

2010

Cosmology

Sponsored by

- . CNRS (Centre National de la Recherche Scientifique)
- . CEA (Commissariat à l'Énergie Atomique)
- . FNRS (Fond National de la Recherche Scientifique)
- . IN2P3 (Institut National de Physique Nucléaire et de Physique des Particules)
- . BSP (Belgian Science Policy)

XLVth Rencontres de Moriond

La Thuile, Aosta Valley, Italy – March 13-20, 2010

2010 Cosmology

© Thê Gioi Publishers, 2010

All rights reserved. This book, or parts thereof, may not be reproduced in any form or by any means, electronic or mechanical, including photocopying, recording or any information storage and retrieval system now known or to be invented, without written permission from the publisher.

Proceedings of the XLVth RENCONTRES DE MORIOND

Cosmology

La Thuile, Aosta Valley Italy

March 13-20, 2010

2010

Cosmology

edited by

Etienne Augé,

Jacques Dumarchez

and

Jean Trân Thanh Vân

The XLVth Rencontres de Moriond
2010 Cosmology

was organized by :

Etienne Augé (IN2P3, Paris)
Jacques Dumarchez (LPNHE, Paris)

with the active collaboration of :

R. Ansari (Orsay),
M. Arnaud (Saclay),
P. Astier (Paris) ,
Ch. Charmousis (Orsay),
F. Combes (Paris),
K. Ganga (Paris),
Y. Giraud-Héraud (Paris),
C. Magneville (Saclay),
S. Maurogordato (Nice),
H. McCracken (Paris)

2010 RENCONTRES DE MORIOND

The XLVth Rencontres de Moriond were held in La Thuile, Valle d'Aosta, Italy.

The first meeting took place at Moriond in the French Alps in 1966. There, experimental as well as theoretical physicists not only shared their scientific preoccupations, but also the household chores. The participants in the first meeting were mainly french physicists interested in electromagnetic interactions. In subsequent years, a session on high energy strong interactions was added.

The main purpose of these meetings is to discuss recent developments in contemporary physics and also to promote effective collaboration between experimentalists and theorists in the field of elementary particle physics. By bringing together a relatively small number of participants, the meeting helps develop better human relations as well as more thorough and detailed discussion of the contributions.

Our wish to develop and to experiment with new channels of communication and dialogue, which was the driving force behind the original Moriond meetings, led us to organize a parallel meeting of biologists on Cell Differentiation (1980) and to create the Moriond Astrophysics Meeting (1981). In the same spirit, we started a new series on Condensed Matter physics in January 1994. Meetings between biologists, astrophysicists, condensed matter physicists and high energy physicists are organized to study how the progress in one field can lead to new developments in the others. We trust that these conferences and lively discussions will lead to new analytical methods and new mathematical languages.

The XLVth Rencontres de Moriond in 2010 comprised three physics sessions:

- March 06 - 13: “Electroweak Interactions and Unified Theories”
- March 13 - 20: “QCD and High Energy Hadronic Interactions”
- March 13 - 20: “Cosmology”

We thank the organizers of the XLVth Rencontres de Moriond:

- A. Abada, J. Conrad, S. Davidson, P. Fayet, J.-M. Frère, P. Hernandez, L. Iconomidou-Fayard, P. Janot, M. Knecht, J. P. Lees, S. Loucatos, F. Montanet, L. Okun, A. Pich, S. Pokorski, D. Wood for the “Electroweak Interactions and Unified Theories” session.
- E. Augé, U. Bassler, E. Berger, S. Bethke, A. Capella, A. Czarnecki, D. Denegri, N. Glover, B. Klima, M. Krawczyk, L. McLerran, B. Pietrzyk, Chung-I Tan, J. Trần Thanh Vân, U. Wiedemann for the “QCD and High Energy Hadronic Interactions” session.
- R. Ansari, M. Arnaud, P. Astier, Ch. Charmousis, F. Combes, J. Dumarchez, K. Ganga, Y. Giraud-Héraud, C. Magneville, S. Maurogordato, H. McCracken for the “Cosmology” session.

and the conference secretariat and technical staff:

V. de Sa-Varanda and C. Bareille, I. Cossin, G. Dreneau, D. Fligiel, N. Ribet, V. Zorica.

We are also grateful to Andrea Righetto, Gioacchino Romani, Erik Agostini and the Planibel Hotel staff who contributed through their hospitality and cooperation to the well-being of the participants, enabling them to work in a relaxed atmosphere.

The Rencontres were sponsored by the Centre National de la Recherche Scientifique, the Institut National de Physique Nucléaire et de Physique des Particules (IN2P3-CNRS), the Commissariat à l’Energie Atomique (DSM and IRFU), the Fonds de la Recherche Scientifique (FRS-FNRS), the Belgium Science Policy and the National Science Foundation. We would like to express our thanks for their encouraging support.

It is our sincere hope that a fruitful exchange and an efficient collaboration between the physicists and the astrophysicists will arise from these Rencontres as from previous ones.

E. Augé, J. Dumarchez and J. Trần Thanh Vân

Contents

Foreword

1. CMB / Polarization

Polarized CMB Foregrounds: What do we know and how bad is it?	C. Dickinson	3
The QUIET experiment	A. Kusaka	7
The QUBIC Experiment: A bolometric interferometer to detect the CMB B-mode polarization	R. Charlassier	11
Instrumental challenges for a future B-mode space instruments	M. Piat	15
On Stokes polarimeters for high precision CMB measurements and mm astronomy measurements	M. Salatino	19
Planck-scale Lorentz invariance violations and CMB polarization data	G. Gubitosi	23
Large-angle anomalies in the microwave background	E. Bunn	27
Desperately seeking non-gaussianity in the cosmic microwave background	G. Rossi	35
Probing non-gaussianities on large scales in WMAP5 and WMAP7 data using surrogates	C. Räth	39
Impact of a causal primordial magnetic field on the Sachs Wolfe effect	C. Bonvin	43
Statistical anisotropy in CMB maps	A. Lewis	47
Λ CDM and the WMAP power spectrum beam profile sensitivity	T. Shanks	53
The Small Scale Angular Anisotropy at 148 GHz as seen by the Atacama Cosmology Telescope	C. Hernandez-Monteagudo	59
Planck status	F. Pajot	65
B-mode CMB spectrum estimation using a pure pseudo cross-spectrum approach	M. Tristram	69
Preparation of the CMB Planck data analysis: estimation of the contamination due to the polarized Galactic emissions	L. Fauvet	73
Component separation in CMB observations	J. Delabrouille	77

2. Clusters / SZ

Forecasting Cosmological Constraints from future X-ray cluster surveys	B. Sartoris	83
Spectroscopic follow-up of the South Pole Telescope galaxy clusters	G. Bazin	87
Beyond the standard lore of the SZE: opportunities offered from future space born mm and sub-mm experiments	S. Colafrancesco	91
Observation model of a Planck-like cluster catalogue	J. Démocles	95
Galaxy Clusters at the Planck time	E. Pointecouteau	99
Galaxy clusters number counts with Sunyaev-Zel'dovich effect and scaling laws evolution	P. Delsart	103
Mass estimates in intermediate redshifts clusters of galaxies	G. Foex	107
Non-thermal emission from galaxy clusters: a Pandora's vase for astrophysics	C. Ferrari	111
Statistical investigation of the non-thermal emission of galaxy clusters	J. Lanoux	119
Studying the Local Group within the CLUES project	S. Gottlöber	123
Merger events with galaxy-gas separation in the hot galaxy cluster A2163	H. Bourdin	127

3. Dark Matter

Dark Matter constraints with the first year of FERMI-LAT data	E. Nuss	133
Excited dark matter versus PAMELA/Fermi	J. Cline	141
Direct searches for dark matter in CMS	B. Clerbaux	145
Searches for Signatures of Dark Matter with the IceCube Neutrino Telescope	E. Strahler	149
Results from the Search for Ultra-High Energy Neutrinos with ANITA-II	A. Vieregg	153
Relativistic trajectories of celestial bodies as a tool to constrain f(R) theories of gravity and dark matter concentration near the Galactic Center	A. Zakharov	157
The large-scale clustering of massive dark matter haloes	V. Desjacques	161
Neutrinos in the intergalactic medium	M. Viel	165
Weighing Neutrinos with the Largest Photometric Redshift Survey: MegaZ DR7	S. Thomas	169
Minimally Parametric Constraints on the Primordial Power Spectrum from Lyman-alpha	S. Bird	173
Is the 2MASS dipole convergent?	M. Chodorowski	177
The CAST experiment: status and perspectives	T. Dafni	181

4. Dark Energy Probes

Type Ia supernovae and Cosmology	N. Regnault	187
SN Ia photometric studies in SNLS	N. Palanque-Delabrouille	195
Gravitational lensing in the Supernova Legacy Survey	T. Kronborg	199
Recent results from the SNfactory experiment	E. Gangler	203
Gravitational lensing and parameter extraction from SNe catalogues	V. Marra	207
Investigating The Uncertainty On The BAO Scale Measured From Future Photometric And Spectroscopic Surveys	A. Abate	211
Constraining Dark Energy with BOSS	N. Busca	215
Characterizing the Universe	A. Blanchard	219
Real-Time Cosmology with Cosmic Parallax and Redshift Drift	M. Quartin	223

5. Theory

Models of Dark energy	E. Copeland	231
Primordial gravitational waves and the local B-polarization of the CMB	J. Garcia-Bellido	239
Charge, domain walls and Dark Energy	J. Pearson	245
Testing generic predictions of dark energy	M. Mortonson	249
The string revolver: how rotation of background galaxies could be a smoking gun for the existence of cosmic strings	D. Thomas	253
Gravitational waves from cosmological phase transitions	C. Caprini	257
F-term uplifted racetrack inflation	M. Badziak	265
Initial conditions in hybrid inflation: exploration by MCMC technique	S. Clesse	269
Conformal Invariance, Dynamical Dark Energy and the CMB	E. Mottola	275

6. Herschel

Modeling Galaxy Clustering in the Cosmic Infrared Background	A. Pénin	285
--	----------	-----

7. Testing the Cosmological Model

No Evidence for Dark Energy Dynamics from a Global Analysis of Cosmological Data	P. Serra	293
The Gamma-Ray View of the Extragalactic Background Light	J. Finke	299
Constraints on the linear fluctuation growth rate from future surveys	C. Di Porto	303

8. Reionization / Radio

Efficiently Simulating the High-Redshift 21-cm Signal with 21cmFAST	A. Mesinger	309
Fast large volume simulations of the 21 cm signal from the reionization and pre-reionization epochs	M. Santos	315
Cosmological observations in the radio domain: the contribution of extragalactic sources	A. Tartari	321
Cosmic structure formation at high redshift	I. Iliev	325
Distribution of Maximal Luminosity of Galaxies in the Sloan Digital Sky Survey	E. Regos	329

9. Posters

A multifrequency method based on the Matched Multifilter for the detection of point sources in CMB maps	L. Fernando Lanz	337
Planck-HFI time ordered data analysis	D. Girard	339
Clustering of Radio Galaxies	W. Godlowski	341
Void Merging Trees in Hierarchical Clustering	E. Tigrak	343
SuperNova Legacy Survey 5-years sample analysis : a new differential photometry technique	N. Fourmanoit	345
Dark energy accretion onto black holes	V. Dokuchaev	347
Measuring unified DM and DE properties with 3D cosmic shear	S. Camera	349
Multi-scalar field cosmology from SFT: Exactly solvable approximation	A. Koshelev	351
On leptogenesis and lepton asymmetry effects in the early Universe	D. Kirilova	355

1. CMB / Polarization

Polarized CMB Foregrounds: What do we know and how bad is it?

Clive Dickinson

*Jodrell Bank Centre for Astrophysics, School of Physics & Astronomy,
University of Manchester, Oxford Rd, Manchester, M13 9PL, U.K.*



Polarized foregrounds are going to be a serious challenge for detecting CMB cosmological B-modes. Both diffuse Galactic emission and extragalactic sources contribute significantly to the power spectrum on large angular scales. At low frequencies, Galactic synchrotron emission will dominate with fractional polarization $\sim 20 - 40\%$ at high latitudes while radio sources can contribute significantly even on large ($\sim 1^\circ$) angular scales. Nevertheless, simulations suggest that a detection at the level of $r = 0.001$ might be achievable if the foregrounds are not too complex.

1 CMB foregrounds overview

For high sensitivity measurements, once systematics are made negligible, component separation to remove foregrounds represents the ultimate limit to the precision in which the CMB, and therefore cosmological parameters, can be measured. Diffuse Galactic radiation consists of at least 3 components including synchrotron emission produced by relativistic electrons spiralling in the Galactic magnetic field, free-free emission from electrons accelerated by ionized gas and thermal dust emission due to black-body radiation from dust grains at temperatures of a few tens of degrees Kelvin. Other mechanisms are thought to contribute at some level. In particular, electro-dipole emission from ultra-small rapidly spinning dust grains may be a significant contributor at frequencies < 100 GHz. Fortunately, at least for cosmologists, the CMB anisotropies in total-intensity are larger than the Galactic emission, over a significant fraction of the sky and over a few decades in frequency range i.e. $\sim 30 - 150$ GHz. Extragalactic sources, which are typically point-like relative to the experimental beam, are a major foreground on small angular scales, typically $< 1^\circ$ or $\ell > 200$. Their removal is usually achieved by masking/fitting the brightest sources, and making a statistical correction of the residual sources in the power spectrum.

The situation for polarization is different. Both Galactic and extragalactic radiation are significantly polarized, at the few to tens of a per cent level. Although the CMB E-mode fluctuations are at the 10% level, the B-mode fluctuations are at least an order of magnitude lower than this, and possibly much smaller. It is therefore quite clear that CMB polarization measurements will be seriously affected by foregrounds. In this article, I summarise some new results for polarization of diffuse Galactic emission and extragalactic sources.

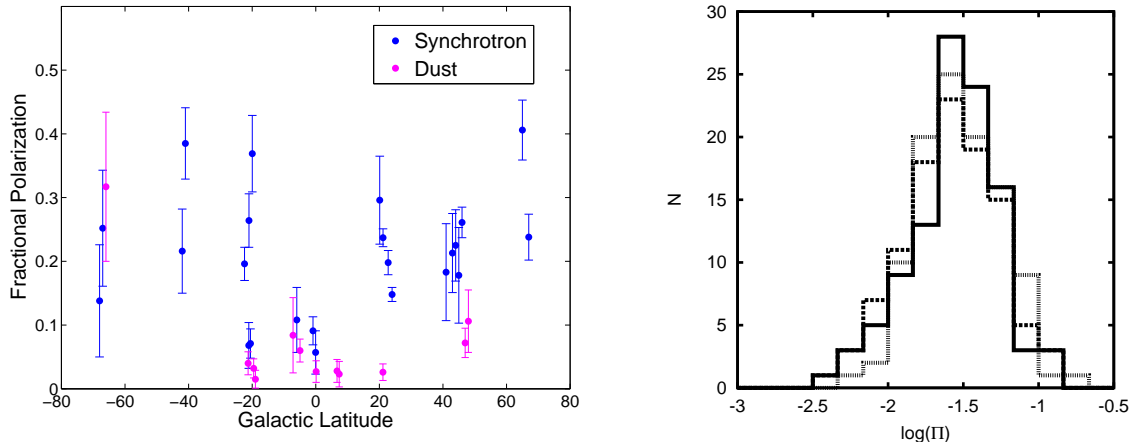


Figure 1: *Left*: Fractional polarization of diffuse foregrounds as a function of Galactic latitude. *Right*: Fractional polarization of radio sources.

2 Template analysis of WMAP data in polarization

Very little is known about the details of diffuse polarized foregrounds. Kogut et al.⁹ studied the global properties of the synchrotron and dust polarized emission, assuming the synchrotron polarization angle given by WMAP K-band and dust polarization angle given by a model map of starlight absorption. More recently, Macellari et al.¹⁰ used a template cross-correlation analysis by fitting total-intensity templates to the polarization data directly. The analysis amounts to fitting total-intensity maps to polarized intensity ($P = \sqrt{Q^2 + U^2}$) at a resolution of $N_{side} = 32$, by minimizing the χ^2 . A statistical noise bias was subtracted from P and correlations between Q and U were taken into account, by using the WMAP noise covariance matrix supplied by the WMAP team, degraded to $N_{side} = 32$. Pixel-pixel correlations were not taken into account, but are typically small ($\sim 1\%$). The main limitation of this method is that if the polarization angles of individual components are not the same, cross-terms appear that can bias the result. However, we do not expect the angles to be significantly different on large angular scales.

The left panel of Fig. 1 shows the fractional polarizations for the synchrotron- and dust-correlated components at K-band (23 GHz) as a function of Galactic latitude. The synchrotron polarization fraction is low ($\sim 5\%$) at low Galactic latitudes, as expected from depolarization along the line-of-sight. At high latitudes, the synchrotron fractional polarization increases to $\sim 15 - 40\%$; at $|b| > 20^\circ$ the average is 19%. We detect a dust-correlated signal, with an average polarization fraction of $2.9 \pm 0.6\%$. This is consistent with the expectation for spinning dust, although magneto-dipole emission cannot be ruled out. The H α -correlated signal, expected to be due to free-free emission, has little or no polarization, with an all-sky average of $0.6 \pm 0.7\%$.

3 Contribution of polarized extragalactic sources

Extragalactic sources are known to exhibit polarization. At frequencies > 100 GHz, there is very little information at all, except to note that the polarization must be relatively small for most galaxies (e.g. Seiffert et al.¹²). At frequencies < 100 GHz, radio surveys such as the NVSS at 1.4 GHz (Condon et al.³) have accurately characterised source counts down to a few mJy. However, the polarization properties are still not well known, except for the brightest sources. Recently, Jackson et al.⁸ observed bright (> 1 Jy) sources detected by WMAP (Hinshaw et al.⁷) with the Very Large Array (VLA) in polarization at 8.4, 22 and 43 GHz. The right panel of Fig. 1 shows the distribution of polarization fractions, Π , for sources detected at all

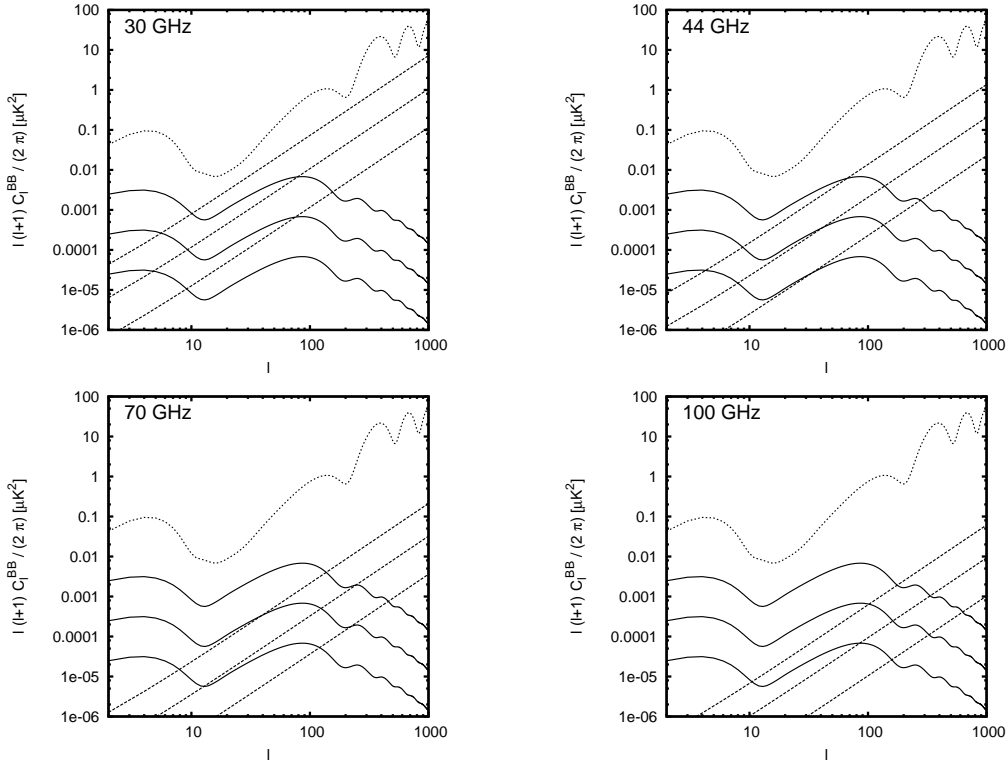


Figure 2: Projected power spectra of radio sources at 30, 44, 70 and 100 GHz. The dotted line shows the theoretical CMB E-mode spectrum while the solid lines are the CMB B-mode spectra for $r = 0.1, 0.01, 0.001$. The dashed lines show the power spectra of radio sources for different intensity flux density cut-offs, $S_{\text{cut}} = 1, 0.1, 0.01$ Jy.

3 VLA frequencies. The distributions at 8.4, 22 and 43 GHz are almost identical and can be approximated by a Gaussian distribution in $\log(\Pi)$. The median value is $\simeq 2\%$ with an average of $\simeq 3.5\%$. This allows us to estimate the contribution of point sources to the CMB power spectrum in polarization. Fig. 2 shows the source power spectra at 4 frequencies and for 3 different flux cut-off values. We have assumed no clustering of radio sources, and that the spectra and polarization fractions do not vary at lower flux densities. It is clear that, even at large angular scales ($\sim 1^\circ$), extragalactic sources will need to be removed if one is to try to detect $r \sim 0.001$. In particular, at low frequencies the power from radio sources will dominate B-modes at $r = 0.001$ even when a large number of sources have been removed. To measure CMB B-modes at this level, accurate statistical corrections in the power spectrum will need to be applied.

4 What tensor-to-scalar ratio can be achieved?

Without detailed knowledge of polarized foregrounds, it is difficult to calculate the lowest value of the tensor-to-scalar ratio, r , that might be achieved with a future CMB mission (e.g. CMBpol/EPIC, Bpol). However, using simple models, normalized to the approximate levels that we see in current experiments, we can estimate the ultimate r -value, assuming the foregrounds are relatively simple. It should be remembered that component separation is likely to set the limit on the lowest r -value that can be achieved.

As part of a white paper in preparation for the U.S. 2010 decadal review and the CMBpol design study for a future CMB polarisation satellite, Dunkley et al.⁵ investigated the issue of foreground removal. Using the Planck Sky Model, a simulation of diffuse foregrounds was produced at a range of frequencies, as proposed for a particular configuration of the EPIC

Table 1: Forecasted 1σ uncertainties on the tensor-to-scalar ratio, r , for a fiducial value $r = 0.01$.

Method	Description	$\ell < 15$	$\ell < 150$
Fisher	Assumed 10% residual foregrounds	0.014	0.00052
Parametric	Power-law indices	0.003	—
Blind	SMICA	—	0.00055

satellite. In polarization, this consisted of synchrotron and thermal dust components, based on the model of Miville-Deschénes et al.¹¹. White noise was added, in accordance to the EPIC design. No extragalactic sources were added and CMB lensing was not considered.

A number of techniques were used to estimate the sensitivity to r that could be achieved, including a Fisher-matrix calculation, parametric fitting with various assumptions (Eriksen et al.⁶), and a blind component separation method (Delabrouille et al.⁴). Two ℓ ranges were considered, to take into account that lensing of E-modes into B-modes will be a major challenge for $\ell > 15$. The results are summarised in Table 1. The results suggest that $r \sim 0.01$ should be relatively easily achievable, so long as the foregrounds are not significantly more complex than we expect. If we assume that lensing B-modes can be removed, then $r < 0.001$ may be attainable with ultra-sensitive instruments; see also Betoule et al.². However, foregrounds (including lensing) are likely to make detecting $r < 10^{-4}$ impossible. It is clear, however, that accurate data over the frequency range of a few GHz to ~ 1 THz is needed to characterize and understand foregrounds so that they can be accurately removed from sensitive CMB data.

Acknowledgments

CD acknowledges an STFC Advanced Fellowship and an ERC grant under the FP7.

References

1. Battye, R. A., Browne, I. W. A., Peel, M. W., Jackson, N. J., Dickinson, C. 2009, MNRAS, submitted (arXiv:1003.5846).
2. Betoule, M., Pierpaoli, E., Delabrouille, J., Le Jeune, M., & Cardoso, J.-F. 2009, A&A, 503, 691
3. Condon, J. J., Cotton, W. D., Greisen, E. W., Yin, Q. F., Perley, R. A., Taylor, G. B., & Broderick, J. J. 1998, AJ, 115, 1693.
4. Delabrouille, J., Cardoso, J.-F., & Patanchon, G. 2003, MNRAS, 346, 1089
5. Dunkley, J., et al. 2009, American Institute of Physics Conference Series, 1141, 222
6. Eriksen, H. K., Jewell, J. B., Dickinson, C., Banday, A. J., Górski, K. M., & Lawrence, C. R. 2008, ApJ, 676, 10
7. Hinshaw, G., et al. 2009, ApJS, 180, 225.
8. Jackson, N., Browne, I. W. A., Battye, R. A., Gabuzda, D., & Taylor, A. C. 2010, MNRAS, 401, 1388.
9. Kogut, A., et al. 2007, ApJ, 665, 355
10. Macellari, N., Piepaoli, E., Dickinson, C., Vaillancourt, J.. 2010, MNRAS, submitted.
11. Miville-Deschénes, M.-A., Ysard, N., Lavabre, A., Ponthieu, N., Macías-Pérez, J. F., Aumont, J., & Bernard, J. P. 2008, A&A, 490, 1093
12. Seiffert, M., Borys, C., Scott, D., & Halpern, M. 2007, MNRAS, 374, 409

The QUIET experiment

A. Kusaka for the QUIET Collaboration

*Enrico Fermi Institute and Kavli Institute for Cosmological Physics, University of Chicago,
Chicago, Illinois 60637 U.S.A.*

The Q/U Imaging ExperimenT (QUIET) is a ground-based radiometer array designed to measure the polarization of the cosmic microwave background (CMB). In Phase I, it measures the CMB polarization at angular scales of $25 \lesssim \ell \lesssim 1000$ in the frequencies 95 GHz and 44 GHz. QUIET employs a unique radiometer technology, ‘radiometer on chip,’ which integrates monolithic microwave integrated circuits (MMIC) of high electron mobility transistor (HEMT) amplifiers into a receiver module. This technology enables us to assemble the world’s largest polarimeter array using the HEMT amplifier devices. In these proceedings, we review the QUIET instrument and report on the status of Phase I, observing since October 2008. We also mention prospects for QUIET Phase II.

1 Introduction

The anisotropy of the CMB polarization has yet to be fully explored. It can be decomposed into a curl-free component, or E-modes, and divergence-free component, or B-modes. The E-modes, since their first detection¹, have been measured and characterized by various experiments and are consistent with the predictions of the standard Λ CDM model. The B-modes, on the other hand, remain entirely elusive. While the E-modes are sensitive to the scalar density fluctuations in the early Universe, the B-modes would be evidence primordial gravitational waves, which are sourced only by the inflation. The detection of B-modes in CMB polarization is not only the smoking gun of inflation, but also a unique opportunity to measure the energy scale of the inflationary potential^{2,3}.

QUIET Phase I and Phase II are among current and next generation experiments aiming for the detection of the inflationary B-modes. Deployed on the Chajnantor plateau in Chile, QUIET Phase-I started its observation with its 44 GHz receiver in October 2008. After nine months of successful observation, we deployed the 95 GHz receiver replacing the 44 GHz one and the observation resumed in August 2009. Among numerous CMB experiments, QUIET stands out with its unique receiver technology. Here we describe the instrumentation, the site, and observation strategy, as well as the current status of the analysis of 44 GHz receiver data.

2 Instrument

We measure the CMB polarization power spectra using receiver arrays at multiple frequencies. In Phase I, the instrument consists of two arrays at 95 GHz and 44 GHz with 90 and 19 receiver elements, respectively. The array is coupled to the optics comprising platelet-array feedhorns⁶ and a 1.4 m Mizuguchi-Dragone reflective telescope^{7,8}. The optics achieves the beam size of 12 arcmin (27 arcmin) in full-width-half-maximum at 95 GHz (44 GHz), defining the sensitive

Table 1: QUIET Phase-I experiment summary.

Frequencies (GHz)	95 / 44
Angular resolutions (arcmin)	12 / 27 in full-width-half-maximum
Number of receiver elements	90 / 19
Array sensitivity ($\mu\text{K}\sqrt{\text{s}}$)	57 / 64
Detector type	HEMT
Polarization modulation	Phaseswitch (4 kHz and 50 Hz), sky and boresight rotations
Telescope optics	Mizuguchi-Dragone
Field centers (J2000 RA,DEC)	(181°, -39°), (78°, -39°), (12°, -48°), (341°, -36°)
Field size	15° × 15° each
Observation	August 2009~ / October 2008~June 2009

angular scale of $\ell \lesssim 1000$ ($\ell \lesssim 400$). Table 1 summarizes the Phase-I instrument and observing.

Large focal-plane arrays are achieved by a breakthrough in millimeter-wave circuit technology and packaging at JPL⁴, which miniaturizes the correlation polarimeter and enables mass production. Each array element is based on a QUIET module: a pseudo-correlation receiver comprising HEMT low-noise amplifiers, phase shifters, detector diodes, and passive components (Fig. 1). The 95 GHz (44 GHz) module dimensions are 3.2 cm × 2.9 cm (5.1 cm × 5.1 cm). The polarization properties of the CMB can be expressed by two linear polarization (Q and U) Stokes parameters. Each module measures both of the linear polarization parameters simultaneously when its inputs are coupled through the septum polarizer^a, which splits the incoming radiation into left- and right-circular polarizations⁵. Pseudo-correlation technique provides not only sensitivity to Q and U polarizations but also makes the polarimeter immune to gain fluctuations and unpolarized signals. Phase modulation occurs at 4 kHz, which is faster than the $1/f$ knee frequency of the atmosphere, amplifiers, and diode detectors. In addition to the 4 kHz phase modulation occurring in one of the amplifier chains, the phase switch in the second chain is also modulated at lower frequency of 50 Hz. This ‘double demodulation’ cancels out spurious instrumental polarization that can arise if there are transmission differences between the two phase states in either of two phase shifters.

The performances of the QUIET modules are fully calibrated, characterized and verified in the field through observations in Phase I. The mean sensitivity of a module is $0.5 \text{ mK}\sqrt{\text{s}}$ ($0.25 \text{ mK}\sqrt{\text{s}}$) for 95 GHz (44 GHz), making up the combined array sensitivity of $57 \mu\text{K}\sqrt{\text{s}}$ ($64 \mu\text{K}\sqrt{\text{s}}$). The achieved $1/f$ knee frequencies are typically well below the telescope scan frequency of 0.05–0.1 Hz, thus minimizing the sensitivity degradation due to the $1/f$ noise.

3 Site and Observation

QUIET is located at 5080-m altitude on the Chajnantor plateau in Chile using the platform of CBI⁹. Chajnantor offers exceptional conditions for radio astronomy because of its high altitude and low water vapor¹⁰. Under median conditions, the zenith sky brightness at 95 GHz (44 GHz) is 5–6 K (9 K).

We started Phase-I observations in October 2008 with the 44-GHz receiver array. The observing season finished in June 2009 after collecting over 3500 hours of data. After the deployment of the 95-GHz receiver array replacing the 44-GHz one, observing resumed in August 2009 and continues. We have already collected more than 3000 hours of 95-GHz data by the end of March 2010 and expect to collect an additional 4500 hours by the end of 2010.

^aIn Phase I, six (two) out of 90 (19) modules of the 95-GHz (44-GHz) array are coupled to assemblies of ortho-mode transducers and magic tees, instead of to the septum polarizers, providing sensitivity to the temperature anisotropy of the CMB.



Figure 1: A 95-GHz module with the radiometric components integrated (left) and the 90-element 95-GHz array under assembly (right).

QUIET observes the four CMB patches listed in Table 1. Each scan is performed with a half amplitude of 7.5° and repointed when the sky has drifted by 15° , making up deep coverages of $\simeq 15^\circ \times 15^\circ$ on each patch. The observing scan is a periodical scan in azimuth with the speed of $\simeq 6^\circ/\text{s}$, with a fixed elevation and rotation angle about the optical axis. We use two means to achieve parallactic-angle coverage: sky rotation from diurnal sky motion and weekly rotation about the optical axis (boresight rotation).

About 10% of our observing time is dedicated to calibrations. Calibrations of polarization angle, spurious polarization due to leakage from I (intensity) to Q/U, and the responsivity are of importance. We calibrate these by combining daily and/or weekly observations of astronomical sources such as the Moon, Jupiter, and Taurus A; and the ‘skydip’ (scanning the telescope up and down in elevation), which is performed once per 90 minutes. Supplemented by measurements using a broad-band polarized noise source and a rotating wire-grid, we achieve the required calibration precision for Phase I. We also spend $\sim 10\%$ of observation time scanning galactic plane for the purposes of calibration and galactic science.

4 Analysis

Our two independent analysis pipelines employ different and complementary techniques: one uses pseudo- C_ℓ estimators^{11,12} and the other is based on maximum-likelihood map-making and power-spectrum estimation^{13,14}. It is critical to cut data contaminated by fluctuations of environmental or instrumental origin. Such selection criteria are under development using results obtained from the null-test suite described below.

Our policy is to not look at polarization power spectra until the criteria are defined and the data pass a variety of predefined null tests, each designed to validate our understanding of a particular possible systematic effect. In each test, the data are split into two subsets; CMB maps (\mathbf{m}_1 and \mathbf{m}_2) are made from each half, and we compute the power spectrum of the difference map ($\mathbf{m}_{\text{diff}} \equiv [\mathbf{m}_1 - \mathbf{m}_2]/2$), to check consistency with zero signal.

One example is to split the data into those obtained from Q-sensitive channels and U-sensitive ones. Excess power should arise in this null spectrum if there were instrumental systematic effects that show up differently in those channels. A preliminary result for this null test using 44 GHz data is shown in the left panel of Fig. 2, where the power spectra are consistent with zero signal as expected. Each division has 16 bins, 8 bins in E-mode and B-mode power. A test suite of 32 divisions makes a total of 512 points that should be consistent with zero. The right panel of Fig. 2 shows the distribution of the χ^2 values of those points for one of our CMB patches. The data distribution is consistent with that from Monte Carlo simulations, validating our selection criteria and noise model.

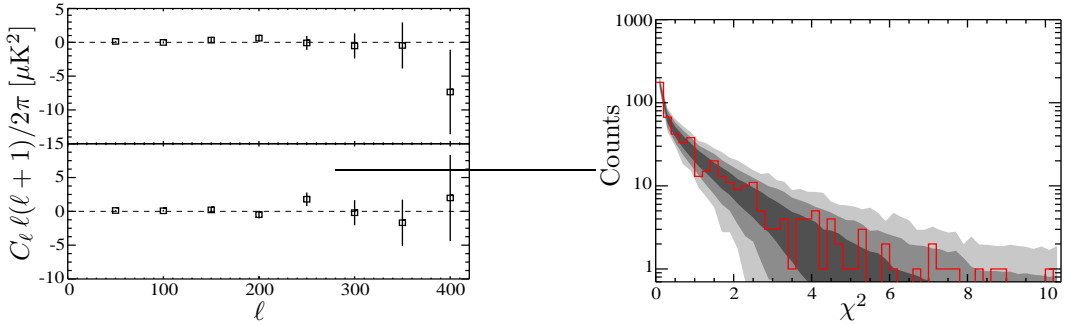


Figure 2: The left panel shows a preliminary null power spectrum obtained by differencing data sets from Q-sensitive and U-sensitive diodes. The right panel is the χ^2 distribution of the null power spectra of 32 divisions, where the red histogram and the shaded region correspond respectively to the data and expectation from Monte Carlo simulation. Both are only for one of the four CMB patches we observe and from the 44 GHz receiver data.

5 Future Prospects: Phase-II

Phase II will consist of three separate telescopes with four cryostats: three will house identical 95-GHz arrays of 499 elements and one houses an array consisting of 61 elements of 44 GHz and 18 elements of 30 GHz polarimeters for control against foreground contamination due to synchrotron radiation from our galaxy. The sensitivity of Phase II allows us to possibly detect B-modes from primordial gravitational waves, or to put a stringent limit on the tensor-to-scalar ratio r of $\simeq 0.01$.

Acknowledgments

Support for the QUIET instrument and operations comes through the NSF cooperative agreement AST-0506648. Support also provided by AST-04-49809, DE-AC02-05CH11231, JSPS KAKENHI (A) 20244041, and by the Strategic Alliance for the Implementation of New Technologies (SAINT). Some work presented was performed on the Joint Fermilab–KICP Supercomputing Cluster, supported by grants from Fermilab, the Kavli Institute for Cosmological Physics, and the University of Chicago. We are particularly indebted to the engineers who maintained and operated the telescope: J. Cortes, C. Jara, F. Munoz, and C. Verdugo.

References

1. J. M. Kovac *et al.*, *Nature*, 420, 772–787, (2002).
2. U. Seljak and M. Zaldarriaga, *Phys. Rev. Lett.*, 78, 2054 (1997).
3. M. Kamionkowski, S. Kosowsky, and A. Stebbins, *Phys. Rev. Lett.*, 78, 2058 (1997).
4. T. Gaier *et al.*, *New Astronomy Rev.*, 47, 1167–1171 (2003).
5. J. Bornemann and V. A. Labay, *IEEE Trans. MTT*, 43, 95 (1995).
6. J. Gunderson and E. Wollack, *Journal of Physics: Conference Series*, **155** 012005 (2009).
7. Y. Mizugutchi, M. Akagawa and H. Yokoi, *IEEE Antennas and Propagation Society International Symposium*, Vol. 14, pp. 2-5 (1976).
8. C. Dragone, *Bell Syst. Tech. J.*, vol. 57, pp. 2663–2684 (1978).
9. A. C. S. Readhead *et al.*, *Astrophys. J.*, 609:498–512 (2004).
10. S. Radford, *ASP Conf. Ser.* 266, 148 (2002).
11. G. Chon *et al.*, *MNRAS*, 350, 914–926 (2004).
12. F. K. Hansen and K. M. Górski, *MNRAS*, 343, 559–584 (2003).
13. M. A. J. Ashdown *et al.*, *A&A*, 467, 761 (2007).
14. H. K. Eriksen *et al.*, *ApJ*, 676, 10 (2008).

The QUBIC Experiment

A bolometric interferometer to detect the CMB B-mode polarization

Romain CHARLASSIER¹ on behalf of the QUBIC collaboration

¹*Laboratoire APC – Université Paris Diderot-Paris 7 – CNRS*

QUBIC is a dedicated CMB B-mode experiment based on a novel instrumental technique, bolometric interferometry, which could combine some very specific advantages of interferometry in terms of systematics control and the advantages of bolometric techniques in terms of sensitivity. We introduce bolometric interferometry key concepts and give the specifications of the QUBIC instrument. A first module is planned to be installed at the Concordia station (Antarctica) in 2012; the final instrument will have the sensitivity to detect a tensor to scalar ratio of 0.01 with one effective year of data. QUBIC is a collaboration between France, Ireland, Italy, U.K. and U.S.A, which results from the merging of the MBI and BRAIN projects.

1 Context

1.1 Detecting CMB B-mode

Measuring the Cosmic Microwave Background (CMB) B-mode polarisation appears nowadays as the most powerful way to place constraints on inflationary theories. The detection of such a weak signal is however a tremendous experimental challenge. Future experiments will need, in addition to a high statistical sensitivity, a reliable foreground removal and an unprecedented control of systematic effects¹².

1.2 The path towards bolometric interferometry

Most future B-mode experiments (EBEX⁹, PLANCK¹⁰, SPIDER¹¹, PolarBear) will have a similar imaging concept, sharing the same kind of instrumental systematic errors. Another kind of instrumental concept has proven successful in the past : the DASI⁷ and CBI⁸ interferometers, which were the first experiments to detect E-mode polarization of the CMB. Unfortunately, the sensitivity of this kind of instrument (heterodyne interferometer) is intrinsically limited because they rely on coherent detection : the electromagnetic signals collected by the horns are amplified (by HEMTs) and mixed to lower frequencies before being correlated by pairs. Another strong limitation is the cost of the correlator (which does not grow linearly with the number of horns N since $N(N - 1)/2$ correlations must be done).

Bolometric interferometry offers a promising alternative for detecting B-modes, which combines some very specific advantages of interferometry in terms of systematics control and those of bolometric techniques in terms of sensitivity.

2 Bolometric Interferometry : key concepts

2.1 Fizeau combination

The QUBIC instrument concept is represented on figure 1. A bolometric interferometer can be seen as a millimetric version of the first interferometer ever dedicated to astronomy, the Fizeau one, which was obtained by placing a mask with two holes in front of a telescope; the millimetric sky is directly observed in our case through an array of back-to-back horns, acting as diffractive pupils. Interference patterns are formed in the focal plane of the beam combiner (which is just a telescope). This focal plane is filled with an array of bolometers, which are sensitive to polarisation.

A rotating half-wave plate (HWP) is located after the array of reemitting horns in order to modulate the polarisation (in the same way as for imaging experiments). It can be shown that the power measured by a bolometer located at \vec{d}_p , is:

$$R_{\vec{d}_p}(t) = S_I(\vec{d}_p) \pm \cos(4\omega t) S_Q(\vec{d}_p) \pm \sin(4\omega t) S_U(\vec{d}_p) \quad (1)$$

where ω is the HWP angular velocity and where S_X is defined by:

$$S_X(\vec{d}_p) = \int X(\vec{n}) |A_s(\vec{d}_p - \vec{n})|^2 d\vec{n} \quad (2)$$

where $X = \{I, Q, U\}$ stands for the Stokes parameters. This quantity S_X is usually called the *dirty image* in interferometry : this is an image of the sky filtered by the *baselines* (which are the vectors defined by every pair of horns, in wavelength units). Equivalently, this is an image of the sky observed through the *synthesized beam* $A_s(\vec{d}_p - \vec{n})$, which is approximately given by the discrete Fourier transform of the horn distribution. This beam has much more structure than a Gaussian function (it is for instance the product of a Gaussian by a sinc function in the case of a square-grid array of horns having Gaussian primary beams).

The dirty image can equivalently be written as a linear combination of the *visibilities*. These are the standard observables in traditionnal radio-interferometry : the Fourier transform of the sky field observed through the primary beam. The CMB power spectra are roughly given by the variance of these visibilities in the flat sky approximations.

We therefore see that there are two ways to deal with the data measured by a bolometric interferometer: one can make maps of the sky observed through the synthesized beam (the data analysis is then very close that of an imager) or one can invert the linear system instantaneously and store the visibility measurements (the data analysis is then very close that a heterodyne CMB interferometer). We are studying which way is better.

2.2 Sensitivity

We have shown^{1,2} that the sensitivity of a bolometric interferometer is roughly equivalent to that of an imager having the same number of horns, provided that the horn distribution presents a high degree of redundancy: the average number of redundant baselines should scale as the number of horns. This condition would be satisfied by the QUBIC compact square-grid array.

The question of bandwidth often used to be raised about our concept by specialists in radio-interferometry; indeed, if the raw sensitivity of detectors grows as the square root of the bandwidth, there is a secondary effect, known as *bandwidth smearing* which can largely degrade the global sensitivity of an interferometer. However we have shown³ that this sensitivity loss is very acceptable in the QUBIC case (about a factor 1.6 loss for 25% bandwidth).

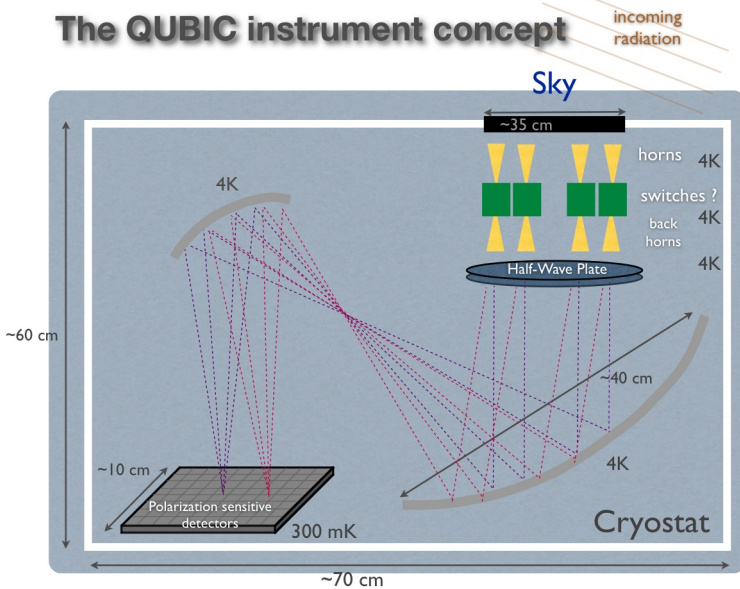


Figure 1: The QUBIC instrument concept is a millimetric Fizeau interferometer with image-plane beam combination (see text).

2.3 Self-calibration

The high degree of redundancy of the QUBIC horn array enables a powerful self-calibration procedure. The main idea is to take advantage of the fact that in an ideal instrument, redundant visibilities (defined by redundant baselines) should exactly equal each other, while in a real experiment, they will slightly differ because of systematic errors. These small differences can be used to calibrate the gains, phases and polarization couplings of each channel (these quantities are the sources of instrumental errors when mis-estimated). We emphasize the fact that this self-calibration procedure is very different from the usual calibration used in imaging experiments that must rely on models of the calibration source.

The use of redundant baselines for self-calibration is a known but rather uncommon method in radio-interferometry⁶. Traditionally, radio-interferometers aim at achieving the maximal angular resolution; with a fixed number of antennas, it is usually best to arrange them to optimize the sampling in Fourier space, rather than to maximize redundancy.

In our case, we will need a self-calibration period during which we will measure separately the $N(N - 1)/2$ visibilities : this would be possible thanks to polarized switches inserted between each back-to-back horn pair.

Details on this self-calibration procedure will be given in an article in preparation.

3 The QUBIC collaboration

The MBI⁴ and BRAIN⁵ collaborations, which were both involved in bolometric interferometry development, decided to join their efforts in 2008. The BRAIN collaboration has already launched three site testing (atmosphere, logistics) pathfinder campaigns at Dôme C during the Antarctic summers 2006, 2007 and 2009. The MBI collaboration has built a four horn prototype interferometer, MBI-4, and taken data in 2008 and 2009. Fringes have been observed, that demonstrate bolometric interferometry with Fizeau combination. QUBIC is now a worldwide collaboration between France (APC Paris, CESR Toulouse, CSNSM Orsay, IAS Orsay), Ireland (Maynooth University), Italy (Università di Roma La Sapienza, Università di Milano Bicocca),

United Kingdom (University of Manchester) and USA (University of Wisconsin, Brown University, Richmond University).

3.1 The Dôme C site

We plan to install the QUBIC instrument in the French/Italian Antarctica Concordia Station located at the Dôme C site (3233 m altitude). This site offers many advantages for millimetric astronomy : a very low brightness temperature of its atmosphere (around 14 K) and excellent transmission due to its very low precipitable water vapor level, its exceptional atmospheric stability within the polar vortex, and a low sun set on the horizon. These favorable experimental conditions are furthermore available most of the year.

3.2 Instrumental R&D

Important instrumental developments are going on within the QUBIC collaboration regarding the instrument's key components.

Detectors. Our collaborators at APC are currently developing filled TES arrays (which will be combined with a polarized grid), while our collaborators at Università di Roma La Sapienza are developing KIDs array.

HWP & switches. Our collaborators at the University of Manchester are now developing saphire and metal-mesh achromatic half-wave plates. They are also taking charge of the development of polarized switches in wave guide (which are required for a self-calibration procedure).

Combiner. Our collaborators at Maynooth University and at Università di Milano Bicocca are designing the fast off-axis telescope which carries out the beam combination.

3.3 Instrument specifications

A possible configuration of the QUBIC instrument would be as follows: 2x3 modules of 144/256/512 back-to-back horns in a compact square array at respectively 90/150/220 GHz (25% bandwidth). The focal plane of each module \simeq 900 Transition Edge Sensors. The primary beams would have a FWHM of 14° . The cryogenics would involve a 4K pulse-tube cooler for each module and a 100-300 mK dilution unit for the focal plane. The multipole range would be approximately $25 \leq \ell \leq 150$. Such an instrument would allow us to reach $r \sim 0.01$ in one year of continuous operation at Dôme C. The QUBIC collaboration intends to deploy a first module in 2011/2012. More details and references can be found at www.qubic.org.

References

1. Charlassier, R. et al., 2009, A&A v497, p963 [arXiv:0806.0380](https://arxiv.org/abs/0806.0380).
2. Hamilton, J.-Ch. et al. 2008, A&A v491, p923 [arXiv:0807.0438](https://arxiv.org/abs/0807.0438).
3. Charlassier, R. et al. 2010, A&A 514, A37, [arXiv:0910.1864](https://arxiv.org/abs/0910.1864).
4. Timbie, P.T. et al. 2006, New Ast. Rev., v50, p999.
5. Charlassier, R. et al. 2008, Proceed. 43rd "Rencontres de Moriond" on Cosmology, [arXiv:0805.4527v1](https://arxiv.org/abs/0805.4527v1).
6. Pearson T. J. & Readhead A. C. S., 1984, Ann. Rev. A&A, 22:97-130.
7. Kovac, J. et al. 2002, Nature, v420 pp772-787.
8. C. R. Contaldi *et al.*, 2002, [arXiv:astro-ph/0210303](https://arxiv.org/abs/astro-ph/0210303).
9. P. Oxley *et al.*, 2004 Proc. SPIE Int. Soc. Opt. Eng. 5543 320 [arXiv:astro-ph/0501111](https://arxiv.org/abs/astro-ph/0501111).
10. Planck Collaboration, 2006 [arXiv:astro-ph/0604069](https://arxiv.org/abs/astro-ph/0604069).
11. Crill, B. et al., 2008, Proc. SPIE, Vol. 7010, [arXiv:0807.1548](https://arxiv.org/abs/0807.1548).
12. J. Bock et al., 2006, "Task Force on CMB Research" [arXiv:astro-ph/0604101](https://arxiv.org/abs/astro-ph/0604101).

Instrumental challenges for a future B-mode space instruments

M. Piat

Astroparticule et Cosmologie (APC), Université Paris Diderot, 10 rue Alice Domon et Léonie Duquet, 75013 Paris, France

The detection of the B-mode polarisation of the CMB is today one of the major challenge in observational Cosmology. Dedicated space missions have been imagined to characterise this small signal which could be a major discovery for Cosmology and fundamental Physics. A discussion on some instrumental challenges is proposed, with a focus on the detectors and polarisation modulator sub-systems.

1 Introduction

Our understanding of the origin and evolution of the Universe has made remarkable progress during the last decade, thanks in particular to observations of the Cosmic Microwave Background (CMB). What is now known as the standard cosmological model (or concordance model) is able to explain a number of diverse and ever increasingly detailed observations. The model also predicts the existence of primordial gravitational waves, generated during an explosive period of expansion known as inflation¹. This prediction remains yet to be tested and is the motivation for a lot of research effort since these primordial gravity waves should have imprint particular features on the CMB polarisation: the B-modes. This signal is expected very weak with an RMS of less than $200\text{nK}_{\text{CMB}}$, at least 3 orders of magnitude lower than the CMB temperature anisotropies. The level of B-modes depends on the scalar-to-tensor ratio r which is today constrained at $r < 0.24$ at 95% confidence limit².

The detection of gravity waves from inflation would not only be a major discovery for cosmology, but also for all of fundamental Physics. It would satisfy one of the primary objectives of modern Physics to detect these waves predicted by Einstein's General Relativity. It would furthermore be an indication of the quantum nature of gravity, for the excitation mechanism of inflation is inherently semi-classical (usually reserved otherwise for quantum fields). Finally, these B-modes would offer direct access to physics at energies inaccessible in the laboratory and probably related to grand unification. For example, the amplitude of the B-mode would immediately give us the energy scale of inflation and hence the characteristic energy scale of unification physics.

While detection of this primordial B-mode signal will probably be done from ground (if $r > 0.01$), the precise characterisation of the angular power spectrum will certainly require measurements from space. Dedicated space missions have therefore been designed in feasibility studies both in the US and in Europe. This paper presents some of the challenges to develop such space instruments. The focus is made on detector arrays and polarisation modulator.

2 Polarisation dedicated space mission

Space environment and especially the second Lagrange point L2 offers several advantages for CMB observation: the thermal environment is cold and stable, no emission nor fluctuations from atmosphere, passive cooling down to about 40K could be obtained as first cryogenic stage, the whole sky could be mapped allowing to recover large angular scales. These leads both US and Europe to propose dedicated CMB polarisation missions to the space agencies^{3,4,5}.

As an example, the BPol concept was proposed in 2007 to answer the ESA Cosmic Vision call^{4,5}. It consisted on 8 refractive telescopes, covering the frequency range between 70GHz and 353GHz in 5 bands (see figure 1). This design allows for a constant angular resolution in the CMB channels. The focal plane was covered with 100mK polarisation sensitive bolometers coupled to the telescopes thanks to corrugated horns. Two radiometers looking directly on the sky were added at 45GHz in order to map the galactic synchrotron and free-free emission. Such a large frequency coverage allows for mapping and removing to some extend the foreground emission of our Galaxy⁶. The scanning strategy was a combination of rotation and nutation in order to cover a large fraction of the sky in a short time and with different polarisation angles.

Such a mission was nevertheless not selected today, mainly because the technology is thought



Freq. band (GHz)	45	70	100	143	217	353
$\Delta\nu$	30%	30%	30%	30%	30%	30%
ang. res.	15deg	68'	47'	47'	40'	59'
# horns	2	7	108	127	398	364
det. noise ($\mu K \cdot \sqrt{s}$)	57	33	53	53	61	119
Q & U sens. ($\mu K \cdot \text{arcmin}$)	33	23	8	7	5	10
Tel. diam. (mm)	45	265	265	185	143	60

Figure 1: Artist view of the BPol satellite and principal characteristics of this instrument.

to be not mature enough and also because the space agencies want to have a first detection. The European Space Agency (ESA) nevertheless recommended "focussed technology activities to enable a sufficiently mature mission concept which could be submitted by community in response to future ESA Calls for Missions."

This kind of mission is certainly a challenge but technological solutions are available to make it real. The french phase 0 study SAMPAN^{7,4} has been especially very useful in this process. This study has indeed been done on collaboration with engineers from the french space agency CNES, from Thales and Air Liquide and with scientists. It has demonstrate for example that the passive cooling of forward V-grooves could be obtained efficiently down to about 40K. The main challenges remains in the detection chain: the detector arrays and the polarisation modulation.

3 Detector arrays

To be background limited, the detectors must be wideband ($\Delta\lambda/\lambda \simeq 20-30\%$) and need to have Noise Equivalent Power (NEP) of $3 - 8.10^{-18} W.Hz^{-1/2}$. The scanning strategy constrains the detector time constant to be typically lower than 10ms. Finally, to reach a sensitivity needed for B-modes, depending on the design, some thousands of detectors are needed in the focal plane. A recent feedback from the Planck satellite indicates that immunity to cosmic ray hits could be a concern for a future CMB polarisation satellite⁹. Such constraint has therefore to be taken into account at the beginning of the project.

Bolometers cooled to very low temperature ($T \leq 0.3K$) are currently the best detectors for low

spectral resolution $\lambda/\Delta\lambda$ detection from about $100\mu\text{m}$ to 3mm . The other technology that could be used is radiometers. They are based on high frequency amplifiers with noise temperature that becomes closer and closer to the quantum limit given by $T_{QL} = h\nu/k$. It can nevertheless be shown that space born measurements of the CMB leads to a very low power background on the detectors which gives a strong advantage for bolometers⁸. On the low frequency part, bolometers tend to be difficult to manufacture and radiometers are probably unavoidable for frequencies lower than about 50GHz , where the sky signal is mainly dominated by free-free and synchrotron emission from our Galaxy. Large bolometer arrays are today being manufactured

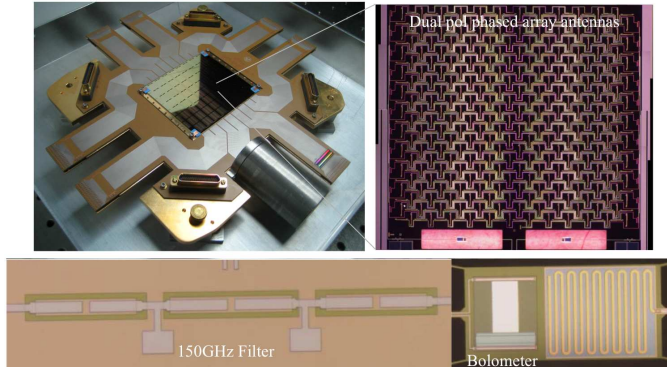


Figure 2: Example of a bolometer arrays made at Caltech-JPL¹⁰. It consists of 64 detectors, each is based on a dual polarisation phased-array antenna that couples the RF signal to a bolometer through a microstrip line filter centered at 150GHz . This kind of detectors are now being used on the BICEP2 instruments¹¹.

and used for ground based and balloon born CMB observations (figure 2). They are based on Transition Edge Sensors (TES) that are easier to multiplex at very low temperature. We refer to a previous publications⁸ and references therein for a more detailed discussion on this subject.

4 Polarisation modulation

Up to now, the measurement of Stokes parameters with bolometers is obtained by subtracting the signals from two perpendicular polarised detectors. This method induces instrumental systematic effects since the 2 detection chains do not behave exactly in the same way¹². The use of a system to modulate the incident polarisation allows to measure the Stokes parameters with each single detectors and therefore avoid this problem. If this polarisation modulator is used continuously (not stepwise), it could remove $1/f$ noise efficiently¹⁶ which could also simplify the scanning strategy. A polarisation modulator is nevertheless not always necessary, especially if the $1/f$ noise of the instrument is well controlled and if the scanning strategy allows for rapid revisit of the pixels by each detectors at different angles⁷.

Probably the most used (or planned to be used) polarisation modulator is the Half Wave Plate (HWP)¹³ which modulates the sky polarisation at 4 times the rotating speed θ . Such a system could nevertheless induce systematic effects as clearly seen in the data from Maxipol¹⁵ which was the first CMB instrument to use a HWP. The thermal emission of the modulator itself could induce a parasitic effect at 4θ and parasitic reflections in the optical path could generate 4θ signal^{13,14}. This could be reduced by cooling the HWP and adding antireflection coating.

Another promising way to modulate the polarisation is by using planar phase shifters. This will allow to realise new detection architecture like the pseudo-correlator scheme¹⁷ or bolometric interferometry¹⁸. The possibility to use this kind of architecture was quoted in the BPol proposal⁴. An example of such component is shown figure 3. It consists of a superconducting transmission line where the quasiparticles density is modulated by changing the DC current or the temperature. This induces a modulation of the kinetic inductance and therefore a variation

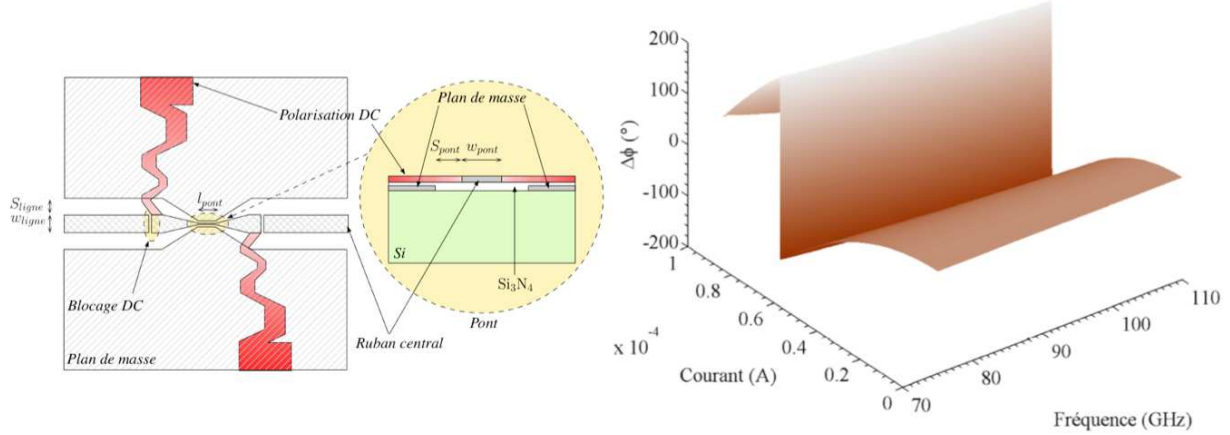


Figure 3: Design of a superconducting phase shifter and simulated phase shift as a function of frequency and DC current¹⁹

of the electric length of the lines¹⁹. This design is very promising and a prototype is being designed for a test of the concept between 10GHz and 20GHz. The Technology Readiness Level (TRL) of such component is nevertheless low and further R&T effort is needed.

5 Conclusion

Two instrumental challenges in the detection chain of a dedicated CMB polarisation satellite have been discussed. TES arrays are today used in ground based and balloon born instruments. The integration is a complex issue and a system approach is needed to avoid unexpected sensitivity degradation. Polarisation modulators are probably unavoidable but a careful optical design should be done and comprehensive characterisations should be performed. Other modulation technics using planar technology is today being studied but need TRL improvement.

References

1. P. Leahy, these proceedings
2. D. Larson et al., WMAP-7, Power Spectra and WMAP-Derived Parameters (2010)
3. J. Bock et al., arXiv:0805.4207 (2008)
4. <http://www.b-pol.org>
5. P. De Bernardis et al., Experimental Astronomy **23**, Issue 1 (2009)
6. C. Dickinson, these proceedings
7. F.R. Bouchet et al., SF2A-2005 (2005)
8. M. Piat, proceedings of Moriond Cosmology session (2008)
9. F. Pajot, these proceedings
10. C.L. Kuo et al., Proc. SPIE **6275**, 62751M (2006)
11. A. Orlando et al., LTD13, AIP Conference Proceedings **1185**, 471 (2009)
12. C. Rosset et al., arXiv:1004.2595
13. M. Salatino, these proceedings
14. M. Salatino et al, arXiv:1006.5392v2, (2010)
15. B.R. Johnson et al., ApJ **665**, Issue 1 (2007)
16. C.J. MacTavish et al., ApJ **689**, Issue 2 (2008)
17. G. Yassin et al., Physica C **466**, 115 (2007)
18. R. Charlassier, these proceedings
19. A. Ghribi, Ph.D. thesis (2009)

ON STOKES POLARIMETERS FOR HIGH PRECISION CMB MEASUREMENTS AND MM ASTRONOMY MEASUREMENTS

M. SALATINO and P. DE BERNARDIS

*Department of Physics University of Rome “la Sapienza”, p.le Aldo Moro, 2
00185, Rome, Italy*

Several on-going and future experiments use a Stokes polarimeter (i.e. a rotating wave plate followed by a steady polarizer and by an unpolarized detector) to measure the small polarized component of the Cosmic Microwave Background. The expected signal is typically evaluated using the Mueller formalism. In this work we carry-out the signal evaluation taking into account the temperatures of the different optical devices present in the instrument, their non-idealities, multiple internal reflections, and reflections between different optical components. This analysis, which exploits a new description of the radiation transmitted by a half wave plate, can be used to optimize the experimental setup as well as each of its optical components. We conclude with an example of application of our analysis, studying a cryogenic polarization modulator developed for detecting the interstellar dust polarization.

1 Introduction

The most ambitious challenge in Experimental Cosmology today is the precision measurement of the polarized signal of the Cosmic Microwave Background (CMB). Given the tiny amplitude of the polarized component with respect to the unpolarized one, its extraction is very complicated. Several on-going and future CMB experiments, like EBEX¹, BRAIN², BICEP-2³, QUBIC⁴, SPIDER⁵, LSPE⁶, B-Pol⁷, CMB-Pol⁸, and astrophysical ones, like PILOT⁹ and BLAST-pol¹⁰, will detect the polarized component of the signal of interest (CMB or interstellar dust polarization) by means of a rotating a Half Wave Plate (HWP) followed by a fixed polarizer, both located in front of the detector.

Using the Stokes parameters and the Mueller matrix formalism, the power detected when an ideal HWP rotates at angular speed ω in front of an ideal polarizer is¹¹:

$$S_{ideal}(\theta) = \frac{1}{2}[S_0 + S_1 \cos 4\theta + S_2 \sin 4\theta]; \quad (1)$$

where $\theta = \omega t$ and S_i are the Stokes parameters of the radiation under analysis. The linearly polarized radiation is thus modulated at frequency $4f = 2\omega/\pi$. Only the radiation transmitted by the HWP + polarizer stack have been included. In general, we need to include in the analysis also the thermal emission from all the optical devices and from the radiative background. Moreover the non-idealities of the devices, the multiple internal reflections and the reflections between distinct devices modify the signal detected by the polarimeter. In Sec. 2 we describe the behavior of a real polarimeter. We provide simulations of the signal detected by a typical CMB experiment in Sec. 3. Before concluding summarizing our results (Sec. 5), we present the Cryogenic Waveplate Rotator (CWR), a system which will modulate the polarized component of the interstellar dust in the PILOT balloon-borne experiment (Sec. 4).

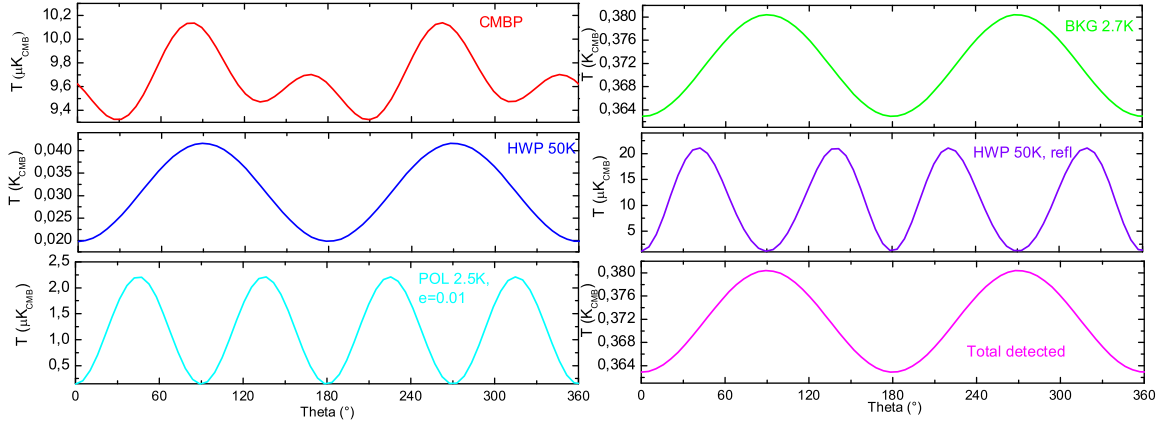


Figure 1: Simulation of the different contributions to the power detected in a Stokes polarimeter at 150 GHz, vs rotation angle of the waveplate. From top left to bottom right: CMB polarization, unpolarized radiative background with temperature 2.7 K, polarized emission of the HWP at 50 K transmitted to the polarizer and the same reflected back by the polarizer, polarized emission of the polarizer ($T_p = 2.5 K$, $\epsilon_p = 0.01$), total signal detected by the bolometer.

2 Modeling a real polarimeter

The Mueller formalism as used above provides a simplistic description of the radiation transmitted by an ideal HWP; in particular, it assumes that the 100 % of the incident radiation is transmitted, independently of the incidence angle, and that the phase difference ϕ is frequency-independent. In the Adachi formalism¹², instead, the phase difference depends on the frequency of the incident wave, on the thickness of the crystal d , on the extraordinary n_e and ordinary n_o refraction index of the birefringent crystal.

Here we use a new description of the HWP¹³ that takes into account multiple internal reflections. These depend on the optically activity of the anisotropic HWP crystal (OAMR, Optically Active Multiple Reflections), and we also include the frequency dependence of the refraction indices. From the total transmitted and reflected electric fields we have built two new Mueller matrices: one for the transmitted stokes vector and the other for the reflected one; the matrix elements depend on n_e , n_o , ϕ , the reflectivity, and the transmissivity of the anisotropic medium in a complex way. For a real HWP, M_{HWP}^{real} , in normal incidence approximation the multiple reflections create non-vanishing off-diagonals terms, not present in the ideal one, $diag(M_{HWP}^{ideal}) = (1, 1, -1, -1)$. For example, at 150 GHz, a typical Mueller matrix for the HWP is:

$$M_{HWP}^{real} = \begin{pmatrix} 0.773 & -0.006 & 0 & 0 \\ -0.006 & 0.773 & 0 & 0 \\ 0 & 0 & -0.773 & -0.033 \\ 0 & 0 & 0.033 & -0.773 \end{pmatrix}. \quad (2)$$

We also take into account the spectral dependence of the refraction indices and of the absorption coefficients which are assumed to decrease linearly with the temperature of the HWP.

A polarizer emits linearly polarized radiation; in the Stokes polarimeter this emission is reflected back by the rotating HWP, and after the crossing through the polarizer, is modulated at a frequency $4f$. The unpolarized radiative background, following the same optical path of the astrophysical signal, is instead modulated at $2f$ by small non-idealities in the wave plate. Small

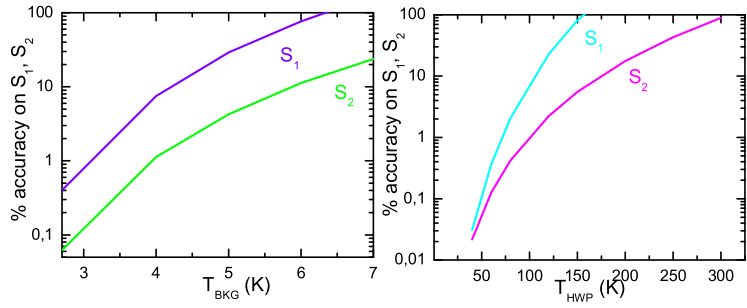


Figure 2: Accuracy for the detection of linear CMB polarization versus the temperature of the radiative background (left) and of the HWP (right).

Table 1: Features of the spurious signals produced by a real polarimeter.

EFFECT	MOD.	AMPL.
radiative background at 2.7 K	$2f$	15 mK
polarized emission of the polarizer at 2.5 K reflected by the HWP	$4f$	$2.1 \mu\text{K}$
polarized emission of the HWP at 50 K transmitted by the polarizer	$2f$	22 mK
polarized emission of the HWP at 50 K reflected by the polarizer	$4f$	$3 \mu\text{K}$
polarized emission of the HWP at 4 K reflected by the polarizer	$4f$	$0.6 \mu\text{K}$

differences in the absorbtion coefficients of the HWP, fews 10^{-3} , produce a polarized emission; it is modulated at $2f$ ($4f$) when is transmitted (reflected back) by a polarizer (and successively by the HWP)¹³.

For a Λ -CDM model, with tensor to scalar ratio $r = 0.1$, the expected detected signal due only to the CMB, has a typical (rms) amplitude of about $0.7 \mu\text{K}$. We consider the normal incidence approximation and an incoming monochromatic ray at 150 GHz. Going through a real absorbing HWP the signal amplitude does not change much ($0.6 \mu\text{K}$), but the heights of the peaks become uneven, due to a spurious $2f$ component (Fig. 1). From our model, we find a number of spurious effects, as quantified in Tab. 1.

The result of the sum of these emissions, with respect to the CMB signal, depends on the relative angle between the CMB polarization angle and the orientation of the wire grid. Despite of the large amplitude of the 2θ components, they are easily removable from the cosmological signal by means of a high-pass filter. The $4f$ spurious signals, on the contrary, cannot be removed; being at the same frequency, they contaminate the cosmological signal by an amount which depends on the physical temperature of the optical components: at 2.5 K the spurious signal is about 4 times the CMB one, while at 1 K it decreases below 4% of the CMB one. We conclude that it is certainly necessary to cool down the polarizer and the HWP, and to reduce the radiative background.

3 Saturation effects

Bolometric detectors, used at these frequencies, are non linear and start to saturate if the detected signals become too large. In a slightly saturated bolometer a pure 2θ signal acquires a 4θ component, plus higher order terms. Therefore, non linearities place upper limits on the radiative background we can tolerate in a CMB polarization experiment. Given a 1% saturation

for signals of the order of 200 mK_{CMB} , we find that if we want to detect the S_1 and S_2 parameters with, at least, 10% accuracy, we must reduce the radiative background below 4.5 K (Fig. 2).

A possible solution for removing these troublesome spurious signals could be using an array of polarizers, one per detector, with different wire grid orientations, in place of a single wire grid covering all the array. In this way, the spurious emissions having different phases partially cancel each other. PSBs are naturally providing this advantage, if properly oriented in the array.

4 The Cryogenic Waveplate Rotator

In the near future PILOT⁹, a balloon experiment with 1024 bolometers cooled down to 0.3 K, will observe the polarized emission from the Galactic plane and the cirrus clouds at high Galactic latitudes, in two bands centered on 545 and 1250 GHz. The cryogenic waveplate rotator (CWR)^{14 15} will modulate the astrophysical signal at a frequency of $4f$, rotating a 4K HWP. The CWR works in a step and integration mode, exploiting an innovative mechanical system driven by a step motor running at room temperature. The CWR controls, in a completely automated way, the position of the crystal with an accuracy better than 0.03° , stopping in pre-selected positions sensed by a 3-bit optical encoder made with optical fibers.

5 Conclusions

We have shown a few examples of contamination of Stokes Polarimeter data due to the polarized emission of the polarizer reflected back by the rotating HWP, to the unpolarized radiative background, which follows the same path of the target signal, going through a non-ideal waveplate, and to the polarized emission of the HWP reflected and transmitted by a polarizer. This study has used a new description of the HWP which takes into account the optically active multiple reflections inside the crystal and which describes the radiation transmitted and reflected from the birefringent medium. The non linear behavior of the bolometric detector produces a 4θ signal from the large $2f$ spurious signals; this means that even if the $2f$ signal can be removed post-detection, its level should be kept low enough that the linearity of the detector is not challenged. This sets upper limits, less than about 10 K, for the allowed radiative background in a given experiment. Our simulations also show the necessity of cooling the polarizer down to about 1 K and the HWP to 4 K.

References

1. P. Oxley *et al*, *Proc. of SPIE* **5543**, 320 (2004).
2. G. Polenta *et al*, *New. Astron. Rev.* **51**, 256 (2007).
3. J. Kovac *et al*, *Bulletin of the American Astronomical Society* **38**, 913 (2007).
4. Kaplan J. *et al*, *Proc. of Blois Conference “Windows on the Universe”* in press (2009).
5. B. Crill *et al*, *Proc. of SPIE* **7010**, 70102P (2008).
6. P. de Bernardis *et al*, *Nuclear Physics B* **194**, 350 (2009).
7. P. de Bernardis *et al*, *Exp. Astron.* **23**, 5 (2009).
8. J. Bock *et al*, astro-ph/0906.1188 (2009).
9. J. P. Bernard *et al*, *EAS Publication Series* **23**, 189 (2007).
10. G. Marsden, *et al*, *SPIE Conference Proceedings* astro-ph/0805.4420 (2008)
11. E. Collett in *Polarized light.*, Marcel Dekker, Inc. (New York, 1993).
12. S. Adachi S. and E.M. Kennaugh, *IEEE Trans. on microwave th. and tech.* **8**, 520 (1960).
13. M. Salatino and P. de Bernardis, in prep. (2010).
14. M. Salatino *et al*, *Mem. S.A.It.* **79**, 905 (2008).
15. M. Salatino and P. de Bernardis, submitted to *Exp. Astron.* (2010).

PLANCK-SCALE LORENTZ INVARIANCE VIOLATIONS AND CMB POLARIZATION DATA

GIULIA GUBITOSI

*Dipartimento di Fisica, Università di Roma “La Sapienza”
and Sez. Roma1 INFN, P.le A. Moro 2, 00185 Roma, Italy
giulia.gubitosi@roma1.infn.it*

Some models of spacetime quantization leading to violations of Lorentz symmetries predict a minute effect of birefringence for the propagation of photons. For Cosmic Microwave Background (CMB) photons, which have some degree of linear polarization, this results in a rotation of their polarization direction. The effect is greatly amplified by their long time of propagation, and could have observably large implications for analyses of CMB polarization. Here we mainly report the results of previous works^{1,2,3}, in which it is shown that for the most studied model of quantum-spacetime-induced birefringence, available BOOMERanG 2003 and WMAP data can be used to establish a bound of Planck-scale significance. We give forecasts on the sensitivities achievable by future CMB polarization measures and we comment on how systematic effects of CMB experiments could influence these constraints. As a final point we discuss how Lorentz violations can also produce non-isotropic birefringence effects.

Motivations to study Planck-scale physics come from quantum-gravity research, that essentially tries to solve the problem of finding a common description for quantum and general-relativistic phenomena, to be used in the physical situations in which both of them are non-negligible. The lacking of a unifying theory, despite all the efforts made toward it, can be traced back to the difficulties encountered in accessing experimentally the ultra-high energy (and correspondingly the ultra-short length) scale at which these phenomena should be relevant. So it is clear the crucial importance of looking for physical situations in which one could find clues of what the quantum-gravity theory should look like.

One of the most common expectations emerging from quantum-gravity research is that spacetime should show some quantum properties (such as discreteness, coordinates noncommutativity or fuzziness) when probed at scales of the order of the Planck length $L_P \sim 10^{-35} m$. It is commonly agreed that this quantization may cause a deformation of spacetime symmetries, which acquire some “quantum” features themselves⁴, leading to violations of Lorentz symmetries. Among the many ways in which these violations could show up, much studied are possible consequences on particles’ energy-momentum dispersion relations⁶, characterized by corrective terms governed by the Planck scale $E_P \sim 10^{28} eV$. In the high-energy regime, to the first order in $\frac{1}{E_P}$, the modified dispersion relation for photons takes the form

$$E \simeq p + \frac{\eta}{E_P} p^2, \quad (1)$$

where η is a dimensionless parameter governing the amplitude of the correction.

It has been also studied the case^{6,7} in which two states with opposite helicity behave differently, obeying different dispersion relations

$$E_{\pm} \simeq p \pm \frac{\eta_*}{E_P} p^2. \quad (2)$$

Since in this case the two helicity states of the electromagnetic waves have different phase velocity, linearly polarized monochromatic radiation rotates its polarization vector during propagation^a. This behaviour is known as *in-vacuo* birefringence, due to its similarity with the birefringence effects observed when light propagates in materials with chiral molecules.

Modifications of photon dispersion relation of the form $\frac{p^2}{E_P}$ can be formalized through an effective field theory for electrodynamics with mass-dimension five corrections to the standard Maxwell Lagrangian density. A well-studied model (both on the theoretical and the phenomenological sides) is the one proposed by Myers and Pospelov⁵, in which the electromagnetic tensor $F_{\mu\nu}$ is coupled to a fixed four vector n_{α} and the nonrenormalizable operator in the Lagrangian has a coupling constant proportional to $\frac{1}{E_P}$, to ensure that the new physics effects originate at the Planck scale:

$$\mathcal{L} = -\frac{1}{4}F_{\mu\nu}F^{\mu\nu} + \frac{1}{2E_P}n^{\alpha}F_{\alpha\delta}n^{\sigma}\partial_{\sigma}(n_{\beta}\varepsilon^{\beta\delta\gamma\lambda}F_{\gamma\lambda}) \quad (3)$$

Until now only a simplified version of the model has been studied, in which the four-vector n_{α} has the spatial components set to zero ($n_{\alpha} = \{n_0, 0, 0, 0\}$), so that space isotropy is preserved, and only invariance under boost transformations is violated^b. Within this assumption, the Lagrangian density takes the form:

$$\mathcal{L} = -\frac{1}{4}F_{\mu\nu}F^{\mu\nu} + \frac{\xi}{2E_P}F_{0j}\varepsilon^{jkl}\partial_0F_{kl} \quad (4)$$

where $\xi \equiv (n_0)^3$ is the parameter governing the amplitude of non-standard effects so that its ratio with E_P sets the scale at which new phenomena are originating. Constraining ξ roughly to order one means testing new effects originating genuinely at the Planck scale. From the above Lagrangian a birefringent behavior of photons can be deduced^{5,1}, of the kind of (2) with $\eta_* = \xi$, so, if the field is linearly polarized, after propagation for a time T its polarization vector will rotate of an angle¹

$$\alpha(T) = 2\frac{\xi}{E_P}p^2T. \quad (5)$$

This formula has a peculiar energy dependence. If we want to test the rotation using CMB photons, for which the energy redshift due to the universe expansion can not be neglected, the above formula has to be corrected. For a photon traveling from epochs with redshift z toward us, where it is measured to have momentum p_0 , the total rotation angle is given by

$$\alpha(z) = \frac{2\xi}{E_P} \frac{p_0^2}{H_0} \int_0^z \frac{(1+z')}{\sqrt{\Omega_m(1+z')^3 + \Omega_{\Lambda}}} dz' \quad (6)$$

where H_0 is the value of the Hubble function today, Ω_m and Ω_{Λ} are respectively the matter and dark energy densities and we assumed a standard Λ CDM cosmological model.

The reason why it is actually possible to constrain this rotation effects using CMB photons is that their production process is very well understood, and it is known to produce partially linearly polarized radiation, and to be parity invariant⁸. Expanding the polarization pattern on the sky in spherical harmonics it is possible to separate the modes with different properties under

^aIf one considers non-monochromatic waves, when the propagation time is sufficiently long the polarization ends up disappearing⁷.

^bThis choice clearly is not reference frame independent. We discuss later this issue.

parity transformations (the so-called “electric” and “magnetic” modes of polarization). Due to parity invariance of the original polarization pattern, we would expect to see only parity-even modes (the “electric” ones). Parity-odd modes are produced instead from the parity-even ones if a rotation of polarization occurs. We have analyzed WMAP5 and BOOMERanG2003 data. The results are reported in Table 1. Notice that since the two experiments detect photons with slightly different energies, we cannot give a joint estimate on α , which is energy-dependent, but we have to rely on the ξ parameter.

Experiment	$\alpha \pm \sigma(\alpha)$	$\xi \pm \sigma(\xi)$
WMAP (94 GHz)	-1.6 ± 2.1	-0.09 ± 0.12
BOOMERanG (145 GHz)	-5.2 ± 4.0	-0.123 ± 0.096
WMAP+BOOMERanG	-	-0.110 ± 0.075

Table 1: Mean values and 1σ error on α (in degrees) and ξ .

The constraints on ξ are

$$-0.260 < \xi < 0.040 \quad (7)$$

at 95% confidence level, which are even beyond the desired Planck scale sensitivity. We have also given an estimate of the sensitivities reachable with the recently-launched PLANCK satellite and some other future experiments (see Table 2 and also the more detailed table reported in our previous work¹, where we report also the sensitivities reachable with an ideal cosmic-variance limited experiment).

Experiment	Channel	$\sigma(\alpha)$	$\sigma(\xi)$
PLANCK	100+143+217	-	$8.5 \cdot 10^{-4}$
Spider	145	0.27	$6.1 \cdot 10^{-3}$
EPIC	70+100+150+200	-	$1.0 \cdot 10^{-5}$

Table 2: Expected 1σ error for PLANCK 70, 100, 143, 217 GHz, Spider 145 GHz, EPIC 70, 100, 150, 220 GHz and two ideal CVL experiment at 150 GHz and 217 GHz on α (in degrees) and ξ .

Thanks to the multi-frequency data provided by some of these experiments, exploiting the energy dependence peculiar of Planck scale effects will make it possible to give quite stringent limits on ξ up to 10^{-5} and disentangle this kind of rotation effect from other phenomena giving analogous signatures in CMB polarization data. An example are systematic effects. To this regard, we have checked how much a misalignment of the polarimeters, which could mimic a polarization rotation effect, could have influenced our constraints². For multi-frequency experiments it is possible to exploit the peculiar energy dependence to disentangle a genuine rotation due to Planck-scale birefringence from other effects. On the other hand, this issue is particularly worrisome in single-frequency experiments like BOOMERanG. So we considered a realistic miscalibration of BOOMERanG polarimeters of 0.9 ± 0.7 degrees, which leads to a different estimate on α : $\alpha = -4.3 \pm 4.1$ degrees. This weakens the (already faint) indication of rotation we found before. The estimate on ξ , including also WMAP data, becomes $\xi = 0.097 \pm 0.075$.

We have shown that present CMB polarization data provide sensitivity to the Planck scale birefringence parameter ξ of order 10^{-1} . Actually there are analyses exploiting astrophysical sources that are able to put much more stringent constraints (using Crab Nebula observations allows to put the limit⁹ $|\xi| \leq 10^{-9}$). But it is necessary to be very careful in comparing these limits, since they are obtained in different reference frames and ξ is actually related to the time component of a four vector (the limit of 10^{-9} on ξ translates into a limit of 10^{-3} on n_0). In particular one could have $n_\alpha = (0, 1, 1, 1)$ in some reference frame, but then in another reference frame moving with velocity $\beta = 10^{-3}$ with respect to the first one one would have n_0 of order 10^{-3} . And this value for β is of the same order of magnitude of the relative velocity between CMB reference frame and our galactic cluster reference frame.

So it is clear the importance on putting bounds all the four components of n_α . And when studying the phenomenological consequences of the Lagrangian (3) another feature emerges that suggests caution when interpreting the bounds on the model (4) with only n_0 different from zero. In fact when also the spatial components of the vector are considered, the photon dispersion relation becomes direction-dependent³:

$$\omega_\pm = |\vec{p}| \pm \frac{|\vec{p}|^2}{E_P} (n_0 + \vec{n} \cdot \hat{p})^3. \quad (8)$$

If n_α is space-like, there are some propagation directions for the photons, in which they behave classically. So using point-like astrophysical sources to constrain Lorentz violations induced by the Lagrangian (3) can be misleading^c. To this respect CMB data can be very competitive in constraining the general model, since CMB radiation covers almost all the sky and so is capable of giving a better statistics than point-like astrophysical sources.

References

1. G. Gubitosi, L. Pagano, G. Amelino-Camelia, A. Melchiorri and A. Cooray, arXiv:0904.3201 [astro-ph.CO].
2. L. Pagano *et al.*, arXiv:0905.1651 [astro-ph.CO].
3. G. Gubitosi, G. Genovese, G. Amelino-Camelia and A. Melchiorri, arXiv:1003.0878 [Unknown].
4. G. Amelino-Camelia and S. Majid, Int. J. Mod. Phys. A **15** (2000) 4301 [arXiv:hep-th/9907110].
5. R. C. Myers, M. Pospelov, Phys. Rev. Lett. 90 (2003) 211601
6. R. Gambini and J. Pullin, Phys. Rev. D **59** (1999) 124021 [arXiv:gr-qc/9809038].
7. R. J. Gleiser and C. N. Kozameh, Phys. Rev. D **64** (2001) 083007 [arXiv:gr-qc/0102093].
8. W. Hu, Phys. Rev. D **62** (2000) 043007 [arXiv:astro-ph/0001303].
9. L. Maccione and S. Liberati, JCAP **0808** (2008) 027 [arXiv:0805.2548 [astro-ph]].

^cBesides the completely blind directions, in a quite large fraction of the sky the birefringent effect can be weakened of a significant amount³

LARGE-ANGLE ANOMALIES IN THE MICROWAVE BACKGROUND

E.F. BUNN

*Physics Department, University of Richmond
28 Westhampton Way, Richmond, VA 23173, USA*

Several claims have been made of anomalies in the large-angle properties of the cosmic microwave background anisotropy as measured by WMAP. In most cases, the statistical significance of these anomalies is hard or even impossible to assess, due to the fact that the statistics used to quantify the anomalies were chosen a posteriori. On the other hand, the possibility of detecting new physics on the largest observable scales is so exciting that, in my opinion, it is worthwhile to examine the claims carefully. I will focus on three particular claims: the lack of large-angle power, the north-south power asymmetry, and multipole alignments. In all cases, the problem of a posteriori statistics can best be solved by finding a new data set that probes similar physical scales to the large-angle CMB. This is a difficult task, but there are some possible routes to achieving it.

1 Introduction

Our understanding of cosmology has advanced extremely rapidly in the past decade, due in large part to observations of cosmic microwave background (CMB) anisotropy, particularly the data from the Wilkinson Microwave Anisotropy Probe (WMAP).^{1,2,3,4} As a result of these and other observations, a “standard model” of cosmology has emerged, consisting of a Universe dominated by dark energy and cold dark matter, with a nearly scale-invariant spectrum of Gaussian adiabatic perturbations^{5,6} of the sort that would naturally be produced in an inflationary epoch.

The all-sky CMB maps made by WMAP provide a unique window on the Universe, probing larger scales and earlier times than any other data. Not surprisingly, therefore, researchers have scrutinized the maps carefully for evidence of nonstandard phenomena on large scales. In most ways, there is remarkable agreement between the standard model and the large-angle properties of the WMAP data; however, several anomalies have been noted on the largest scales, including among others a lack of large-scale power,^{2,7,8} alignment of low-order multipoles,^{8,9,10,11} and hemispheric asymmetries^{12,13,14}. The WMAP collaboration has conducted a thorough review and analysis of the claimed anomalies.¹⁵

The significance of and explanations for these puzzles are uncertain, largely because of the problem of a posteriori statistics. The typical sequence of events in the discovery of a CMB anomaly is as follows: some unusual feature is noticed in the data, and afterwards (a posteriori) a statistic is devised to quantify the unusualness of this feature. The p -values from such a statistic cannot be taken at face value: in any moderately large data set, it is always possible to find something that looks odd, and a statistic engineered to capture that oddness will have an artificially low probability. Chance fluctuations can therefore incorrectly seem to be in need of explanation.

Figure 1 illustrates this with a simple toy example. A Gaussian random map was made

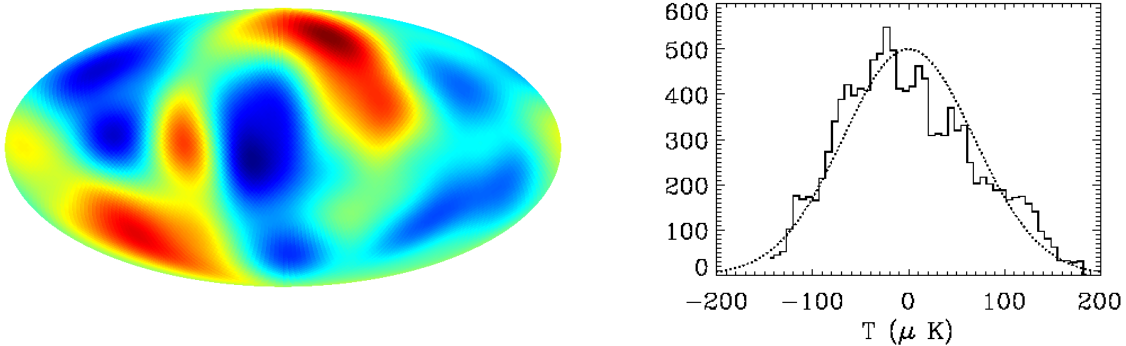


Figure 1: A toy example of the dangers of a posteriori statistics. The left panel shows a Gaussian, statistically isotropic simulation of a CMB map, smoothed to show only large-scale anisotropy. As the right-panel shows, the one-point probability distribution of the anisotropy has an unusually high skewness. This skewness can be “explained” by noting the presence of a pair of almost perfectly antipodal extreme hot spots.

that by chance has noticeable positive skewness. Someone looking for an explanation for this skewness might be tempted to examine the most extreme hot spots in the map and would find that they are almost perfectly antipodal. The probability that a map’s two most extreme hot spots are as far apart as in this map is less than 1%. One might be tempted to speculate on the possible explanations for this unlikely pair of hot spots, but of course there is none.

One can (and from a formal statistical point of view, arguably one must) dismiss the entire subject of CMB anomalies because of this problem, but I believe that a more nuanced view is called for. Scientists often by necessity use non-rigorous (or even “invalid”) statistical methods, especially in preliminary analyses. As long as we maintain a skeptical stance and seek further tests that can be done of any hypotheses that result from such an analysis, these methods can yield fruitful insights. Considering the importance of finding ways to test the largest-scale properties of the Universe, I suggest that is neither necessary nor wise to dismiss the subject out of hand.

In this paper, I will not discuss all of the claims of anomalies but rather focus on the three that in various ways seem to me most interesting: the large-scale power deficit, evidence for hemispheric power modulation, and alignment of low-order multipoles. I will also discuss possible future directions for testing hypotheses arising from these anomalies.

2 Lack of large-scale power

Ever since the first all-sky CMB maps were made by the COBE satellite,¹⁶ questions have been raised about the low amplitude of fluctuations on the largest angular scales. In the observed angular power spectrum, the quadrupole (the largest-scale data point) is lower than expected, although given the large cosmic variance in the quadrupole as well as the need to mask part of the sky, this discrepancy is not extremely statistically significant. The lack of large-scale power appears more striking when viewed in real space rather than the spherical harmonic space of the power spectrum. As Figure 2 illustrates, the two-point correlation function is very close to zero for all angles $\theta \gtrsim 60^\circ$, unlike typical simulations.

To quantify this behavior, the statistic $S_{1/2}$ is defined to be¹⁷

$$S_{1/2} = \int_{-1}^{1/2} [C(\theta)]^2 d\cos\theta. \quad (1)$$

The value of this statistic is low compared to simulations at a confidence level of approximately

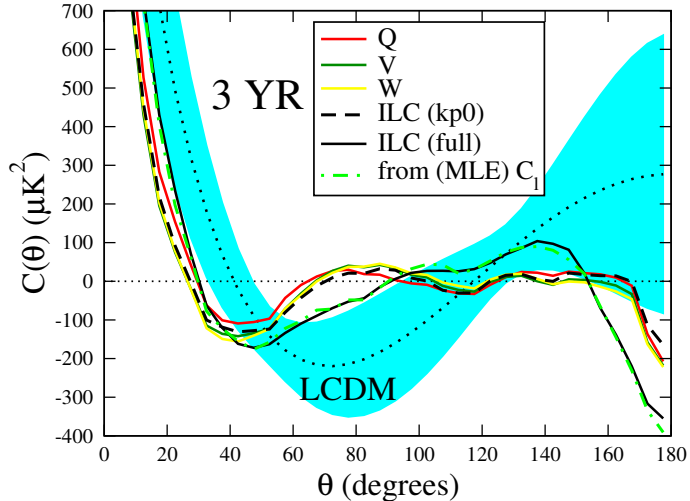


Figure 2: From Copi et al.⁷ two-point correlation function for the three-year WMAP data. The blue band shows the expected range from simulations.

99.8%.⁷

This statistic is of course a prime example of an “invalid” a posteriori statistic, chosen to quantify an already-noticed odd feature in the data, so this confidence level must be interpreted with skepticism. On the other hand, the two-point correlation function is one of the simplest and most natural quantities to compute from a CMB sky map — for many years, in fact, it was the chief way CMB anisotropy was quantified. The qualitative difference between the observed WMAP correlation function and theoretical predictions is therefore intriguing.

If we tentatively assume that the lack of large-scale power does require an explanation, then it is natural to ask what form that explanation might take. We can rule out one broad class of explanations, namely those that involve a statistically independent additive contaminant to the data.^{7,18} The reason is that such a contaminant always biases the expected amount of large-scale power up, rendering the low observed value less likely, not more. It is clear that a contaminant always adds power in an rms sense: the quadrupole (or any other multipole) is simply the quadrature sum of the contributions from the true CMB anisotropy and the contaminant. But I am making the stronger statement that the entire probability distribution shifts in such a way that a low value of the power becomes more improbable (e.g., Figure 3). This statement is true whether the lack of large-scale power is quantified by the observed quadrupole⁷ or by the statistic $S_{1/2}$.¹⁸ It is independent of any assumptions about the statistics of the contaminant, as long as it is independent of the intrinsic CMB anisotropy.

For example, this result rules out an undiagnosed foreground as an explanation for the power deficit. While it is possible that a foreground could cancel the intrinsic large-scale power, such a chance cancellation is always *less* likely than the power coming out low without the contaminant. In fact, if a foreground contaminant is invoked for some other reason (e.g., to explain one of the other anomalies), it will exacerbate the large-scale power deficit problem.

In addition to foreground contaminants, some more exotic models also fall into the category ruled out by this model, such as ellipsoidal models¹⁹, some models with large-scale magnetic fields²⁰, etc.

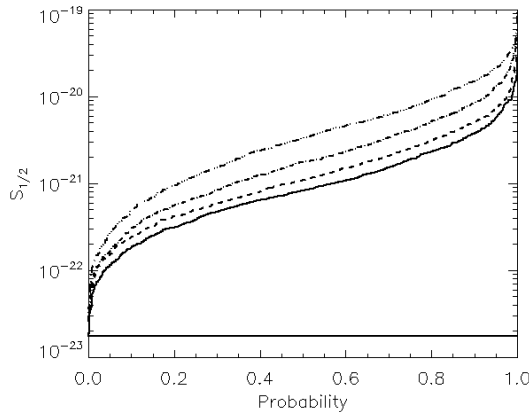


Figure 3: From Bunn & Bourdon¹⁸. The solid curve shows the cumulative probability distribution for the statistic $S_{1/2}$. The dashed curves show the distributions for various anisotropic (ellipsoidal) models. At any given value of $S_{1/2}$, the probability is always largest for the standard model.

3 Hemisphere asymmetry

In the standard cosmological paradigm, CMB anisotropy is generated by a statistically isotropic random process, meaning that all directions should be, on average, identical. However, there appears to be a large-scale modulation in power in the WMAP sky maps: more fluctuation power is seen in one hemisphere than in the opposite hemisphere. Figure 4a illustrates this power asymmetry.

Figure 4b shows an important test of this anomaly performed by Hansen et al.¹⁴. The WMAP data are filtered into non-overlapping ranges of multipoles: $l = 2 - 101, 102 - 201, \dots$. In each case, the direction is found that maximizes the power asymmetry (i.e., maximizing the ratio of power in a hemisphere centered on that direction to power in the opposite hemisphere). In the standard model, these directions should all be independent random variables, but they are clearly closely correlated with each other. Even if the initial detection of a power asymmetry is contaminated by the problem of a posteriori statistics, this close correlation provides a largely independent test that is relatively free of this contamination.

I believe that this test provides strong evidence that the power asymmetry is truly present in the data, but this does not mean that it is cosmological. As indicated in the Figure, the power-maximizing direction is quite close to the south ecliptic pole. If this alignment is not a coincidence, then the hemisphere asymmetry has a local cause, perhaps related to the WMAP scan strategy.

4 Multipole alignments

The alignment of low-order multipoles, especially the quadrupole and octopole ($l = 2, 3$) may have received the most attention of all of the claimed anomalies. For each multipole, one can define a plane in which the fluctuations preferentially lie, using an angular-momentum statistic⁸ or multipole vectors¹⁰. These directions are expected to be independent of each other but are surprisingly closely aligned. In addition, the directions perpendicular to these planes are close to both the CMB dipole and the ecliptic plane (see Figure 5). Depending on which of these surprises one chooses to consider and how one chooses to quantify them, it is easy to get p -values of 10^{-3} or less⁹. (Of course, as with the hemisphere asymmetry, if there is a cosmological explanation for the alignments, then the alignment with the ecliptic must be a mere coincidence.)

Yet again the problem of a posteriori statistics rears its head. The lowest p -values arise from

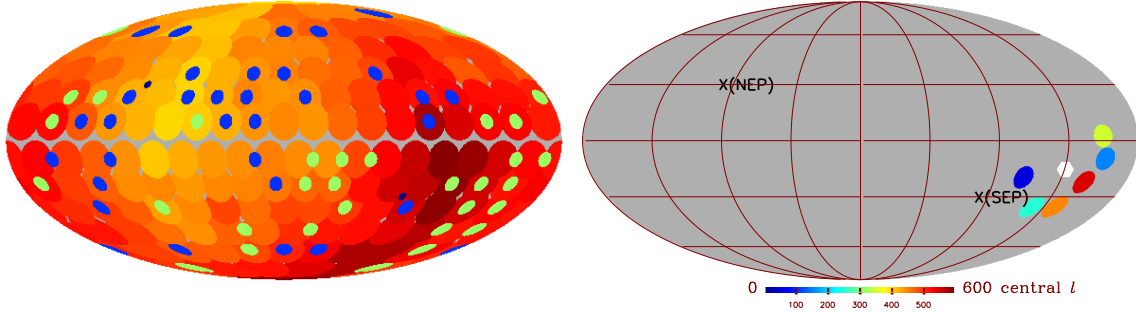


Figure 4: The left panel (from Eriksen et al.¹²) illustrates the hemisphere asymmetry seen in WMAP. The color of each large disk indicates the ratio of power in a hemisphere centered on the disk to power in the opposite hemisphere, considering only multipoles $l = 2-63$. The right panel (from Hansen et al.¹⁴) shows the directions yielding maximum power asymmetry for different ranges of multipoles.

considering alignment of things that have been seen to be aligned. It is difficult to know how to correct this for the various alignments that could have been seen but weren't. Reasonable people can (and do) differ over how much weight to give to the various multipole alignments. In my opinion, it is impossible to be confident that the observed alignments are significant, but it is reasonable to use them to generate hypotheses for future examination and then look for ways to test these hypotheses with new data sets that are independent of the large-angle CMB.

5 Possible explanations and future tests

If we tentatively assume that a given anomaly is “real” (i.e., not merely a statistical fluctuation amplified by an a posteriori statistic), then it is natural to ask what explanations might be possible. Possibilities include systematic errors, foreground contaminants (although not in the case of the power deficit), or more exotic explanations involving new physics. Examples from the latter category are theories that define a preferred direction in space, either through spontaneous isotropy breaking²¹ or by the presence of a vector field during inflation²².

Because the alternative theories generally have additional free parameters (and usually include the standard model as a limiting case), they typically can provide better fits to the data. A model selection criterion is required to decide whether the improved goodness of fit is worth the “cost” of a more complex theory. Perhaps the most natural such criterion is the Bayesian evidence ratio^{23,24,25,26,27,28,29}, which is essentially the factor by which the posterior probability ratio of two theories is increased, in comparison to the prior ratio, by the acquisition of the new data. The evidence ratio automatically disfavors complicated theories (i.e., those with large parameter spaces) unless the improvement in fit is correspondingly large; in other words, it automatically incorporates a form of Occam's razor. Recent work^{26,29} has attempted to quantify the Bayesian evidence ratios for certain classes of theories. Figure 6 illustrates an example, in which we quantify the degree to which the quadrupole-octopole alignment improves the likelihood of spontaneous isotropy breaking and preferred direction models. Although the evidence ratios exceed 1, indicating that the more complicated models go up in probability as a result of the multipole alignment, the improvement is extremely modest. In general, one does not pay much attention to Bayesian evidence ratios unless they are far larger than these values²³.

Because of the uncertainties surrounding the interpretation of the statistics of the various CMB anomalies, they should be regarded chiefly as potentially useful guides in formulating hypotheses for further testing. The essential next step, therefore, is to find new data sets that can be used to test any such hypotheses. To be specific, we need to find data sets that probe comparable physical scales to the large-angle CMB (i.e., gigaparsec scales in comoving

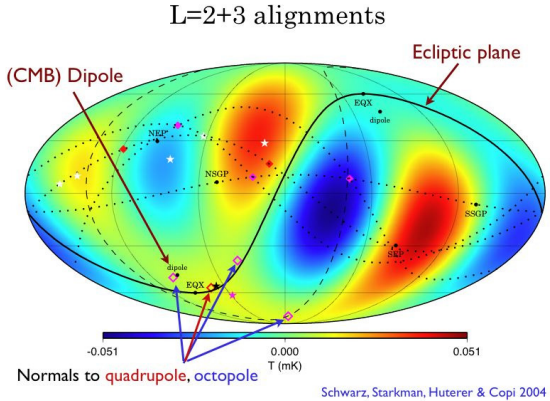


Figure 5: From Schwarz et al.⁹ The quadrupole plus octupole of the WMAP data. Several directions that can be computed from these multipoles are indicated, along with the orientations of the ecliptic and dipole.

coordinates) but that are independent of the CMB anisotropy modes, which have already been measured to the cosmic-variance limit. Finding such data sets is nontrivial, of course, but it may not be impossible.

The first natural place to look is to CMB polarization. For any given anomaly, one can imagine devising (a priori) statistical tests to be performed on polarization maps to look for the anomaly's presence. For example, one can compute the two-point correlation function of a map of E-type CMB polarization, and see if it shows the same lack of large-angle power as the temperature anisotropy. Because there are correlations between temperature and E polarization, this is not, strictly speaking, an independent test, but in practice it is nearly so: as Figure 7 shows, the predicted probability distribution for an $S_{1/2}$ statistic computed from a polarization map is essentially independent of the value of $S_{1/2}$ for temperature. When CMB polarization data are good enough to allow reliable estimation of the correlation function, we can compute $S_{1/2}$. If it is anomalously low, then we have found independent evidence that this puzzle requires an explanation.

Unfortunately, this test is likely to be of less value than it might initially appear: the bulk of the large-angle power in CMB polarization data comes from photons that last scattered at low redshift (after reionization), and hence probes far smaller length scales than the corresponding temperature data. Thus even if there is a cosmological explanation for the lack of large-scale temperature correlations, we would probably not expect to find confirmation of it in polarization. The same conclusion would likely apply to tests of other anomalies. A polarization map does in principle contain information on large length scales that is independent of the temperature data, but it is not obvious (at least to me) that this information can be separated from the reionization signal in a way that would allow a clear test of the anomalies.

There are other possibilities for independent probes of perturbations on gigaparsec scales. Since the CMB anisotropy primarily probes the surface of last scattering, methods that sample the interior of our horizon volume will generically provide independent data sets. One method that might prove promising in the future is the Kamionkowski-Loeb effect:³⁰ by measuring the polarization of the Sunyaev-Zel'dovich-scattered photons coming from a galaxy cluster, one can infer the CMB temperature quadrupole measured at that cluster's location and look-back time. A sample of such cluster measurements can be used to reconstruct modes on length scales corresponding to the CMB modes at $l \sim 5$.^{31,32} This is a challenging task, but the generation of telescopes currently being developed, such as SPTPol and ACTPol, are capable of achieving it.

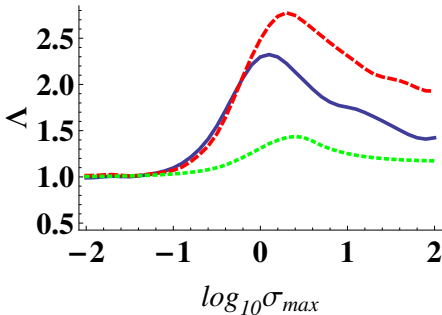


Figure 6: An illustration of the use of Bayesian evidence to decide whether anomalies in the data warrant adoption of a more complicated model. The quantity plotted is the Bayesian evidence ratio comparing various anisotropic models (two based on the idea of spontaneous isotropy breaking and one involving a preferred direction during inflation) with the standard model. The statistic used in computing the evidence ratio is based on the multipole vector method of quantifying quadrupole-octopole alignment. For further details, see Zheng & Bunn.²⁹

6 Conclusions

The subject of large-angle CMB anomalies remains controversial, largely because of the difficulty in interpreting a posteriori statistics. While reasonable people can and do conclude that the correct attitude is to dismiss the subject entirely, I believe that a more nuanced view is appropriate, in which we view some anomalies as providing hints of possible new directions to explore. With this attitude, it is of course essential to seek rigorous tests of any hypotheses generated. Such tests may be difficult but not impossible to find.

Acknowledgments

This work was supported by US National Science Foundation Awards 0507395 and 0908319. I thank the Laboratoire Astroparticule-Cosmologie of the Université Paris VII for their hospitality during some of the time this work was prepared.

References

1. G. Hinshaw *et al.*, *Astrophys. J. Supp.* **148**, 135 (2003).
2. C. L. Bennett *et al.*, arXiv:astro-ph/0302207 (2003).
3. G. Hinshaw *et al.*, *Astrophys. J. Supp.* **170**, 288 (2007).
4. N. Jarosik *et al.*, arXiv:1001.4744 (2010).
5. D. Larson *et al.*, arXiv:1001.4635 (2010).
6. E. Komatsu *et al.*, arXiv:1001.4538 (2010).
7. C. J. Copi *et al.*, *Phys. Rev. D* **75**, 023507 (2007).
8. A. de Oliveira-Costa *et al.*, *Phys. Rev. D* **69**, 063516 (2004).
9. D. J. Schwarz *et al.*, *Phys. Rev. Lett.* **93**, 221301 (2004).
10. C. J. Copi, D. Huterer and G. D. Starkman, *Phys. Rev. D* **70**, 043515 (2004).
11. A. Hajian, astro-ph/0702723 (2007).
12. H. K. Eriksen *et al.*, *Astrophys. J.* **605**, 14 (2004).

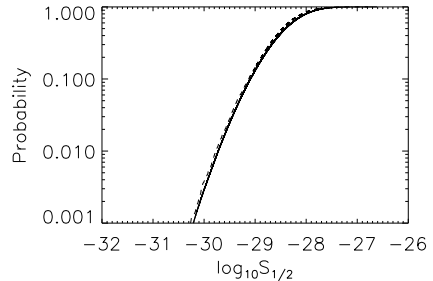


Figure 7: The cumulative probability distribution of the statistic $S_{1/2}$ for E-mode polarization, as predicted by the standard model. The solid curve shows the overall probability distribution, derived from simulations based on a standard Λ CDM model. The dashed curve is the probability distribution conditioned on extremely low values (first percentile) of the *temperature* $S_{1/2}$ statistic. The close correspondence of the curves shows that a low value of $S_{1/2}$ for polarization may be regarded as independent, to a good approximation, of the measurement of a low $S_{1/2}$ in temperature.

13. P. E. Freeman *et al.*, *Astrophys. J.* **638**, 1 (2006).
14. F. K. Hansen *et al.*, *Astrophys. J.* **704**, 1448 (2009).
15. C. L. Bennett *et al.*, arXiv:1001.4758 (2010).
16. G. F. Smoot *et al.*, *Astrophys. J. Lett.* **396**, L1 (1992).
17. D. N. Spergel *et al.*, *Astrophys. J. Supp.* **148**, 175 (2003).
18. E. F. Bunn and A. Bourdon, *Phys. Rev. D* **78**, 123509 (2008).
19. L. Campanelli, P. Cea and L. Tedesco, *Phys. Rev. Lett.* **97**, 131302 (2006).
20. J. D. Barrow, P. G. Ferreira and J. Silk, *Phys. Rev. Lett.* **78**, 3610 (1997).
21. C. Gordon *et al.*, *Phys. Rev. D* **72**, 103002 (2005).
22. L. Ackerman, S. M. Carroll and M. B. Wise, *Phys. Rev. D* **75**, 083502 (2007).
23. H. Jeffreys, *Theory of Probability* (Oxford University Press, 1961).
24. K. Land and J. Magueijo, *Mon. Not. Royal Astron. Soc.* **378**, 153 (2007).
25. H. K. Eriksen *et al.*, *Astrophys. J. Lett.* **660**, L81 (2007).
26. J. Hoftuft *et al.*, *Astrophys. J.* **699**, 985 (2009).
27. A. R. Liddle, *Mon. Not. Royal Astron. Soc.* **377**, L74 (2007).
28. G. Efstathiou, *Mon. Not. Royal Astron. Soc.* **388**, 1314 (2008).
29. H. Zheng and E. F. Bunn, arXiv:1003.5548 (2010).
30. M. Kamionkowski and A. Loeb, *Phys. Rev. D* **56**, 4511 (1997).
31. E. F. Bunn, *Phys. Rev. D* **73**, 123517 (2006).
32. L. R. Abramo and H. S. Xavier, *Phys. Rev. D* **75**, 101302 (2007).

DESPERATELY SEEKING NON-GAUSSIANITY IN THE COSMIC MICROWAVE BACKGROUND ^a

GRAZIANO ROSSI

Korea Institute for Advanced Study, Hoegiro 87, Dongdaemun-Gu, Seoul 130 – 722, Korea



The statistics of pixels above or below a temperature threshold (excursion sets) is a powerful tool for studying departures from Gaussianity in Cosmic Microwave Background (CMB) maps, since there are no free parameters involved. Using a large set of simulated full-sky realizations with different levels of the non-linearity parameter f_{NL} , we compute the spatial distribution and clustering of pixels above/below threshold. We find an enhancement in the clustering of cold excursion set regions, which increases linearly with f_{NL} and is particularly sensitive at angular scales of about 75 arcmin. We provide analytical insights of this effect in the limit of weak non-Gaussianity, using the Edgeworth expansion. We also propose several statistical tests to maximize the detection of a local primordial non-Gaussian signal, including an optimal selection of the threshold level.

1 Gaussianity or non-Gaussianity?

Studies on primordial non-Gaussianity are currently very topical in cosmology, since data from the Wilkinson Microwave Anisotropy Probe (WMAP)² seem to disfavor a Gaussian scenario.^{3,4} However, a clear detection of non-Gaussianity is still missing, while a variety of anomalies have been reported in the literature.^{5,6,7} In a previous work, we also pointed out an interesting feature present in the CMB anisotropy, which cannot be explained in the context of Gaussian random fields: a striking difference in the clustering between hot and cold CMB pixels above (or below) a fixed temperature level.⁸ Cold temperature patches seem to cluster more than hot excursion sets regions, at relatively large angular scales. Is this a distinct manifestation of primordial non-Gaussianity? Here we provide an answer, by constructing simulated non-Gaussian maps and by performing a thorough pixel clustering analysis. Some analytical understanding is also developed: the excursion sets statistics, well-defined in the framework of Gaussian random fields,⁹ is extended to models with primordial non-Gaussianity of the local type.¹⁰ On a general

^aTitle freely inspired from a paper by Press & Rybicki (1997).¹

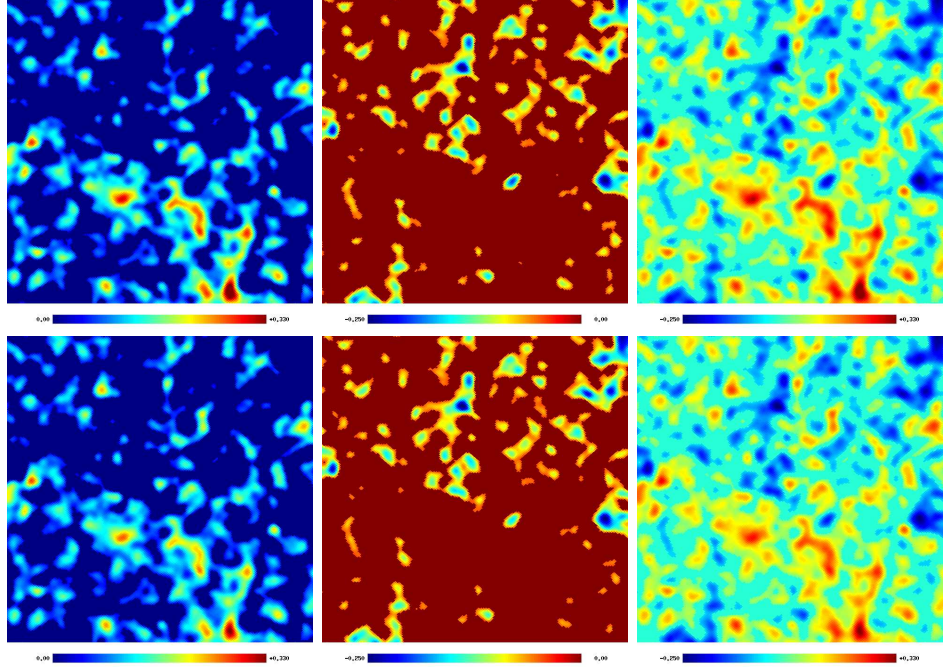


Figure 1: A $\sim 10^\circ \times 10^\circ$ patch of the simulated CMB sky with primordial Gaussianity [top panels], and with primordial non-Gaussianity of the local type when $f_{\text{NL}} = 500$ [bottom panels], smoothed with a Gaussian beam of 30'. Regions below $\nu = 0.50$ [left panels], above $\nu = -0.50$ [central panels], or both below $\nu = 0.50$ and above $\nu = -0.50$ [right panels] are set to zero. The temperature scale is in mK, ranging from -0.250 to +0.330.

ground, it is imperative not to assume *a posteriori* statistics based on some previous knowledge of the expected type of non-Gaussianity; rather, the correct strategy is to select an *a priori* method, and then test its effectiveness on a real (or simulated) data set. Deviations from Gaussianity are important, as they can potentially open new windows into the physics of the very early-universe, and affect significantly the large-scale structure pattern.

2 Simulating non-Gaussianity

Non-Gaussian simulations of the CMB temperature anisotropy are constructed as explained in Chingangbam & Park (2009).¹¹ The key point of the procedure is to calculate the standard spherical harmonic coefficients $a_{\ell m}$ as an integral in real, rather than in Fourier space. Figure 1 shows an example of a $\sim 10^\circ \times 10^\circ$ patch of the sky. Top panels are Gaussian realizations, while in the bottom panels $f_{\text{NL}} = 500$. A Gaussian smoothing with a FWHM of 30 arcmin is applied. Regions below the temperature threshold $\nu = \delta/\sigma = 0.50$ (left panels), above $\nu = -0.50$ (central panels), or both below and above the two thresholds (right panels) are set to zero. Differences between the Gaussian and the non-Gaussian scenarios are minimal; hence, the main challenge is to devise statistical techniques which amplify such small differences.

3 Excursion sets statistics: the *a priori* method

3.1 Basic theory

In presence of weak non-Gaussianity of the local f_{NL} type, the number density of excursions set pixels is given by:

$$n_{\text{pix}}^{\text{NG}}(\nu) = \frac{N_{\text{pix,tot}}}{4\pi} \cdot \left\{ \frac{\text{erfc}(\nu/\sqrt{2})}{2} + \frac{\sigma S^{(0)}}{6\sqrt{2\pi}} (\nu^2 - 1) e^{-\nu^2/2} \right\}. \quad (1)$$

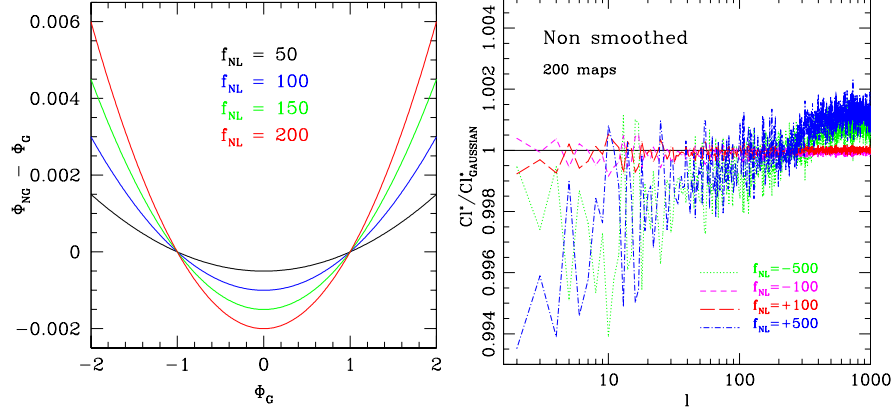


Figure 2: [Left] Difference between Gaussian and non-Gaussian potentials, as a function of the local non-linearity parameter f_{NL} . [Right] Average power spectrum extracted from 200 simulated maps, expressed in units of the corresponding Gaussian power spectrum. Four different values of f_{NL} are shown, as indicated in the figure.

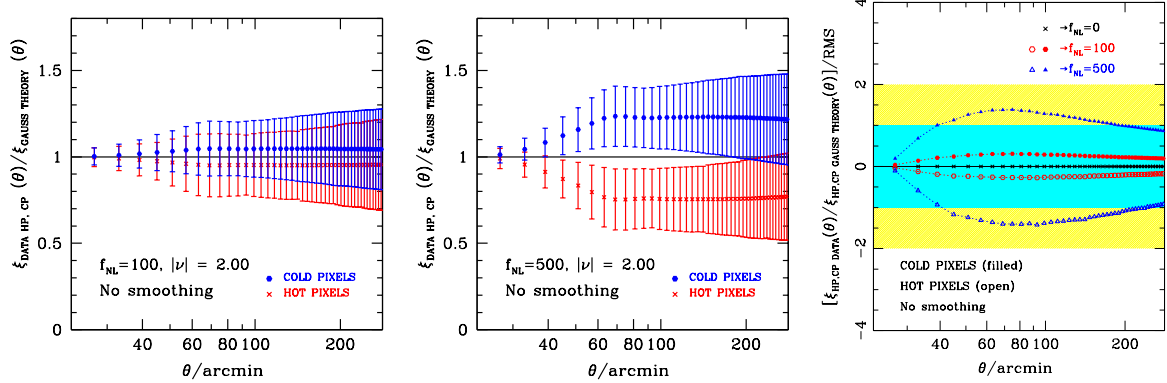


Figure 3: Measurements of the hot (cold) pixel clustering above (below) threshold, from the simulated maps. [Left and central] Non-Gaussian correlations when $f_{NL} = 100$ and 500 , normalized by the expectations from a Gaussian signal. [Right] Same as the previous two panels, but in rms units. There is a 2σ effect when $f_{NL} = 500$.

The underlying one-dimensional probability distribution function (*pdf*) is then:

$$p(\nu)d\nu \sim \frac{1}{\sqrt{2\pi}}e^{-\nu^2/2} \cdot \left\{ 1 + \frac{\sigma S^{(0)}}{6}\nu(\nu^2 - 3) \right\} d\nu. \quad (2)$$

Using the bivariate Edgeworth expansion is it possible to express similarly $p(\nu_1, \nu_2, \theta)$, the two-dimensional *pdf*. The clustering strength of pixels above/below threshold is then given by:

$$1 + \xi_\nu(\theta) = \int_\nu^\infty d\nu_1 \int_\nu^\infty d\nu_2 p(\nu_1, \nu_2, \theta) / \left[\int_\nu^\infty p(\nu) d\nu \right]^2. \quad (3)$$

3.2 Main results

In Figure 2, the left panel shows the difference between Gaussian and non-Gaussian potentials as a function of f_{NL} . Note the very small scale along the y-axis: this is the reason why it is hard to distinguish between simulated maps with various degrees of non-Gaussianity. The right panel in Figure 2 displays the non-Gaussian power spectrum extracted from the simulated maps and averaged over 200 realizations, in units of the Gaussian one. Unless f_{NL} is large, the power spectrum alone is not a good indicator of non-Gaussianity. Figure 3 displays measurements of the hot and cold pixel clustering above/below threshold, from the simulations. The left and

central panels show correlations when $f_{\text{NL}} = 100$ and 500 , respectively. Those are normalized by the expectations from a Gaussian signal. For positive and large non-Gaussianity, the clustering of the cold pixels is enhanced with respect to that of the hot ones. The effect is of the order of 2σ if $f_{\text{NL}} = 500$, as shown in the right panel of the same figure – in rms units.

4 Future directions

We extended the statistics of the excursion set pixels to models with primordial non-Gaussianity of the local f_{NL} type. This is a powerful method, because there are no free parameters involved. Using simulated maps and some analytic guidance, we characterized the number density and the clustering strength of pixels above/below threshold, in presence of non-Gaussianity. We found a distinct non-Gaussian behavior in the clustering of the hot and cold patches, as shown in Figure 3. This feature is a distinct manifestation of primordial non-Gaussianity (i.e. a peculiar enhancement in the clustering of the cold versus hot excursion set regions), so it can be used to disentangle a Gaussian signal from a non-Gaussian one. Our previous WMAP 5-year data analysis pointed towards this effect,⁸ and it constituted our primary motivation in pursuing this work. Future goals include the study of derived statistics which could minimize cosmic variance, the inclusion of inhomogeneous noise and of other observational artifacts in our simulations, and the applications of the analytic formalism developed here to peaks – rather than pixels. Repeating a similar analysis at the Planck resolution is also the subject of work in progress.

Acknowledgments

Many thanks to Changbom Park and Pravabati Chingangbam for providing the maps of this study, and for many useful discussions. I would also like to thank the organizers of the “45th *Rencontres de Moriond*” for a very nice and fruitful meeting . I acknowledge the use of the *Legacy Archive for Microwave Background Data Analysis (LAMBDA)*, support for which is provided by the National Aeronautics and Space Administration (NASA) Office of Space Science. Some of the results in this work have been derived using the *HEALPix* package.¹²

References

1. Press, W. H., & Rybicki, G. B. 1997, *Astronomical Time Series*, 218, 61
2. Komatsu, E., et al. 2010, arXiv:1001.4538
3. Yadav, A. P. S., & Wandelt, B. D. 2008, *Physical Review Letters*, 100, 181301
4. Smith, K. M., Senatore, L., & Zaldarriaga, M. 2009, *Journal of Cosmology and Astro-Particle Physics*, 9, 6
5. Cruz, M., Martínez-González, E., Vielva, P., Diego, J. M., Hobson, M., & Turok, N. 2008, *MNRAS*, 390, 913
6. Pietrobon, D., Cabella, P., Balbi, A., de Gasperis, G., & Vittorio, N. 2009, *MNRAS*, 682
7. Kim, J., & Naselsky, P. 2010, arXiv:1002.0148
8. Rossi, G., Sheth, R. K., Park, C., & Hernández-Monteagudo, C. 2009, *MNRAS*, 399, 304
9. Bond, J. R. and Efstathiou, G., 1987, *MNRAS*, 226, 655-68
10. Rossi, G., Chingangbam, P., & Park, C. 2010, arXiv:1003.0272
11. Chingangbam, P., & Park, C. 2009, *Journal of Cosmology and Astro-Particle Physics*, 12, 19
12. Górski, K. M. et al., 1999, in Proc. MPA/ESO Conf. “Evolution of Large-Scale Structure: From Recombination to Garching”

PROBING NON-GAUSSIANITIES ON LARGE SCALES IN WMAP5 AND WMAP7 DATA USING SURROGATES

C. RÄTH¹, G. ROSSMANITH¹, G. E. MORFILL¹, A. J. BANDAY^{2,3}, K. M. GÓRSKI^{4,5}

¹*Max-Planck-Institut für extraterrestrische Physik, Giessenbachstr. 1, 85748 Garching, Germany*

²*Centre d'Etude Spatiale des Rayonnements, 9, Av du Colonel Roche, 31028 Toulouse, France*

³*Max-Planck-Institut für Astrophysik, Karl-Schwarzschild-Str. 1, 85741 Garching, Germany*

⁴*Jet Propulsion Laboratory, California Institute of Technology, Pasadena, CA 91109, USA*

⁵*Warsaw University Observatory, Aleje Ujazdowskie 4, 00 - 478 Warszawa, Poland*

Probing Gaussianity represents one of the key questions in modern cosmology, because it allows to discriminate between different models of inflation. We test for large-scale non-Gaussianities in the cosmic microwave background (CMB) in a model-independent way. To this end, so-called first and second order surrogates are generated by first shuffling the Fourier phases belonging to the scales not of interest and then shuffling the remaining phases for the length scales under study. Using scaling indices as test statistics we find highly significant signatures for both non-Gaussianities and asymmetries on large scales for the WMAP data of the CMB. We find remarkably similar results when analyzing different ILC-maps based on the WMAP five and seven year data. Such features being independent from the map-making procedure would disfavor the fundamental principle of isotropy as well as canonical single-field slow-roll inflation - unless there is some undiscovered systematic error in the collection or reduction of the CMB data or yet unknown foreground contributions.

1 Introduction

One of the key questions in cosmology is to probe the Gaussianity of the primordial density fluctuations, because it allows to discriminate between different models of inflation. While the simplest model of inflation, namely single-field slow-roll inflation⁷, predicts that the temperature fluctuations of the cosmic microwave background (CMB) correspond to a (nearly) Gaussian, homogeneous, and isotropic random field, more complex models may give rise to non-Gaussianity (NG). Models in which the Lagrangian is a general function of the inflaton and powers of its first derivative can lead to scale-dependent non-Gaussianities, if the sound speed varies during inflation^{7,8}. Similarly, string theory models that give rise to large non-Gaussianity have a natural scale dependence⁹. Possible deviations from Gaussianity have been investigated in studies based on e.g. the WMAP data of the CMB (see e.g. Komatsu et al.⁷ and references therein) and claims for the detection of non-Gaussianities and other anomalies, like hemispherical power asymmetry, the 'axis of evil', the Cold Spot etc. have been made. However, most of the tests on non-Gaussianities do not take into account any possible scale-dependency. In this contribution we apply the formalism of surrogate data sets, which was recently adapted to CMB data analysis¹⁰, to test for non-Gaussianities on large scales in the WMAP data. Special emphasis is put on a comparison of the WMAP five year data with the WMAP seven year data.

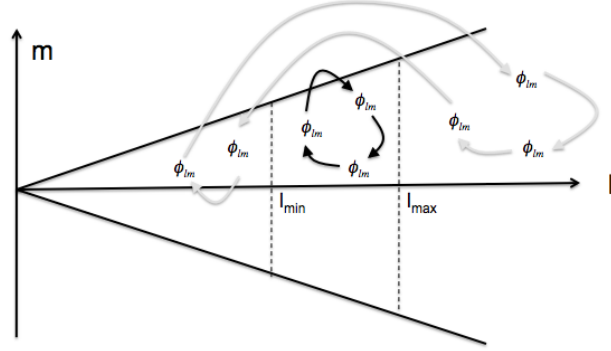


Figure 1: Schematic view of the shuffling procedure on the l - m -plane for generating the first and second order surrogates. The gray arrows indicate the phase permutations for obtaining first order surrogates and the black arrows show the shuffling for making the second order surrogates.

2 Data Sets

We use the foreground-cleaned Internal Linear Combination (ILC) maps generated and provided by the WMAP-team on the basis of the five year (WMAP5)⁷ and seven year (WMAP7)⁷ data. For comparison we also analysed the five year ILC-map (NILC5) produced by Delabrouille et al.⁷, which was generated pursuing a needlet-based approach for removing the foreground contributions.

3 Surrogates and Scaling Indices

The model-independent test for scale-dependent non-Gaussianities is based on the use of so-called surrogate data sets. As test statistics for NGs we use scaling indices. Both methods were introduced and described in detail previously^{7,8,9}. Here, we briefly review the main points of the two formalisms.

3.1 Surrogates

Consider a CMB map $T(\theta, \phi)$, where $T(\theta, \phi)$ is Gaussian distributed, which can easily be achieved by a rank-ordered remapping of the temperatures onto a Gaussian distribution. We calculate the Fourier transform of $T(\theta, \phi)$. The complex valued coefficients a_{lm} , $a_{lm} = \int d\Omega_n T(n) Y_{lm}^*(n)$ can be written as $a_{lm} = |a_{lm}| e^{i\phi_{lm}}$ with $\phi_{lm} = \arctan(Im(a_{lm})/Re(a_{lm}))$. The linear or Gaussian properties of the underlying random field are contained in the absolute values $|a_{lm}|$, whereas all higher order correlations (HOCs) – if present – are encoded in the phases ϕ_{lm} and the correlations among them. To ensure that the distribution of the phases is uniform, we also perform a rank ordered remapping of the phases ϕ_{lm} . To test for scale-dependent NGs we first generate a first order surrogate map, in which any phase correlations for the scales, which are not of interest (here: the small scales), are randomized. This is achieved by a random shuffle of the phases ϕ_{lm} for $l > l_{cut}$, $0 < m \leq l$, where $l_{cut} = 20$ throughout this study and by performing an inverse Fourier transformation. Second, N (here: $N = 500$) realizations of second order surrogate maps are generated for the first order surrogate map, in which the remaining phases ϕ_{lm} with $1 < l \leq l_{cut}$, $0 < m \leq l$ are shuffled while the already randomized phases for the small scales are preserved. In Fig. ?? the phase shuffling procedure for generating first and second order surrogates is schematically visualized.

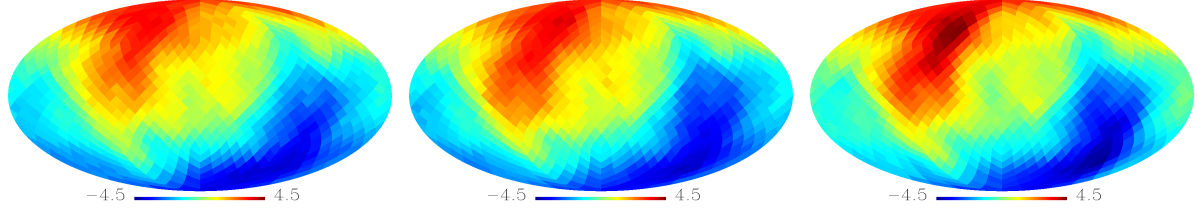


Figure 2: Deviation S as derived from rotated upper hemispheres for $\langle \alpha(r_{10}) \rangle$ for the WMAP5 ILC map (left), the WMAP7 ILC map (middle) and the needlet-based ILC map (right).

3.2 Scaling Indices

To compare the two classes of surrogates, we calculate local statistics in the spatial domain, namely scaling indices (SIM) as described previously^{7,8}. In brief, scaling indices estimate local scaling properties of a point set P . The spherical CMB data can be represented as a three-dimensional point distribution $P = \vec{p}_i = (x_i, y_i, z_i), i = 1, \dots, N_{pixels}$ by transforming the temperature fluctuations into a radial jitter. For each point \vec{p}_i the local weighted cumulative point distribution ρ is calculated $\rho(\vec{p}_i, r) = \sum_{j=1}^{N_{pixels}} e^{-(\frac{d_{ij}}{r})^2}$ with $d_{ij} = \|\vec{p}_i - \vec{p}_j\|$. The weighted scaling indices $\alpha(\vec{p}_i, r)$ are then obtained by calculating the logarithmic derivative of $\rho(\vec{p}_i, r)$ with respect to r , $\alpha(\vec{p}_i, r) = \frac{\partial \log \rho(\vec{p}_i, r)}{\partial \log r}$. Using the above-given expression for the local weighted cumulative point distribution ρ , the following analytical formula for the scaling index α

$$\alpha(\vec{p}_i, r) = \frac{\sum_{j=1}^N 2(\frac{d_{ij}}{r})^2 e^{-(\frac{d_{ij}}{r})^2}}{\sum_{j=1}^N e^{-(\frac{d_{ij}}{r})^2}} \quad (1)$$

is obtained. For each pixel we calculated scaling indices for ten different scales, $r_1 = 0.025, \dots, r_{10} = 0.25$ in the notation of Räth et al.⁷.

4 Results

For each scale we calculate the mean ($\langle \alpha \rangle$) of the scaling indices $\alpha(\vec{p}_i, r)$ derived from a set of pixels belonging to rotated hemispheres. The differences of the two classes of surrogates are then quantified by the σ -normalised deviation $S(Y) = (Y_{surro1} - \langle Y_{surro2} \rangle) / \sigma_{Y_{surro2}}$, $Y = \langle \alpha(\vec{p}_i, r_j) \rangle$, $j = 1, \dots, 10$, surro1: first order surrogate, surro2: second order surrogate. Fig. ?? shows the deviation $S(\langle \alpha(r_{10}) \rangle)$ as derived from pixels belonging to the respective upper hemispheres for 768 rotated reference frames for the three ILC-maps under study. The z-axis of the respective rotated reference frame pierces the center of the respective colour-coded pixel.

Statistically significant signatures for non-Gaussianity and ecliptic hemispherical asymmetries become immediately obvious, whereby the patterns of asymmetry remain remarkably similar for the three maps. Interestingly enough, we obtain slightly larger deviations for the WMAP7 map ($S_{min} = -3.99$, $S_{max} = 3.73$) as compared to the WMAP5 map ($S_{min} = -3.87$, $S_{max} = 3.51$). We find the largest deviation ($S_{min} = -4.36$, $S_{max} = 4.5$) for the NILC map, which can be considered as a more precise full-sky CMB temperature map than the ILC maps generated by the WMAP team⁷. Thus, the level of non-Gaussianity systematically increases, when the underlying CMB-map becomes less noisy and less foreground contaminated.

To quantify the similarity of the patterns of asymmetry in the three maps we calculate the cross-correlation $C(r)$ of the $S(Y)$ -maps derived from the three input maps as a function of the scaling range r . The results are shown in fig. ?? (left). For each scaling range r the three maps are highly correlated among each other with $C(r)$ always being larger than 0.87. The highest correlations are found for the largest scales r , where $C(r)$ reaches values of 0.98 and more. Thus,

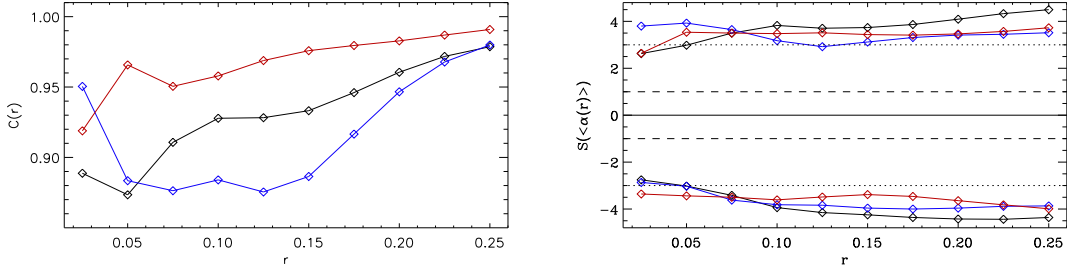


Figure 3: Left side: Cross correlation coefficient $C(r)$ for the $S(Y)$ -maps as a function of the scaling range r . Black: NILC vs. WMAP5, blue: NILC vs. WMAP7 and red: WMAP5 vs. WMAP7. Right side: Minimal and maximal values of the σ -normalized deviations $S(Y)$ for the rotated hemispheres for each scaling range r . Black: NILC, blue: WMAP5 and red: WMAP7.

on all scales r the patterns of asymmetry are very similar for each input map. On the right hand side of fig. ?? we show the minimum and maximum of S as a function of r . Except for the smallest r 's we obtain for each map stable 3σ -deviations for both extrema, where – once again – the NILC map always yields the largest deviations for scaling ranges $r > 0.1$.

5 Conclusions

In conclusion, we detect highly significant signatures for asymmetries and non-Gaussianities for large scales ($l < 20$) in the WMAP five and seven year data. The increase of the signal with decreasing noise as well as the very high correlations between the significance maps points towards an intrinsic nature of the detected anomalies, which are independent of the map making procedure. Such features would disfavor the fundamental principle of isotropy as well as canonical single-field slow-roll inflation – unless there is some undiscovered systematic error in the collection or reduction of the CMB data or yet unknown foreground contributions. Thus, further tests are required to rule out other systematic effects as origin of the detected anomalies.

Acknowledgments

Many of the results in this contribution have been obtained using HEALPix⁷. We acknowledge the use of LAMBDA. Support for LAMBDA is provided by the NASA Office of Space Science. Finally, CR would like to thank the organisers for a very enjoyable meeting.

References

1. A. H. Guth, *Phys. Rev. D* **23**, 347 (1981).
2. C. Armendariz-Picon, T. Damour and V. Mukhanov, *Physics Letters B* **458**, 209 (1999).
3. J. Garriga and V. Mukhanov, *Physics Letters B* **458**, 219 (1999).
4. M. Lo Verde *et al.*, *Journal of Cosmology and Astro-Particle Physics* **4**, 14 (2008).
5. E. Komatsu *et al.*, *Astrophys. J. Suppl. Ser.* **180**, 330 (2009).
6. B. Gold *et al.*, *Astrophys. J. Suppl. Ser.* **180**, 265 (2009).
7. B. Gold *et al.*, arXiv:1001.4555.
8. J. Delabrouille *et al.*, *Astron. & Astrophys.* **493**, 835 (2009).
9. C. Räth *et al.*, *Phys. Rev. Lett.* **102**, 131301 (2009).
10. C. Räth, P. Schuecker and A. J. Banday, *Mon. Not. R. Astron. Soc.* **380**, 466 (2007).
11. G. Rossmanith *et al.*, *Mon. Not. R. Astron. Soc.* **399**, 1921 (2009).
12. K. M. Górski *et al.*, *Astrophys. J.* **622**, 759 (2005).

IMPACT OF A CAUSAL PRIMORDIAL MAGNETIC FIELD ON THE SACHS WOLFE EFFECT

C. BONVIN

CEA, IPhT, URA 2306, F-91191 Gif-sur-Yvette, France.

E-mail: camille.bonvin@cea.fr

We present an analytical derivation of the Sachs Wolfe effect sourced by a primordial magnetic field, generated by a causal process, such as a first order phase transition in the early universe. As for the topological defects case, we apply the general relativistic junction conditions to match the perturbation variables before and after the phase transition, in such a way that the total energy momentum tensor is conserved across the transition. We find that the relevant contribution to the magnetic Sachs Wolfe effect comes from the metric perturbations at next-to-leading order in the large scale limit. The leading order term is strongly suppressed due to the presence of free-streaming neutrinos. We derive the neutrino compensation effect and confirm that the magnetic Sachs Wolfe spectrum from a causal magnetic field behaves as $\ell(\ell + 1) C_\ell^B \propto \ell^2$ as found in the latest numerical analyses.

1 Introduction

The origin of the large scale magnetic fields observed in galaxies and clusters is still unknown: one of the possible explanations is that they have been generated in the primordial universe. A primordial magnetic field of the order of the nanoGauss could leave a detectable imprint in the cosmic microwave background (CMB) anisotropies^{1,2,3,4}. Here we concentrate on its effect on the temperature CMB spectrum at large scales and more particularly on the Sachs Wolfe effect. The motivation is that conflicting results exist in the literature regarding the ℓ -dependence of the Sachs Wolfe effect induced by a causal primordial magnetic field: the analytical analysis of¹ found $\ell(\ell + 1) C_\ell^B$ scaling as ℓ^{-1} or more negative, and the same result was found in the numerical calculation of²; on the other hand,^{3,4,5} found $\ell(\ell + 1) C_\ell^B$ scaling as ℓ^2 . The aim of this paper is to explain this discrepancy analytically (for a more detailed derivation see⁶).

We assume that a magnetic field is generated in the early universe by a sudden phase transition, as for example the electroweak (EW) phase transition. We consider a stochastic magnetic field with no background component and we suppose that the magnetic energy momentum tensor is first order in perturbation theory. We study the effect of the magnetic field on the metric and fluid (matter plus radiation) perturbations by solving analytically Einstein's and conservation equations in the long wavelength limit. We take into account the neutrinos in our derivation. In order to connect the solutions before and after the magnetic field generation, we match the geometry and the fluid variables at the phase transition time, so that the induced three metric and the extrinsic curvature are continuous⁷. This implies the conservation of the total energy momentum tensor across the phase transition, and it completely determines the metric and fluid perturbation variables after the magnetic field generation. Before neutrino decoupling, we find that at leading order in the large scale expansion $k/\mathcal{H} \ll 1$, the metric perturbation Φ

is proportional to $\Phi \propto \Pi_B(\mathcal{H}/k)^2$, where Π_B is the magnetic field anisotropic stress. This induces a contribution in the CMB spectrum scaling as $\ell(\ell+1)C_\ell^B \propto \ell^{-1}$, and consistent with^{1,2}. However, once neutrinos decouple and start free-streaming, they acquire a non-zero anisotropic stress, which acts to compensate and reduce the magnetic field one^{4,8}. We demonstrate that this compensation drastically reduces the leading order contribution to the CMB spectrum, and that the dominant contribution becomes the one from the next-to-leading order in the $k/\mathcal{H} \ll 1$ expansion, which induces then $\ell(\ell+1)C_\ell^B \propto \ell^2$, as found in^{3,4,5}.

2 Solutions for the metric and fluid variables

In this section we solve for the metric and fluid perturbations. We consider only scalar perturbations on a spatially flat Friedmann background, and we work with gauge invariant variables. We consider a stochastic primordial magnetic field with spectral index $n \geq 2$ because of its causal generation⁹: $\langle B_i(\mathbf{k})B_j^*(\mathbf{q}) \rangle = (2\pi)^3\delta(\mathbf{k} - \mathbf{q})(\delta_{ij} - \hat{k}_i\hat{k}_j)A k^n$, where A is the amplitude of the spectrum. We work under the one-fluid MHD approximation, meaning that the conductivity of the universe is high, so that we can neglect the electric field. The magnetic field is characterised by its energy density ρ_B , anisotropic stress π_B and Lorentz force ℓ_B that describes the momentum exchange between the magnetic field and the primordial fluid. These quantities satisfy the relation $\rho_B/2 = \pi_B + 3\ell_B/(2k)$, coming from momentum conservation. To solve for the metric and fluid perturbations, we combine the system of Einstein's and conservation equations into a second order differential equation for the gauge invariant variable D , corresponding to the total (matter plus radiation) density perturbation in the velocity-orthogonal slicing. The equation is

$$\begin{aligned} \ddot{D} + (1 + 3c_s^2 - 6w)\mathcal{H}\dot{D} + 3\mathcal{H}^2 \left[-\frac{1}{2} - 4w + \frac{3}{2}w^2 + 3c_s^2 + \frac{c_s^2}{3} \left(\frac{k}{\mathcal{H}} \right)^2 \right] D = \\ \frac{\mathcal{H}^2}{1+a} \left[2 - 3w + 3c_s^2 - \frac{a}{1+a} - \frac{1}{3} \left(\frac{k}{\mathcal{H}} \right)^2 \right] \Omega_B + \frac{2\mathcal{H}^2}{1+a} \left[1 + 6w - 3c_s^2 + \frac{a}{1+a} + \frac{1}{3} \left(\frac{k}{\mathcal{H}} \right)^2 \right] \Pi_B \\ + 2\mathcal{H}^2 \left[-2w + 3c_s^2 + 3w^2 + \frac{w}{3} \left(\frac{k}{\mathcal{H}} \right)^2 \right] \pi_F - 2\mathcal{H}w\dot{\pi}_F, \end{aligned} \quad (1)$$

where a dot denotes derivative with respect to conformal time η , π_F is the anisotropic stress of the matter plus radiation fluid, $\Omega_B = \rho_B/\rho_{\text{rad}}$ and $\Pi_B = \pi_B/\rho_{\text{rad}}$. To determine the Sachs Wolfe effect, we need to solve this equation for scales which are over the horizon at recombination. Therefore, we can drop the terms proportional to $(k/\mathcal{H})^2$.

We split the universe's evolution in three stages: before magnetic field generation, between magnetic field generation and neutrino decoupling, and after neutrino decoupling. Before magnetic field generation, the universe is filled with matter and radiation only, for which we consider adiabatic initial conditions. Since at early time neutrinos are coupled to photons, their anisotropic stress is zero. Consequently, the two last lines of Eq. (1) vanish and we solve the homogeneous equation for D ¹⁰. At time η_B , the magnetic field is generated by a causal process that we assume to act 'fast', *i.e.* within one Hubble time, as for example a sudden phase transition. After η_B , the second line in Eq. (1) acts as a source for D . We solve it using the Wronskian method. In order to connect the solutions before and after the field generation, we match the variables in such a way that the total energy momentum tensor is conserved across the transition. Following what has been done in⁷ for the analogous case of the topological defects, we find that this matching imposes the continuity of the variables ϕ and V at the phase transition (see Eqs. (36) of⁷). Finally, at time η_ν , neutrinos decouple and start to free stream. They acquire a non-zero anisotropic stress π_ν that acts as a new source term in Eq. (1): $\pi_F = R_\nu\pi_\nu$ (where $R_\nu \equiv \rho_\nu/\rho_{\text{rad}} = 0.4$). Solving Eq. (1) using the Wronskian method requires to know the time evolution of the neutrino anisotropic stress, π_ν . The evolution of π_ν in the presence of an

external constant anisotropic stress has been studied in⁸ (see also⁴). The neutrino anisotropic stress quickly adjusts to the external one and compensates it (see appendix B of⁶ for a detailed derivation of π_ν). The final time dependence of π_ν is rather complicated (Eq. (B.12) of⁶) , but it can be approximated by $\pi_\nu(y) = \frac{3\Pi_B}{R_\nu} \left(\frac{y_\nu^2}{y^2} - 1 \right) - \frac{40a_1}{15+4R_\nu} y(y - y_\nu)$, where $y = \eta/\eta_{\text{rec}}$ and a_1 is related to the amplitude of the primordial potential. With this approximation, we can solve analytically for D .

3 Sachs Wolfe effect at leading order in the long wavelength expansion

With our solution for D valid through the whole universe's history, we compute the metric variables Φ and Ψ and the velocity perturbation V , using Einstein's equations. We then split the fluid into its individual components and solve for the photon density perturbation $D_{g\gamma}$ and velocity perturbation V_γ , using standard adiabatic initial conditions. With this we compute the Sachs Wolfe contribution to the temperature anisotropy at large scales, given by (see *e.g.*¹⁰)

$$\begin{aligned} \frac{\Delta T^B}{T}(k, \eta_0) &\simeq \frac{D_{g\gamma}(k, \eta_{\text{rec}})}{4} + \Psi(k, \eta_{\text{rec}}) - \Phi(k, \eta_{\text{rec}}) \\ &\simeq -\frac{12 \left[4y_{\text{rec}}^2(y_B - 2y_\nu) + y_{\text{rec}}(4y_B + 5y_\nu^2 - 8y_\nu) + 6y_\nu^2 \right] \Pi_B}{y_{\text{rec}}^4(2 + y_{\text{rec}})^3} \frac{\Pi_B}{x_{\text{rec}}^2} \equiv f(y_{\text{rec}}, y_\nu, y_B) \frac{\Pi_B}{x_{\text{rec}}^2}, \end{aligned} \quad (2)$$

where $x_{\text{rec}} \equiv k\eta_{\text{rec}} \ll 1$ for superhorizon scales at recombination. This contribution is proportional to the magnetic field generation time (*e.g.* $y_B \simeq 10^{-12}$ for generation at the EW phase transition), and to the neutrino decoupling time, $y_\nu \simeq 10^{-6}$. It is therefore strongly suppressed: $f(y_{\text{rec}}, y_\nu, y_B) \simeq 10^{-6}$. This contribution corresponds to the effect of the magnetic field anisotropic stress from its time of generation to the neutrino decoupling time. The subsequent magnetic contribution to the Sachs Wolfe effect, arising from y_ν up to recombination time, is cancelled by the free-streaming neutrinos. With the above result we compute the CMB spectrum. Neglecting the integrated Sachs-Wolfe, and using that, for a causal magnetic field with $n \geq 2$, the power spectrum of the magnetic field anisotropic stress is constant in k up to the damping scale k_D ^{1,3,4}

$$\langle \Pi_B(\mathbf{k}) \Pi_B^*(\mathbf{q}) \rangle = (2\pi)^3 \delta(\mathbf{k} - \mathbf{q}) |\Pi_B(k)|^2 \quad \text{with} \quad |\Pi_B(k)|^2 = \bar{\Pi} \frac{\langle B^2 \rangle^2}{\bar{\rho}_{\text{rad}}^2} \frac{1}{k_D^3}, \quad \text{we find}^5 \quad (3)$$

$$\ell(\ell+1)C_\ell^B \simeq f^2(y_{\text{rec}}, y_\nu, y_B) g^2(\eta_{\text{rec}}) \bar{\Pi} \frac{\langle B^2 \rangle^2}{\bar{\rho}_{\text{rad}}^2} \frac{\eta_0}{\eta_{\text{rec}}} \frac{1}{(\eta_{\text{rec}} k_D)^3} \frac{2\ell(\ell+1)}{8\ell^3 + 12\ell^2 - 2\ell - 3}, \quad (4)$$

where $g(y_{\text{rec}})$ denotes the visibility function. Therefore, we find that the CMB spectrum scales as $1/\ell$, as in^{1,2}, rather than as ℓ^2 as found in^{3,4}. The reason why refs.^{3,4} do not find the $1/\ell$ dependence is because the initial conditions that they insert into their Boltzmann code are derived after neutrino decoupling, when the magnetic field anisotropic stress has already been compensated by the neutrino one. Eq. (4) shows that the period of time between magnetic field generation and neutrino decoupling leaves an imprint on the CMB spectrum. This imprint is however much too small to be observable. Therefore, we now proceed to compute analytically the next order contribution in the $k/\mathcal{H} \ll 1$ expansion, that will lead to a ℓ^2 -dependence in the CMB spectrum.

4 Next-to-leading order contribution to the Sachs Wolfe

In order to compute the next-to-leading order contribution to the temperature anisotropy, we need to solve for the metric variables at next-to-leading order in the $k/\mathcal{H} \ll 1$ expansion. The

easiest way to compute this order is to use the curvature perturbation $\zeta \equiv -\Phi + \frac{2}{3(1+w)} \left(\Psi - \frac{\dot{\Phi}}{\mathcal{H}} \right)$. Indeed, starting from the leading order solution that we computed for D , we can calculate the next-to-leading order in the curvature ^a. We use then this solution to compute the next-to-leading order in Φ , by integrating from the definition of ζ . This can be done analytically if we approximate the time evolution of the neutrino anisotropic stress at next-to-leading order as $\pi_\nu(y) = (d_1\Omega_B + d_2\Pi_B)(y - y_\nu)^2 x_{\text{rec}}^2$, where d_1 and d_2 are two arbitrary constants that we determine from the conservation equations of the neutrino and photon fluids. With this, we find for the temperature anisotropy at next-to-leading order $\frac{\Delta T}{T}^B \simeq -0.2\Omega_B - 2.7\Pi_B$.

The energy density spectrum and the cross-correlation one have been calculated in ^{1,3,4}, and they share the same k -dependence as the anisotropic stress spectrum, Eq. (3). Denoting $\bar{\Omega}$ the amplitude of the energy density spectrum and \bar{C} the cross-correlation one, we find for the CMB spectrum

$$\ell(\ell+1)C_\ell^B \simeq g^2(\eta_{\text{rec}}) \left[0.04\bar{\Omega} + 7.29\bar{\Pi} + 0.54\bar{C} \right] \frac{\langle B^2 \rangle^2}{\bar{\rho}_{\text{rad}}^2} \frac{\ell(\ell+1)}{\pi(\eta_0 k_D)^2}. \quad (5)$$

Therefore, we confirm that the next-to-leading order contribution to the Sachs Wolfe effect scales as $\ell(\ell+1)C_\ell^B \propto \ell^2$, as found numerically in ^{3,4}.

5 Conclusion

In this work we present an analytical computation of the Sachs Wolfe effect induced by a primordial magnetic field. We have restricted our analysis to a magnetic field generated by a causal process, such as a first order phase transition. In this case, the initial conditions for the metric and fluid variables are determined unambiguously by imposing conservation of the total energy momentum tensor across the transition. Using these initial conditions, we have computed analytically the leading order and next-to-leading order magnetic contribution to the Sachs Wolfe effect. We have found that the leading order contribution is sourced only by the magnetic field anisotropic stress, and leads to a CMB spectrum scaling as $1/\ell$. However, this contribution is strongly suppressed once the magnetic field anisotropic stress is compensated by the one of the neutrinos. As a consequence, the dominant contribution to the Sachs Wolfe is the next-to-leading order one, that generates a CMB spectrum scaling as ℓ^2 . Our analytical work solves therefore the discrepancy regarding the ℓ -dependence of the magnetic Sachs Wolfe.

References

1. T. Kahnashvili and B. Ratra, *Phys. Rev. D* **75**, 023002 (2007).
2. D.G. Yamazaki, K. Ichiki, T. Kajino and G.J. Mathews, *Phys. Rev. D* **77**, 043005 (2008).
3. D. Paoletti, F. Finelli and F. Paci, *MNRAS* **396**, 523 (2009); F. Finelli, F. Paci and D. Paoletti, *Phys. Rev. D* **78**, 023510 (2008); D.G. Yamazaki, K. Ichiki, T. Kajino and G.J. Mathews, *Phys. Rev. D* **81**, 023008 (2010).
4. J.R. Shaw and A. Lewis, *Phys. Rev. D* **81**, 043517 (2010).
5. C. Caprini, F. Finelli, D. Paoletti and A. Riotto, *JCAP* **0906**, 021 (2009).
6. C. Bonvin and C. Caprini, arXiv:1004.1405.
7. N. Deruelle, D. Langlois and J.P. Uzan, *Phys. Rev. D* **56**, 7608 (1997).
8. K. Kojima, T. Kajino, G.J. Mathews, *JCAP* **1002**, 018 (2010).
9. R. Durrer and C. Caprini, *JCAP* **0311**, 010 (2003).
10. R. Durrer, *The Cosmic Microwave Background*, Cambridge University Press 2008.

^aNote that the magnetic field does not affect the curvature at leading order, $\mathcal{O}(1/x_{\text{rec}}^2)$. It is therefore still conserved on large scales.

Statistical anisotropy in CMB maps

Antony Lewis

Department of Physics & Astronomy, University of Sussex, Brighton BN1 9QH, UK

Duncan Hanson

Institute of Astronomy and Kavli Institute for Cosmology, Madingley Road, Cambridge, CB3 0HA, UK.

Abstract

We describe a nearly optimal method to test for small Gaussian statistical anisotropies in Cosmic Microwave Background temperature maps. We show how to account for realistic sky-coverage, anisotropic instrumental noise, and effects from beam asymmetries, providing a fast and robust method to derive cosmological constraints from real data. We apply our estimators to the WMAP temperature maps: we first constrain an empirically motivated spatial modulation of the observed CMB fluctuations, reproducing marginal evidence for a dipolar modulation pattern with amplitude 7% at $l \lesssim 60$, but demonstrate that the effect decreases at higher multipoles and is $\lesssim 1\%$ at $l \sim 500$. We also look for evidence of a direction-dependent primordial power spectrum, finding no evidence for signal. However accounting for beam asymmetries is crucial to reach this conclusion: we find that the anisotropy due to non-circular beams is highly significant and must be subtracted to infer constraints on the primordial power spectrum.

1 Introduction

The temperature fluctuations of the Cosmic Microwave Background (CMB) are often assumed to be a realization of a statistically isotropic Gaussian random field, in which case the statistical properties of the fluctuations are completely described by the power spectrum $\langle \Theta_{lm} \Theta_{l'm'}^* \rangle = \delta_{ll'} \delta_{mm'} C_l^{\Theta\Theta}$. However there are already tantalizing hints in the WMAP data for violation of statistical isotropy (see e.g. Ref. [1] and references therein). It is therefore important to have robust methods to test the isotropy assumption.

We discuss estimators to constrain Gaussian but anisotropic models, such that the statistics are still fully described by a covariance matrix, but it is no longer diagonal. We shall assume that the off-diagonal terms are perturbatively small, as indicated by the good fit to statistically isotropic models. There are many good reasons to consider such models. Secondary effects that are linear in the CMB temperature result in a guaranteed signal of this form at the $\mathcal{O}(10^{-3})$ level: gravitational lensing [2], patchy reionization [3] and the doppler shifting due to the motion of our frame relative to the CMB, for example, may be thought of in this context and should become observable with the upcoming generation of CMB measurements. Many non-linear effects and non-standard models can be considered as a fixed modulation of an initially Gaussian field, which is still Gaussian but anisotropic if the modulation is considered fixed. More speculatively, recently proposed anisotropic models of inflation could lead to primordial fluctuations that are anisotropic [4, 5].

Assuming that the instrumental noise is also Gaussian, the rigorous approach to an analysis of these models is clear: calculate the log-likelihood \mathcal{L} of the observed CMB, given by

$$-\mathcal{L}(\hat{\Theta}|\mathbf{h}) = \frac{1}{2} \hat{\Theta}^\dagger (\mathbf{C}^{\hat{\Theta}\hat{\Theta}})^{-1} \hat{\Theta} + \frac{1}{2} \ln \det(\mathbf{C}^{\hat{\Theta}\hat{\Theta}}), \quad (1)$$

where \mathbf{h} are parameters characterizing the anisotropy, $\hat{\Theta}$ is the observed CMB and $\mathbf{C}^{\hat{\Theta}\hat{\Theta}} \equiv \mathbf{C}^{\Theta\Theta} + \mathbf{C}^{NN}$ is its covariance, incorporating the theoretical (anisotropic) covariance as well as instrumental noise. In this work, we will take a quadratic estimator approach, expanding the likelihood to low order in the anisotropy. This approach is not a new one: it was originally

discussed for the purpose of lens reconstruction by Ref. [6], and some of the estimators that we will discuss here have also been derived for full-sky coverage as minimum-variance estimators with quadratic form [7, 3, 8, 9]. In this paper we will generalize these estimators for application to real data.

Although we will frame our discussion here on Gaussian but statistically anisotropic models, we note that every statistically anisotropic Gaussian model is related to a statistically isotropic but non-Gaussian model: if there is a preferred direction, taking the direction as being a random variable (e.g. by a random rotation) makes the distribution statistically isotropic at the expense of complicating the statistics [10]. In the statistically isotropic interpretation the anisotropy estimators we discuss would always have zero expectation, but the non-zero disconnected four-point function gives the estimators a variance above that expected for a Gaussian isotropic field, giving an equivalent means of detection.

We shall focus on the CMB temperature, since this is measured with much lower noise than the polarization, especially on smaller scales. This paper summarizes results from Refs. [11, 12].

2 Anisotropy estimators

We begin by introducing the methodology of anisotropy estimation as a likelihood maximization, loosely following Hirata and Seljak who pioneered this approach for CMB lensing [6].

Differentiating the likelihood of Eq. (1) with respect to a set of parameters \mathbf{h} which characterize the anisotropy gives

$$\frac{\delta \mathcal{L}}{\delta \mathbf{h}^\dagger} = -\frac{1}{2} \hat{\Theta}^\dagger (\mathbf{C}^{\hat{\Theta}\hat{\Theta}})^{-1} \frac{\delta \mathbf{C}^{\hat{\Theta}\hat{\Theta}}}{\delta \mathbf{h}^\dagger} (\mathbf{C}^{\hat{\Theta}\hat{\Theta}})^{-1} + \frac{1}{2} \text{Tr} \left[(\mathbf{C}^{\hat{\Theta}\hat{\Theta}})^{-1} \frac{\delta \mathbf{C}^{\hat{\Theta}\hat{\Theta}}}{\delta \mathbf{h}^\dagger} \right]. \quad (2)$$

The trace term results in a “mean field” over realizations of the observed CMB. To see this, consider the identity $\text{Tr}(\mathbf{A}) = \langle \mathbf{x}^\dagger \mathbf{A} \mathbf{C}^{-1} \mathbf{x} \rangle$, where \mathbf{A} is any matrix and \mathbf{x} is a vector of Gaussian random variables with covariance \mathbf{C} . Making this substitution with $\mathbf{C} = \mathbf{C}^{\hat{\Theta}\hat{\Theta}}$ and maximizing the likelihood by setting $\delta \mathcal{L} / \delta \mathbf{h}^\dagger = 0$ gives the simple equation

$$\frac{\delta \mathcal{L}}{\delta \mathbf{h}^\dagger} = \langle \mathcal{H} \rangle - \mathcal{H} = 0, \quad (3)$$

where

$$\mathcal{H} = \frac{1}{2} \left[(\mathbf{C}^{\hat{\Theta}\hat{\Theta}})^{-1} \hat{\Theta} \right]^\dagger \frac{\delta \mathbf{C}^{\hat{\Theta}\hat{\Theta}}}{\delta \mathbf{h}^\dagger} \left[(\mathbf{C}^{\hat{\Theta}\hat{\Theta}})^{-1} \hat{\Theta} \right]. \quad (4)$$

The maximum-likelihood (M-L) point can be determined iteratively using Newton’s method

$$\mathbf{h}_{i+1} = \mathbf{h}_i - \left[\frac{\delta}{\delta \mathbf{h}^\dagger} (\langle \mathcal{H} \rangle - \mathcal{H})^\dagger \Big|_i \right]^{-1} (\langle \mathcal{H} \rangle_i - \mathcal{H}_i), \quad (5)$$

where quantities subscripted with i are evaluated for the estimate \mathbf{h}_i of the i^{th} iteration.

We are working under the assumption that any anisotropy which we will be studying is “weak”, and so a single iteration of Eq. (5), starting from $\mathbf{h} = \mathbf{0}$ should give a sufficiently accurate estimate of \mathbf{h} . For simplicity, the derivative term is replaced with its ensemble average

$$\left\langle \frac{\delta}{\delta \mathbf{h}^\dagger} (\langle \mathcal{H} \rangle - \mathcal{H})^\dagger \right\rangle = \left\langle \frac{\delta}{\delta \mathbf{h}^\dagger} \frac{\delta \mathcal{L}}{\delta \mathbf{h}} \right\rangle = \left\langle \frac{\delta \mathcal{L}}{\delta \mathbf{h}^\dagger} \frac{\delta \mathcal{L}}{\delta \mathbf{h}} \right\rangle = \left[\langle \mathcal{H} \mathcal{H}^\dagger \rangle - \langle \mathcal{H} \rangle \langle \mathcal{H} \rangle^\dagger \right] = \mathcal{F},$$

where \mathcal{F} is the Fisher matrix. Putting all of this together, we have an approximate, quadratic maximum-likelihood (QML) estimator of the form

$$\hat{\mathbf{h}} = \mathcal{F}^{-1} [\tilde{\mathbf{h}} - \langle \tilde{\mathbf{h}} \rangle]. \quad (6)$$

The inverse Fisher matrix can be thought of as the estimator normalization, as well as its covariance in the limit of no anisotropy. The quadratic part of the estimator is given by

$$\tilde{\mathbf{h}} = \mathcal{H}_0 = \frac{1}{2} \bar{\Theta}^\dagger \frac{\delta C^{\hat{\Theta}\hat{\Theta}}}{\delta \mathbf{h}^\dagger} \bar{\Theta} \Big|_{\mathbf{h}=0} = \frac{1}{2} \sum_{lm, l'm'} \left[\frac{\delta C_{lm, l'm'}^{\hat{\Theta}\hat{\Theta}}}{\delta \mathbf{h}^\dagger} \right]_{\mathbf{h}=0} \bar{\Theta}_{lm}^* \bar{\Theta}_{l'm'}, \quad (7)$$

where $\bar{\Theta} = (C^{\hat{\Theta}\hat{\Theta}})^{-1}|_0 \hat{\Theta}$ is the observed sky after application of inverse-variance filtering with $\mathbf{h} = \mathbf{0}$. The inverse-variance filtering can be calculated relatively quickly by using conjugate gradients with a good preconditioner [13, 14]. The resulting quadratic estimator can often be re-cast in a form that can be calculated quickly using real-space filtered fields.

The QML formalism makes it straightforward to construct estimators for any form of Gaussian but statistically anisotropic model which is accurately parameterized as a linear function of a set of parameters \mathbf{h} . The $\langle \tilde{\mathbf{h}} \rangle$ ‘mean field’ term in Eq. (6) is the term that must be subtracted to account for anisotropies of non-cosmological origin. In general it can be evaluated by Monte Carlo simulations, and will include anisotropic effects from non-uniform sky coverage, anisotropic noise, beam asymmetries, and any other relevant systematics. A simple analytic model that can be used to simulate and then subtract the beam asymmetry mean field for WMAP is described in Ref. [12].

We will test the assumption of statistical anisotropy in the WMAP 5-year maps, which are provided in HEALPix format at $N_{\text{side}} = 512$ [15]. The mean field and estimator normalization are generally determined for each data map using Monte-Carlo simulations.

3 Modulation on the sky

A popular form of modulation anisotropy which has been tested in the literature is given by

$$\Theta_f(\hat{\mathbf{n}}) = [1 + f(\hat{\mathbf{n}})]\Theta_f^i(\hat{\mathbf{n}}), \quad (8)$$

where $\Theta_f^i(\hat{\mathbf{n}})$ is some intrinsic statistically isotropic CMB temperature, $f(\hat{\mathbf{n}})$ is a modulating field, and the f subscript denotes restriction to some range of angular scales (e.g. $l \leq l_{\text{max}}$). The dipole part of $f(\hat{\mathbf{n}})$ has received particular attention since the work of Ref. [16], which found evidence for a large-scale hemispherical power asymmetry in the WMAP data. This pathfinding work was followed by more rigorous likelihood analyses [17, 18, 19], and recently Refs. [20, 21] have extended the analysis to smaller angular scales, arguing for increased detection significance as more data is added. Previous analyses were limited by computational requirements to multipoles $l \leq 80$, but with the QML estimator no such difficulties arise, so we can extend our analysis to the limit of current observations. We apply our QML estimators to estimate f_{1m} , the dipole components of the modulation field (we find no evidence for anomalies in the other low moments). Our results for $l_{\text{max}} \lesssim 60$ show some evidence for a $\sim 7\%$ dipole modulation in the direction of $(l, b) = (225^\circ, -22^\circ) \pm 24^\circ$, but only at $\mathcal{O}(99\%)$ significance (not accounting for the a posteriori choices). We have tested that the apparent dipolar modulation of low multipoles cannot be explained by the cold spot or other anomalies at $l < 10$. However we find that the large modulation indicated by the low- l data does not persist on smaller scales, constraining the modulation to $\lesssim 1\%$ at $l \sim 500$, consistent with the tight constraint on the anisotropy in the quasar distribution [22].

4 Primordial Power Anisotropy

Refs. [5, 4, 23] consider anisotropic models of the early universe, where at late times the universe isotropizes so that the only evidence is an angular-dependent power spectrum on large scales: the primordial spectrum $\mathcal{P}_\chi(\mathbf{k})$ depends on the direction of \mathbf{k} and not just the magnitude.

Again we can apply our QML estimators to constrain the anisotropy parameters, in this case the multiple moments of $\mathcal{P}_\chi(\mathbf{k})$. If we exclude beam asymmetry effects from the mean-field term, we find a highly significant quadrupolar signal aligned with the ecliptic plane [11]. This arises because of a similarity in form between anisotropies generated by beams and the anisotropy due to an anisotropic primordial power spectrum, with the preferred direction of the beam signal being set by the symmetry of the WMAP scanning strategy. However when we include beam asymmetries in the mean field subtraction, the quadrupolar signal is consistent with isotropy (except in W4, where we find an additional asymmetry that can be explained as due to noise correlations). We can constrain any component of a quadrupolar primordial power spectrum to be less than 7%, so there is no evidence for statistical anisotropy in the primordial power spectrum.

References

- [1] C. L. Bennett et al. Seven-Year Wilkinson Microwave Anisotropy Probe (WMAP) Observations: Are There Cosmic Microwave Background Anomalies? 2010.
- [2] Antony Lewis and Anthony Challinor. Weak gravitational lensing of the cmb. *Phys. Rept.*, 429:1–65, 2006.
- [3] Cora Dvorkin and Kendrick M. Smith. Reconstructing Patchy Reionization from the Cosmic Microwave Background. *Phys. Rev.*, D79:043003, 2009.
- [4] A. E. Gümrükçüoğlu, Carlo R. Contaldi, and Marco Peloso. Inflationary perturbations in anisotropic backgrounds and their imprint on the CMB. *JCAP*, 0711:005, 2007.
- [5] Lotty Ackerman, Sean M. Carroll, and Mark B. Wise. Imprints of a Primordial Preferred Direction on the Microwave Background. *Phys. Rev.*, D75:083502, 2007.
- [6] Christopher M. Hirata and Uros Seljak. Analyzing weak lensing of the cosmic microwave background using the likelihood function. *Phys. Rev.*, D67:043001, 2003.
- [7] Cora Dvorkin, Hiranya V. Peiris, and Wayne Hu. Testable polarization predictions for models of CMB isotropy anomalies. *Phys. Rev.*, D77:063008, 2008.
- [8] Anthony R. Pullen and Marc Kamionkowski. Cosmic Microwave Background Statistics for a Direction- Dependent Primordial Power Spectrum. *Phys. Rev.*, D76:103529, 2007.
- [9] Cristian Armendariz-Picon. Footprints of Statistical Anisotropies. *JCAP*, 0603:002, 2006.
- [10] Pedro G. Ferreira and Joao Magueijo. The closet non-Gaussianity of anisotropic Gaussian fluctuations. *Phys. Rev.*, D56:4578–4591, 1997.
- [11] Duncan Hanson and Antony Lewis. Estimators for CMB Statistical Anisotropy. *Phys. Rev.*, D80:063004, 2009.
- [12] Duncan Hanson, Antony Lewis, and Anthony Challinor. Asymmetric Beams and CMB Statistical Anisotropy. 2010.
- [13] Siang Peng Oh, David N. Spergel, and Gary Hinshaw. An Efficient Technique to Determine the Power Spectrum from Cosmic Microwave Background Sky Maps. *Astrophys. J.*, 510:551, 1999.
- [14] Kendrick M. Smith, Oliver Zahn, and Olivier Dore. Detection of gravitational lensing in the cosmic microwave background. *Phys. Rev.*, D76:043510, 2007.

- [15] G. Hinshaw et al. Five-Year Wilkinson Microwave Anisotropy Probe (WMAP) Observations: Data Processing, Sky Maps, & Basic Results. *Astrophys. J. Suppl.*, 180:225–245, 2009.
- [16] Frode K. Hansen, A. J. Banday, and K. M. Gorski. Testing the cosmological principle of isotropy: local power spectrum estimates of the WMAP data. *Mon. Not. Roy. Astron. Soc.*, 354:641–665, 2004.
- [17] D. N. Spergel et al. Wilkinson Microwave Anisotropy Probe (WMAP) three year results: Implications for cosmology (v1). 2006.
- [18] Christopher Gordon. Broken Isotropy from a Linear Modulation of the Primordial Perturbations. *Astrophys. J.*, 656:636–640, 2007.
- [19] Hans K. Eriksen, A. J. Banday, K. M. Gorski, F. K. Hansen, and P. B. Lilje. Hemispherical power asymmetry in the three-year Wilkinson Microwave Anisotropy Probe sky maps. *Astrophys. J.*, 660:L81–L84, 2007.
- [20] F. K. Hansen, A. J. Banday, K. M. Gorski, H. K. Eriksen, and P. B. Lilje. Power Asymmetry in Cosmic Microwave Background Fluctuations from Full Sky to Sub-degree Scales: Is the Universe Isotropic? 2008.
- [21] J. Hoftuft et al. Increasing evidence for hemispherical power asymmetry in the five-year WMAP data. *Astrophys. J.*, 699:985–989, 2009.
- [22] Christopher M. Hirata. Constraints on cosmic hemispherical power anomalies from quasars. 2009.
- [23] Nicolaas E. Groeneboom and Hans Kristian Eriksen. Bayesian analysis of sparse anisotropic universe models and application to the 5-yr WMAP data. *Astrophys. J.*, 690:1807–1819, 2009.

Λ CDM and the WMAP power spectrum beam profile sensitivity

Utane Sawangwit & Tom Shanks

*Department of Physics, Durham University, South Road,
Durham DH1 3LE, England*

We first discuss the sensitivity of the WMAP CMB power spectrum to systematic errors by calculating the raw CMB power spectrum from WMAP data. We find that the power spectrum is surprisingly sensitive to the WMAP radiometer beam profile even at the position of the first acoustic peak on ≈ 1 degree scales. Although the WMAP beam profile core is only $12.6'$ FWHM at W, there is a long power-law tail to the beam due to side-lobes and this causes significant effects even at the first peak position. We then test the form of the beam-profile used by the WMAP team which is based on observations of Jupiter. We stacked radio source beam profiles as observed in each WMAP band and found that they showed a wider profile in Q, V, W than the Jupiter profile. We have now checked that this is not due to any Eddington or other bias in our sample by showing that the same results are obtained when radio sources are selected at 1.4GHz and that our methods retrieve the Jupiter beam when it is employed in simulations. Finally, we show that the uncertainty in the WMAP beam profile allows the position as well as the amplitude of the first peak to be changed and how this could allow simpler cosmologies than standard Λ CDM to fit the CMB data.

1 Introduction

The standard Λ CDM cosmological model is a quite perplexing mixture of impressive observational successes (e.g. Hinshaw *et al.*¹, Komatsu *et al.*², Hicken *et al.*³, Kessler *et al.*⁴) coupled with wider implications which make the model complicated to the point of implausibility (eg Weinberg⁵). Some fundamental and astrophysical issues for the standard model are as follows:

- The exotic, weakly interacting, particles envisaged as candidates for the dark matter component of the standard model are still undetected in the laboratory (eg Aprile *et al.*⁶).
- The inclusion of a cosmological constant means that ratio of the vacuum energy density to the radiation energy density after inflation is 1 part in 10^{100} , a fine-tuning coincidence which leads to appeals to the anthropic principle for an explanation (eg Efstathiou⁷).
- Even if fine-tuning arguments are regarded as unsatisfactory, the problem is that inflation was set up to get rid of fine-tuning in terms of the ‘flatness’ problem (Guth⁸) and so the introduction of more fine-tuning with the cosmological constant appears circular.
- Λ has the wrong sign for string theorists who prefer a negative Λ than a positive Λ , ie a cosmology which is approximately Anti-de Sitter rather than de Sitter (eg Witten⁹).
- The standard inflationary model predicts not just one but $10^{10^{77}}$ Universes (Steinhardt¹⁰).

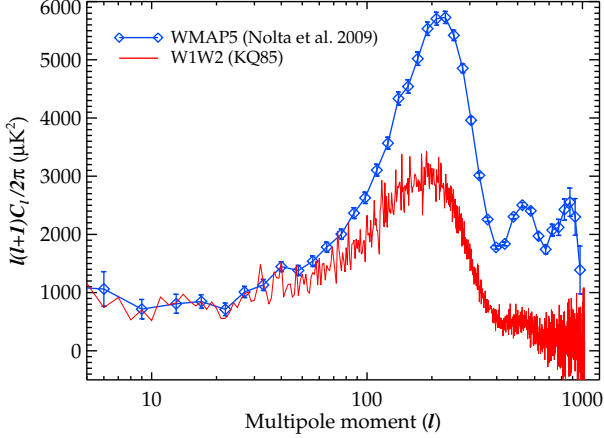


Figure 1: The red line shows the raw WMAP W band power spectrum estimated from the cross-correlation of the WMAP5 W1 and W2 maps. The blue diamonds + line shows the final WMAP5 spectrum after ‘de-beaming’ using the Jupiter beam(+‘cut-sky’ correction). The large effect of de-beaming even at the first acoustic peak ($\approx 1\text{deg}$) is caused by beam sidelobes, even though the beam’s Gaussian core has a width of only $12.^{\circ}6$ FWHM.

- Astrophysically, any CDM model in the first instance predicts a featureless mass function for galaxies whereas the galaxy luminosity function shows a sharp ‘knee’ feature (eg Benson *et al.*¹¹).
- CDM models predict that large structures should form last and therefore should be young whereas, observationally, the largest galaxies and clusters appear old (eg Cowie *et al.*¹²).
- To fix the above two problems, large amounts of feedback (eg Bower *et al.*¹³) are invoked which results in more energy now being used to prevent stars forming than in forming them under gravity.

2 WMAP CMB Power Spectrum

The above issues mean that the standard model requires remarkable observations in its support and the most remarkable of these is represented by the acoustic peaks in the CMB power-spectrum as measured by WMAP (eg Hinshaw *et al.*¹⁴) and other CMB experiments. Much therefore depends on the accuracy of these observations and in particular on the position of the first acoustic peak at wavenumber $l=220$ or $\approx 1\text{deg}$. A first peak at scales as large as these strongly favours a CDM model. Attempts have been made to move the first peak using cosmic foregrounds such as large clusters via the SZ effect (Myers *et al.*¹⁵, Bielby *et al.*¹⁶) or gravitational lensing (Shanks¹⁷) or even inhomogeneous reionisation at $z \approx 10$ but generally the effects have been small.

At first sight, it seems unlikely that any observational effect of the resolution of CMB radiometers such as those used by WMAP on the position and amplitude of the first peak could be significant. The highest resolution of the WMAP satellite comes at the 94GHz W band where the core of the beam profile has $12.^{\circ}6$ FWHM (eg Page *et al.*¹⁸) and it seems unlikely that such a narrow beam profile would have an effect at the ≈ 1 degree scale of the first peak. However, Sawangwit and Shanks¹⁹ have recalculated the WMAP5 power spectrum, C_l , by cross-correlating the maps from the W1 and W2 detectors as an example. This raw spectrum is compared in Fig. 1 to the WMAP5 spectrum that is usually fitted by the standard model and large differences can be seen even at the scale of the first acoustic peak, where the raw spectrum is a factor of ≈ 2 lower than expected. Most of the reason for this difference ($\approx 70\%$) is the effect

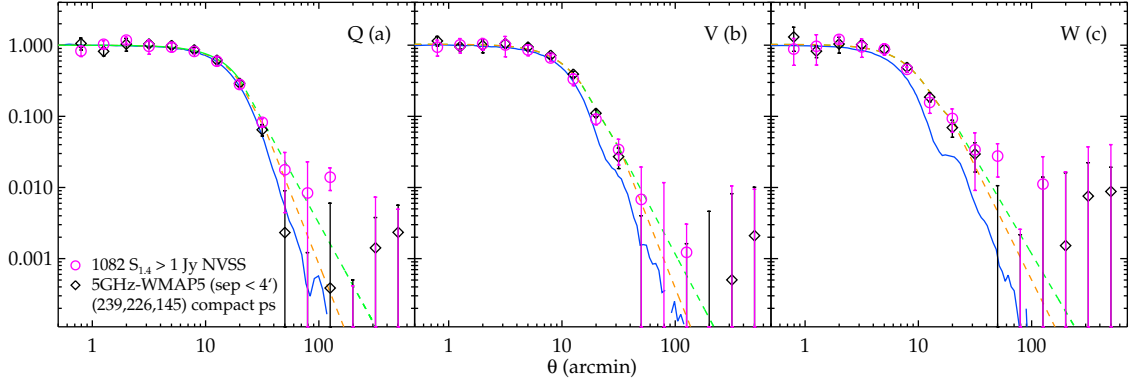


Figure 2: Stacked radio source beam profiles for the Q, V and W WMAP bands. Open black diamonds represent sources from the WMAP catalogue of Wright *et al.* and open magenta circles represent NVSS sources. The Jupiter beam is shown in each case (blue solid line). The radio source profiles appear wider than the Jupiter profiles particularly in the V and W bands. The dashed green and red lines are the power-law fits of Sawangwit and Shanks to the observed WMAP radio source profiles.

of the WMAP beam profile with the remainder being due to sky incompleteness. Although the W band beam profile has its narrow, $12.^{\circ}6$, core, it also has wide sidelobes which fall off as a power-law with angle, rather than as a Gaussian. The WMAP beam profile is usually estimated by measuring bright planetary sources such as Jupiter and the beam must be known to high accuracy at 1 degree scales where the profile reaches 0.1% of its peak value. Thus the effects of ‘de-beaming’ are $\approx 70\%$ of the first peak height and even more at the position of the second and third peaks.

3 Testing the WMAP beam using radio sources

The sensitivity of the WMAP power spectrum to the beam profile suggests that it is important to test the profile used by the WMAP team. Sawangwit and Shanks¹⁹ stacked the CMB data at the positions of $\approx 150 - 250$ WMAP5 radio sources as catalogued by Wright *et al.*²⁰, excluding all sources identified as extended in ground-based, higher resolution 5GHz surveys (see Fig. 2). They found that at the Q, V and W bands, the stacked source profiles looked increasingly broad and broader than the Jupiter profile on scales of $10 - 30'$. Beyond these scales, the noise on the stacked radio-source profile means that little information about the profile can be obtained by this method. Sawangwit & Shanks¹⁹ also found more marginal evidence that the profile width may increase as source flux decreases, possibly suggesting that there was a non-linearity in the WMAP flux scale.

In Fig. 2 we also show a new WMAP stack on the positions of a flux limited selection of NVSS sources at the 1.4GHz frequency, now rejecting any source with a neighbour within a 1 degree radius. As can be seen, we find an almost exactly similar result to that based on selecting sources from the WMAP5 catalogue. We have further found that the result reproduces in the sample of sources detected using the ‘CMB-free’ method of Chen and Wright²¹. Sawangwit²² has also checked our result in 100 CMB sky simulations, each containing a similar number of sources as in the WMAP5 source list and with each source assuming the Jupiter beam profile. We found that in this simulated case our stacked radio source profile retrieved the Jupiter beam almost perfectly. All of these tests suggest that our results are not subject to any ‘Eddington bias’ or any other bias.

4 Other models that fit the WMAP CMB Power Spectra

Sawangwit and Shanks¹⁹ fitted power-laws to the WMAP radio source beam profile (see Fig. 2) and showed how sensitive the height of the first acoustic peak is to relatively small deviations away from the Jupiter profile. Here we show that beam profiles that are consistent with the radio sources can also significantly shift the *position* of the first peak from the standard $l = 220$ multipole to $l > 300$. We do this by reverse engineering a beam profile, $b_s(\theta)$, from the square of the beam window function, b_l , obtained by dividing the C_l of a model with $\Omega_{baryon} = 1$, $H_0 = 35 \text{ km s}^{-1} \text{Mpc}^{-1}$ and $\tau = 0.35$ (Shanks^{24,25,26}) by the ‘raw’, W1W2 C_l shown in Fig. 1. Transforming back to the beam profile, $b_s(\theta)$, leaves a profile which shows a ‘ringing’ at large θ and which oscillates between positive and negative values. After only taking the small-scale part of the profile which is positive and ‘squeezing’ the profile to smaller scales by 25% to compensate for the loss of the negative parts gives us a ‘do-it-yourself’ profile for the large scales. At $\theta < 20'$ we fit the radio source profile with a Gaussian and then an exponential which helps match the Gaussian smoothly onto the large scale part. The resulting profile is shown in Fig. 3, where it is compared to the WMAP and NVSS radio source W band profile and the Jupiter profile. It is the spike at $\approx 35'$ which is vital to move the $l = 220$ peak to match the $\Omega_{baryon} = 1$, C_l peak at $l = 330$. The resulting ‘diy’ debeamed W band C_l compares well to the theoretical $\Omega_{baryon} = 1$, low H_0 C_l on which it is based (see Fig. 4); the raw W1W2 C_l is also shown. Beyond $l = 600$ where the S/N for the WMAP spectrum drops, the C_l from the QUAD experiment (Brown *et al.*²³) is also plotted. Again, we see broad agreement with the $\Omega_{baryon} = 1$ model, although there is some detailed disagreement with QUAD peak positions at $l > 1000$.

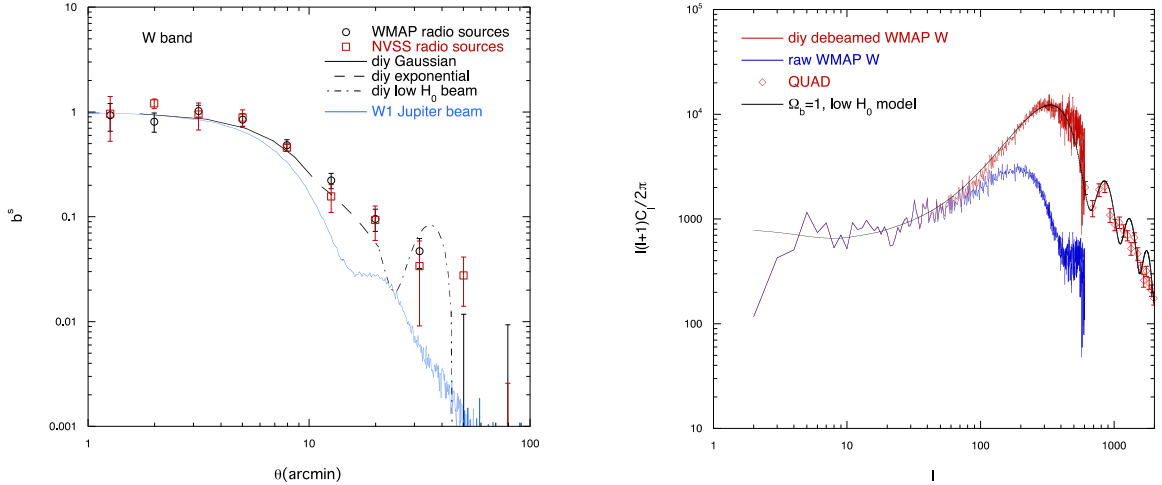


Figure 3: A partly ‘reverse-engineered’ or ‘do-it-yourself’ W band beam profile comprising a Gaussian in Fig. 3 is shown as the red line and the $\Omega_{baryon} = 1$, low H_0 model is also compared to the QUAD results at $l > 600$ (red open circles).

5 Conclusions

We have discussed various fundamental and astrophysical problems for the standard Λ CDM cosmological model, including its requirement for undiscovered physics in terms of the weakly interacting CDM particle and in the one part in 10^{100} fine-tuning in terms of the small size of the cosmological constant. But the model has received overwhelming support from CMB

experiments such as WMAP in terms of the position of the first acoustic peak in the power spectrum. However, Sawangwit and Shanks¹⁹ have shown the high sensitivity of the amplitude of the first acoustic peak to the detailed form of the WMAP instrumental beam profile and that stacking unresolved radio sources indicates wider beams than expected in the Q, V and W bands. Here we have shown that a WMAP W band beam which is not inconsistent with the radio source beam profile can also reproduce the power spectrum of a simple inflationary model with $\Omega_{baryon} = 1$ and a low value of H_0 . This model produces a peak at multipole $l = 330$ rather than $l = 220$. It also reproduces the broad form, although not the detailed peak positions, of the observed power spectrum in the $600 < l < 2000$ region from e.g the QUAD experiment. However, the $l = 330$ WMAP peak was basically ‘reverse-engineered’ to fit the $\Omega_{baryon} = 1$ model, using the freedom afforded by the loose constraints on the stacked radio source profiles at scales $\theta > 30'$ and it remains to be seen whether the actual WMAP beam is consistent with this very simple cosmological model.

Acknowledgments

We acknowledge the WMAP team for making their data freely and publicly available. Utane Sawangwit acknowledges a Royal Thai Government Scholarship for PhD funding.

References

1. G. Hinshaw *et al*, *ApJS* **148**, 135 (2003).
2. E. Komatsu *et al*, *ApJS* submitted, arXiv:1001.4538 (2010).
3. M. Hicken *et al*, *ApJS* **700**, 1097 (2009).
4. R. Kessler *et al*, *ApJS* **185**, 32 (2009).
5. S. Weinberg, *Rev. Mod. Phys* **61**, 1 (1989).
6. E. Aprile *et al*, *Phys. Rev. Lett.* submitted, arXiv:1005.0380 (2010).
7. G.P. Efstathiou, *MNRAS* **274**, L73 (1995).
8. A.H. Guth, *Phys. Rev. D* **23**, 347 (1981).
9. E. Witten, <http://theory.tifr.res.in/strings/Proceedings/witten/22.html> (2001).
10. P.J. Steinhardt, in *The Very Early Universe*, eds: Gibbons, GW, Hawking, SW and Siklos, STC (Cambridge: Cambridge University Press, 1983).
11. A.J. Benson *et al*, *AJ* **599**, 38 (2003).
12. L.L. Cowie, A. Songaila and E. Hu, *AJ* **112**, 839 (1996).
13. R.G. Bower *et al*, *MNRAS* **370**, 645 (2006).
14. G. Hinshaw *et al*, *ApJS* **180**, 225 (2009).
15. A.D. Myers *et al*, *MNRAS* **347**, L67 (2004).
16. R.M. Bielby and T. Shanks, *MNRAS* **382**, 1196 (2007).
17. T. Shanks, *MNRAS* **376**, 173 (2007).
18. L. Page *et al*, *ApJS* **148**, 39 (2009).
19. U. Sawangwit and T. Shanks, *MNRAS* accepted, arXiv:0912.0524 (2010).
20. E.L. Wright *et al*, *ApJS* **180**, 283 (2009).
21. X. Chen and E.L. Wright, *ApJ* **694**, 222 (2009).
22. U. Sawangwit, PhD thesis, Durham Univ., in prep. (2010).
23. M.L. Brown, *ApJ* **705**, 978 (2009).
24. T. Shanks, *Vistas in Astronomy*, 28, 595 (1985).
25. T. Shanks *et al* in *Observational Tests of Cosmological Inflation*, Eds. T Shanks, AJ Banday, RS Ellis, CS Frenk and AW Wolfendale, (Kluwer, Dordrecht, 1991).
26. T. Shanks in *Maps of the Cosmos*, Eds. MM Colless, L Staveley-Smith and R Stathakis (ASP, San Francisco, 2005).

The Small Scale Angular Anisotropy at 148 GHz as seen by the Atacama Cosmology Telescope

Carlos Hernández-Monteagudo

*Max Planck Institute für Astrophysik (MPA), Karl Schwarzschild Str.1, Garching bei München,
D-85741, Germany*

The small scale anisotropy pattern of the Cosmic Microwave Background (CMB) encodes precious cosmological information, in the form of both effects arising at very young stages of the Universe and at much more recent epochs. Here we present the observations of the Atacama Cosmology Telescope of a southern strip centered at ecliptic declination $\delta = -53^0$ and spanning the R.A. range $0^h - 7^h 36^m$. With an angular resolution close to 1 arcmin, this telescope sweeps the sub-degree and arcminute range ($l \in [400, 8000]$). Once the brightest point sources are removed, the angular power spectrum of the covered field reveals the damped acoustic peak structure expected for CMB intrinsic temperature anisotropies in the *Silk damping tail*, which is buried by an excess at multipoles higher than $l = 2,500$. This excess can be explained by a single Poisson distributed population of unresolved point sources, and prompts no evidence for clustered point sources nor SZ from a galaxy cluster population. This allows setting the constraint of $\sigma_8 < 0.85$ at 95% CL after assuming an $A_{\text{SZ}} \propto \sigma_8^7$ scaling for the Sunyaev-Zel'dovich (SZ) power spectrum as described by the model of Sehgal et al. [16]

1 Introduction

1.1 The CMB sky

In the Standard Cosmological scenario, the Cosmic Microwave Background (CMB) radiation is a thermal photon bath that was released when the universe was $\sim 400,000$ years old, at the time when the electrons in the medium recombined the protons to form neutral hydrogen, and radiation (formerly linked to matter via Thomson scatter) started to propagate freely in space. Although isotropic to the level of 10^{-5} , this radiation field contains small inhomogeneities in the angular intensity and polarization distribution that encode precious information of our universe at the time of hydrogen recombination. These anisotropies are prominent at the angular scales corresponding to the angle subtended by the sound horizon of the universe at that epoch. Indeed this is a fundamental angular scale, since it generates harmonics or acoustic peaks in the anisotropy pattern of the CMB intensity. On much smaller angular scales (corresponding to few arcmins and below), the imperfect coupling of photons with electrons via Thomson scattering blurred the anisotropies in the photon distribution, in such a way that the anisotropy pattern shows an exponential decrease that is known as the *Silk damping tail*. The detection of the first (bigger in angular scale) acoustic peaks prompted the determination of the angular distance to the surface of last scattering (where recombination took place), together with strong constraints on the energy density of baryons and cold dark matter in our universe, [e.g., 3, 7, 9].

This field of *intrinsic* CMB anisotropies crosses the observable universe before reaching the observer, and in its journey it witnesses an evolving universe with uneven matter and gravi-

tational potential distributions. The CMB photons are hence deflected by those gravitational fields, and this introduces a *smoothing* of the acoustic peak anisotropy structure in the damping tail. The extent of this effect of gravitational lensing on CMB intensity anisotropies has not been detected yet, since there are no high precision observations of the CMB fluctuations at such small angular scales.

1.2 Secondary anisotropies and foregrounds

As the CMB radiation flies towards the observer, density fluctuations in the universe grow hierarchically, giving first rise to stars (that re-ionize the medium), clusters, galaxies and clusters of galaxies. In this scenario, there is a wealth of processes than modify the CMB angular and spectral pattern. During the reionization of the medium, the free electrons interact again with the CMB photons via Thomson (e.g, Siuniaev [19]) and resonant [2] scattering, while at later stages the CMB radiation undergoes red and blue shifting when crossing gravitational potential wells in evolution, [13, 15]. All these are just some of the *secondary anisotropies* imprinted on the CMB.

On the smallest angular scales some of the dominant CMB secondary anisotropies are associated to galaxy clusters. These structures are the largest bound objects in the universe, and contain a large amount of hot electrons that scatter CMB photons. If these electrons are hot enough, then there exists an energy transfer to the CMB photon field that translates into a spectral distortion of the CMB black body spectrum (which manifests as *frequency dependent* temperature anisotropies). This is the so-called thermal Sunyaev-Zel'dovich effect [hereafter tSZ, 17]. Even if there is no energy transfer in the scattering, the cluster's peculiar motion introduces a Doppler kick to *all* CMB photons, that is proportional to the projection of that peculiar velocity along the observer's line of sight. This is known as the kinematic Sunyaev-Zel'dovich effect, [hereafter kSZ, 18]. Galaxy clusters constitute an important cosmological tool, since their abundance and peculiar velocities tell us about the dynamics ruling the growth of structure in our universe.

There are also other astrophysical sources that add their emission on the CMB photon bath, the most important being radio and star forming galaxies. Accretion phenomena on supermassive black holes in galaxies accelerate particles and generate radio emission that can be seen from very large distances, [10, 11]. On the other hand, merging episodes in galaxies trigger star forming activity. The newly born stars produce a background of UV radiation that is absorbed by dust particles, which re-emit this energy in the millimeter and sub-millimeter range, and is then redshifted into the microwave range. All these point sources constitute *contaminants* to CMB observations, and their flux and angular distribution on the sky must be understood if CMB anisotropies are to be properly distinguished and interpreted.

CMB experiments like the Atacama Cosmology Telescope ^a[hereafter ACT, 6] or the South Pole Telescope [14] are by first time probing the angular scales in which all these effects are of relevance, providing a first glance to the physics behind them.

2 Observations and Data Analysis

The results presented in this and successive sections attempt to summarise those presented in more detail in this paper [1], to which we refer for a deeper description of the observations and their analysis.

The Atacama Cosmology Telescope operates from Cerro Toco, at an elevation of 5190 m in the chilean Atacama desert, where the median precipitable water vapor (PWV) was 0.49 mm for the data presented here. It is an off-axis Gregorian telescope with a main mirror of 6 m diameter,

^a<http://www.physics.princeton.edu/act/>

and is observing the sky in three bands centered at 148 GHz, 218 GHz and 277 GHz. We present here the data taken from mid-August to December 2008 with the Millimeter Bolometer Array Camera (MBAC). This camera consists on three set of detector arrays, each containing 1000 transition edge sensor (TES) bolometers and centered in one of the three central frequencies quoted above, although here we shall present the analysis of the data corresponding to 148 GHz only. More particularly, we shall focus on an area of 228 deg^2 , centered around a band of declination $\delta = -53^\circ$ spanning the RA range from 0^h to 7^h36^m . For the 148 GHz band, the effective elliptical beam of the telescope has full widths at half-maximum (FWHM) at $1.40'$ by $1.34'$, [8]. The telescope is scanning at a constant elevation of 50° , the first half of each observing night the rising field in the eastern sky, the second half the same setting field in the western sky. This ensures cross-linking observations in celestial coordinates, while minimizing the changes in the local observing conditions of the telescope. After cutting observations made under high values of PWV or instrument performance tests and data coming from detectors with abnormal behavior, the effective sensitivity of the remaining 148 GHz data is close to $30 \mu\text{K} \text{ s}^{1/2}$ in CMB temperature units. Uranus is used for calibration, with a temperature uncertainty at the 6% level caused by uncertainties in the planet's brightness temperature and in the solid angle of the telescope. A similar level of indetermination in the calibration is found when using WMAP data [7] for cross-calibration. The pointing errors for the considered field are close to $5''$ after following 20 known radio sources in preliminary maps. After iteratively solving the mapping equation projecting the detector data on the sky, we end up with $N_{pix} \sim 10^7$ pixels of $30'' \times 30''$ size in a Cylindrical equal-area projection. In this process, low frequencies (more affected by the atmospheric emission) were down-weighted, and other systematics associated to detector correlations, the common mode, and the atmospheric gradient were accounted and corrected for. The resulting map is shown in Fig. (1), where the three panels show the a temperature map (top), a difference map (center) and the sensitivity map for the field under consideration, (bottom).

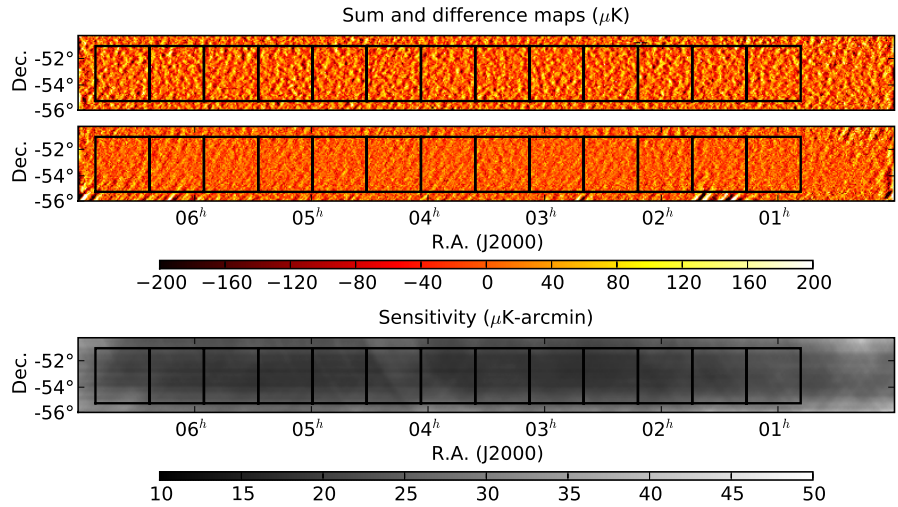


Figure 1: ACT southern field at 148 GHz (top panel), followed by a difference map (middle panel) and the sensitivity map (bottom panel). The thirteen square $4^0.2 \times 4^0.2$ patches used in the power spectrum computation are also shown.

Regarding point sources, a matched filter approach using noise weighting was used to identify all pixels above 5σ with at least three neighbors above 3σ as point sources. In the 228 deg^2 of the patch, this threshold roughly corresponds to 20 mJy, and yielded 108 point source detections, 105 were identified as radio sources present in radio catalogs, one in the 2MASS infrared catalog,

and the remaining two not having previously detected counterparts. The source count and flux densities compared well with the radio models of Toffolatti et al. [20] and de Zotti et al. [5]. An area of 10 arcmin^2 was masked around each source before computing the angular power spectrum, ($\sim 2.3 \text{ deg}^2$ in total), although other masks inferred from galaxy clusters' positions and radio catalogs were built and used, yielding negligible changes in power spectrum estimates.

The field is first filtered with a squared sine function in Fourier space in order to remove the large scale contamination introduced by the instrument, scan strategy and atmospheric contamination. Next it is divided into 13 different patches, of $4^0.2 \times 4^0.2$ size each. For each patch, four different maps are obtained after storing data from four different but successive nights, providing four independent estimates of the sky for each field. Following the procedure given by Das et al. [4], the maps are prewhitened (which avoids to great extent the leakage from low to high spatial/angular frequencies – or multipoles l -s). All possible cross and auto-power spectra for the four maps of each patch are then computed, after applying the mask and the adaptively weighted multi-taper method outlined in Das et al. [4] with $N_{\text{tap}} = 5$ tapers at resolution parameter $N_{\text{res}} = 3$. This method increases the coupling between different multipoles, so that power spectrum estimates are binned in annuli of width $\Delta l \simeq 300$ rather than $\Delta l \simeq 90$ as it would correspond for patches of size $4^0.2$, ($\Delta l \simeq 2\pi/\theta_{\text{patch}} \simeq 90$). These power spectrum estimates are then divided by the mode coupling matrix introduced by the masking and tapering, and corrected by the bias introduced by the high-pass filter, the pre-whitening filter and the beam. The resulting quantities should be *unbiased* estimates of the sky angular power spectrum.

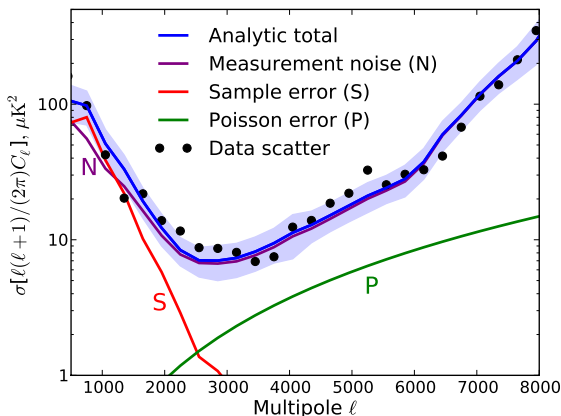


Figure 2: Comparison of the scatter in the power spectrum estimates obtained from subsets of data (filled circles) with the analytical predictions for the noise, sample error and Poisson source contributions, (solid lines).

At every multipole bin b centered at $l = l_b$ and for each patch j we compute the angular power spectrum (defined as $\mathcal{D}_b^j = l_b(l_b + 1)/(2\pi)C_{l_b}$) as the average of the 6 cross-power spectra estimated from the four independent maps. The dispersion of these power spectrum estimates around the average value provides an idea of the uncertainty of the patch estimate \mathcal{D}_b^j . The inverse of this dispersion is used as a patch weight (w_j) when combining power spectrum estimates for the 13 patches into a final and unique estimate for every multipole bin b ,

$$\mathcal{D}_b = \frac{\sum_{j=1}^{13} w_j \mathcal{D}_b^j}{\sum_{j=1}^{13} w_j}. \quad (1)$$

The covariance matrix of the power spectrum estimates $\Sigma_{b,b'} \equiv \langle \Delta \mathcal{D}_b \Delta \mathcal{D}_{b'} \rangle$ is computed from the dispersion of each patch estimate around the average value of Eq.(1). A simple analytical model for this covariance matrix including the instrumental noise (estimated from the difference

of the average auto-power spectra and cross-power spectra for each patch), the sample error (due to the finite patch area), and the Poisson scatter (introduced by the unresolved population of point sources and galaxy clusters) reproduced the measured diagonal terms of $\Sigma_{b,b'}$, as Fig.(2) shows. The power of the difference maps (from the four different maps per patch) is found to be compatible with zero, and no evidence for anisotropy in the power spectrum is found.

3 Results

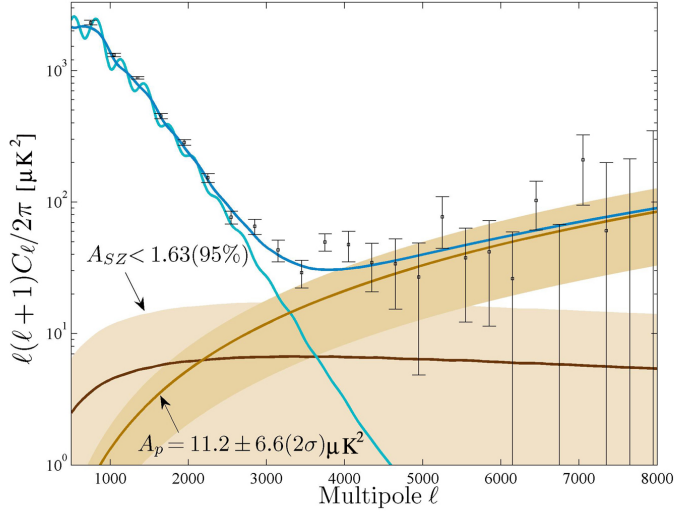


Figure 3: Angular power spectrum measured in the ACT southern field at 148 GHz.

The binned power spectrum estimates, ranging from $l = 800$ up to $l = 8,000$ are shown in Fig.(3). For $l < 2,500$, the measured anisotropy power is compatible with the accordingly smoothed Λ CDM WMAP – 5th year prediction [after including BAO and SN data, blue solid line, 7], but above $l \simeq 2,500$ there exists a clear excess. We model the measured angular power spectrum at 148 GHz as

$$\mathcal{D}_b = \mathcal{D}_b^{CMB} + A_{SZ} \mathcal{D}_b^{SZ} + A_p \left(\frac{l}{3000} \right)^2 + \mathcal{D}_b^{corr}. \quad (2)$$

While \mathcal{D}_b^{CMB} gives the intrinsic CMB prediction, the SZ power spectrum template (\mathcal{D}_b^{SZ}) considers both the (dominant) tSZ and the kSZ components, and is obtained from the cosmological simulations of Sehgal et al. [16]. The scaling factor A_{SZ} accounts for offsets of real data with respect to this prediction. For Poisson distributed sources the power spectrum scaling is $\propto l^2$, and A_p provides its normalization at $l = 3000$. The multipole pattern for clustered sources is more complicated. Motivated by the scaling of the galaxy correlation function $\xi(\theta) \sim \theta^{-0.8}$ [12], which yields $C_l \sim l^{-1.2}$, we adopted the scaling $\mathcal{D}_b^{corr} = A_{corr} \left(\frac{l_b}{3000} \right)$. By introducing the above estimated power spectrum covariance matrix $\Sigma_{b,b'}$ in the definition of the data likelihood, we solve for the probability distribution of the model parameters A_{SZ} , A_p and A_{corr} . We find marginalized constraints on $A_p = 11.2 \pm 3.3 (\mu\text{K})^2$, but no evidence for any SZ contribution ($A_{SZ} < 1.63$ at the 95 % CL), which translates into the constraint $\sigma_8 < 0.85$ at 95% CL if one assumes a $A_{SZ} \propto \sigma_8^7$ scaling.

4 Future Prospects

Future observations at 220 GHz and 280 GHz should allow to better separate the contribution from SZ (which cancels at 220 GHz) and IR sources, whose clustering properties should be more easily accessible at these higher frequencies too. The peculiar motion of clusters might as well be detected by first time by looking at cluster's positions in the 220 GHz maps in which the tSZ is greatly suppressed. Apart from a better characterization of the radio and IR source populations, upcoming data should also enable the study of lensing of intrinsic CMB anisotropies and the chase for missing baryons.

References

- [1] The ACT Collaboration, et al. 2010, arXiv:1001.2934
- [2] Basu, K., Hernández-Monteagudo, C., & Sunyaev, R. A. 2004, *A& A*, 416, 447
- [3] Bennett, C. L., et al. 2003, *ApJS*, 148, 1
- [4] Das, S., Hajian, A., & Spergel, D. N. 2009, *Ph.Rv.D*, 79, 083008
- [5] de Zotti, G., Ricci, R., Mesa, D., Silva, L., Mazzotta, P., Toffolatti, L., & González-Nuevo, J. 2005, *A& A*, 431, 893
- [6] Fowler, J. W., & ACT Collaboration 2006, *Bulletin of the American Astronomical Society*, 38, 1227
- [7] Hinshaw, G., et al. 2009, *ApJS*, 180, 225
- [8] Hincks, A. D., et al. 2009, arXiv:0907.0461
- [9] Jarosik, N., et al. 2010, arXiv:1001.4744
- [10] McCarthy, P. J. 1993, *Annu.Rev.Astron.Astrophys.*, 31, 639
- [11] Miley, G., & De Breuck, C. 2008, *Astron.Astrophys.Rev.*, 15, 67
- [12] Peebles, P. J. E. 1980, Research supported by the National Science Foundation. Princeton, N.J., Princeton University Press, 1980. 435 p.,
- [13] Rees, M. J., & Sciama, D. W. 1968, *Nature*, 217, 511
- [14] Ruhl, J., et al. 2004, *SPIE*, 5498, 11
- [15] Sachs, R. K., & Wolfe, A. M. 1967, *ApJ*, 147, 73
- [16] Sehgal, N., Bode, P., Das, S., Hernández-Monteagudo, C., Huffenberger, K., Lin, Y.-T., Ostriker, J. P., & Trac, H. 2010, *ApJ*, 709, 920
- [17] Sunyaev, R. A., & Zeldovich, Y. B. 1972, *Comments on Astrophysics and Space Physics*, 4, 173
- [18] Sunyaev, R. A., & Zeldovich, Y. B. 1980, *MNRAS*, 190, 413
- [19] Siumiaev, R. A. 1977, *Soviet Astronomy Letters*, 3, 268
- [20] Toffolatti, L., Argueso Gomez, F., de Zotti, G., Mazzei, P., Franceschini, A., Danese, L., & Burigana, C. 1998, *MNRAS*, 297, 117

PLANCK STATUS

F. PAJOT ON BEHALF OF THE PLANCK COLLABORATION

Institut d'Astrophysique Spatiale, Bât. 121, Université Paris Sud-11, 91405 Orsay Cedex, France



The Planck satellite has been operating with outstanding success since its launch on May 14th 2009. This paper gives a brief description of the operations and an outline of the status of the spacecraft and its instruments. It recalls the pre-launch performance of the instruments and the main scientific objectives of the mission.

1 Planck goals

The Planck^a satellite (Fig. 1) is the 3rd generation space CMB experiment (Lamarre et al. ¹). It aims at a gain of a factor 2.5 in angular resolution and one order of magnitude in sensitivity with respect to WMAP. It is nearly photon noise limited in the CMB channels (100-217 GHz) and its temperature power spectrum sensitivity is limited by the ability to remove the foreground emissions. For this purpose it has a very broad frequency coverage from 30 GHz to 1 THz. The HFI (High Frequency Instrument) is based on direct detectors (bolometers) cooled to 100mK distributed in 6 bands from 100 to 857 GHz read in total power mode with a white noise from 10 mHz to 100Hz (no 1/f noise in the signal range). The LFI (Low Frequency instrument) uses coherent detection based on HEMT amplifiers distributed in 3 bands from 30 to 70 GHz, with photometric reference loads on the 4 K box of the HFI focal plane unit. The Planck *Blue Book* (<http://www.rssd.esa.int/Planck>) gives all detailed informations about the Planck mission and its goals.

^aPlanck (<http://www.esa.int/Planck>) is an ESA project with instruments provided by two scientific Consortia funded by ESA member states (in particular the lead countries: France and Italy) with contributions from NASA (USA), and telescope reflectors provided in collaboration between ESA and a scientific Consortium led and funded by Denmark.



Figure 1: The Planck satellite in the Centre Spatial Guyannais clean hall S1B in Kourou before its integration in the fairing of the Ariane 5 ECA launcher (credit ESA-CNES-Arianespace / Optique Video du CSG - L. Mira).

2 Planck operations

All informations and illustrations are taken from public information at the time of the conference. The injection of the spacecraft on the L2 orbit was performed on July 2nd 2009. At the same time the HFI detectors reached their operating temperature close to 100 mK (Fig. 2). The calibration and performance verification activities followed until August 13th 2009. The 4K cryocooler unexpectedly shut down on August 6th 2009: the HFI cryochain was lost but recovered to the same operating point in 6 days. This did not reoccur since. The spacecraft operation is very smooth, with only minor events on pointing and thermal control. The scanning strategy is fully implemented. The first light survey (August 13th-27th 2009) was followed by the first all-sky survey in continuity until February 13th 2010. The second all-sky survey is in progress.

2.1 Planck status

The 4 stages of the cooling chain are regulated at their nominal temperatures: the 18 K stage at 17.5 K, the 4 K stage at 4.72 K, the 1.6 K stage at 1.38 K. The dilution is regulated at 101 mK, operated with the lowest flow of isotopes providing a potential 30 months survey duration. The HFI detectors at their 103 mK operating temperature behave exactly as during ground tests. For more information on Planck, refer to the special issue of A&A on Planck pre-launch status papers (in press).

2.2 Planck data processing

The timelines consisting in circles (20 to 40 typ. per pointing) are processed into rings: the very stable pointing (5-10 arcsec) allows an efficient removal of glitches. The solar activity is at its minimum. This translate into a higher cosmic particules rate getting into the Solar system.

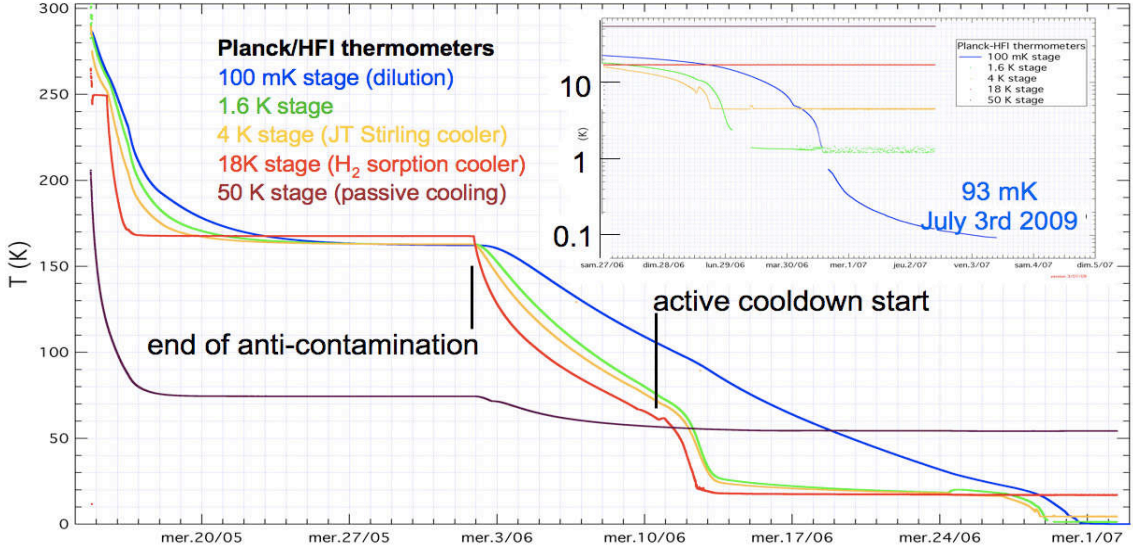


Figure 2: Cooldown profile of the Planck instruments cryochain.

The time transfert function is being carefully determined because it directly impacts the CMB spectrum. A first order calibration is derived from the CMB dipole or from the Galaxy in the day to day trend analysis. The mapmaking process already produced tantalizing pictures such as the one presented in the ESA/HFI/LFI press releases. All sky absolute calibration will be performed on the CMB orbital dipole or on the FIRAS data. Polarisation maps require relative band to band fine calibration, as well as beams, side lobes and far side lobes determination. At all levels, a strict control of the systematics is needed to reach the most ambitious CMB science goals of Planck.

3 Conclusion

In August 2010 the DR2 "first all sky survey" internal data release will be released to the Planck scientists. These data are the basis for early papers on foregrounds which should be original, robust, and submitted by the end of 2010. They will be presented in January 2011 at a dedicated Planck conference in Paris on the missions performances, foreground emissions, and implications on the CMB science. At the same time the early release compact sources catalogue (ERCSC) public release will be done. The nominal mission (2 surveys) internal release is planned beginning of 2011, and its public release in mid-2012. The operations extention is approved by ESA until November 2011, for a 4 all sky surveys expected total duration of the mission. The potential impact of the extended mission on the CMB science is large. In particular an improved B-mode detection potential have been shown in Efstathiou and Gratton².

References

- [1] Lamarre, J-M., Puget, J-L., Bouchet, F. et al., 2003, New Astronomy Review, 47, 1017.
- [2] Efstathiou, G., and Gratton, S., 2009, JCAP, 6, 11.

B-mode CMB spectrum estimation using a pure pseudo cross-spectrum approach

M. Tristram

Laboratoire de l'Accélérateur Linéaire

CNRS Université Paris 11, Bâtiment 200, Orsay, France

I describe the pure pseudo-spectrum formalism for the estimation of the Cosmic Microwave Background polarized power spectra, as proposed by [Smith 2006] and extended to incorporate cross-spectra of the multiple maps of the same sky area by [Grain et al. 2009]. I summarize the performance of the method as compared to other existing algorithms and their implementations. In particular, I show that the statistical uncertainty of the estimated B-mode spectra is typically found to be within a factor ~ 2 of the variance derived from the most optimistic Fisher matrix predictions accounting only for the sampling and noise uncertainty of the B-modes alone. I conclude that the presented formalism thanks to its speed and efficiency can provide an interesting alternative to the CMB polarized power spectra estimators based on the optimal methods.

1 Introduction

The reliable characterization and scientific exploitation of the polarized Cosmic Microwave Background (CMB) Anisotropy signal is one of the main challenges facing the CMB research at the present. We discuss the CMB power spectrum estimation via the pure pseudo spectrum technique as published in [Grain et al. 2009]¹. Pseudo- C_ℓ algorithms provide a computationally quick and flexible framework for estimating the power spectra. However, it has been long recognized² that a straightforward application of the pseudo spectrum technique to cut-sky polarized CMB maps leads to the so-called "*E*-to-*B*" leakage, or power aliasing. A consequence of which the cosmologically important information contained in the CMB *B*-modes is overwhelmed by the statistical uncertainty of the (much larger) *E*-modes. [Grain et al. 2009]¹ propose an approach that relies on a suitably chosen sky apodization to remove from the map harmonic modes which are neither solely *E* nor *B* as introduced by [Smith 2006]³.

2 Angular Power Spectrum Estimation

Maps of I, Q and U components of the CMB signal are decomposed into spherical harmonics $a_{\ell m}^T$, $a_{\ell m}^E$ and $a_{\ell m}^B$. From these coefficients, one can construct the 6 angular power spectrum : C_ℓ^{TT} , C_ℓ^{EE} , C_ℓ^{BB} , C_ℓ^{TE} , C_ℓ^{TB} and C_ℓ^{EB} . Systematic effects need to be taken into account in this process. In particular, beam smoothing effects or partial coverage of the sky must be accounted for. Even for full sky missions, foreground residuals usually still dominate the noise in the Galactic plane. To avoid any contamination of the angular power spectra, a mask is applied to suppress pixels in which parasitic signal are strong, leading to less than full-sky effective coverage. Angular power spectra estimators can be separated in two main categories:

- Maximum Likelihood methods^{5,7,6} which estimate angular power spectra using the angular correlation function M by maximizing the probability of C_ℓ considering the maps T :

$$\mathcal{P}(C_\ell|T) \propto \exp \left[-\frac{1}{2} (T^T M^{-1} T + \text{Tr}(\ln M)) \right].$$

The algorithm scales as $\mathcal{O}(N_{\text{bins}} N_{\text{pix}}^3)$ for CPU time and $\mathcal{O}(N_{\text{pix}}^2)$ for memory. This implies that maximum likelihood methods are not well adapted to surveys such as Planck which should deliver high resolution maps with more than 10^7 pixels.

- Pseudo- C_ℓ methods^{8,9,10,11} compute the angular power spectra directly from the observed maps before correcting for instrumental effects such as beam smoothing effects (B_ℓ), partial sky coverage ($M_{\ell\ell'}$ which is computed analytically using the spherical transform of the weight mask) or filtering of data (F_ℓ). The biased spectrum (called pseudo-spectrum) \tilde{C}_ℓ rendered by the direct spherical harmonics transform of a partial sky map is different from the full sky angular spectrum C_ℓ but their ensemble average are linked by :

$$\langle \tilde{C}_\ell \rangle = \sum_{\ell'} M_{\ell\ell'} F_{\ell'} B_{\ell'}^2 \langle C_{\ell'} \rangle + \langle \tilde{N}_\ell \rangle.$$

$\langle \tilde{N}_\ell \rangle$ is the noise contribution to the estimated pseudo-spectra and vanishes, whenever the noise in the two data sets is not correlated, as for example, in a case of two data sets produced by two different experiments or two uncorrelated detectors of a single experiment. This emphasizes one of the biggest advantages of the cross-spectrum based estimators, which do not need such a correction. Pseudo- C_ℓ estimators make use of the fast spherical harmonics transform that scales in $\mathcal{O}(N_{\text{pix}}^{3/2})$. Moreover they are often nearly optimal in practice (at least for temperature). Nevertheless, they need a precise description of the instrument (beam, filtering, noise) that requires a large number of Monte-Carlos.

3 E-B mixing

Due to the limited sky coverage, and non-uniform, pixel-dependent weights, the above pseudo- C_ℓ estimator is biased and its average over CMB realizations, $\langle \tilde{C}_\ell^X \rangle$, involves a mixing between different ℓ modes (or bins) and polarization states ($X = E, B$). The latter can be described by a so-called *mixing kernel* $M_{\ell\ell'}$. The unbiased estimator C_ℓ^X is thus obtained by inverting the following linear system,

$$\begin{pmatrix} M_{\ell\ell'}^{\text{diag}} & M_{\ell\ell'}^{\text{off}} \\ M_{\ell\ell'}^{\text{off}} & M_{\ell\ell'}^{\text{diag}} \end{pmatrix} \begin{pmatrix} C_{\ell'}^E \\ C_{\ell'}^B \end{pmatrix} = \begin{pmatrix} \tilde{C}_\ell^E - N_\ell^E \\ \tilde{C}_\ell^B - N_\ell^B \end{pmatrix}. \quad (1)$$

In the ensemble average sense the above expression is unbiased as a result of a subtle cancellation of the E mode power present in the pseudo- B and E spectra. Such a cancellation does not however apply to the variance of the estimator and as a result the variance of the spectra of one type will include a contribution from the other preventing any detection of the primordial B-mode (figure 1).

4 Pure pseudo- C_ℓ estimators for cross-spectrum

Using the two differential operators $\mathbf{D}_s^{E(B)}$ which generalize to arbitrary spin the operators used in [Bunn et al. 2003]², we can write the harmonic representation of the field $\mathbf{P} = (Q, U)$ in the

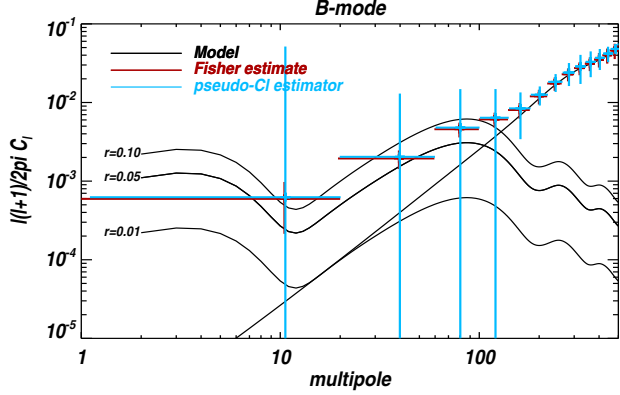


Figure 1: B-mode reconstruction with error bars from a Fisher analysis (red) and a pseudo- C_ℓ estimator (blue) based on a B-mode with $r=0.05$. The shown B-mode spectrum (black) is decomposed into primordial (plotted for three different values of $r=0.01, 0.05, 0.1$) and lensing parts.

E/B subspace. We introduce the sky coverage setting $W = 1$ for pixel in the sky area and $W = 0$ elsewhere. In particular, for the B mode

$$\begin{aligned} a_{\ell m}^B &= \int_{4\pi} W \cdot (Q, U) \times D^B Y_{\ell m} \\ &= \int_{\Omega} D^B(Q, U) \times Y_{\ell m} + \oint_{C_{\Omega}} (Q, U) \partial Y_{\ell m} + \oint_{C_{\Omega}} \partial(Q, U) Y_{\ell m} \end{aligned} \quad (2)$$

The two contour integrals represent the so-called "ambiguous" modes that are responsible for the E-to-B leakage. Pseudo- C_ℓ estimators of the polarization power spectra which do not mix E and B modes can be constructed in projecting the polarization fields on the "pure" E and B subspaces². Pure B multipoles on a partial sky are defined as follows³:

$$\begin{aligned} a_{\ell m}^B &= \int_{4\pi} (Q, U) \times D^B(W Y_{\ell m}) \\ &= \int_{\Omega} W \cdot D^B(Q, U) \times Y_{\ell m} + \oint_{C_{\Omega}} (Q, U) \times \partial(W Y_{\ell m}) + \oint_{C_{\Omega}} \partial(Q, U) \times W Y_{\ell m} \end{aligned} \quad (3)$$

We choose W a spin-0 window function in order to satisfy the Dirichlet and Neumann conditions on the boundary of the observed sky region. Such conditions on the window function are optimized for the estimated multipoles to be free of a E/B leakage due to partial sky either analytically or numerically^{3,4,1} (figure 2). This translates into vanishing mixing matrices

$$M_{\ell \ell'}^{off} = 0.$$

Our numerical implementation proceeds in two steps¹:

1. from the spin-0 window function W_0 , we define two spin-weighted windows

$$W_1 = \partial W \text{ and } W_2 = \partial^2 W$$

2. we calculate the pure multipoles $a_{\ell m}^{(s)}$ of the s -spin fields $\tilde{P}_s = W_s^\dagger(Q + iU)$. The pure estimated multipoles coefficients then reads as linear combinations of the $a_{\ell m}^{(s)}$

$$\mathcal{A}_{\ell m}^B = a_{\ell m}^{(2)} + \lambda_{1,\ell} a_{\ell m}^{(1)} + \lambda_{0,\ell} a_{\ell m}^{(0)} \quad (4)$$

The code is fully parallel (both in CPU time and memory) and very fast (less than 30min for 1000 simulations on 1024 procs) using the *pureS2HAT* library¹². We can recover the B-mode angular power spectrum without bias and with a significant improvement in the level of error bars compared to "standard" pseudo- C_ℓ methods (figure 3).

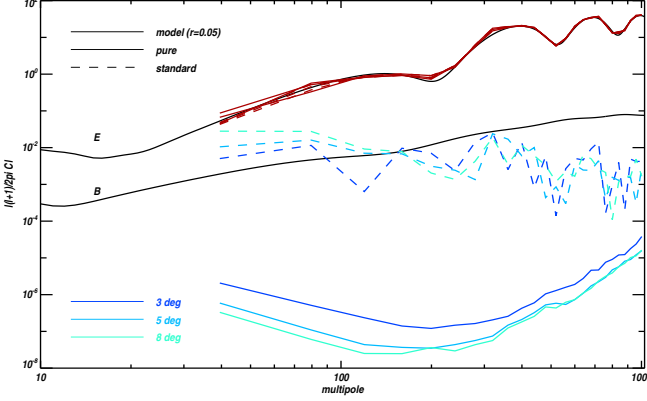


Figure 2: Leakage from E to B in the case of standard estimator (dashed line) and pure estimator (solid line) using three different apodization length : 3, 5 and 8 deg. Remaining leakage at high multipoles is induced by pixel effects.

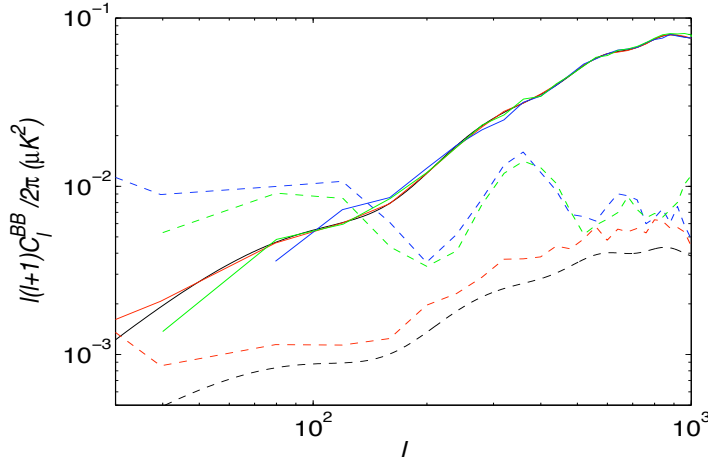


Figure 3: B-mode angular power spectrum estimation (solid lines) and their MC-estimated variance as compared with the input (black solid) and Fisher variance (black dashed) from various estimators : Xpol standard estimator (blue), SpicePol standard estimator (green), Xpure pure estimator (red). figure by H. Nishino (KEK)

References

1. Grain J., Tristram M., Stompor R., 2009, Physical Review D **79** 123515
2. E.F. Bunn, M. Zaldarriaga, M. Tegmark, & A. de Oliveira-Costa, Phys. Rev. D **67**, 023501 (2003)
3. K.M. Smith, Phys. Rev. D **74** 083002 (2006)
4. K.M. Smith & M. Zaldarriaga, Phys. Rev. D **76**, 0043001, (2007)
5. Bond J R, Jaffe A H and Knox L 1998 Physical Review D **57** 2117
6. Borrill J 1999a Physical Review D **59** 27302
7. Tegmark M 1997 Physical Review D **55** 5895
8. Peebles P J E and Hauser M G 1974 ApJS **28** 19
9. Wandelt B D, Hivon E and Gorski K M 2001 Physical Review D **64** 083003
10. E. Hivon, K.M. Górski, C.B. Netterfield, B.P. Crill, S. Prunet, & F. Hansen, Astrophys. J., **567**, 2, (2002)
11. M. Tristram, J.F. Macias-Pérez, C. Renault & D. Santos, MNRAS, **358**, 833, (2005)
12. www.apc.univ-paris7.fr/~radek/pureS2HAT.html

Preparation to the CMB Planck analysis : contamination due to the polarized galactic emission

L. Fauvet, J.-F. Macías-Pérez

*LPSC, Université Joseph Fourier Grenoble 1, CNRS/IN2P3, Institut National Polytechnique de Grenoble, 53 avenue des Martyrs,
38026 Grenoble cedex, France*

The Planck satellite experiment, which was launched the 14th of may 2009, will give an accurate measurement of the anisotropies of the Cosmic Microwave Background (CMB) in temperature and polarization. This measurement is polluted by the presence of diffuse galactic polarized foreground emissions. In order to obtain the level of accuracy required for the Planck mission it is necessary to deal with these foregrounds. In order to do this, have developed and implemented coherent 3D models of the two main galactic polarized emissions : the synchrotron and thermal dust emissions. We have optimized these models by comparing them to preexisting data : the K-band of the WMAP data, the ARCHEOPS data at 353 GHz and the 408 MHz all-sky continuum survey. By extrapolation of these models at the frequencies where the CMB is dominant, we are able to estimate the contamination to the CMB Planck signal due to these polarized galactic emissions.

1 Introduction

The PLANCK satellite² which is currently in flight and acquiring data, should give the most accurate measurement of the anisotropies of the CMB in temperature and polarization with a sensitivity of $\Delta T/T \approx 2 \times 10^{-6}$ and an angular resolution of 5 arcmin. Thanks to its range of frequencies between 30 and 857 GHz it will give a great amount of information about galactic and extra-galactic emissions. In order to obtain the level of accuracy required for the Planck mission it is necessary to deal with these foregrounds and the residual contamination due to these foreground emissions. While, for the full sky, these emissions have the same order of magnitude than the CMB in temperature, they dominate by a factor 10 in polarization². The principal polarized Galactic microwave emissions come from 2 effects: thermal dust emission and synchrotron emission. The synchrotron is well constrained by the 408 MHz all-sky continuum survey⁷, by Leiden [Leiden/DRAO] between 408 MHz and 1.4 GHz¹⁶, by Parkes at 2.4 GHz⁵, by the MGLS *Medium Galactic Latitude Survey* at 1.4 GHz¹⁵ and by the satellite WMAP *Wilkinson Microwave Anisotropies Probe* (see e.g.⁸). The synchrotron emission is due to ultrarelativistic electrons spiraling in the large-scale galactic magnetic field. The thermal dust emission which has already been constrained by IRAS¹³ and COBE-FIRAS³ is due to dust grains heated by the the interstellar radiation field. Those grains emit a polarized submillimetric thermal radiation³ as observed by e.g. ARCHEOPS¹. The polarization of these two types of radiation is orthogonal to the field lines. We developed models of those emissions using the 3D galactic distribution of the magnetic field and the matter density. The models are constrained using pre-existing data and used to estimate the residual contamination to the CMB Planck signal due to these

polarized galactic emissions.

2 3D modelling of the Galaxy

A linearly polarized emission¹⁰ at a given frequency ν in GHz, can be described by the Stokes parameters I, Q and U. For the polarized foreground emissions integrated along the line of sight we obtain, for synchrotron:

$$I_s = I_{\text{Has}} \left(\frac{\nu}{0.408} \right)^{\beta_s}, \quad (1)$$

$$Q_s = I_{\text{Has}} \left(\frac{\nu}{0.408} \right)^{\beta_s} \frac{\int \cos(2\gamma) p_s n_e (B_l^2 + B_t^2)}{\int n_e (B_l^2 + B_t^2)}, \quad (2)$$

$$U_s = I_{\text{Has}} \left(\frac{\nu}{353} \right)^{\beta_s} \frac{\int \sin(2\gamma) p_s n_e (B_l^2 + B_t^2)}{\int n_e (B_l^2 + B_t^2)}, \quad (3)$$

where B_n , B_l and B_t are the magnetic field components along, longitudinal and transverse to the line of sight. The polarization fraction p_s is set to 75%. I_{Has} is the template map⁷. The maps are extrapolated at all the Planck frequencies using the spectral index β_s which is a free parameter of the model.

For the thermal dust emission the Stokes parameters are given by:

$$I_d = I_{\text{sf}d} \left(\frac{\nu}{353} \right)^{\beta_d}, \quad (4)$$

$$Q_d = I_{\text{sf}d} \left(\frac{\nu}{353} \right)^{\beta_d} \int n_d \frac{\cos(2\gamma) \sin^2(\alpha) f_{\text{norm}} p_d}{n_d}, \quad (5)$$

$$U_d = I_{\text{sf}d} \left(\frac{\nu}{353} \right)^{\beta_d} \int n_d \frac{\sin(2\gamma) \sin^2(\alpha) f_{\text{norm}} p_d}{\int n_d}, \quad (6)$$

where the polarization fraction p_d is set to 10 %, β_d is the spectral index (set to 2.0) and f_{norm} is an empirical factor, fitted to the ARCHEOPS data. The $I_{\text{sf}d}$ map is the model 8 of Schlegel *et al.*¹³.

The models are based on an exponential distribution of relativistic electrons on the Galactic disk, following⁴, where the radial scale h_r is a free parameter. The distribution of dust grains n_d is also exponential¹. The Galactic magnetic field is composed a regular and a turbulent components. The regular component is based on the WMAP team model¹² which is close to a logarithmic spiral to reproduce the shape of the spiral arms⁶. The pitch angle p between two spiral arms is a free parameter of the model. The turbulent component is described by a Kolmogorov's law⁶ spectrum with a relative amplitude A_{turb} .

3 Comparison to data

We computed Galactic profiles in temperature and polarization for various bands in longitude and latitude and various values of the free parameters. In order to optimize these 3D models we compare them to Galactic profiles computed with preexisting data using a χ^2 test. For the synchrotron emission in temperature, we use the 408 MHz all-sky continuum survey⁷ as shown on Figure 1. In polarization we use the K-band WMAP 5 years data. The thermal dust emission model is optimized using the polarized ARCHEOPS data¹ at 353 GHz.

The best fit parameters for the 3D model in polarization are given in Table 1. The results are consistent for the three sets of data. In particular we obtain compatible results for the

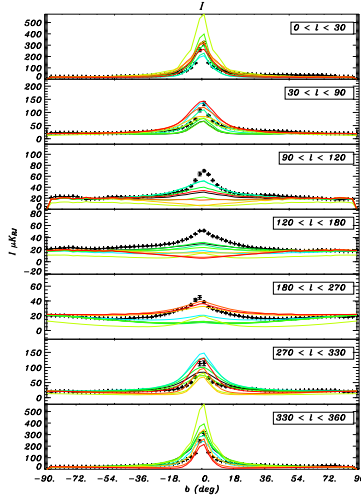


Figure 1: Galactic profiles in temperature at 408 MHz Haslam data in black and our synchrotron emission model for various values of the pitch angle p (from green to red).

synchrotron and thermal dust emission models. A_{turb} and h_r are poorly constrained as was already the case in Sun *et al*¹⁴. The best fit value of the pitch angle p is compatible with results obtained by other studies^{14,12}. The best fit value for the spectral index of the synchrotron emission is lower than the value found by^{14,12}, but this is probably due to the choice of normalisation for the regular component of the magnetic field. With these models we reproduce the global structure of the data (see for instance the Figure 1) apart from the Galactic Center.

Table 1: Best fit parameters for synchrotron and thermal dust emission models.

	p (deg)	A_{turb}	h_r	β_s	χ^2_{min}
<i>WMAP</i>	$-30.0^{+40.0}_{-30.0}$	< 1.25 (95.4 % CL)	> 1 (95.4 % CL)	$-3.4^{+0.1}_{-0.8}$	5.72
<i>HASLAM</i>	$-10.0^{+70.0}_{-60.0}$	< 1.25 (95.4 % CL)	$5.0^{+15.0}_{-2.0}$	\emptyset	5.81
<i>ARCHEOPS</i>	-20^{+80}_{-50}	< 2.25 (95.4 % CL)	\emptyset	\emptyset	1.98

4 Conclusions

From the above best fit parameters we estimated the contamination of the CMB PLANCK data by the polarized galactic emissions. We compared power spectra computed with simulations of the CMB PLANCK data^a. Figure 2 shows the temperature and polarization power spectra at 143 GHz for the CMB simulation (red) and the Galactic foreground emissions, obtained by applying a Galactic cut $|b| < 15^\circ$ (black). The foreground contamination seems to be weak but for the B modes an accurate foreground subtraction is extremely important concerning the detection of the primordial gravitational waves.

References

1. A. Benoît *et al*, A&A **424**, 512 (2004)
2. The Planck Consortium, 2004, *Planck : The Scientific Program*

^aWe used cosmological parameters for the Λ CDM-like model proposed in⁹ with a tensor to scalar ratio of 0.03.

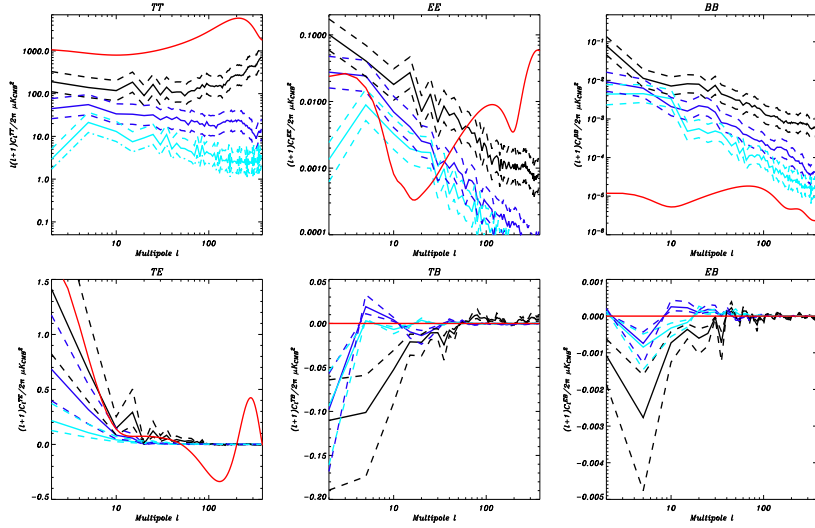


Figure 2: Clockwise from top left : power spectra $C_l^{TT}, C_l^{EE}, C_l^{BB}, C_l^{TE}, C_l^{TB}, C_l^{EB}$ at 143 GHz applying a galactic cut of $|b| < 15^\circ$ (black), $|b| < 30^\circ$ (blue) and $|b| < 40^\circ$ (cyan) (see text for details).

3. F. Boulanger *et al*, A&A **312**, 256 (1996)
4. R. Drimmel & D.N. Spergel, ApJ **556**, 181 (2001).
5. A. Duncan *et al*, A. & A. **350**, 447 (1999).
6. J. L. Han *et al*, A&A **642**, 868 (2006).
7. C.G.T Haslam *et al*, A&AS **47**, 1 (1982).
8. G. Hinshaw *et al*, ApJS **170**, 288 (2007).
9. E. Komatsu *et al*, ApJS **180**, 306 (2009)
10. A. Kosowsky, Ann. Phys. **246**, 49 (1996).
11. M. -A. Miville-Deschénes *et al*, A&A accepted **astro-ph/08023345**, 2008 (.)
12. L. Page *et al*, ApJSS **170**, 335 (2007).
13. D. J. Schlegel, D. P. Finkbeiner & M. Davies, ApJ **500**, 525 (1998).
14. X.H. Sun *et al*, A & A manuscript **astro-ph/0711.1572v1**, 2008 (.)
15. B. Uyaniker *et al*, A & A.S.S. accepted **astro-ph/9905023v1**, 1999 (.)
16. M. Wolleben *et al*, A.& A. **448**, 411 (2006).

COMPONENT SEPARATION IN CMB OBSERVATIONS

J. DELABROUILLE

*CNRS – Laboratoire APC, 10 rue A. Domon et L. Duquet
75013 Paris, France*

In these proceedings, we discuss the extraction, in WMAP 5 year data, of a clean CMB map, of foreground emission (dominated by emission of the interstellar medium of our galaxy), and of the tiny signal from Sunyaev Zel'dovich effect in the direction of known galaxy clusters. The implementation of an Internal Linear Combination method locally in both pixel and harmonic space, with the use of a decomposition of WMAP maps onto a frame of spherical needlets, permits to extract a full sky CMB map, with good accuracy even in regions close to the galactic plane. Proper subtraction of this estimated CMB from WMAP original observations provides us with CMB-free foreground maps, which can be used for the analysis of the emission of the galactic interstellar medium and for detecting and measuring emissions from compact sources. Finally, while the Sunyaev-Zel'dovich cannot be detected for individual clusters in WMAP data, due to lack of spatial resolution and sensitivity, a stacking analysis of tentative detections towards a number of known ROSAT clusters permits to detect the SZ effect in WMAP data and measure how the SZ flux scales with cluster mass and X-ray luminosity.

1 Introduction

The separation of emissions from different astrophysical or cosmological origin in Cosmic Microwave Background (CMB) observations is a crucial aspect of CMB data analysis. Component separation consists in extracting maps (or any set of relevant parameters) describing the emission of individual components of interest, from a set of observations containing emissions from several such components¹. For this purpose, one makes use of prior information about the morphology or the shape of individual components, about their color (emission law as a function of wavelength), about their statistical independence. Sky emission as observed by the WMAP satellite contains essentially emission from CMB anisotropies, from the galactic interstellar medium (ISM), and from a small number of strong radiosources. Other emissions, such as the Sunyaev-Zel'dovich (SZ) emission from galaxy clusters, or the emission from a background of numerous and unresolved radio and infrared sources, are too faint to be clearly seen in WMAP data. In these proceedings, we discuss briefly some recent work on the extraction of a clean CMB map, of maps of foreground emission, and of the detection of thermal SZ effect towards a set of 893 known ROSAT clusters.

2 A clean CMB map from WMAP data

The CMB is a very special component. Its spectral emission law is perfectly known theoretically. Its anisotropies are known to be very close to Gaussian, and are not significantly correlated to other emissions (with the exception of a small correlation with tracers of large scale structure such

as galaxies and clusters of galaxies, as such large scale structure can induce CMB anisotropies via the Integrated Sachs-Wolfe effect).

The simplest model of multifrequency CMB observations such as those of the WMAP satellite is $\mathbf{x} = \mathbf{a}s + \mathbf{n}$, where \mathbf{x} is the vector of observations (e.g. five maps), \mathbf{a} is the response to the CMB for all observations (e.g. a vector with 5 entries equal to 1 if WMAP data only are considered) and \mathbf{n} is the noise (including any foreground contaminants). Here it is assumed (for the moment) that all observations are at the same resolution. Assuming that we know the noise covariance \mathbf{R}_n , the (generalised) least square (GLS) solution gives an estimate \hat{s}_{GLS} of s as follows:

$$\hat{s}_{\text{GLS}} = \frac{\mathbf{a}^t \mathbf{R}_n^{-1}}{\mathbf{a}^t \mathbf{R}_n^{-1} \mathbf{a}} \mathbf{x} = \frac{\mathbf{a}^t \mathbf{R}_x^{-1}}{\mathbf{a}^t \mathbf{R}_x^{-1} \mathbf{a}} \mathbf{x} \quad (1)$$

where the noise covariance matrix \mathbf{R}_n is a 5×5 matrix, and \mathbf{R}_x is the covariance matrix of the total signal including CMB. The last equality comes from the fact that, recalling that $\mathbf{R}_x = \mathbf{R}_n + \sigma^2 \mathbf{a} \mathbf{a}^t$, where σ^2 is the variance of the CMB, and making use of the inversion formula:

$$[\mathbf{R}_n + \sigma^2 \mathbf{a} \mathbf{a}^t]^{-1} = \mathbf{R}_n^{-1} - \sigma^2 \frac{\mathbf{R}_n^{-1} \mathbf{a} \mathbf{a}^t \mathbf{R}_n^{-1}}{1 + \sigma^2 \mathbf{a}^t \mathbf{R}_n^{-1} \mathbf{a}} \quad (2)$$

we have $\mathbf{a}^t \mathbf{R}_x^{-1} \propto \mathbf{a}^t \mathbf{R}_n^{-1}$.

In the absence of prior information about the foregrounds, the GLS solution cannot be implemented using \mathbf{R}_n^{-1} in equation 1. Diagonal terms in \mathbf{R}_n contain contributions from instrumental noise and from foregrounds, whereas off-diagonal terms arise from the covariance of the foreground emission between WMAP channels, which is not known *a priori*.

An alternate solution is to use the so-called Internal Linear Combination (ILC) method, which estimates the CMB as the linear combination of the input maps with minimum variance (in fact, minimum power) and unit response to CMB. The ILC CMB estimate is:

$$\hat{s}_{\text{ILC}} = \frac{\mathbf{a}^t \hat{\mathbf{R}}_x^{-1}}{\mathbf{a}^t \hat{\mathbf{R}}_x^{-1} \mathbf{a}} \mathbf{x} \quad (3)$$

where $\hat{\mathbf{R}}_x$ is the empirical covariance matrix of the observations, i.e. an estimate of the true covariance \mathbf{R}_x , estimated on the observed maps. Hence, the ILC method is, in some sense, an approximation of the GLS method. The ILC uses, instead of the unknown \mathbf{R}_n or \mathbf{R}_x , the empirical covariance matrix $\hat{\mathbf{R}}_x$ of the observations.

An ILC estimate of the CMB map from WMAP data has been obtained by a number of authors. The ILC solution is just a linear combination of the inputs. However, it is clear that the optimal linear combination should depend on scale as well as on the region of the sky considered. This can be achieved by implementing the ILC using wavelets of some sort on the sphere. Here we use a decomposition on a needlet frame. The initial observations (WMAP and a 100 micron map tracing the dust emission) are decomposed in sets of needlet coefficients, for a set of scales and a set of pixels on the sphere. The 100 micron observation helps subtracting dust emission on small scales, which is otherwise essentially significant in the W channel only (and hence cannot be removed by linear combinations of WMAP channels alone). The ILC is then implemented independently on sets of such coefficients, and a final CMB map, at full WMAP W channel resolution, is obtained by reconstructing the full sky CMB from the needlets coefficients of the CMB map obtained in this way². The resulting map is displayed in figure 1. Comparison with earlier work shows that the needlet ILC (NILC) map is less contaminated by galactic foregrounds than most other ILC maps obtained by various authors without making use of the needlet decomposition. The NILC CMB map can be downloaded from a dedicated web page^a.

^ahttp://www.apc.univ-paris7.fr/APC/Recherche/Adamis/cmb_wmap-en.php

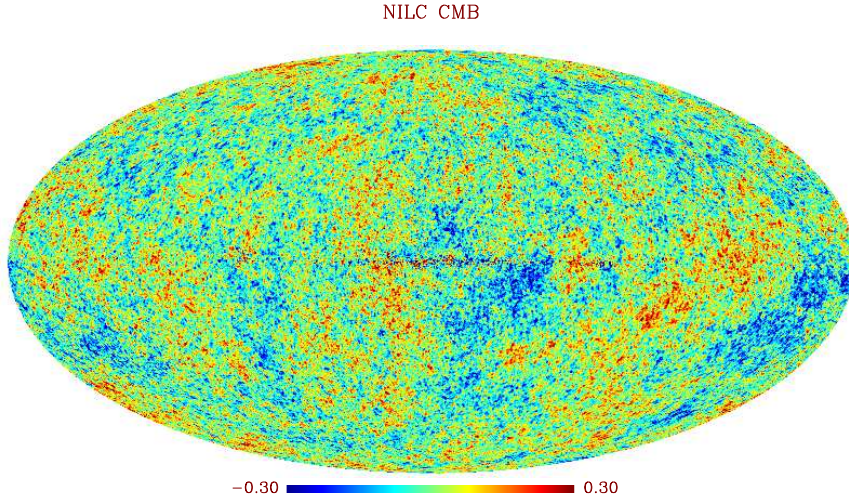


Figure 1: CMB map obtained with WMAP 5 year data by needlet ILC (units are mK thermodynamic).

3 Foreground emission in WMAP data

Once a clean CMB map has been obtained, it is quite natural to subtract it from the original observations to get foreground maps free of CMB contamination. It should be noted, however, that on small scales the CMB map at the resolution of the WMAP W channel contains more noise than CMB. Direct subtraction of the CMB map from the observation of one WMAP channel, with simple smoothing to put it at the resolution of the channel considered, would result in significant small scale extra noise. This noise, in addition, would be correlated from channel to channel. Hence, we subtract from each band-averaged map a Wiener-filtered version of the NILC CMB map³. After this is done, latitude-dependent additional smoothing, using a Gaussian beam which maximizes the signal to noise ratio at that latitude, is performed. The impact of the various stage of the processing for a patch of the WMAP K-band map at moderate galactic latitude ($l = 70^\circ$, $b = -30^\circ$) is illustrated in figure 2.

4 Cluster SZ emission in WMAP data

The thermal SZ effect, due to inverse Compton scattering of CMB electrons off hot electrons in intra-cluster gas, leaves in principle a detectable (albeit small) imprint in CMB observations. WMAP, however, is not an ideal instrument for its detection. The pixel sensitivity is not quite good enough, and the angular resolution of 15 to 60 arcminutes (depending on the channel) does not permit to resolve the large majority of galaxy clusters.

Given a cluster profile and the WMAP beam profiles for all frequency bands, one can build multifrequency matched filters⁴ to detect clusters in WMAP data. A blind search does not yield any significant detection. It is possible, however, to look for known SZ clusters observed by ROSAT, using a prior model profile derived from X-ray observations for each of them. The detection does not depend much on this profile, as for unresolved clusters the actual cluster profile on the maps is essentially set by the beam.

For each individual ROSAT cluster, no significant SZ signal is detected, even when making use of prior information about the cluster location and profile. It is possible, however, to average the estimated SZ flux (the Y_{SZ} parameter) from clusters in redshift bins, in bins of X-ray luminosity, or in bins of mass (the mass being estimated from the X-ray flux). The SZ signal is then clearly detected. This permits to measure how the SZ flux depends on the cluster mass

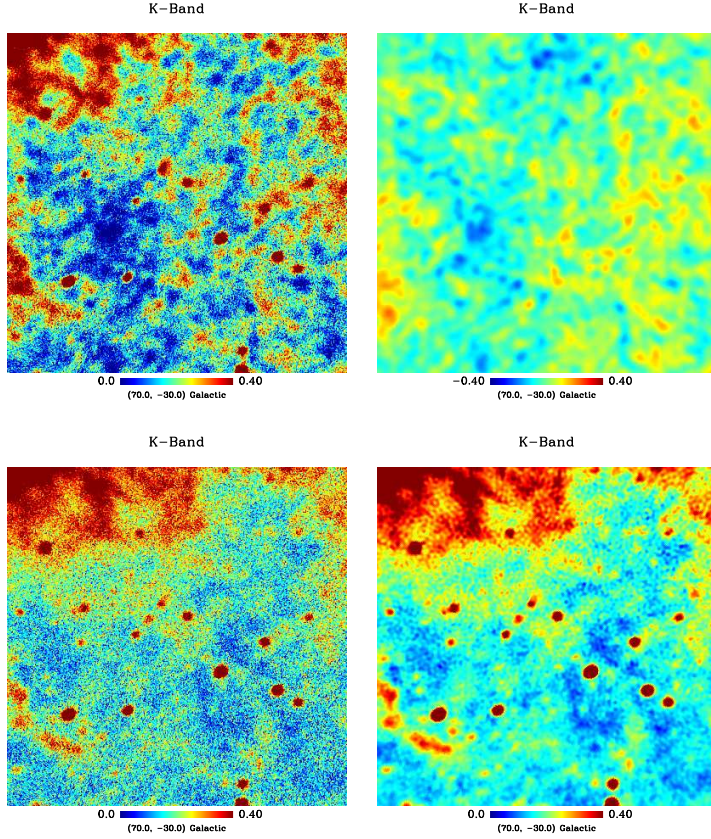


Figure 2: Top: left = K-band map, right = CMB. Bottom: left = after CMB subtraction, right = after filtering.

and on the X-ray luminosity. Hence, even if clusters are not detected individually, a filter which makes use both of the frequency dependence and of the expected profile of the clusters permits to extract relevant information about a component which is, in this data set, very subdominant. The reader is invited to look for additional details in the relevant publication⁵.

5 Conclusion

Component separation is an important aspect of the analysis of CMB observations. Examples of extraction of the CMB, foreground emission, and thermal SZ effect from WMAP data have been discussed. No single component separation method is optimal for the extraction of all components. Instead, one has to design methods adapted to the component(s) of interest and to the scientific objectives. A component separation pipeline must chain several such methods and put them all in a coherent frame. This is becoming crucial for upcoming sensitive experiments, for which instrumental noise will be a subdominant source of error as compared to the confusion due to emissions from a large number of astrophysical processes.

References

1. J. Delabrouille and J.-F. Cardoso, *Lecture Notes in Physics* **665**, 159 (2009)
2. J. Delabrouille *et al.*, *A&A* **493**, 835 (2009).
3. T. Ghosh *et al.*, ArXiv preprint astro-ph/1006.0916 (2010)
4. J.-B. Melin, J. Bartlett and J. Delabrouille, *A&A* **459**, 341 (2006)
5. J.-B. Melin *et al.*, ArXiv preprint astro-ph/1001.0871 (2010)

2. Clusters / SZ

FORECASTING COSMOLOGICAL CONSTRAINTS FROM FUTURE X-RAY CLUSTER SURVEYS

BARBARA SARTORIS, STEFANO BORGANI

Dipartimento di Fisica, Sezione di Astronomia, Università di Trieste, Via Tiepolo 11, I-34143 Trieste, Italy

*INAF-Osservatorio Astronomico di Trieste, Via Tiepolo 11, I-34143 Trieste, Italy
INFN, Sezione di Trieste, Via Valerio 2, I-34127 Trieste, Italy*

We present forecasts for constraints on deviations from Gaussian distribution of primordial density field perturbations from future X-ray surveys of galaxy clusters. We use the WFXT surveys that have high-sensitivity and wide-area to detect about 2.5×10^5 extended sources, and to provide reliable measurements of robust mass proxies for about 2×10^4 clusters. Computing the Fisher-Matrix for number counts and large-scale power spectrum of clusters, we constrain at once nine cosmological parameters and four nuisance parameters, which define the relation between cluster mass and X-ray flux, using the so-called self-calibration approach. Because of the scale dependence of large-scale bias induced by local-shape non-Gaussianity, we find that the power spectrum provides strong constraints on the non-Gaussianity f_{NL} parameter, which complement the stringent constraints on the power spectrum normalization, σ_8 , from the number counts. To quantify the joint constraints on the two parameters, σ_8 and f_{NL} , that specify the timing of structure formation for a fixed background expansion, we define the figure-of-merit $FoMs_{FT} = (\det [Cov(\sigma_8, f_{NL})])^{-1/2}$. We find that our surveys constrain deviations from Gaussianity with a precision of $\Delta f_{NL} \simeq 10$ at 1σ confidence level, with $FoMs_{FT} \simeq 39$. We point out that constraints on f_{NL} are weakly sensitive to the uncertainties in the knowledge of the nuisance parameters. As an application of non-Gaussian constraints from available data, we analyse the impact of positive skewness on the occurrence of XMMU-J2235, a massive cluster $z \simeq 1.4$. Its presence turns out to be a rather unlikely event, even evading either the available constraints on f_{NL} or on σ_8 .

1 Introduction

Generalizations of the most standard model of inflation give rise to seed primordial density fluctuations that follow a non-Gaussian probability distribution¹. Therefore, testing at what precision we can measure possible deviations from Gaussianity with available and future observations has important implications on our understanding of the mechanism that seeded density fluctuations in the early Universe.

Analyses of the Cosmic Microwave Background (CMB) provide at present the highest constraints on the amount of allowed non-Gaussianity², but non-Gaussian perturbations are also expected to leave their imprint on the pattern of structure growth, at least in two different ways. First, a positively skewed distribution provides an enhanced probability of finding large overdensities, that means that the probability of forming large collapsed structures enhances at high redshift, changing the timing of structure formation and the shape and evolution of the mass function of dark-matter halos. Second, non-Gaussianity affects the large-scale clustering of halos in such a way that the linear biasing parameter acquires a scale dependence. This modifies

the power spectrum of the distribution of any tracer of cosmic structures at small wavenumbers and offers a unique way of testing the nature of primordial fluctuations.

To test non-Gaussianity in the regimes where its effects are more apparent, we need surveys that cover a large enough volume at high redshift and whose sensitivity and angular resolution are high enough to warrant an accurate measurement of robust mass proxies. Surveys with these characteristics can be provided by an already proposed X-ray telescope, WFXT³, in which a *Wide* survey covering most part of the extragalactic sky is complemented by a *Medium* and by a *Deep* surveys.

In our analysis⁴ we derive forecasts, based on the Fisher–Matrix approach, on the capability of future X-ray cluster surveys such WFXT to constrain deviations from Gaussian perturbations.

2 Method

The deviation of primordial density fluctuations distribution from the Gaussian one can be parameterize writing the Bardeen’s gauge invariant potential Φ as $\Phi = \Phi_G + f_{NL} * (\Phi_G^2 - \langle \Phi_G^2 \rangle)$, where f_{NL} is the parameter that denotes the amplitude of the deviation from Gaussianity and is related to the skewness of the distribution. If the distribution of primordial density perturbations is not Gaussian, it cannot be fully described by a power spectrum expressed as $P_\Phi(\mathbf{k}) = B k^{n-4}$, but we need higher-order moments such as the bispectrum. In particular, different models of inflation give rise to different shapes of the bispectrum: we adopt the *local shape*, one giving the largest effects especially on bias, for which the bispectrum is maximized for configurations in which one of the three momenta is much smaller than the other two (“squeezed” configurations).

Through the presence of skewness and bispectrum two of the ingredients that critically affect the observed properties of the cluster population are influenced by non-Gaussian initial conditions: the halo mass function and the linear bias of dark-matter halos. For non-Gaussian mass function different prescriptions exist: we adopt the one from Lo Verde et. al. (2008)⁵ (Eqs. (4.19) and (4.20) of that paper), where the authors approximated the probability distribution for the smoothed dark-matter density field using the Edgeworth expansion. The non-Gaussian halo bias can be written, following Matarrese & Verde (2008)⁶, as the sum a Gaussian term and a term encapsulates the non-Gaussian dependence on the scale.

Our analysis is based on computing the Fisher Matrix (FM) for the information provided by the evolution of mass function and power spectrum of galaxy clusters.

An important problem in cluster analysis is that we don’t actually measure the mass of clusters so we have to relate, under some assumptions, the observable quantities like luminosity or temperature, to the halo mass; this gives rise to a systematic bias in the estimation of the mass and an intrinsic scatter. We include them, both function of redshift, following Lima & Hu (2005)⁷ in our analysis. According to the self-calibration approach⁸, the model parameters entering in the FM estimate are nine cosmological parameters (reference values from WMAP-7) and 4 nuisance parameters, defining the clusters observable–mass relation.

To include clustering information in deriving FM survey forecasts we follow the approach by Tegmark (1997)⁹ where different scales are weighted by the effective volume, means the volume accessible by the survey at redshift z at wavenumber k weighted by the shot noise level associated the the cluster distribution.

An alternative method to include clustering information is the so called count-in-cell approach⁷: one makes a partition of the sky area covered by a survey into regular cells of a fixed angular size and then computes the fluctuations in the cluster counts within such cells. Since this method does not explicitly include the covariance between counts within different cells¹⁰, it only samples clustering at a fixed angular scale. Cunha et al. (2010)¹¹ use the count-in-cell approach by also including the information from the covariance. Therefore, in the count-in-cell approach the information on the large-scale power spectrum is conveyed by the covariance terms.

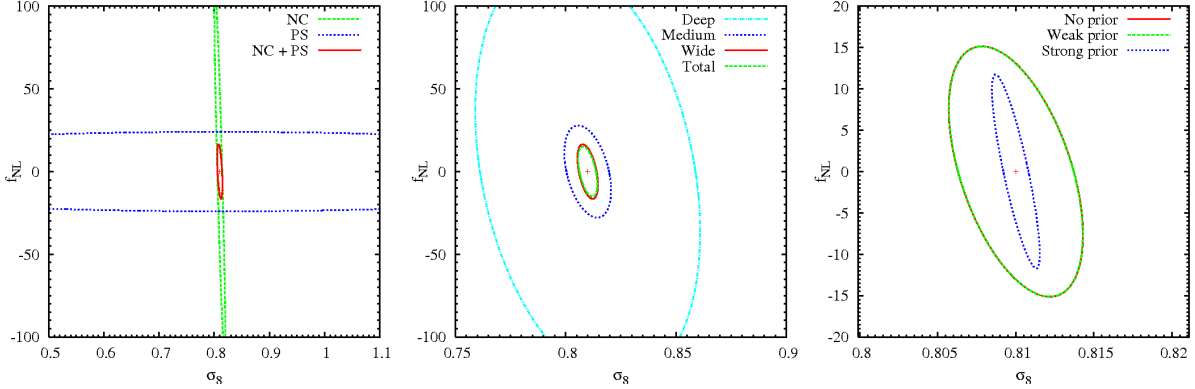


Figure 1: Constraints at the 68 per cent confidence level on non-Gaussian parameter f_{NL} and power spectrum normalization σ_8 : **Left:** coming from number counts alone (short-dashed green curve), power spectrum alone (dotted blue curve) and from the combination of the two (solid red curve). The analysis refer to the clusters detected in the Wide Survey. *No prior* is assumed for the values of the nuisance parameters. **Center:** from the Deep, Medium and Wide surveys (dot-dashed cyan, dotted blue and solid red curves, respectively), by combining number counts and power spectrum information, by using no priors on the nuisance parameters. Also shown with the short-dashed green curve are the constraints obtained from the combination of the three surveys. *No prior* is assumed for the values of the nuisance parameters. **Right:** by assuming *no prior* (solid red curve), *weak prior* (dashed green) and *strong prior* (dotted blue) on the nuisance parameters. Constraints are obtained by combining cluster number counts and power spectrum information for the three surveys together. The FM from Planck experiment is included in the calculation of all constraints.

3 Results

We present ⁴ forecasts on constraints from non-Gaussian models. These results will be shown in terms of constraints on the σ_8 – f_{NL} plane after marginalizing over the other cosmological and nuisance parameters. The reason for this choice is that, for a fixed Friedmann background, σ_8 and f_{NL} are the two parameters which determine the timing of structure formation and, therefore, the evolution of number density and large-scale clustering of galaxy clusters. Information on such constraints are quantified by introducing the figure-of-merit for structure formation timing defined , in analogy with ¹², as $\text{FoM}_{\text{SFT}} = (\det[\text{Cov}(\sigma_8, f_{\text{NL}})])^{-1/2}$. The main results obtained from our analysis can be summarized as follows.

- 1) Power spectrum and number counts of galaxy clusters are highly complementary in providing constraints (Fig. 1, left pannel): while number counts are highly sensitive to the value of σ_8 , the weak sensitivity of the high-end of the mass function to non-Gaussianity provides only very weak constraints on f_{NL} ; conversely, the scale-dependence of bias makes the power spectrum a powerful diagnostic for non-Gaussianity, while providing only loose constraints on σ_8 .
- 2) Combining number counts and power spectrum information for the three surveys turns into $\Delta f_{\text{NL}} \simeq 10$ for the 1σ uncertainty with which a deviation from Gaussianity associated to a “local shape” model can be constrained. Correspondingly, we find $\text{FoM}_{\text{SFT}} \simeq 39$ for the figure-of-merit of structure formation timing (Fig. 1, center pannel). Most of the constraining power is provided by the Wide survey for two main reasons. First, the Wide survey provides the largest statistical baseline out to $z \simeq 1.5$, when including all clusters down to the mass limit corresponding to detection. This implies a better determined mass function and, therefore, stronger constraints on σ_8 . Second, the larger area coverage of the Wide survey allows it to better sample long-wavelength modes, where the scale-dependence of the bias induced by non-Gaussianity can be better assessed, thus turning into stronger constraints on f_{NL} .

- 3) We presented results by assuming prior on cosmological parameters from Planck experiment and *no prior* knowledge on the nuisance parameters: this is probably too much a conservative approach, in view of the calibration of the relation between robust mass proxies (e.g., Y_X and M_{gas}) and X-ray luminosity for a large number of clusters within the planned surveys. In the right pannel of figure 1 we show the effect of assuming a prior knowledge of the nuisance parameters. If we assume the *weak priors* for these parameters, constraints are very slightly improved. Quite interestingly, even assuming the *strong prior* (i.e. nuisance parameters fixed) improves the constraints on σ_8 , while having a relative smaller impact on those for f_{NL} .
- 4) As an application of non-Gaussian constraints from available data, we analyse the impact of positive skewness on the occurrence of XMMU-J2235, a massive distant cluster recently discovered at $z \simeq 1.4$. We confirm that in a WMAP-7 Gaussian Λ CDM cosmology, within the survey volume, $\simeq 5 \times 10^{-3}$ objects like this are expected to be found. To increase the probability of finding such a cluster by a factor of at least 10, one needs to evade either the available constraints on f_{NL} or on the power spectrum normalization σ_8 .

Acknowledgments

WE thank our collaborators: C. Fedeli, L. Moscardini, S. Matarrese, P. Rosati and J. Weller. BS thanks the organizers of Moriond meeting for the award of a grant.

References

1. Bartolo N., et al. 2004 Phys. Rept., 402, 103
2. Komatsu, E., et al. 2010, arXiv:1001.4538
3. Giacconi, R., et al. 2009, astro2010: The Astronomy and Astrophysics Decadal Survey, 2010, 90
4. Sartoris, B., Borgani, S., Fedeli, C., Matarrese, S., Moscardini, L., Rosati, P., & Weller, J. 2010, arXiv:1003.0841
5. LoVerde M., et al. 2008, Journal of Cosmology and Astro-Particle Physics, 4, 14
6. Matarrese S., Verde L., 2008, ApJ, 677, L77
7. Lima M., Hu W., 2005, Phys. Rev. D, 72, 043006
8. Majumdar S., Mohr J. J., 2003, ApJ, 585, 603
9. Tegmark M., 1997, Physical Review Letters, 79, 3806
10. Oguri M., 2009, Physical Review Letters, 102, 211301
11. Cunha, C., Huterer, D., & Dore, O. 2010, arXiv:1003.2416
12. Albrecht A., et al. 2009, ArXiv e-prints, 0901.0721

Spectroscopic follow-up of the South Pole Telescope galaxy clusters

G. Bazin

*Department of Physics, Ludwig-Maximilians-Universität, Scheinerstr. 1, 81679 München, Germany
Excellence Cluster Universe, Boltzmannstr. 2, 85748 Garching, Germany*

We present the spectroscopic follow-up of 3 galaxy clusters detected using the Sunyaev-Zel'dovich Effect (SZE) with the South Pole Telescope. We obtained the redshift of several member galaxies (from 18 to 37) and derived dynamical masses using the velocity dispersion of each cluster. In the near future, we hope to get additional data to provide a dynamical scaling relation between the SZE flux and the cluster mass competitive and complementary to other probes like X-ray observations.

1 Introduction

The Sunyaev-Zel'dovich Effect (SZE) is a small distortion of the CMB spectrum by Compton scattering of the CMB photons with the hot gas of the clusters (Sunyaev and Zel'dovich 1972). This provides an interesting method to detect massive galaxy clusters because the SZE is almost redshift-independent (Carlstrom et al. 2002). The 10-m South Pole Telescope (SPT, Carlstrom et al. 2009) was designed for large scale, multifrequency surveys of the CMB with arcminute resolution (Ruhl et al 2004). Therefore, the SPT survey is well suited to deliver large, essentially mass selected samples of clusters that extend over the full redshift range where those clusters exist. Indeed, we published the discovery of 4 high mass SPT clusters in Staniszewski et al. (2008) and recently submitted a new catalog with 17 additional SPT clusters from our initial 200 deg² survey (Vanderlinde et al. 2010). The SPT survey continues and will cover more than 1400 deg² by the end of the 2010 season.

To study cosmic acceleration using clusters (Haiman et al 2001) requires that the SPT cluster selection be very carefully characterized, and the relationship between cluster SZE signatures and cluster mass (the scaling relation) be understood over a broad redshift and mass range. The evolution of cluster mass with the redshift puts direct constraints on the growth of structures and therefore on the expansion history of the Universe (e.g. Vikhlinin et al. 2009). Thus, the accuracy reached in the scaling relation has a direct impact on the cosmological constraints provided by the SPT cluster sample.

Galaxy velocity dispersions are known to be a good mass proxy because galaxies are not affected by the hydrostatic state of the gas in the cluster. Therefore, velocity dispersions do not depend on the gas physics such as magnetic fields, AGN feedback and cosmic rays. Evrard et al. (2008) showed an intrinsic scatter of 5% on the mass using velocity dispersions derived from N-body numerical simulations. A key issue is possible kinematic biases of galaxies relative to dark matter. This systematic is expected to be a 10% effect (e.g. Carlberg et al. 1990), making it appropriate for us to obtain a dispersion mass calibration with this statistic precision and thus, at the level of the systematics uncertainties affecting the X-ray mass calibration (Vikhlinin

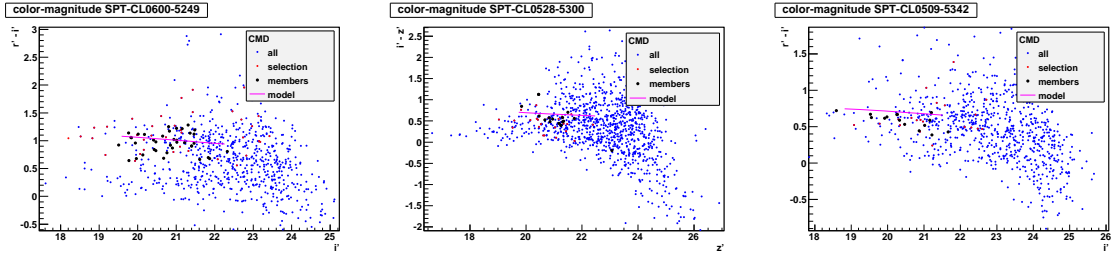


Figure 1: Selection of the red sequence (red dots) on color-magnitude diagrams. The identified members are indicated in black.

et al. 2009).

In this paper, we present the first dynamical mass estimates for 3 clusters detected by the SPT.

2 Observations

2.1 SPT-SZE

The SPT survey observed a uniform 196 deg² area (177.5 deg² after point-source masking) for 1500 hr in 2008 (Carlstrom et al. 2009). Details of the data processing, map-making, cluster extraction and significance estimates are given in Vanderlinde et al. 2010. We report the spectroscopic follow-up of 3 SPT clusters at $S/N > 5$ in their SZE decrement at 150 GHz and in an intermediate range of redshift ($0.46 < z < 0.77$).

2.2 Optical imaging

The Blanco Cosmology Survey (BCS) is an NOAO survey program to obtain deep optical griz imaging over 100 deg² in a subset of the SPT 05hr and 23hr fields (Ngeow et al. 2009, High et al. 2010). The BCS data typically reach 5σ AB depths of 24.75, 24.65, 24.35 and 23.5 in $g'r'i'z'$. BCS data was available for 2 of our clusters: SPT-CLJ0528-5300 and SPT-CLJ0509-5342.

For SPT-CLJ0600-5249 that fell outside the BCS coverage, $g'r'i'z'$ Magellan imaging was obtained as part of a larger program to get an optical confirmation of the SPT clusters. The observing strategy was to expose roughly 100s in $g'r'i'z'$, to search for a cluster in the images and to continue additional exposures if none was found (see High et al 2010 for additional informations).

2.3 Gemini spectroscopy

Multi-object spectroscopy towards the 3 clusters was acquired on the 8.1-m Gemini South telescope from UT December 2009 to January 2010. Galaxies with $r' - i'$ or $i' - z'$ color consistent with a cluster red-sequence at the appropriate redshift (Song et al. 2010) and having non-stellar PSFs in the Gemini i-band pre-image were used to populate two masks, allowing us to get 40-45 spectra/cluster using the R150-G5326 grism and the GG455-G0329 filter. Figure 2.3 represents the selected red sequence for each of our clusters as well as the identified members. For each mask, the total exposure time was 90 min, 30 min and 40 min for SPT-CL0528-5300, SPT-CLJ0509-5342 and SPT-CLJ0600-5249 respectively.

The IRAF Gemini reduction package was used for standard CCD processing. The wavelength-calibrated 2D spectra were sky-subtracted using an in-house routine, after which the 1D spectra were extracted from the coadded 2D spectra.

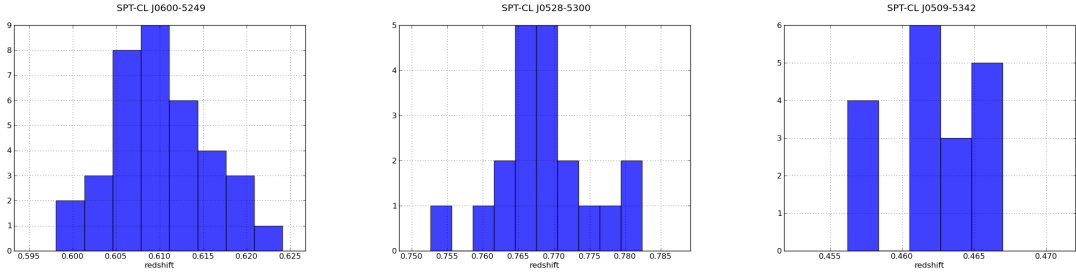


Figure 2: Redshift dispersions

3 Results

3.1 Redshifts

We developed our own tool to compute the redshift for galaxies exhibiting absorption features. This algorithm relies on a χ^2 minimization between the observed spectrum and the SDSS early-type galaxy template. The convergence of the algorithm was checked by visual inspection and judged by the presence of absorption lines.

We got secure redshifts for roughly half of the selection and selected the cluster members by a 3σ clipping around the mean value. Eventually, we identify the redshift for 37/74, 18/39 and 20/43 members for SPT-CLJ0600-5249, SPT-CLJ0509-5342 and SPT-CLJ0528-5300 respectively.

3.2 Velocity dispersion

Because the redshift distributions of our clusters (figure 3.2) are not gaussian, we used the robust biweight estimator of Beers et al. (1990) to estimate the mean velocity and velocity dispersion. The errors (68% confidence interval) are gotten from bootstrap resampling. The obtained velocity dispersions are 1070_{-100}^{+200} km/s, 720_{-70}^{+90} km/s and 1160_{-190}^{+370} km/s for SPT-CLJ0600-5249, SPT-CLJ0509-5342 and SPT-CLJ0528-5300 respectively.

We derived dynamical masses for our clusters following the Evrard et al. 2008 calibration between the line-of-sight velocity dispersion and the halo mass. The uncertainty in the derived mass is largely dominated by the poisson noise in the velocity dispersion since $M \sim \sigma^3$. Table 3.2 summarize our results for these 3 clusters.

Cluster	SZ S/N	redshift	σ (km/s)	M_{200} ($10^{14} M_\odot$)
SPT-CLJ0600-5249	9.28	0.61	1070_{-100}^{+200}	$10.4_{-2.8}^{+7.1}$
SPT-CLJ0509-5342	6.61	0.46	720_{-70}^{+90}	$3.5_{-1.0}^{+1.5}$
SPT-CLJ0528-5300	5.45	0.77	1160_{-190}^{+370}	$12.0_{-5.2}^{+15.3}$

Table 1: Dynamical masses

Compared to the SZ derived masses given in Vanderlinde et al. 2010, our dynamical mass is in agreement within 1σ for SPT-CLJ0509-5342 ($M_{\text{SZ}} = 5.43 \pm 1.24$) and tends to be overestimated for SPT-CLJ0600-5249 and SPT-CLJ0528-5300 ($M_{\text{SZ}} = 6.61 \pm 1.34$ and $M_{\text{SZ}} = 3.67 \pm 0.95$ respectively). Given that we only have 3 dispersions available, further studies on more clusters are needed to efficiently compare our masses with SZ mass estimates and with other proxies like X-ray.

In the near future, we hope to obtain spectroscopic observation time at the Gemini, Magellan and VLT telescopes. These observations would allow us to calibrate a scaling relation relying on dynamical masses and to put some constraints on the evolution of this relation dividing the full sample in several redshift bins. We also aim to compare the systematics between dynamical mass measurement and masses derived using others probes like X-rays.

References

1. Beers *et al*, *The Astronomical Journal* **100**, 32 (1990).
2. Carlstrom *et al*, *The Astrophysical Journal* **352**, 29C (1990).
3. Carlstrom *et al*, *ARA&A* **40**, 643 (2002).
4. Carlstrom *et al*, submitted (arXiv/0907.4445).
5. Evrard *et al*, *APJ* **672**, 122-137 (2008).
6. High *et al*, submitted (arXiv/1003.0005).
7. Ngeow *et al*, *BAAS* **41**, 335 (2009).
8. Ruhl *et al*, *SPIE* **5498**, 11 (2004).
9. Song *et al*, in prep.
10. Staniszewski *et al*, *The Astrophysical Journal* **701**, 3241 (2008).
11. Sunyaev and Zel'dovich, *CASP* **4**, 173 (1972)
12. Vanderlinde *et al*, submitted (arXiv/1003.0003).
13. Vikhlinin *et al*, *APJ* **692**, 1060V (2009).

Beyond the standard lore of the SZE: opportunities offered from future space born mm and sub-mm experiments.

S. COLAFRANCESCO

ASDC-ASI, Via G. Galilei, c/o ESA-ESRIN, 00040 Frascati, Italy



The SZ effect is a unique tool to study the complex physics of cluster atmospheres because it is sensitive to the specific features of the spectra of the various electronic populations. Multi-frequency observations of galaxy clusters indicate, in fact, that the atmospheres of these systems consist of a complex structure of thermal (hot and warm) and non-thermal (with different origin and spectra) distribution of electrons (and protons) which is, therefore, far from its modelling as a single, thermal electronic plasma. This evidence requires to go beyond the standard lore of the SZ effect. Such a task is challenging for both the theoretical aspects of their modelling and for the experimental goals to be achieved, but it will return a large amount of physical information. In such a context, the coming SZ experiments from space will open a new path in the exploration of the SZ effect as a probe for Cosmology and Astro-Particle Physics

1 Galaxy cluster physics: more than basics

The electronic distribution of the atmospheres of galaxy clusters is neither simple nor unique. There are, in fact, various matter components in clusters that can provide different sources of electrons: baryons, relativistic plasmas, Dark Matter annihilation.

Many galaxy clusters contain, in addition to the thermal intra-cluster gas, a population of relativistic electrons (with $E_e \approx 16 \text{ GeV} B^{-1/2} (\nu/\text{GHz})^{1/2} \sim \text{a few GeV}$ to radiate at $\nu \gtrsim 30 \text{ MHz}$ in a μG magnetic field) which produce a diffuse radio emission (radio halos and/or relics) via synchrotron radiation in a magnetized atmosphere (see, e.g., Govoni & Feretti 2004 for a review). The origin of such relativistic electrons is not clear and models of bottom-up production (i.e., re-accelerated by intra-cluster turbulence) or top-down origin (i.e., secondarily produced by Dark Matter WIMP annihilation) can fit the observed radio-halo features (see Ferrari at this Meeting). The presence of Extreme UV/soft X-ray excesses in a few nearby clusters indicate the presence of an additional population of secondary relativistic electrons or a combination of warm (reproducing the EUV excess) and (quasi-)thermal (reproducing the hard X-ray excess

by bremsstrahlung) populations of distinct origins (see Colafrancesco 2008 for a review and references therein). The evidence for further physical phenomena occurring in the cluster atmospheres – e.g., non-thermal heating in the cluster cores (see, e.g., Colafrancesco, Dar & DeRujula 2004, Colafrancesco & Marchegiani 2008 and references therein), AGN and radio-galaxy feedback, intra-cluster cavities (McNamara et al. 2005) and radio bubbles (Birzan et al. 2004) filled with relativistic electrons, multi-scale magnetic fields (see, e.g., Govoni & Feretti 2004) – imply the presence of additional electronic components with peculiar spectral and spatial characteristics. Finally, the viable Dark Matter candidate annihilation/decay can produce copious amounts of secondary electrons with a spatial distribution which is strictly related to that of the original DM (see Colafrancesco et al. 2006).

In conclusion, cluster electronic atmospheres are a complex combination of thermal (hot and warm) and non-thermal (quasi-thermal due to stochastic acceleration, relativistic due to DM annihilation and/or to AGN injection) distributions with different energy spectra and spatial distributions. Each one of the electron populations which reside in the cluster atmosphere inevitably produces a distinct SZE with peculiar spectral and spatial features (see, e.g., Colafrancesco 2007 for a review). To describe the various forms of SZE in a unique and consistent theoretical framework, we must go beyond the standard lore of the SZE.

2 Beyond the standard lore of the SZ effect

The generalized relativistic expression for the SZE which is valid in the Thomson limit ($\gamma h\nu \ll m_e c^2$ in the electron rest frame) for a generic electron population and includes also the effects of multiple scatterings and the combination with other electron populations has been derived by Colafrancesco et al. (2003). According to these results, the spectral distortion of the CMB spectrum observable in the direction of the specific structure is

$$\Delta I(x) = 2 \frac{(k_B T_{CMB})^3}{(hc)^2} y \tilde{g}(x) , \quad (1)$$

with $x \equiv h\nu/k_B T_{CMB}$, where the Comptonization parameter y is

$$y = \frac{\sigma_T}{m_e c^2} \int P_e d\ell , \quad (2)$$

in terms of the total pressure P_e of the electronic populations. The spectral function $\tilde{g}(x)$ is

$$\tilde{g}(x) = \frac{m_e c^2}{\langle \varepsilon_e \rangle} \left\{ \frac{1}{\tau_e} \left[\int_{-\infty}^{+\infty} i_0(xe^{-s}) P(s) ds - i_0(x) \right] \right\} \quad (3)$$

in terms of the photon redistribution function $P(s)$ and of $i_0(x) = I_0(x)/[2(k_B T_{CMB})^3/(hc)^2] = x^3/(e^x - 1)$, where $\langle \varepsilon_e \rangle \equiv \frac{\sigma_T}{\tau_e} \int P_e d\ell$ is the average energy of the electron plasma (see Colafrancesco et al. 2003) and $\tau_e = \sigma_T \int d\ell n_e$ is the optical depth of the electron population.

In addition to the intensity spectral distortion (see eq.1), a polarization of the SZE arises ubiquitously as a consequence of the Compton scattering process (see Leahy et this Meeting). Analogously to the derivation for the SZE intensity, a general derivation of the polarization patterns of the SZE can be obtained in the full relativistic approach and for a generic combination of electron populations in terms of the generalized expressions of the Stokes parameters of the polarized radiation after the SZE process (Colafrancesco & Tullio 2010 in preparation).

3 Observational strategy

To fully exploit the richness of the physical information contained in the SZE, a spectro-polarimetric study of the SZE signals is required. The simultaneous study of the SZE spectral

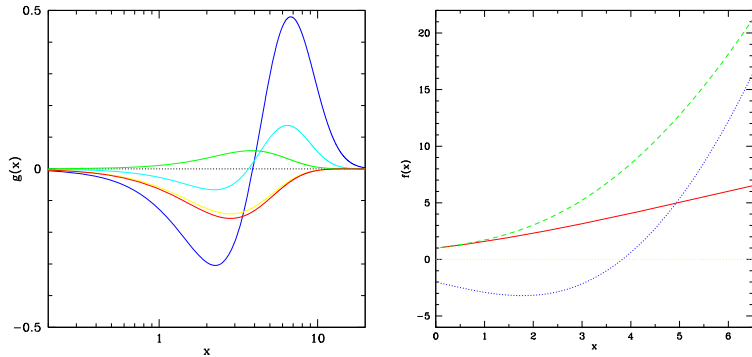


Figure 1: The spectral shape of the SZE intensity from various electronic populations (left): thermal IC gas (blue), warm gas (cyan), relativistic electrons (yellow), DM-produced secondary electrons (red). The kinematic SZE is also shown for positive and negative values of the peculiar velocity (green curves). The spectral shape of the polarized SZE is also shown for various polarization mechanisms (right): the CMB quadrupole and the SZE due to transverse gas motion both (red solid), the SZE due to double scattering in the cluster thermal gas (dotted) and due to the cluster bulk motion (dashed). The zero level of the polarized SZE is also drawn.

and polarization features over a wide frequency range (from ~ 100 to ~ 500 GHz), and with the appropriate spatial resolution (\sim arcsec to arcmin) for the large variety of astrophysical cases (see Colafrancesco 2007), is only possible from space since the atmosphere blocks most of the high frequency microwave radiation coming from these cosmic structures, leaving only a few frequency bands available for ground-based observations.

To achieve the wide spectral range necessary for the full study of the SZE spectra with imaging capabilities (with resolution of \sim arcsec to arcmin), a Fourier Transform spectrometer would be an optimal experimental solution. Specific technical solutions for space-borne projects using Martin-Puplett architecture (Martin & Puplett 1970) have been presented for studies of space experiments (see DeBernardis et al. 2010). These experimental solutions allow a clean differentiation of the spectra coming from two independent inputs covering two continuous areas of the telescope focal plane, so that the measured spectrum is the difference in the spectra of the target source and an offset reference field. For this differential configuration, even small SZE signals can be extracted from a strong background generated, e.g., by the CMB itself, and the intrinsic emission from the telescope, in addition to other signals from the Earth and other astronomical foreground sources. With such experimental choice, a large detector array can be arranged in the focal plane of a sub-mm telescope, thus increasing the mapping speed. A low-to-medium resolution configuration (i.e., a ~ 1 to 10 GHz resolution, but constant over a large frequency band) for the spectrometer envisaged here is completely suitable to study the smooth features of the continuum SZE spectra (see Fig.2). In addition, the experimental design of such instrument allows to evolve it into an spectro-polarimeter that is sensitive to any polarization orientation, thus allowing to extract even small polarized fractions from the SZE signal.

With a 12 m diameter dish the angular resolution, which is limited by diffraction at the telescope entrance aperture, goes from ≈ 1 arcmin FWHM at 100 GHz, to ≈ 12 arcsec FWHM at 500 GHz. With a reduced 4 (3) m diameter dish, the corresponding angular resolution, of the previous bands used to measure the SZE are $\approx 3(4)$ arcmin FWHM and $\approx 0.6(1)$ arcmin FWHM, respectively. The capabilities of such experimental device must be coupled to high-sensitivity detectors to fully exploit the large amount of information enclosed in the SZE signal. Achievable photon noise limited NEP of each detectors can be (with the technology today available) in the range $\sim 10^{-17}$ W/ $\sqrt{\text{Hz}}$ to $\sim 10^{-19}$ W/ $\sqrt{\text{Hz}}$ for a passive or active cooling, respectively, therefore allowing full exploitation of even the smallest SZE signals.

We finally note that spectroscopic and polarimetric devices operating in the sub-mm and

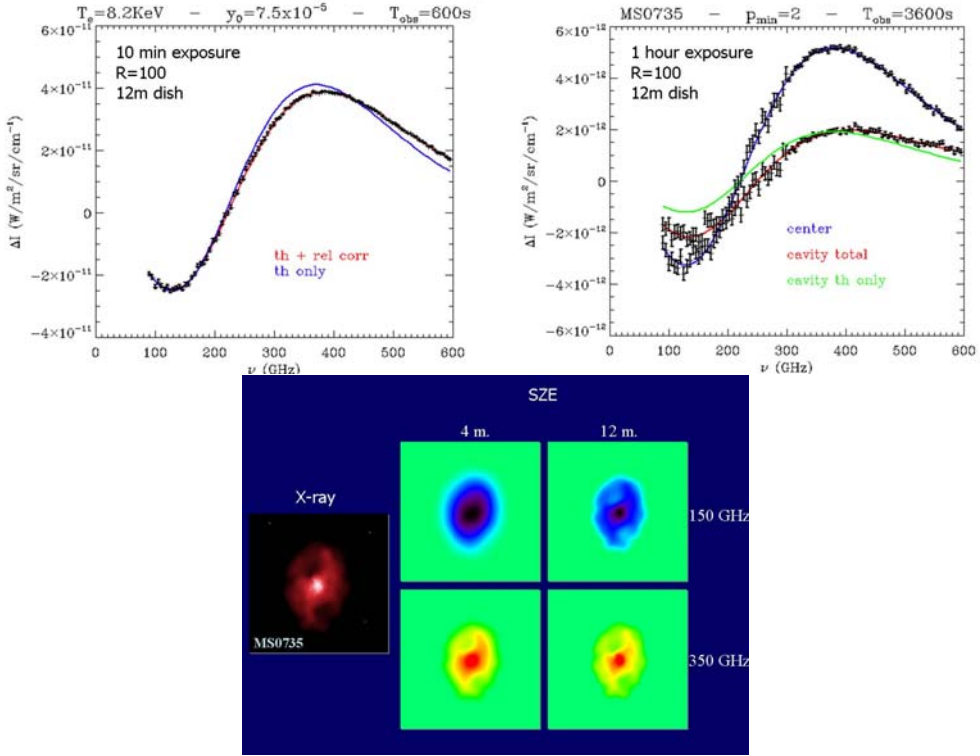


Figure 2: SZE spectra obtainable with typical exposures for Coma (10 min.: upper left) and MS0735+7421 towards one of the cavities (1 hour: upper right). We also show (bottom panel) simulated SZE maps obtainable for the cluster MS0735+7421 at two frequencies (150 and 350 GHz) and for two dish configurations (4 and 12 m).

mm bands enables to explore the physics of a wide range of astrophysical sources, from galaxy clusters to AGNs, from millimeter to starburst galaxies, from galactic molecular clouds, SNRs and star forming regions to planetary atmospheres.

References

1. Birzan, L. et al. 2004, ApJ, 607, 800
2. Colafrancesco, S. 2007, New Astron. Rev., 51, 394
3. Colafrancesco, S. 2008, in Practical Cosmology, Y.V. Baryshev, I.N. Taganov, P. Teerikorpi Eds., p.160-171
4. Colafrancesco, S., Marchegiani, P. & Palladino, E., 2003, A&A, 397, 27
5. Colafrancesco, S., Dar, A. & De Rujula, A. 2004, A&A, 413, 441
6. Colafrancesco, S., Profumo, S. and Ullio, P. 2006, A&A, 455, 21
7. Colafrancesco, S. & Marchegiani, P. 2008, A&A, 484, 51
8. De Bernardis, P. et al. 2010, (arXiv:1002.0867)
9. Govoni, F. & Feretti, L. 2004, IJMPD, 13, 1549
10. Martin, D. & Puplett, E., 1970, Infrared Physics, 10, 105109
11. McNamara, B.R., Nulsen, P.E.J., Wise, M.W. et al. 2005, Nature, 433, 45

Observation model of a Planck-like cluster catalogue

J. Démoclès

*IRFU/Service de Physique des Particules - CEA/DSM - CNRS, Bât. 141, CEA-Saclay,
F-91191 Gif-sur-Yvette Cedex, France*

We present a model, relying on a simulation of the millimetric sky and taking into account known clusters properties, which predicts the observed flux distribution and completeness of a Planck-like cluster catalogue. A Fisher matrix application of this model is shown here.

1 Introduction

The galaxy clusters are the largest structures formed by gravitational collapse. Their abundance is a powerful cosmological probe. In particular, the Sunyaev-Zel'dovich effect provides a way of observing galaxy cluster in millimetric wavelenghts by the characteristic deformation it induces in the CMB spectrum. Furthemore, it provides a mass proxy which is found to be robust with the dynamical state of the cluster.

Nevertheless, the exploitation of the SZ cluster catalogues requires to quantify and understand the systematic effects which affect cluster detection. This can be obtained through a Monte-Carlo based on a reliable simulation of the sky taking into account instrumental effects and on an unbiased cluster extraction algorithm. In addition, we need a reliable association procedure which allows the identification of the recovered clusters among the detected sources.

We present an observation model which directly links the theoretical expectation for cluster abundance in function of SZ flux (Y) and redshift (z) to the observed one in terms of photometry, contamination and completeness.

During all this study, we use Λ CDM model. The cosmological parameters are assumed to be $\Omega_M = 0.3$, $\Omega_\Lambda = 0.7$, $\sigma_8 = 0.8$ and $h = 0.75$.

2 Monte-Carlo simulation

Our simulated maps contain the four main astrophysical components of the millimetric sky which are the primordial CMB anisotropies (excluding the dipole), the bright infra-red (IR) galaxies, the IR emission of the Galaxy and SZ clusters.

The cluster abundance is computed using Jenkins et al [3] mass function. The scaling relations to link cluster mass with its observable properties and cluster profiles are derived from published relation based on X-rays observation [2]. The clusters are assumed elliptical following the prescription of Cooray (2000).

We assume white instrumental noise so that the pixel noise is : $nois_{pix} = n_{eqT} \times \sqrt{N_{BOL} \times t_{pix}}$ where n_{eqT} is the noise at each frequency band, N_{BOL} the number of bolometers at this particular frequency and t_{pix} the time spent on each pixel. These are given following the experiment

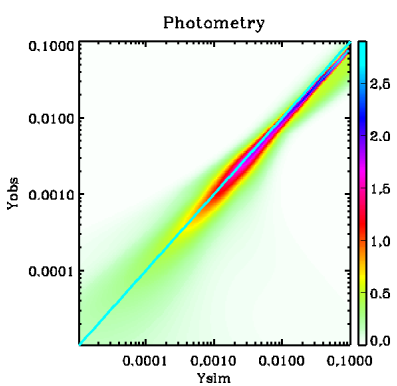


Figure 1: Model of photometry corrected from the threshold effect

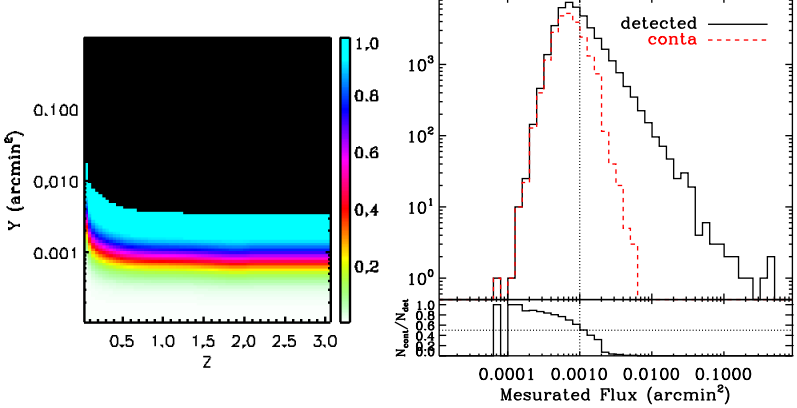


Figure 2: Model of completeness.

Figure 3: Contamination

characteristics as given for a Planck-like nominal survey. In particular, we simulate the sky outside the Galactic plan.

Using a wavelet ILC component separation, we recover a noisy SZ map that we convolute with a Gaussian and apply SExtractor to extract the clusters. This provides a catalogue of detected sources without any assumption on the cluster shape or profile.

We need to identify the true detected clusters among all the sources to characterize the detected catalogue. This is done through an association algorithm based on cluster position in the map. We determine a spherical region around each cluster of the simulated catalogue starting by the brightest ones. The radius of this region d_{ASSO} varies in function of the flux and the size of the cluster. We plot the histograms of the number of associated clusters in function of their distance of association for different ranges of cluster flux and size to determine its dependancies. These distributions exhibit a global maximum before decreasing and flattening at $d_{ASSO} \approx 0.5 \times \theta_{200}$ for the resolved clusters ($\theta_{200} \geq 5$ arcmin). We fix a distance of association of 5 arcmin for the unresolved clusters. We estimate the rate of false association given by the flat tail of the distribution at 1% to 2% (depending on the cluster sizes).

3 Observation model

The observation model is a tool which allows to take into account the survey limitations in the predictions of the cosmological constraints. It quantifies the systematics in the photometry, completeness and contamination.

The photometry is the error on the measured flux. It is really important because it is the mass estimator. Therefore, this error has to be taken into account in addition to the expected dispersion of the mass-SZ flux relation when one intends to compare the observation with the theory. Then, for a theoretical number of clusters of N_{th} and given the experiment, we will observe N_{det} sources which is the sum of the true recovered clusters N_{obs} and the contamination N_{cont} . While the contamination is directly given by the association process, the number of detected cluster is obtained through the application of the selection function of the survey on the theoretical distribution of clusters. Thus, in the plan (Y, z), we can write :

$$\frac{dN_{obs}}{dz dY_{obs}}(z, Y_{obs}) = \int \frac{dN_{th}}{dz dY_{th}}(z, Y_{th}) \times C(z, Y_{th}) \times P(Y_{th} | Y_{obs}) \quad (1)$$

where $C(z, Y_{th})$ is the completeness and $P(Y_{th} | Y_{obs})$ the photometry of the observed catalogue.

Here, we computed each quantities separately.

3.1 Photometry

When we compare the reconstructed flux with the corresponding simulated one, there are mainly two aspects and each one can be described by a Gaussian :

- the first one is the increase of the dispersion. It is the global resolution of the photometry.
- the second one is the systematic effects at low and high flux. At low flux, we see a bias due to a threshold effect. As we approach to the detection threshold only the clusters for which the noise fluctuations make them brighter will be detected. This induces a bias illustrated by a systematic overestimation of the flux of the faint clusters. On the contrary at high flux, we underestimate the flux of the brightest clusters due to their extension on the sky.

In addition to the effects described above, we notice a systematic offset of the measured flux. Indeed it is 10% up to 20% under the simulated value for a measured flux spanning from $Y_{obs} \sim 9 \times 10^{-4}$ to $\sim 2 \times 10^{-1}$ arcmin 2 . This indicates that the flux is not integrated over the full size of the cluster but corresponds instead to only $\approx 0.8 - 0.7 \times R_{200}$ ^a.

To isolate the effect of the photometry from the selection effect of the flux limited selection, we symmetrise the distribution at low flux. The value of the flux where the threshold effect starts is given by the position of the second gaussian when its mean becomes lower than the mean of the first gaussian. In the case of the Planck-like experiment it is found to be at $Y \approx 6 \times 10^{-3}$ arcmin 2 . The result is shown in figure 1.

3.2 Completeness

The completeness of the catalogue comes from the efficiency of detecting a cluster depending on its characteristics, here taken as its redshift and integrated flux. Using the results of the Monte-Carlo, we estimate the completeness by computing the ratio between the distribution of the simulated clusters and the distribution of the recovered clusters in the plan (Y, z).

At each redshift, the completeness is well described by a Fermi-Dirac function :

$$P(Y, z) = 1 - \frac{1}{1 + \exp((Y - Y_A(z))/Y_B(z))}$$

where $Y_A(z)$ is the value of the flux for which the completeness fall at 50% of the simulated sample and $Y_B(z)$ is the slope. The slope increases and the 50% threshold decreases as we go towards high redshift. Indeed, at high z, the signal becomes more concentrated whereas at low z, clusters are more extended so the signal is dimmer. Both the slope and the threshold evolution flatten around $z \sim 1$.

3.3 Contamination

The contamination is given by the number of sources detected but not associated to any simulated clusters. As expected, it is almost 100% of the sources detected at low flux ($Y \sim 10^{-4}$ arcmin 2) and fall close to zero at high flux with a 50% contamination at $Y \sim 10^{-3}$ (figure 3).

^aThe radius where the density of the cluster is 200 times larger than the critical density of the Universe $\rho_c(z)$ at the redshift of the cluster

4 Fisher analysis

The method and results presented here are general to compute the selection function of a SZ survey. Only the parameters of the fits used to model the photometry and the completeness change. We compute the observation model in the case of a smaller survey but with a higher resolution allowing a larger fraction of clusters to be resolved.

A straightforward application of this model is to use it to compute the observed abundance of clusters $dN_{obs}/dzdY$ which is used to constrain the cosmological parameters. We use the formalism of the Fisher matrix to compute the sensibility on Ω_M , Ω_Λ and σ_8 . We compare the results obtained assuming a simple cut in flux at 50% of completeness at high redshift, with those using our model.

The result is shown in figure 4 a) and b). Using a simple cut in flux leads to an optimistic estimation of the constraints. The difference is mainly due to the fact that we overestimate the number of clusters especially at low redshift compared to the case based on the model of completeness.

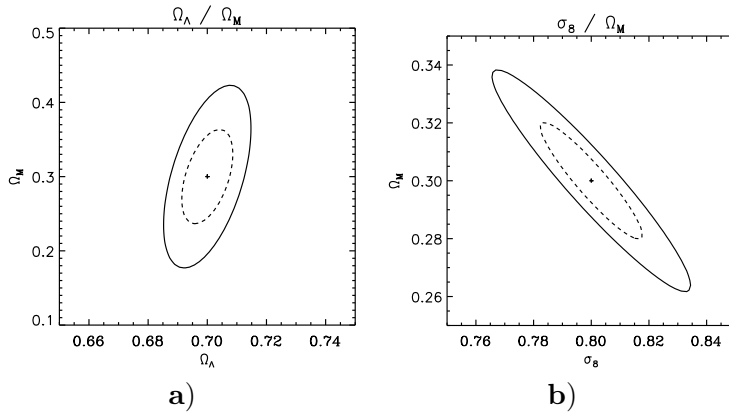


Figure 4: **Prediction of the cosmological constraints** assuming all the other parameters known : a) In the plan Ω_Λ, Ω_M . b) In the plan σ_8, Ω_M . The dashed lines are the constraints obtained with a simple cut in flux in the theoretical abundance of clusters and the solid lines are obtained with the application of the model of completeness.

5 Discussion and conclusions

We presented an observation model which offers analytical expressions to characterise SZ cluster catalogues. It includes a photometric characterisation, a completeness and contamination modeling for large SZ surveys.

It is a way to directly relate theoretical cluster distribution to the observed one taking into account all the systematics due to the reconstruction of the clusters. In particular, the angular size of the clusters is an issue for both the completeness and the photometry, extended clusters (mostly low redshift ones) being less accurately reconstructed. It is crucial to take this fact into account when exploiting SZ cluster catalogues to cosmology.

Acknowledgments

I would like to thank the organizers for a very interesting and enjoyable conference and my colleagues from the SPP and SAp at CEA-Saclay for useful discussions and suggestions.

References

1. J.B. Juin, D. Yvon, A. Réfrégier et C. Yèche, A&A **465**, 57-65, Jan. 2007
2. Arnaud M., Pratt G. W., Piffaretti R. et al , ArXiv e-prints, Oct 2009
3. A. Jenkins et al, MNRAS **321**, 372-384, Sep. 2001

GALAXY CLUSTERS AT THE PLANCK TIME

E. POINTECOUTEAU

on behalf of members of Planck project
“multi-wavelengths cluster science”

*CESR, Université de Toulouse/CNRS, 9. avenue du colonel Roche, BP44346, 31028
Toulouse, France*

The Planck Surveyor satellite currently surveying the whole sky is expected to detect more than a thousands clusters of galaxies via their Sunyaev-Zel'dovich signature on the CMB. This catalogue will be one of the major scientific outcome of this mission. Beyond number counts and 2D correlation functions, the optimisation of the scientific exploitation of this catalogues will require the combination of Planck data with ancillary data such as optical and X-ray data. In this perspective I will discuss the current status for this mission in terms of predictions, detection methods, assembly of X-ray ancillary data, physical information expected from combined optical/X-ray/SZ joint analysis and scientific objectives of envisioned multi-wavelengths follow-up programs.

1 Introduction

With the launch of the Planck Surveyor satellite this spring, a new window is opening for the study of galaxy clusters. Hundreds of new massive halos are expected to be detected by the Planck satellite via their Sunyaev-Zeldovich effect [SZE – 21]. Their studies at the Planck frequencies and their follow-up at other wavelengths (such as in X-rays) will shed new light on our understanding of the formation and evolution of these large scale structures, and on their tight link to the overall matter and energy content of the Universe.

In the standard model of hierarchical structure formation, clusters form through gravitational collapse of dark matter (DM) around primordial over-densities [3]. The population of clusters is a powerful tool in cosmology as well as in the study of the formation and evolution of structures. Their mass function, $N(M, z)$, their spatial distribution, their content in gas, are directly correlated with the (dark and baryonic) matter and energy content of the Universe, thus to the power spectrum of primordial density fluctuations, $P(k)$. Cosmological constraints from clusters are complementary to constraints from the Cosmic Microwave Background (CMB) or from supernovae. Also, clusters are especially fitted to probe the Universe bellow $z = 2$, where the effect of dark energy is predominant [1, 11]. In the standard model, the collapse of structure is mainly driven by gravitation. However, we know that non-gravitational processes play an important role in the formation and in the evolution of structures: pre-heating of the gas by AGNs or supernovae, galactic winds, radiative cooling, metal enrichment... [e.g 6, 23, 20]. The respective roles of all these processes have still to be understood and disentangled. They can be studied through their impact on the overall structural and scaling properties of clusters. [e.g 7, 18, 19, 2]. The inaccurate knowledge we currently have of these statistical properties limits our ability to properly understand the history of clusters formation, its coupling with the galaxy

formation and evolution.

In this framework, we highlight in this paper the expectation and work plans from the catalogue of Planck detected clusters.

2 The Planck satellite and the SZ effect

The Planck Surveyor satellite was lauch on May 14th 2009. After one year, Planck has already surveyed the whole sky in the frequency range of 30-857 GHz. With the primary scientific objective of mapping the temperature fluctuations of the Cosmic Microwave Background [CMB – 15], Planck also provide access to secondary anisotropies such as the Sunyaev-Zel'dovich effect [SZE – 21]. Indeed the inverse Compton scattering of CMB photons by the hot ICM electrons shifts the energy distribution of CMB photons towards higher temperature. This effect therefore produces a characteristic distortion of the CMB spectrum in the direction of galaxy clusters. The intensity of this thermal SZE is directly proportional to the electron thermal pressure integrated along the line of sight (i.e the ICM pressure). A companion effect is due to the intrinsic cluster velocity in a comobile volume. This Doppler effect, or kinetic SZE, is at least an order of magnitude smaller than the thermal SZE. The following equations gives the basics of SZ quantities.

The thermal SZE monochromatic brightness is expressed as:

$$\left. \frac{\Delta I_\nu}{I_\nu} \right|_{th} = y f(x) \quad (1)$$

where $f(\nu, T_e)$ depicts the spectral shape of the SZE which has a second-order dependance to the hot gas temperature due to weakly relativistic electrons [16]. e subscript refers to electron intra-cluster quantities. y is the Comptonisation parameter, which reads as:

$$y = \frac{k}{m_e c^2} \sigma_T \int_l T_g(r) n_e(r) dl' \quad (2)$$

The measure SZE flux can be expressed as:

$$F_{SZ} = \int_\Omega y' d\Omega' \int_\nu f(\nu', kT) d\nu' \quad (3)$$

where Y is the integrated Comptonisation parameter:

$$Y = \int_\Omega y(\Omega') d\Omega' = \frac{kT}{m_e c^2} \frac{\sigma_T}{d_A^2} N_e \propto f_{gas} kT \frac{M_{tot}}{d_A^2} \quad (4)$$

As shown by the equation above, the SZ flux is directly proportional to the ICM thermal pressure, i.e $P_{gas} = M_{gas} \times T_{gas}$, thus to the cluster total mass (through the gas fraction, f_{gas}).

3 Expectations from the Planck all sky survey

Assuming a Λ CDM comology, current predictions for the Planck survey gives a range of ~ 1000 - 1500 clusters to be detected in the Planck survey. It will provide us with a unique, all sky, mass limited, complete cluster sample that should be efficient up to high redshifts. It is worth to stress that massive and distant clusters are rare objects, thus the most constraining for cosmology and formation of structures in a Universe where evolution is driven by gravitation.

Taking into account the Planck sensitivity, we expect to detect hot and massive clusters (i.e $M > 3 - 6 \times 10^{14} M_\odot$, $kT > 5 - 7$ keV) are expected to be detected in the survey. One of the baseline method for cluster detection in the Planck data is based on a multi-matched filter

approach as described in Melin et al. [12]. From the overlap of Planck SZ measurements and X-ray catalogues of clusters, we will constrain the SZ scaling relations in the local Universe as well as their evolution up to $z \simeq 0.5$. Constraints on relations such as the $Y - M$ and $Y - L_X$ will provide solid basis to further study the physics of formation of massive clusters. Moreover, on the basis of known catalogues of clusters (from the X-rays or the optical), we should be able to push down the Planck detection limit via *stacking* analysis, thus to investigate the SZ scaling relations down to a lower mass regime compared to what is accessible from direct measurements. For instance, to date we know nearly 2000 X-ray clusters [see the homogenised compilation by 14], mainly from the ROSAT all sky survey cluster catalogues [NORAS and REFLEX – 4, 5] and from ROSAT serendipitous catalogues.

To date, we know only a handful of clusters above $z = 0.6$ and with $kT > 7$ keV. Beyond this redshift and temperature, we expect from 100 to 200 new detected clusters in the Planck survey. A considerable increase in number that will allow us to investigate in details the statistical properties of the high mass end of the distant cluster population. More specifically we will look at the ICM X-ray properties of these new SZ clusters (i.e L_X , kT , M_{gas}); derive their (distributions in) dynamical mass (under the hypothesis of the HE and sphericity) and entropy; look at their content in gas (i.e f_{gas}); calibrate the evolution of the $Y_{SZ} - M$ relation at high z , mandatory to proceed with the full scientific exploitation of a catalogue of SZ clusters, especially in cosmology.

These objectives obviously require for each cluster candidate: (i) an optical identification and redshift estimation, (ii) a cross-combination of Planck SZ data with X-ray observations of these clusters. Therefore, we will undertake a systematic optical and X-ray follow-ups of a well defined and selected sample of new detected Planck clusters. Validation and identification work are inherent to such survey mission [e.g SPT – 22, 10]. An optical follow-up will deliver a photometric/spectrometric measurement of their redshift, a prerequisite quantity. The scientific implications of an X-ray follow-up are deeper as X-ray and SZE probe the same physical component of clusters, the hot intra-cluster gas. As these clusters are massive, they are expected to be X-ray luminous even at high redshifts (i.e $0.8 < z < 1.0$): $f_X[0.5-2 \text{ keV}] > 10^{13} \text{ erg/s/cm}^2$. Such fluxes are encouraging for the perspective of an X-ray follow-up program with XMM-Newton. We can compare to similar existing X-ray observation of high redshift clusters. For instance, the temperature of MS 1054-0321 ($z = 0.83$, $f_X[0.5-2 \text{ keV}] = 2.5 \times 10^{13} \text{ erg/s/cm}^2$) was derived with a 10% precision with an exposure time of 25ks [8]. So based on the aforementioned expected number of high redshift clusters and considering an exposure time of 25-50ks per target, as an indication of what could be done with XMM-Newton, we would need a large program to follow-up few tenth of Planck selected new clusters.

Complementary ground based SZE follow-up might prove very useful as well. Ground based SZE facilities have higher angular resolution than Planck (of the order of 1 arcmin wrt 5-10 arcmin). The combination of SZ detailed images with X-ray images (even when no X-ray spectroscopy is available) can lead to good enough estimation of physical properties such as the gas temperature (thus the cluster mass) as originally demonstrated by Pointecouteau et al. [17], Kitayama et al. [9]. More recently such a method have been successfully applied to high resolution SZ data from the APEX telescope [13] showing impressive and promising results for the cluster internal structure study.

4 Conclusion

The Planck satellite is currently surveying the sky and is expected to provide us with the detection of about 1000-1500 clusters. From this unique all sky survey, we will study the statistical properties of clusters via cross-correlation with their X-ray or optical properties. The all sky coverage of Planck will also provide us with a unique opportunity to draw a sub-sample of SZ selected distant massive clusters, and follow it at various wavelengths to scrutinize the

distant clusters properties.

This overall characterisation accross redshifts will allow us to provide strong constraints on the evolution of massive halos, and altogether, in the framework of the study of galaxy clusters, Planck should allow us to derive constraints to address questions among which: (i) How do non-gravitational processes produce departure from the simplest gravitational model. (ii) How does the ICM history depends on each of these physical individual processes. (iii) How do cluster of galaxies evolve. (iv) How do the first large scale structures form. (iv) What cosmological constraints can we draw from Planck clusters studies.

Acknowledgments

We thank the organisers for the very enjoyable conference. EP is grateful to N. Aghanim and J.-L. Puget for their support, and M. Arnaud, R. Piffaretti, G. Pratt, J.-B. Mellin, J. Bartlett and A. Chamballu for providing material use in his presentation. EP acknowledges the support of grant ANR-06-JCJC-0141.

References

- [1] Allen, S. W., et al. 2004, MNRAS, 353, 457
- [2] Arnaud, M., Pratt, G. W., Piffaretti, R., et al. 2009, eprint arXiv:0910.1234
- [3] Bertschinger, E. 1985, ApJ Suppl., 58, 39
- [4] Böhringer, H., Voges, W., Huchra, J. P., et al. 2000, ApJ Suppl., 129, 435
- [5] Böhringer, H., Schuecker, P., Guzzo, L., et al. 2004, A&A, 425, 367
- [6] Borgani, S., Murante, G., Springel, V., et al. 2004, MNRAS, 348, 1078
- [7] Croston, J. H., Pratt, G. W., Böhringer, H., et al. 2008, A&A, 487, 431
- [8] Gioia, I. M., Braito, V., Branchesi, M., et al. 2004, A&A, 419, 517
- [9] Kitayama, T., Yoshida, N., Susa, H., & Umemura, M. 2004, ApJ, 613, 631
- [10] High, F. W., et al. 2010, arXiv:1003.0005
- [11] Mantz, A., Allen, S. W., Rapetti, D., et al., 2009, eprint arXiv:0909.3098
- [12] Melin, J.-B., Bartlett, J. G., & Delabrouille, J. 2006, A&A, 459, 341
- [13] Nord, M., et al. 2009, A&A, 506, 623
- [14] Piffaretti, Arnaud, M., R., Pointecouteau, E., et al., 2010, in preparation.
- [15] The Planck Collaboration, 2006, “The Scientific Programme of Planck”, arXiv:astro-ph/0604069
- [16] Pointecouteau, E., Giard, M., & Barret, D. 1998, A&A, 336, 44
- [17] Pointecouteau, E., Hattori, M., Neumann, et al., 2002, A&A, 387, 56
- [18] Pratt, G. W., Croston, J. H., Arnaud, M., & Böhringer, H. 2009, A&A, 498, 361
- [19] Pratt, G. W., et al. 2010, A&A, 511, A85
- [20] Schindler, S. & Diaferio, A. 2008, Space Science Reviews, 134, 363
- [21] Sunyaev, R. A. & Zeldovich, Y. B. 1972, Comments on Astrophysics and Space Physics, 4, 173
- [22] Vanderlinde, K., et al. 2010, arXiv:1003.0003
- [23] Voit, G. M. 2005, Reviews of Modern Physics, 77, 207

GALAXY CLUSTERS NUMBER COUNTS WITH SUNYAEV-ZEL'DOVICH EFFECT AND SCALING LAWS EVOLUTION

PIERRE DELSART

*Laboratoire Astrophysique de Toulouse-Tarbes, Université Paul Sabatier
14 avenue Edouard Belin, 31400 Toulouse, France*

The study of the galaxy cluster population is a powerful tool to determine the properties of the Universe. However their inner properties must be well understood. In this paper, I present results from X-ray study. By modeling the temperature function of the clusters, I will show that there is an inconsistency between the model and the observation for the distant cluster, can be explain by a new kind of heating not being taken into account in the standard scaling laws. With a Monte-Carlo Markov Chain method, I constrain this heating called redshift evolution and I will demonstrate this latter modify both the cluster number counts in the X-ray band and also for the Sunyaev-Zel'dovich effect.

Introduction

The galaxy clusters are the biggest objects in the Universe and a very good representation of the content of the Universe. Their population can be used to gather information on the properties of the Universe. The local population gives information on the cosmology whereas the distant population gives information on the evolution of the growth factor of the structure and on evolution of the Universe. Because they are very sensitive to the growth factor and the geometry, they can be used to place constraint on the cosmological parameters.

1 Cluster modeling

The population of galaxy cluster is a powerful cosmological tool to determine nature of our Universe. The main ingredient to estimate this population is the mass function. This function was developped at first by Press and Schechter¹⁰ using numerical simulation of a spherical collapse. Hence, for a given mass we can write the density of objects by the following relation :

$$N(M) = \frac{\rho}{M} f(\nu) \frac{d\sigma}{dM} \quad \text{where} \quad f(\nu) = \sqrt{\frac{2}{\pi}} \exp\left(-\frac{\nu^2}{2}\right) \quad (1)$$

with $\nu = \frac{\delta(z)D(z,\Omega_m)}{\sigma(M)D(0,\Omega_m)}$, $\delta(z)$ the critical overdensity at a redshift z (revoir), $\sigma(M)$ the amplitude of the density fluctuation inside a sphere of mass M and D the growth factor of the structures. However, because the Press and Schechter mass function underestimates the population of massive objects, I decided to use the Sheth, Mo and Tormen mass function¹².

$$f(\nu) = C \sqrt{\frac{2A}{\pi}} \left(1 + \frac{1}{(A\nu^2)^Q}\right) \exp\left(-\frac{A\nu^2}{2}\right) \quad (2)$$

Name	Number	Mean redshift	Temperature interval (keV)	Energy band (keV)
Local sample	~ 40	0.05	3-10	0.5-2
400 square degrees ¹⁵	~ 30	0.5	3-11	0.5-2
MACS ³	12	0.6	7-11.6	0.1-2.4

Table 1: Summary of the used samples to calculate the observational temperature function

with $A = 0.707$, $C = 0.3222$, $Q = 0.3$. Other arguments to explain my choice are : the function is well defined at every masses and is in good agreement with the numerical simulations.

But, if we make measurements on a cluster, especially on the mass, we get either a bias or a very bad precision. That's why, it was suggested by Kaiser in 1991⁶ to study the relation between the mass and another observable quantity. The galaxy clusters are a result of a gravitational collapse and they are virialized objects. This means that their kinetic energy compensate the gravitational collapse. So, one can derive a relation between the mass and the temperature of the object. This relation is called the scaling law, and for this work I used the one below :

$$T = A_{TM} (hM_v)^{2/3} \left(\Omega_M \frac{\Delta(z, \Omega_M)}{178} \right)^{1/3} (1 + z) \quad (3)$$

where T is the temperature of the cluster in keV, A_{TM} a normalization constant, M_v the virial mass expressed in 10^{15} solar mass, Ω_M the matter density parameter, z the redshift and $\Delta \times \bar{\rho} = \frac{3M_\Delta}{4\pi r_\Delta}$. From this point, it becomes easy to calculate the population of galaxy clusters using the temperature, that I call hereafter the temperature function. In that way, the temperature function is related to the mass by the following relation :

$$N(> k_B T)_{theo} = \int_0^T N(M) \frac{dM}{dX} dX \quad (4)$$

Note that the above definition gives the density of objects hotter than a given temperature.

2 Constraints from X-ray observations

To place constraints means that is necessary to compare the observations to a model. The model of the clusters' population is given in the paragraph (1). In this part, I develop the estimation of the observational temperature function. From table (1), I assessed the clusters population and their standard deviation by the estimators below⁴ :

$$N(> k_B T)_{obs} = \sum_i \frac{1}{V_{max,i}} \quad (5)$$

$$\sigma^2(> k_B T)_{obs} = \sum_i \frac{1}{V_{max,i}^2}$$

In this work, the statistical analysis was made by a bayesian approach. I used the COSMOMC package⁸, which estimates the maximum likelihood of the parameters, thanks to the Monte-Carlo Markov Chain method. For this, the CMB data from WMAP 7yr⁵, the SN data from SDSS⁷, LOWZ, ESSENCE, HST, the power spectrum of the SDSS LRG DR7¹¹ and my own temperature function were combined in order to place constraints on the cosmological parameters and also on the A_{TM} parameter from the scaling relation $M_v - T$. Note, in that way, the A_{TM} parameter is constrained auto-consistently with the cosmological parameters.

The first analysis was only made with the local sample in order to get the cosmology. The figure (1) show the result of this analysis. The model, represented by the blue solid line, is in good agreement with the observations.

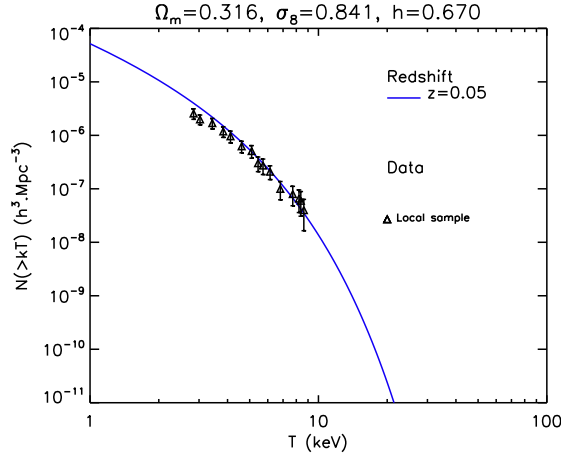


Figure 1: Temperature function of the local sample

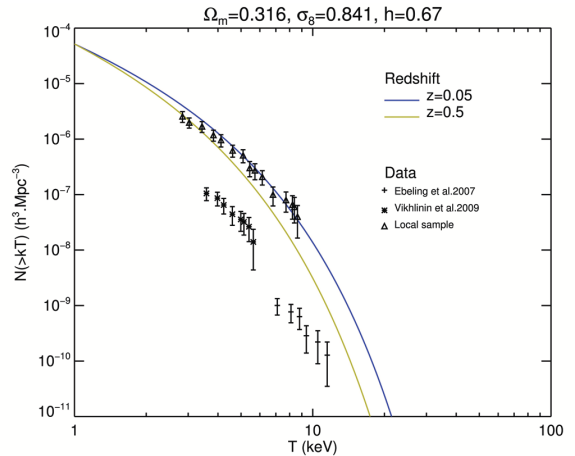


Figure 2: Temperature function of the local and deep samples

The complication comes from the distant clusters. The figure (2) shows the model, in yellow solid line, for a sample with a mean redshift of $z = 0.5$. In this case, the local model is still consistent with the observations but not the deep model. As mentioned previously, the cosmology is well determined by the local population. In other words, the problem is not in the cosmology but elsewhere.

In order to remove this inconsistency, Blanchard et al. 2000² and Vauclair et al. 2003¹⁴ suggested to add a redshift evolution in the scaling law $M_v - T$. This comes to multiply the standard scaling relation by $(1 + z)^\beta$. Consequently, with the combination of the previous datasets, it becomes easy to constrain this new parameter β in the same way as the other parameters. A new statistical analysis was performed including this latter parameter, what is shown on the figure (3). Now the deep model is in good agreement with the observations where the result of the analysis gives $A_{TM} = 7.22$ keV and $\beta \sim -1$.

3 Sunyaev-Zel'dovich number counts

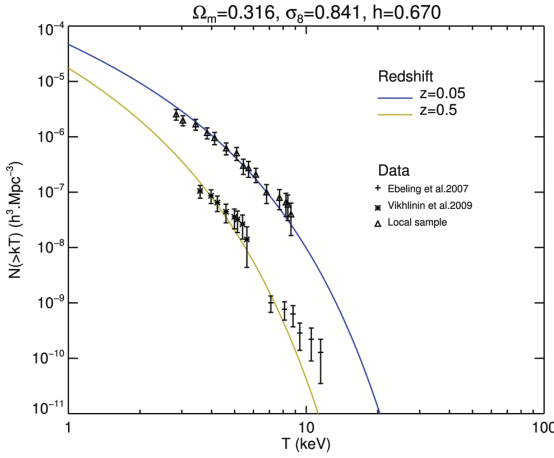


Figure 3: Temperature function of the local and deep samples including the evolution

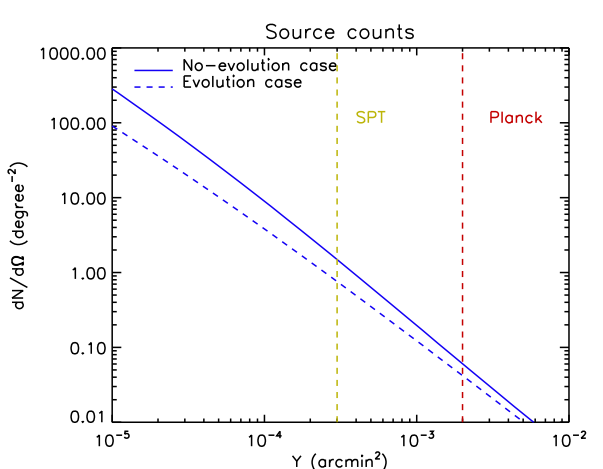


Figure 4: Sunyaev-Zel'dovich source.

The Sunyaev-Zel'dovich (SZ hereafter) effect is an inverse Compton scattering of the CMB photons on the electrons of the cluster gas. The result of this collision is a shift in frequency (or a shift in energy). This can be seen as distortion of the blackbody spectrum with a null point near 220GHz, an absorption part before this point and an emission part after.

The estimation of the SZ clusters number counts is performed in the same way as previously. The scaling relation used here is between the mass and the SZ flux. The latter is given by $S_{SZ} = j(\nu) \times Y^l$, where $j(\nu)$ is a frequency function and Y , the Y-Compton parameter. In order to compare different experiences, the frequency function is removed. Hereafter I will call the SZ flux the Y-Compton parameter. Thus the SZ scaling relation can be written as :

$$Y = 2.49 \cdot 10^{-4} A_{TM} \times f_B \times M_v^{5/3} h^{8/3} \times \left(\Omega_m \frac{\Delta(z, \Omega_m)}{178} \right)^{1/3} \times D^{-2} \quad (\text{in arcmin}^2) \quad (6)$$

Note that in the above equation, the X-ray scaling relation with redshift was inserted because the definition of Y is $Y \propto M \times T$. The reason why I added the redshift evolution is because the effect of this latter is strong on the X-ray population as shown in figure (3). Consequently the figure (4) shows the clusters number counts with the case without evolution (solid line) and with evolution (dashed). Also, the two vertical dashed lines are the SZ flux threshold of Planck and South Pole Telescope (SPT hereafter) selected from the work of Melin et al. 2006⁹ in an optimistic case (2.10^{-3} and 3.10^{-4} arcmin² respectively for Planck and SPT). This plot shows that the redshift evolution of the scaling law modifies the number count by a factor of about 2 for Planck and of about 3 for SPT.

Conclusion

The galaxy clusters demonstrated that they are a powerful tool for determining the properties of the Universe. But, through this work, they also demonstrated that they must be well understood before being used as cosmological test. In this work, I focused on the scaling relations of these objects. I showed, in the X-ray band, that the models are inconsistent with the observation when the distant population is studied. To remove this disagreement, I added a new parameter called the redshift evolution and I constrained this parameter auto-consistently with the cosmological parameters. The result of this analysis provided a value for this parameter $\beta \sim -1$, thus modifying strongly the temperature function at high redshift. For the SZ population estimation, I had to take this result into account and the consequence was a difference by a factor of 2 to 3 between a case without redshift evolution and with evolution.

References

1. Barbosa, D., Bartlett, J. G., Blanchard, A. and Oukbir, J, *A&A* **314**, 13 (1996)
2. Blanchard, A., Sadat, R., Bartlett, J. G. and LeDour, M, *A&A* **362**, 809 (2000)
3. Ebeling, H., et al., *ApJL* **661**, L33 (2007)
4. Henry, J. P, *JKAS* **37**, 371 (2004)
5. Jarosik, N., et.al., submitted to *Astrophysical Journal Supplement Series* (2010)
6. Kaiser, N, *ApJ* **383**, 104 (1991)
7. Kessler, R., et al., *ApJS* Accepted for publication (2010)
8. Lewis, A. and Bridle, S, *Phys. Rev. D* **66**, 103511 (2002)
9. Melin, J. B., Bartlett, J. G. and Delabrouille, J, *A&A* **429**, 417 (2005)
10. Press, W. H. and Schechter, P, *ApJ* **187**, 425 (1974)
11. Reid, B. A., et al., submitted to *MNRAS*, arxiv.org/abs/0907.1659
12. Sheth, R. K., Mo, H. J., and Tormen, G, *MNRAS* **323**, 1 (2001)
13. Sunyaev, R. A. and Zeldovich, Y. B, *Comments on Astrophysics and Space Physics* **4**, 173 (1972)
14. Vauclair, S. C., et al., *A&A* **412**, L37 (2003)
15. Vikhlinin, A., et al., *ApJ* **692**, 1033 (2009)

MASS ESTIMATES IN INTERMEDIATE REDSHIFT CLUSTERS OF GALAXIES

G. FOEX¹, G. SOUCAIL¹, M. LIMOUSIN⁴, E. POINTECOUTEAU², M. ARNAUD³, G.W. PRATT³, H. CHEN³

¹*LATT, CNRS and Université de Toulouse, 14 Av. E. Belin, F-31400 Toulouse, France*

²*CESR, CNRS and Université de Toulouse, 9 Av. du Colonel Roche, F-31028 Toulouse, France*

³*CEA/IRFU/Service d'Astrophysique, CEA Saclay, France*

⁴*LAM, CNRS and Université de Provence Aix-Marseille 1, 38 rue Joliot-Curie, 13388 Marseille cedex 13, France*

We present preliminary results from the gravitational lensing follow-up of the X-ray brightest clusters (i.e. the most massive) selected from a representative sample of intermediate redshift ($0.4 < z < 0.6$) galaxy clusters observed with XMM-Newton, the EXCPRES sample (Evolution of X-ray Properties in a REpresentative Sample). Using high-quality multi-color wide field imaging obtained with MegaCam at CFHT, we performed a weak lensing investigation of these clusters. We derived a direct total mass (dark matter and baryons) estimated from the weak lensing shear signal and another from the hydrostatic equilibrium hypothesis from the X-ray. We present a comparison of the lensing analysis with the X-ray results and discuss preliminary implications for the derivation of a reliable cluster mass in this sparsely-studied redshift range.

1 Introduction

Clusters of galaxies have been attracting considerable interest for their cosmological applications for more than three decades (e.g. Perrenod¹). Most surveys aimed at determining the observed cluster abundance and the cluster mass function are based on the so called scaling relations, i.e. the relations that give an estimate of the mass from observables such as the temperature or the richness of the cluster. Therefore, it is of prime importance to characterise these relations (normalisation, scatter) with accurate mass measurements on some well defined samples of clusters. Here we present a preliminary analysis of a sample of clusters at intermediate redshifts, using the complementarity of lensing and X-ray-derived mass estimates. In the following we mainly focus on the calibration/validation of the lensing estimates. Further, an ongoing work involves the calibration of these mass proxies.

2 Data

The initial sample of clusters is EXCPRES, a sample of medium-distant clusters selected by their X-ray luminosity, without consideration of their morphological characteristics (Arnaud *et al.*, in prep.) . The sample lies in the redshift range $[0.4 < z < 0.6]$ and covers a wide dynamic range in temperature ($2.5 < kT < 12$ keV), which is necessary to fully assess the evolution of cluster scaling and structural properties. This sample is the distant equivalent of the local representative sample REXCESS² and covers the same X-ray temperature range. Each of the 20 clusters of the EXCPRES sample were observed with XMM-Newton with deep pointings (a minimum of 25 ks for each cluster, depending on the cluster X-ray flux). More details about this sample can be found in Arnaud *et al.* (in preparation).

For the WL analysis, we selected all clusters with total X-ray luminosity $L_X > 5 \cdot 10^{44}$ erg s⁻¹ (i.e. only the most massive ones). This limit is close to a mass limit and allows to keep clusters in different

dynamical stages (merging clusters, cool core ones, etc ...). In total 11 clusters fulfill the criteria. For each cluster, we have megacam (@ CFHT) observations in 4 bands (g' , r' , i' and z') in good seeing conditions and large exposure time (7200 sec. in the r' band, which is used for the lensing analysis).

3 Methodology

For each cluster, we perform an X-rays (see e.g. Arnaud³ for a global review on the method) and WL analysis. X-ray mass profiles are produced for all clusters (Pratt *et al.*, in prep.). Density and temperature profiles, derived including projection and PSF effects, are also produced (e.g., Croston *et al.*⁴, Pratt & Arnaud⁵ and Pointecouteau *et al.*⁶); the total masses are then calculated assuming the standard assumptions of hydrostatic equilibrium and spherical symmetry. With the WL analysis, we derive shear profiles (Foex *et al.*, in prep.) following a standard procedure (e.g. Bartelmann *et al.*⁷ for theoretical and technical details of WL with galaxy clusters). Both the shear and mass profiles are then fitted to analytical models (e.g. the NFW profile⁸ motivated by numerical simulations of dark matter) to allow a direct comparison between the two methods.

Our WL pipeline can be summarized as following. First we detect the objects on the images with SExtractor⁹, measure their parameters (e.g. flux, magnitude, size) and sort the stars and the galaxies. The second step is to measure the shape of the galaxies corrected by the PSF field (we have used here IM2SHAPE¹⁰). The third step is to select the background galaxies. We use a magnitude cut to remove most of the foreground members and a color/magnitude selection to reject most of the cluster members (located within the red sequence of the cluster). We also estimate photo-z (with HYPERZ¹¹) and use them as an extra selection criterion by integrating the (normalized) probability distribution in redshift (PDZ) to determine the most probable redshift range for each galaxy.

This standard procedure in building a weak lensing mass is hampered by several difficulties due to the moderately-high redshift of our clusters. The fraction of foreground galaxies not sheared by the cluster is quite significant in the catalogues and they have to be eliminated with care. The photo-z criteria are therefore of prime importance but they imply that the background galaxy density is cut by a factor of 2 for a given observed depth compared to low redshift clusters. Moreover the shear γ and the convergence κ are two quantities that are proportional to the geometrical factor $\beta(z_l, z_s) = D_{ls}/D_{os}$ (e.g. Hoekstra *et al.*¹²). For clusters at high redshifts, β covers a broad range of values for the redshifts of background galaxies and we need to determine $\langle \beta(z) \rangle$ averaged over the right redshifts distribution $p(z)$. To estimate $p(z)$, we use the photo-z distribution of galaxies detected in the CFHTLS Deep fields. The photo-z catalogue was kindly produced by R. Pello with HYPERZ and validated with spectroscopic redshifts from the VVDS survey. The main advantage is that these data were taken with the same instrument (Megacam@CFHT) and the same filters. It is thus straightforward to apply the selection cuts used to build up our catalogues of background galaxies to the Deep catalogues and have an accurate value $\langle \beta(z) \rangle$ on a similar distribution as the one detected behind each cluster.

In addition to these intrinsic difficulties, each step of the WL pipeline introduces uncertainties that need to be corrected as much as possible in order to avoid any bias or systematic in the final mass reconstructions. This is especially true for the measurement of the galaxies shape parameters. To test our pipeline and the way we implement the IM2SHAPE software, we used the STEP simulations¹³ provided to the lensing community. With these simulations we can characterize the PSF residuals and the shear calibration of the method. Our pipeline gives an underestimate of 10% for the shear which translates into a +10% correction to the measured shear profiles.

Another uncertainty comes from the purity and the completeness of the background galaxy catalogues. We built simulated catalogues to adjust the PDZ threshold above which a galaxy can be classified as a background member. This must be a compromise between a strong reduction of the source density which increases the noise in the shear profile and a limit in the foreground contamination which otherwise introduces some shear dilution.

The last limitation in the mass reconstruction comes from the fact that at these redshifts (0.4-0.6), we

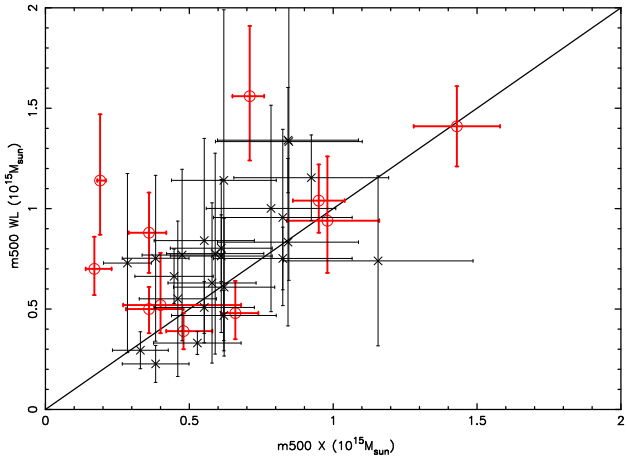


Figure 1: Weak lensing mass estimates (y-axis) versus X-ray estimates (x-axis). The black crosses are the clusters from B07 and D06. The red open circles are the clusters used in this work.

cannot expect too many radial bins and this reduces the spatial resolution because the linear size of the bins is large compared to the dimension of the virial radius. Thus we lose information near the center of the cluster and we have only a few points to fit analytical models, increasing the error on the mass estimates.

4 Results

For each cluster we fitted a NFW profile (two free parameters, the concentration c and the mass M_{500}) separately to the mass profile obtained with the X-ray analysis and to the shear profile derived from the lensing analysis. Not surprisingly, the WL analysis is unable to constrain the central mass distribution of the clusters. This impacts the possibility to evaluate the concentration parameter c which strongly depends on the inner radial profile. Therefore we chose to fit only M_{500} with the shear profiles and c is fixed to the fiducial value $c = 4$ derived from the c-M relation (e.g. Duffy *et al.*¹⁴) for a typical mass and redshift corresponding to our clusters.

4.1 Comparison of the mass estimates

We compare our approach with previous studies where detailed comparisons between lensing and X-ray mass estimates were proposed: at lower redshifts, Zhang *et al.*¹⁵ used the lensing masses from Bardeau *et al.*¹⁶ (B07) and Dahle¹⁷ (D06) and compared them to their X-ray estimates. Figure 1 shows our results overplotted. The agreement is satisfying although the scatter between the two mass estimates is still large and there remain some discrepancies which can be discussed.

First, our sample was build to be unbiased towards any specific kind of clusters, so we expect to have unrelaxed or dynamically disturbed clusters. In these cases, the X-ray mass estimates are questionable and more detailed 2D and 3D analysis are necessary to better characterise these clusters.

The WL masses can also be uncorrect. The extraction of this signal crucially depends on the quality of the data like the bright star contamination (with extended diffraction wings or ghost images), the depth and the seeing of the images (crucial factors to have high densities of background galaxies). We can also invoke the presence of other mass structures (filaments, sub-clumps, ...) that can distort the radial WL analysis.

In the present work, the X-ray mass estimates have smaller uncertainties than the lensing ones (Figure 1). With the high sensitivity of XMM-Newton and the deep pointings, the final error bars of the X-ray masses are considerably reduced. On the contrary the WL analysis is done with ground-based data and despite the high quality of the CFHT seeing these data cannot compete efficiently. However, we observe

a good correspondance between the masses for most of the sample : WL gives robust masses that can be used to calibrate the mass proxies with a completely different approach than X-ray and this remains valid up to $z \sim 0.5$ or higher.

4.2 Combining the two data sets

Although the X-ray mass estimates have lower error bars compared to the WL ones, we tried to combine the two data sets, taking advantage of the qualities of each method (information on the central parts and small error bars for the X-ray, lesser dependance on the dynamical state and large scale measure for the lensing analysis). Previous works have already proposed to combine the two methods for data of similar quality (e.g. Mahdavi *et al.*¹⁸). In the present case, we simply implemented a global fit of the X-ray mass profile and the reduced shear profile, with a global χ^2 minimisation and no weighting of the data sets. As expected the final results are mainly driven by the X-ray data ($M_{X+WL}/M_X \sim 1$), because of the smaller error bars on the mass profiles than the shear profiles and we do not improve the mass estimates (i.e. $err_{X+WL}/err_X \sim 1.1$) compared to the X-ray only analysis.

5 Conclusion

We have performed an X-ray and WL analysis of 11 medium-distant galaxy clusters, resulting in a set of two mass estimates that are completely independant. We have pointed out the difficulties of conducting a WL analysis at high redshifts and characterised the limitations of such an analysis (quality of the data, WL approximation, shear calibration, spatial resolution). The relatively good agreement we found between the WL and X-ray analysis seems to validate our WL analysis at high redshifts and we will be able to use it as a second robust mass estimate. The next step will be to calibrate the scaling relations (M-T, M-L_X, ...) that are mandatory to derive cosmological informations from large surveys of galaxy clusters via their mass function. Moreover, we will be able to put constraints on the model of structure formation and their evolution with time by comparing our results with the local sample REXCESS.

References

1. S. C. Perrenod, *ApJ* **236**, 373 (1980).
2. G. W. Pratt and J. H. Croston and M. Arnaud and H. Böhringer, *A&A* **498**, 361 (2009).
3. M. Arnaud in *Background Microwave Radiation and Intracluster Cosmology*, ed. F. Melchiorri & Y. Rephaeli, 2005.
4. J. H. Croston *et al*, *A&A* **459**, 1007 (2006).
5. G. W. Pratt and M. Arnaud, *A&A* **394**, 375 (2002).
6. E. Pointecouteau *et al*, *A&A* **423**, 33 (2004).
7. M. Bartelmann and P. Schneider, *Phys. Rep.* **340**, 291 (1999).
8. J. F. Navarro and C. S. Frenk and S. D. M. White, *ApJ* **490**, 493 (1997).
9. E. Bertin and S. Arnouts, *Phys. Rep.* **117**, 393 (1996).
10. S. Bridle and S. Gull and S. Bardeau and J.-P. Kneib in *Proceedings of the Yale Cosmology Workshop: "The Shapes of Galaxies and their Dark Halos"*, ed. Natarajan P., 2002.
11. M. Bolzonella and J.-M. Miralles and R. Pelló, *A&A* **363**, 476 (2000).
12. H. Hoekstra and M. Franx and K. Kuijken, *ApJ* **532**, 88 (2000).
13. C. Heymans *et al*, *MNRAS* **368**, 1323 (2006).
14. A. R. Duffy and J. Schaye and S. T. Kay and C. Dalla Vecchia, *MNRAS* **390**, L64 (2008).
15. Y.-Y. Zhang *et al*, *ApJ* **482**, 451 (2008).
16. S. Bardeau *et al*, *A&A* **470**, 449 (2007).
17. H. Dahle, *ApJ* **653**, 954 (2006).
18. A. Mahdavi *et al*, *ApJ* **664**, 162 (2007).

Non-thermal emission from galaxy clusters: a Pandora's vase for astrophysics

C. FERRARI

*Université de Nice Sophia Antipolis, CNRS, Observatoire de la Côte d'Azur,
Laboratoire Cassiopée, Nice, France*

The existence of cosmic rays and weak magnetic fields in the intracluster volume has been well proven by deep radio observations of galaxy clusters. However a detailed physical characterization of the non-thermal component of large scale-structures, relevant for high-precision cosmology, is still missing. I will show the importance of combining numerical and theoretical works with cluster observations by a new-generation of radio, Gamma- and X-ray instruments.

1 Introduction

Deep radio observations of the sky have revealed the presence of extended (~ 1 Mpc) radio sources in about 50 merging galaxy clusters (see [1, 2] and references therein). This diffuse radio emission is not related to unresolved radio-galaxies, but rather to the presence of relativistic particles ($\gamma >> 1000$) and magnetic fields of the order of μGauss in the intracluster volume. The physical mechanisms responsible for the origin of this non-thermal intracluster component are matter of debate (e.g. [3, 4]), as well as the effects of intracluster cosmic rays (CRs) and magnetic fields on the thermodynamical evolution and mass estimate of galaxy clusters (e.g. [5, 6]). A deep understanding of the evolutionary physics of *all* the different cluster components (dark matter, galaxies, thermal and non-thermal intracluster medium – ICM) and of their mutual interactions is indeed essential for high-precision cosmology with galaxy clusters [7].

In the following, I will give an overview of our current knowledge of the non-thermal component of galaxy clusters. I will also stress the importance of a new generation of multi-wavelength telescopes – such as the *Low Frequency Array (LOFAR)*, and the Gamma- and hard X-ray (HXR) satellites *Fermi* and *NuSTAR* – for a deep understanding of the non-thermal cluster physics. The ΛCDM model with $H_0 = 70 \text{ km s}^{-1}\text{Mpc}^{-1}$, $\Omega_m = 0.3$ and $\Omega_\Lambda = 0.7$ has been adopted.

2 The discovery of the non-thermal intracluster component: radio observations

The presence of intracluster CR electrons (CR_{es}) and magnetic fields was pointed out in 1970 by Willson [8], whose detailed radio analysis of the Coma cluster followed the first detection in 1959 of a noticeably diffuse cluster radio source – Coma C – by Large et al. [9].

Diffuse cluster radio sources are very elusive. On the one hand their low-surface brightness ($\sim \mu\text{Jy/arcsec}^2$ at 1.4 GHz) requires low angular resolution observations in order to achieve the necessary signal-to-noise ratio. On the other hand complementary high-resolution observations are needed in order to identify and remove emission from point sources. Samples of clusters hosting diffuse radio sources started to be available from the 90's (e.g. [10]), with the advent

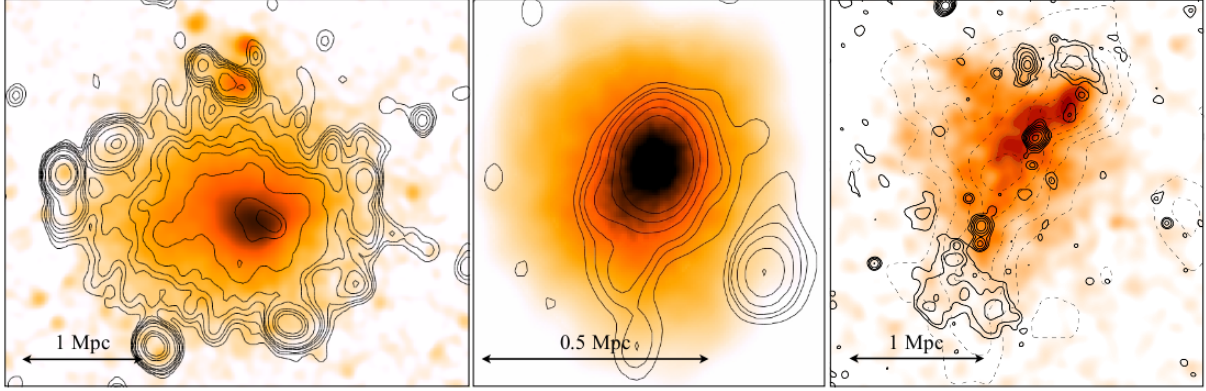


Figure 1: The galaxy clusters Abell 2163 (left), RX J1347.5-1145 (middle) and ZwCl 2341.1+0000 (right) observed in X-rays (brown scale image) and at radio wavelengths (solid contours) (adapted from [15, 16, 18]). A2163 is the hottest Abell cluster and it hosts one of the most luminous radio halos [15]. A radio-mini halo is at the center of the most X-ray luminous cluster RX J1347.5-1145 [16]. Double radio relics have been discovered in ZwCl 2341.1+0000 [18]. Diffuse radio emission has also been detected in this cluster along the optical filament of galaxies shown here by dashed contours [19].

of continuum radio surveys such as the NVSS [11]. It emerged that the non-thermal plasma emitting at radio wavelengths could be not a common property of galaxy clusters (see [12] and references therein). It was also found that a common feature of intracluster radio sources is a steep synchrotron spectral slope ($\alpha \gtrsim 1^a$, [13]). Based on the observed difference in other physical properties (e.g. position in the host cluster, size and morphology) a working classification with three main classes of intracluster radio sources was soon adopted [14]:

- *radio halos* are extended ($\gtrsim 1$ Mpc) sources that have been detected at the centre of merging clusters. Their morphology is similar to the X-ray morphology of the cluster (Fig. 1, left panel);
- *radio mini-halos* are smaller sources ($\lesssim 500$ kpc) located at the centre of cool-core clusters. They surround a powerful radio galaxy (Fig. 1, middle panel);
- *radio relics* have extensions similar to halos and are also detected in merging clusters, but they are usually located in the cluster outskirts and have an elongated morphology (Fig. 1, right panel). In some clusters double relics have been detected (see [17, 18] and references therein).

The discovery of a non-thermal intracluster component through radio observations has opened a number of astrophysical questions: How do cosmic rays and magnetic fields originate within the intracluster volume? Are all the clusters hosting a non-thermal component? How does it affect the thermodynamical evolution and the mass estimates of galaxy clusters? As detailed in the following sections, new observational facilities will allow us to address most of these open questions in the next few years.

3 Non-thermal component of galaxy clusters: the known and unknown

3.1 Magnetic fields

The intensity of intracluster magnetic fields can be measured [4, 20]:

^a $S(\nu) \propto \nu^{-\alpha}$

- through Faraday rotation measures (RM) of polarized radio sources within / behind clusters (current measurements: $\sim 1\text{--}10 \mu\text{Gauss}$);
- by comparing synchrotron radiation from diffuse radio sources with non-thermal HXR emission due to Inverse Compton (IC) scattering of CMB photons by relativistic electrons (current measurements: $\sim 0.1\text{--}0.3 \mu\text{Gauss}$);
- by assuming energy equipartition between intracluster CRs and magnetic fields (current measurements: $\sim 0.1\text{--}1.0 \mu\text{Gauss}$);
- through the study of cold fronts in merging galaxy clusters (current measurements: $\sim 10 \mu\text{Gauss}$).

The discrepancy between these different measurements can indeed be related to the complex structure of intracluster magnetic fields. Magnetic field models where both small and large scale structures coexist must be considered, as recently shown by joint observational and numerical studies (e.g. [21, 22]). A radial decline of the magnetic field strength has also been observed in agreement with different magneto-hydrodynamic simulations ([23, 24] and references therein). This can have important consequences in comparing, for instance, volume averaged magnetic field measurements (such as those obtained through the equipartition and IC methods) with RM estimates, that are very sensitive to local variations in the magnetic field and ICM structure. Consistent magnetic field measurements have been recently obtained in Coma by firstly determining a model of magnetic field strength, radial profile and power spectrum, and then deriving with the different methods an average magnetic field strength over the same cluster volume [23]. Finally, magnetic field measures based on IC scattering of CMB photons have also to take into account the controversial detection of HXR flux from galaxy clusters (Sect. 3.3) and that radio ($\approx 1.4 \text{ GHz}$) and XHR ($\approx 50 \text{ keV}$) radiations come from different populations of intracluster relativistic electrons [20].

Magnetic fields at the observed intensity level ($\approx 1 \mu\text{Gauss}$) could result from amplification of seed fields through adiabatic compression, turbulence and shear flows associated to the hierarchical structure formation process. Seed fields could have been created by primordial processes and thus fill the entire volume of the universe, or through different physical mechanisms, such as the “Biermann battery” effect in merger and accretion shocks, or the outflow from AGN and starburst galaxies in proto-clusters at $z \approx 4\text{--}6$ (see [25] for a recent review).

3.2 *Cosmic rays*

Different mechanisms can produce CRs in galaxy clusters. Primary relativistic particles can be accelerated by processes internal to cluster galaxies, i.e. galactic winds or AGNs, and then ejected into the intracluster volume. Intracluster CRs gyrate around magnetic field lines which are frozen in the ICM. The expected diffusion velocity of relativistic particles being of the order of the Alfvén speed ($\sim 100 \text{ km/s}$), CRs need $\gtrsim 10 \text{ Gyr}$ to propagate over radio halo and relic extensions. The radiative lifetime of relativistic electrons is however much shorter ($\lesssim 0.1 \text{ Gyr}$) due to IC and synchrotron energy losses. Therefore CRs cannot simply be ejected by active galaxies and propagate over the cluster volume, but they have to be continuously (re-)accelerated *in situ* [26]. Electrons can be (re-)accelerated to GeV energies by shocks and turbulence generated by major cluster mergers, and to TeV energies at the strong accretion shocks [27], where cold infalling material plunges in the hot ICM of massive galaxy clusters and shock Mach numbers range between 10 and a few 10^3 (see Fig. 2).

The timescales for energy losses as well as the diffusion timescales are instead longer than the Hubble time for CR protons (CRps). They thus can be continuously accelerated both by internal and by external processes, resulting in an effective accumulation of relativistic and

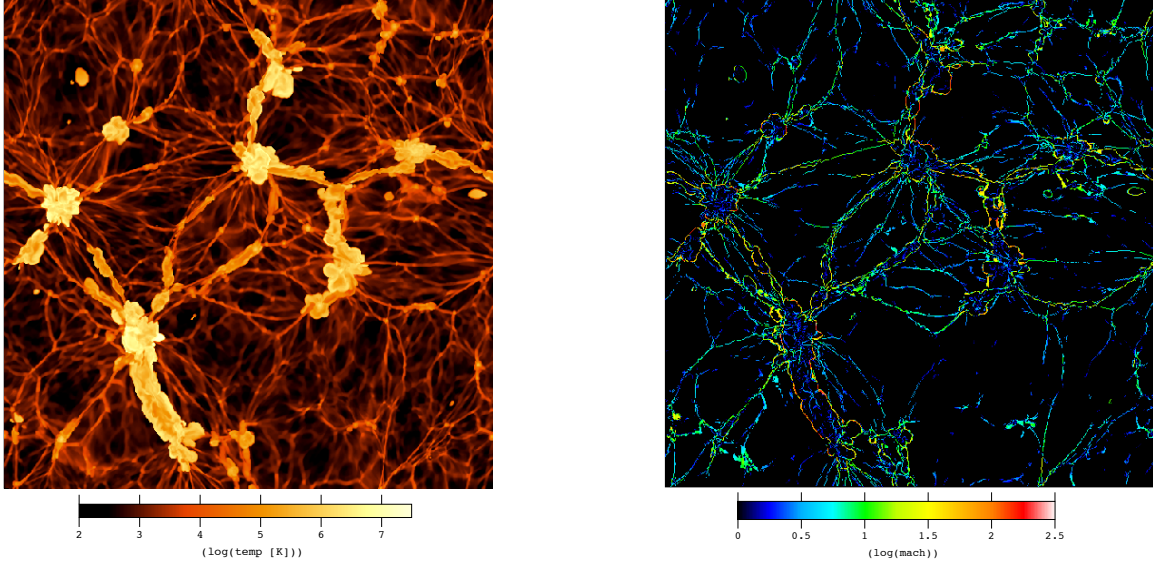


Figure 2: Simulated maps of the gas temperature (left) and Mach number (right) in a region of side 80 Mpc (from [29]). Accretion shocks (due to large scale matter infall on massive clusters) have significantly higher Mach numbers compared to shocks that develop in the central regions of major merging clusters. Accretion shocks are expected to be highly efficient sources of particle acceleration, with steeper spectra of injection compared to the shocks internal to clusters.

ultra-relativistic CR ps in clusters. Hadronic CRs can subsequently produce Gamma-rays and secondary relativistic electrons through inelastic collisions with the ions of the ICM (see e.g. [28] and references therein). Other possible physical mechanisms that could accelerate electrons up to ultra-relativistic energies (TeV–PeV) are related to interactions of CMB photons with ultra-relativistic CR ps [30], and/or very high energy intracluster Gamma-ray photons [31]. Dark matter annihilation can also be a source of secondary relativistic electrons and positrons [32].

Relativistic electrons observed at radio wavelengths can thus have a secondary origin [33], and/or have been (re-)accelerated by ICM shocks and turbulence developed during cluster mergers [34, 35]. Current radio observational results are mostly in agreement with this latter hypothesis (e.g. [36]). The strongest point leading to this conclusion is the fact that giant radio halos and relics have been detected up to now only in merging clusters. However, as detailed in Sect. 3.3, deeper radio, Gamma-ray and HXR observations are required to get firm conclusions about the origin of intracluster CR es .

At the light of current results different questions still need to be answered. First of all we have to understand if relativistic electrons are really hosted *only* in merging systems (as present radio observations suggest) or if *all* clusters have a radio halo/relic. In addition extended radio sources have not been detected in *all* merging clusters. If shocks and turbulence related to cluster mergers are the mechanisms responsible for electron re-acceleration, the absence of observational evidence of intracluster CR es in several merging systems could be related to other physical effects. The observed correlation between radio power and cluster mass seems to indicate that only very massive cluster mergers are energetic enough to accelerate electrons at relativistic velocities in the intracluster volume [12]. This scenario needs however to be tested through higher sensitivity radio observations, since the non-detection of radio halos/relics in many merging clusters could be related to a lack of sensitivity of current instruments. Deep future radio surveys (Sect. 4) will allow us to study the evolution of the luminosity function of radio halos, giving important constraints on current models for electron acceleration in galaxy clusters [37].

Table 1: The non-thermal ‘‘Pandora’s vase’’ for galaxy clusters. We can expect multi-wavelength emission and particle acceleration from different kinds of interactions between: (**first row**) intracluster magnetic fields, CMB photons and ICM ions, and (**first column**) relativistic / ultra-relativistic cosmic rays accelerated by different possible physical mechanisms in galaxy clusters (see Sect. 3.2). Note in addition that the interaction between CMB photons and intracluster Gamma-ray photons can produce ultra-relativistic CRes.

&	MAGNETIC FIELDS	CMB PHOTONS	ICM IONS
REL. CRes	Radio emission (Synchrotron)	Hard X-rays (Inverse Compton)	
REL. CR _{ps}			Gamma-rays + Secondary CRe (Hadronic collisions)
ULTRA-REL. CRes	Hard X-rays (Synchrotron)	Gamma-rays (Inverse Compton)	
ULTRA-REL. CR _{ps}		Ultra-rel. CRes (Bethe-Heitler)	

3.3 A multi-wavelength view of the non-thermal intracluster component

An increasing number of theoretical and numerical analyses (e.g. [38, 39]) are exploring the possibility that a combination of CR protons and electrons of primary and secondary origin can reproduce the multi-wavelength radiation of the non-thermal intracluster component. Besides synchrotron radio emission from GeV electrons and intracluster magnetic fields, we can expect (see also Table 1):

- *HXR emission* from IC scattering of CMB photons by GeV electrons or from synchrotron emission of TeV electrons;
- *Gamma-ray emission* from IC scattering of CMB photons by TeV electrons or from inelastic collision of CR_{ps} with the ions of the CMB.

Radio synchrotron emission from galaxy clusters is now firmly confirmed (Sect. 2). Evidence of non-thermal (IC) HXR emission from several clusters hosting diffuse radio sources has been obtained mostly through the X-ray satellites *Beppo-SAX* and *RXTE* (e.g. [40, 41]). The detection and nature (thermal or non-thermal) of the HXR excess in galaxy clusters is however strongly debated ([42] and references therein). Up to now, only upper-limits have been derived for the Gamma-ray emission of galaxy clusters, which imply a CR energy density less than 5-20% of the thermal cluster energy density. If we assume intracluster magnetic fields of the order of μ Gauss (Sect. 3.1) and cluster radii of a few Mpc, it can easily be derived that intracluster CR and magnetic field energy densities are not far from equipartition [43].

4 Perspectives

In order to make a proper comparison between observational results and current theoretical models about the origin and physical properties of the non-thermal intracluster component, we

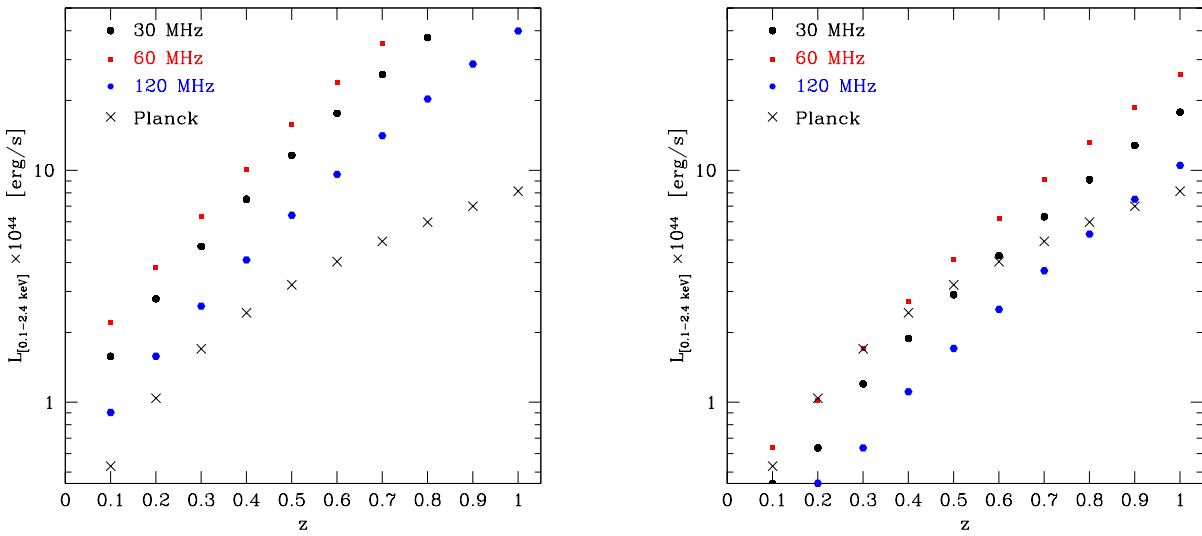


Figure 3: Evolution with redshift of the X-ray luminosity limit of clusters whose diffuse radio emission can be detected with *LOFAR* at 30, 60 and 120 MHz down to the sensitivity limit of the All-Sky Survey (left) and Deep Survey (right), at a resolution of 21 arcsec, assuming to detect at least 50% of the radio flux at 10σ level (our estimates). The detection limits expected for the *Planck* cluster catalogue are shown with black crosses (courtesy of A. Chamballu and J. Bartlett).

need multi-frequency observations of *statistical* samples of clusters hosting diffuse radio sources. The study of galaxy cluster SED ^b from Gamma-rays to low radio frequencies, for instance, is essential to discriminate between the different particle acceleration scenarios and to improve the measure of magnetic field intensity (see e.g. [44]).

In the next decades several radio facilities – such as *LOFAR*, *LWA*, *ASKAP*, *MeerKAT* and, last but not least, *SKA* – will allow to significantly improve our knowledge about the radio emission of the non-thermal intracluster component (e.g. [45]). We are now assisting to the opening of a spectral window largely unexplored by previous radio telescopes ($\nu < 200$ MHz) thanks to *LOFAR*. Due to the steep synchrotron spectrum of halos and relics, the detection of diffuse cluster radio sources is favored at this low frequencies (see Fig. 7 in [2]). The planned *LOFAR* All-Sky survey is expected to detect about 350 radio halos at redshift $z \lesssim 0.6$ [46].

At other wavelengths and based on what detailed in previous sections, important constraints about the non-thermal cluster emission are expected from the Gamma-ray *Fermi* satellite, and from telescopes observing in the HXR band, such as *NuSTAR* and, possibly, *IXO* (e.g. [39]). The detection of statistical samples of radio halos and relics through on-going and up-coming radio surveys (e.g. “K.P. Extragalactic Surveys” of *LOFAR* [47], “EMU” survey of the *ASKAP* telescope^c) will need complementary multi-frequency projects for:

- obtaining complementary cluster catalogs to verify the presence of galaxy clusters corresponding to diffuse radio sources (see for instance the nice complementarity between the clusters that could be detected with *LOFAR* All-Sky and Deep Surveys and with *Planck*, Fig. 3);
- getting a precise physical characterization of the detected cluster – and in particular of its redshift, mass and dynamical state – in order to test current models of CR acceleration.

^bSpectral Energy Distribution

^c<http://www.atnf.csiro.au/people/rnorris/emu/>

To conclude, after the huge progress in the last fifteen years of our knowledge of the evolutionary physics of cluster galaxies and of the thermal ICM, we are now living in the “golden age” for non-thermal cluster studies: the opening of the few spectral windows largely unexplored by astronomical observations (i.e. the HXR, Gamma-ray and low-frequency radio bands) will allow us to study the non-thermal physics of galaxy clusters with unprecedented statistics and thoroughness.

Acknowledgments

I warmly thank the organizers of the Cosmology Moriond meeting for having invited me to this interesting and enjoyable conference. Thanks also go to Franco Vazza for his careful reading of the paper and his very useful comments. I acknowledge financial support by the Agence Nationale de la Recherche through grant ANR-09-JCJC-0001-01.

References

- [1] Feretti, L. & Giovannini, G., in *Lecture Notes in Physics*, Vol. 740, 143, A Pan-Chromatic View of Clusters of Galaxies and the Large-Scale Structure, ed. M. Plionis, O. López-Cruz, & D. Hughes (Berlin Springer Verlag, 2008)
- [2] Ferrari, C. *et al.*, *Space Science Reviews* **134**, 93 (2008)
- [3] Jaffe, W. J., *ApJ* **212**, 1 (1977)
- [4] Govoni, F. & Feretti, L, *IJMPD* **13**, 1549 (2004)
- [5] Sharma, P. *et al.*, *arXiv:0909.0270* (2009)
- [6] Laganà, T. F. *et al.*, *A&A* **510**, 76 (2010)
- [7] Arnaud, M., in *Background Microwave Radiation and Intracluster Cosmology*, 77, Proceedings of the International School of Physics ”Enrico Fermi”, ed. F. Melchiorri & Y. Rephaeli (IOS Press, The Netherlands, and Società Italiana di Fisica, Bologna, Italy, 2005)
- [8] Willson, M. A. G., *MNRAS* **151**, 1 (1970)
- [9] Large, M. I. *et al.*, *Nature* **183**, 1663 (1959)
- [10] Giovannini, G. *et al.*, *NewA* **4**, 141 (1999)
- [11] Condon, J. J. *et al.*, *AJ* **115**, 1693 (1998)
- [12] Giovannini, G. & Feretti, L., 2002, in *Astrophysics and Space Science Library*, Vol. 272, 197, Merging Processes in Galaxy Clusters, ed. L. Feretti, I. M. Gioia, & G. Giovannini, (Kluwer Academic Publishers, Dordrecht, 2002)
- [13] Kempner, J. C. & Sarazin, C. L., *ApJ* **548**, 639 (2001)
- [14] Feretti, L. & Giovannini, G., in *IAU Symposium*, Vol. 175, 333, Extragalactic Radio Sources, ed. R. D. Ekers, C. Fanti, & L. Padrielli (1996)
- [15] Feretti, L. *et al.*, *A&A* **373**, 106 (2001)
- [16] Gitti, M. *et al.*, *A&A* **470**, 25 (2007)
- [17] Bonafede, A. *et al.*, *A&A* **494**, 429 (2009)

- [18] van Weeren, R. J. *et al.*, *A&A* **506**, 1083 (2009)
- [19] Giovannini, G. *et al.*, *A&A* **511**, 5 (2010)
- [20] Carilli, C. L. & Taylor, G. B., *ARA&A* **40**, 319 (2002)
- [21] Govoni, F. *et al.*, *A&A* **460**, 425 (2006)
- [22] Guidetti, D. *et al.*, *A&A* **483**, 699 (2008)
- [23] Bonafede, A. *et al.*, *A&A* **513**, 30 (2010)
- [24] Vacca, V. *et al.*, *arXiv:1001.1058* (2010)
- [25] Dolag, K., *et al.*, *Space Science Reviews* **134**, 311 (2008)
- [26] Sarazin, C. L., in *Astrophysics and Space Science Library*, Vol. 272, 1, Merging Processes in Galaxy Clusters, ed. L. Feretti, I. M. Gioia, & G. Giovannini, (Kluwer Academic Publishers, Dordrecht, 2002)
- [27] Miniati, F. *et al.*, *ApJ* **542**, 609 (2000)
- [28] Aharonian, F. *A&A* **495**, 27 (2009)
- [29] Vazza, F. *et al.*, *MNRAS* **395**, 1333 (2009)
- [30] Inoue, S. *et al.*, *ApJ* **628**, 9 (2005)
- [31] Timokhin, A. N. *et al.*, *A&A* **417**, 391 (2004)
- [32] Profumo, S. & Ullio, P., *arXiv:1001.4086* (2010)
- [33] Dennison, B., *apj* **239**, L93 (1980)
- [34] Enßlin T. A. *et al.*, *A&A* **332**, 395 (1998)
- [35] Brunetti, G. *et al.*, *MNRAS* **320**, 365 (2001)
- [36] Brunetti, G. *et al.*, *A&A* **670**, 5 (2007)
- [37] Cassano, R. *et al.*, *MNRAS* **369**, 1577 (2006)
- [38] Pfrommer, C. *et al.*, *MNRAS* **385**, 1211 (2008)
- [39] Brunetti, G., in *Revista Mexicana de Astronomia y Astrofisica Conference Series*, Vol. 36, 201 (Revista Mexicana de Astronomia y Astrofisica Conference Series 2009)
- [40] Fusco-Femiano, R. *et al.*, *ApJ* **513**, L21 (1999)
- [41] Rephaeli, Y. *et al.*, *ApJ* **511**, L21 (1999)
- [42] Ferrari, C. *AIPC* **1126**, 277 (2009)
- [43] Vannoni, G. *et al.*, *arXiv:0910.5715* (2009)
- [44] Colafrancesco, S. & Marchegiani, P., *A&A* **502**, 711 (2009)
- [45] Feretti, L. *et al.*, *NewAR* **48**, 1137 (2004)
- [46] Cassano, R. *et al.*, *A&A* **509**, 68 (2010)
- [47] Röttgering, H. J. A. *astro-ph/0610596* (2006)

STATISTICAL INVESTIGATION OF THE NON-THERMAL EMISSION OF GALAXY CLUSTERS

J. LANOUX, E. POINTECOUTEAU, M. GIARD, L. MONTIER

*Centre d'Etude Spatiale des Rayonnements, CNRS/Université de Toulouse, 9 Avenue du colonel Roche,
BP 44346, 31028 Toulouse Cedex 04, France*

A diffuse non-thermal component has now been observed in massive merging clusters. To better characterise this component, and to extend analyses done for massive clusters down to a lower mass regime, we are conducting a statistical analysis over a large number of X-ray clusters (from ROSAT based catalogues). By means of their stacked radio and X-ray emissions, we are investigating correlations between the non-thermal and the thermal baryonic components. We will present preliminary results on radio-X scaling relations with which we aim to probe the mechanisms that power diffuse radio emission ; to better constrain whether the non-thermal cluster properties are compatible with a hierarchical framework of structure formation ; and to quantify the non-thermal pressure.

1 Introduction

Galaxy clusters are the largest gravitationally bound systems of the Universe. Most of their mass is in the form of dark matter ($\sim 85\%$). A few percents is in the form of galaxies. The rest ($\sim 12\%$) is in the form of diffuse hot gas, which is the intracluster medium. This gas cools down via thermal Bremsstrahlung emission observed at X-ray wavelengths. But diffuse radio sources were also observed in ~ 50 massive and merging clusters. Their radio emission is related to highly relativistic electrons and magnetic fields that populate the intracluster space. These non-thermal components are observed at radio wavelengths due to their synchrotron emission. To date, there are two main hypothesis to explain their origin: violent acceleration processes such as mergers occurring during clusters lifetime, and secondary electrons injected during proton-proton collisions. We observe three different types of diffuse radio sources in galaxy clusters: halos, relics and mini-halos (e.g. Ferrari et al. 2008⁵ for a review). The non-thermal component contributes to the total pressure of the intracluster medium and can bias mass proxies up to $\sim 15\%$ (Dolag et al. 2000⁴).

Gas properties are following dark matter properties (e.g. Arnaud 2005¹ for a review). Studying the correlation between the thermal and the non-thermal components then allow us to observe whether the population of electrons is following the gas, and so the dark matter in the process of structure formation. Liang et al. (2000)⁸ were the first to show a correlation between the radio and X-ray luminosities in galaxy clusters. This correlation was confirmed by subsequent works such as Giovannini et al. (2009)⁷ or Brunetti et al. (2009, B09 hereafter)². But this correlation has only been highlighted for samples of massive clusters with radio halos or relics and showing features of merging processes.

In this work, we study this correlation down to a lower mass regime of clusters. So far, we have been limited by the sensitivity of radio observations. For instance, Cassano et al.

(2008)³ searched for radio halos in clusters using the NVSS and the GMRT. They found that for clusters with X-ray luminosities higher than 10^{45} erg/s, only 40% showed radio halos, and that this percentage decreases rapidly with lower X-ray luminosities. Moreover, radio halos and relics have only been found in merging clusters, i.e. in clusters dynamically disturbed. However, it is not trivial to derive the dynamical state of clusters from available data. Therefore, we investigated the correlation via a statistical approach. We applied statistical and stacking tools to a X-ray (RASS) and a radio (NVSS) all-sky surveys, working with large cluster catalogues derived from ROSAT.

We used the following Λ CDM cosmology: $H_0 = 70 \text{ km s}^{-1} \text{ Mpc}^{-1}$, $\Omega_m = 0.3$ and $\Omega_\Lambda = 0.7$.

2 Data sets and catalogues

We made use of a X-ray and a radio survey : the ROSAT All Sky Survey (RASS) in the 0.1-2.4 KeV band and the NRAO VLA Sky Survey (NVSS) at 1.4 Ghz that covers the entire sky north of a declination of -40° .

We used a compilation of X-ray cluster catalogues assembled by Piffaretti et al. (2010)⁹. This compilation was homogenised to give physical quantities within an over-density δ_{500} such as R_{500} , L_{500} , M_{500} , etc. This compilation is based on RASS catalogues such as NORAS, REFLEX, NEP, BCS,... and serendipitous catalogues from ROSAT PSPC such as 400SD, SHARC,... We used 1,428 clusters of this compilation for which we produce estimates of L_{radio} and L_X .

3 Methodology

We derive L_X and L_{radio} from the RASS and NVSS using the following steps :

- In order to weight properly the luminosities, we masked the brightest point sources outside an aperture of R_{500} around the location of each cluster of our list using associated catalogues: the Bright and Faint Source Catalogues for the RASS, and the NVSS Source Catalogue for the NVSS.
- We then computed count rates and radio fluxes within R_{500} taking into account the local background. For the radio fluxes, we derive as well an estimate of the radio luminosities after the removal of point sources within R_{500} .
- We derived X-ray and radio luminosities within R_{500} . Assuming a standard self-similar evolution (Arnaud 2005¹), we scaled all luminosities as $L_X \propto n_e^2 V \propto h^{-1}(z)$ and $L_{radio} \propto n_e V \propto h(z)$ with $h(z) = h_0 \sqrt{(1+z)^3 \Omega_M + \Omega_\Lambda}$.
- From the computed X-ray and radio luminosities, we draw the $L_{radio} - L_X$ correlation using bisector methods taking into account the errors in both directions.

4 Sanity Checks

In order to double-check the validity of our X-ray and radio luminosities, we performed a series of sanity checks and tests. We compared our X-ray luminosities with those of Piffaretti et al. (2010)⁹. Beside a few outliers, we are in very good agreement with their luminosities. The cross-check of our radio luminosities was more problematic as we don't have large samples. We compared them with the radio luminosities of 20 out of 24 clusters from the sample of B09², and we are compatible with their luminosities.

We then reproduced the computation of our X-ray and radio luminosities for 1,500 random positions on the sky with $|b| > 15^\circ$. To derive those, we attributed an artificial redshift, R_{500}

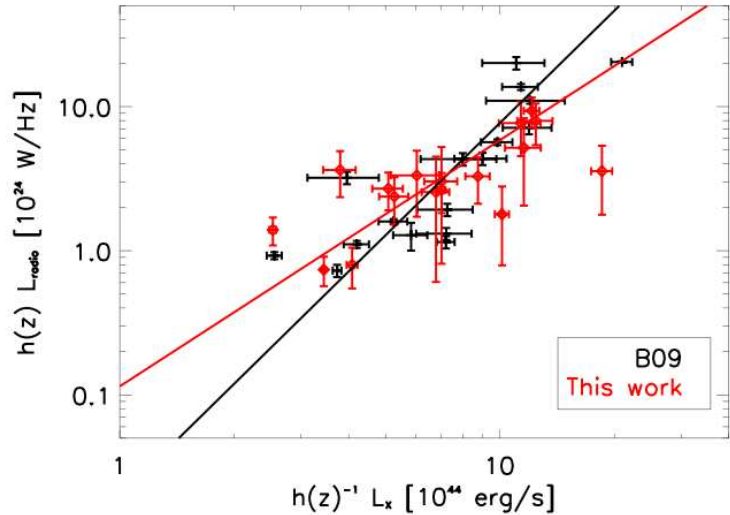


Figure 1: Distribution of 20 clusters from the sample of B09 in the radio-X luminosity plane. Black points mark luminosities from their work, red points mark our computed luminosities for the same clusters. Solid lines show the corresponding $L_{radio} - L_X$ best fits.

and kT_{500} accordingly to the respective distributions of those quantities in our list of clusters. We performed F-tests and Kolmogorov-Smirnov tests between the distributions of clusters and of random fields. The results of both tests are compatible with 0, and the distributions are therefore different.

Finally, we drew the $L_{radio} - L_X$ correlation for the random fields, and we found a flat correlation. Nevertheless, the fit showed a nonzero mean radio background. Thus, we subtracted it from all our luminosities (Figure 2, right panel).

5 $L_{radio} - L_X$ correlation

As a first step, we reproduced the work of B09. We plotted their clusters and correlation. We then identified those clusters in our list of clusters and we plotted them as well as the corresponding correlation using our computed luminosities (Figure 1). We derived a slope of ~ 1.7 . B09 derived a slope of ~ 2.6 for luminosities corrected from evolution (~ 2.2 with no evolution). We are marginally compatible with their results. However, it matches very well the slope of ~ 1.7 derived with linear methods (e.g. Feretti et al. 2005⁶ for 16 clusters, Giovannini et al. 2009⁷ for 33 clusters).

In a second step, we drew the $L_{radio} - L_X$ correlation for the clusters of our list (Figure 2, left panel). We compared the results obtained with the two different radio luminosities that we computed (luminosities with all the fluxes within an aperture of R_{500} , and luminosities subtracted from known point sources). We found the same slope, but with a lower normalization for the *cleansed* luminosities. We then drew the correlation for a sub-selection of 476 clusters with $L_X > 5 \times 10^{43}$ erg/s ($M > \sim 10^{14} M_\odot$). We then binned our X-ray luminosities in bins of equal number of clusters, i.e. 60. We fitted the binned data and derived a slope of ~ 0.9 .

6 Discussion and Conclusion

We have investigated the $L_{radio} - L_X$ correlation for clusters of galaxies. We extended this analysis down to a lower mass regime ($M > 10^{14} M_\odot$) with respect to previous works dealing

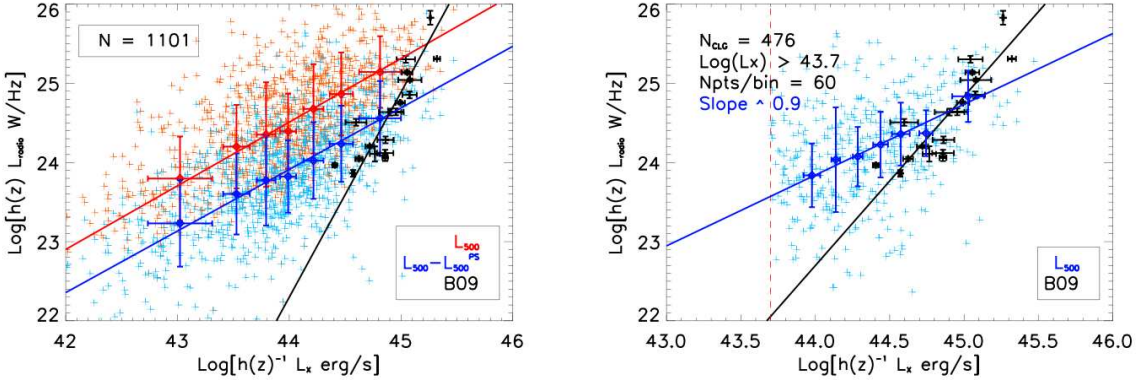


Figure 2: Distribution of clusters in the radio-X luminosity plane for clusters of our list (*left panel*) and for clusters with X-ray luminosity higher than 5×10^{43} erg/s (*right panel*). Red crosses mark individual radio luminosities with all the fluxes within R_{500} , blue crosses mark individual radio luminosities with the fluxes subtracted from known point sources, and black points mark clusters from the sample of B09. Diamonds mark binned luminosities.

Solid lines show the corresponding $L_{radio} - L_X$ best fits.

with limited samples of massive and dynamically disturbed clusters.

We found a correlation with a flatter slope (~ 0.9) compared to pre-cited works. This is likely to be explained by the fact that our radio luminosities contains a component of unresolved point sources. In other terms, all the point sources (i.e. AGN) are not subtracted within R_{500} . This population of unresolved AGN (in the used radio data, i.e. NVSS data) may be the main contributor to our radio luminosities on the top of a diffuse emission linked to the intracluster medium.

To go further in this analysis, we need to quantify the contribution of AGN in the radio emission of galaxy clusters. This will allow us to constrain the population of AGN in dense media ; to characterize diffuse radio emissions of clusters down to the low mass regime ; and to probe the mechanisms that power them.

Acknowledgments

We are deeply indebted to Rocco Piffaretti for providing us with his homogenised compilation of X-ray catalogues with which this work was carried out. JL, EP and LM acknowledge the support of grant ANR-06-JCJC-0141.

References

1. Arnaud, M., *Background Microwave Radiation and Intracluster Cosmology* (2005) [[arXiv:astro-ph/0508159](https://arxiv.org/abs/astro-ph/0508159)]
2. Brunetti, G., Cassano, R., Dolag, K., and Setti, G., *A&A* **507**, 661 (2009)
3. Cassano, R., Brunetti, G., Venturi, T., et al., *A&A* **480**, 687 (2008)
4. Dolag, K., Schindler, S., *A&A* **364**, 491 (2000)
5. Ferrari, C., Govoni, F., Schindler, et al., *Space Sci. Rev.* **134**, 93 (2008)
6. Feretti, L., *X-Ray and Radio Connections* (2005b) [[arXiv:astro-ph/0406090](https://arxiv.org/abs/astro-ph/0406090)]
7. Giovannini, G., Bonafede, A., Feretti, L., et al. *A&A* **507**, 1257 (2009)
8. Liang, H., Hunstead, R. W., Birkinshaw, M., and Andreani, P., *ApJ* **544**, 686 (2000)
9. Piffaretti, R., et al., *A&A* , (to be submitted) (2010)

STUDYING THE LOCAL GROUP WITHIN THE CLUES PROJECT

S. GOTTLÖBER¹, N. LIBESKIND¹, G. YEPES², Y. HOFFMAN³

¹*Astrophysical Institute Potsdam, An der Sternwarte 16, 14482 Potsdam, Germany*

²*Grupo de Astrofísica, Universidad Autónoma de Madrid, Madrid E-28049, Spain*

³*Racah Institute of Physics, The Hebrew University of Jerusalem, Givat Ram, Israel*

Within the CLUES project (<http://clues-project.org> — Constrained Local UniversE Simulations) we perform numerical simulations of the evolution of the local universe, the best observed part of the universe. We discuss the radial distribution of matter in the Local Group halos as well as the preferred directions of infall of satellites.

1 Introduction

During the last decade a flat Friedmann universe whose mass-energy content is dominated by a cosmological constant (the Λ term), a cold dark matter (CDM) component and baryons became the standard model of cosmology. This model specifies the cosmological expansion history, within which structures on all scales have been formed starting from tiny initial density fluctuations. The knowledge of the physical laws governing the dynamics of the dark matter and baryons in the expanding universe provide the framework within which a successful model of galaxy formation can be developed. The basic paradigm of cosmological structure formation suggests the dark matter forms halos, within which galaxy formation takes place via complex baryonic physics. This process can be followed by numerical simulations which take into account the gravitational interaction and clumping of matter as well as in some approximation the baryonic physics. This approximation includes the radiative cooling of the baryonic gas, the formation of stars and the feedback of these stars on the baryonic gas.

Cosmological simulations must cover a large dynamical and mass range. A representative volume of the universe should be large, but this comes at the expense of the mass resolution. A smaller volume could possibly be not representative. To overcome this problem we simulate the evolution of a small volume which, however, is specifically designed to represent the observed local universe. The algorithm of constrained realisations of Gaussian field provides a very attractive method of imposing observational data as constraints on the initial conditions and thereby yielding structures which can closely mimic those in the nearby universe. The prime motivation of the CLUES project (<http://clues-project.org> — Constrained Local UniversE Simulations) is to construct simulations that reproduce the local cosmic web and its key 'players', such as the Local Supercluster, the Virgo cluster, the Coma cluster, the Great Attractor and the Perseus-Pisces supercluster. Observational data of the nearby universe is used as constraints on the initial conditions and thereby the resulting simulations reproduce the observed large scale structure. The implementation of the algorithm of constraining Gaussian random fields¹ to observational data and a description of the construction of constrained simulations has been described in more detail in Gottlöber et al.⁶.

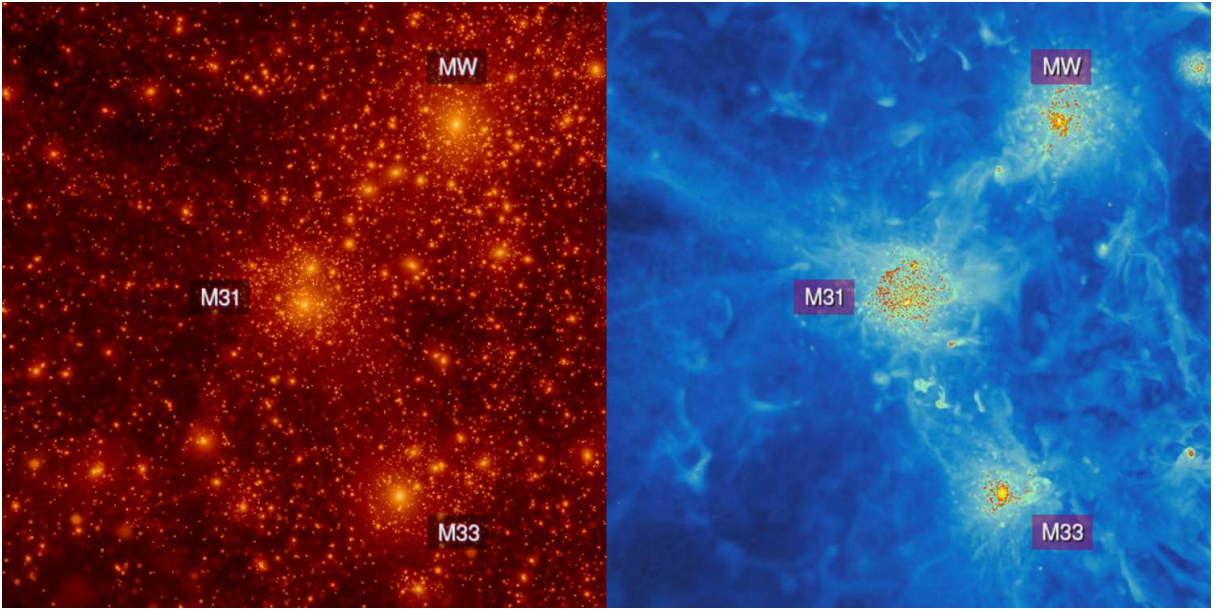


Figure 1: Left panel: The dark matter distribution in the simulated Local Group. Right panel: The gas distribution in the same region.

We run our simulations within the standard Λ CDM model assuming a WMAP3² cosmology with $\Omega_m = 0.24$, $\Omega_b = 0.042$, $\Omega_\Lambda = 0.76$ with a power spectrum normalisation of $\sigma_8 = 0.73$ and slope $n = 0.95$ slope of the power spectrum. We used the PMTree-SPH code **GADGET2**³ to simulate the evolution of a cosmological box with side length of $L_{\text{box}} = 64h^{-1}\text{Mpc}$.

Using a constrained realisations of the initial conditions we are able to simulate the evolution of our local group in an environment which closely mimics the environment of the observed local group. In order to improve the mass resolution in the region of interest we simulate the evolution of a sphere of radius $2h^{-1}\text{Mpc}$ using the full resolution (equivalent to 4096^3 particles in the box) whereas outside this region, the simulation box is populated with lower resolution (i.e higher mass) particles. We have used the same set of initial conditions to run two simulations, one with dark matter only and another one including gas dynamics. For the second one we populate only the high resolution region by dark matter and gas particles. We follow the clustering of gas particles using an subgrid model⁴ which includes cooling, star formation and supernova feedback. Thus we are able to achieve high resolution and follow gas-dynamical processes in the region of interest, while maintaining the correct external gravitational environment by following the evolution of more massive dark matter particles on low computational costs.

2 The Local Group

The three main galaxies of our simulated Local Group - the Milky Way (MW), M31 and M33 - have been reproduced with masses in good agreement with the observed masses of these objects. In Figure 1 we show the dark matter and gas distribution in and around these three objects. One can clearly see the three main objects of the local group as well as a number of smaller objects. In order to identify and study all isolated objects as well as objects residing inside another one (called sub-halos) we have used the AHF halo finder⁵, which locates local over-densities as prospective halo centres. For each isolated halo the virial radius r_{vir} has been computed and the properties of the halo are related to the mass distribution inside a sphere of virial radius. Sub-haloes are defined as haloes which lie within the virial radius of a more massive halo, their host halo. Since sub-haloes are embedded within the enlarged density of their host halo their

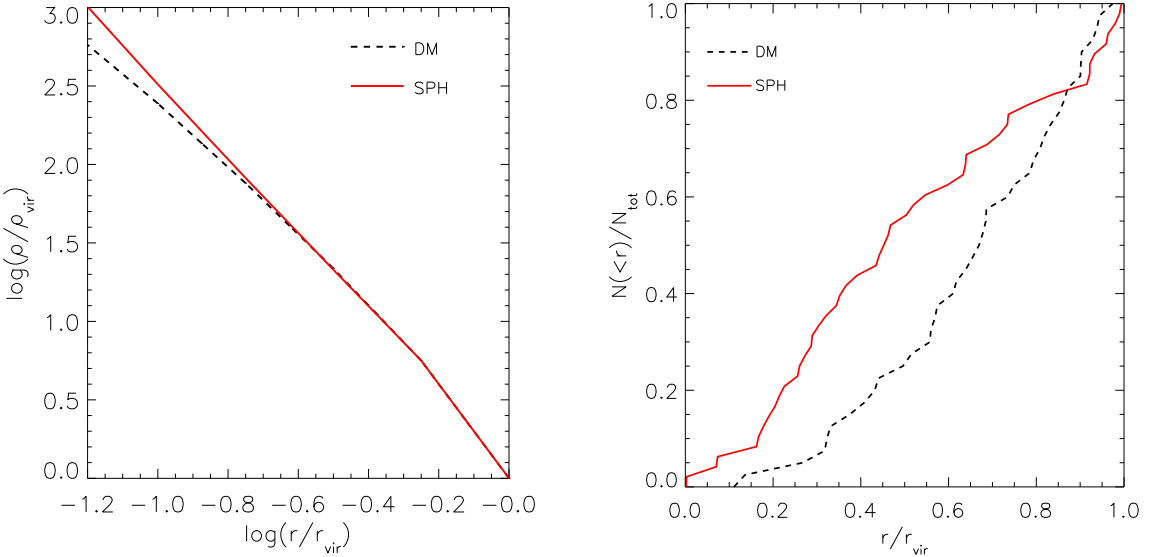


Figure 2: Left panel: The average total matter density profile of the three main halos in the DM (black) and SPH (red) simulations, normalised to the virial radius and virial over-density. Right panel: The cumulative radial density profile of sub-halos. The solid and dashed lines show this quantity for SPH and DM sub-haloes (respectively) with $z = 0$ masses larger than $2 \times 10^8 h^{-1} M_{\odot}$.

size cannot be characterised by their virial radius but rather by a characteristical upturn of the density. The corresponding distance is assigned as the sub-halo's radius and the sub-halo's properties are calculated within this radius. We follow the evolution of halos and sub-halos by cross-correlating haloes in consecutive simulation outputs using the particle ids which are stored within the AHF module.

In Fig. 2, left panel we plot the mean density profile averaged over the three main halos (MW, M31, M33) in the DM only and gas-dynamical simulations. Across most of the halo's radius the density profiles are the same: only within $\sim 0.1 r_{\text{vir}}$ does the total density profile in the SPH simulation rise significantly above the DM one⁷. In Fig. 2, right panel we show the cumulative radial profile of sub-halos in the DM only and gas-dynamical simulations at $z = 0$. We only consider sub-halos with masses larger than $2 \times 10^8 h^{-1} M_{\odot}$, in order to roughly obtain the right number of satellites per host. One can clearly see, that the substructures in the SPH simulation are significantly more centrally concentrated than in the DM one. Simply put, this is due to the interplay between adiabatic contraction, tidal stripping and dynamical friction. In simulations with cooling, baryonic substructures grow deeper potential wells, which inhibit tidal stripping by allowing substructures to retain more mass, making the satellites more massive and thus more prone to dynamical friction. This feature does not depend on sub-halo mass⁷. This result is consistent with Weinberg et al.⁸, who compared the radial distribution of much more massive substructures ($M_{\text{sub}} \sim 10^{10} M_{\odot}$) in more massive systems ($M_{\text{host}} \sim 10^{12-14} M_{\odot}$) in dark matter only and SPH simulations of galaxy groups.

Of interest to the $z = 0$ spatial distribution of satellites, is the question of whether satellites are uniformly or anisotropically accreted. In order to address this issue, we defined a dynamic coordinate system locked on the members of the Local Group. We then record each time a satellite (with mass larger than $2 \times 10^7 h^{-1} M_{\odot}$) enters the virial radius. In Fig. 3 left panel, we show the angular distribution on the sky of these satellite entry points and note that it is inconsistent with a uniform distribution. Furthermore, the angular pattern of infalling satellites seen at r_{vir} , mimics that of satellites crossing shells located much further out, for example at $3 r_{\text{vir}}$ (Fig. 3, right panel). This implies the existence of a collimated flow of satellites that

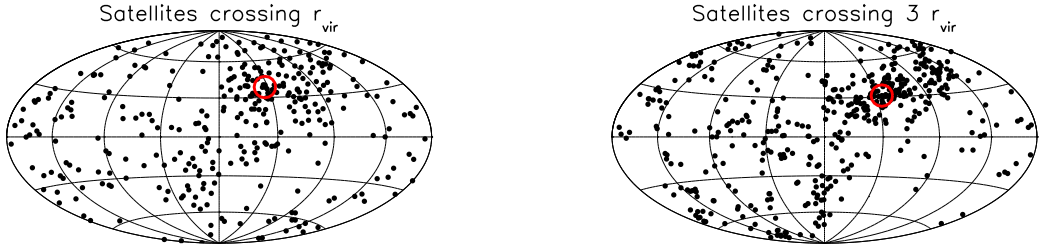


Figure 3: The location on the sky of accretion points for satellites entering the virial radius (left panel) and for those crossing shells $3 r_{\text{vir}}$ (right panel). The red circles indicate the region on the sky with the highest density of entry points. Not only are the accretion points not uniformly distributed over the sphere, but the angular pattern is coherent over a large radial extent.

originates far from the virial radius, thus providing halos with a preferred direction from which to accrete satellites.

Acknowledgments

NIL is supported by the Minerva Stiftung of the Max Planck Gesellschaft. YH has been partially supported by the ISF (13/08). GY acknowledges support of MICINN (Spain) through research grants FPA2009-08958, AYA2009-13875-C03-02 and CONSOLIDER-INGENIO SyEC (CSD2007.0050). SG acknowledges support of MICINN (Spain) through the Consolider-Ingenio 2010 Programme under grant MULTIDARK CSD2009-00064. The simulations described here were performed and analysed at the Leibniz Rechenzentrum Munich (LRZ) and at the Barcelona Supercomputing Center (BSC). We thank DEISA for giving us access to computing resources in these centers through the DECI projects SIMU-LU and SIMUGAL-LU. We would like to thank Kristin Riebe for providing us Figure 1 made with PMviewer^a of Arman Khalatyan.

References

1. Y. Hoffman, E. Ribak, *ApJL* **380**, L5 (1991)
2. D. N. Spergel, R. Bean, O. Doré, M. R. Nolta, C. L. Bennett, et al. *ApJS* **170**, 377 (2007)
3. V. Springel, *MNRAS* **364**, 1105 (2005)
4. V. Springel, L. Hernquist, *MNRAS* **339**, 289 (2003)
5. S. R. Knollmann, A. Knebe, *ApJS* **182**, 608 (2009)
6. S. Gottlöber, Y. Hoffman, G. Yepes, in: *High Performance Computing in Science and Engineering*, Springer-Verlag, 2010
7. N.I. Libeskind, G. Yepes, A. Knebe, S. Gottlöber, Y. Hoffman, S. R. Knollmann, *MNRAS* **401**, 1889 (2010)
8. D. H. Weinberg, S. Colombi, R. Davé, N. Katz, *ApJS* **678**, 6 (2008)

^a<http://pmviewer.sourceforge.net/>

Merger events with galaxy-gas separation in the hot galaxy cluster A2163.

H. Bourdin¹, M. Arnaud², P. Mazzotta¹, G.W. Pratt², J.-L. Sauvageot², R. Martino¹, S. Maurogordato³, A. Cappi^{3,4}, C. Ferrari³ and C. Benoist³

¹ Dipartimento di Fisica, Università degli Studi di Roma ‘Tor Vergata’,

² Laboratoire AIM, IRFU/Service d’Astrophysique - CEA/DSM - CNRS - Université Paris Diderot

³ Université de Nice Sophia-Antipolis, CNRS, Observatoire de la Côte d’Azur, UMR 6202

⁴ INAF - Osservatorio Astronomico di Bologna

Located at $z=0.203$, A2163 is a rich galaxy cluster showing outstanding gas properties –in particular exceptionally high X-ray luminosity and average temperature–, but also a powerful and extended radio halo. We present a multiwavelength analysis about merger events observable in this hottest cluster. From XMM-Newton and Chandra spectral-imaging, we evidence the westwards motion of a cold gas clump embedded in the hotter atmosphere of A2163, and delimited by a cold front. From gas brightness and temperature profile analysis performed in two opposite regions of the main cluster, we show that average pressure of the Intra-Cluster Medium (ICM) have been raised behind the moving cold clump, leading to a strong ICM departure from hydrostatic equilibrium possibly due to shock heating. Interestingly, we further show that this gas clump has been spatially separated from a galaxy sub-cluster recently detected from optical data. In a similar way to what has been observed in the so-called “bullet cluster”, 1E0657-56, we infer from these findings a merging scenario where a fast sub-cluster has been accreted along the East-West elongation of A2163, while his gas content has been spatially segregated from galaxies. Extensively observed at various wavelenghts, A2163 would thus provide us a secondary case study of gas-galaxy separation in a merging galaxy cluster.

1 Introduction

A2163 is a rich galaxy cluster (richness class 2) located at $z = 0.203$. After initial X-ray detection by HEAO 1 A-1 [1], combined observations by the Ginga and Einstein X-ray satellites revealed the extraordinary properties of its hot gas content, with exceptionally high luminosity and average temperature [$L_X = 10.2 \times 10^{38}$ W, $kT = 13.9$ keV, 2]^a. Follow-up observations have further revealed several signatures of major merger events at various wavelengths in this hottest cluster. ROSAT observations showed an irregular X-ray morphology [3], while ASCA observations revealed complex thermal structure [4], more recently confirmed from Chandra data [5, 6, 7]. Evidence for clear cluster substructuring has been seen in weak lensing [see e.g. 8, 9] and in the galaxy density distribution [10]. Moreover, A2163 is known to host a prominent radio halo [11, 12] and to be a possible source of non thermal hard X-ray emission [13, 14]. Due to its high thermal energy content, A2163 is also a favoured target for SZ observations. A recent analysis of optical data [10, hereafter, M08] has revealed the complex galaxy structure and dynamics in A2163, where a main cluster, A2163-A, is connected to a smaller sub-cluster to the North, A2163-B, via a galaxy bridge. The main cluster, A2163-A, itself has two brightest galaxies (BCG1 and

^a 10^{38} W $\equiv 10^{45}$ erg.s $^{-1}$; X-ray luminosity has been corrected for luminosity distance assuming $H_0 = 70$ km s $^{-1}$ Mpc $^{-2}$, and $\Lambda = 0.7$.

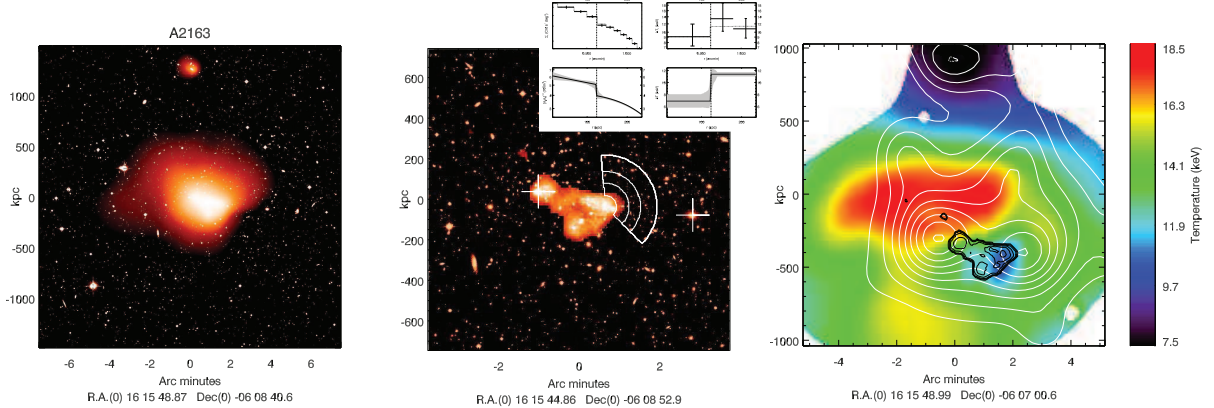


Figure 1: A2163. Left and middle panels: X-ray emission overlaid on galaxy maps. Optical observations performed at the MPI 2.2m telescope, see also [10]. X-ray images obtained from B-spline wavelet analyses of a Chandra exposure in the 0.5-2.0 keV band. Left: overall cluster emission. Middle: high resolution details corresponding to angular sizes lower than 2 arcmin. Inserted plot: ICM brightness (top-left) and projected temperature (top-right) profiles corresponding to the sector illustrated on the map, with 3d modelling of the ‘cold-front’ density and temperature jumps (bottom left and right, respectively). Right panel: ICM temperature maps obtained from wavelet spectral-imaging analysis of the EPIC-XMM-Newton data set. Black iso-contours from high resolution Chandra residue (same as bottom-left map); white iso-density contours from galaxy density map (see also [10]).

BCG2), a bimodal morphology, and an exceptionally large velocity dispersion (1434 ± 60 km s $^{-1}$). From analyses of XMM-Newton and Chandra observations of the Intra-Cluster Medium (ICM), we investigate the merger scenario involving the various components of A2163.

2 A gas ‘bullet’ crossing the main cluster atmosphere separately from galaxies

The Chandra-ACIS brightness map in the left panel of Fig. 1 show us the complex and irregular morphology of the ICM in A2163. This map reveals us a main component (A2163-A) and a Northern sub-cluster (A2163-B), the main component itself appearing irregular with an eastern extension at large scale and a triangular shape in the central region. As shown on the middle panel of Fig. 1, restricting a wavelet analysis of this data set to high resolution details has enabled us to separate a brightness peak located close to the brightest cluster galaxy (BCG1, see also M08) from a sharp-edged, wedge-shaped feature located to its west. Interestingly, overlaying the high resolution image obtained from this wavelet analysis to a gas temperature map (EPIC-XMM-Newton data) enables us to associate the wedge-like feature with a cold clump. The 3d structure of this cool core has been investigated by extracting the brightness and temperature profiles corresponding to the ICM sector illustrated on Fig. 1. Consistent with disrupted density and temperature distributions, these profiles identify the western edge of the cool core as a cold front. By analogy with 1E0657-56 (the so-called ‘bullet-cluster’, [15]), the location of the cold front with respect to the wedge-shaped residual emission might indicate the westwards motion of a stripped cool core embedded in the hotter atmosphere of A2163-A.

To try and constrain the history of a possible sub-cluster infall associated with this cool core, in the right panel of Fig. 1 we overlay the galaxy iso-density contours obtained from WFI data (see also M08) on the ICM temperature map of A2163. As discussed in M08, the galaxy iso-density contours map a complex, bimodal galaxy distribution in A2163-A. This bimodal distribution corresponds to an E-W elongation of the cluster dark matter halo, as revealed from weak lensing analysis [9]. Interestingly, we now observe that the less dense of the two galaxy sub-clusters in A2163-A is located near the cool core, but is separated from it at a projected distance of about 30 arcsec. Its location to the west of the cool core suggests a scenario in which a sub-cluster has crossed the A2163-A complex from east to west; the offset wedge-shaped

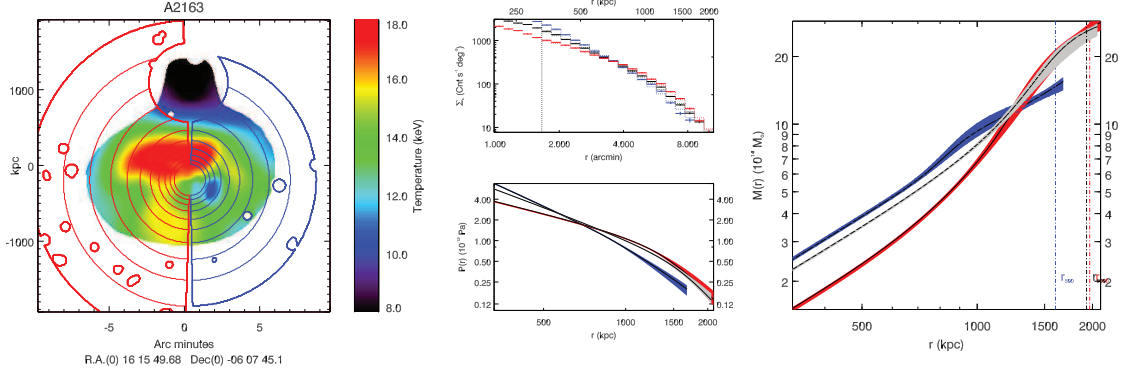


Figure 2: Left panel: A2163 gas temperature map with two complementary profile extraction regions overlaid. Middle panel: Gas surface brightness (top) and ICM pressure profiles (bottom) modelled to fit the surface brightness and projected temperature corresponding to the overall cluster (in black) and the eastern and western cluster sectors shown on the map (in red and blue, respectively). Right panel: A2163 mass profiles computed assuming ICM hydrostatic equilibrium in the same colour-coded cluster regions.

residual emission then suggests sub-cluster gas loss gas due to ram pressure of the main cluster atmosphere, leading to its present separation from the constituent galaxies.

3 Merger effect on the gas pressure

The evidence for a gas ‘bullet’ separated from its galaxies crossing the A2163 atmosphere suggests that the main cluster has recently accreted a sub-cluster along the East-West direction. In order to investigate the effects of this major merger event on the ICM thermodynamics, we extracted three sets of ICM brightness and temperature profiles corresponding to the eastern and western cluster sectors shown on Fig. 2, and to the overall cluster A2163-A. Fitting spherically symmetric distributions of the ICM density and temperature to these projected profiles has enabled us to model the ICM pressure structure in the two complementary cluster regions, and in the overall cluster. As observed for the brightness profiles, the eastern and western pressure profiles differ in the innermost region of A2163-A, then cross each other at a radial distance of about 800 kpc, above which the eastern profile has a higher pressure than the western profile by a factor ~ 2 . This pressure excess may be related to ICM shock heating behind the crossing ‘bullet’, leading to an adiabatic compression of the gas. The overall cluster pressure profile seems to reflect the higher pressure values corresponding to the eastern cluster sector, so that the on-going merger event is likely to have strongly disturbed the shape of the overall cluster pressure profile.

4 Mass measurements

The exceptionally high ICM temperature of A2163 and the evidence of an ongoing major merger event in its central region makes this cluster an interesting test case for cluster mass measurements. Assuming hydrostatic equilibrium, the ICM density and temperature profiles used to model gas pressure have been used to derive the integrated cluster mass profile, shown as a grey shaded area in the left panel of Fig. 2. The total cluster mass estimate, $M_{500} = 24.7^{+0.5}_{-0.9}$, obtained from this profile is inconsistent with the estimate obtained from the Y_X proxy, defined as the product of gas mass $M_{g,500}$ and average temperature kT [16], and expected to be robust to merger events from numerical simulations of cluster evolution: $M_{500,Y_X} = 18.7^{+2.0}_{-2.4}$. To investigate the origins of this inconsistency, we derive two additional integrated cluster mass profiles using the density and temperature profiles from the eastern and western cluster sectors shown

in Fig. 2. The eastern and western cluster mass profiles significantly differ in shape. We observe that the western profile has a higher integrated mass than the eastern profile near the cluster centre but then flattens at a lower radius, leading to a lower integrated mass estimate in the cluster outskirts. Similar to the pressure profiles, we further observe that the overall cluster mass profile appears to reflect the pressure of the eastern cluster side. The inconsistency observed between eastern and western profiles show us that the shock heating of the cluster ICM induced by the accretion may have transiently taken gas away from hydrostatic equilibrium in this region. For this reason, the cluster mass estimates assuming hydrostatic equilibrium in this region and hence in the overall cluster are likely to be overestimated. Assuming hydrostatic equilibrium in the western cluster side might instead provide with us an estimate of the cluster mass before the on-going merger event, $M_{500,HE,West} = 14.5^{+0.6}_{-0.3}$, while the sub-cluster accretion might have raised the total cluster mass up to the value provided by the Y_X proxy: $M_{500,Y_X} = 18.7^{+2.0}_{-2.4}$.

5 Discussion and conclusions

From evidence of a stripped cool core crossing the main cluster atmosphere separately from a nearby galaxy overdensity, we infer that A2163 might have recently accreted a sub-cluster along its East-West elongation. We suggest that this merger event has shocked the main-cluster atmosphere, and adiabatically compressed the ICM behind the crossing cool core. This indication of shock heating and the evidence of a galaxy-gas separation lead us to infer that the sub-cluster has been accreted to a supersonic velocity. Shock heating may further have transiently pulled cluster gas away from hydrostatic equilibrium, leading to large uncertainties on the cluster mass estimate from X-ray analysis. Assuming the Y_X proxy to indicate the mass of the overall system A2163 and the western cluster sector to represent the ICM in hydrostatic equilibrium before sub-cluster accretion, we may infer a merger scenario between two sub-units of mass-ratio 1:4, leading to the present system with mass $M_{500,Y_X} \simeq 1.9 \times 10^{15} M_\odot$.

A fast sub-cluster accretion with evidence of galaxy-gas separation was first seen in 1E 0657-56, the so-called ‘bullet cluster’ [15]. It is interesting to note that both 1E 0657-56 and A2163 are exceptionally massive, favouring ram pressure stripping of the gas content of an incoming sub-cluster due both to the high density of these accreting cluster atmospheres, and by exceptionally high collision velocities assuming free fall encounters. It is thus likely that the comparable mass of A2163 and 1E 0657-56 has favoured similar merger scenarios. Moreover, both 1E 0657-56 and A2163 exhibit similar global properties such as exceptionally high luminosity and gas temperature (about 15 and 12 keV for 1E0657-56 and A2163, respectively), and powerful emission from an extended radio halo. These common properties are likely point to the recent dissipation of a large amount of kinetic energy through shock heating and turbulence.

As extensively studied in the textbook case of the ‘bullet cluster’, observing a high-velocity sub-cluster accretion within a massive cluster may provide interesting constraints on ICM physics, galaxy evolution, and dark matter properties. Better constraints on the dynamics of the exceptional merger event in A2163 would thus be obtained from deeper X-ray or SZ observations, and high resolution weak lensing analyses.

1. M. P. Kowalski et al., 1984. *ApJS*, 56:403.
2. M. Arnaud et al., 1992. *ApJ*, 390:345.
3. D. Elbaz et al., 1995. *A&A*, 293:337.
4. M. Markevitch et al., 1994. *ApJ*, 436:L71.
5. M. Markevitch & A. Vikhlinin, 2001. *ApJ*, 563:95.
6. F. Govoni et al., 2004. *ApJ*, 605:695.
7. M. S. Owers et al., 2009. *ApJ*, 704:1349.
8. G. Squires et al., 1997. *ApJ*, 482:648.
9. M. Radovich et al., 2008. *A&A*, 487:55.
10. S. Maurogordato et al., 2008. *A&A*, 481:593.
11. L. Feretti et al., 2001. *A&A*, 373:106.
12. L. Feretti et al., 2004. *A&A*, 423:111.
13. Y. Rephaeli et al., 2006. *ApJ*, 649:673.
14. E. T. Million & S. W. Allen, 2009. *MNRAS*, 399:1307.
15. M. Markevitch et al., 2002. *ApJ*, 567:L27.
16. A. V. Kravtsov et al., 2006. *ApJ*, 650:128.

3. Dark Matter

DARK MATTER CONSTRAINTS WITH THE FIRST YEAR OF FERMI-LAT DATA

T. YLINEN^{†,a} and E. NUSS[‡],
on behalf of the Fermi-LAT Collaboration

[†]*Department of Physics, Royal Institute of Technology, AlbaNova University Center, SE-106 91 Stockholm, Sweden - School of Pure and Applied Natural Sciences, University of Kalmar, SE-391 82 Kalmar, Sweden - The Oskar Klein Centre for Cosmoparticle Physics, AlbaNova University Center, SE-106 91 Stockholm, Sweden*

[‡]*Laboratoire de Physique Théorique et Astroparticules, Université Montpellier 2, CNRS/IN2P3, Montpellier, France*

Our understanding of the Universe today includes overwhelming observational evidence for the existence of an elusive form of matter that is generally referred to as dark. Although many theories have been developed to describe its nature, very little is actually known about its properties. The launch of the Fermi Gamma-ray Space Telescope in 2008 opened a new window for the indirect experimental search for dark matter through high-energy gamma-rays. The principal instrument onboard, the Large Area Telescope (LAT), is designed to measure gamma-rays with energies ranging from 20 MeV to more than 300 GeV. The first year of *Fermi*-LAT data has allowed for a large variety of dark matter searches and we present here a review of the results from the different analyses.

1 Introduction

The existence of dark matter (DM) was first proposed already in 1933 by Zwicky¹, after studying the radial velocities of eight galaxies in the Coma galaxy cluster. The observed velocity dispersion was unexpectedly large, which suggested additional matter that was non-luminous (so-called “dark” hereafter). A large variety of observations supporting the existence of such matter have been performed since then and relate to the Big Bang Nucleosynthesis (BBN)², gravitational lensing³ and the cosmic microwave background (CMB)⁴. The most visual evidence of DM to date comes from the merging galaxy cluster 1E 0657-558 (“Bullet Cluster”), where a clear separation of the mass (determined from gravitational lensing) and the X-ray emitting plasma can be seen⁵.

Combined, these observations have constrained the fractions of the energy density in the Universe in the form of matter and in the form of a cosmological constant to $\Omega_M \sim 0.3$ and $\Omega_\Lambda \sim 0.7$, respectively, with ordinary baryonic matter only constituting about $\Omega_B \sim 0.05$ ⁶. Non-baryonic matter therefore seems to be the dominating form of matter in the Universe.

A favored model of the Universe that is in reasonable agreement with observations is the so-called Λ CDM model, which features long-lived and collisionless Cold Dark Matter (CDM) and a contribution from a cosmological constant (Λ).

^aSpeaker

A potential candidate for the CDM, that naturally provides the correct present-day relic abundance of DM, are Weakly Interacting Massive Particles (WIMPs). These are thought to annihilate or decay into Standard Model particles and one of the possible resulting particles are gamma-rays. These gamma-rays can be categorized into continuum signals and spectral line signals, which are produced mainly through the decay of neutral pions created in the hadronization of e.g. quark-antiquark final states and via loop-suppressed channels directly into monochromatic gamma-rays, respectively.

Continuum signals represent excesses in the overall energy spectrum that can not be accounted for by the existing components, which include the diffuse galactic emission, the isotropic diffuse emission and point sources. This type of search is limited by the precision to which the existing components can be described.

Many viable DM candidates can also give rise to spectral lines via annihilation or decay channels directly into monochromatic gamma-rays. The final state then constitutes one gamma-ray and some other particle X with a mass of M_X , which can e.g. be another gamma-ray, a Z-boson, a Higgs boson, a neutrino or a non-Standard Model particle. The photon energy E_γ , produced in a non-relativistic annihilation process, is then given by the equation $E_\gamma = M_\chi (1 - M_X^2/4M_\chi^2)$, where M_χ is the mass of the DM particle. The corresponding equation for decays is provided by the substitution $M_\chi \rightarrow M_\chi/2$.

An observation of a spectral line would be a “smoking-gun” for DM, since no other astrophysical process should be able to produce it. However, many models also predict either low branching fractions or low cross-sections for those channels, which means that a halo with a large central concentration, the existence of substructure that boosts the signal or the Sommerfeld enhancement⁷ might be needed to be able to observe the signal.

The distribution of DM on galactic and sub-galactic scales is currently still a matter of debate but plays an important role in the detection of DM signals. A phenomenological halo density profile is generally used to describe most of the observed rotation curves of galaxies and it is based on N-body simulations. This smooth and spherically symmetric profile is given by Eq. 1,

$$\rho(r) = \frac{\delta_c \rho_c}{(r/r_s)^\gamma [1 + (r/r_s)^\alpha]^{(\beta-\gamma)/\alpha}}, \quad (1)$$

where r is the angular radius from the galactic center, r_s is a scale radius, δ_c is a characteristic dimensionless density, and $\rho_c = 3H^2/8\pi G$ is the critical density for closure. A variety of halo profiles following this equation exist and differ in the values of the (α, β, γ) parameters. Two examples of profiles that are commonly used are the Navarro, Frenk and White (NFW) model with $(1, 3, 1)$ ⁸ and the isothermal profile with $(2, 2, 0)$ ⁹. Another halo profile, which is observationally favored, is the Einasto profile^{10,11}. The Einasto profile takes the form as given in Eq. 2,

$$\rho_{\text{Einasto}}(r) = \rho_s e^{-(2/a)[(r/r_s)^a - 1]}, \quad (2)$$

where ρ_s is the core density and a is a shape parameter.

For a specified halo profile, the total energy-dependent flux of gamma-rays from annihilating DM is the sum of the fluxes from the different final states of branching fraction B_f and depends on the mass of the DM particle, the velocity-averaged cross-section $\langle \sigma v \rangle$, the solid angle Ω of the observed region-of-interest and the integral of the square of the halo profile over the line-of-sight according to Eq. 3.

$$\frac{d\Phi}{dE_\gamma}(E_\gamma, \phi, \theta) = \frac{1}{4\pi} \frac{\langle \sigma v \rangle}{2M_\chi^2} \sum_f \frac{dN_\gamma^f}{dE_\gamma} B_f \times \int_{\Delta\Omega(\phi, \theta)} d\Omega' \int_{\text{LoS}} \rho^2(\vec{r}(l, \phi', \theta')) dl \quad (3)$$

In the extragalactic case, the flux is the integrated flux from all redshifts. The equation above therefore also depends on the optical depth, which governs the absorption, an assumed model for the enhancement of the annihilation signal due to substructure and the parametrization of the energy content in the Universe.

2 Fermi Large Area Telescope

The Fermi Gamma-ray Space Telescope (also called *Fermi*), was successfully launched on a Delta II heavy launch vehicle from Cape Canaveral in Florida, USA, on June 11, 2008. The satellite was formerly known as the Gamma-ray Large Area Space Telescope (GLAST) but was renamed after its launch. The satellite orbits the Earth at an altitude of about 565 km and with an inclination angle of about 25.6° . One orbit takes about 90 minutes and full-sky coverage is reached in only two orbits. The satellite consists of two detector systems, the Large Area Telescope (LAT) and the Gamma-ray Burst Monitor (GBM).

The LAT covers the approximate energy range from 20 MeV to more than 300 GeV. The instrument is a pair-conversion telescope, designed to measure the electromagnetic showers of incident gamma-rays over a wide field-of-view while rejecting incident charged particles with an efficiency of 1 to 10^6 . It consists of a 4×4 array of 16 identical modules on a low-mass structure. Each of the modules has a gamma-ray converter tracker for determining the direction of the incoming gamma-ray and a calorimeter for measuring its energy. The tracker array is surrounded by a segmented anti-coincidence detector. In addition, the whole LAT is shielded by a thermal-blanket micro-meteoroid shield.

The performance and sensitivity of the LAT are unprecedented. The field of view is ~ 2.4 sr (at 1 GeV), the effective area > 1 GeV is ~ 8000 cm 2 on-axis and the energy resolution is $< 15\%$ at energies > 100 MeV.

3 Dark matter searches

The *Fermi*-LAT instrument allows for a large variety of searches for dark matter in the gamma-ray region. The sensitivity of such searches, however, depends on the spatial region selected for the search. Any region has its advantages and disadvantages. Although the galactic center region has fairly large photon statistics, it is affected by source confusion and a strong diffuse photon background. Alternative locations, which may give a better signal-to-noise ratio include for example dark matter satellites (substructures containing only dark matter), dwarf spheroidal galaxies (substructures with optical counterparts but with high mass-to-light ratios) and galaxy clusters at high galactic latitudes, where the photon background is lower and the source identification is better. The extragalactic background has large photon statistics, but is limited by astrophysical uncertainties.

We present here the results from all dark matter searches performed by the *Fermi*-LAT Collaboration after one year of observations.

3.1 Clusters of galaxies

Clusters of galaxies are a distant source type but they are dark matter dominated and typically at high galactic latitudes, which make them ideal targets for DM searches.

In this analysis, six clusters were selected from the HIghest X-ray FLUX Galaxy Cluster Sample (HIGFLUGCS) catalog and an unbinned likelihood fit with both spatial and spectral models was performed. No significant gamma-ray emission was, however, detected from the selected clusters for 11 months of data¹². Assuming an NFW profile, the upper limits at 95%

confidence level, shown in Fig. 1, begin to constrain the allowed phase space, especially for models where the results from the PAMELA experiment are interpreted in terms of DM annihilations.

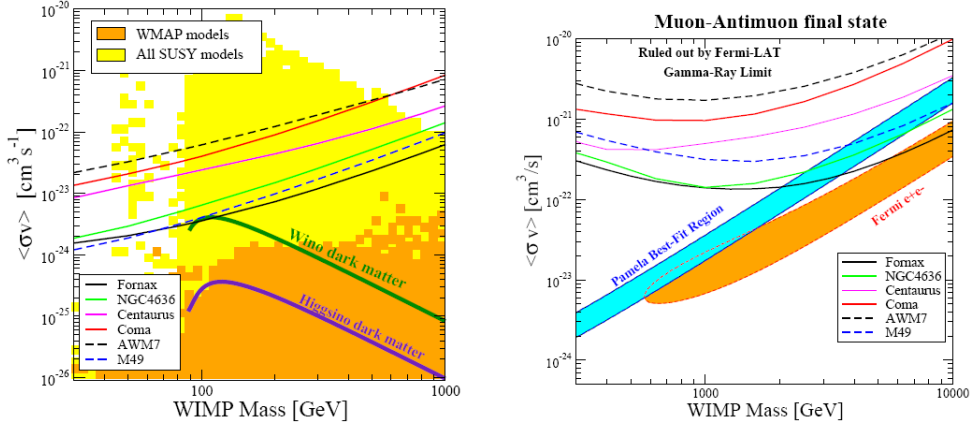


Figure 1: Upper limits at 95% confidence level for cluster of galaxies and for assumed $b\bar{b}$ (*left*) and $\mu^+\mu^-$ final states (*right*)¹².

3.2 Cosmological dark matter

The search for cosmological DM includes the contribution from DM from all halos at all redshifts. The search is based on the measured isotropic diffuse gamma-ray background emission¹³ and a number of cases have been considered. These include 4 annihilation clustering enhancement models, 3 particle physics models for dark matter, 2 absorption models and 2 upper limit calculations (conservative and stringent). For more details, see¹⁴. As can be seen in Fig. 2, the upper limits can be very constraining for some cases. However, there are large uncertainties in the modeling of the evolution of DM structure and substructure as well as in the estimation of the isotropic background, which make the interpretation more challenging.

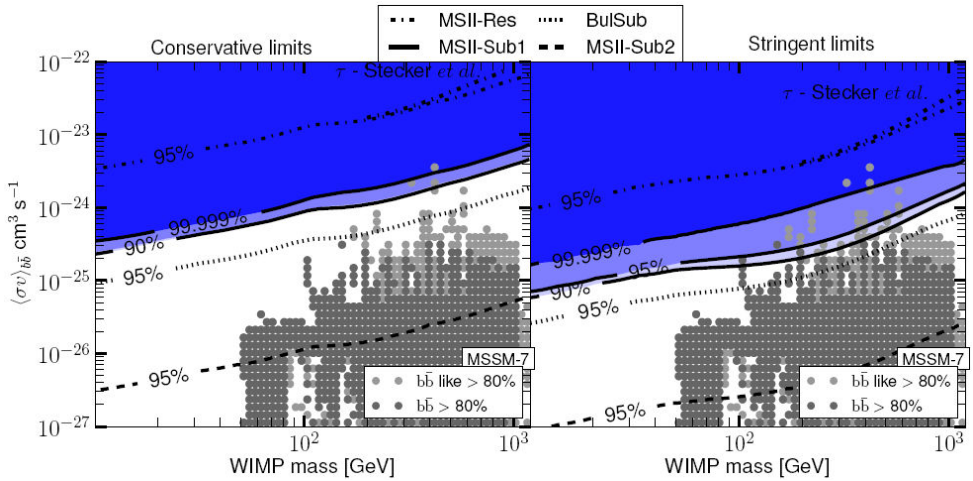


Figure 2: Upper limits for cosmological dark matter for an assumed $b\bar{b}$ final state in the conservative (*left*) and stringent (*right*) case¹⁴.

3.3 Galactic center

The galactic center (GC) coincides with the cusped part of the theorized DM halo density profile, which is expected to be the strongest source of gamma-rays from DM annihilations.

The literature devoted to the possible signatures from DM in the gamma-ray region at the GC is extensive. The vicinity of the GC, however, also constitutes the most violent and active region of our galaxy and harbors numerous objects capable of accelerating cosmic rays to very high energies. The resulting gamma-rays are produced by inverse Compton scattering of electrons or pion decays following from e.g. proton-proton interactions.

A bright and very high energy gamma-ray point source has been observed by several other experiments and it is now widely considered to be a standard astrophysical source associated either with the bright compact radio source Sgr A* or with the candidate pulsar wind nebula G359.95-0.04¹⁵. This source is a formidable background for DM studies in this region.

In Fig. 3, a preliminary fit from the ongoing analysis of the GC region is shown¹⁶. The observed region is composed of the square $7^\circ \times 7^\circ$ around the GC and the modeled components include the galactic diffuse emission, based on GALPROP, the isotropic diffuse emission and point sources from the first *Fermi*-LAT catalog. As can be seen in the figure, the model mostly reproduces the data within the uncertainties, but a residual gamma-ray emission is left, not accounted for by the above model. However, the disentanglement of a potential DM signal requires a detailed understanding of the conventional astrophysics.

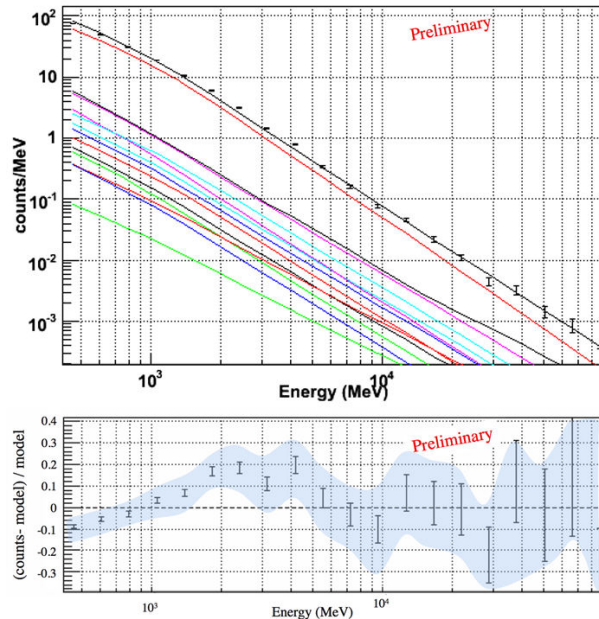


Figure 3: A preliminary fit (top) and residuals (bottom) to the gamma-rays from the galactic center region¹⁶.

3.4 Dark matter subhalos

DM subhalos can be categorized into DM satellites and optically observed dwarf spheroidal galaxies. The former represent substructures that contain only DM. These may then shine in radiation from DM annihilations/decays. The analysis is at the time of writing still ongoing. However, preliminary results on 10 months of *Fermi*-LAT data include no detection of such structures.

The second category refer to low luminosity optically observed galaxies that are companions to a larger host galaxy. They are characterized by high mass-to-light ratios in the range 10-1000, which makes them dark matter dominated. Many of them are also nearby.

In the analysis, 14 dwarf spheroidal galaxies were selected, based on their proximity, galactic latitude and dark content as inferred from recent stellar velocity measurements¹⁷. A binned profile likelihood search on 11 months of *Fermi*-LAT data, assuming an NFW halo profile, was

then performed. No gamma-ray excesses were, however, observed and 8 limits with DM densities inferred from stellar data were derived. As is shown in Fig. 4, the upper limits at 95% confidence level are beginning to constrain the mSUGRA, MSSM and AMSB parameter spaces.

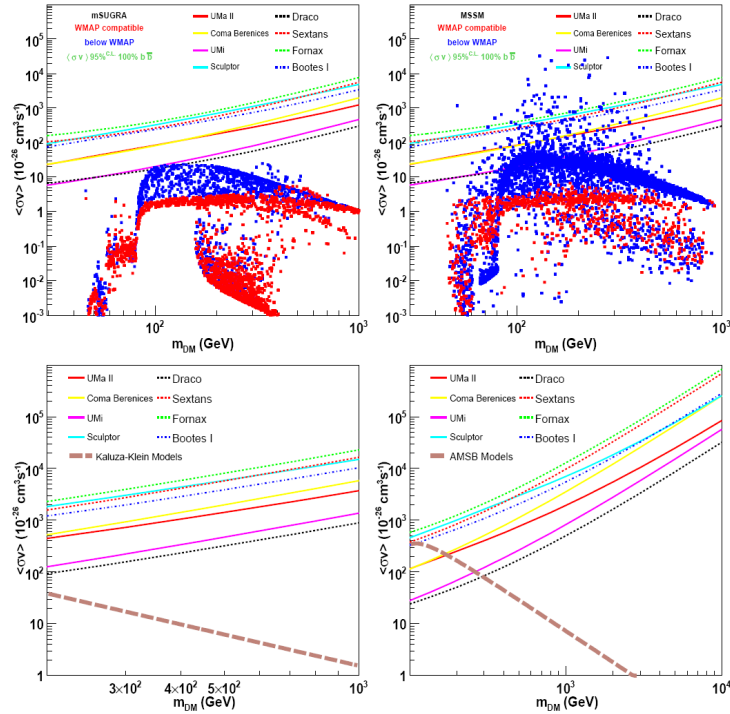


Figure 4: Upper limits at 95% confidence level as compared to mSUGRA, MSSM, Kaluza-Klein and AMSB parameter spaces using data from dwarf spheroidal galaxies with the *Fermi*-LAT¹⁷.

A dedicated analysis on a specific dwarf spheroidal galaxy, Segue 1, has also been performed¹⁸. The analysis combines a binned likelihood analysis with CMSSM parameter scans via **DarkSUSY** using a nested sampling algorithm. However, the disfavoured models are already strongly disfavoured by relic density constraints.

3.5 Spectral lines

The search for spectral lines from dark matter consists of an unbinned fit to the data using the profile likelihood technique and can be used for both detection and upper limits. The likelihood model is constructed within the **RooFit** framework and requires an accurate modeling of the energy dispersion of the detector. These are determined from full detector simulations at specified energies and interpolations at intermediate energies. The data selection used for the spectral line search differs from standard analyses, since additional cuts with respect to the public data event class have been performed in order to reduce the charged particle contamination. In addition, the profile energy has been used instead of the standard energy.

The region-of-interest, chosen for this search, is defined by the sum of the regions $|b| > 10^\circ$ and a square of $20^\circ \times 20^\circ$ around the galactic center. Point sources inherent in a preliminary point source catalog, corresponding to 11 months of *Fermi*-LAT data, were masked.

The search did not result in a detection and upper limits on the velocity-averaged cross-section and the decay lifetime at 95% confidence levels were calculated¹⁹ as is shown in Fig. 5. These are still about a factor of 10 from the allowed MSSM and mSUGRA parameter spaces. However, the results disfavor, by a factor of 2–5, a model where the wino is the lightest supersymmetric particle²⁰. At 170 GeV, the model predicts $\langle\sigma v\rangle_{\gamma Z} = 1.4 \times 10^{-26} \text{ cm}^3 \text{ s}^{-1}$.

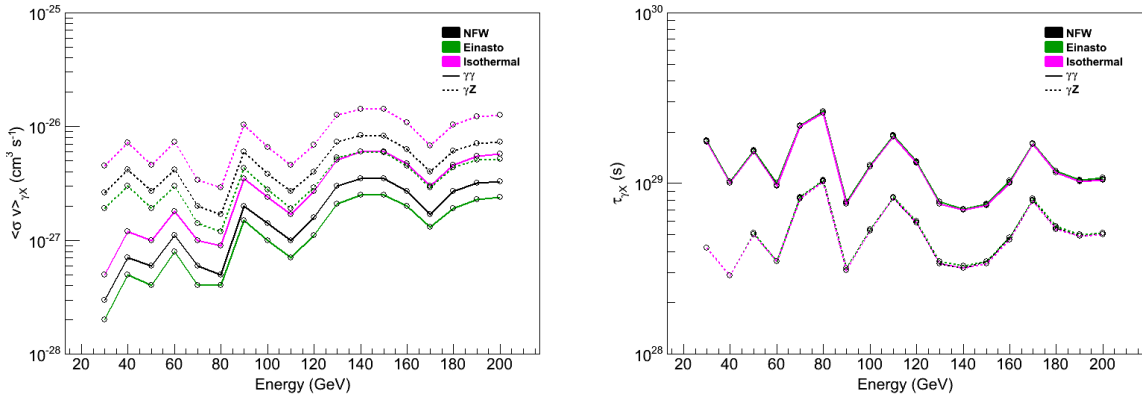


Figure 5: Upper limits at 95% confidence level on the cross-section (*left*) and the decay lifetime (*right*).

3.6 Electrons and positrons

The *Fermi*-LAT instrument can also be used to measure electrons and positrons, but the lack of a magnet prohibits the separation of the two. This kind of study is most relevant for cosmic-ray propagation models and the investigation of possible nearby sources, but a rejection power of 10^3 – 10^4 for protons is required. This is achieved via a separate series of trigger settings and cuts on detector variables.

The preliminary spectrum from combining a low-energy and high-energy analysis is shown in Fig. 6 in addition to an intermediate step in the analysis that shows the separation of electrons from hadrons for data and simulation²¹. The results indicate that any reasonable model (e.g. GALPROP), where a simple continuous distribution of sources is assumed, is not compatible with the measured spectrum.

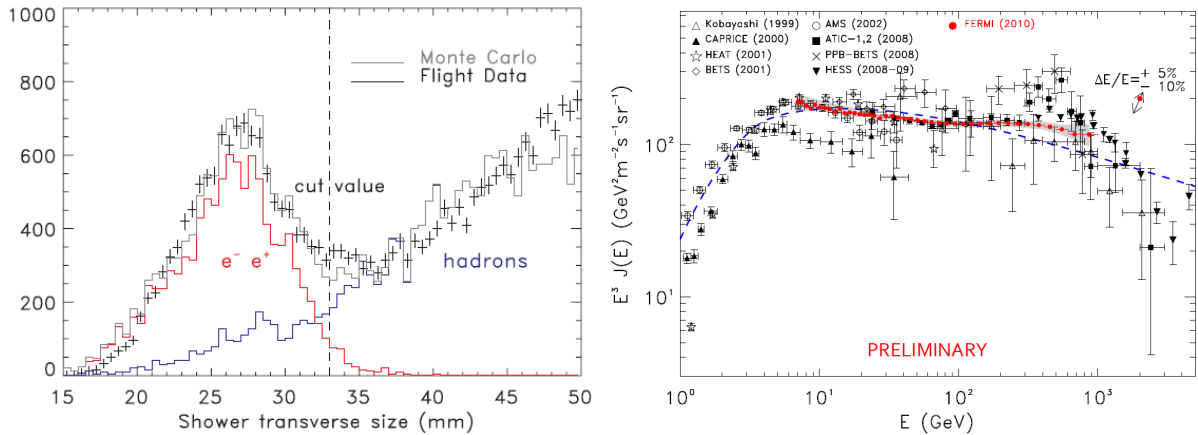


Figure 6: An intermediate step in the analysis chain (*left*) and preliminary electron-positron spectrum (*right*).

Many possible interpretations of the shape of the measured spectrum, in combination with the results from other experiments and measurements, have been suggested. These include e.g. nearby pulsars, source stochasticity and a revision of our understanding of cosmic-ray acceleration^{22,23}. Although a DM contribution is not required to explain the measurements, it cannot be ruled out at this point either.

4 Summary and conclusions

Fermi Gamma-ray Space Telescope has opened a new era in DM searches and a large variety of analyses have been developed for clusters of galaxies, DM subhalos, cosmological DM and spectral lines. No significant detections have been made, but constraints that start to probe the available phase space have been put on the annihilation cross-section and decay lifetimes. In addition, several ongoing analyses are now being finalized, including studies of DM satellites and the complicated galactic center region. The *Fermi* mission is expected to continue for 5-10 years and the future therefore promises a plethora of interesting results.

Acknowledgments

The *Fermi*-LAT Collaboration acknowledges generous ongoing support from a number of agencies and institutes that have supported both the development and the operation of the LAT as well as scientific data analysis. These include the National Aeronautics and Space Administration and the Department of Energy in the United States, the Commissariat à l'Energie Atomique and the Centre National de la Recherche Scientifique / Institut National de Physique Nucléaire et de Physique des Particules in France, the Agenzia Spaziale Italiana and the Istituto Nazionale di Fisica Nucleare in Italy, the Ministry of Education, Culture, Sports, Science and Technology (MEXT), High Energy Accelerator Research Organization (KEK) and Japan Aerospace Exploration Agency (JAXA) in Japan, and the K. A. Wallenberg Foundation, the Swedish Research Council and the Swedish National Space Board in Sweden. Additional support for science analysis during the operations phase is gratefully acknowledged from the Istituto Nazionale di Astrofisica in Italy and the Centre National d'Études Spatiales in France.

References

1. F. Zwicky, *Helvetica Physica Acta* **6**, 110 (1933).
2. S. Sarkar, *Rep. Prog. Phys.* **59**, 1493 (1996).
3. J.A. Tyson, G.P. Kochanski & I.P. Dell'Antonio, *Astrophysical J.* **498**, L107 (1998).
4. D.N. Spergel, et al., *Astrophysical J. Suppl.* **170**, 377 (2007).
5. D. Clowe, et al., *Astrophysical J.* **648**, L109 ((2006)).
6. P. Ullio, et al., *Phys. Rev. D* **66**, 12 (2002).
7. M. Lattanzi & J. Silk, *Phys. Rev. D* **79**, 083523 (2009).
8. J.F. Navarro, C.S. Frenk & S.D. White, *Astrophysical J.* **490**, 493 (1997).
9. J.N. Bahcall & R.M. Soneira, *Astrophysical J. Suppl.* **44**, 1980 (73).
10. J. Einasto, *Trudy Instituta Astrofiziki Alma-Ata* **5**, 87 (1965).
11. D. Merritt, et al., *Astrophysical J.* **132**, 2685 (2006).
12. A.A. Abdo, et al. (*Fermi*-LAT Collaboration), [arXiv:astro-ph/1002.2239] (2010).
13. A.A. Abdo, et al., (*Fermi*-LAT Collaboration), *Phys. Rev. Lett.* **104**, 101101 (2010).
14. A.A. Abdo, et al. (*Fermi*-LAT Collaboration), *J. Cosm. Astropart. Phys.* **04**, 014 (2010).
15. C. van Eldik, et al., (H.E.S.S. Collaboration), [arXiv:astro-ph/0709.3729] (2007).
16. V. Vitale & A. Morselli, (*Fermi*-LAT Collaboration), [arXiv:astro-ph/0912.3828] (2009).
17. A.A. Abdo, et al. (*Fermi*-LAT Collaboration), *Astrophysical J.* **712**, 147 (2010).
18. P. Scott, et al., *J. Cosm. Astropart. Phys.* **01**, 031 (2010).
19. A.A. Abdo, et al. (*Fermi*-LAT Collaboration), *Phys. Rev. Lett.* **104**, 091302 (2010).
20. G. Kane, R. Lu, & S. Watson, *Phys. Lett. B* **681**, 151 (2009).
21. A.A. Abdo, et al. (*Fermi*-LAT Collaboration), *Phys. Rev. Lett.* **102**, 181101 (2009).
22. D. Grasso, et al., *Astropart. Phys.* **32**, 140 (2009).
23. P. Blasi, *Phys. Rev. Lett.* **103**, 051104 (2009).

EXCITED DARK MATTER VERSUS PAMELA/FERMI

J.M. CLINE

CERN Theory Division, CERN, Case C01600, CH-1211 Genève, Switzerland

and

McGill University, Department of Physics, 3600 University St., Montréal, Qc H3A2T8, Canada



Excitation of multicomponent dark matter in the galactic center has been proposed as the source of low-energy positrons that produce the excess 511 keV γ rays that have been observed by INTEGRAL. Such models have also been promoted to explain excess high-energy e^\pm observed by the PAMELA, Fermi/LAT and H.E.S.S. experiments. We investigate whether one model can simultaneously fit all three anomalies, in addition to further constraints from inverse Compton scattering by the high-energy leptons. We find models that fit both the 511 keV and PAMELA excesses at dark matter masses $M < 400$ GeV, but not the Fermi lepton excess. The conflict arises because a more cuspy DM halo profile is needed to match the observed 511 keV signal than is compatible with inverse Compton constraints at larger DM masses.

1 Galactic cosmic ray anomalies and DM collisions

There are several hints of unexplained sources of electrons and positrons in our galaxy, which could be due to collisions of dark matter (DM). The longest-standing one is the excess of 511 keV γ rays from the galactic center, first seen by balloon-borne detectors in the 1970's, and most recently measured by the SPI spectrometer aboard the INTEGRAL satellite (for a review, see ref.¹). More recently, a number of experiments have found evidence for e^\pm at higher energies, in excess of those understood to be coming from known sources. Among these, PAMELA² reports an excess in the positron fraction at energies of 10 – 100 GeV, while the Fermi Large Area Telescope (LAT)³ and H.E.S.S.⁴ observe an excess of $e^+ + e^-$ in the 100 – 1000 GeV energy range.

Although many different astrophysical explanations have been proposed as the source of the low-energy positrons that produce the 511 keV signal, there is no consensus.^a Pulsars have

^afor example, the argument of ref.⁵ that low-mass x-ray binaries are most likely source has been criticized in ref.⁶.

been proposed as a likely source of the PAMELA and Fermi leptons (see for example refs. ^{7,8}) but the uncertainties in the parameters characterizing such sources still leave room for other interpretations.

Although DM annihilations had previously been suggested as the source of some of these anomalies, ref. ⁹ was the first to point out a class of DM models that could potentially explain all of them (and a few others: the WMAP haze and the DAMA/LIBRA annual modulation). Namely, these are models where the DM has a mass M near the TeV scale, and has several components that acquire naturally small mass splittings $\delta M \lesssim 1$ MeV from radiative corrections. A new hidden sector Higgs or gauge boson with mass $\mu \lesssim 1$ GeV mediates annihilations of the DM into e^\pm but not antiprotons (since $\mu < 2m_p$), of which no excess has been observed by PAMELA. All of this can be economically achieved by assuming the hidden sector gauge symmetry is nonabelian and spontaneously breaks near the GeV scale. Then the mediator is one of the gauge bosons B_μ , which can mix with the standard model hypercharge Y_μ through the dimension-5 gauge kinetic mixing operator $\Lambda^{-1} \Delta^a B_{\mu\nu}^a Y^{\mu\nu}$, where Δ^a is a hidden sector Higgs field in the adjoint representation that gets a VEV. Some of the simplest examples involving SU(2) gauge symmetry were considered by us in ref. ^{10,11}.

2 Exciting Dark Matter in the Galactic Center

The excited DM mechanism (XDM) for explaining the 511 keV excess was first proposed in ref. ¹³. The ground state DM particles undergo inelastic scattering to the excited state by $\chi_1\chi_1 \rightarrow \chi_2\chi_2$, followed by decays $\chi_2 \rightarrow \chi_1 e^+ e^-$ into nonrelativistic e^\pm . However a quantitative computation of the excitation cross section was not used there, and ref. ¹⁴ argued that the rate of excitation was too small to account for the observations unless many partial waves were at their maximum values allowed by unitarity.

In refs. ^{10,12} we numerically computed the excitation cross section by solving the Schrödinger equation, and showed that indeed the suspicion of ref. ¹⁴ was correct, the rate of e^+ production is too small, even varying all the model parameters and DM halo properties over a wide range.

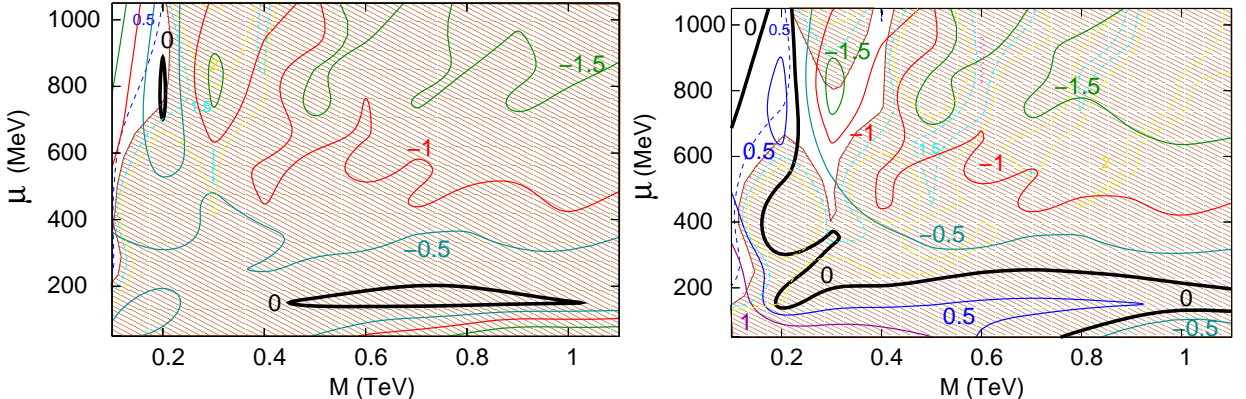


Figure 2: Left: contours of the rate of positron production, $\log(R_{e^+}/R_{\text{obs}})$ (for INTEGRAL 511 keV γ rays) in plane of gauge boson mass μ versus DM mass M for $\delta M_{23} = 100$ keV mass splitting and halo Einasto profile parameters $\alpha = 0.17$, $r_s = 15$ kpc, $\rho_\odot = 0.4$ GeV/cm³, $v_0 = 250$ km/s.¹⁸ Heavy contours match the observed rate. Dashed curves are contours of inverse Compton (IC) signal over IC bound. Shaded regions are excluded by IC constraint. Right: same, but with $\delta M_{23} = 25$ keV, $\alpha = 0.20$, $r_s = 15$ kpc, $\rho_\odot = 0.3$ GeV/cm³, $v_0 = 220$ km/s.

At the same time, we proposed a solution, involving the existence of a stable excited state that undergoes scattering $\chi_2\chi_2 \rightarrow \chi_3\chi_3$, followed by the decay $\chi_3 \rightarrow \chi_1 e^+ e^-$. This can have a smaller mass gap $\delta M_{23} \sim 100$ keV which is easier to excite in DM collisions than the larger one $\delta M_{13} > 2m_e$. This “inverted mass hierarchy” is shown in figure 1.

Figure 2 (left panel) shows an example of our new contours for the rate of positron production compared to the observed rate in the $M-\mu$ plane,¹⁸ using the mass splitting $\delta M_{23} = 100$ keV, and the gauge coupling $\alpha_g = 0.031$ (M/TeV) required for getting the right relic density.¹¹ The DM density profile is taken to be of the Einasto form,

$$\rho = \rho_\odot \exp \left[-\frac{2}{\alpha} \left(\left(\frac{r}{r_s} \right)^\alpha - \left(\frac{r_\odot}{r_s} \right)^\alpha \right) \right] \quad (1)$$

with $\rho_\odot = 0.4$ GeV/cm³, $r_\odot = 8.3$ kpc, $\alpha = 0.17$, $r_s = 15$ kpc, consistent with best-fit values of N -body simulations,¹⁷ and a high value of the circular velocity $v_0 = 250$ km/s. In this example, the heavy contours show that there exist parameters leading to a large enough rate, but these tend to disappear rapidly if one increases the values of δM_{23} (since the χ_2 states do not have enough kinetic energy to produce χ_3), or α or r_s (since then ρ becomes too small in the central region of the galaxy, reducing the rate). This can be compensated by decreasing δM on the other hand, as illustrated in the right panel of fig. 2. The shaded regions are ruled out by constraints on inverse Compton gamma rays,¹⁶ as we discuss in the next section. Fig. 3 shows that the more cuspy DM profile with $\alpha = 0.17$ gives a better fit to the angular distribution of the 511 keV signal.

3 High energy e^\pm from annihilations

Although in refs.^{10,11} we showed that the XDM mechanism with inverted mass hierarchy can work for the 511 keV signal, we did not consider whether it could also be compatible with the PAMELA and Fermi lepton excesses. The same model can also explain the high energy leptons through annihilation to hidden sector gauge bosons, $\chi_1\chi_1 \rightarrow BB$, followed by the decays $B \rightarrow e^+ e^-$.¹⁵ However, this scenario has come under increasing pressure from various constraints, the most stringent being due to inverse Compton scattering of e^\pm on starlight in the galaxy, which should produce γ rays with energies up to several hundred GeV. Demanding that this new source not exceed recent observations excludes the annihilating DM interpretation of Fermi leptons unless the galactic DM density profile is less cuspy near the center¹⁶ than is generally expected on the basis of N -body simulations of halo evolution.¹⁷ This limit requires taking small values of $\delta M \lesssim 100$ keV in order to get a large enough rate for 511 keV γ rays, as illustrated in fig. 2.

The ability of the models to explain the high-energy lepton observations while respecting the IC constraints are summarized in figure 4 taken from ref.¹⁹. The left figure is an example using a cuspy halo profile compatible with the PAMELA and 511 keV excesses, at $M < 400$ GeV, while the right one shows the result of a noncuspy profile where the PAMELA and Fermi excesses can be marginally explained, but not the 511 keV.

4 Conclusions

We have found that annihilating multistate DM can explain two out of three galactic cosmic ray anomalies, either PAMELA/Fermi or PAMELA/INTEGRAL, but not all three simultaneously.

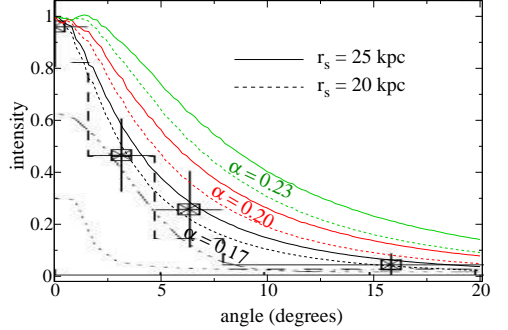


Figure 3: Observed angular distribution of INTEGRAL 511 keV signal, and theoretical predictions for different Einasto parameter values $\alpha = 0.17, 0.20, 0.23$, $r_s = 20, 25$ kpc.

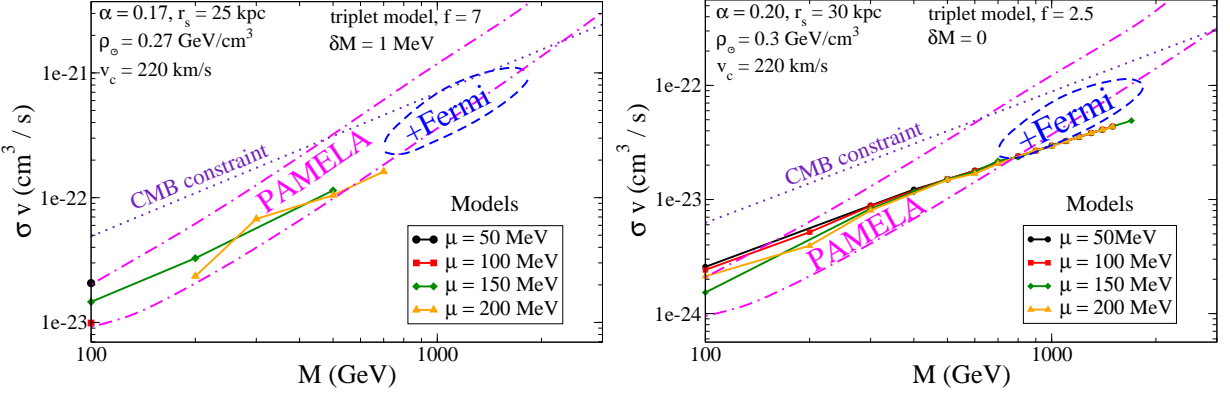


Figure 4: Allowed regions for PAMELA and Fermi lepton excess in σv - M plane,¹⁹ and predictions of multistate DM annihilation that are compatible with inverse Compton constraint. Left: for Einasto parameters $\alpha = 0.17$, $r_s = 25$ kpc, $\rho_\odot = 0.28$ GeV/cm 3 ; Right: for $\alpha = 0.20$, $r_s = 30$ kpc, $\rho_\odot = 0.3$ GeV/cm 3 . $1/f$ is fraction of total DM mass density occupied by annihilating DM ground state χ_1 .

Although it is possible to marginally predict all the correct rates using Einasto profile parameter $\alpha = 0.20$, the angular distribution of 511 keV γ rays is too wide in this case. Of the two possibilities, the PAMELA/INTEGRAL combination seems preferable from the standpoint of the required DM halo parameters, since in this case we are able to adopt standard values that are quite compatible with N -body simulations of galactic structure evolution. Moreover we can match the anomalous lepton rates well for PAMELA/INTEGRAL. The PAMELA/Fermi possibility requires stretching the halo parameters to their maximal values, while only marginally giving a large enough rate of leptons, yet a small enough rate of associated inverse Compton γ rays.

References

1. R. Diehl and M. Leising, arXiv:0906.1503.
2. O. Adriani *et al.* [PAMELA Collaboration], Nature **458**, 607 (2009) [arXiv:0810.4995].
3. A. A. Abdo *et al.* [Fermi LAT Collaboration], Phys. Rev. Lett. **102**, 181101 (2009) [arXiv:0905.0025].
4. F. Aharonian *et al.* [H.E.S.S. Collaboration], [arXiv:0905.0105].
5. G. Weidenspointner *et al.*, Nature **451**, 159 (2008).
6. R. M. Bandyopadhyay, J. Silk, J. E. Taylor and T. J. Maccarone, [arXiv:0810.3674].
7. D. Hooper, P. Blasi and P. D. Serpico, JCAP **0901**, 025 (2009) [arXiv:0810.1527].
8. D. Grasso for the Fermi-LAT collaboration, arXiv:0907.0373.
9. N. Arkani-Hamed, *et al.*, Phys. Rev. D **79**, 015014 (2009) [arXiv:0810.0713].
10. F. Chen, J. M. Cline and A. R. Frey, Phys. Rev. D **79**, 063530 (2009) [arXiv:0901.4327].
11. F. Chen, J. M. Cline and A. R. Frey, Phys. Rev. D **80**, 083516 (2009) [arXiv:0907.4746].
12. F. Chen, J. M. Cline, A. Fradette, A. R. Frey and C. Rabideau, Phys. Rev. D **81**, 043523 (2010) [arXiv:0911.2222].
13. D. P. Finkbeiner and N. Weiner, [arXiv:astro-ph/0702587].
14. M. Pospelov and A. Ritz, Phys. Lett. B **651**, 208 (2007) [arXiv:hep-ph/0703128].
15. P. Meade *et al.*, Nucl. Phys. B **831**, 178 (2010) [arXiv:0905.0480].
16. M. Papucci and A. Strumia, [arXiv:0912.0742].
17. J. F. Navarro *et al.*, arXiv:0810.1522.
18. F. Chen, J. Cline, A. Frey, “Stable excited dark matter and galactic 511 keV γ rays,” in preparation.
19. M. Cirelli and J. M. Cline, arXiv:1005.1779 [hep-ph].

Direct searches for dark matter in CMS

B. CLERBAUX

*IIHE(ULB-VUB), Université Libre de Bruxelles, bd du Triomphe,
1050 Brussels, Belgium*

On behalf of the CMS Collaboration



Many models propose candidates for dark matter, the most popular being supersymmetry and models with extra spatial dimensions. Direct search for dark matter in CMS is presented in these frameworks, with emphasis on topologies with missing transverse energy.

0.1 *Introduction : the LHC and CMS*

The LHC has provided its first proton-proton collisions at 900 GeV and 2.36 TeV center-of-mass energy at the end of 2009. The high energy run, with 7 TeV in the center-of-mass, started in March 2010 at the time of the conference. The CMS detector is described in detail elsewhere¹. To perform the commissioning of the detector, the CMS collaboration has made extensive use of (i) cosmic-ray muon data taken performed in summer 2009 and (ii) 900 GeV and 2.36 TeV proton-proton collision data. This ensured excellent performance of the CMS detector before high energy data taking, and has permitted CMS to publish a first physics paper on minimum bias events² already in February 2010. The total integrated luminosity expected to be collected by CMS in the years 2010 and 2011 is expected to be around 1 fb^{-1} . This report describes the CMS potential for discovery, using simulated (by Monte-Carlo technique) data.

0.2 *Dark matter searches*

Three paths are actually followed in the search for dark matter (DM) production : (i) direct detection experiments, searching for WIMP interactions with nuclei, (ii) indirect DM searches (searching for γ -ray annihilation products of WIMPS, astronomical measurements, satellite based experiments, ...), and (iii) searches at colliders. These three methods are complementary. The advantages of collider searches, in particular at the LHC, are a large center-of-mass

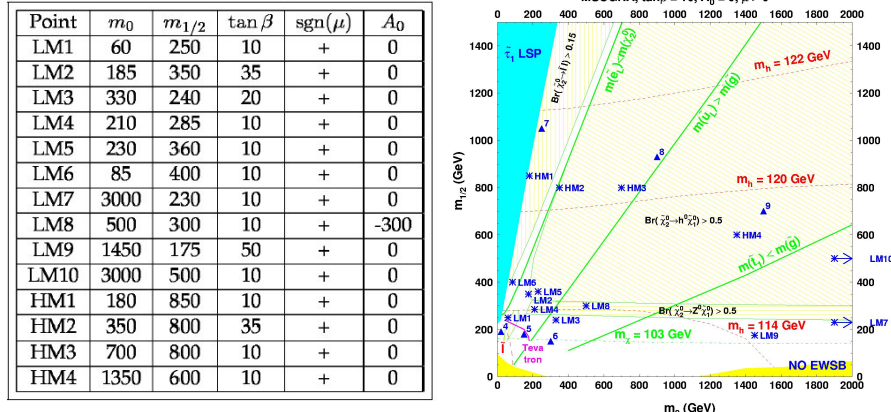


Figure 1: MSUGRA benchmark points (see text) studied by CMS.

energy, a potentially large cross section production for new state production, and the possibility to investigate detailed properties as masses and couplings.

Many models provide candidates for DM. The most popular models are supersymmetry, where the DM candidate is the lightest stable particle (LSP), for example the lightest neutralino or the gravitino, and models with extra spatial dimensions, in which the DM candidate is the lightest stable "Kaluza-Klein" particle.

In order to lower the number of free parameters, the search is often performed in the mSUGRA framework, in which only five free parameters are left : M_0 , the common boson mass at the GUT scale; $M_{1/2}$, the common fermion mass at the GUT scale; $\tan\beta$, the ratio of the two Higgs vacuum expectation values; A_0 , the common GUT trilinear coupling; and μ , the sign of the Higgs potential parameter. Constraints can be set by the relic density, measured for example by WMAP.

CMS studied scenarios corresponding to benchmark points in mSUGRA, in parameter-space region consistent with other experiment results (LEP, WMAP), with focus on significantly different event topologies. This allows easy comparison between different experiments. The benchmark points are shown in Figure 1 in the $M_{1/2}$ and M_0 plane, together with a table of the values of the five corresponding mSUGRA parameters. In the following, emphasis is put on LM1 (in the bulk region, at low M_0 and low $M_{1/2}$ values), and LM9 (in the focus point region, at high M_0 and low $M_{1/2}$ values).

0.3 SUSY final states with MET + multi-jets

In SUSY searches, the easiest topology for a discovery at LHC is the final state with missing transverse energy (MET) and multi-jets³. The production rate is high : as an example, for sgluino and squark masses of the order of 1 TeV, a rate of one event per day is expected for an instantaneous luminosity of $10^{31} \text{ cms}^{-2} \text{ s}^{-1}$ (the design LHC luminosity being $10^{34} \text{ cms}^{-2} \text{ s}^{-1}$). The challenge of this channel is the control of an important background ($Z \rightarrow \nu\bar{\nu}$, $t\bar{t}$, QCD) using data driven methods. The irreducible background from $Z \rightarrow \nu\bar{\nu} + \text{jets}$ can be measured directly from data from $Z \rightarrow \mu\mu + \text{jets}$ events or $\gamma + \text{jet}$ events, where the $\mu\mu$ pair or the γ is removed to mimic MET due to the escaping $\nu\bar{\nu}$ pair⁴.

Another analysis strategy aims at being as much as possible independent of MET measurements. It uses the variable $\alpha_T = \sqrt{E_T(\text{jet2})/E_T(\text{jet1})}/\sqrt{2(1 - \cos\Delta\phi)}$, where E_T is the transverse energy of the jet and $\Delta\phi$ the azimuthal angle between the two jets. This variable distinguishes between the QCD background (where jets are usually back to back and $\alpha_T \approx 0.5$) and the signal (typically at higher values of α_T). The α_T distribution for analysis considering

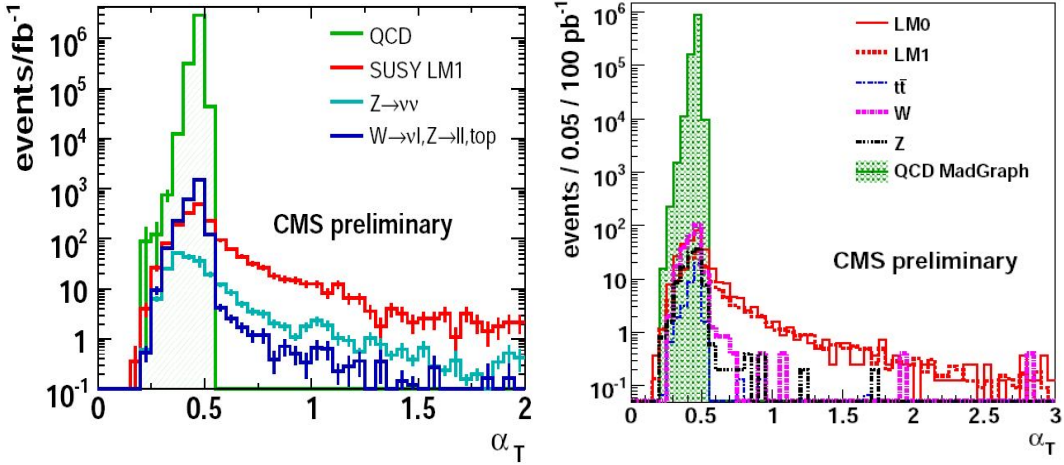


Figure 2: The α_T distribution; left: for di-jets ($\sqrt{s} = 14$ TeV and $L = 1 \text{ fb}^{-1}$); right: for multi-jets ($\sqrt{s} = 10$ TeV and $L = 100 \text{ pb}^{-1}$).

the two highest E_T jets (di-jets)⁵ at $\sqrt{s} = 14$ TeV and $L = 1 \text{ fb}^{-1}$ is presented in Figure 2 (left), and for multi-jets production⁶ at $\sqrt{s} = 10$ TeV and $L = 100 \text{ pb}^{-1}$ in Figure 2 (right). In the latter case, the discrimination power of α_T against Standard Model background from QCD events provides, for favourable SUSY benchmark points, signal over background ratios of 4 to 8, depending on the considered jet multiplicity bin.

0.4 SUSY final states with MET + jets + leptons

This channel has lower production rate and lower background than the MET + jets channel. It is characterised by a decay chain of a squark or a gluino into a slepton, via for example heavy neutralinos, giving in the final state MET and two isolated leptons with the same flavour and opposite charges. The typical shape of the 2 lepton invariant mass distribution ("mass edges") can shed light on neutralino and slepton masses. This distribution is presented in Figure 3 for $\sqrt{s}=10$ TeV and $L = 1 \text{ fb}^{-1}$ for the mSUGRA points LM1 and LM9. The CMS 5σ discovery potential for LM1 (LM9) is expected to be achieved already with $L=250$ (350) pb^{-1} ⁷.

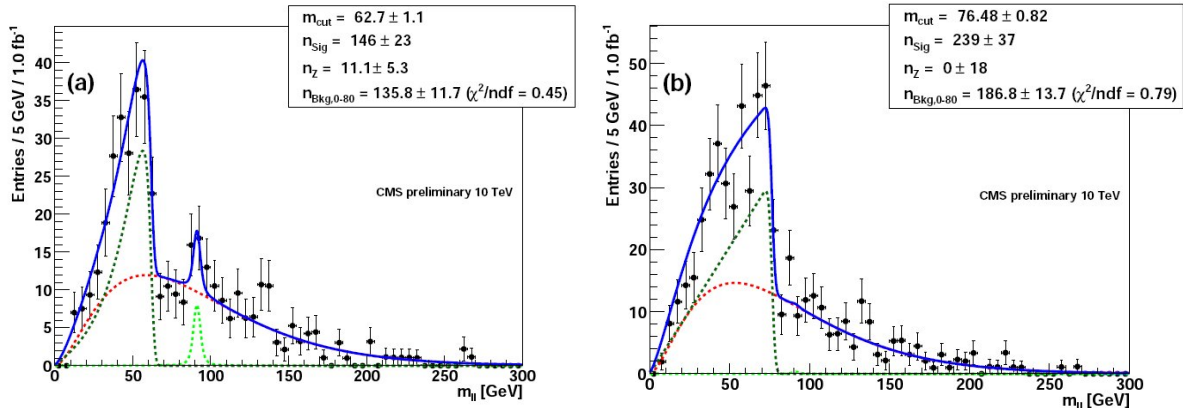


Figure 3: Two lepton invariant mass distribution for $\sqrt{s}=10$ TeV and $L = 1 \text{ fb}^{-1}$, for two mSUGRA points; left : LM9; right : LM1.

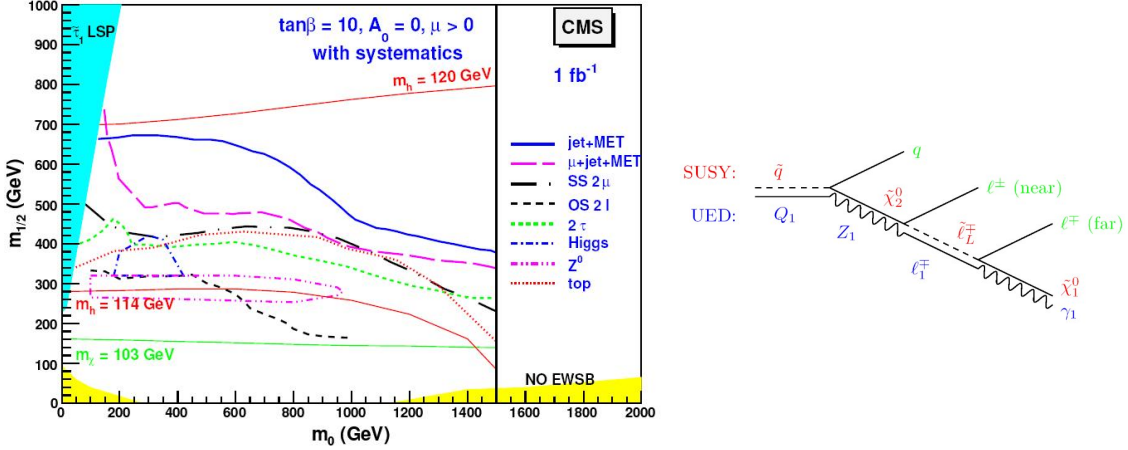


Figure 4: Left : CMS discovery potential ($\sqrt{s}=14$ TeV and $L = 1 \text{ fb}^{-1}$) for different channels; right : diagram of a cascade decay for a squark in SUSY or for a Q1 in Universal Extra-Dimension.

0.5 Summary and discussion

A summary of the CMS discovery potential in different channels³ is given in Figure 4 (left) for mSUSGRA ($\tan\beta = 10$, $A_0 = 0$ and $\mu > 0$), for $\sqrt{s}=14$ TeV and $L = 1 \text{ fb}^{-1}$. The MET+jets channel is observed to have the highest sensitivity. While the excess of events in some of these searches can be observed with already a handful of data, it is important to realize that understanding the origin of the excess may take some substantial time.

Indeed, similar signatures can be realized in the case of other models. For example, in the Universal Extra-Dimension (UED) model, a new extra compact dimension is introduced, in which all Standard Model fields can propagate. Phenomenologically, the model predicts the existence of new states (called "Kaluza-Klein" (KK) towers). This model leads to signatures very similar to those of SUSY : several jets, large MET, leptons, and opposite sign dilepton mass edges. A difference, however, is that KK-partners have the same spin as the Standard Model ones. As an example, Figure 4 (right) shows the diagram of a cascade decay for a squark in SUSY or for a "Kaluza-Klein" heavy quark in the Universal Extra-Dimension (UED) model, leading to similar final states.

References

1. CMS Collaboration, "The CMS experiment at the CERN LHC", JINST 3:S08004,2008
2. CMS Collaboration, "Transverse momentum and pseudorapidity distributions of charged hadrons in pp collisions at $\sqrt{s} = 0.9$ and 2.36 TeV", JHEP 02 041, 2010, arXiv:1002.0621v2 [hep-ex]
3. CMS Collaboration, "CMS Physics TDR: Volume II (PTDR2), Physics Performance", CERN-LHCC-2006-021, June 2006, J. Phys. G: Nucl. Part. Phys. 34 995-1579
4. CMS Collaboration, "Data-Driven Estimation of the Invisible Z Background to the SUSY MET Plus Jets Search", CMS PAS SUS-08-002
5. CMS Collaboration, "SUSY searches with dijet events", CMS PAS SUS-08-005
6. CMS Collaboration, "Search strategy for exclusive multi-jet events from supersymmetry at CMS", CMS PAS SUS-09-001
7. CMS Collaboration, "Discovery potential and measurement of a dilepton mass edge in SUSY events at $\sqrt{s} = 10$ TeV", CMS PAS SUS-09-002

SEARCHES FOR SIGNATURES OF DARK MATTER WITH THE ICECUBE NEUTRINO TELESCOPE

E. STRAHLER for the ICECUBE COLLABORATION^a
*Interuniversity Institute for High Energies, Vrije Universiteit Brussel,
Pleinlaan 2, Brussels 1050, Belgium*

IceCube is a km³ scale neutrino detector being constructed deep in the Antarctic ice. When complete, IceCube will consist of over 5000 optical modules deployed on 86 strings between 1450 and 2450 m of depth. Of these, 6 strings will comprise a densely packed subarray in the deepest, clearest ice called DeepCore, which will extend the sensitivity of neutrino searches below 100 GeV. In 2010, 77 strings will be operational. IceCube can be used to indirectly probe the spin-dependent dark matter scattering cross-section. Data taken with partial detector configurations has been used to search for neutrino signals of dark matter annihilations in the sun, halo, and galactic center. We present the current state of these searches as well as the projected sensitivity of the full detector.

1 Neutrino Detection

A neutrino traveling through the Earth will occasionally interact with a rock or ice nucleus, resulting in the creation of a daughter lepton. In the case of an electron or tau, the energy will be quickly dispersed in an electromagnetic cascade. A muon, on the other hand, can travel for several kilometers, depending on the medium. These high energy muons emit Cherenkov radiation as they travel, which can be detected if the medium is optically transparent, such as water or ice. By recording the arrival times and intensities of these photons with optical sensors, the direction and energy of the muon and parent neutrino may be reconstructed.

2 The IceCube Telescope

The IceCube detector¹ is an array of Digital Optical Modules (DOMs) deployed on strings in the glacial ice of the South Pole between depths of 1450-1250 m. Scheduled to be completed in 2011, IceCube will consist of over 5000 DOMs on 86 strings. Of these, 6 strings will feature more densely spaced DOMs with higher quantum efficiency, making up a subarray known as DeepCore. DeepCore will increase the sensitivity of the detector at low energies and reduce the threshold to near 10 GeV. In addition, by using the surrounding IceCube strings as a veto, DeepCore will enable searches at low energies in the southern hemisphere, transforming IceCube into a full sky observatory. A surface array, called IceTop, is used for cosmic ray studies and as a muon veto. Each DOM consists of a 25 cm photomultiplier tube (PMT) and associated electronics enclosed in a glass pressure sphere.² Following the 2010 construction season, 79 strings have been deployed, including all 6 strings of DeepCore.

^asee <http://www.icecube.wisc.edu> for full author list

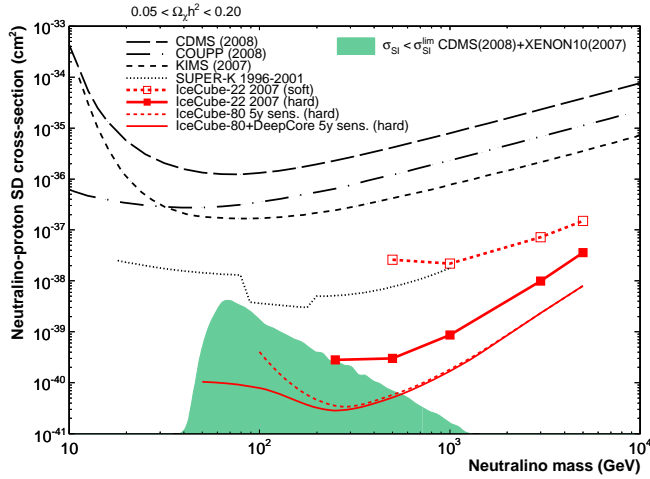


Figure 1: Upper limits on the spin-dependent neutralino-proton scattering cross section for hard (W^+W^-) and soft ($b\bar{b}$) annihilation channels. Results from the 22-string IceCube analysis are shown along with the predicted sensitivity for the completed detector. The shaded region depicts the model space allowed by direct detection experiments.

3 Solar WIMPs

Weakly Interacting Massive Particles (WIMPs) are one of the most promising candidates for the universal dark matter.³ In the Minimally Supersymmetric Standard Model (MSSM), the WIMP can take the form of the lightest neutralino.⁴ These neutralinos are swept up by the sun on its transit through the galactic halo. They scatter weakly with solar nucleons and may become gravitationally bound. Over time, this leads to an accumulation of dark matter in the center of the sun which may then self-annihilate. A flux of neutrinos will be generated which is spectrally dependant on the annihilation channel and neutralino mass and which can be searched for as a point-like source with neutrino telescopes such as IceCube.

Such a search has been performed on data taken with the 22-string configuration of the IceCube detector.⁵ Sophisticated background rejection techniques were employed to suppress background due to cosmic-ray induced muons and neutrinos. Once a final event selection was achieved, a likelihood comparison was made to determine whether a significant excess of neutrino candidates existed from the direction of the Sun. No such excess was detected and limits on the spin-dependent WIMP-proton scattering cross-section were set. These are shown in Fig. 1 and represent the most stringent limits to date. With this analysis, we are beginning to probe the still-allowed parameter space, and the full 86-string detector will be able to meaningfully constrain the models.

Rather than a neutralino, dark matter could arise from Kaluza-Klein excitations in the framework of universal extra dimensions (UED).⁶ In this case, WIMPs would be the lightest KK particle (LKP), with a possible mass range of 300 GeV to several TeV. In the case of an LKP WIMP, the spin-independent WIMP-proton scattering cross-section would be very small, but the spin-dependent contribution could be large enough to probe with neutrino telescopes. Using the same dataset as for neutralino dark matter, a search was made for neutrinos arising from LKP annihilations in the Sun.⁷ The method used was similar to the neutralino search, and no excess from the direction of the sun was observed. Based on the observations, limits on the spin-dependent scattering cross-section were set, as shown in Fig. 2. These first limits already restrict the allowed parameter space and it is expected that the full IceCube detector will be able to provide a factor of 10 improvement in sensitivity.

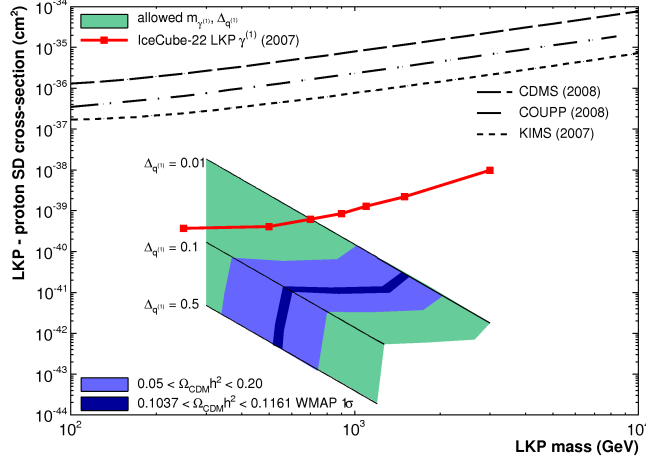


Figure 2: Upper limits on the spin-dependent LKP-proton scattering cross section. Results from the 22-string IceCube analysis are shown from several possible LKP masses. The shaded region depicts the allowed parameter space, while the darker region corresponds to the the favored relic density as measured by WMAP.

4 Dark Matter from the Galactic Halo

IceCube can also be used to probe dark matter annihilation in the halo. The dark matter density profile is dependent on the distance from the galactic center and is highly model dependent. For the analyses considered here, we have chosen to use the Einasto model baseline, while also considering the Moore, NFW, and Kravtsov models. For each, the density profile may be parameterized and integrated along the line of sight. Combined with channel-dependent dark matter annihilation spectra, this allows the calculation of expected neutrino fluxes.

A search was conducted using the 22-string configuration of IceCube for such annihilations.⁸ Since the galactic center is below the viewable horizon, this search focused on the outer halo and looked for a large scale anisotropy in the neutrino event rate from the region surrounding the galactic center, and a region diametrically opposite. No such anisotropy was observed, and limits were set on the self-annihilation cross-section for various potential annihilation channels, shown in Fig. 3.

With the 40-string IceCube detector, a filter was devised to select down-going tracks that originated in the detector volume, by using the upper DOM layers as a veto. This preferentially selected neutrino events, while rejecting cosmic-ray induced muon background and allowed the search to extend to the direction of the galactic center. As in the 22-string search, no anisotropy in event rates was observed between on and off source regions and limits were set on the self-annihilation cross-section. Since the dark matter density profile and hence neutrino rate varies greatly by model close to the galactic center, the average model is shown in Fig. 3.

The results of these analyses are competitive with recent limits derived from Super-Kamiokande data.⁹ It is expected that these limits will improve substantially with the full IceCube detector and the improved vetoing capabilities introduced with DeepCore.

5 Outlook

Following a very successful deployment season, the IceCube detector is nearly complete, with 79 out of 86 strings in the ice. Included in this number is the full DeepCore subarray of 6 strings, which will reduce the energy threshold of IceCube to around 10 GeV. DeepCore will increase the sensitivity of IceCube to low WIMP masses as well as allowing the measurement of neutrino oscillation. In addition, by using the surrounding IceCube strings as a veto, we will be able to

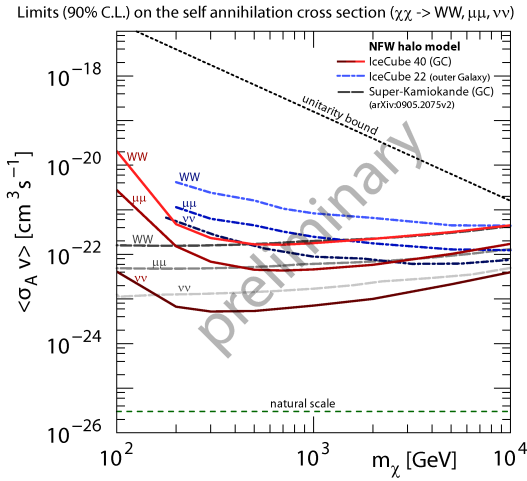


Figure 3: Preliminary upper limits for the dark matter self-annihilation cross-section at 90% C.L. For the 22-string analysis which looked at the outer halo, the bands represent the spread in model predictions. For the 40-string results, the average (Einasto) dark matter density profile is shown. Limits derived from Super-K data are shown for comparison.

extend searches to the southern sky, including the galactic center.

We have performed searches for dark matter annihilations in the sun and galactic halo using partial detector configurations. Results for the 22-string detector have been published, and 40 and 59-string results are forthcoming. To date, no dark matter signal has been detected and limits have been placed on both the spin-dependent WIMP-nucleon scattering cross-section as well as the self annihilation cross-section.

References

1. A. Achterberg *et al.* (IceCube Coll), *Astropart. Phys.* **26**, 155 (2006).
2. R. Abbasi *et al.* (IceCube Coll), *Nucl. Inst. Meth.* **A601**, 294 (2009).
3. V. Rubin and W.K. Ford, *Astrophys. J.* **159**, 379 (1970).
4. M. Drees and M.M. Nojiri, *Phys. Rev. D* **47**, 376 (1993).
5. R. Abbasi *et al.* (IceCube Coll), *Phys. Rev. Lett.* **102**, 201302 (2009).
6. D. Hooper and S. Profumo, *Phys. Rep.* **453**, 29 (2007).
7. R. Abbasi *et al.* (IceCube Coll), *Phys. Rev. D* **81**, 057101 (2010)
8. C. Rott (for the IceCube Coll), *arXiv* 0912.5183.
9. J. Hisano, K. Nakayam, M.J.S. Yang, *arXiv* 0905.2075.

Results from the Search for Ultra-High Energy Neutrinos with ANITA-II

Abigail G. Vieregg for the ANITA Collaboration

*Department of Physics and Astronomy, University of California Los Angeles,
475 Portola Plaza, Los Angeles, CA, USA 90095-1547*

The ANtarctic Impulsive Transient Antenna (ANITA) is an innovative balloon-borne radio telescope, designed to detect coherent Cherenkov emission from cosmogenic ultra-high energy (UHE) neutrinos with energy greater than 10^{18} eV. The second flight of the ANITA experiment launched on December 21st, 2008, and flew for 31 days. We discuss the most sensitive search to date for UHE neutrinos, including calibration techniques, analysis methods, and background rejection. In a blind analysis, we find two candidate neutrino events on a background (thermal and man-made noise) of 0.97 ± 0.42 .

1 Introduction

Ultra-high energy (UHE) neutrino astronomy (above 10^{18} eV) is a new frontier in particle astronomy which promises to open up a window to the UHE distant universe where classical photon and cosmic-ray astronomy is limited. UHE neutrinos may also help reveal the origin of UHE cosmic rays (UHECRs), a longstanding mystery in astrophysics. A population of neutrinos above 10^{18} eV is a “guaranteed” bi-product of the Greisen Zatsepin Kuzmin (GZK) process, whereby cosmic rays above $10^{19.5}$ eV interact with the CMB within tens of Megaparsecs of the source¹. Via a Delta resonance, the interaction yields a pion and a proton or neutron, and the charged pion decay chain produces UHE neutrinos.

The ANtarctic Impulsive Transient Antenna (ANITA) is a Long Duration Balloon experiment that searches for coherent radio Cherenkov emission from electromagnetic cascades induced by UHE neutrinos interacting with the Antarctic ice. Strong, coherent radio emission from UHE electromagnetic showers within a dielectric was first predicted by Askaryan in the 1960’s², and later confirmed in the lab³. Radio frequency (RF) signals at the payload from neutrino interactions are largely vertically-polarized because ANITA views the top of the radially-polarized Cherenkov cone and Fresnel effects at the surface of the ice favor the vertical polarization.

ANITA is also sensitive to radio geosynchrotron emission which reflects off of the Antarctic ice surface from extended air showers of UHECRs. Geosynchrotron emission detected by ANITA is predominantly horizontally polarized because the Earth’s magnetic field in Antarctica is mostly vertically polarized, causing the electrons and positrons in the shower to split horizontally, and Fresnel effects at the reflection surface favor the horizontal polarization.

The first flight of ANITA saw no neutrino candidates⁴. Further analysis of ANITA-I data revealed 16 observed UHE cosmic rays⁵, with energy of order 10^{19} eV.

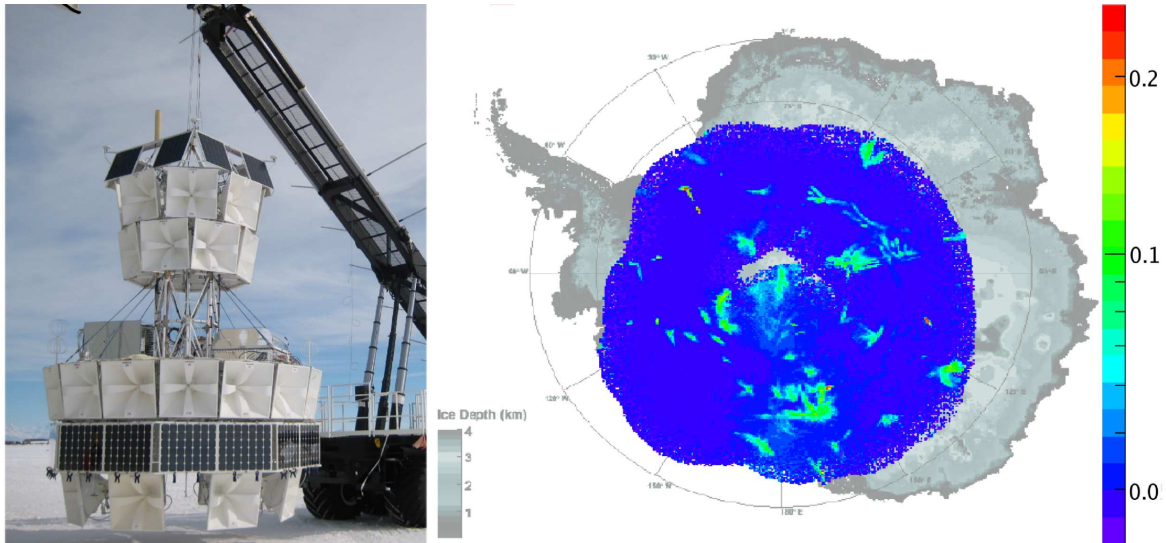


Figure 1: Left: A picture of the ANITA-II payload before launch. Right: An RF image of Antarctica, seen with ANITA-II. The best direction for all 21.2 M Quality Events is shown; the color of each bin is the average value of the peak of the interferometric map for events which fall in that bin.

2 The Second Flight of ANITA

The second flight of ANITA (ANITA-II) launched from Williams Field, Antarctica on December 21, 2008 and landed near Siple Dome after a 31-day flight with 28.5 live days. ANITA-II has 40 quad-ridged horn antennas, is sensitive from 200-1200 MHz, and triggers on fast, broadband signals in the vertical polarization. ANITA-II's sensitivity to UHE neutrinos was improved by about a factor of four compared to ANITA-I because of improvements to the trigger, front-end electronics, flight path, and live time. ANITA-II recorded ~ 26.7 M events, over 98.5% of which are thermal-noise triggers. Figure 1 shows a picture of the ANITA-II payload.

3 Data Analysis

The analysis described here is reported in Reference⁶ and described in detail in Reference⁷. We performed a blind analysis on the data, setting all analysis cuts and estimating the background based on sidebands before looking at events in the hidden signal region, which comprises single, isolated plane-wave events.

For each event, we create an interferometric image in each polarization by cross-correlating waveforms from neighboring antennas and summing the total normalized cross-correlation value for each elevation and azimuth. We construct a “coherently summed” waveform given the direction of the largest peak in either map using the antennas that are closest to that peak. The analysis pointing resolution, determined using ground-to-payload calibration impulses, is $0.2^\circ - 0.4^\circ$ in elevation and $0.5^\circ - 1.1^\circ$ in azimuth, depending on the signal-to-noise ratio (SNR) of the event.

Table 1 shows the number of events cut and the efficiency of each set of cuts in the analysis. Figure 1 shows the best direction for all 21.2 M Quality Events, and the color of each bin is the average value of the peak of the interferometric map for events which fall in that bin. The blue background is consistent with thermal-noise triggers, and can easily be rejected to a level of 2.5×10^{-8} with a set of cuts on the peak value of the interferometric map and the peak envelope of the coherently summed waveform. An expected background of 0.50 ± 0.23 thermal events passes these reconstruction cuts.

Table 1: Event totals vs. analysis cuts and estimated signal efficiencies for ESS spectral shape⁸.

Cut requirement	Passed		Efficiency
	Vpol	HPol	
Hardware-Triggered Events	$\sim 26.7M$		-
(1) Quality Events	$\sim 21.2M$		1.00
(2) Reconstructed Events	320,722		0.96
(3) Not Traverses and Aircraft	314,358		1.00
(4) Isolated Singles	7	4	0.64
(5) Not Misreconstructions	5	3	1.00
(6) Not of Payload Origin	2	3	1.00
Total Efficiency			0.61

The bright spots in Figure 1 are consistent with clusters of man-made noise. After reconstruction cuts, 320,722 Reconstructed Events (mostly clusters of man-made noise) remain, 314,358 of which are not associated with Traverses and Aircraft tracks. Events which remain at this stage are clustered with other events which remain, known places of human activity (camps), and bright spots on the right panel of Figure 1 (Hot Spots).

Any remaining unclustered events are deemed Isolated Singles, and remain in the hidden box. We used seven largely independent methods to estimate that the anthropogenic background remaining after our clustering cuts is 0.65 ± 0.39 vertically polarized (VPol) events and 0.25 ± 0.19 horizontally polarized (HPol) events.

The polarization angle of remaining events is then calculated using Stokes parameters to separate VPol ($> 50^\circ$) and HPol ($< 40^\circ$) events. Two final cuts are applied by hand. Any event that has a high probability of being a Misreconstruction is removed by hand, *e.g.* we remove any event that clearly peaked at a sidelobe of the pattern in the interferometric image. Any remaining event which is clearly of Payload Origin is also removed by hand.

4 Results

After all cuts are applied, two events remain in the VPol channel, and three in the HPol channel. After clustering cuts, the thermal noise background reduces to 0.32 ± 0.15 in each channel. The total background is 0.97 ± 0.42 events in the VPol channel, and 0.67 ± 0.24 events in the HPol channel.

All three HPol events show characteristics which identify them as radio emission from UHECR air showers, reflecting from the ice surface, as described in the ANITA-I results⁵. While ANITA-I saw 16 such events, the much smaller number of HPol events seen in ANITA-II is due to the change of the trigger to favor VPol events to maximize neutrino sensitivity.

In Figure 2 we show some of the characteristics of the two VPol neutrino candidates, including the waveforms, frequency spectra, and interferometric maps. The waveforms and frequency spectra are within the range of simulated neutrino events. We set a limit including systematic errors⁹, shown in the right panel of Figure 2, using the 28.5 day livetime, the energy-dependent analysis efficiency, and the average acceptance from the two independent simulations¹⁰.

The expected limit from this data in the absence of signal, is about a factor of four more sensitive than ANITA-I⁴. The actual limit, shown in Figure 2, includes our two observed candidates. Because ANITA-II saw more than the expected background, the actual limit is only a factor of two better than ANITA-I even though the discovery potential is four times higher for ANITA-II.

ANITA-II's constraint on cosmogenic neutrino models strongly excludes models with maximally energetic UHECR source spectra which saturate other available bounds^{13,14}. ANITA-II is

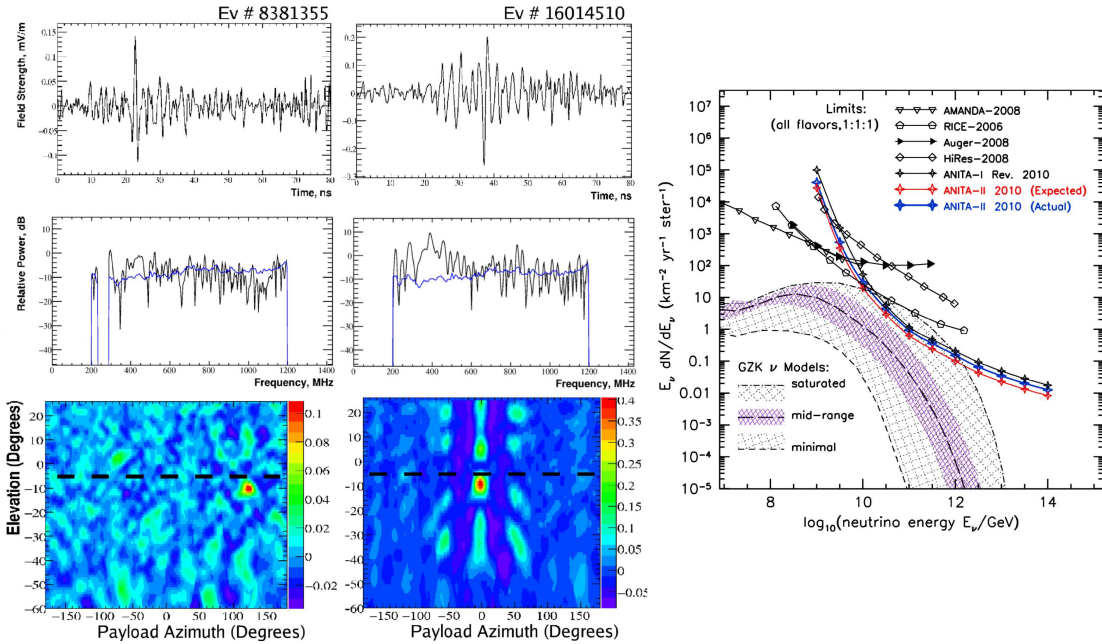


Figure 2: Top: Waveforms of incident field strength for the two surviving VPol events. Event 8381355 is shown filtered between 235–287 MHz to remove weak CW noise from above the horizon. Middle: Corresponding frequency power spectra. Bottom: Corresponding interferometric maps showing the pulse direction. The dashed line is the horizon. Right: ANITA-II limit on the UHE neutrino flux. The red curve is the expected limit before unblinding, based on seeing a number of candidates equal to the background estimate. The blue curve is the actual limit, based on the two surviving candidates. Other limits are from AMANDA, RICE, Auger, HiRes, and a revised limit from ANITA-I^{11,6}. The GZK neutrino model range is determined by a variety of models.^{8,12,13,14,15,16}

now probing several models with strong source evolution spectra that are plausible within current GZK source expectations^{13,14,16}, some at $> 90\%$ confidence level. These are the strongest constraints to date on the cosmogenic UHE neutrino flux.

References

1. Greisen, Phys. Rev. Lett. 16, 748 (1966); Zatsepin and Kuzmin, JETP Lett. 4, 78 (1966).
2. G. Askaryan, Soviet Physics JETP-USSR 14 (2), 441-443 (1962).
3. D. Saltzberg *et al.*, Phys. Rev. Lett. 86, 2802 (2001).
4. P. Gorham *et al.*, Phys. Rev. Lett. 103, 051103 (2009).
5. S. Hoover *et al.*, Submitted to Phys. Rev. Lett., arXiv:1005.0035 (2010).
6. P. Gorham *et al.*, Submitted to Phys. Rev. D, arXiv:1003.2961 (2010).
7. A. Vieregg, Ph.D. Dissertation, UCLA (2010).
8. R. Engel, D. Seckel, T. Stanev, Phys. Rev. D 64, 093010 (2001).
9. Feldman and Cousins, Phys. Rev. D 57 (1998); Conrad *et al.*, Phys. Rev. D 67 (2003).
10. P. Gorham *et al.*, Astropart. Phys. 32, 10-41 (2009).
11. M. Ackermann *et al.*, Ap. J. 675, 1014 (2008); I. Kravchenko, *et al.*, Phys. Rev. D 73, 082002 (2006); J. Abraham *et al.*, Phys. Rev. Lett. 100, 211101 (2008); R. Abbassi *et al.*, Ap. J. 684, 790 (2008).
12. R. Protheroe and P. Johnson, Astropart. Phys. 4, 253 (1996).
13. O. Kalashev *et al.*, Phys. Rev. D 66, 063004 (2002).
14. C. Aramo, *et al.*, Astropart. Phys. 23, 65 (2005).
15. M. Ave *et al.*, Astropart. Phys. 23, 19 (2005).
16. V. Barger, P. Huber, D. Marfatia, Phys. Lett. B 642, 333 (2006).

RELATIVISTIC TRAJECTORIES OF CELESTIAL BODIES AS A TOOL TO CONSTRAIN F(R) THEORIES OF GRAVITY AND DARK MATTER CONCENTRATION NEAR THE GALACTIC CENTER

A. F. ZAKHAROV

*Institute of Theoretical and Experimental Physics, B. Cheremushkinskaya, 25, 117259, Moscow, Russia;
Bogoliubov Laboratory for Theoretical Physics, JINR, 141980 Dubna, Russia*

F. DE PAOLIS, G. INGROSSO

Dipartimento di Fisica, Università del Salento and INFN Sezione di Lecce, Lecce, Italy

A. A. NUCITA

XMM-Newton Science Operations Centre, ESAC, ESA, Madrid, Spain

Trajectories of test bodies may be used for a potential reconstruction, in particular, one can get constraints on a theory choice and/or on a choice of a specific model for a selected object. We mention an opportunity to put limits on alternative theories of gravity from planetary motions in our Solar system. We discuss constraints on DM concentration near the Galactic Center from apocenter shift data.

Shapes of celestial body trajectories may be used for a gravitational potential reconstruction similarly to nuclear physics where people reconstruct interaction potentials. In particular, we use planetary orbits in Solar system to put severe constraints on alternative theories of gravity such a $f(R)$ theory [1, 2, 3].

Advancements in infrared astronomy are allowing to test the scale of the mass profile at the center of our galaxy down to tens of AU. With the Keck and VLT telescopes, the proper motions of several stars orbiting the Galactic Center black hole have been monitored and almost entire orbits, as for example that of the S2 star, have been measured allowing an unprecedent description of the Galactic Center region [4, 5, 6]. Measurements of the amount of mass $M(< r)$ contained within a distance r from the Galactic Center are continuously improved as more precise data are collected. Observations extend down to the periastron distance ($\simeq 3 \times 10^{-4}$ pc) of the S16 star and they correspond to a value of the enclosed mass $\simeq 3.67 \times 10^6 M_\odot$ within $\simeq 3 \times 10^{-4}$ pc [4]. Here and in the following, we use the three component model for the central region of our galaxy based on estimates of enclosed mass proposed in [7]. This model is constituted by the central black hole, the central stellar cluster and the DM sphere (made of WIMPs), i.e.

$$M(< r) = M_{BH} + M_*(< r) + M_{DM}(< r) , \quad (1)$$

where M_{BH} is the mass of the central black hole Sagittarius A*. For the central stellar cluster,

the empirical mass profile is

$$M_*($$
 (2)

with a total stellar mass $M_* = 0.88 \times 10^6 M_\odot$ and a size $R_* = 0.3878$ pc. As far as the mass profile of the DM concentration is concerned, we have assumed a mass distribution of the form [7]

$$M_{DM}($$
 (3)

M_{DM} and R_{DM} being the total amount of DM in the form of WIMPs and the radius of the spherical mass distribution, respectively.

A likelihood analysis has allowed to estimate for the DM mass the value $M_{DM} \simeq 10^5 M_\odot$ while the DM sphere size results to be in the range $(10^{-4} - 1)$ pc. It is clear that present observations of stars around the Galactic Center do not exclude the existence of a DM sphere with mass $\simeq 4 \times 10^6 M_\odot$, well contained within the orbits of the known stars, if its radius R_{DM} is $\lesssim 2 \times 10^{-4}$ pc (the periastron distance of the S16 star in the more recent analysis [6]). However, if one considers a DM sphere with larger radius, the corresponding upper value for M_{DM} decreases (although it tends again to increase for extremely extended DM configurations with $R_{DM} \gg 10$ pc). In the following, we will assume for definiteness a DM mass $M_{DM} \sim 2 \times 10^5 M_\odot$, that is the upper value for the DM sphere in [7] within an acceptable confidence level in the range $(10^{-3} - 10^{-2})$ pc for R_{DM} . As it will be clear in the following, we emphasize that even a such small value for the DM mass (that is about only 5% of the standard estimate $(3.67 \pm 0.19 \times 10^6)$ M_\odot for the dark mass at the Galactic Center [6]) may give some observational signatures.

Evaluating the S2 apoastron shift ^a as a function of R_{DM} , one can further constrain the DM sphere radius since even now we can say that there is no evidence for negative apoastron shift for the S2 star orbit at the level of about 10 mas. In addition, since at present the precision of the S2 orbit reconstruction is about 1 mas, we can say that even without future upgrades of the observational facilities and simply monitoring the S2 orbit, it will be possible within about 15 years to get much more severe constraints on R_{DM} .

We study the motion of stars as a consequence of the gravitational potential $\Phi(r)$ due the mass profile given in Eq. (1). As usual, the gravitational potential can be evaluated as

$$\Phi(r) = -G \int_r^\infty \frac{M(r')}{r'^2} dr' . \quad (4)$$

According to GR, the motion of a test particle can be fully described by solving the geodesic equations. Under the assumption that the matter distribution is static and pressureless, the equations of motion in the PN-approximation become

$$\frac{d\mathbf{v}}{dt} \simeq -\nabla(\Phi_N + 2\Phi_N^2) + 4\mathbf{v}(\mathbf{v} \cdot \nabla)\Phi_N - v^2 \nabla\Phi_N . \quad (5)$$

We note that the PN-approximation is the first relativistic correction from which the apoastron advance phenomenon arises. In the case of the S2 star, the apoastron shift as seen from Earth

^aWe want to note that the periastron and apoastron shifts $\Delta\Phi$ as seen from the orbit center have the same value whereas they have different values as seen from Earth (see Eq. (7)). When we are comparing our results with orbit reconstruction from observations we refer to the apoastron shift as seen from Earth.

(from Eq. (7)) due to the presence of a central black hole is about 1 mas, therefore not directly detectable at present since the available precision in the apoastron shift is about 10 mas (but it will become about 1 mas in 10–15 years even without considering possible technological improvements). It is also evident that higher order relativistic corrections to the S2 apoastron shift are even smaller and therefore may be neglected at present, although they may become important in the future.

The Newtonian effect due to the existence of a sufficiently extended DM sphere around the black hole may cause an apoastron shift in the opposite direction with respect to the relativistic advance due to the black hole. Therefore, we have considered the two effects comparing only the leading terms.

For a spherically symmetric mass distribution (such as that described above) and for a gravitational potential given by Eq. (4), Eq. (5) may be rewritten in the form

$$\frac{d\mathbf{v}}{dt} \simeq -\frac{GM(r)}{r^3} \left[\left(1 + \frac{4\Phi_N}{c^2} + \frac{v^2}{c^2} \right) \mathbf{r} - \frac{4\mathbf{v}(\mathbf{v} \cdot \mathbf{r})}{c^2} \right], \quad (6)$$

\mathbf{r} and \mathbf{v} being the vector radius of the test particle with respect to the center of the stellar cluster and the velocity vector, respectively. Once the initial conditions for the star distance and velocity are given, the rosetta shaped orbit followed by a test particle can be found by numerically solving the set of ordinary differential equations in Eq. (6). As one can see, for selected parameters for DM and stellar cluster masses and radii the effect of the stellar cluster is almost negligible while the effect of the DM distribution is crucial since it enormously overcome the shift due to the black hole (for $R_{DM} = 10^{-3}$ pc). Moreover, as expected, its contribution is opposite in sign with respect to that of the black hole [8]. We note that the expected apoastron (or, equivalently, periastron) shifts (mas/revolution), $\Delta\Phi$ (as seen from the center) and the corresponding values $\Delta\phi_E^\pm$ as seen from Earth (at the distance $R_0 \simeq 8$ kpc from the GC) are related by

$$\Delta\phi_E^\pm = \frac{d(1 \pm e)}{R_0} \Delta\Phi, \quad (7)$$

where with the sign \pm are indicated the shift angles of the apoastron (+) and periastron (−), respectively. The S2 star semi-major axis and eccentricity are $d = 919$ AU and $e = 0.87$ [6]. Taking into account that the present day precision for the apoastron shift measurements is of about 10 mas, one can say that the S2 apoastron shift cannot be larger than 10 mas. Therefore, any DM configuration that gives a total S2 apoastron shift larger than 10 mas (in the opposite direction due to the DM sphere) is excluded. The same analysis is done for two different values of the DM mass distribution slope, i.e. $\alpha = 1$ and $\alpha = 2$ [9, 10]. In any case, we have calculated the apoastron shift for the S2 star orbit assuming a total DM mass $M_{DM} \simeq 2 \times 10^5 M_\odot$. As one can see, the upper limit of about 10 mas on the S2 apoastron shift may allow to conclude that DM radii in the range about $10^{-3} - 10^{-2}$ pc are excluded by present observations for DM mass distribution slopes. We notice that the results of the present analysis allows to further constrain the results [7], where it was concluded that if the DM sphere radius is in the range $10^{-3} - 1$ pc, configurations with DM mass up to $M_{DM} = 2 \times 10^5 M_\odot$ are acceptable. The present analysis shows that DM configurations of the same mass are acceptable only for R_{DM} out the range between $10^{-3} - 10^{-2}$ pc, almost irrespectively of the α value.

We have considered the constraints that the upper limit (presently of about 10 mas) of the S2 apoastron shift may put on the DM configurations at the galactic center. When (in about 10–15 years, even without considering improvements in observational facilities) the precision of S2 apoastron shift will be about 1 mas (that is equal to the present accuracy in the S2 orbit reconstruction) our analysis will allow to further constrain the DM distribution parameters. In particular, the asymmetric shape of the curve in Fig. 1 implies that any improvement in the apoastron shift measurements will allow to extend the forbidden region especially for the

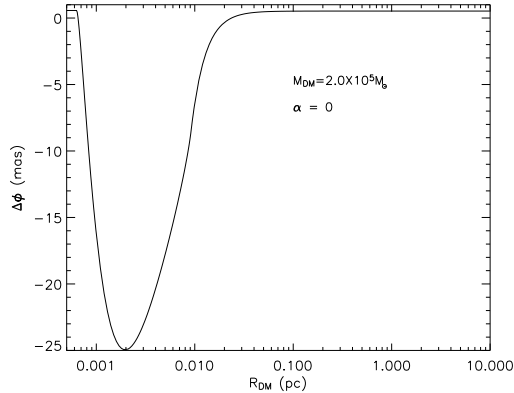


Figure 1: Apoastron shift as a function of the DM radius R_{DM} for $\alpha = 0$ and $M_{DM} \simeq 2 \times 10^5 M_{\odot}$. Taking into account present day precision for the apoastron shift measurements (about 10 mas) one can say that DM radii R_{DM} in the range $8 \times 10^{-4} - 10^{-2}$ pc are not acceptable.

upper limit for R_{DM} . Quantitatively, we have a similar behavior curves for other choices of slope parameters α for DM concentrations. In this context, future facilities for astrometric measurements at a level 10 μ as of faint infrared stars will be extremely useful and they give an opportunity to put even more severe constraints on DM distribution. In addition, it is also expected to detect faint infrared stars or even hot spots orbiting the Galactic Center. In this case, consideration of higher order relativistic corrections for an adequate analysis of the stellar orbital motion have to be taken into account. In our considerations we adopted simple analytical expression and reliable values for R_{DM} and M_{DM} parameters following [7] just to illustrate the relevance of the apoastron shift phenomenon in constraining the DM mass distribution at the Galactic Center. If other models for the DM distributions are considered the qualitative aspects of the problem are preserved although, of course, quantitative results on apoastron shifts may be different.

We thank J. Dumarchez for his kind attention to this contribution.

References

- [1] A. F. Zakharov *et al*, *Phys. Rev. D* **74**, 107101 (2006).
- [2] A. F. Zakharov *et al*, *AIP Conf. Proc.* **966**, 173 (2007).
- [3] A. F. Zakharov *et al.*, *Space Sc. Rev.*, **148**, 301 (2009).
- [4] A. M. Ghez *et al.*, *Astron. Nachr.* **324**, 527 (2003).
- [5] R. Genzel *et al.*, *Astrophys J.* **594**, 812 (2003).
- [6] A. M. Ghez *et al.*, *Astrophys. J.* **620**, 744 (2005).
- [7] J. Hall and P. Gondolo, *Phys. Rev. D* **74**, 063511 (2006).
- [8] A. A. Nucita *et al.*, *Publ. Astron. Soc. Pacific* **119**, 349 (2007).
- [9] A. F. Zakharov *et al*, *Phys. Rev. D* **76**, 62001 (2007).
- [10] A. F. Zakharov *et al*, *Journ. of Phys.: Conf. Ser.* **133**, 012032 (2008).

THE LARGE-SCALE CLUSTERING OF MASSIVE DARK MATTER HALOES

V. DESJACQUES

*Institute for Theoretical Physics, University of Zürich
Winterthurerstrasse 190, 8057 Zürich, Switzerland*

The statistics of peaks of the initial, Gaussian density field can be used to interpret the abundance and clustering of massive dark matter haloes. I discuss some recent theoretical results related to their clustering and its redshift evolution. Predictions from the peak model are qualitatively consistent with measurements of the linear bias of high mass haloes, which also show some evidence for a dependence on the halo mass M beyond the peak height ν . The peak approach also predicts distinctive scale-dependence in the bias of haloes across the baryon acoustic feature, a measurement of which would provide strong support for its validity. For 2σ density peaks collapsing at $z = 0.3$, this residual scale-dependent bias is at the 5-10% level and should thus be within reach of very large simulations of structure formation.

1 Peaks in Gaussian random field

The peak model introduced by¹ assumes that dark matter haloes are associated with peaks of the initial (Gaussian) density field. Although dark matter haloes are the local maxima of the evolved mass distribution, there is a clear correspondence with initial density maxima for massive objects only. In the following, I will focus on the large-scale clustering properties of initial density peaks and show there is nontrivial scale-dependence both in the linear spatial and velocity bias. I will discuss some implications of these results.

2 First order biasing of initial density peaks

Following¹, one usually smoothes the initial density fluctuations at redshift $z_i \gg 1$ with a filter of characteristic mass scale M before identifying local maxima of height ν . Even though density peaks form a well-behaved point process, the large-scale asymptotics of the 2-point correlation and pairwise velocity can be thought of as arising from the continuous bias relation^{6,8}

$$\delta n_{\text{pk}}(\mathbf{x}) = b_\nu \delta_M(\mathbf{x}) - b_\zeta \Delta \delta_M(\mathbf{x}), \quad (1)$$

$$\mathbf{v}_{\text{pk}}(\mathbf{x}) = \mathbf{v}_M(\mathbf{x}) - \frac{\sigma_0^2}{\sigma_1^2} \nabla \delta_M(\mathbf{x}), \quad (2)$$

where δn_{pk} and \mathbf{v}_{pk} are the peak count-in-cell density and velocity, δ_M and \mathbf{v}_M are the initial mass density and velocity field smoothed on scale M , and the (Lagrangian) bias parameters b_ν and b_ζ are

$$b_\nu(\nu, \gamma_1) = \frac{1}{\sigma_0} \left(\frac{\nu - \gamma_1 \bar{u}}{1 - \gamma_1^2} \right), \quad b_\zeta(\nu, \gamma_1) = \frac{1}{\sigma_2} \left(\frac{\bar{u} - \gamma_1 \nu}{1 - \gamma_1^2} \right). \quad (3)$$

Here, $\bar{u} \equiv \bar{u}(\nu)$ denotes the mean curvature of peaks of height ν , $\gamma_1(M) = \sigma_1^2/\sigma_0\sigma_2$ and σ_0 , σ_1 and σ_2 are spectral moments which depend upon the shape of the linear mass power spectrum. Note that b_ζ is strictly positive, whereas b_ν can be positive or negative. In Fourier space, wavemodes of the peak number density $\delta n_{\text{pk}}(\mathbf{k})$ can be obtained by multiplying $\delta_M(\mathbf{k})$ with (here and henceforth, I will omit the dependence on ν and γ_1 for brevity)

$$b_{\text{pk}}(k) = b_\nu + b_\zeta k^2. \quad (4)$$

This defines the spatial peak bias at the first order. In practice, the peak-background split approach, which is based on count-in-cells statistics, can also be used to estimate b_ν ³. In this regards, the linear Lagrangian bias b_ν predicted by the peak model is exactly the same as that returned by the peak-background split argument⁸.

The peak velocity $\mathbf{v}_{\text{pk}}(\mathbf{x})$ as defined in Eq.(2) is consistent with the assumption that initial density peaks move locally with the dark matter. However, the 3-dimensional velocity dispersion of peaks is smaller than that of the mass σ_{-1} , i.e. $\sigma_{\text{vpk}}^2 = \sigma_{-1}^2(1 - \gamma_0^2)$ with $\gamma_0 = \sigma_0^2/\sigma_{-1}\sigma_1$, because large-scale flows are more likely to be directed towards peaks than to be oriented randomly¹. As shown in⁸, this leads to a k -dependence of the peak velocities as can be seen upon taking the divergence of $\mathbf{v}_{\text{pk}}(\mathbf{x})$ and Fourier transforming it,

$$\theta_{\text{pk}}(\mathbf{k}) = \left(1 - \frac{\sigma_0^2}{\sigma_1^2} k^2\right) W(k, M) \theta(\mathbf{k}) \equiv b_{\text{vel}}(k) \theta_M(\mathbf{k}), \quad (5)$$

where $\theta \equiv \nabla \cdot \mathbf{v}$ is the mass velocity divergence and $W(k, M)$ is the Fourier transform of the filter. This defines the *statistical* velocity bias $b_{\text{vel}}(k)$. Note that $b_{\text{vel}}(k)$ does not depend on ν and, for the highest peaks, remains scale-dependent even though the spatial bias $b_{\text{pk}}(k)$ has no k -dependence in this limit.

3 Redshift evolution of the peak correlation

Pairwise motions induced by gravitational instabilities will distort the primeval peak correlation. The gravitational evolution of the correlation of initial density peaks can be addressed with the Zel'dovich ansatz¹⁴, assuming they behave like test particles moving with the dark matter. In this first order approximation, the gravitationally-evolved peak correlation $\xi_{\text{pk}}(r, z)$ is the Fourier transform of the peak power spectrum⁹

$$P_{\text{pk}}(k, z) = G^2(k, z) [b_{\text{vel}}(k) + b_{\text{pk}}(k, z)]^2 P_M(k, 0), \quad (6)$$

where $b_{\text{pk}}(k, z) = D(z_i)/D(z)b_{\text{pk}}(k)$ and the function

$$G^2(k, z) = \left(\frac{D(z)}{D(0)}\right)^2 e^{-\frac{1}{3}k^2\sigma_{\text{vpk}}^2(z)} \quad (7)$$

is a damping term induced by velocity diffusion. It is similar to the propagator $G_\delta(k, z)$ introduced in⁴, although the latter involves the matter velocity dispersion σ_{-1} . The first term in the square bracket reflects the fact that peaks stream towards (or move apart from) each other in high (low) density environments, but this effect is k -dependent owing to the statistical velocity bias. Therefore, the Eulerian and Lagrangian linear bias parameters are related according to

$$b_\nu^E(z) \equiv 1 + \frac{D(z_i)}{D(z)} b_\nu(z_i), \quad b_\zeta^E(z) \equiv \frac{D(z_i)}{D(z)} b_\zeta(z_i) - \frac{\sigma_0^2}{\sigma_1^2}. \quad (8)$$

The first relation is the usual formula for the Eulerian, linear scale-independent bias¹¹. The second relation shows that b_ζ^E approaches $-\sigma_0^2/\sigma_1^2$ with time.

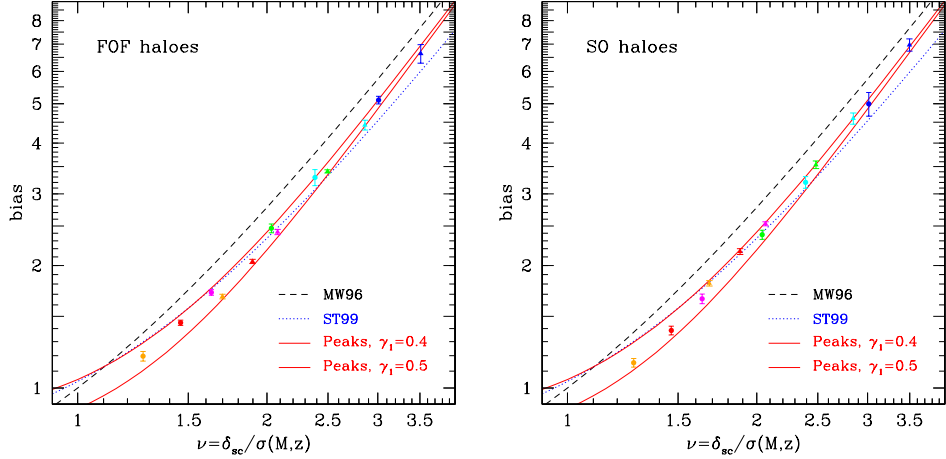


Figure 1: Large-scale bias of dark matter haloes identified with a FOF finder of linking length $b = 0.2$ (left panel) and a SO finder with redshift-dependent overdensity threshold (right panel). Circles and triangles refer to halo samples whose average mass is ~ 1.3 and $5 \times 10^{13} M_\odot/h$, respectively. The dotted and dashed curves are formulae based on the excursion set theory, whereas the solid curves are fits motivated by the peak model.

4 The large-scale bias of dark matter haloes

The large-scale bias contains important information on the abundance and clustering of biased tracers of the density field. To compare theoretical expectations with measurements of dark matter halo bias, I will assume that peaks of height $\nu = \delta_c/\sigma_0(R, z)$ identified in the initial, smoothed density field δ_M are associated with objects of mass M collapsing at redshift z .

The peak model predicts that, for moderate peak height, b_ν^E is significantly smaller than the value $1 + \nu^2/\delta_c$ derived for thresholded regions¹⁰ due to the correlation between the peak height and the peak curvature¹. However, in the limit $\nu \gg 1$, $b_\nu^E(\nu) \approx 1 + (\nu^2 - 3)/\delta_c$ which shows that the evolved linear bias of initial density peaks of height ν indeed converges towards the prediction of¹⁰. This should be compared to well-known expressions derived from the extended Press-Schechter formalism which, in the same limit, evaluate to $b_{\text{MW}}^E(\nu) = 1 + (\nu^2 - 1)/\delta_c$ ¹¹ and $b_{\text{ST}}^E(\nu) \approx 1 + (a\nu^2 - 1)/\delta_c$ ¹². In the latter case, $a = 0.75$ follows from normalising the Sheth-Tormen mass function to N-body simulations. Note that, whereas b_{MW}^E and b_{ST}^E depend only upon the peak height, b_ν^E is a function of both ν and M (through $\gamma_1(M)$).

In Fig. 1, these various predictions are compared with measurements of the linear bias of massive haloes extracted from numerical simulations of structure formation⁷. Error bars show the scatter among various realisations. The measured halo bias appears to depart from the Sheth-Tormen scaling at large ν , in agreement with recent measurements of the halo bias^{2,13}. Furthermore, the data shows evidence for a dependence on M , but the exact magnitude of the effect is sensitive to the halo finder. Because the best choice of filter is a matter of debate, I treat γ_1 as a free parameter and show $b_\nu^E(\nu, \gamma_1)$ for $\gamma_1 = 0.4$ and 0.5 (a Gaussian filter yields $\gamma_1 \approx 0.65$ for the mass range considered), which provide a reasonably good fit to the bias of $\gtrsim 2\sigma$ haloes. Note that the peak expression b_ν^E is also found to match the bias of massive haloes in scale-free cosmologies rather well⁵.

5 Peak biasing and the baryon acoustic oscillation

Having checked that the peak model predicts a large-scale halo bias $b_\nu^E(z)$ consistent with simulations, I consider now the impact of the scale-dependent piece $b_\zeta^E(z)k^2$. The presence of such a term amplifies the contrast of the baryon acoustic oscillation (BAO) in the correlation of initial

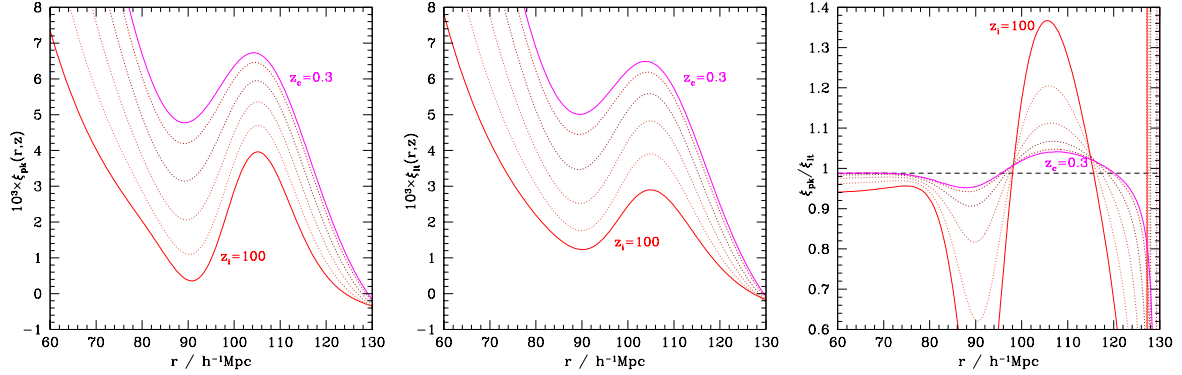


Figure 2: *Left*: Redshift evolution of the baryon acoustic oscillation in the correlation of initial, 2σ density peaks as predicted by Eq.(6). Results are shown at redshift $z = 100, 5, 2, 1, 0.5$ and 0.3 (curves from bottom to top). *Middle*: Same as left panel but for “linear tracers”, for which the correlation simply is $b_\nu^E(z)^2$ times the evolved mass correlation *Right*: The ratio diverges at $r \sim 130 h^{-1}\text{Mpc}$ because zero-crossings do not coincide

density peaks relative to that in the linear theory correlation⁶. Eq.(6) can be used to estimate how much of this effect survives at virialization redshift (a more realistic calculation should include the mode-coupling power).

To emphasise the effect of $b_\zeta^E(z)k^2$, Fig. 2 compares the redshift evolution of the large-scale, 2-point correlation ξ_{pk} of initial density peaks (left) with that of “linear tracers”, ξ_{lt} , for which $P_{\text{lt}}(k, z) \equiv G_\delta^2(k, z)[b_\nu^E(z)]^2 P_M(k, 0)$ (middle). The right panel displays the ratio between the two correlations. Results are shown for 2σ density peaks collapsing at $z_c = 0.3$ and identified on a mass scale $5 \times 10^{13} \text{ M}_\odot/h$ with a Gaussian filter. The relative amplification of the BAO contrast in $\xi_{\text{pk}}(r, z_i)$ induces a scale-dependence in the bias that decays with time owing to the smearing from velocity dispersion. At the collapse redshift however, the model predicts residual scale-dependence across the BAO feature at the 5-10% level (right), a measurement of which in numerical simulations would provide strong support for the validity of the peak approach.

Acknowledgments

I would like to thank the organisers for a very enjoyable meeting.

References

1. J.M. Bardeen, R.J. Bond, N. Kaiser, A.S. Szalay, *Astrophys. J.* **304**, 15 (1986).
2. J.D. Cohn, M. White, *Mon. Not. R. Astron. Soc.* **385**, 2025 (2008)
3. S. Cole, N. Kaiser, *Mon. Not. R. Astron. Soc.* **237**, 1127 (1989).
4. M. Crocce, R. Scoccimarro, *Phys. Rev. D* **73**, 3519 (2006).
5. N. Dalal, M. White, R.J. Bond, A. Shirokov, *Astrophys. J.* **687**, 12 (2008).
6. V. Desjacques, *Phys. Rev. D* **78**, 3503 (2008).
7. V. Desjacques, U. Seljak, I.T. Iliev, *Mon. Not. R. Astron. Soc.* **396**, 85 (2009).
8. V. Desjacques, R.K. Sheth, *Phys. Rev. D* **81**, 3526 (2010).
9. V. Desjacques et al., in preparation (2010).
10. N. Kaiser, *Astrophys. J.* **284**, L9 (1984).
11. H.J. Mo, S.D.M. White, *Mon. Not. R. Astron. Soc.* **282**, 347 (1996).
12. R.K. Sheth, G. Tormen, *Mon. Not. R. Astron. Soc.* **308**, 119 (1999).
13. J.L. Tinker, B.E. Robertson, A.V. Kravtsov, A. Klypin, M.S. Warren, G. Yepes, S. Gottlöber, arXiv:1001.3162
14. Ya.B. Zel'dovich, *Astron. Astrophys.* **5**, 84 (1970)

NEUTRINOS IN THE INTERGALACTIC MEDIUM

MATTEO VIEL

*INAF - Osservatorio Astronomico di Trieste, Via G.B. Tiepolo 11, I-34131 Trieste, Italy
INFN/National Institute for Nuclear Physics, Via Valerio 2, I-34127 Trieste, Italy*

In this talk I will present a numerical modelling of the matter power spectrum at high redshift using full hydrodynamical simulations that incorporate neutrinos in two different ways: either as a set of (fast-moving) particles or by solving the gravitational potential on a particle-mesh grid. I will focus in particular on the mildly non-linear regime probed by Lyman- α forest observations ($z = 2 - 4$ and scales of the order of tens of Mpc). Moreover, I will quantify the impact that neutrinos have on the most relevant quantity, namely the Lyman- α 1D flux power spectrum that probes intergalactic medium (IGM) structures and that at present provides the tightest constraint on the quantity Σm_ν .

1 Introduction

The Lyman- α forest, the absorption of neutral hydrogen along the line-of-sight to distant quasars, is a powerful cosmological tool. Measurements of the matter power spectrum from Lyman- α forest data extend to smaller scales ($\sim 1 - 80$ comoving Mpc) and probe a redshift range ($z = 2 - 4$) complementary to estimates of the matter power spectrum from Cosmic Microwave Background (CMB), galaxy surveys or weak gravitational lensing observations (for a review see^{1,2}). At present the tightest constraints (2σ upper limit) is provided by a combination of large scale structure data set where the most important probe is the SDSS Lyman- α flux power spectrum³ and gives $\Sigma m_\nu < 0.17$ eV⁴. Very important constraints can be achieved also on the coldness of cold dark matter using a combination of high and low resolution data and state-of-the-art simulations^{5,6,7}. While linear theory is sufficient to quantify the impact of neutrinos on large scales and on the cosmic microwave background, the non-linear evolution of density fluctuations has to be taken into account on smaller scales at lower redshift. A range of numerical studies of the effect of neutrinos on the distribution of (dark) matter has been performed some while ago (e.g.⁸ and references therein) with a renewed interest in the last couple of years^{9,10}. These numerical studies of the non-linear evolution have been complemented by analytical estimates based on the renormalization group time-flow approach perturbation theory or the halo model¹¹. The use of Lyman- α forest data for accurate measurements of the matter power spectrum benefits tremendously from the careful modeling of quasar absorption spectra with hydrodynamical simulations (e.g. ^{12,13}). No such modeling has yet been performed including the effect of neutrinos on the matter power and here I will present results of the modeling of Lyman- α forest data in the non-linear regime including the effect of neutrinos by using a modified version of the hydrodynamical code GADGET-3. The results summarized in this talk could be found in this recent paper by Viel, Haehnelt & Springel (2010)¹⁴.

2 Numerical Hydrodynamic Modelling of Neutrinos

We use the hydrodynamical TreePM-SPH (Tree Particle Mesh-Smoothed Particle Hydrodynamics) code GADGET-3, which is an improved and extended version of the code described in Ref.⁷. We have modified the code in order to simulate the evolution of the neutrino density distribution. The neutrinos are treated as a separate collisionless fluid, just like the dark matter. In order to save computational time, most of our simulations assume however that the clustering of neutrinos on small scales is negligible and the short-range gravitational tree force in GADGET's TreePM scheme is not computed for the neutrino particles. This means that the spatial resolution for the neutrino component is only of order the grid resolution used for the PM force calculation, while it is about an order of magnitude better for the dark matter, star and gas particles calculated with the Tree algorithm (gravitational soft. 4 com. kpc/h). We also implemented memory savings such that the number of neutrino particles can be made (significantly) larger than the number of dark matter particles, which helps to reduce the Poisson noise present in the sampling of the (hot) neutrino fluid. In the grid based implementation the power spectra of the neutrino density component is interpolated in a table produced via CAMB of one hundred redshifts in total spanning logarithmically the range $z = 0 - 49$. The gravitational potential is calculated at the mesh points and the neutrino contribution is added when forces are calculated by differentiating this potential. We have checked that we have reached convergence with this number of power spectrum estimates and also explicitly checked that increasing the linear size of the PM grid by a factor two has an impact below the 1% level on the total matter power for the wavenumbers $k < 10h/\text{Mpc}$. For the grid simulations the starting redshift has been chosen as $z = 49$, well in the linear regime. Power spectra are computed for each component separately (gas, dark matter, stars and neutrinos), as well as for the total matter distribution. The results presented refer to a 60 comoving Mpc/h box with 3×512^3 gas+neutrinos+dark matter particles. The PM grid is chosen to be of 512^3 mesh points. Tests have been made to test resolution, dependence on initial redshift, velocities in the initial conditions, different matter content etc. (see¹⁴).

3 Results in Terms Matter and Flux Power Spectra

In Figure 1, we compare the non-linear power spectra from the numerical simulations with the results predicted by linear theory, shown as thick curves. The suppression of the matter power spectrum increases with increasing Σm_ν (recall that these simulations are normalized at the CMB scale). Note the plateau of constant suppression predicted by linear theory, which is approximately described by $\Delta P/P \sim -8 f_\nu$, and depends only very weakly on redshift. Linear theory provides a good description of the matter power spectrum at $z = 2 - 4$ up to scales of about $k \sim 0.4 h/\text{Mpc}$, and the agreement is more accurate for the smaller neutrino masses. The non-linear matter power spectrum does, on the other hand, depend strongly on redshift and the dependence on scale becomes steeper with decreasing redshift. For $\Sigma m_\nu = 0.6 \text{ eV}$, a good fit to the suppression at $z = 3$ in the range that deviates from linear theory, $k (h/\text{Mpc}) \in [0.3, 3]$, is given by $P_{f_\nu}/P_{f_\nu=0} = T_\nu(k) \propto \log_{10}(k)^{-0.15, -0.11, -0.08}$ at $z = 2, 3, 4$, respectively; while for $\Sigma m_\nu = 0.3 \text{ eV}$, we find $T_\nu(k) \propto \log_{10}(k)^{-0.08, -0.06, -0.04}$ at the same redshifts. We also note that the maximum reduction of power shifts to larger scales with decreasing redshift.

The maximum of the non-linear suppression can be described by $\Delta P/P \sim -10.5 f_\nu$ (green thick curves in Fig. 1) for neutrino masses $\Sigma m_\nu = 0.15, 0.3, 0.6 \text{ eV}$, respectively. For the most massive case we considered the suppression is about $\Delta P/P \sim -9 f_\nu$. Our results differ somewhat from those of Ref.⁹, who reported $\Delta P/P \sim -9.8 f_\nu$ (at $z = 0$) while we measure $\Delta P/P \sim -9.5 f_\nu$, apart from the most massive case in which the suppression is smaller, $\Delta P/P \sim -8 f_\nu$. We must remind, however, that the above linear approximation starts to break down for

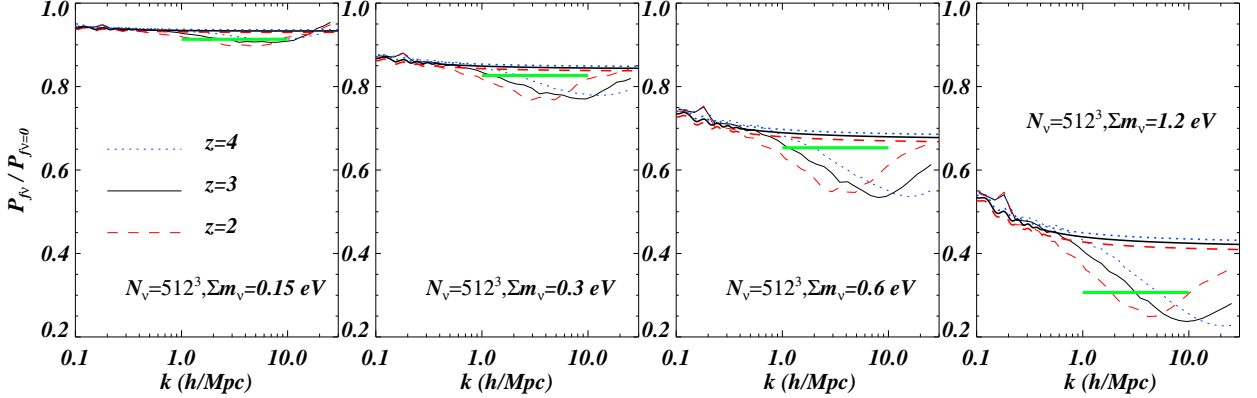


Figure 1: Effect of different f_ν on the matter power and comparison with linear prediction. Ratio between matter power spectra for simulations with and without neutrinos for four different values of the neutrino mass, $\Sigma m_\nu = 0.15, 0.3, 0.6, 1.2$ eV, from left to right. Different line-styles refer to different redshifts: $z = 2$ (red dashed), $z = 3$ (black continuous) and $z = 4$ (blue dotted). Linear theory is shown as the thick curves. An estimate of the overall suppression based on the hydrodynamical simulations is shown as a thick short green line, $\Delta P/P \sim -10.5 f_\nu$.

large neutrino masses and is already very poor for $\Sigma m_\nu = 1$ eV (e.g. ¹¹).

We show the measured flux power spectra for our different simulations in Figure 2. Note that the results have not been smoothed. We recall that the useful range of high resolution spectra reaches to $k = 0.03$ s/km while we can reach to $k \sim 0.018$ s/km with low-resolution SDSS spectra. We are here primarily interested in quantifying the effects over this range of wavenumbers. For $\Sigma m_\nu = 0.15$ eV, the only effect of neutrinos on the flux power is a $< 5\%$ suppression at $z = 4$. As expected the effect becomes larger with increasing neutrino mass. At the largest scales the flux power in the simulations with neutrinos is suppressed by 5, 7 and 15% for $\Sigma m_\nu = 0.3, 0.6$ and 1.2 eV, respectively. There is some dependence of the suppression on wavenumber with an upturn at small scales of about 0.01 s/km and a bump at $k \sim 0.05$ s/km.

4 Conclusions

We presented a suite of full hydrodynamical cosmological simulations that quantitatively address the impact of neutrinos on the (mildly non-linear) spatial distribution of matter and in particular on the neutral hydrogen distribution in the IGM, which is responsible for the intervening Lyman- α absorption in quasar spectra. The free-streaming of neutrinos results in a (non-linear) scale-dependent suppression of power spectrum of the total matter distribution at scales probed by Lyman- α forest data which is larger than the linear theory prediction by about 25 % and strongly redshift dependent. By extracting a set of realistic mock quasar spectra, we quantify the effect of neutrinos on the flux probability distribution function and flux power spectrum. The differences in the matter power spectra translate into a $\sim 2.5\%$ (5%) difference in the flux power spectrum for neutrino masses with $\Sigma m_\nu = 0.3$ eV (0.6 eV). This rather small effect is difficult to detect from present Lyman- α forest data and nearly perfectly degenerate with the overall amplitude of the matter power spectrum as characterised by σ_8 . If the results of the numerical simulations are normalized to have the same σ_8 in the initial conditions, then neutrinos produce a smaller suppression in the flux power of about 3% (5%) for $\Sigma m_\nu = 0.6$ eV (1.2 eV) when compared to a simulation without neutrinos. If we implement the results obtained we can get constraints on neutrino masses using the Sloan Digital Sky Survey flux power spectrum alone and we find an upper limit of $\Sigma m_\nu < 0.9$ eV (2σ C.L.), comparable to constraints obtained from the cosmic microwave background data or other large scale structure probes.

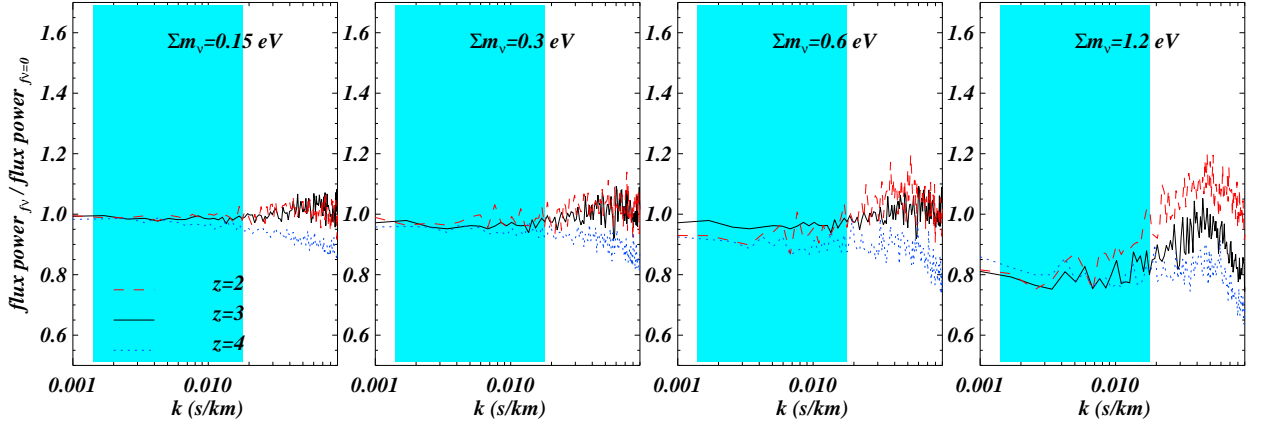


Figure 2: Effect of f_ν on the flux power spectrum. Ratio between flux power spectra with and without neutrinos as a function of wavenumber in s/km. Four different cases are presented with $\Sigma m_\nu = 0.15, 0.3, 0.6, 1.2$ eV, from left to right. Different line-styles refer to different redshifts: $z = 2$ (red dashed), $z = 3$ (black continuous), and $z = 4$ (blue dotted). The shaded area indicates the range of wavenumbers probed by the SDSS flux power spectrum.

Acknowledgments

I am partly supported by ASI/AAE, INFN-PD51 and a PRIN by MIUR. Numerical computations were performed using the COSMOS Supercomputer in Cambridge (UK), sponsored by SGI, Intel, HEFCE and the Darwin Supercomputer of the University of Cambridge High Performance Computing Service, provided by Dell Inc. using Strategic Research Infrastructure Funding from the Higher Education Funding Council for England. Part of the analysis has been performed at CINECA with a Key project on the intergalactic medium obtained through a CINECA/INAF grant. I wish to thank my collaborators on the topic presented here: M.G. Haehnelt and V. Springel.

References

1. H. Bi, A.F. Davidsen *Astrophysical Journal*, **479**, 523 (1997)
2. A.A. Meiksin, 2009, *Reviews of Modern Physics*, **81**, 1405
3. P. McDonald *et al.*, *ApJ*, **635**, 761 (2005).
4. U. Seljak, A. Slosar, P. McDonald, *JCAP*, **10**, 14, (2006)
5. M. Viel, J. Lesgourgues, M. G. Haehnelt, S. Matarrese and A. Riotto, *PRD*, **71**, 063534 (2005).
6. M. Viel, J. Lesgourgues, M. G. Haehnelt, S. Matarrese, A. Riotto, *Phys. Rev. Lett.*, **97**, 071301 (2006)
7. M. Viel *et al.* *Phys. Rev. Lett.*, **100**, 041304 (2008)
8. C.-P. Ma, E. Bertschinger, *ApJ*, **429**, 22, (1994)
9. J. Brandbyge, S. Hannestad, T. Haugbølle, B. Thomsen, *JCAP* **8**, 20 (2008)
10. J. Brandbyge, S. Hannestad, *JCAP*, **5**, 2 (2009)
11. J. Lesgourgues, S. Pastor, *Physics Reports*, **429**, 307 (2006)
12. M. Viel, M. G. Haehnelt and V. Springel, *MNRAS*, **354**, 684 (2004).
13. M. Viel and M. G. Haehnelt, *MNRAS*, **365**, 231 (2006).
14. M. Viel, M. G. Haehnelt and V. Springel, submitted to *JCAP* arXiv:1003.2422 (2010).
15. V. Springel, *MNRAS*, **364**, 1105 (2005);

WEIGHING NEUTRINOS WITH THE LARGEST PHOTOMETRIC REDSHIFT SURVEY: MEGAZ DR7

S.A. THOMAS, F.B. ABDALLA & O. LAHAV

Department of Physics and Astronomy, University College London, Gower Street, London, WC1E 6BT

We present a new upper limit of $\sum m_\nu \leq 0.28$ eV (95% CL) on the sum of the neutrino masses assuming a flat Λ CDM cosmology. This relaxes slightly to $\sum m_\nu \leq 0.34$ and $\sum m_\nu \leq 0.47$ when quasi non-linear scales are removed and $w \neq -1$, respectively. These bounds are derived from a new photometric redshift catalogue of over 700,000 Luminous Red Galaxies (MegaZ DR7) with a volume of $3.3 (\text{Gpc } h^{-1})^3$, extending over the redshift range $0.45 < z < 0.65$ and up to angular scales of $\ell_{\text{max}} = 300$. The data are combined with WMAP 5 CMB fluctuations, Baryon Acoustic Oscillations, type 1a Supernovae and an HST prior. This is the first combined constraint from a photometric redshift catalogue with other cosmological probes. The upper limit is also one of the tightest and ‘cleanest’ constraints on the neutrino mass from cosmology or particle physics. Furthermore, if the aforementioned bounds hold, they all predict that next generation neutrino experiments, such as KATRIN, are unlikely to obtain a detection.

1 Introduction

Studies of the neutrino have traditionally been the realm of particle physics experiments with bounds placed on the splitting *between* the neutrino mass eigenstates from solar, accelerator and atmospheric experiments¹. However, currently both the absolute scale and the hierarchy of the masses remain hidden. KATRIN, a kinematic beta decay experiment², aims to provide a constraint in the future.

Cosmology not only probes the absolute mass scale of the neutrino but is a completely independent method. A cosmological constraint on the sum of the neutrino masses is primarily a constraint on the relic Big-Bang neutrino density Ω_ν . One can relate this density to the sum of the mass eigenstates $\sum m_\nu$ as given by,

$$\Omega_\nu = \frac{\sum m_\nu}{93.14 \text{h}^2 \text{eV}}. \quad (1)$$

The direct effects of the neutrinos depend on whether they are relativistic, non-relativistic and the scale under consideration. Neutrinos have a large thermal velocity as a result of their low mass and subsequently erase their own perturbations on scales smaller than the *free streaming* length. This subsequently contributes to a suppression of the statistical clustering of galaxies over small scales and can be observed in a galaxy survey. The abundance of neutrinos in the Universe can also have a *direct* effect on the primary CMB anisotropies if non-relativistic before the time of decoupling. However, one of the most clear effects at this epoch is a displacement in the time of matter-radiation equality. All these cosmological effects can be used to impose bounds on the neutrino mass.

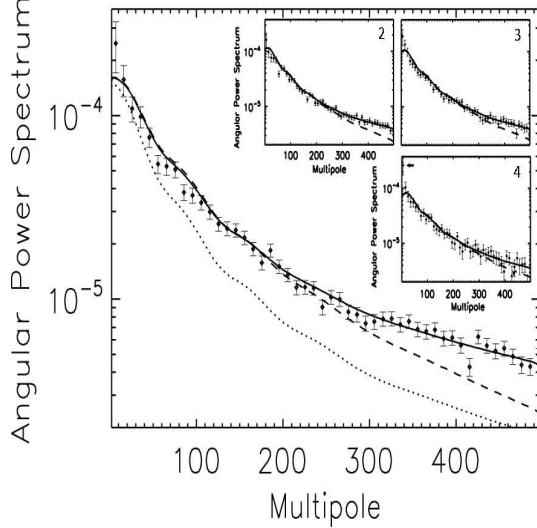


Figure 1: The best fit angular power spectra C_ℓ in the combined analysis (solid lines) are plotted over the MegaZ DR7 data. The panels relate to four redshift bins with width $\Delta z = 0.05$ from $z = 0.45$ (main panel) to $z = 0.65$ (panel 4). The fit is also plotted for linear spectra (dashed lines). The dotted line demonstrates the effect of introducing $\sum m_\nu = 1$ eV neutrinos with all parameters, except Ω_c , held fixed.

In ³ we utilise the *new* SDSS MegaZ LRG DR7 galaxy clustering data that we produce in ⁴ to provide the first photometric galaxy clustering constraint on the neutrino. With an almost comprehensive combination of probes this renders one of the tightest constraints on the neutrinos in cosmology and therefore physics. We assume a flat Universe with Gaussian and adiabatic fluctuations and a constant spectral index. The effective number of neutrinos are fixed to $N_{\text{eff}} = 3.04$. The constant dark energy equation of state is at first set to $w = -1$ and later relaxed. Finally, we consider the neutrinos to be mass degenerate given that current inferred bounds are much greater than the splitting hierarchies.

2 Analysis

Although parameter degeneracies and a mild insensitivity to relativistic neutrinos limit the upper bound one can place on $\sum m_\nu$ with the CMB its high statistical discrimination of the remaining cosmological model facilitates a competitive combination of probes. We therefore start by using the latest 5-year WMAP data and likelihood⁵ to vary seven Λ CDM parameters: $\Omega_b h^2$, $\Omega_c h^2$, Ω_Λ , n_s , τ , $\ln(10^{10} A_s)$ and A_{SZ} , in addition to $\sum m_\nu$. τ , n_s and A_s are defined at $k = 0.002/\text{Mpc}$. The contributions from the Sunyaev-Zeldovich fluctuations are included with the pre-factor A_{SZ} and is allowed to vary as $0 < A_{\text{SZ}} < 2$ ⁵.

Our CMB run yields $\sum m_\nu < 1.271$ eV at the 95% confidence level consistent with⁶. This bound implies the neutrinos were relativistic at decoupling and as such induces a degeneracy between the neutrino masses and Ω_m as well as h . This can be seen in Figure 2 and⁶. This degeneracy can be improved by adding supernovae data from the first year Supernova Legacy Survey and the BAO data from⁷. Our analysis for WMAP + SNe + BAO gives $\sum m_\nu < 0.695$ eV (95% CL) similar to⁶ ($\sum m_\nu < 0.67$ eV).

In order to go beyond such studies we include the MegaZ LRG (DR7) *photometric* redshift survey that will be presented in³, which we have checked to be compatible with earlier SDSS clustering and photo-z analyses⁸. This adds galaxy clustering information that is sensitive to the growth of structure suppressed by the free streaming neutrinos. The SDSS colours provide reliable photometric redshift estimates and, due to their high luminosity, probe a large region of

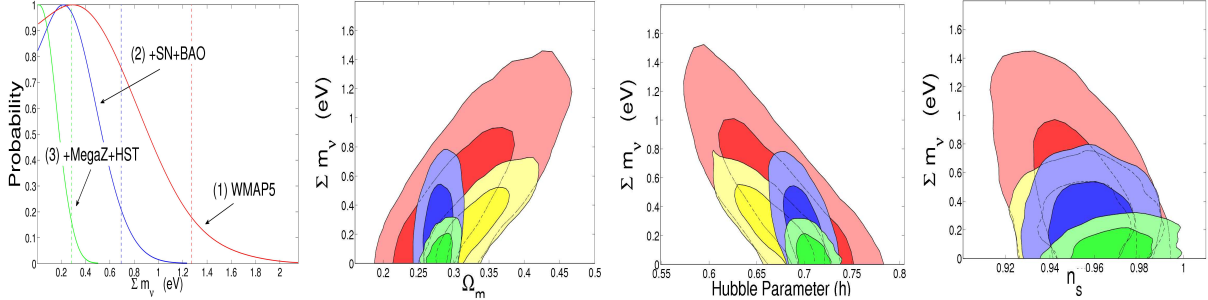


Figure 2: *Left Panel*: The marginalised 1D distribution for the neutrino from three incrementally combined analyses. The vertical dashed lines correspond to 95% CL. *Other Panels*: 68% and 95% marginalised distributions for Ω_m , h and n_s against the total neutrino masses. The contours correspond to (from bottom layer) WMAP-only (red/dark), WMAP+MegaZ (yellow/light), WMAP+SNe+BAO (blue/dark) and WMAP+SNe+BAO+MegaZ+HST (green/light).

cosmic volume. Encapsulating 7746 deg^2 , we utilise 723,556 photometrically determined LRGs in four redshift bins of width $\Delta z = 0.05$ between $0.45 < z < 0.65$ in a spherical harmonic analysis of the galaxy distribution until a maximum multipole $\ell_{max} = 300$. Specifically we use the angular power spectrum defined as,

$$C_\ell \equiv \langle \delta^{2D} \delta^{*2D} \rangle = 4\pi \int \Delta^2(k) W_\ell^2(k) \frac{dk}{k}. \quad (2)$$

where $\Delta^2(k)$ is the dimensionless power spectrum calculated with CAMB. The matter distribution is projected onto a plane in the sky with weight $W_\ell^2(k)$ described by both $W_\ell(k) = \int f(z) j_\ell(kz) dz$ and $f(z) = n(z) D(z) (\frac{dz}{dx})$, with the spherical Bessel function $j_\ell(kz)$, the linear growth factor $D(z)$ and the normalised redshift distribution $n(z)$. The effects of redshift space distortions are included. The likelihood combines the four measured redshift bins and includes the full covariance as a result of photometric errors scattering galaxies between bins and therefore correlating slices. There are four additional parameters included in the study as a result of the galaxy bias in each bin (b_1 , b_2 , b_3 and b_4), i.e. modestly accounting for the redshift dependence. Despite the non-linear contribution becoming significant only at scales $\ell > 300$ we use HALOFIT to model the non-linear power spectrum.

This survey is not only one of the largest to date but is one of the most competitive available. However, these power spectra provide an additional incentive for this combined measurement. This because the BAOs, which were shown to be so advantageous before, can be used in conjunction to MegaZ with no cross-covariance. The BAO data is extracted at $z = 0.2$ and $z = 0.35$, whereas MegaZ is defined at a higher redshift. They therefore constitute independent data.

By combining the MegaZ LRGs as described above with the previous CMB, SNe and BAO data we find a significantly lower bound of $\sum m_\nu < 0.325 \text{ eV}$ at 95% CL. Again, this is roughly a factor 2 improvement in the neutrino masses with the addition of the LRGs and is shown clearly against Ω_m , h and the 1D marginalised distribution in Figure 2.

The information on the growth of structure is paramount to the improvement seen in this study. However, part of this information originates from the quasi-non-linear regime. We repeat the combined analysis with the smaller scales removed. By truncating the multipoles at $\ell_{max} = 200$ this more conservative approach is seen to give a similar but slightly relaxed limit of $\sum m_\nu < 0.393 \text{ eV}$. While this highlights the importance of understanding non-linearities for obtaining the most stringent constraints, it is reassuring that there is still a marked improvement on the previous study (CMB+SNe+BAO) with linear LRGs.

It is also intriguing to compare the input of the LRGs to those of the two distance measures (SNe+BAO). We therefore perform a joint analysis using just the WMAP5 and LRG data, subsequently obtaining the limit $\sum m_\nu < 0.651 \text{ eV}$ at 95% CL. This is comparable to the *spec-*

$\sum m_\nu$ (95% CL)	Analysis
< 1.271 eV	WMAP5
< 0.695 eV	WMAP5 + SNe + BAO
< 0.651 eV	WMAP5 + MegaZ
< 0.344 eV	WMAP5 + SNe + BAO + MegaZ _(ℓ_{200}) + HST
< 0.281 eV	WMAP5 + SNe + BAO + MegaZ + HST
< 0.491 eV	WMAP5 + SNe + BAO + MegaZ _(ℓ_{200}) + HST
< 0.471 eV	WMAP5 + SNe + BAO + MegaZ + HST

Table 1: A summary of the bounds placed³ on $\sum m_\nu$. ℓ_{200} corresponds to the truncation in the maximum multipole scale. The top constraints are for $w = -1$; the bottom for $w \neq -1$, marginalised over.

troscopic DR7 galaxy clustering addition to the CMB in⁹ with $\sum m_\nu < 0.62$ eV and illustrates the development of photometric surveys as a competitive tool for the future.

We conclude by further restricting the parameter space with the addition of the new HST prior¹⁰ on h to the WMAP5 + SNe + BAO + MegaZ DR7 run. With this the final limit is reduced to $\sum m_\nu < 0.28$ eV. This is one of the tightest constraints in the literature. The angular power spectra C_ℓ corresponding to the best fit values are plotted in Figure 1 with the galaxy clustering data. An overview of all the neutrino bounds are displayed in Table 1. For $w \neq -1$ the tighter bound relaxes slightly to $\sum m_\nu < 0.47$ eV. We note that biasing *could* act to mimic the neutrino signature over smaller scale analyses. As a gauge of this effect we implement, as an example, the ‘Q-model’¹¹; resulting in a combined constraint (all data) of $\sum m_\nu < 0.44$ eV.

3 Conclusions

Using the biggest ever large scale structure survey we have set bounds on the neutrino masses at $\sum m_\nu < 0.28$ eV ($\ell_{\max} = 300$) and $\sum m_\nu < 0.34$ eV ($\ell_{\max} = 200$) at 95% CL, when combined with WMAP5+SNes+BAO+HST data. This is the first ever determination of neutrino masses from a photometric galaxy redshift survey. Not only have we shown that photometric redshifts can be used for this problem, but also that such a galaxy survey is competitive with all currently available geometric probes (SNe+BAO) or spectroscopic clustering when added to the CMB. Our constraint is one of the tightest current bounds available without the use of data from Lyman- α ¹², which is prone to systematics. Further, all our results show that KATRIN’s projected 90% sensitivity ($\sum m_\nu < 0.6$ eV) leaves an unlikely neutrino mass detection.

References

1. T. Schwetz, *et al.*, New Journal of Physics. **10** 113011 (2008)
2. J. Wolf, *et al.*, [arXiv:astro-ph/0810.3281].
3. S.A. Thomas, F.B. Abdalla and O. Lahav., Submitted [arXiv:astro-ph/0911.5291].
4. S.A. Thomas, F.B. Abdalla and O. Lahav., In Prep.
5. J. Dunkley, *et al.*, ApJS **180** 306-329 (2008)
6. E. Komatsu, *et al.*, ApJS **180** 330-376 (2009)
7. W. Percival, *et al.*, MNRAS **381** 1053-1066 (2007)
8. C. Blake, *et al.*, MNRAS **374** 1527-1548 (2007)
9. B. Reid, *et al.*, Submitted [arXiv:astro-ph/0907.1659].
10. A.G. Riess, *et al.*, ApJ **699** 539-563 (2009)
11. S. Cole, *et al.*, MNRAS **362** 505-534 (2005)
12. U. Seljak, *et al.*, JCAP **10** 14 (2006)

Minimally Parametric Constraints on the Primordial Power Spectrum from Lyman-alpha

Simeon Bird

Institute of Astronomy and Kavli Institute for Cosmology, University of Cambridge, Cambridge, UK

Current analyses of the Lyman-alpha forest assume that the primordial power spectrum of density perturbations obeys a simple power law, a strong theoretical assumption which should be tested. Employing a large suite of numerical simulations which drop this assumption, we reconstruct the shape of the primordial power spectrum using Lyman-alpha data from the Sloan Digital Sky Survey (SDSS). Our method combines a minimally parametric framework with cross-validation, a technique used to avoid over-fitting the data. Future work will involve predictions for the upcoming Baryon Oscillation Sky Survey (BOSS), which will provide new Lyman-alpha data with vastly decreased statistical errors.

1 Introduction

The Lyman- α forest is the name given to a series of absorption lines in quasar spectra, caused by the scattering of photons via interaction with neutral hydrogen at redshifts 2 – 4. At these redshifts, a large proportion of the baryon density of the universe is contained within hydrogen clouds. Most of the hydrogen is ionized, but a small fraction remains neutral, and absorbs photons via the Lyman- α transition. Hence, the Lyman- α forest is sensitive to the matter power spectrum on scales of a few Mpc, making it the only currently available probe of fluctuations at these weakly non-linear scales. A number of authors have examined the constraints obtainable from the Lyman- α forest in the past, including Croft et al¹, Gnedin & Hamilton², Viel, Haehnelt & Springel³.

Previous analyses of constraints from the Lyman- α forest have assumed that the primordial power spectrum is described by a nearly scale-invariant power law. This deserves further attention for a number of reasons. First, it is a strong assumption; if the data are inconsistent with it, derived constraints could be biased to some extent. Second, it is a generic prediction of inflationary models; hence, any test of a power law primordial power spectrum which cannot be attributed to data systematics is a test of inflation. Third, of all current datasets, the Lyman- α constrains the smallest cosmological scales; thus, it provides the best opportunity presently available to understand the overall shape of the power spectrum. To do this, we shall reconstruct the primordial power spectrum in a minimally parametric way, using a technique called cross-validation to robustly recover the signal. If the data are in agreement with theoretical expectations, the recovered power spectrum will be nearly scale-invariant. In these Proceedings, we discuss a minimally parametric framework for constraining the primordial matter power spectrum, the cross-validation technique, and the methodology for obtaining constraints from observations. Finally, some preliminary results are presented.

2 Flux Power Spectrum

In the case of Lyman- α , the observable is not a direct measurement of the clustering properties of tracer objects, as in galaxy clustering, but the statistics of absorption along a number of quasar sightlines. It is easiest to work with the statistics of the flux, \mathcal{F} , defined as

$$\mathcal{F} = \exp(-\tau), \quad (1)$$

where τ is the optical depth. The primary observable here is the one dimensional flux power spectrum, P_F ,

$$P_F(k) = |\tilde{\mathcal{F}}(k)|^2, \quad (2)$$

where $\tilde{\mathcal{F}}$ is the Fourier transform of the flux, evaluated as a function of distance along the line of sight,

$$\tilde{\mathcal{F}}(k) = \int \mathcal{F}(x) e^{ikx} dx. \quad (3)$$

Current constraints on P_F are given by McDonald et al⁴, determined from ~ 3000 SDSS quasar spectra.

In order to simulate the observable flux power spectrum from a given set of primordial fluctuations, a large N -body simulation is required. This makes it impractical to directly calculate P_F for every possible set of input parameters; instead simulations are run for a representative sample. Other results are obtained via interpolation, using the following scheme of Viel & Haehnelt⁵. The flux power spectrum is assumed to be given by a Taylor expansion around some best-fit model. For a vector of parameters p_i , with best-fit model parameters p_i^0 , the flux power spectrum P_F is given by

$$P_F(p_i) = P_F(p_i^0) + \Sigma_i (p_i - p_i^0) \frac{\partial P_F}{\partial p_i} + \Sigma_i (p_i - p_i^0)^2 \frac{\partial^2 P_F}{\partial p_i^2}. \quad (4)$$

Numerical simulations are used to calculate the derivatives of the flux power spectrum. Each parameter is varied independently, and the total change in the flux power spectrum is assumed to be a linear combination of the change due to each parameter, i.e.,

$$\delta P_F = \frac{\delta P_F}{\delta p_1} \delta p_1 + \frac{\delta P_F}{\delta p_2} \delta p_2 + \dots \quad (5)$$

Figure 1 shows the error due to this approximation for a sample input primordial power spectrum. The error is around 1% on scales probed by current Lyman- α data ($k = 0.4 - 2 h \text{ Mpc}^{-1}$), which is a small contribution to the total error, allowing us to proceed with confidence. Further checks on interpolation errors are in progress, and are expected to give similar results.

3 Power Spectrum Reconstruction

Previous analyses of the Lyman- α forest^{3,8} have assumed the primordial power spectrum is a nearly scale-invariant power law, of the form

$$P(k) = A_s \left(\frac{k}{k_0} \right)^{n_s - 1}. \quad (6)$$

As discussed above, we seek to test whether the data supports this assumption by reconstructing the power spectrum with smoothing splines^a, as proposed in Sealfon et al⁶. Smoothing splines are used because they have good continuity properties and are particularly suited to formulation of a cross-validation penalty.

^aSplines are piecewise cubic polynomials with globally continuous first and second derivatives, completely specified by their values at a series of knots, where the polynomials meet.

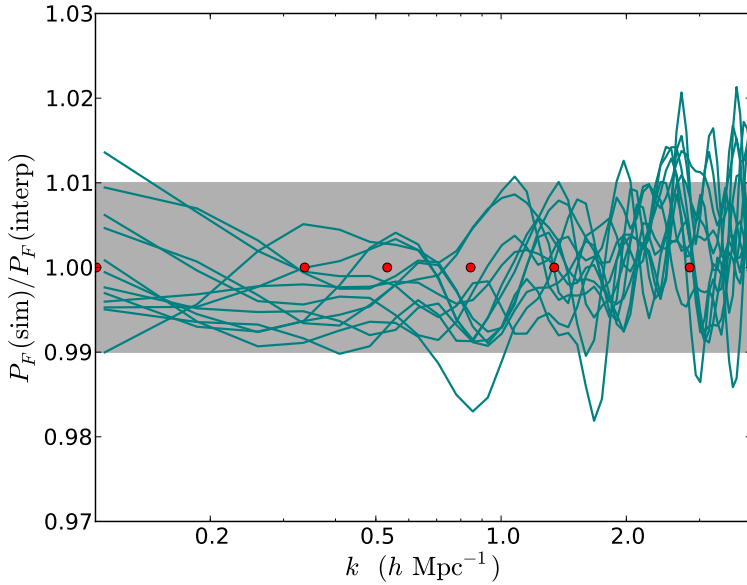


Figure 1: The difference between the flux power spectrum as obtained from interpolation, using Eq. 4, and directly by simulation. Each line represents simulation output at a different redshift bin, between $z = 2.0$ and $z = 4.2$. Red dots show the positions of spline knots. The grey band shows 1% error bars.

4 Cross-Validation

Any minimally parametric formalism, when applied to noisy data, runs the risk of over-fitting the data. One way to avoid this problem is a technique called cross-validation, described in Peiris & Verde⁷. This technique assumes that noise in the data takes the form of additional small-scale structure, and thus power spectra with superfluous fluctuations should be penalised. This penalty is implemented by adding an extra term to the likelihood function, \mathcal{L} :

$$\log \mathcal{L} = \log \mathcal{L}(\text{Data}|P(k)) + \lambda \int_k dk (P''(k))^2. \quad (7)$$

Here λ , the penalty weight, is a free parameter. In the limit $\lambda \rightarrow \infty$ this likelihood becomes functionally identical to linear regression, while $\lambda \rightarrow 0$ is appropriate in the case of noiseless data. In order to determine the optimal value for λ , the data points are first divided into two sets, the training set, or CV1, and the validation set, or CV2. CV1 and CV2 are composed of alternating data bins. Next, to calculate the CV score, a value is chosen for λ , and the best fit power spectrum based on the CV1 dataset is found. The χ^2 is then calculated for this power spectrum with the CV2 dataset. This is repeated, replacing CV1 with CV2 and vice versa, and the CV score is the sum of both χ^2 values.

The key to cross-validation is that signal in the CV1 dataset will predict signal in the CV2 dataset well, while noise in CV1 will predict noise in CV2 poorly. The optimal choice of λ is therefore the one which allows maximal predictivity between CV1 and CV2; in other words, minimizes the CV score.

5 Results

We performed a large grid of N -body simulations using Gadget-II⁹. Convergence checks were carried out to ensure P_F was not significantly affected by simulation settings¹⁰, such as particle

resolution or box size. Initial conditions included a variety of input power spectra, on scales ranging from $k = 0.45 - 2 h \text{ Mpc}^{-1}$.

A significant departure from a power law primordial power spectrum translates to a detectable feature in the flux power spectrum, which is more noticeable at higher redshifts. This is due to the way in which the matter power spectrum evolves: a feature in the matter power spectrum will create extra non-linear growth on smaller scales, making the feature in P_F stand out less. The results of the simulations provide a mapping between primordial and flux power spectra, which in turn provides a likelihood function for any given primordial power spectrum from SDSS data. The full data analysis, including cross-validation, is currently being carried out.

6 Future Prospects

The best constraints on the flux power spectrum currently come from the Sloan Digital Sky Survey (SDSS⁴), which contains ~ 3000 quasar sightlines. In the near future, better constraints will be available from the Baryon Acoustic Oscillation Sky Survey (BOSS¹¹), part of SDSS-III. This will contain 160000 quasar spectra between redshifts of 2.2 and 3, and should further increase the statistical power of the Lyman- α forest. We plan to make forecasts for BOSS in forthcoming work¹².

7 Acknowledgements

I thank my collaborators in this work, Hiranya Peiris, Matteo Viel and Licia Verde, for useful discussions. I am supported by STFC and by Pembroke College Cambridge. This work was performed using the Darwin Supercomputer of the University of Cambridge High Performance Computing Service (<http://www.hpc.cam.ac.uk/>), provided by Dell Inc. using Strategic Research Infrastructure Funding from the Higher Education Funding Council for England.

References

1. Croft R.A.C., Weinberg D. H., Bolte M., Burles S., Hernquist L., Katz N., Kirkman D., Tytler D., 2002, ApJ, 581, 20
2. Gnedin N.Y., Hamilton A.J.S., 2002, MNRAS, 334, 107
3. Viel M., Haehnelt M.G., Springel V., 2004, MNRAS, 354, 684
4. McDonald P., Seljak U., Burles S., et al, 2006, Ap. J. Suppl., 163, 80-109
5. Viel M., Haehnelt M.G., 2006, MNRAS, 365, 231-244
6. Sealfon C., Verde L., Jimenez R., 2005, PRD 72, 103520
7. Peiris H., Verde L., 2008, JCAP 0807:009
8. McDonald P., Seljak U., Cen R., Shih D. et al, Ap.J. 635 761-78
9. Springel V., 2005, MNRAS, 364 1105-1134, astro-ph/0505010
10. Heitmann K., White M., Wagner C., Habib S., Higdon D, 2010, Ap.J 715, 104-121
11. SDSS collaboration, see Sec. 3 of <http://www.sdss3.org/collaboration/description.pdf>
12. Bird S., Peiris H., Viel M., Verde L., in preparation

IS THE 2MASS DIPOLE CONVERGENT?

Michał CHODOROWSKI & Maciej BILICKI

*N. Copernicus Astronomical Center,
Bartycka 18, 00-716 Warsaw, Poland*

Gary A. MAMON

*Institut d'Astrophysique de Paris (UMR 7095: CNRS & UPMC),
98 bis Bd Arago, F-75014 Paris, France*

Thomas JARRETT

*Spitzer Science Center, California Institute of Technology,
Pasadena, CA 91125, USA*

We study the growth of the clustering dipole of galaxies from the Two Micron All Sky Survey (2MASS). We find that the dipole does not converge before the completeness limit of the 2MASS Extended Source Catalog, i.e. up to about $300 \text{ Mpc}/h$. We compare the observed growth of the dipole with the theoretically expected, conditional growth for the ΛCDM power spectrum and cosmological parameters constrained by *WMAP*. The observed growth turns out to be within 1σ confidence level of the theoretical one, once the proper observational window of the 2MASS flux dipole is included. For a contrast, if the adopted window is a top hat, then the predicted dipole grows significantly faster and converges to its final value at a distance of about $200 \text{ Mpc}/h$. We study the difference between the top-hat window and the window for the flux-limited 2MASS survey and we conclude that the growth of the 2MASS dipole at effective distances greater than $200 \text{ Mpc}/h$ is only apparent. Eventually, since for the window function of 2MASS the predicted growth is consistent with the observed one, we can compare the two to evaluate $\beta \equiv \Omega_m^{0.55}/b$. The result is $\beta \simeq 0.38 \pm 0.05$, which gives a rough estimate of $\Omega_m \simeq 0.2 \pm 0.1$.

1 Introduction

For more than 20 years now, many attempts have been made to measure the peculiar gravitational acceleration of the Local Group of galaxies (LG). Such a measurement is possible with the use of all-sky galaxy catalogues, under the assumption that visible (luminous) matter is a good tracer of the underlying density field.

The general procedure is to calculate the so-called *clustering dipole* of a galaxy survey, \mathbf{d} , and use it to infer the acceleration of the LG, \mathbf{g} . Within linear theory of gravitational instability, these two quantities are proportional, although under several assumptions. First, the survey should cover the whole sky; second, the observational proxy of the gravitational force should have known properties and last but not least, the survey should be deep enough for the dipole to be convergent to the final value that we want to measure. If one or more of these assumptions are not met, the dipole \mathbf{d} is a biased estimator of the acceleration \mathbf{g} and the inference of the latter from the former may be done only when the mentioned effects are properly accounted for.

We focus on the third of these effects, i.e. the question of convergence of the clustering dipole, using the data from the Two Micron All Sky Survey (2MASS, Skrutskie et al.¹⁵) Extended Source Catalog (XSC). The XSC is complete for sources brighter than $K_s \simeq 13.5^{\text{mag}}$ ($\sim 2.7 \text{ mJy}$) and resolved diameters larger than $\sim 10\text{--}15 \text{ arcsec}$. The near-infrared flux is particularly useful for the purpose of large-scale structure studies as it samples the old stellar population, and hence the bulk of stellar mass, and is minimally affected by dust in the Galactic plane (Jarrett⁴).

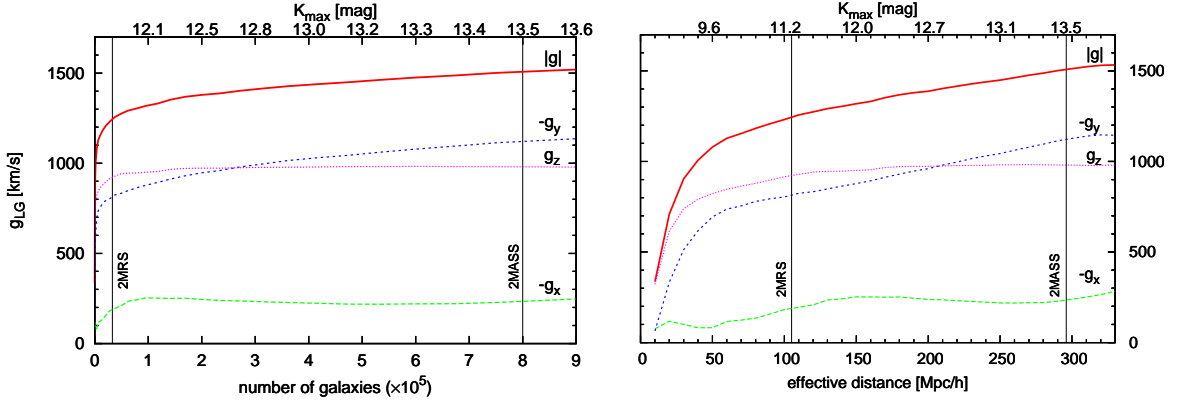


Figure 1: Growth of the 2MASS clustering dipole. *Left*: as a function of the number of galaxies used for the calculation. *Right*: as a function of the effective distance. Top axes show corresponding cut-off magnitudes. Solid lines represent the amplitude of the dipole; dotted and dashed lines illustrate Galactic Cartesian components.

The gravitational instability scenario of large-scale structure formation relates peculiar velocities of galaxies with their peculiar gravitational accelerations. In linear theory, this relation has a particularly simple form (Peebles¹³):

$$\mathbf{v} = \beta \mathbf{g}, \quad (1)$$

where $\beta \equiv \Omega_m^{0.55}/b$, Ω_m is the current value of the cosmological density parameter of non-relativistic matter, b is the linear biasing parameter and the acceleration \mathbf{g} is expressed in units of velocity. Applying Eq. (1) to the motion of the Local Group as a gravitationally bound system, we can evaluate the β parameter from LG's peculiar velocity and acceleration. If we have some additional knowledge on the biasing, we can estimate the value of the density parameter Ω_m .

The velocity of the LG is known from the dipole component of the temperature distribution of cosmic microwave background (CMB). When reduced to the barycenter of the LG, it equals to $v_{CMB} = 622 \pm 35$ km/s in the direction $(l, b) = (272^\circ \pm 3^\circ, 28^\circ \pm 5^\circ)$ in Galactic coordinates. As for the acceleration of the LG, it can be estimated from a two-dimensional all-sky catalog, i.e. one containing astro- and photometric data only, provided that we know the behaviour of the mass-to-light ratio in the band(s) of the survey.

2 Growth of the 2MASS dipole

The main interest of the study presented here was to examine the growth of the clustering dipole of galaxies from 2MASS XSC as a function of increasing depth of the sample. For that purpose we used positions and fluxes in the near-infrared K_s band ($2.16\ \mu\text{m}$), obtained from the catalog^a, corrected for extinction and other effects, such as Zone of Avoidance. The growth was calculated by decrementing the minimum flux of the objects in the sample (i.e. incrementing the maximum K_s magnitude). Results are presented in Fig. 1. The left panel shows the growth of the dipole as a function of the number of galaxies, together with Galactic Cartesian components. Such a presentation was used by Maller et al.¹¹ and would suggest convergence of the dipole, just as they concluded. However, a linear scale in the number of galaxies on the x -axis is not a convenient measure of the sample depth. What is needed is a linear scale *in distance* on the abscissa. For that purpose we related magnitudes of galaxies with effective distances. As an estimator of the latter we propose the median value of distance given the flux. Its calculation involves the luminosity function (LF) parameters for a given band. For the LF in the K_s band

^ahttp://pegasus.phast.umass.edu/data_products/all_sky_catalog/index.html

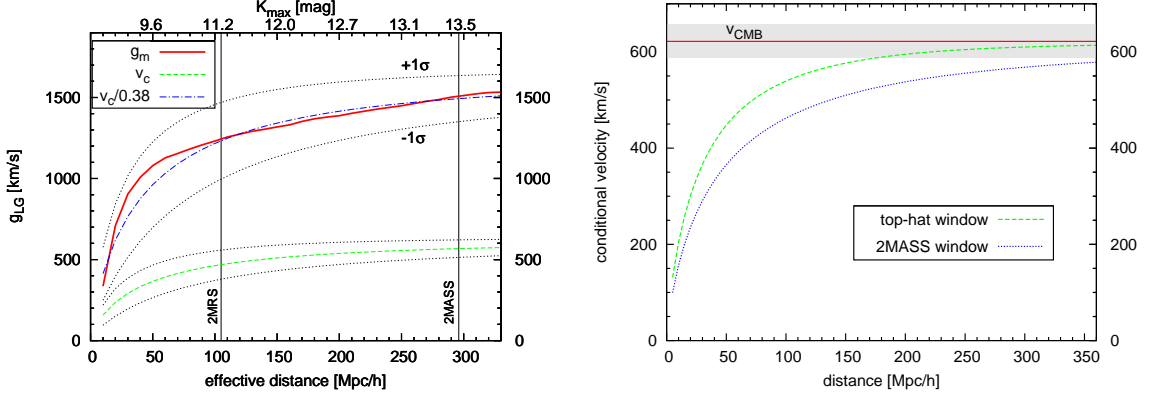


Figure 2: *Left:* Growth of the 2MASS clustering dipole (solid line), compared with the theoretical expectation for conditional velocity of the Local Group in the Λ CDM model (dashed line) and the latter rescaled by the β parameter (dot-dashed line). The dotted lines show 1σ variances for the theoretical curves. *Right:* Theoretically predicted conditional velocity of the Local Group for known v_{CMB} using two different observational windows: the flux window of 2MASS (dotted line) and top-hat (dashed line). The horizontal solid line is the velocity of the Local Group with respect to the CMB and the shaded strip represents confidence intervals of the v_{CMB} measurement.

as given by Jones et al.⁷, we find $r_{\text{eff}} \simeq 0.59 \times 10^{0.2K} \text{Mpc}/h$ for the magnitude K . This proxy of distance is used in the right panel of Fig. 1. The growth of the clustering dipole up to the completeness limit of 2MASS XSC ($\approx 300 \text{Mpc}/h$) is now evident.

3 Observations vs. theory

Taken at face value, this divergence is consistent with the findings of some other authors, who used various datasets and methods. On the other hand, it contradicts existing claims of convergence (even at scales as small as $60\text{--}100 \text{Mpc}/h$). However, this discrepancy most probably stems from the different nature of catalogs and methods used for the calculation, and in particular is due to distinct *observational windows*. Knowledge of these windows is necessary to correctly confront such results and is also essential if we want to make comparisons with theoretical expectations.

We thus pose the following question: is the behaviour of the 2MASS flux dipole consistent with the predictions of the currently accepted cosmological model, namely Lambda–Cold–Dark–Matter (Λ CDM)? Looking for the answer, we compare our results with the expectation value for the amplitude of the acceleration of the LG *knowing* its peculiar velocity. The relevant formulae can be found in Juszkiewicz et al.⁸ and Lahav et al.⁹. Results are presented in Fig. 2 (left panel). The expectation value of the acceleration (dot-dashed line) is obtained from the conditional velocity (dashed line) rescaled by the β parameter according to Eq. (1). This velocity, calculated from eq. (8a) of Juszkiewicz et al.⁸, includes the CDM power spectrum (PS) of density fluctuations and the observational window of the 2MASS flux-limited survey. For the former we use the linear PS of CDM as given by Eisenstein & Hu² together with *WMAP* 5-year cosmological parameters (Hinshaw et al.⁵). The latter is the window calculated by Chodorowski et al.¹

As can be seen in the left panel of Fig. 2, the observed growth of the 2MASS dipole is well within the 1σ range of the theoretical prediction rescaled by $\beta = 0.38$. In the right panel of Fig. 2 we compare the prediction for the 2MASS window with the one for top-hat (i.e. a sphere of radius R). The latter window is appropriate for all-sky catalogues that include redshifts (as for example the 2MASS Redshift Survey, 2MRS, Huchra et al.⁶). It is noticeable that the expectation value of the conditional velocity (without rescaling) for the 2MASS window is far from converging to the limit of $v_{\text{CMB}} = 622 \text{ km/s}$ even for r approaching $300 \text{ Mpc}/h$. On the contrary, the theoretically expected dipole measured through a top-hat window has clearly converged to v_{CMB} for $r \simeq 300 \text{ Mpc}/h$. It should be noted, however, that even for all-sky redshift surveys, such

as 2MRS, the convergence of the dipole is rather unlikely before some $200 \text{ Mpc}/h$, contrarily to the measurement of Erdoğdu et al.³, where it is claimed that the contribution from structure beyond $6000 \text{ km/s} (= 60 \text{ Mpc}/h)$ is negligible (but cf. Lavaux et al.¹⁰). We can see that for the latter distance, the conditional velocity for the top-hat window has reached only 75 per cent of its final value.

The slower convergence of the dipole measured through the 2MASS window compared to the top-hat case is easy to understand. In redshift space, the contribution to the flux dipole from, for instance, a galaxy cluster will come from distances of plus/minus several megaparsecs around the true value (the so-called Fingers of God). In the case of angular data only, numerous faint galaxies of the cluster will contribute to the flux at effective distances that are *significantly* greater than the true distance of the cluster.

The preliminary errorbars for our measurement of β can be evaluated from the error in v_{CMB} ($\sim 6\%$) and taking the theoretical σ_g as a measure of the uncertainty on g ($\sim 9\%$). This altogether results in $\Delta\beta \simeq 0.05$. The value of $\beta = 0.38 \pm 0.05$ is in accordance with Erdoğdu et al.³ and only slightly below the lower confidence limit of Pike & Hudson¹⁴. Using the biasing $b_{K_s} = 1.1 \pm 0.2$ from Maller et al.¹² we obtain a rough estimate of the density parameter: $\Omega_m \simeq 0.2 \pm 0.1$.

More details of the study presented here will be given in a forthcoming paper. In the future, we also plan to apply the maximum likelihood method to the 2MASS data, as described in Chodorowski et al.¹, for an *optimal* calculation of the β parameter and its errors.

Acknowledgments

This publication makes use of data products from the Two Micron All Sky Survey, which is a joint project of the University of Massachusetts and the Infrared Processing and Analysis Center/California Institute of Technology, funded by the National Aeronautics and Space Administration and the National Science Foundation. M.B. and M.C. were partially supported by the Polish Ministry of Science and Higher Education under grant N N203 0253 33, allocated for the period 2007–2010.

References

1. Chodorowski M.J., Coiffard J.-B., Bilicki M., Colombi S., Ciecielag P., *Mon. Not. Roy. Astr. Soc.* **389**, 717 (2008)
2. Eisenstein D.J., Hu W., *Astroph. Jour.* **496**, 605 (1998)
3. Erdoğdu P. et al., *Mon. Not. Roy. Astr. Soc.* **368**, 1515 (2006)
4. Jarrett T., *Publ. Astr. Soc. Aus.* **21**, 396 (2004)
5. Hinshaw G. et al., *Astroph. Jour. Suppl. Ser.* **180**, 225 (2009)
6. Huchra J. et al., in Colless M., Staveley-Smith L., Stathakis R., eds., Proc. IAU Symp. 216, *Maps of the Cosmos*, Astron. Soc. Pac., San Francisco, 170 (2005)
7. Jones D.H., Peterson B.A., Colless M., Saunders W., *Mon. Not. Roy. Astr. Soc.* **369**, 25 (2006)
8. Juszkiewicz R., Vittorio N., Wyse R.F.G., *Astroph. Jour.* **349**, 408 (1990)
9. Lahav O., Kaiser N., Hoffman Y., *Astroph. Jour.* **352**, 448 (1990)
10. Lavaux G., Tully R.B., Mohayaee R., Colombi S., *Astroph. Jour.* **709**, 483 (2010)
11. Maller A.H., McIntosh D.H., Katz N., Weinberg M.D., *Astroph. Jour. Let.* **598**, L1 (2003)
12. Maller A.H., McIntosh D.H., Katz N., Weinberg M.D., *Astroph. Jour.* **619**, 147 (2005)
13. Peebles P.J.E., *The Large-Scale Structure of the Universe*, Princeton University Press, Princeton, New Jersey (1980)
14. Pike R.W., Hudson M.J., *Astroph. Jour.* **635**, 11 (2005)
15. Skrutskie M.F. et al., *Astron. Jour.* **131**, 1163 (2006)

THE CAST EXPERIMENT: STATUS AND PERSPECTIVES

T. DAFNI, on behalf of the CAST Collaboration

*Laboratorio de Física Nuclear y Astropartículas, University of Zaragoza,
50008 Zaragoza, Spain*

CAST (CERN Axion Solar Telescope) is looking for axions coming from the Sun, using an LHC decommissioned prototype dipole magnet as a converter of axions into detectable x-rays. The experiment started data-taking in 2002 and has used different configurations, keeping the magnet bores under vacuum and using ^4He as buffer gas. It has put the most restrictive limits of the axion-to-photon coupling constant of $g_{a\gamma} < 8.8 \times 10^{-11} \text{ GeV}^{-1}$ for axion masses up to $m_a \sim 0.02 \text{ eV}/c^2$ and $g_{a\gamma} < 2.2 \times 10^{-10} \text{ GeV}^{-1}$, for masses between $0.02 \text{ eV} < m_a < 0.39 \text{ eV}$. CAST is sensitive for the first time to realistic QCD-axion models at the sub-eV scale. Since 2008, ^3He has been used inside the magnet, intending to reach even higher axion masses. Here we present the current status of the experiment as well as a short discussion on the future prospects of the helioscope technique.

1 Introduction

Axions are hypothetical particles which give an elegant solution to the strong-CP problem. They could have been produced in early stages of the Universe, which makes them good candidates for the Dark Matter. One of the processes they could have been produced is the so-called misalignment (or re-alignment) effect. These relic axions could be the main component of the Cold Dark Matter, if their masses fall in the 10^{-6} eV to 10^{-3} eV range. Microwave cavity experiments are the most sensitive to these axions, like the Axion Dark Matter Experiment (ADMX)¹, which is scanning this low axion mass range. Axions could also have been thermally produced and therefore could be part of the Hot Dark Matter. In any case their mass should not exceed 1 eV, in order to be compatible with the latest CMB data.²

Axions couple to gluons, and thus couple to nucleons and mix with pions. However the cornerstone of all experimental efforts to look for axions so far, has been their coupling to photons, (present as well in all QCD-axion models). This property allows for an axion-to-photon conversion (and viceversa) in the presence of an electromagnetic field, also known as the Primakoff effect. Therefore, axions could be produced in the core of stars like the Sun, through the conversion of the blackbody photons in the solar plasma. In 1983, Sikivie³ suggested that the inverse effect could take place; if we provided the axions with an appropriate magnetic field as they are streaming out of the Sun, so as to reconver them to photons, which should be easily detectable. This introduced the *helioscope* concept. CAST has been the third helioscope built so far and the most sensitive one.⁴ It was preceded by the pioneering experiment of the Rochester, Brookhaven, Florida collaboration^{5,6} and by Sumico⁷.

2 The CERN Axion Solar Telescope

The CERN Axion Solar Telescope (CAST) is looking for axions produced in the center of the Sun (Figure 1(b)). In order to re-convert the axions to photons, it is using a decommissioned LHC prototype dipole magnet which can reach 9 T along its 10 m-length. The magnet has two bores, with an aperture of 14.5 cm^2 each, and is sitting on a moving platform allowing it to align itself with the center of the Sun for approximately 1.5 h during sunrise and 1.5 h during sunset. The energy range of the expected signal is between 1 and 10 keV (Figure 1(a)), and its rate is dependent on the very weak axion-photon coupling. Therefore, low background x-ray detectors are necessary in order to have a high sensitivity.

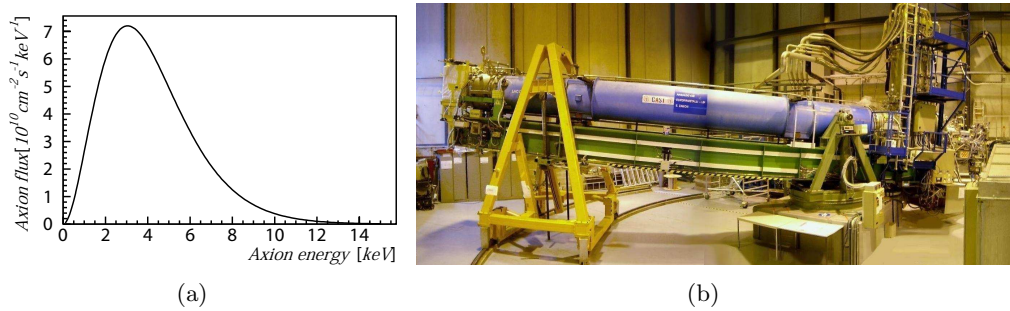


Figure 1: a) The solar axion flux as expected on the earth. It spans between 1 and 10 keV with a mean energy of 4.2 keV. b) A photograph of the CAST Experiment.

Phase I of the physics program of CAST started in 2002, when data were taken keeping the magnet bores under vacuum. At the time, three different types of detectors were covering the ends of the magnet looking for axions. A multiwire TPC was occupying the two bores looking for ‘sunset’ axions,⁸ while a micromegas detector⁹ and a CCD were looking for ‘sunrise’ axions. The CCD is coupled to an x-ray focusing device, forming part of an x-ray telescope prepared for x-ray astronomy space missions, and which increases significantly the signal-to-background ratio.¹⁰ In the absence of an axion signal, the experiment published the most restrictive limit on the axion-to-photon coupling constant to $g_{a\gamma} < 8.8 \times 10^{-11} \text{ GeV}^{-1}$ for axion masses up to $m_a \sim 0.02 \text{ eV}/c^2$.¹¹

In 2005, the experiment passed to its second phase, when a buffer gas was introduced in appropriate steps inside the magnet bores in order to restore coherence and therefore sensitivity for specific axion masses, higher than those reached in the previous configuration. During 2006, ${}^4\text{He}$ was used as buffer gas and it took approximately 160 discrete pressure steps for CAST to scan the axion-mass region up to $0.39 \text{ eV}/c^2$, supplying an upper limit for the axion-to-photon coupling constant of $g_{a\gamma} < 2.2 \times 10^{-10} \text{ GeV}^{-1}$.¹² CAST entered for the first time in the QCD-favoured axion model band. Because ${}^4\text{He}$ condensates in higher pressures (and thus masses), in order to continue with the scanning of higher masses ${}^3\text{He}$ had to be employed. During 2007 the gas system was being adapted to using the new gas. At the same time, several upgrades of different parts of the setup were made. One of them regarded the detectors: the TPC was replaced by two, new generation, micromegas detectors, which have shown very low background levels.¹³

Data-taking with ${}^3\text{He}$ started in 2008. Until the end of 2009, CAST had scanned the axion masses up to $0.85 \text{ eV}/c^2$. Recently the experiment restarted data taking, aiming at reaching $m_a \sim 1.1 \text{ eV}/c^2$ by the end of 2010. In Figure 2 the results of the experiment so far are summarised.

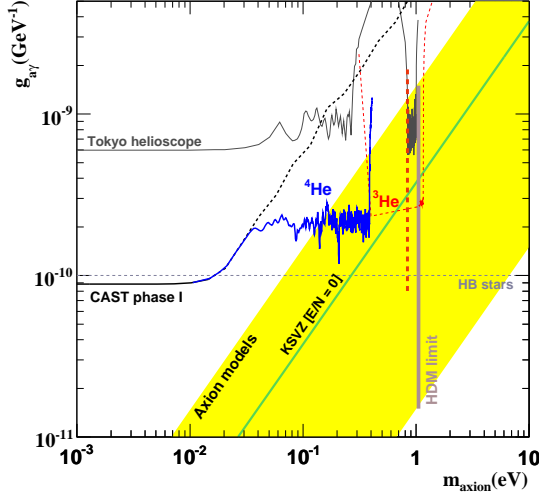


Figure 2: A combined exclusion line at 95% CL with CAST data both of phase I (black line),¹¹ when the magnet bores were in vacuum and the ⁴He run (red line).¹² For comparison, other laboratory limits such as the Tokyo helioscope^{7,7} as well as the cosmological upper limit on the axion.² The yellow-shaded area indicates the region of theoretical preference for QCD axion models. The thin dashed line in red, indicates the sensitivity expected to be reached in the ³He phase. The thick vertical dashed line in orange indicates approximately the progress of CAST data taking with ³He until the end of 2009.

3 Towards a new generation of helioscopes

CAST is the most sensitive helioscope built so far. The main advantages it presents with respect to the previous two are its powerful magnet and the x-ray telescope system. The Collaboration has already started active discussions regarding the future generation of axion helioscopes. Eq. 1

$$g \propto (BL)^{\frac{1}{2}} A^{\frac{1}{4}} (b^{\frac{1}{8}} / t^{\frac{1}{8}}) \quad (1)$$

shows the parameters on which the sensitivity of such devices depends. It can be easily seen that the domains which one could aim to improve are three: the exposure time, considering, for example, a platform that could increase the movement span of the magnet; detectors with zero background and the use of focusing devices, in order to enhance signal sensitivity and efficiency; and a new, powerful magnet with a big aperture. From the contribution of the three parameters in the equation, the effect of a new magnet is evidently the strongest one.

CAST has been actively discussing the near, middle and long-term future, based on the present and near-future technology innovations regarding magnets. An effort has been invested on the understanding of the current detectors used in the experiment, which have shown background levels compatible with zero, as well as the possibility to employ another x-ray focusing device apart from the x-ray telescope. The discussions so far point at encouraging prospects, as shown in figure 3^a. Moreover, the combination of Helioscope experiments and Dark matter axion searches (namely ADMX), would lead to the exploration of large parts of the model region for QCD axions in the coming decade.

4 Conclusions

CAST is the most sensitive axion helioscope built so far. Although axions may still elude direct detection, the results of the experiment have put the most stringent constraints on the coupling

^aThis has been discussed in detail in the presentation of T. Papaevangelou in ¹⁴

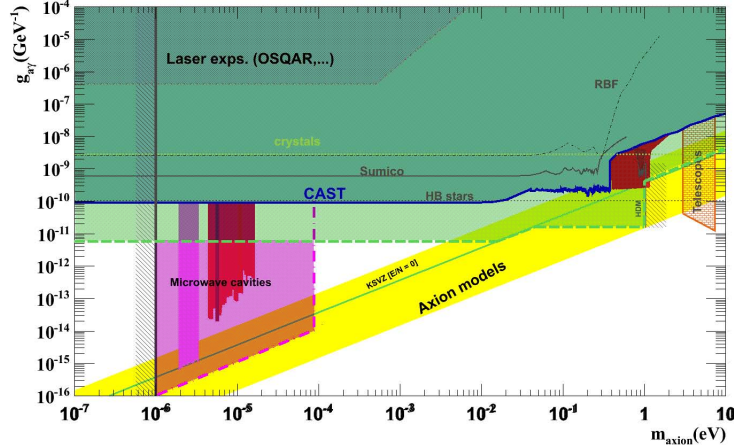


Figure 3: A global view of the Axion and axion-like particles map. The current limits set by CAST and other experiments (helioscopes, laser experiments, microwave cavity experiments) are shown. The limits of the mass set by the CMB data, astrophysical limits (HB stars) and cosmological limits (Overclosure) are presented as well. Also depicted are the prospects of the next generation helioscopes (dashed green line and green-shaded area), a simulation result of the prospects for a new magnet in the near future, with the current detectors of CAST. The sensitivity is enhanced by one order of magnitude over the whole mass range, entering well in the yellow band of the most favoured axion models. Furthermore, the future of the microwave cavity experiments (dashed purple line and purple-shaded area). One can see that in the next decade the bulk of the yellow area, denoting the region of theoretical preference for axion models, could be explored.

constant of axions to photons, reaching for the first time sensitivities at the QCD-favoured axion models level. Currently the experiment is taking data at the higher end of axion rest masses, with the aim to cover the range up to $1.02 \text{ eV}/c^2$. At the same time, CAST is exploring the possibility to build a helioscope of the next generation, with the help of a powerful and higher aperture magnet, which would push the sensitivity of the experiment at least one order of magnitude.

References

1. S. J. Asztalos et al., *Phys. Rev. D* **69**, 011101 (2004), astro-ph/0310042.
2. S. Hannestad et al., *J. Cosmol. Astropart. Phys.* JCAP 0804(2008)019.
3. P. Sikivie, *Phys. Rev. Lett.* **51**, 1415 (1983).
4. K. Zioutas et al., *Nucl. Instrum. Methods A* **425**, 480 (1999).
5. K. van Bibber et al., *Phys. Rev. D* **39**, 2089 (1989).
6. D. M. Lazarus et al., *Phys. Rev. Lett.* **69**, 2333 (1992).
7. S. Moriyama et al., *Phys. Lett.* B434, 147 (1998), hep-ex/9805026.
8. D. Autiero et al., *New J. Phys.* 9:171 (2007).
9. P. Abbon et al., *New J. Phys.* 9:170 (2007).
10. M. Kuster et al., *New J. Phys.* 9:169 (2007).
11. S. Adriamonje et al., *J. Cosmol. Astropart. Phys.* JCAP 04(2007)010.
12. E. Arik et al., *J. Cosmol. Astropart. Phys.* JCAP 02(2009)008.
13. S. Aune et al., *Nucl. Instrum. Methods A* **604**, 15-19 (2009).
14. T. Papaevangelou et al., Towards the new generation of axion helioscopes (CAST), Workshop on “New Opportunities in the Physics Landscape at CERN”, 2009.

4. Dark Energy Probes

Type Ia Supernovae and Cosmology

N. Regnault

LPNHE, IN2P3/CNRS, Universités Paris 6 and Paris 7

We review recent progress in supernova cosmology. We discuss inconsistencies recently unveiled by the SDSS-II collaboration, between distance measurements performed with the SALT2 and MLCS2k2 light curve fitters. Finally, we briefly review the main systematics affecting the measurements of the dark energy equation of state with type Ia supernovae.

1 Introduction

Comparing nearby and distant type Ia supernova luminosities allows one to study the relation between luminosity distance and redshift and to constrain the expansion history of the Universe. Twelve years ago, relying on the first distant supernova samples obtained in the 1990s, two independent teams reported that the expansion of the Universe seems to be accelerating^{1,2}. This acceleration implies either modifications of gravity on cosmological scales, or the existence of a fluid with negative pressure, called “Dark Energy”³.

This result was confirmed by complementary cosmological probes^{4,5}. With more observations than basic parameters, we have over-constrained the standard cosmological model, and found a consistent explanation, with Dark Energy accounting for over 75% of the total energy density of the Universe. To unveil the nature of Dark Energy one must measure its equation of state parameter w , defined as the ratio of its pressure p_X over its density ρ_X : $w = p_X/\rho_X$. SN Ia observations remain a key ingredient in this measurement. They give access to the history of the expansion in the redshift range $0.01 < z < 1$, when Dark Energy started to dominate over matter.

Given the size of the current SN Ia samples (~ 1000 nearby and distant SNe Ia), systematic uncertainties now dominate the error budgets. Recent studies seem to suggest that the uncertainty on cosmological parameters is much larger than previously assessed and that the uncertainties related to the empirical modeling of SNe Ia have been largely underestimated. In this short review, we will examine these claims. We will also discuss the main sources of uncertainties affecting the current results.

2 Constraining the Cosmic Expansion History with Type Ia Supernovae

Type Ia supernovae are rare (1 SN / galaxy / millennium), bright (10^{10} solar luminosities) and transient (~ 1 month) events. They are quite easily identified using spectroscopy. Spectra taken around maximum luminosity reveal broad absorption features from materials ejected at speeds of $\sim 20,000$ km/s. SN Ia spectra are characterized by their lack of hydrogen lines, and the presence of strong silicon features. These observations suggest that SNe Ia come from the thermonuclear explosion of white dwarfs having reached the Chandrasekhar mass by accreting

mass from a companion. However, the exact nature of the companion (evolved main sequence star, red giant, white dwarf) is not precisely known, nor are the ignition scenarios and the explosion mechanisms (detonation, deflagration, delayed detonation...) ⁶.

Type Ia supernovae display an impressive homogeneity. The dispersion of their maximum restframe luminosity in the Johnson B -band does not exceed 40%. More importantly, the SN Ia restframe luminosity is correlated with the shape of their light curves, and with their restframe colors. Taking into account these two relations — respectively known as the “brighter-slower” and “brighter-bluer” relations — allows one to reduce the dispersion of the standardized maximum luminosities to about 15%. Hence, SNe Ia permit to measure (relative) luminosity distances on cosmological scales with an remarkable precision of about 7%.

Several methods have been developed to derive standardized luminosity distances from multi-band SN Ia light curve measurements. They all rely on empirical models of the supernova light curves, build from a training sample of well measured SNe. Currently, two approaches are in wide use in the community. We discuss them briefly below.

2.1 The MLCS Distance Estimator

The Supernova Multicolor Light Curve Shape method (MLCS2k2⁹) allows one to directly derive a standardized luminosity distance from a supernova light curve, measured in several bands in the observer frame. The model is trained on a set of nearby supernovae *with known relative distances*. Light curve templates in a set of pre-defined filters are derived from this training sample, allowing to interpolate between the observations. Since the supernovae that enter the cosmological measurements span a large redshift range, observer frame magnitudes of supernovae at higher redshifts do not cover the same spectral region. To account for this effect, K-corrections are applied to the light curve points. MLCS2k2 uses tabulated K-corrections that depend on the supernova redshift, color and epoch, determined from a sample of about 100 nearby supernova spectra, covering a large range in phase.

MLCS2k2 parametrizes the diversity of SNe Ia with a single parameter, Δ . The prediction of the model, at a given epoch τ (relative to the maximum of luminosity) and in a given observer band f may be written as:

$$m_f(\tau) = \mu + A_f^{MW}(\tau) + K_{ff'}(\tau) + M_{f'}(\tau) + p_{f'}(\tau)\Delta + q_{f'}(\tau)\Delta^2 + A_{f'}^{Host}(\tau) \quad (1)$$

f' denote the corresponding restframe filters ($UBVRI$) for which the model is defined, $K_{ff'}$ is the K -correction, A_f^{MW} is the absorption by the Milky way and $A_{f'}^{Host}$ is the absorption by dust in the SN host galaxy. M , p and q are the model vectors, determined during the training set. Finally, μ is the “true” (standardized) distance modulus.

This parametrization encodes a series of strong assumptions. First, it assumes that SN Ia form a one dimensional family, whose diversity may be accurately parametrized using the single parameter Δ . It also assumes that the model accurately captures the full color diversity of SNe Ia and that any remaining color dispersion is entirely due to dust reddening (in the SN host galaxy). Finally, absorption by dust in the Milky-Way or in the host galaxy is parametrized with the Cardelli-Clayton-Mathis (CCM) law¹³. In particular, we have explicitly, for example in the B band: $A_B = R_B \times E(B - V)$ with $R_B = 4.1$. In order to ensure that the estimates of A are positive, the authors apply a prior, which is determined using simulations.

From a multiband supernova light curve, the trained model gives an estimate of μ along with its uncertainty, as well as an estimate of the extinction by dust in the host galaxy. Then, the standardized distance moduli are compared with the cosmology predictions:

$$\mu_i = \mu(z, \vec{\theta}) \equiv 5 \log_{10} \left(\frac{d_L(z_i, \vec{\theta})}{10\text{pc}} \right) \quad (2)$$

where $d_L(z)$ is the Hubble parameter-free luminosity distance, and $\vec{\theta}$ is the vector of cosmological parameters. The MLCS method was used by the High-z Supernova Search in the discovery of cosmic acceleration. Since then it has been used in many projects^{11,12,10,21}.

2.2 Fitting Standardized Distances along with the Cosmology

An alternate approach consists in determining a subset of observables from the supernova light curves (or possibly spectra), and then try to combine these observables in order to minimize empirically the dispersion in the Hubble diagram.

In practice, three quantities are usually estimated from the supernova light curves (1) the restframe magnitude of the supernova in a reference band, usually *B*-Johnson (m_B^*) (2) a light curve shape parameter, such as the *stretch* parameter as defined in Perlmutter *et al*¹ (3) and a restframe color of the supernova, c . These quantities are estimated using an empirical light curve model, itself derived from a training set. Following the original approach proposed by Tripp⁷, they are combined to form a standardized distance modulus μ :

$$\mu = m_B^* + M_B + \alpha(s - 1) - \beta c \quad (3)$$

As shown above, μ is then compared to the predictions of the cosmological models under study, $\mu(z, \vec{\theta})$. In the equation above α accounts for the brighter-slower relation, β , for the brighter-bluer relation, and M_B is the restframe absolute magnitude of type Ia supernovae (fully degenerated with H_0). These three quantities are nuisance parameters. They are usually fit along with the cosmological parameters and then marginalized over.

Several light curve fitters have been developed by various collaborations in order to determine m_B^* , s and c from the supernova light curves. As an example, the Supernova Legacy Survey (SNLS)¹⁴ have developed SALT2¹⁵ and SiFTO¹⁶. These two models do not apply K-corrections to the data, but attempt to directly predict the observed supernova fluxes as a function of SN epoch from a restframe spectral sequence $F(\lambda, \tau)$, using the telescope passband functions $F(\lambda)$. The SALT2 model determines $F(\lambda, \tau)$ using a large training set incorporating over a hundred supernova observed simultaneously photometrically and spectroscopically. The model parametrization may be written as:

$$F(\lambda, \tau) = x_0 [M_0(\lambda, \tau) + x_1 M_1(\lambda, \tau)] \exp(c CL(\lambda)) \quad (4)$$

where x_0 , x_1 and c are respectively the restframe flux in the reference (*B*) band, x_1 a shape parameter, and c a color parameter. $M_0(\lambda, \tau)$ is the mean spectral sequence, while $M_1(\lambda, \tau)$ describes the variations that go with the shape parameter (analog to a first component in a PCA decomposition). Finally, $CL(\lambda)$ describes a color law. $M_0(\lambda, \tau)$, $M_1(\lambda, \tau)$ and $CL(\lambda)$ are all empirical functions (modeled as splines) determined during the training.

With this approach, the treatment of supernova diversity of foregrounds is totally agnostic. First, it is not assumed that the supernova-to-supernova color variations is due to dust extinction. Instead, it is accounted for empirically as can be seen in equation 3. Furthermore, they do not assume that CCM law applies for dust in distant galaxies. Instead, SALT2 re-determines empirically a color law $CL(\lambda)$ during the training set. Another advantage of this approach, is that the supernova luminosity information is not used in the training. Hence, the training set can be supplemented with several hundreds of high-quality distant supernova light curves, such as those published by the SNLS or SDSS-II.

Note that alternate methods have also been developed, following the same approach, but using different standardization observables. For example, CMAGIC^{17,18} utilizes a linear relationship found in the color-magnitude diagram of SNe Ia for an extended period of time after maximum. Other methods rely on correlations between SN Ia luminosities and spectral flux ratios or on the equivalent width of selected spectral features^{19,20}.

3 Are SN Ia Luminosity Distance Measurements Reliable ?

In an attempt to estimate the impact of the assumptions made by the various light curve fitters on the cosmology, Kessler *et al* ²¹ analyze the first year SDSS-II dataset (supplemented with nearby, SNLS, ESSENCE, and HST data) with two different light curve fitters: MLCS2k2 and SALT2. Combining supernova constraints with the WMAP-5 year results, and with the measurements of the BAO feature in the SDSS Luminous Red Galaxy sample ²², they obtain two estimates of w . Using MLCS2k2 they find: $w = -0.76 \pm 0.07(stat) \pm 0.11(sys)$, while using SALT2 they obtain: $w = -0.96 \pm 0.06(stat) \pm 0.12(sys)$ respectively. These two estimates are incompatible at the 2σ -level. This result has had a strong impact on the community and deserves some discussion.

The source of these discrepancies is analyzed in detail in Kessler *et al*. They show that the differences can be explained by two effects:

1. First, there seem to be an anomaly in the SN models in the region of rest frame U -band. This effect is easily tested by studying the difference between the SDSS-II SN distance moduli computed without including the restframe data corresponding to the observer frame passbands ($\mu_{no\ U}$), or including it ($\mu_{with\ U}$) as a function of the redshift: $(\mu_{no\ U} - \mu_{with\ U})(z)$ Both SALT2 and MLCS2k2 seem to exhibit this anomaly.
This effect has been studied on more recent SNLS data, with an updated SALT2 training and an updated photometric calibration ²³. It has been shown that it can be completely explained by the impact of an inaccurate calibration of the SNLS first year sample on the training of SALT2. For the MLCS2k2 fitter, this effect may also be explained by the inclusion of inaccurately calibrated U -band data. Ground-based U -band observations are indeed notoriously difficult to calibrate. Indeed, the atmospheric transmission is extremely variable around ~ 300 nm, and the atmospheric cutoff is also variable, making the effective passband ill-defined.
2. The second effect tracked by Kessler *et al*, is related to the treatment of supernova colors. As discussed above, MLCS2k2 assumes that the observed color variation is not intrinsic to the supernova, but due to dust. Furthermore, MLCS2k2 ensures that the fitted extinction is positive, using a prior. Hence, as noted by Kessler *et al*, since there high-redshift SNe tend to have bluer colors, the distant moduli estimated using both methods will differ: the method relying on SALT2 will assign them larger luminosities and distances, hence the differences in the estimates of w . Furthermore, the authors show that the shape of the prior on supernova colors has a very strong impact on w , that can be as large as $\Delta w \sim 0.2$, explaining the main part of the effect.

There is still ongoing controversy around these two explanations. More details may be found in ^{21,23}. To summarize the situation, we may point out that:

1. the U -band anomaly has disappeared from the more recent SALT2 trainings. This is mainly due to changes in the photometric calibration of the SNLS survey. There is evidence that currently available U -band photometry suffer from large photometric errors: the dispersion of rest-frame U -band data is much lower for high- z data than for nearby data. Furthermore, there is significant tension in the residuals from the cosmological fit between the nearby and distant data if U -band is included.
2. there is evidence that the β correction in equation 3 does not identify with the R_B parameter of the Cardelli law. Indeed, $R_B \sim 4.1$, while the cosmology fits have consistently yield $\beta \sim 2$ over the last decade. This low value suggests either a very unusual extinction law in the environment of SNe Ia (either in their host galaxy, or in dust shells around the SN), or an intrinsic color variation that dominates the effect of dust.

3. there is evidence from the SALT2 training (and also from the SiFTO training) that SNe Ia follow a color law that cannot be explained by the Cardelli-Clayton-Mathis law.

As a conclusion, the causes of the discrepancies observed by Kessler *et al* have been identified. They seem to be related to photometric calibration (a solvable issue, in principle) and potentially incorrect assumptions (that may always be relaxed).

4 Systematic Uncertainties

The most recent measurements of w with SNe Ia are now dominated by systematic uncertainties. For example, the SDSS-II collaboration reports systematics twice as large as the statistical uncertainties. Next generation large surveys such as DES^a will study thousands of SNe Ia, while LSST^b will derive cosmological constraints with more than 10^5 supernovae. In this section, we examine a few selected systematics that dominate the current budgets.

4.1 Photometric Calibration

Measuring SN Ia luminosities relies on precision photometry performed with CCD imagers. The photometric calibration of these imagers is a key ingredient of the cosmological measurements with SNe Ia. Indeed, the cosmological information comes from comparing the luminosity distances of distant supernovae, observed in the redder bands of the imagers (~ 800 nm), with the distances of nearby SNe, observed at bluer wavelengths (around 400 nm). Therefore, a good control of the flux intercalibration of the imager passbands is essential. Otherwise, a redshift-dependent bias may affect the distance estimates.

Calibration consists in two steps: first, the observations are standardized onto some magnitude system, using a catalog of standard stars^{24,25,26,27}. Then, it is necessary to convert from the standard system into fluxes. This is done using a fundamental flux reference, i.e. a source with known magnitudes and a well measured spectral energy distribution (SED). Modern supernova surveys have greatly benefited for the Hubble Space Telescope (HST) CALSPEC^c calibration program²⁸. CALSPEC tied the flux calibration of the HST on observations of pure hydrogen white dwarfs whose spectra were known theoretically. This calibration was then propagated to a larger sample of spectrophotometric standards.

Modern surveys such as SNLS or SDSS-II have put significant efforts in improving the calibration of their datasets^{29,30}. Interestingly enough, both surveys have independently devised very similar strategies, anchoring their flux calibration on red CALSPEC standards. The precision obtained with the current strategies is slightly less than 1% in the visible, and of about 2% in the near-infrared (z -band). Despite these efforts, photometric calibration is still the dominant contribution to the systematic uncertainty budgets.

It is likely that the precision of $\sim 0.1\%$ in all bands, required by future surveys such as LSST will not be attained by these methods. One has to keep in mind indeed, that the CALSPEC flux calibration ultimately relies on theoretical models of pure hydrogen white dwarfs. Hence, there is some unknown systematic uncertainty associated with it. Several cosmology groups have started R&D programs, to calibrate the imagers with dedicated illumination systems^{31,32,33,34}. This will allow to tie the imager flux calibration on laboratory standards instead of astrophysical objects.

^a<http://www.darkenergysurvey.org/>

^b<http://www.lsst.org>

^c<http://www.stsci.edu/hst/observatory/cdbs/calspec.html>

4.2 Modeling of Supernova Light Curves

The analysis of SN Ia light curves requires empirical models trained from real data. Aside from the controversies around the MLCS- or SALT-like approaches, there are additional sources of systematics, coming from the finite size of the training sample, and also from various assumptions made in the implementation of the model. Both may be quantified and propagated into the analysis (see²³ for details). For SNLS for example, there are always smaller (up to a factor 2) than the calibration uncertainties.

4.3 Gravitational Lensing

Gravitational lensing of SN light due to the presence of Dark Matter haloes along the line of sight is expected to affect the SN signal, causing increased dispersion in the Hubble diagram. The distortion is asymmetric, most SN being slightly demagnified, while some are strongly magnified. For current large surveys such as SNLS, the impact of lensing is negligible, however, it may become an issue for future surveys targeting $z > 1$ supernovae^{35,36}.

A 2σ detection of the lensing signal in the supernova data has been published by SNLS^{40,41}. With more data, it may become a powerful probe of mass of galaxies embedded in the dark matter haloes.

4.4 Evolution of SN Ia

Evolution of SNe Ia luminosities with redshift is fully degenerate with cosmology. Observationally, it can be tested either by comparing the properties of nearby and distant supernovae, or by studying the correlations of these properties with those of their host galaxies (which are known to evolve with redshift).

Modern surveys have undertaken large efforts to detect differences in the spectral properties (ejecta velocities, equivalent width...) of nearby and distant supernovae^{38,37,39}. No systematic differences between both population have been detected yet. Before, Astier *et al* had performed a similar test on the light curve properties of nearby and distant SNe and obtained negative results.

Another way to test for evolution is to study whether the standardization relations evolve with redshift. Kessler *et al*²¹ unveiled a strong decrease of β with redshift using SALT2 and MLCS2k2. These results have been put under scrutiny by the SNLS collaboration²³. The measurement of β is very sensitive to the estimate of the uncertainties affecting the color estimates. It was shown that with more sophisticated color-error modeling the effect became much smaller than that measured by Kessler *et al*, and it was concluded that there is no evidence for an evolution of α and β given the size of the current samples.

4.5 Host Galaxy Environment

Another test for evolution consists in comparing the SN Ia photometric properties, such (stretch and color) with the properties of their host galaxies (star formation rate, mass...). It is known that galaxy properties evolve with redshift. Hence, any unaccounted-for correlation between SNe luminosities and their host galaxies properties could translate into a redshift-dependent bias affecting the SN Ia distance estimates.

Several authors^{42,43,44,45,46} have shown that the width of SN Ia light curves is correlated with the host galaxy morphology. Sullivan *et al*⁴⁷ confirmed this result, using SNLS data and stellar evolutionary models fitted on the galaxy colors: SNe Ia have a tendency to exhibit a smaller light curve width when exploding in a passive environment. Hence, it was shown that there is a correlation between the SN Ia properties and their environment. However this effect was fully accounted for by the brighter-slower relation.

More recently, several authors^{48,47,49} published evidence that SN Ia residuals from the Hubble diagram are correlated with host galaxy mass. The correlation between the SN absolute luminosities and the galaxy properties are still weak (4σ at best), but the effect on the peak absolute magnitude is substantial, of the order of 0.08 mag. There is no physical explanation for this effect yet. It was shown however that splitting the sample by host galaxy mass, and fitting for a different peak absolute magnitude for each sub-sample corrects for the effect.

4.6 Combining the Systematic Uncertainties

Most identified systematics affecting the distances to supernovae (calibration, light curve fitter training, selection bias ...) are correlated and redshift-dependent. As a consequence, it is necessary to publish the full covariance matrix of the supernova luminosity distances, so that SN data can be used without loss of information. Up to very recently, this information was not available, with the consequence that most subsequent analyses just ignored them⁴. This situation has changed recently, as authors started to provide that information^{50,21}.

5 Conclusion

Supernova cosmology has been a very active field over the last decade. Large surveys such as SNLS and SDSS-II have started rolling out very high quality distant SN Ia samples of a few hundred supernovae. The precision of the measurements is now limited by the quality of the low- z datasets, and by the intercalibration of the high- z and low- z data.

There has been a controversy recently on the size of the systematic errors associated with the empirical modeling of SNe Ia, as the SDSS-II collaboration published two incompatible estimates of w from the same dataset. A careful analysis of these results show that these discrepancies mostly come from photometric calibration problems in the U -band, and from incorrect assumptions in the treatment of supernova colors.

The uncertainties affecting the cosmological parameter estimates is now dominated by systematic uncertainties. However, a careful analysis shows that all identified systematics may be reduced as the size of the supernova samples grows. As an example, the quality of the empirical light curve models will be improved with larger training samples. For the first time, correlations between residuals in the Hubble diagrams and the environment of SNe Ia have been detected. However, it has been shown that taking into account the host galaxy properties in the cosmological fit corrects for the effect. Despite substantial progress and considerable efforts invested by the supernova surveys, photometric calibration remains the dominant contribution to the systematic error budgets and obtaining the precision required by the future surveys will be a considerable challenge.

References

1. Perlmutter *et al* *Astrophysical Journal* **517**, 565 (1999)
2. Riess *et al* *Astronomical Journal* **116**, 1009 (1998).
3. Frieman *et al* *Annual Review of Astronomy & Astrophysics* **46**, 385 (2008)
4. Komatsu *et al* ArXiv **1001.4538**, (2010).
5. Percival *et al* *Monthly Notices of the Royal Astronomical Society* **381**, 1053 (2007).
6. Hillebrandt, W. and Niemeyer, J. C. *Annual Review of Astronomy & Astrophysics* **38**, 191 (2000).
7. Tripp, R. *Astronomy & Astrophysics* **331**, 815 (1998)
8. Riess, A. G. *et al* *Astrophysical Journal* **473**, 88 (1996)
9. Jha, S. *et al* *Astrophysical Journal* **659**, 122 (2007)

10. Wood-Vasey, W. M. *et al* *Astrophysical Journal* **666**, 694 (2007)
11. Riess, A. G. *et al* *Astrophysical Journal* **607**, 665 (2004)
12. Riess, A. G. *et al* *Astrophysical Journal* **659**, 98 (2007)
13. Cardelli J. A. *et al* *Astrophysical Journal* **345**, 245 (1989)
14. Astier, P. *et al* *Astronomy & Astrophysics* **447**, 31 (2006)
15. Guy, J. *et al* *Astronomy & Astrophysics* **466**, 11 (2007)
16. Conley, A. *et al* *Astrophysical Journal* **681**, 482 (2008)
17. Wang, L. *et al* *Astrophysical Journal* **590**, 944 (2003)
18. Conley, A. *et al* *Astrophysical Journal* **644**, 1 (2006)
19. Nugent, P. *Astrophysical Journal Letters* **455**, L147+ (1995)
20. Bailey, S. *et al* *Astronomy & Astrophysics* **500**, 17 (2009)
21. Kessler, R. *et al* *The Astrophysical Journal Supplement* **185**, 32 (2009)
22. Eisenstein, D. J. *et al* *Astrophysical Journal* **633**, 560 (2005)
23. Guy, J. *et al* *Astronomy & Astrophysics* , accepted (2010)
24. Landolt, A. U. *Astronomical Journal* **88**, 439 (1983)
25. Landolt, A. U. *Astronomical Journal* **104**, 340 (1992)
26. Landolt, A. U. *Astronomical Journal* **137**, 4186 (2009)
27. Smith, J. A. *Astronomical Journal* **123**, 2121 (2002)
28. Bohlin, R. C. *Astronomical Journal* **111**, 1743 (1996)
29. Holtzman08, J. A. *et al* *Astronomical Journal* **136**, 2306 (2008)
30. Regnault, N. *Astronomy & Astrophysics* **506**, 999 (2009)
31. Juramy, C. *et al* *SPIE* **7014**, (2008)
32. Barrelet, E. *et al* *Nuclear Instruments and Methods in Physics Research Section A* **585**, 93 (2008)
33. Stubbs, C. W. *et al* *Astronomical Society of the Pacific Conference Serie* **364**, 373 (2007)
34. Stubbs, C. W. *et al* *ArXiv* **1003.3465**, (2010)
35. Holz, D. E. & Linder, E. V. *Astrophysical Journal* **631**, 678 (2005)
36. Bergström, L. *et al* *Astronomy & Astrophysics* **358**, 13 (2000)
37. Brödner, T. J. *et al* *Astronomy & Astrophysics* **477**, 717 (2008)
38. Balland, C. *et al* *Astronomy & Astrophysics* **507**, 85 (2009)
39. Blondin, S. *et al* *Astronomical Journal* **131**, 1648 (2006)
40. Kronborg, T. *et al* *Astronomy & Astrophysics* **514**, 44 (2010)
41. Jonsson, J. *et al* *Monthly Notices of the Royal Astronomical Society* **405**, 535 (2010)
42. Hamuy, M. *et al* *Astronomical Journal* **109**, 1 (1995)
43. Hamuy, M. *et al* *Astronomical Journal* **112**, 2398 (1996)
44. Hamuy, M. *et al* *Astronomical Journal* **120**, 1479 (2000)
45. Riess, A. G. *et al* *Astronomical Journal* **117**, 707 (1999)
46. Gallagher, J. S. *et al* *Astrophysical Journal* **635**, 208 (2005)
47. Sullivan, M. *et al* *Monthly Notices of the Royal Astronomical Society* **406**, 782 (2010)
48. Kelly, P. L. *et al* *Astrophysical Journal* **715**, 743 (2010)
49. Lampeitl, H. *et al* *ArXiv* **1005.4687**, (2010)
50. Kowalski, M. *et al* *Astrophysical Journal* **686**, 749 (2008)

SNIa photometric studies in SNLS

N. PALANQUE-DELABROUILLE
(on behalf of the SNLS experiment)

Bat. 141, IRFU-SPP, CEA Centre de Saclay, 91191 Gif sur Yvette, Cedex, France

The discovery of accelerated expansion using supernova surveys has been one of the most surprising discoveries in cosmology in the past ten years. Present and future surveys, among which SNLS, JDEM or LSST, are based on samples of a few hundreds to a million supernovae. The measurement of their spectroscopic redshifts to investigate dark energy properties is already by far the limiting aspect of such surveys. In this paper, I will discuss and illustrate with SNLS data an approach based solely on photometry to both select supernova candidates and determine their redshift.

1 Introduction

From 2003 to 2008, the Supernova Legacy Survey (SNLS) collected data with the MegaCam imager, a 1 square degree array of 36 CCD with a total of 340 million pixels, over four 1-square degree fields. The data were obtained in a rolling search mode, with a typical time sampling of one point every three to four nights, in four different visible frequency bands g_M , r_M , i_M and z_M . The instrument and scanning strategy were designed specifically for the detection of Type Ia supernovae (SNIa) in the redshift range between 0.2 and 1.0.

The standard SNIa selection for the cosmological analyses in SNLS¹ are based on real-time detection and follow-up spectroscopy (thereafter RTA for Real Time Analysis). Despite the significant amount of time allocated to SNLS for the spectroscopy of its candidates, a spectrum could be obtained for roughly half of them only. This justified additional studies based solely on photometry. The SNLS photometric analyses described here are independent of the RTA, based on different data processing and selection. As such, they can provide a cross-check to estimate possible biases of the standard scenario. They can also be used for studies requiring larger sets of SNIa, as well as for the selection of other transients. For instance, a photometric analysis of the SNLS data has already led to the identification of a sample of 117 core-collapse supernovae (SNCC), from which was derived the most precise measurement to-date of the rate of SNCC at a mean redshift $z \sim 0.3$ (Bazin et al., 2009²).

These proceedings present two major steps towards the use of SNIa from pure photometric studies, i.e. without requiring any spectroscopic information, to derive cosmological constraints. The photometric identification of SNIa, summarizing work which can be found in Bazin et al. (2010) in prep., is described in section 2. The determination of the photometric redshift of SNIa (see Palanque-Delabrouille et al., 2010³ for details) is presented in section 3.

2 SNIa photometric identification

2.1 Detection catalog

Image subtraction was used to search for the appearance of transient events in the 3-year SNLS data (from 2003 to 2006) and to measure their light curves. Because most of the signal from SNIa in the redshift range $[0.2; 1.0]$ is expected to lie in the i_M band, this is where the catalog of detections was built, leading to $\sim 300,000$ events.

These were dominated mostly by saturated signals from bright objects which were not perfectly subtracted, by a large contribution from AGNs and a lesser one from variable stars. Unlike supernovae which are expected to have a flat light-curve before the explosion or a year after, AGNs and long-term variable stars usually exhibit variations over several years. Pollution of the measurements from saturated stars also produces random signals over the entire light curve. Most of the background detections were thus rejected by criteria based on the simultaneity of the signal between the various filters, and on considerations of light curve stability outside the time range of the main fluctuation. This led to a catalog of about 1500 detections.

To proceed with the selection of SNIa, a redshift information is required. The detections were therefore matched with galaxies from an external catalog of galactic photometric redshifts⁴ obtained from stacked images of the same fields. Whenever possible (successful match between the event and a unique host galaxy, and available photometric redshift for the galaxy) the events were assigned the photometric redshift z_{gal} of their host galaxy. This reduced the catalog to ~ 1200 detections with an assigned photometric redshift.

2.2 SNIa selection

The SALT2⁵ light curve fitter was applied simultaneously over the four-band light curves of each event to provide an estimate of the colour C , the stretch X_1 and the rest-frame B band peak magnitude m_B , under the assumption that the event was a SNIa. These characteristics were used to further select SNIa and discriminate against two major contaminations:

- core-collapse supernovae,
- SNIa which were accidentally assigned a photometric redshift z_{gal} significantly different from their actual redshift.

The selection criteria were set up using synthetic SNIa, synthetic SNCC, and the subset of our events which happened to have also been selected in the RTA. The latter then have a spectroscopic redshift available (z_{spe}) and a confirmed type (Ia or CC).

The major steps of the analysis are described below.

Long duration events ($X_1 > 4$) were rejected because almost none of the SNIa fall in that category, in contrast to almost all the plateau core-collapse and about 10% of the other SNCC.

As illustrated in figure 1 (left plot), rejecting extreme colors (requiring $|C| < 0.35$) was very efficient against both types of contaminants. While SNIa have $\langle C \rangle = 0$ with a r.m.s. of 0.1, SNCC exhibit instead $\langle C \rangle = 0.3$. The constrain on color thus rejected 40% of the remaining SNCC. In addition, a strong correlation was observed between events fitted with extreme color values and events with a bad redshift assignment: about 70% of the synthetic SNIa with $|z_{\text{gal}} - z_{\text{spe}}| > 0.2$ were removed by the above constraint on color.

The final major step to purify the photometric sample of SNIa was based on color magnitude diagrams, as the one illustrated in figure 1 (right plot). In these diagrams, SNIa populate a thin band while SNCC lie in a broad region which is shifted w.r.t. the SNIa band.

The photometric analysis briefly summarized above selected a total of 485 SNIa. A fraction of these (175 SNIa, thereafter the “identified” sample) had also been selected in the RTA pipeline; they were confirmed as Type Ia from spectroscopy, and their redshift was measured at the same time. They can therefore be used as a test sample to compare their characteristics with those

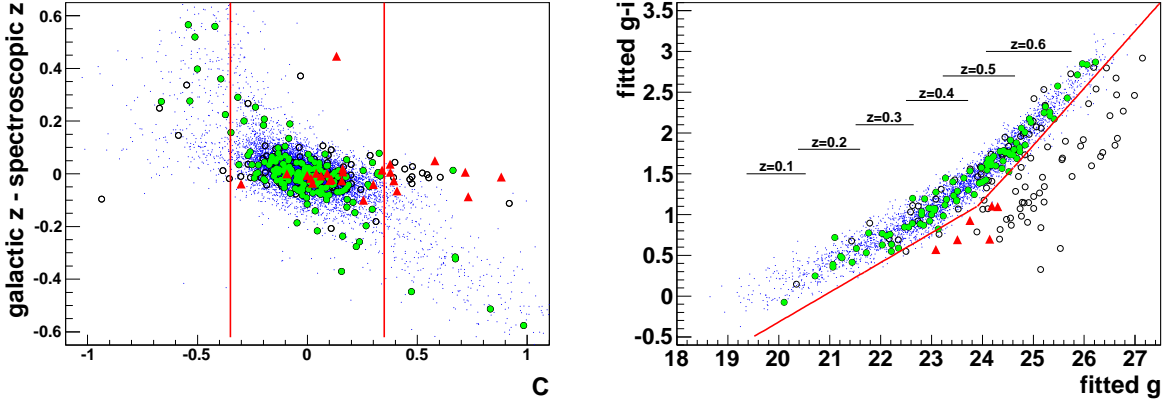


Figure 1: Left: Difference in redshift assignments $z_{\text{gal}} - z_{\text{spe}}$ as a function of color C . Extreme values are rejected. Right: $g - i$ vs. g color-magnitude diagram. Events below the red curve are rejected. In both plots, synthetic SNIa are in dotted blue, data in black circles. Green filled circles stand for data events spectroscopically confirmed as SNIa, and red triangles for spectroscopically confirmed SNCC.

of the additional SNIa solely selected from photometry (310 SNIa) and thereafter called the “unidentified” sample. The main difference between the two subsamples lies in their magnitude distribution. Because in SNLS a spectrum could only be obtained for events brighter than $i \sim 23.4$, the unidentified sample extends about 1 magnitude deeper than the identified one. This translates into an average redshift of 0.6 (resp. 0.9) for the identified (resp. unidentified) sample. Despite this difference, both subsamples exhibit similar properties. For instance, when limited to a common range of bright events ($i < 23$), both subsamples exhibit similar dependences of the residuals to the Hubble diagram with color or with stretch (the so-called “brighter-bluer” and “brighter-slower” relations).

This photometric selection increased by about a factor of 2 the set of SNIa found in the SNLS data. These can already allow new studies where additional statistics is necessary (e.g. to split the events into subsamples). From simulated SNCC, the contamination of this photometric sample was estimated to be ~ 0 from plateau SNCC and of $\sim 3\%$ from other SNCC.

3 SNIa photometric redshift

The above analysis was using the host galaxy photometric redshift as the assigned supernova redshift. We saw however that the external catalog can be incomplete (resulting in a 17% loss in our case). We can also assign the wrong host (resulting in an arbitrary supernova redshift). Even when all goes well, the uncertainty on a galaxy photometric redshift is at present only of order 5%. It is thus reasonable to assume that using the time-dependent information available in supernovae light curves could result in a redshift with smaller uncertainties. The derivation of a supernova redshift from its light curve is the aim of the work presented in this section.

Because, by definition, the redshift of the supernova shifts its spectrum towards larger wavelengths, the amount of flux measured in the four bands of SNLS is also affected. The main information about redshift is thus contained in the observed colors of a SNIa. The measurement of the time-evolution of these colors, through the use of the full multi-band light curves, is crucial to break inherent color-redshift degeneracies.

Recently, both the SNLS³ and the SDSS⁶ experiments have developed methods to estimate supernova redshifts using light curve fitters, where the redshift is determined as any of the other free parameters. One of the main difficulties in such a procedure is the mandatory initialization of the parameters, to avoid falling in an arbitrary local minimum. The initialization is usually done in several steps. In SNLS, the first step is a scan of the fit χ^2 as a function of redshift,

where both color C and stretch X_1 are fixed to 0. This yields an initial estimate of the redshift used thereafter. A second fit, with a Gaussian prior set on color, is done to determine the stretch value. The last fit, with redshift and stretch constrained to the result of the second step, lets the color unconstrained in order to estimate its value.

The performance of the method is estimated using the SNIa (whether spectroscopically confirmed or selected with the photometric analysis of section 2) which have their redshift (or that of their host) known from spectroscopy. The results are illustrated in figure 2.

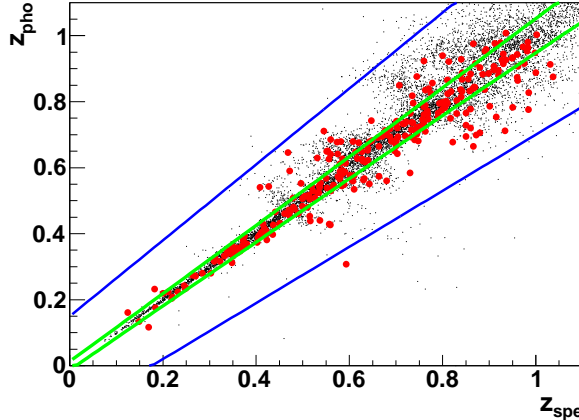


Figure 2: Photometric (z_{pho}) vs. spectroscopic (z_{spe}) redshift of SNIa. The green lines are for $z_{\text{pho}} = z_{\text{spe}} \pm 0.022(1 + z_{\text{spe}})$, representing the average precision attained up to $z = 1$, and the blue lines for $z_{\text{pho}} = z_{\text{spe}} \pm 0.15(1 + z_{\text{spe}})$ to visualize the catastrophic redshifts. Red circles for data SNIa, black points for simulated ones.

The resolution was defined as $\sigma_{\Delta z/(1+z)} \equiv 1.48 \times \text{median}[|\Delta z|/(1+z)]$ (a robust estimate of the r.m.s.), and the outlier rate η , or rate of catastrophic errors, as the proportion of events with $|\Delta z|/(1+z) > 0.15$. With the method summarized here, we obtained $\sigma_{\Delta z/(1+z)} = 0.022$ on average over the entire redshift range and $\eta = 0.7\%$. This is a significant improvement over the current performance of galactic photometric redshifts, where typically $\sigma_{\Delta z/(1+z)} = 0.037$ and $\eta = 5.5\%$.

SNIa photometric redshifts of this precision will be useful for future experiments (such as the Large Synoptic Survey, the Dark Energy Survey or Pan-STARRS) which aim to discover up to millions of Type Ia supernovae but without spectroscopy for most of them.

One should keep in mind, however, that it might remain useful to use the SNIa photometric redshift as an improvement for an already selected sample of SNIa (based for instance on a redshift coming from the host galaxy, as described here). The reason is that an analysis combining both the identification of SNIa and their redshift determination from the SNIa light curves only (without spectroscopy nor using an external catalog of host galaxy photometric redshift) might result in a larger contamination from SNCC for instance. Such a combined analysis will be the topic of a future study.

References

1. P. Astier *et al*, *Astron. & Astrophys.* **447**, 31 (2006).
2. G. Bazin *et al*, *Astron. & Astrophys.* **499**, 653 (2009).
3. N. Palanque-Delabrouille *et al*, *Astron. & Astrophys.* **in print**, arXiv:0911.1629 (2010).
4. O. Ilbert *et al*, *Astron. & Astrophys.* **457**, 841I (2006).
5. J. Guy *et al*, *Astron. & Astrophys.* **466**, 11G (2007).
6. R. Kessler *et al*, arXiv:1001.0738.

GRAVITATIONAL LENSING IN THE SUPERNOVA LEGACY SURVEY

T. KRONBORG, D. HARDIN, J. GUY, P. ASTIER, C. BALLAND, S. BASA, R. G. CARLBERG,
A. CONLEY, D. FOUCHEZ, I. M. HOOK, D. A. HOWELL, J. JÖNSSON, R. PAIN, K. PEDERSEN,
K. PERRETT, C. J. PRITCHET, N. REGNAULT, J. RICH, M. SULLIVAN,
N. PALANQUE-DELABROUILLE and V. RUHLMANN-KLEIDER

LPNHE, Université Pierre et Marie Curie, Université Paris Diderot, CNRS-IN2P3, France

Dark Cosmology Centre, Niels Bohr Institute, University of Copenhagen, Denmark

University Paris 11, Orsay, France

LAM, CNRS, BP8, Marseille, France

Department of Physics and Astronomy, University of Toronto, Canada

CPPM, CNRS-IN2P3 and Université Aix-Marseille II, France

Department of Astrophysics, University of Oxford, UK

INAF, Osservatorio Astronomico di Roma, Italy

Las Cumbres Observatory Global Telescope Network, Goleta, CA 93117

Department of Physics, University of California, Santa Barbara, CA 93106-9530

Department of Physics and Astronomy, University of Victoria, Canada

IRFU, CEA/Saclay, Gif-sur-Yvette, France

The observed brightness of Type Ia supernovae is affected by gravitational lensing caused by the mass distribution along the line of sight introducing an additional dispersion into the Hubble diagram. We look for evidence of lensing in the SuperNova Legacy Survey (SNLS) 3-year data set by measuring the correlation between the residuals from the Hubble diagram and the gravitational magnification based on a modeling of the mass distribution of foreground galaxies. We find evidence of a lensing signal with a 2.3σ significance. The current result is limited by the number of SNe, their redshift distribution, and the other sources of scatter in the Hubble diagram. We show that for the full SuperNova Legacy Survey sample (~ 400 spectroscopically confirmed Type Ia SNe and ~ 200 photometrically identified Type Ia SNe), there is an 80% probability of detecting the lensing signal with a 3σ significance.

1 Introduction

Type Ia supernovae (SNe Ia) have become an essential tool of observational cosmology. Although SNe Ia can be calibrated to be good standard candles, they are affected by systematic effects such as gravitational lensing.

Magnification of SNe Ia can be estimated in 2 ways. The Hubble diagram residuals, computed assuming the best fit cosmological model, give an indirect measure of the SN magnification. The magnification can, on the other hand, also be estimated by modeling the foreground galaxy mass distribution using galaxy photometric measurements together with derived mass-luminosity relations for galaxies and dark matter halo models. If a correlation between these two estimates is found, it could give interesting insight in the modeling of the mass distribution of the foreground galaxies. The SNLS sample is currently the best suited sample for a possible detection of such a signal thanks to its large number of SNe Ia at high redshift. In this analysis

we present the correlation between the magnification of the SNLS SNe derived from photometric measurements of the foreground galaxies (together with chosen mass-luminosity relations) and the residuals from the Hubble diagram.

2 Data

The SuperNova Legacy Survey consists of an imaging survey which is part of the Canada-France-Hawaii Telescope Legacy Survey and a spectroscopic survey done on 8m class telescopes (VLT^{2,1}, Gemini^{10,5} and Keck telescopes⁸). The imaging was done with the MegaCam imager which detects and monitors the light curves of the SNe, over four different fields of 1 deg² (called D1, D2, D3, D4). The "rolling" search method was used for the *griz* bands, which means observing the same field every 3-4 days during dark and gray time for as long as it remains visible. Images in *u* are also used in this analysis. The 3-year data set consists of 233 spectroscopically confirmed Type Ia supernovae used for cosmological purposes.

3 Estimating the supernovae magnification

We here briefly describe the analysis steps followed to calculate the supernovae magnifications. For a thorough explanation see Kronborg et al.?

The first step is to obtain a high quality galaxy catalog. The galaxy catalogs are built for each field on deep image stacks in the *ugriz* filters. The source detection and photometry is performed using SExtractor V2.4.4⁴ in double image mode. The detection is made in the *i* band. Two categories of objects have to be identified and excluded in the catalog : stars, and the host galaxies of the SNe. Certain areas also need to be masked out.

We need an estimate of the redshift and the rest-frame *B*, *V* and *U* band absolute magnitudes for each galaxy. We have chosen to use a template based code where different templates of galaxy spectra are fitted to the actual measurements. The templates have been optimized using galaxies with spectroscopic redshift from the DEEP-2 survey^{6,7}. As for the resolution of the code, it has been estimated using galaxies with spectroscopic redshift from the VVDS¹² and has been proven similar to the resolution of the CFHTLS photometric redshifts provided by Ilbert et al. 2006¹¹.

The next step is to convert the observed luminosity of each galaxy into a mass estimate using formerly established mass-luminosity relations. For this purpose, the rest-frame *B*-band absolute magnitude of the galaxy is used. Boehm et al. 2004³ and Mitchell et al. 2005¹³ have measured the relation between the absolute magnitude and the velocity dispersion for spirals and ellipticals respectively. In addition, the *U*–*V* color is used to separate the galaxies into a red and a blue population.

The last step is to compute the magnification for each SN. We select the galaxies along the line of sight and use the publicly available software Q-LET⁹, which makes use of the multiple lens plane method. The galaxy halos are modeled as Singular Isothermal Spheres (SIS).

4 Results

The 3-year SNLS data set used in this analysis contains 233 spectroscopically confirmed Type Ia supernovae in the redshift range 0.2-1.05 after quality cuts. However due to masking, we retain 171 SNe for the analysis. The SNLS Hubble diagram exhibits a r.m.s scatter of 0.16 mag.

4.1 Expected Signal

Before presenting the results, it is useful to have an idea of what to expect. As a criterion for a lensing signal detection we have chosen to calculate the weighted correlation coefficient, ρ ,

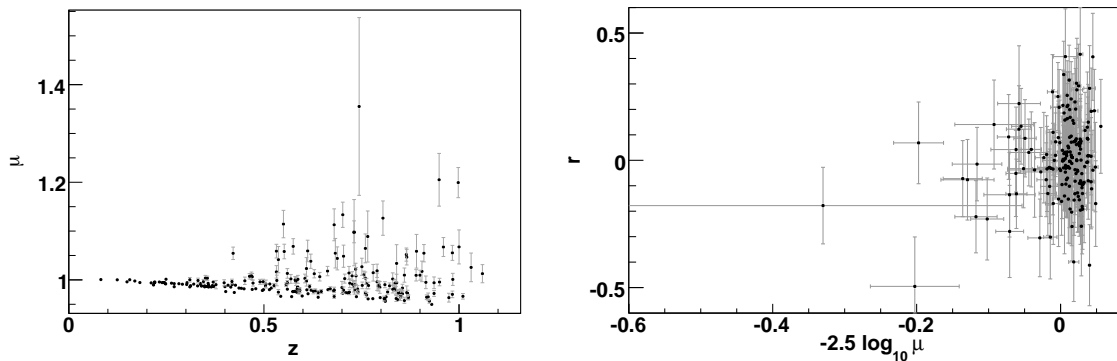
weighting with the inverse of the Hubble residual variance which has been found optimal for a signal detection.

We first simulated a large number of correlated samples similar to the 3-year SNLS sample. We compared the distribution of the weighted correlation coefficient of these samples with that of uncorrelated samples. We find that for the current sample there is 50 % probability of finding a 2.5σ significance correlation or better and 35 % probability of detecting a 3σ signal.

For the final SNLS sample we expect ~ 400 spectroscopically confirmed Type Ia supernovae and ~ 200 photometrically identified Type Ia supernovae. For this sample we find that there is 80% probability of detecting a 3σ signal or more.

Another question to be addressed is how the errors influence the possibility of a signal detection. We find that the signal detection is highly dominated by the scatter in the SN Hubble residuals which is not likely to decrease significantly in the near future. As a consequence improving the signal detection will require better statistics and, if possible, higher redshift SNe.

4.2 Magnification



(a) Magnification factor of the SNLS supernovae versus redshift. Most of the SNe are slightly demagnified whereas some are significantly magnified.

Figure (a) show the magnification, μ of each of the 171 SN as a function of redshift. As expected, most SNe are demagnified with respect to a homogeneous universe and some are significantly magnified. Moreover, the magnification distribution peaks at a value slightly lower than one and presents a long magnification tail.

4.3 Correlation

We are searching for a correlation between the Hubble residuals from a best fit cosmological model and the estimated magnifications of the supernovae based on foreground galaxy modeling. In Figure (b) we show a plot of the Hubble residuals, r , versus the estimated magnification in magnitudes.

The weighted correlation coefficient for this sample is $\rho = 0.18$. To evaluate the strength of the correlation we calculate the distribution of the weighted correlation coefficient for an uncorrelated sample and compare it with the obtained value for our sample. The uncorrelated samples are drawn by randomly associating Hubble residuals and expected magnifications of the real sample. The probability of finding a larger weighted correlation coefficient than the measured one from an uncorrelated sample is 1%, corresponding a 2.3σ detection.

In order to test the scale of galaxy mass estimates, we fit the slope a relating Hubble residuals and expected magnifications : $\langle r \rangle = a \langle \mu_m \rangle$ and find $a = 0.65 \pm 0.30$. Hence the data are consistent with the input mass-luminosity relations at the 1.2σ level, with a precision of 30%.

Using random lines of sight in the real data, we can estimate the increase of Hubble diagram scatter expected from gravitational lensing, as a function of redshift. This can be roughly described as $\sigma(\mu_m) = 0.08 \times z$. Alternatively, if we use the value of a derived from a fit of the relation between Hubble residuals and magnifications, we obtain a lower value $\sigma(\mu_m) = (0.05 \pm 0.022) \times z$.

5 Conclusion

We have calculated the expected magnification of the SNLS 3-year sample from the foreground galaxy properties and searched for a correlation with residuals from the Hubble diagram. A correlation is detected at the 99% CL, compatible with a slope of 1. The expected magnifications cause an extra scatter in the Hubble diagram approximated by $0.08 \times z$, which becomes $(0.05 \pm 0.022) \times z$ once the mass-luminosity relations are calibrated with the supernova data. Simulations also point to the fact that a signal detection is dominated by the number of SNe, their redshift distribution and the scatter in the SN residuals. Reducing the scatter in the estimated magnification by increasing the photometric redshift precision or reducing the scatter in the input mass-luminosity relations have little effect on the probability of a signal detection.

Finally, simulations using the true galaxy catalog show that using the full SNLS data set (~ 400 expected spectroscopically confirmed Type Ia SNe and ~ 200 photometrically identified Type Ia SNe) there is 80% chance of detecting a 3σ signal or more.

Acknowledgments

TK acknowledges the support of the French ministry of Education and Research and the Dark Cosmology Centre funded by the Danish National Research Foundation. We thank O. Ilbert for providing us with high resolution photometric redshifts in the COSMOS field prior to publication. We also thank Michel Fioc, Damien Le Borgne and Jens Hjort for useful discussions. This research has made use of the NASA/ IPAC Infrared Science Archive, which is operated by the Jet Propulsion Laboratory, California Institute of Technology, under contract with the National Aeronautics and Space Administration. The data reduction was carried out at the IN2P3 computing center in Lyon, France.

References

1. C. Balland, et al., *A&A* **507**, 85 (2009).
2. S. Baumont, et al., *A&A* **491**, 567 (2008).
3. A. Boehm, et al., *VizieR Online Data Catalog* **342**, 97 (2004).
4. M. Bertin, S. Arnouts, *A&AS* **117**, 393 (1996).
5. T. J. Bronder, et al., *A&A* **477**, 717 (2008).
6. M. Davis, et al., *SPIE* **4834**, 161-172 (2003).
7. M. Davis, et al., *ApJ* **660**, L1 (2007).
8. R. S. Ellis, et al., *ApJ* **674**, 51 (2008).
9. C. Gunnarsson, et al., *Journal of Cosmology and Astro-Particle Physics* **3**, 2 (2004).
10. D. A. Howell, et al., *ApJ* **634**, 1190 (2005).
11. O. Ilbert, et al., *A&A* **457**, 841 (2006).
12. O. Le fevre, et al., *A&A* **417**, 839 (2004).
13. J. L. Mitchell, et al., *ApJ* **622**, 81 (2005).

RECENT RESULTS FROM THE SNFACTORY EXPERIMENT.

E. GANGER, for the SNFactory collaboration.

*IPNL, Université Lyon/Université Lyon-I, Campus de la Doua, 4, rue Enrico Fermi,
69622 Villeurbanne Cedex*

From 2004 to 2009, around 200 Supernovae of Type 1a spectrophotometric time series were collected by the SNIFS instrument at the 2.2 UH telescope, with an unprecedented accuracy of 2% on the spectral absolute calibration. With such a unique sample, we used classical standardization techniques in order to assess the sample natural dispersion after ad-hoc corrections, and found a value of 0.16 mag. We also designed new standardization techniques based on spectral features in order to reduce further this dispersion to 0.13 mag. In particular, using dust-insensitive spectral indicators allows to correct for pure intrinsic variability of the luminosity, and derive color law parameters.

1 Introduction

1.1 *SNIa and cosmology*

Type Ia supernovae (SNIa) are thought to be thermonuclear explosions of carbon-oxygen white dwarfs approaching the Chandrasekhar limit either by accretion of material from a companion, the favored scenario, or by coalescence of two white dwarves, as it was put into evidence in some cases, in particular in our observations of SN2007if⁷.

By comparing the luminosity of distant and nearby objects, one is able to cancel out the effect of the intrinsic luminosity and the Hubble constant and to show an accelerated expansion of the universe. Along with other probes, it is possible to derive cosmological parameters in a concordant model, and to put constraints on the nature of dark energy, providing a large sample of objects. Current data sets^{4,5} exhibit a limited number of nearby objects, taken in conditions where the selection biases and the quality is difficult to assess. A set of hundreds of nearby objects is a prerequisite of future experiments such as the JDEM project in order to enhance their figure of merit.

1.2 *Purpose of a spectrophotometric survey of nearby SNIa*

The SNFactory experiment focuses on nearby supernovae, targeting them in the Hubble flow ($0.03 < z < 0.08$) which is a tradeoff between peculiar motion of the galaxies and the time needed to achieve a sufficient signal to noise. While the acquisition of hundreds of nearby objects will reduce the uncertainty on cosmological parameters by anchoring the Hubble diagram at low redshift, the high apparent luminosity of these objects allow to acquire spectral series with photometric accuracy.

Such a set is unique, and will be a reference set to train supernovae model fitters and calibrate the luminosity to color and lightcurve shape, and K-corrections. New standardization techniques

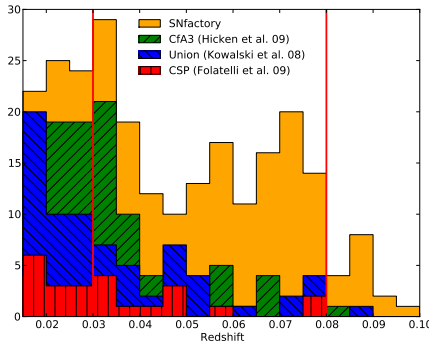


Figure 1: Redshift of SNFactory Type Ia supernovae.

can be also developed, exploiting the spectral features of the supernovae. These features can also be used to refine the sub-typing of SNIa and to serve as an input to computational supernovae explosion models, in order to constrain the physics of the explosion. They can serve as a reference for evolution studies, when similar data will become available at high redshift.

2 SNFactory

2.1 The search

The supernovae of the SNFactory program come mainly from a dedicated search, with the addition of some IAUC circular and Astronomer’s Telegram objects. They were screened and followed by a custom built integral field spectrograph, SNIFS.

The dedicated search was performed without assumptions on already existing galaxies in the field when defining the pointing, in order to minimize the selection biasses with respect to hosts. It was conducted at the 1.2m Samuel Oschin Schmidt telescope at Palomar Observatory as part of the Palomar-QUEST survey using the QUEST-II camera⁶.

2.2 The SNIFS instrument.

The followup instrument, SNIFS, is permanently mounted on the UH 2.2m telescope, and in operation three nights a week with at least a one night gap between each, from March to December. It is operational since 2004 and reached full operations during 2006.

It comprises two spectroscopic channels, with integral field technology. The incoming beam is split by a dichroic filter and projected in each channel on a 15×15 microlens array, representing a $6.4'' \times 6.4''$ field of view with a sampling of $0.43''$. The light is then dispersed by a grism so that the blue channel covers $3200\text{--}5200 \text{ \AA}$ at a dispersion of 2.5 \AA/pixel , and the red channel covers $5100\text{--}10000 \text{ \AA}$ at a dispersion of 2.9 \AA/pixel . In addition, a photometric channel equipped with a multifilter monitors a surrounding field of view of $10' \times 5'$ in order to derive the differential night-to-night extinction ratio for exposures on the same object by photometric analysis of stars in the field. It provides also as an input in order to reconstruct the PSF in the spectroscopic channel.

2.3 The dataset

During the 2004–2008 period, SNFactory discovered about 1000 supernovae of all types, 700 including third party discoveries were typed by the SNIFS instrument. Out of the 450 SNIa thus confirmed, 190 were followed with more than 5 epochs, which amounts to 3000 spectra. Some

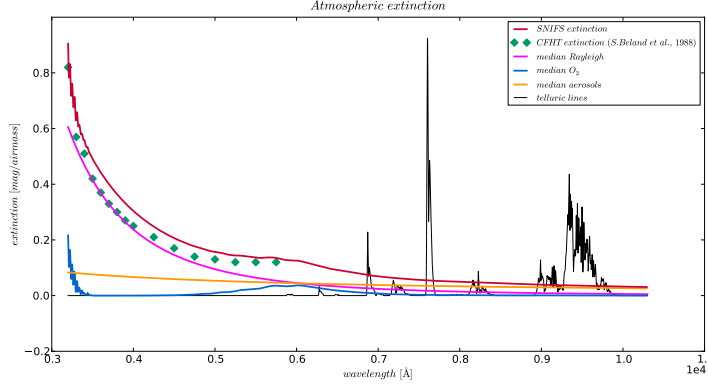


Figure 2: Atmospheric extinction derived at Mauna Kea by the SNIFS standard stars network

supernovae proved themselves worthwhile as individual objects and were subject of individual studies^{1,7,8}. This sample more than doubles the available statistics from existing sets in our target redshift range, and is unique in its nature, providing spectrometry with photometric precision all along the light-curve, as shown on figure 1.

3 Data analysis and first results

3.1 Calibration status

The data reduction pipeline involves classical CCD preprocessing, extraction of individual spectra from the CCD, classical wavelength and relative flux calibration using arc and continuum lamp exposures. In order to obtain an absolute flux calibration, we used exposures of standard stars. When the night is photometric, this calibration can be propagated to the science object, whereas in non-photometric conditions, an additional extinction found to be grey was applied on an object per object basis. It was determined using the photometric channel. The airmass dependance of the flux calibration varies with time, and the contribution from different components, Rayleigh diffusion, ozone, aerosols and telluric lines was calibrated on a day by day basis using exposures on standard stars at different airmass to derive a nightly calibration solution. The average atmospheric extinction is presented on figure 2.

The precision obtained on the calibration was derived from standard stars calibrated as if there were supernova, and comparing to their reference curves. Its normalized mean absolute deviation is 1.7% on photometric nights and 3.2% on non-photometric nights, the color term between adjacent bands being 1.1% on average. In order to assess the calibration on supernovae, which are fainter and for which a structured background has to be subtracted, we compared the flux in synthetic filters to the SALT2 fit³ for the object, and obtained a dispersion of 6.0%, mostly due to the model accuracy or the object variability.

3.2 Hubble diagram dispersion

At the present stage of data analysis, Supernovae were extracted with the assumption that the structured background is linear. The obtained spectral timeseries were integrated on a set of custom top hat filters and the resulting lightcurves were fit by a SALT2 model³ in order to extract their stretch and color parameters. Then, a cosmological fit was performed, and the residuals to the fit were found to have a dispersion of 0.16 magnitudes, which is the usual dispersion observed on far supernovae by this technique, and is of excellent quality for nearby objects.

In order to reduce further this dispersion, various techniques were used. First, K-correction-less analysis uses a set of custom filters which are redshift-dependant, in order to integrate the

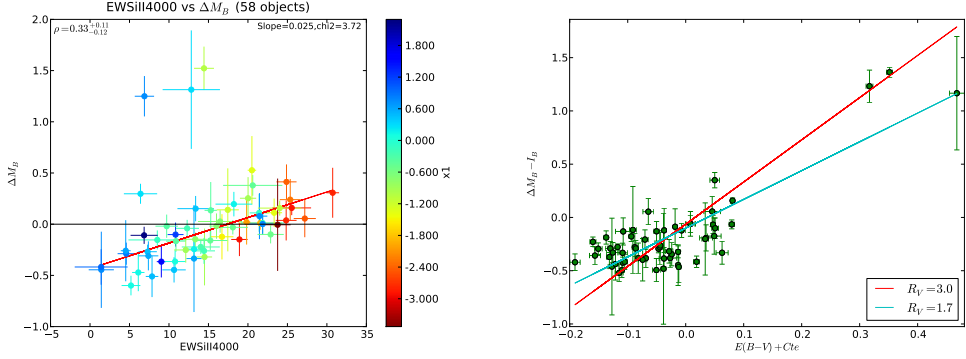


Figure 3: Left : correlation of EWSiII4000 and Hubble diagram residuals. Right : Hubble residuals with respect to color excess after intrinsic contribution subtraction.

same portion of the spectrum in the rest frame. This technique can reduce the dispersion to 0.14 magnitudes.

Alternate metrics for the intrinsic parameters were also proposed. A new flux ratio variable was introduced ², which is shown to be a replacement of both color and stretch, and gives a final resolution of 0.13 mag. Classical indicators, such as the pseudo-equivalent width of the SiII(4130)Å feature were also used in replacement of the stretch parameter. When fitting the Hubble diagram with this equivalent with in place of the stretch, the resulting dispersion is 0.16 mag also, proving that this spectral indicator is a measurement of intrinsic properties of the object.

3.3 Determination of color law

As the SiII(4130) equivalent width is insensitive to the dust reddening of the spectrum, we can derive, from the residuals to the Hubble diagram ΔM_B a correction law for intrinsic luminosity I_B with respect to this equivalent width. Then the difference $\Delta M_B - I_B$ contains mostly the effect of color, be it dust reddening of intrinsic, and a residual of intrinsic dispersion. This measure can be repeated in any band, and in particular, we can define the color, corrected from the intrinsic variation, as $E(B - V) = \Delta M_B - I_B - \Delta M_V - I_V$. Assuming the color term is mostly dust, it is possible to fit for a Cardelli law. The fit is very sensitive on the assumption made on the covariances between all the terms, and the value of 3.1 can't be excluded from preliminary analyses.

1. G. Aldering, et al., *ApJ* **650**, 510 (2006)
2. JS. Bailey, et al. , *A&A* **500**, L17 (2009)
3. J. Guy, et al. , *A&A* **466**, 11 (2007)
4. M. Hicken, et al., *ApJ* **700**, 1097 (2009)
5. M. Kowalski, et al., *ApJ* **686**, 749 (2008)
6. D. Rabinowitz, et al., in *Bulletin of the American Astronomical Society*, **35**, 162 (2003).
7. R. Scalzo, et al., *ApJ* **713**, 1073 (2010)
8. R. Thomas, et al., *ApJ* **654L**, 53 (2009)

Gravitational lensing and parameter extraction from SNe catalogues ^a

Valerio Marra

Department of Physics, University of Jyväskylä, PL 35 (YFL), FIN-40014 Jyväskylä, Finland

Helsinki Institute of Physics, University of Helsinki, PL 64, FIN-00014 Helsinki, Finland

We reanalyze the supernovae data from the Union Compilation including the weak lensing effects caused by inhomogeneities. We compute the lensing probability distribution function for each background solution described by the parameters Ω_M , Ω_Λ and w in the presence of inhomogeneities, which are designed to mimic the observed large-scale structures. We then perform a likelihood analysis in the space of FLRW-parameters and compare our results with the standard approach. We find that the inclusion of lensing can move the best-fit model significantly towards the cosmic concordance of the flat Λ CDM model, improving the agreement with the constraints coming from the CMB and BAO.

Introduction. In the standard approach SNe observations are analyzed in the framework of homogenous FLRW models. However, the universe is known to be inhomogenous, showing a distribution of clusters and filaments surrounding much emptier voids of size $\approx 10 - 100$ Mpc. A known effect of these structures on any set of standard candles is weak gravitational lensing. Weak lensing can cause either brightening or dimming of the source depending on whether the matter column density along the line of sight is larger or smaller than the FLRW value.

The fundamental quantity describing this statistical magnification is the lensing probability distribution function (PDF). The lensing PDF is specific both to the given FLRW model, and to the particular spectrum of inhomogeneities introduced. It is not currently possible to extract the lensing PDF from the observational data and we have to resort to theoretical models. Here we use the approach based on the stochastic modelling of the inhomogeneities introduced in Ref.³. This method combines the flexibility in modelling with a fast performance in obtaining the lensing PDF. To compute one lensing PDF, the numerical implementation `turboGL 0.4`³ takes, with an ordinary desktop computer, a time of order of a second. This speed performance makes it feasible to do an *ab initio* likelihood analysis in the space of FLRW-models endowed with inhomogeneities. In this letter we will perform such an analysis for the Union SNe Compilation⁴.

We will treat inhomogeneities as perturbations over the FLRW model which is parametrized as usual by the present Hubble expansion rate $H_0 = 100h$ km s⁻¹ Mpc⁻¹, the present matter density parameter Ω_M and the present dark energy density parameter Ω_Λ and a constant equation of state w . We fix the radiation density to $\Omega_R = 4.2 \cdot 10^{-5}h^{-2}$. For inhomogeneities we use a “meatball” model consisting of randomly placed spherical halos made of ordinary and dark matter. In principle these halos need not be virialized, and the spherical symmetry assumption is not very restrictive³.

^aContribution to the proceedings of the 45th Rencontres de Moriond, Cosmology Session, March 13-20, 2010. Work done in collaboration with L. Amendola, K. Kainulainen and M. Quartin and based on¹, where more details and references can be found.

Here we use a simple single-mass halo model which is completely parametrized by the comoving distance between halos λ_c , the halo proper radius R_p and the density profile. We choose the latter to be the NFW profile⁶ with a concentration parameter $c \simeq 6.7$ and we assume that the halos have virialized with a contrast of 200 at a redshift z_{vir} , whereby (for a given z_{vir}) the corresponding R_p can be taken constant. The halo mass is related to the comoving density $n_c \equiv \lambda_c^{-3}$ by $\rho_c \Omega_M = M n_c$. For numerical values we used $\lambda_c = 12.6 h^{-1} \text{Mpc}$, and correspondingly $M = 5.6 \cdot 10^{14} h^{-1} \Omega_M M_\odot$, and $z_{\text{vir}} = 0.8$. The numerical value of R_p depends on the background matter density at z_{vir} . For the Λ CDM model $R_p \simeq 0.7 h^{-1} \text{Mpc}$.

Lensing. The meatball model incorporates quantitatively the crucial feature that photons can travel through voids and miss the localized overdensities. This feature is not present, for example, in “swiss-cheese” models where the bubble boundaries are designed to have compensating overdensities. Such models have indeed been shown to have on average little lensing effects^{7,8}. The key quantity is the lens convergence κ , which in the weak-lensing approximation is

$$\kappa(z_s) = \int_0^{r_s} dr G(r, r_s) \delta_M(r, t(r)). \quad (1)$$

Here $\delta_M(r, t)$ is the matter density contrast and $G(r, r_s) = \frac{3H_0^2 \Omega_M}{2c^2 a(t(r))} \frac{f_k(r) f_k(r_s - r)}{f_k(r_s)}$, where the functions $a(t)$, $t(r)$ and $r(z)$ correspond to the FLRW model, $r_s = r(z_s)$ is the comoving position of the source at redshift z_s and the integral is evaluated along the unperturbed light path. Also, $f_k(r) = \sin(r\sqrt{k})/\sqrt{k}$, r , $\sinh(r\sqrt{-k})/\sqrt{-k}$ depending on the spatial curvature $k > = < 0$, respectively. Neglecting the second-order contribution of the shear, the shift in the distance modulus caused by lensing is expressed solely in terms of κ : $\Delta m(z) = 5 \log_{10}(1 - \kappa(z))$. In Ref.³ a fast and easy way to obtain the convergence PDF for these meatball models was derived. In short, the formula for the convergence Eq. (1) is replaced by a discretized probabilistic expression:

$$\kappa(\{k_{im}\}) = \sum_{i=1}^{N_S} \sum_{m=1}^{N_R} \kappa_{1im} (k_{im} - \Delta N_{im}). \quad (2)$$

Here κ_{1im} is the convergence due to one halo, at a comoving distance r_i , which the photon path intercepts with an impact parameter b_m . The quantity k_{im} in Eq. (2) is a Poisson random variable of parameter $\Delta N_{im} = n_c \Delta V_{im}$, which gives the expected number of halos within the bin volume ΔV_{im} . That is, Eq. 2 defines a convergence as a function of a *configuration* $\{k_{im}\}$ of halos along an arbitrary line of sight from the observer to the source. The lensing PDF P_{wl} is then constructed from a large sample of random configurations $\{k_{im}\}$. Note that the expected convergence computed from Eq. (2) is zero, consistent with photon conservation in weak lensing, because for a Poisson distributed variable the expected value coincides with its parameter.

Likelihood function. After the raw lensing PDF $P_{\text{wl}}(\Delta m)$ has been computed for a given set of FLRW-parameters and redshifts, it still has to be convolved with the intrinsic source brightness distribution P_{in} : $P(\Delta m, z_s) = \int dy P_{\text{wl}}(y, z_s) P_{\text{in}}(\Delta m - y)$. We take P_{in} to be a gaussian in the distance moduli. The actual intrinsic distribution should be a universal function if the SN are similar at all distances. However, following Ref.⁴, we will combine all observational (gaussian by assumption) uncertainties in quadrature with the intrinsic distribution, whereby P_{in} becomes an effective distribution specific for each SN event $P_{\text{in}}(x) \rightarrow P_{\text{SN}}(x, \sigma_i)$. The likelihood function for a single SN-observation is then

$$L_i(\mu) = \int dy P_{\text{wl}}(y, z_i) P_{\text{SN}}(\Delta m_i - \mu - y, \sigma_i), \quad (3)$$

where $\Delta m_i = m_{o,i} - m_{t,i}$, $m_{o,i}$ is the observed magnitude and the corresponding FLRW prediction is related to the luminosity distance d_L by $m_{t,i} = 5 \log_{10} d_L(z_i)/10 \text{pc}$. The parameter μ is

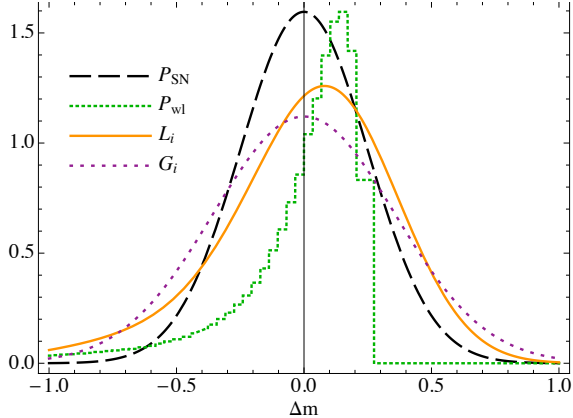


Figure 1: PDFs for a SN with $\sigma = 0.25$ mag at $z_s = 1.5$ in the Λ CDM model.

an unknown offset sum of the SNe absolute magnitudes, of k -corrections and other possible systematics. Note also that L_i inherits the vanishing mean of P_{wl} and that its variance is simply given by the sum of the variances of the convolving PDFs. We define the total likelihood function as the product of all independent likelihood functions, further marginalized over μ :

$$L(\Omega_M, \Omega_\Lambda, w) = \int d\mu \Pi_i L_i(\mu). \quad (4)$$

Since μ is degenerate with $\log_{10} H_0$ we are effectively marginalizing also over the expansion rate of the universe. A replacement of $P_{\text{wl}}(y, z)$ by a *cosmology-independent* gaussian with a variance² $\sigma \equiv 0.093z$, would reduce Eq. (4) to the form used in the analysis of Ref.⁴. Typical forms of P_{wl} , P_{SN} and $L_i(\mu = 0)$ have been illustrated in Fig. 1. Also shown for later use is G_i , which is a gaussian with the same variance of $L_i(0)$.

Results and Conclusions. We run a global likelihood analysis using the formula (4) for two different setups: first in the (Ω_M, w) -space for flat ($\Omega_k = 0$) w CDM models and second in the $(\Omega_M, \Omega_\Lambda)$ -space for a non-flat Λ CDM model ($w = -1$) using the Union SNe Compilation of Ref.⁴. We show our results in Fig. 2 as confidence level contours for $\chi^2 = -2 \log L$. For comparison we have performed the analysis also using the standard P_{SN} distribution (as done in Ref.⁴) and the distribution G_i . The idea for using G_i is that it takes into account the *cosmology-dependent* extra dispersion coming from lensing, but neglects the skewness of the true distribution. So, the contours relative to G_i give an idea of how much of the difference from the standard analysis comes from the widening of the intrinsic distribution, and how much from the skewness of the actual PDF. As it is evident from Fig. 2, the 1σ contours are basically determined by the cosmology-dependent widening, whereas the skewness starts to be relevant between the 2 and 3σ levels. The general trend favoring models with smaller Ω_M follows from the fact that lensing effects in general make the fit slightly worse with than without lensing⁹. The effect comes both from the cosmology-dependent widening and from the skewness of the distributions, and it is obviously more pronounced for larger matter densities. This can be seen directly from Eq. (1), where the magnitude of the lensing effects is explicitly seen to be proportional to Ω_M . The overall movement of the best-fit model then follows the degeneracy of the FLRW models.

We have presented a reanalysis of the supernovae data from the Union Compilation including the lensing effects caused by inhomogeneities. Unlike in the analysis of Ref.⁴, where the lensing effects are accounted for by adding in quadrature a small z -dependent variance to the other statistical and systematic errors, we compute the actual probability distribution functions for each different FLRW-model with a spectrum of inhomogeneities designed to mimic the observed

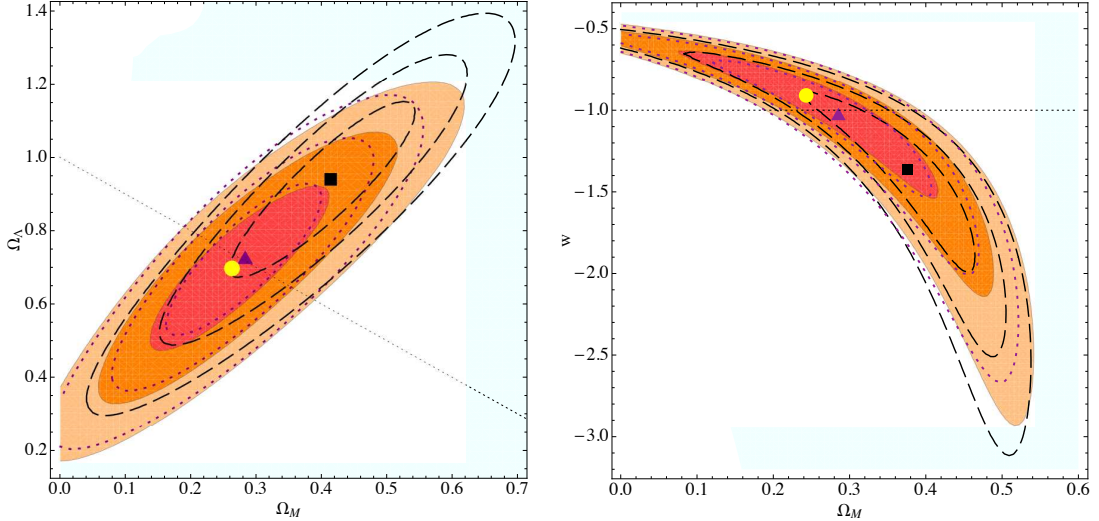


Figure 2: 1, 2 and 3σ confidence level contours in the $(\Omega_M, \Omega_\Lambda)$ -space for a non-flat Λ CDM model (left) and in the (Ω_M, w) -space for flat w CDM models (right) with the halos described in the text. The results using the full likelihood of Eq. (4) are shown as filled contours and the best-fit model by a disk. The results relative to the gaussian G_i are shown by dotted lines with a triangle, the ones relative to the unlensed P_{SN} are shown by dashed lines with a square and correspond to the ones of Ref. ⁵ (without systematics).

large-scale structures. In particular the large voids that dominate the late-time universe were imposed in the model by concentrating all matter into halos. Accordingly, we chose the halos to have the mass of a very large cluster, *i.e.* of order $10^{14} h^{-1} M_\odot$, which then corresponds to an interhalo distance of order $10 h^{-1} \text{Mpc}$. We found that including inhomogeneities significantly changes the likelihood contours (the likelihood peaks, for instance, move of around 1σ) and clearly improves the concordance of the supernova data with the CMB and the BAO, which may be used to strengthen the case for the standard Λ CDM model.

One should be reminded that our findings could change if other effects caused by large-scale inhomogeneities are introduced, e.g., selection or redshift effects. It also remains to be seen how a more realistic inhomogeneous distribution, providing a better fit to the matter power spectrum, would affect these weak-lensing corrections to the SNe contours.

References

1. L. Amendola, K. Kainulainen, V. Marra and M. Quartin, arXiv:1002.1232 [astro-ph.CO].
2. D. E. Holz, E. V. Linder, *Astrophys. J.* **631**, 678 (2005).
3. K. Kainulainen and V. Marra, *Phys. Rev. D* **80**, 123020 (2009). *turbogL* is available at: <http://www.turbogl.org>
4. M. Kowalski *et al.*, *Astrophys. J.* **686**, 749 (2008).
5. C. Park, J. R. Gott III, A. L. Melott and I. D. Karachentsev, *Astrophys. J.* **387**, 1 (1992); S. F. Shandarin and C. Yess, *Astrophys. J.* **505**, 12 (1998).
6. J. F. Navarro, C. S. Frenk and S. D. M. White, *Astrophys. J.* **462** (1996) 563; J. F. Navarro, C. S. Frenk and S. D. M. White, *Astrophys. J.* **490** (1997) 493.
7. V. Marra, E. W. Kolb, S. Matarrese and A. Riotto, *Phys. Rev. D* **76**, 123004 (2007); V. Marra, E. W. Kolb and S. Matarrese, *Phys. Rev. D* **77**, 023003 (2008).
8. N. Brouzakis, N. Tetradis and E. Tzavara, *JCAP* **0804**, 008 (2008); R. A. Vanderveld, E. E. Flanagan and I. Wasserman, *Phys. Rev. D* **78**, 083511 (2008); W. Valkenburg, *JCAP* **0906**, 010 (2009).
9. This effect was noted also in: K. Kainulainen, V. Marra, *Phys. Rev. D* **80**, 127301 (2009).

Investigating The Uncertainty On The BAO Scale Measured From Future Photometric And Spectroscopic Surveys

Alexandra Abate

Laboratoire de l'Accélérateur Linéaire, IN2P3-CNRS, Université de Paris-Sud, BP. 34, 91898 Orsay Cedex, France

The Large Synoptic Survey Telescope (LSST) is a wide (20,000 sq.deg.) and deep *ugrizy* imaging survey which will be sited at Cerro Pachon in Chile. A major scientific goal of LSST is to constrain dark energy parameters via the baryon acoustic oscillation (BAO) signal. Crucial to this technique is the measurement of well-understood photometric redshifts, derived from the survey *ugrizy* imaging. Here we present the results of the effect of simulated photometric redshift (PZ) errors on the reconstruction of the BAO signal. We generate many “Monte Carlo” simulations of galaxies from a model power spectrum using Fast Fourier Transform techniques. Mock galaxy properties are assigned using an algorithm that reproduces observed luminosity-color-redshift distributions from the GOODS survey. We also compare these results to those expected from a possible future spectroscopic survey such as BigBOSS.

1 Introduction

In the early universe, when the temperature is high enough so the photons and baryons are coupled through Compton scattering in a plasma, the cosmological density fluctuations create sound waves which propagate through this plasma. At around a redshift of 1000 the temperature of the universe drops to a level at which the Compton scattering is no longer efficient, effectively stalling the sound waves at the epoch of recombination. The distance these sound waves could travel in the time between the formation of the perturbations and the epoch of recombination imprinted a *characteristic scale* into the spectrum of density perturbations. Because the universe has a significant fraction of baryons, theory predicts that this characteristic scale will also be imprinted in the late-time spectrum of density perturbations. Since galaxies are expected to form in the regions that are overdense in baryons and dark matter, and because this is driven by where the initial perturbations were, there should be a small excess of galaxies at this characteristic scale away from other galaxies. At recombination this scale is roughly 150 Mpc, and it appears in the power spectrum of density fluctuations as a damped harmonic sequence, a series of *wiggles*, which are what is known as the baryon acoustic oscillations (BAO). The position of these wiggles measured as a function of redshift reveals information about dark energy.

It has been shown^{1,2} that it is possible to measure BAO using a photometric redshift survey. The advantage of using photometric redshifts over spectroscopic redshifts is that they are much less expensive (time consuming) to obtain and so a much larger volume of the universe can be surveyed. Since the BAO feature is observed on fairly large scales, a volume even larger than this must be surveyed in order to obtain a measurement with enough statistical significance to measure the cosmological parameters precisely. The disadvantage of photometric redshifts is that they have large errors and the exact distribution of these errors is currently not well understood. Here we present an early result from our simulations of the performance of LSST,

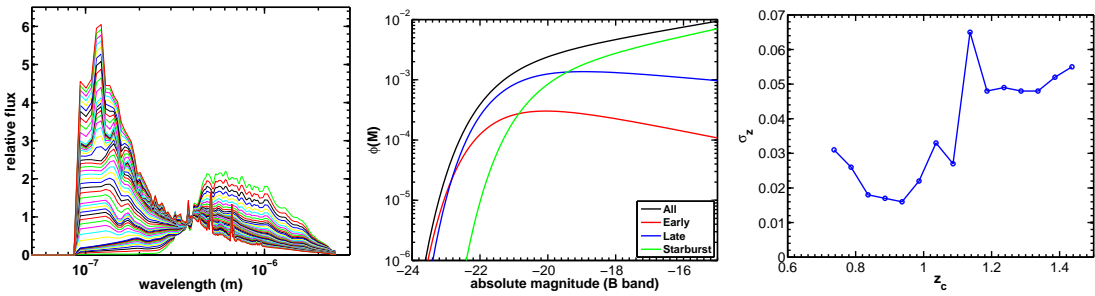


Figure 1: *LHS*: Interpolated SED library, all normalised to the same value at $0.4\mu\text{m}$; *Center*: GOODS type-specific luminosity functions at $0.75 < z < 1$; *RHS*: Fitted standard deviation of photometric redshift errors in each redshift slice of the simulation.

a future photometric wide-field survey, in measuring the BAO signal.

2 The Large Synoptic Survey Telescope

The Large Synoptic Survey Telescope (LSST) will be the first of a next generation of ground based optical telescopes. It seeks to investigate important scientific problems of the next decade: probing dark energy and dark matter, taking an inventory of the Solar System, exploring the transient optical sky, and understanding galaxy formation and the structure of the Milky Way. All these diverse science goals require wide-field repeated deep imaging of the sky in many optical bands.

LSST will carry out such a survey by imaging 20,000 deg² of the sky in six broad photometric bands *ugrizy*, imaging each region of sky roughly 2000 times (1000 pairs of back-to-back 15-sec exposures) over a ten-year survey lifetime. After 10 years, with 1000 visits (2x15s exposures), it is anticipated LSST will yield a coadded map of the sky with a 5- σ depth for point sources of $r \sim 27.5$. For more details on the science goals and capabilities that will be provided by LSST, see the LSST Science Book³.

3 Simulation of mock galaxy catalogs

We take a model linear theory matter power spectrum and generate Gaussian realisations of over-densities. Each over-density is assigned N_i galaxies where N_i depends on the value of the over-density and the expected mean number density of galaxies at the relevant redshift. The mean number density of galaxies as a function of redshift is calculated by integrating the GOODS luminosity functions (LFs)⁴, shown in the center panel of Fig. 1.

Each galaxy in the simulation is assigned an absolute magnitude and a broad spectral type: early-type, late-type or starburst. This is done by creating a probability distribution using the galaxy-type specific LFs measured from GOODS⁴, again see the center panel of Fig. 1. We then create a library of spectral energy densities (SEDs) of different galaxy types by interpolating the CWW⁵ and Kinney⁶ empirical galaxy templates, which cover the range of galaxy types from early to starburst, shown in the left-hand panel of Fig. 1. We randomly assign each galaxy an SED with a prior based on its original broad spectral type. Using the information simulated so far for each galaxy (specifically: z , absolute magnitude and SED) we calculate the observed apparent magnitudes in each LSST filter including the expected photometric and systematic errors³. We verify the simulation method by comparing our own simulation of the GOODS data to the real GOODS data.

Photometric redshifts are reconstructed using a χ^2 fitting technique using the galaxy luminosity function as a prior. Our code produces reasonable distributions of the photometric redshift errors: $z_{\text{phot}} - z_{\text{spec}}$. The right-hand panel of Fig. 1 shows the fitted standard deviation

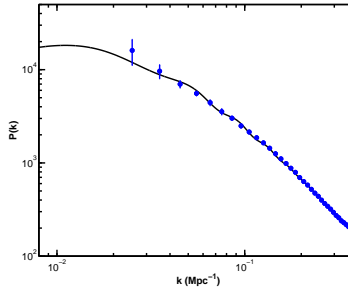


Figure 2: Power spectrum measured from the simulation described in Sections 3 and 4.

of $z_{phot} - z_{spec}$ in different redshift slices of $\Delta z = 0.05$ in the simulation. The precision after $z = 1$ worsens as expected due to the Balmer break having transitioned out of the y band and the Lyman break having yet to enter the u band.

4 Early simulation result

We have simulated just a small survey at this stage: 5 Gpc³ covering $0.7 < z < 1.4$ and assuming 100 visits of the simulated survey area.

We compute the power spectrum using a direct Fourier transform method as outlined in Blake et al. (2007)². To measure the precision on the BAO scale we use the “wiggles only”⁷ method: dividing the measured power spectrum by a smooth reference power spectrum given by the Eisenstein and Hu⁸ “no-wiggles” fitting formula. The “wiggles only” power spectrum is then well approximated by a decaying sinusoid:

$$\frac{P(k)}{P_{ref}} = 1 + Ak \exp \left[- \left(\frac{k}{0.1h\text{Mpc}^{-1}} \right)^\gamma \right] \sin \left(\frac{2\pi k}{k_a} \right) \quad (1)$$

where k_a represents the acoustic scale.

We find the precision on the measurement of the acoustic scale from this simulation to be 3%, corresponding to an error on the dark energy equation of state w (assumed constant) of 16%. Performing a simple extrapolation to an equivalent simulation covering the LSST volume suggests the precision of the acoustic scale measurement for LSST from BAO would be 0.4%, corresponding to an error on w of about 2%.

5 LSST vs BigBOSS

BigBOSS⁹ is a proposed *spectroscopic* survey to measure BAO. Though it will have more precise redshifts than LSST it will cover less volume and observe less galaxies, see Table 1. It is interesting to compare the expected errors on the power spectrum for idealised versions of both surveys.

An analytic expression for the expected fractional errors on the power spectrum under some simplifying assumptions is given below:

$$\frac{\sigma_P}{P} = \sqrt{\frac{2(2\pi)^3}{V} \frac{1}{4\pi k^2 dk} \left(\frac{P + 1/n}{P} \right) \frac{1}{\langle \exp(-(k_z \sigma_z)^2) \rangle_k}} \quad (2)$$

The above equation incorporates uncertainties due to sample variance, shot noise and the photometric redshift errors, assumed to have a Gaussian distribution with a standard deviation which is constant across the survey. For BigBOSS essentially $\sigma_z = 0$.

Fig. 3 shows Eq. 2 plotted for the LSST survey (blue/dark solid line) and the BigBOSS survey (green/light solid line). On the left-hand side optimistic photometric redshift errors for

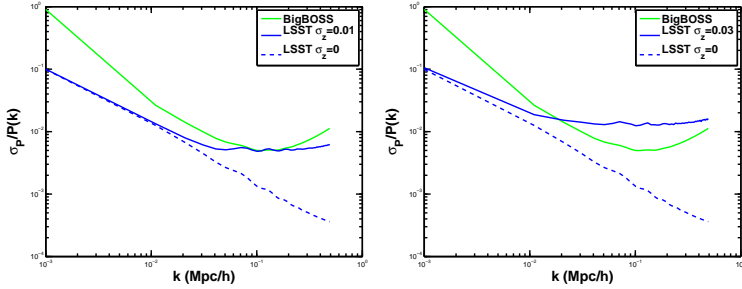


Figure 3: Expected power spectrum errors for BigBOSS and LSST as given by Eq. 2. On the left-hand side optimistic photometric redshift errors for LSST are assumed ($\sigma_z = 0.01$), and on the right-hand side, more conservative ones ($\sigma_z = 0.03$).

Table 1: Comparison of BigBOSS and LSST

Survey	redshift range	Sky Area (sq.deg)	Volume (Mpc/h) ³	N gals
BigBOSS	0.20 < z < 2.0	14,000	3×10^{10}	3×10^7
LSST	0.15 < z < 3.0	20,000	1×10^{11}	10^{10}

LSST are assumed ($\sigma_z = 0.01$), and on the right-hand side, conservative ones ($\sigma_z = 0.03$). The blue dashed line is for LSST with zero photometric redshift errors. The figure shows that BigBOSS becomes shot noise dominated around the BAO scale. To produce competitive constraints with BigBOSS LSST must achieve a photometric redshift precision of $\sigma_z = 0.01$, though LSST performs far superior to BigBOSS on large scales for both assumed error models.

6 Conclusions

From our current simulations we find that:

- Our simulation produces a realistic observed galaxy catalog.
- Computation of photometric redshifts produces expected error distribution.
- Using our current small survey simulation we have shown that a direct 3D power spectrum estimation with photometric redshifts can produce a reasonable constraint on k_{BAO} : $\Delta k_a / k_a = 3\%$
- LSST is competitive with BigBOSS even on the BAO scale, it is superior at large scales. $\Delta k_a / k_a = 0.3\%$ (BigBOSS/LSST optimistic)
 $\Delta k_a / k_a = 0.6\%$ (LSST conservative)

References

1. C. Blake, and S. Bridle MNRAS **363**, 1329 (2005).
2. C. Blake, A. Collister, S. Bridle and O. Lahav MNRAS **374**, 1527 (2007).
3. LSST Science Collaborations: *The LSST Science Book*, arXiv:astro-ph **0912.0201v1**, <http://www.lsst.org/lsst/scibook> (2009).
4. T. Dahlen et al. ApJ **631**, 126 (2005).
5. G.D. Coleman, C.C. Wu and D.W. Weedman ApJS **43**, 393 (1980)
6. A.L. Kinney et al. ApJ **467**, 38 (1996).
7. C. Blake, and K. Glazebrook ApJ **594**, 665 (2003).
8. D.J. Eisenstein and W. Hu ApJ **496**, 605 (1998).
9. D.J. Schlegel et al. arXiv:astro-ph **0904.0468**, (2009)

Constraining Dark Energy with BOSS

Nicol'as G. Busca

APC - Université de Paris 7, Laboratoire APC 10, rue Alice Domon et Léonie Duquet 75205 Paris Cedex 13, Paris

The Baryon Oscillation Spectroscopic Survey (BOSS) will measure the redshift of 1.5 million luminous red galaxies (at $z \sim 0.6$) and 160,000 high redshift quasars ($z > 2.3$). By using the baryon acoustic oscillation scale as a physically calibrated ruler, BOSS will determine the absolute cosmic distance scale with a precision of 1% at $z = 0.35$, 1.1% at $z = 0.6$ and 1.5% at $z = 2.5$ and achieve tight constraints on the equation of state of dark energy. BOSS has been taking data in a stable manner since the end of 2009 and has currently observed about 2% of the final survey surface.

1 Introduction

This last decade has witnessed exceptional progress in the understanding of the Universe at large scales. Very precise observations shaped the current theory for the evolution of the universe since the end of inflation: the Λ -CDM model. However, the Λ -CDM model is far from being completely satisfactory since it contains at least two ingredients which seem *ad-hoc*: the dark matter and the dark energy.

The possibility of a direct detection of dark matter particles might be within reach of current generation experiments, if the recent results from DAMA/LIBRA¹, Edelweiss² and CDMS³ turn out to be the “tip of the iceberg”. The increased exposure of the next runs will tell. At the same time, the LHC will also start probing the parameter space of dark matter models.

While there are working models for dark matter (for instance, those based on supersymmetric particles), the nature of dark energy is darker. Why is the dark energy density so small? Why are we observing the universe right when it became dominant? What is dark energy anyway?

Wide field astronomy will bring essential pieces to this cosmic puzzle. In the next decade, data from many experimental efforts will constrain the nature of dark energy⁴ by constraining its equation of state. The Baryon acoustic Oscillations Spectroscopic Survey (BOSS) is already underway. BOSS is part of the SDSS-III and will measure the peak in the two-point correlation function due to baryon acoustic oscillations (BAO) with percent-precision. Comparison of the sound horizon at decoupling with this observed scale leads then to constraints on cosmological parameters. The measurement will be done in two redshift ranges with two different techniques: in the range $0.3 < z < 0.6$ by means of the spatial distribution of luminous red galaxies (LRG) and in the range $2.3 < z < 3$ by means of the correlations among peaks and troughs in the Ly- α forests of distant quasars.

In these proceedings, I will briefly review the physics of baryon acoustic oscillations in the context of BOSS, and the expected constraints that BOSS will pose on the equation of state of dark energy.

2 Baryon Acoustic Oscillations

Baryon acoustic oscillations arise due to the tight coupling between baryons and photons in the hot, dense primordial plasma. During this tight coupling phase, perturbations in the baryon-photon fluid are unable to grow, but rather propagate as sound waves. After decoupling ($z \sim 1000$) baryons and photons decouple and sound waves are frozen in the initial distribution of baryons. The gravitational collapse then governs the evolution of this initial distribution. The imprint of the initial distribution of sound waves should then be observable in the late time distribution of matter (see *e.g.* ⁶).

The typical distance between overdensities is expected to be the size of the sound horizon at decoupling, nearly $100\text{Mpc}/h$, and this “acoustic scale” can then be used as a physically calibrated ruler. Since the initial distribution of sound waves is also imprinted as the pattern of anisotropies in the CMB, experiments such as WMAP or Plank directly measure the acoustic scale at decoupling. Measurements of the distribution of matter as a function of redshift are tantamount to a measurement of the acoustic scale which can be used to constrain the expansion history of the universe.

With enough statistics, one can measure the acoustic scale both along and across the line of sight which implies direct measurements of two cosmological distances: the Hubble parameter $H(z)$ and the angular diameter distance $d_A(z)$.

This method is expected to be highly robust since the acoustic scale is much larger than the scale of non-linear gravitational collapse.

3 The BOSS experiment

BOSS is the main SDSS-III dark time project. It uses the SDSS 4m telescope, with a field of view of 7 deg^2 . BOSS is a fully spectroscopic survey which will observe $10,000\text{ deg}^2$ in the sky. BOSS makes several improvements with respect to the previous spectroscopic surveys of SDSS-I and SDSS-II: the coverage of the spectrograph is increased to the range $3,700\text{ \AA}$ - $9,600\text{ \AA}$, 1,000 of 2 arcsec in diameter will replace the 640 fibers of 3 arcsec in diameter, all BOSS fibers will be devoted to either LRG or quasar targets (previously only 10-15% of galaxy targets were LRGs or quasars). BOSS is expected to spectroscopically observe nearly 1,600,000 LRGs at $0.15 < z < 0.7$ and 160,000 quasars at $z > 2.3$.

These two types of observations, LRGs and quasars, sample the matter distribution in different ways. LRGs represent a discrete sampling of the underlying matter distribution. The correlation function can be recovered by the standard technique developed by Landy and Szalay ⁵. In contrast, quasars provide a sampling of matter by their Ly α forest. The absorption features in the Ly α forest are due to the presence of neutral hydrogen in the line of sight of a given quasar. The matter distribution is then sampled by an ensemble of “skewers”, each for each quasar line of sight. The correlation function can be recovered in the correlation of absorption features in the forest.

The LRG technique has been exploited by the previous SDSS surveys and the acoustic peak in the LRG distribution has already been observed ⁷. BOSS will make of this detection a precision measurement by increasing the statistics by over a factor of 10. The quasar-Ly α technique is promising (see *e.g.* [?]) but its power to measure the acoustic scale has not yet been demonstrated experimentally.

4 Constraints from BOSS

With its $10,000\text{ deg}^2$ area, BOSS is within a factor of two of the cosmic variance limit for BAO measurement precision at $z < 0.6$ so no future experiment can do substantially better in

this regime. As illustrated in figure 1(left), BAO measurements provide an interesting cross-calibration with type Ia SN at intermediate redshift range, and extend the Hubble diagram to much higher redshifts.

The capabilities of BOSS can be characterized by using the standard parametrization of the equation of state of dark energy: $w(z) = w_0 + w_1 z$. The Hubble parameter is then given by:

$$H^2(z) = \Omega_m(1+z)^3 + \Omega_r(1+z)^4 + \Omega_K(1+z)^2 + \Omega_X(1+z)^{3w(z)} \quad (1)$$

where Ω_i is the present fraction of the critical density in the species i and X denotes dark energy. The angular diameter distance is then:

$$d_A = |K|^{-1} f(|K|^{1/2} \chi), \quad \chi = \int_0^z \frac{dz}{H(z)} \quad (2)$$

where $f(x) = \sinh(x)$, x , $\sin(x)$ for an open, flat or closed universe respectively and $|K|$ is the spatial curvature.

A, somewhat optimistic, estimation of the expected uncertainties in w_0 and w_1 can be obtained via a Fisher analysis by assuming that all other cosmological parameters in equation 1 are fixed to their current best fit values and that both $H(z)$ and $d_A(z)$ are measured in 3 low z (from LRGs) and 3 high z (from quasars) slices with nominal uncertainties at the percent level (a more thorough treatment that rather marginalizes over these parameters and includes other systematic effects can be found in ⁸).

Figure 1(left) shows the 90% constraints in the $w_0 - w_1$ plane coming from $H(z)$ alone (blue), $d_A(z)$ (black) and combined (red).

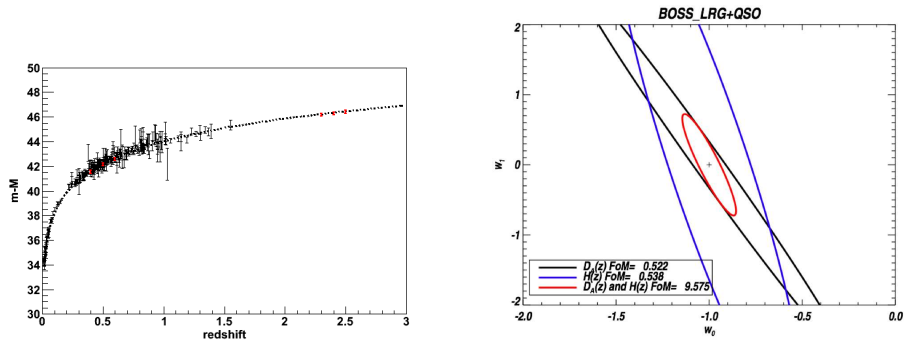


Figure 1: **left:** Equivalent data points from BOSS in the Hubble diagram (red) and current SN-Ia data from the union compilation. **right:** constraints on the dark energy equation of state.

5 Conclusions

BOSS is a high-precision experiment to measure the acceleration of the Universe using the baryon acoustic oscillation technique, with low systematic uncertainties. BOSS will be the largest effective volume yet surveyed for large scale structure, and will sample the distribution of matter using two different tracers: LRGs at $z \approx 0.6$ and the absorption in the Ly α forest of quasars. The LRG survey will measure a quarter of a million Fourier modes at $k < 0.2hMpc^{-1}$

⁸. The BOSS Ly α will provide complimentary high redshift constraints.

BOSS will provide an impressive advance over our current and near future state of knowledge. The area of the constraints in the $w_0 - w_1$ plane is expected to get reduced by over a factor of 10. But this observation understates the capabilities of BOSS. Clear evidence for departures from the (w_0, w_1) parametrization would provide a direct insight into the physics of the cosmic acceleration. The “guaranteed” return of BOSS is much tighter constraints on the parameters of dark energy, but the “discovery” potential is larger still.

1. R. Bernabei et al. (DAMA), *First results from DAMA/LIBRA and the combined results with DAMA/NaI* Eur. Phys. J. C56, 333 (2008)
2. E. Armengaud et al., *First results of the EDELWEISS-II WIMP search using Ge cryogenic detectors with interleaved electrodes*, arXiv:0912.0805v1
3. Z. Ahmed et al. *Results from the Final Exposure of the CDMS II Experiment*, arXiv:0912.3592v1
4. report by the ESA-ESO Working Group on fundamental cosmology: arXiv:astro-ph/0610906, DETF report: arXiv:astro-ph/0609591v1
5. S.D. Landy and A.S. Szalay *Bias and variance of angular correlation functions*. Astrophys.J. 412:64 (1993).
6. D.J. Eisenstein, H. Seo, M. White *On the Robustness of the Acoustic Scale in the Low-Redshift Clustering of Matter*, Astrophys. J. 664:660-674 (2007)
7. D.J. Eisenstein et al, *Detection of the baryon acoustic peak in the large-scale correlation function of SDSS luminous red galaxies*, Astrophys.J. 633:560-574 (2005)
8. <http://www.sdss3.org/collaboration/description.pdf>
9. M. Kowalski et al, *Constraints from New, Old and Combined Supernova Datasets*, Astrophys.J. 686:749-778 (2008).
10. P. McDonnald and D. Eisenstein, *Dark energy and curvature from a future baryonic acoustic oscillation survey using the Ly α forest*, arXiv:astro-ph/0607122v1

Characterizing the Universe

A. BLANCHARD, L. FERRAMACHO

*LATT, OMP, Université de Toulouse, 14 Av E.Belin
31 400 Toulouse, France*

Y. ZOLNIEROWSKI

*LAPP, Université de Savoie, Chemin de Bellevue
74940 Annecy le Vieux, France*

The classical cosmological tests, SNIa Hubble diagram, CMB, BAO and power spectrum of galaxies are allowing tight constraints on the main parameters of Lambda Cold dark matter dominated universes. However, these constraints are established with several assumptions, the high accuracy one obtain on these constraints does not mean that the actual characteristics of the universe are known at the same precision level. Furthermore, astrophysical considerations may lead to additional sources of uncertainties. These issues and their present status are discussed.

1 Introduction

The progress in our knowledge about the universe has been remarkable over the last fifteen years. Three sets of observational data are particularly important in this respect: type Ia supernovae Hubble diagram, measurements of the fluctuations of the CMB, mainly provided by WMAP and the measurement of the large scale distribution of galaxies which is supposed to trace the underlying dark matter distribution. Measurements of the Hubble constant, the lensing signal on large scale, or the properties of x-ray clusters provide some other constraints –among many others– that can be added, but until now these have not reached the same level of recognition by the community. In order to illustrate the achieved precision we provide a table of constraints which has been recently published (Ferramacho et al., 2009) and then discussed some of the possible limitations. Most of the content of this proceedings is based on this work as well as on L.Ferramacho PhD thesis.

One can see that a high precision is achieved on most of the cosmological parameters, between 1% and 5% for most of them, although the progress may not look so spectacular when compared with the first table published using WMAP data (Spergel et al., 2003). Maybe the most spectacular result is the one on the universe curvature: $\Omega_k = -0.005 \pm 0.0121$ (which we regard as a 1% precision estimation...). Obviously, the actual precision one can achieve depends on the number of free parameters of the model. This is illustrated by the fact that constraints change slightly when curvature or $w \neq -1$ are allowed. However, results remain remarkably stable: this reinforces the success of the model.

Table 1: Summary of the posterior distributions mean values for the different sets of parameters constrained, with the corresponding 68% confidence intervals. These constraints are established by combining the three main data sets of cosmological relevance: SNIa Hubble diagram, CMB fluctuations and power spectrum of galaxies. The presented results have been established using a Bayesian analysis (using the COSMOMC tool) to combine the likelihood of each data set and different parameters sets were considered. Final constraints are very similar to those obtained with information reduced on one number like the R distance parameter for CMB.

Parameter	Vanilla	Vanilla + Ω_k	Vanilla + w	Vanilla + $\Omega_k + w$
$\Omega_b h^2$	0.0227 ± 0.0005	0.0227 ± 0.0006	0.0228 ± 0.0006	0.0227 ± 0.0005
$\Omega_{cdm} h^2$	0.112 ± 0.003	0.109 ± 0.005	0.109 ± 0.005	0.109 ± 0.005
θ	1.042 ± 0.003	1.042 ± 0.003	1.042 ± 0.003	1.042 ± 0.003
τ	0.085 ± 0.017	0.088 ± 0.017	0.087 ± 0.017	0.088 ± 0.017
n_s	0.963 ± 0.012	0.964 ± 0.013	0.967 ± 0.014	0.964 ± 0.014
$\log(10^{10} A_s)$	3.07 ± 0.04	3.06 ± 0.04	3.06 ± 0.04	3.06 ± 0.04
Ω_k	0	-0.005 ± 0.007	0	-0.005 ± 0.0121
w	-1	-1	-0.965 ± 0.056	-1.003 ± 0.102
Ω_Λ	0.738 ± 0.015	0.735 ± 0.016	0.739 ± 0.014	0.733 ± 0.020
Age	13.7 ± 0.1	13.9 ± 0.4	13.7 ± 0.1	13.9 ± 0.6
Ω_m	0.262 ± 0.015	0.270 ± 0.019	0.261 ± 0.020	0.272 ± 0.029
σ_8	0.806 ± 0.023	0.791 ± 0.030	0.816 ± 0.014	0.788 ± 0.042
z_{re}	10.9 ± 1.4	11.0 ± 1.5	11.0 ± 1.5	11.0 ± 1.4
h	0.716 ± 0.014	0.699 ± 0.028	0.713 ± 0.015	0.698 ± 0.037

2 Possible systematics

The above results are impressive but one should keep in mind that these constraints are established within a specific model: the inflation based Cold Dark Matter picture. For instance, the initial power spectrum of fluctuations is assumed to be a power law. Relaxing this assumption may widen the constraints and it is unclear if there is a way to establish constraints without such an assumption. Other factors may degrade the above constraints, such as an inaccurate model of the bias between galaxies and dark matter distribution when using LSS data.

2.1 Estimators of large scale structure

Currently the power spectrum derived from redshift surveys is used in order to characterize the galaxy distribution function. This is what has been used when deriving parameters in Table 1 using the power spectrum published with the DR5 SDSS release (Tegmark et al. 2006). However, we have also investigated the same type of constraints using the correlation function as statistical description for the galaxy distribution (Eisenstein et al. 2005). Furthermore, a correction for non linear effects has to be included and these papers provide slightly different prescriptions for doing so. The fact of using such different modellings and estimators can lead to appreciable differences in some of the estimated parameters, sometimes larger than the statistical uncertainties.

2.2 Supernovae evolution

Another source of uncertainty to consider is the possibility of evolution in the intrinsic luminosity of type Ia supernovae. Constraints based on the SNIa Hubble diagram actually rely on the assumption that the luminosity (after correction for lightcurve duration and color) does not evolve with redshift. Although there might be good arguments for that, there are no way to confirm this hypothesis. An approach consists therefore to examine whether some evolution is allowed and whether it would be detectable. For this we have investigated a specific model for

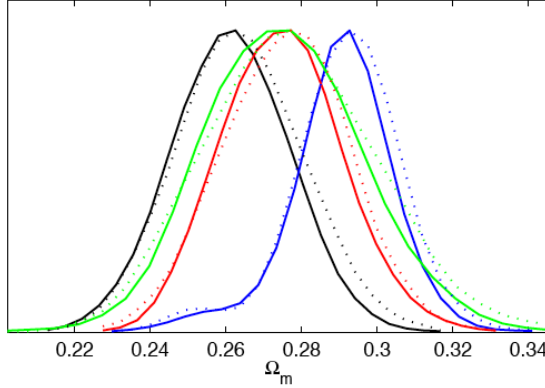


Figure 1: Likelihood on the density parameter using different estimators and correcting factors for non-linearities. The (black) line on the left shows the result using the Tegmark et al. (2006) power spectrum, as well as their non-linear recipe. The (red) curve in the middle shows the likelihood estimation using the correlation function provided by Eisenstein et al. (2005) using their non-linear correction. The second curve (green) correspond to the case where the curvature is left free. The (blue) curve on the right shows the likelihood estimation using the correlation function and the Tegmark et al. non-linear correction.

the evolution:

$$\Delta m(z) = K \frac{t_0 - t(z)}{t_0 - t(z=1)}$$

where t_0 is the present age of the universe in Gyr and $t(z)$ is the age of the universe at the redshift of the supernova explosion. K is therefore the typical change in magnitude due to evolution at a redshift $z = 1$. For this specific form of evolution, a cosmological constant is not needed anymore to explain supernovae data! Other forms of evolution have been investigated by Linden et al. (2009). The results showed that evolution is actually tightly constrained to be close to 0. Therefore previous results based on the supernovae diagram were entirely legitimate.

Table 2: Similar to Table 1, but including an evolution parameter for the supernovae luminosity

Parameter	Vanilla	Vanilla + Ω_k	Vanilla + w	Vanilla + Ω_k + w
$\Omega_b h^2$	0.0228 ± 0.0006	0.0227 ± 0.0005	0.0227 ± 0.0006	0.0226 ± 0.0006
$\Omega_{cdm} h^2$	0.110 ± 0.004	0.109 ± 0.005	0.113 ± 0.005	0.111 ± 0.005
θ	1.042 ± 0.003	1.042 ± 0.003	1.042 ± 0.003	1.042 ± 0.003
τ	0.088 ± 0.017	0.087 ± 0.017	0.085 ± 0.017	0.085 ± 0.016
n_s	0.968 ± 0.013	0.965 ± 0.013	0.963 ± 0.014	0.960 ± 0.014
$\log(10^{10} A_s)$	3.07 ± 0.04	3.06 ± 0.04	3.07 ± 0.04	3.06 ± 0.04
Ω_k	0	-0.002 ± 0.007	0	-0.017 ± 0.013
w	-1	-1	-1.112 ± 0.148	-1.33 ± 0.242
K	-0.042 ± 0.042	-0.035 ± 0.042	-0.105 ± 0.091	-0.133 ± 0.077
Ω_Λ	0.747 ± 0.017	0.745 ± 0.020	0.756 ± 0.022	0.744 ± 0.022
Age	13.6 ± 0.1	13.7 ± 0.4	13.6 ± 0.1	14.5 ± 0.7
Ω_m	0.253 ± 0.017	0.257 ± 0.025	0.244 ± 0.022	0.272 ± 0.029
σ_8	0.801 ± 0.026	0.794 ± 0.029	0.846 ± 0.068	0.867 ± 0.060
z_{re}	11.1 ± 1.5	11.0 ± 1.4	10.9 ± 1.5	10.8 ± 1.4
h	0.725 ± 0.017	0.720 ± 0.036	0.748 ± 0.038	0.703 ± 0.042

The drawback of these conclusions is that the ability for future supernovae projects to

provide additional constraints will depend on their ability to disentangle possible evolution with an accuracy better than a tenth of magnitude at redshift 1.

3 Conclusion

The first conclusion of our study is that Λ CDM is in excellent agreement with observations after the improvement in data quality and quantity over the last ten years. Alternative views, including the orthodox ones like $w \neq -1$ or including curvature do not offer any competitive picture, in the sense that none of these alternative viewss provides an appreciable improved description of present-day data. Although this success does not prove the theory to be right, it confirms that the theory is a scientific theory that could have been disproved, but is still alive and well!

References

1. Eisenstein, D. J., Zehavi, I., Hogg, D. W., et al., *ApJ*, **633**, 560 (2005)
2. Ferramacho, L. D., Blanchard, A., & Zolnierowski, Y. *A&A*, **499**, 21 (2009)
3. Linden, S., Virey, J.-M., & Tilquin, A. *A&A*, **506**, 1095 (2009)
4. D.N. Spergel et al, *ApJS*, **148**, 175 (2003)
5. Tegmark, M., Eisenstein, D., Strauss, M. A. et al., *PhRvD*, **74**, 12 (2006)

Real-Time Cosmology with Cosmic Parallax and Redshift Drift

Miguel Quartin

Instituto de Física, Universidade Federal do Rio de Janeiro, CEP 21941-972, Rio de Janeiro, RJ, Brazil

Institut für Theoretische Physik, Universität Heidelberg, Philosophenweg 16, 69120 Heidelberg, Germany

Two recently proposed techniques, involving the measurement of the cosmic parallax and redshift drift, provide novel ways of directing probing (over a time-span of several years) the background metric of the universe and therefore shed light on the dark energy conundrum. The former makes use of upcoming high-precision astrometry measurements to either observe or put tight constraints on cosmological anisotropy while the latter employs high-precision spectroscopy to give an independent test of the present acceleration of the universe. Both effects constitute but two examples of the upcoming field of Real-Time Cosmology.

1 Introduction

Observational cosmology is undergoing a fast evolution, with the increase of available data and a better understanding of the connections between models and observations. The once undisputed principles of homogeneity and isotropy are being questioned by several observations of large scale structures¹. This is remarkable, since the Cosmic Microwave Radiation (CMB) is widely regarded a strong evidence for the Λ CDM model which is firmly based on these two principles (sometimes extended to three by an extra assumption of flatness).

Large-scale violations of the cosmological principle of homogeneity have been invoked as explanations for the cosmic acceleration enigma (see e.g. [2,3,4,5](#)); the possibility of other often neglected cosmological quantities (such as shear, vorticity and anisotropic curvature) influencing future observations are still not completely resolved [6,7](#). If one is to take into account these possibilities, the quest for new observables for dark energy becomes a valuable one.

Any violation of the cosmological principle means that a simple Friedmann-Robertson-Walker (FRW) metric can no longer be adopted. Arguably the simplest possibility is to adopt in place of the FRW metric the spherically symmetric structure of the Lemaître-Tolman-Bondi (LTB) metric, as suggested by various authors (e.g. [2,3,4,5](#)) ever since the discovery of acceleration. The LTB metric allows for two spatial degrees of freedom that could be employed to reproduce any line-of-sight expansion rate and any line-of-sight inhomogeneity. In particular, LTB models can mimic the observed accelerated expansion rate $H(z)$ and the observed source number counts at the same time⁸. Because of both this flexibility and the isotropy with respect to the center observer, ruling out the LTB model is not a trivial task.

Although we sometimes take for granted that in cosmology we can only access the surface of a single light cone, this is by no means true. We can in fact receive CMB light scattered from distant sources, for instance from the hot intra-cluster medium of galaxy clusters through the Sunyaev-Zel'dovich effect, which comes from inside our light cone. Two additional techniques recently proposed explore instead the *exterior* of our present light cone by observing the same

sources at two different instants of time: the so-called Sandage effect ⁹ or redshift drift ^{10,11,12}, and the Cosmic Parallax (CP) ^{13,14,15,16,12}. In other words, these methods probe two or more different (albeit very close) light cones. The first method relies on high-precision spectroscopy while the latter requires high-precision astrometry.

The redshift drift and the cosmic parallax form a new set of “real-time” cosmic observables. Following ¹², here we briefly review the feasibility of measuring each in the context of LTB void models: the redshift drift with the proposed European Extremely Large Telescope (E-ELT) instrument CODEX ¹⁷; the CP with the Gaia Satellite ^{18,19}.

Most of the results here presented are discussed more extensively in ¹².

2 LTB Void Models

The LTB metric can be used to describe spherically symmetric inhomogeneous models. Although most authors consider the observers to be at the center of symmetry for simplicity, there is no *a priori* reason for that and one should consider the possibility of off-center observers. The maximum off-center distance observationally allowed must be in-between 26 (assuming no peculiar velocity of the observer) and 100 Mpc ^{20,21,22,12}. Following ¹² we will stick to a conservative estimate of 30 Mpc and consider 3 LTB void models, dubbed: “Model I”, “Model II” and “cGBH Model”.

3 Cosmic Parallax and Redshift Drift in LTB

It has been known for a long time ⁹ that for any expanding cosmology the redshift z of a given source is not a constant in time. In effect, observation of dz/dt gives one a direct measurement of the expansion of the universe, and is one of the few direct ways of measuring directly $H(z)$ (along with e.g. longitudinal acoustic oscillations). The prospect of doing so was revisited in ¹⁰. This redshift drift has been investigated for a variety of dark energy models currently pursued in the literature ^{23,24,25} and it is interesting to note that most of them predict a very similar redshift profile for the effect, all very close to the one generated by the Λ CDM model. In Λ CDM, the redshift drift is positive in the region $0 < z < 2.4$ but becomes negative for higher redshift. On the other hand, a dark-energy mimicking giant void produces a very distinct z dependance of this drift, and in fact one has dz/dt always negative ¹².

4 Measuring the Redshift Drift with CODEX

The possibility of detecting the redshift drift at the (E-ELT) using the high-precision spectrograph CODEX ^{17,25} was analyzed in a couple of papers ^{23,24,25}. Contrary to most dark energy models, LTB void models can be told apart from Λ CDM with a 4σ credibility level with 10 years of observation ¹².

It is important to note that a larger observational time-frame allows not only for a larger redshift drift (which is linear in time) but also for smaller error bars (as more photons are collected) and, a higher S/N (which increases as $\sqrt{\Delta t}$) can be achieved. In other words, the “effective signal” increases with $\Delta t^{3/2}$ if one assumes a proportional telescope time is maintained.

Figure 1 depicts the Sandage effect for different dark energy models for three possible (complete observation) time-spans: 5, 10 and 15 years. Also plotted are the forecasted error bars obtainable by CODEX at the E-ELT. Here we are assuming that the time spent observing each quasar is the same, and this accounts for larger error bars at high redshift due to the lower apparent magnitudes of the corresponding quasars (see ¹²). Table 1 contains the corresponding χ^2 and σ -levels for 5, 10 and 15 years. As can be seen, void models could be detected/ruled out at over 4σ with less than a decade of mission-time.

Model	5 years	10 years	15 years
Models I / II	1.1σ	6.2σ	12.5σ
	$\chi^2 = 6.5$	$\chi^2 = 52$	$\chi^2 = 176$
cGBH Model	$.5\sigma$	4.3σ	9.2σ
	$\chi^2 = 3.7$	$\chi^2 = 30$	$\chi^2 = 100$

Table 1: Estimated achievable confidence levels by the CODEX mission in 5, 10 and 15 years.

One very interesting aspect of using the Sandage effect to probe void models is the fact it is model-independent to a good degree. In fact, although in the cGBH model the signal is a little smaller, both Models I and II here studied never differ by more than 0.1σ and except for tiny differences close to the void edge (barely resolvable in Figure 1), they both predict the very same redshift drift profile. These models should be good representatives of this whole class of these dark-energy mimicking LTB void models.

5 Measuring the Cosmic Parallax with Gaia

Distance measurements are one of the most fundamental challenges in astronomy. Measuring a possible apparent change in the relative position of cosmological sources like quasars in any anisotropic expansion scenario, dubbed in ¹³ cosmic parallax, is one of the next challenges for astrometry. In particular, missions that perform *global astrometry* over the entire celestial sphere are preferred because: (i) increasing the number of measurement helps increasing the required accuracy; (ii) cosmic parallax is an all-sky effect, the multipole expansion of which depend on (and therefore is a signature of) the underlying anisotropic model.

Figure 1 illustrates the possibility of detecting the cosmic parallax with Gaia for a possible, though arbitrary, redshift binning. Depicted are $\Delta_t\gamma$ for two sources at the same shell for the 3 LTB void models studied in ¹² and for a time span of 10 (top), 20 (middle) and 30 (bottom plot) years, together with Gaia forecast statistical error bars. An extension to 10 or more years allow smaller error bars and here too we can approximate the errors to scale as $(\Delta t)^{-1/2}$. For $z > 3$, the error bars get much larger and the CP is quite small, so that higher- z bins do not add much. Here we are not considering the two main source of systematics identified in ¹².

Since the cosmic parallax signal is directly proportional to such a distance, one could also phrase the argument of detection in a different way. If we ignore the CMB dipole (and all other) dipolar-anisotropy constraints and leave the off-center distance as a free parameter, how well could Gaia constrain it? To estimate this one need only calculate, for a given number of mission years, what is the off-center distance that would produce a 1σ detection. Table 2 summarizes the results for all 3 models in 6, 10, 20 and 30 years. Interestingly, although a Gaia-like mission requires around 20 years to reach the constraining level of the CMB dipole, already with 6 years it is an equivalent or even better probe of dipolar anisotropy in comparison to current supernovae datasets, which only limit such a distance to around 200-400 Mpc depending on the model ²².

Clearly, the Gaia mission with its nominal duration of 6 years cannot detect the cosmic parallax in void models. Note, however, that a detection could in principle be somewhat facilitated for two reasons. First, earlier estimates for Gaia hinted to the possibility of detecting up to 1 million quasars, which is twice the value we are considering here. Second, we only considered here a simplified strategy of binning quasars in redshift, which amounts to comparing the cosmic parallax of sources at same distances. But in principle one should also compare quasars at different redshifts, and this could lead to an average higher signal.

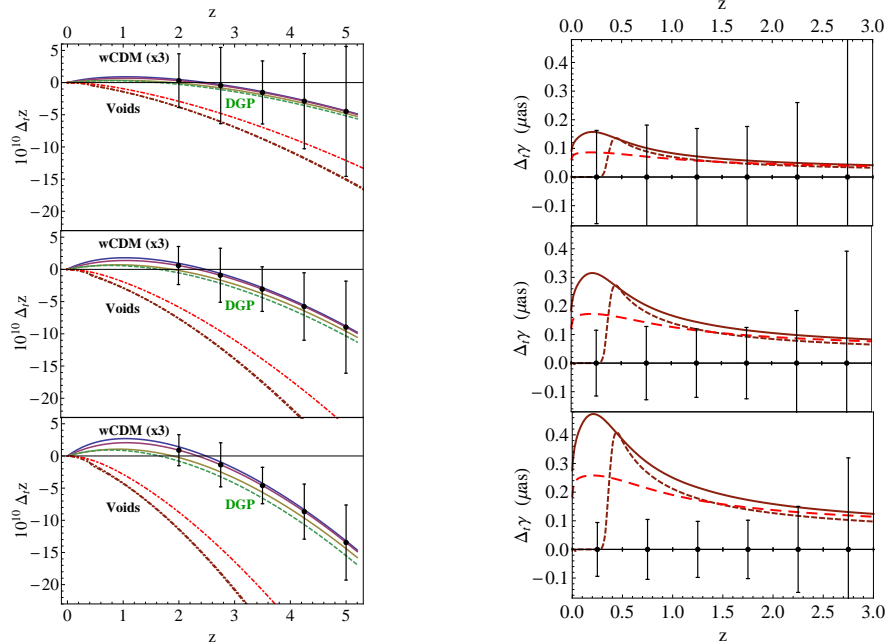


Figure 1: Redshift drift for different dark energy models for a total mission duration of 5 (top), 10 (middle) and 15 (bottom plot) years and CODEX forecast error bars. In each plot, the upper 3, solid lines represent wCDM models for $w = -1.25$ (uppermost), $w = -1$ (second) and $w = -0.75$ (third). The green, dashed line corresponds to a DGP model. The three bottommost, dot-dashed lines stand for 3 void models¹². Note that a 4σ separation between voids and Λ CDM can be achieved in a decade. $\Delta_t\gamma$ for two sources at the same shell for the same 3 LTB models and for a time span of 10 (top), 20 (middle) and 30 (bottom plot) years, together with Gaia forecast statistical error bars. Here we are not considering the two main systematics discussed in¹².

One final note: more general (non-LTB) anisotropic models will not produce a simple dipole^{16,15} and their cosmic parallax can be more easily distinguished from local effects.

6 Conclusions

Cosmic Parallax and redshift drift constitute two new observables for dark energy. In the case of LTB void models, they add to the limited number of tests that can be employed to distinguish them from an accelerating FRW universe, possibly eliminating an exotic alternative explanation to dark energy. It turns out that the best hope to attain a clear-cut discrimination between LTB and FRW is with the redshift drift effect, since the LTB expansion is always decelerated. We find that a 4σ separation can be achieved with E-ELT in less than 10 years, much before the same experiment will be able to distinguish between competing models of dark energy. A Gaia-like mission, on the other hand, can only achieve a reasonable detection of a void-induced cosmic parallax in the course of 30 years.

Nevertheless, CP remains an important tool and in fact one of the most promising way to probe general late-time cosmological anisotropy, as already discussed in^{13,16}. In particular, even if it only lasts 6 years Gaia should constrain late-time anisotropies similarly to current supernovae catalogs, but in an independent way. Also, in Λ CDM it can be used to measure our own peculiar velocity with respect to the quasar reference frame and consequently to the CMB, therefore providing a new and promising way to break the degeneracy between the intrinsic CMB dipole and our own peculiar velocity. We are currently investigating this possibility and results will be published in a subsequent paper.

Direct kinematic tests such as redshift drift and CP are conceptually the simplest probe of expansion and of anisotropy since their interpretation do not rely on calibration of standard

Model	6 years	10 years	20 years	30 years
Model I	143	66	23	13
Model II	235	109	39	21
cGBH Model	214	99	35	19

Table 2: Estimated off-center distance constraints (in Mpc) from the Gaia (or an extended Gaia-like) mission in 6, 10, 20 and 30 years, in the limit where the two considered systematics are arbitrarily distinguished apart.

candles/rulers nor depend on evolutionary or selection effects (as for galaxy ages and number counts). The fact that in both CP and redshift drift the “effective signal” increases as $(\Delta t)^{3/2}$ shows that these new real-time cosmology effects can become some of the most effective long-term dark energy probes. For the same reason, the Sandage and CP effects have also the potential to become the best inhomogeneity and (late-time) anisotropy tests, respectively. Combined, they will form an important direct test of the FRW metric.

Although the odds of Gaia having fuel to last 10 or more years are small, one can consider Gaia as making a first sub-miliarcsecond astrometric sky-map, which could be confronted with any future global-astrometry mission. Since any proper motion signal increases linearly with time, any future mission with a global astrometric accuracy *at least* as good as Gaia can be used to detect the CP (or any other kind of late-time anisotropy) signal. In between missions, however, the effective signal grows only linearly in Δt .

Other real-time cosmology effects will be reviewed in an upcoming paper ²⁶.

1. C. Copi, D. Huterer, D. Schwarz and G. Starkman, arXiv:1004.5602v1 (2010).
2. N. P. Humphreys, R. Maartens and D. R. Matravers, *Astrophys. J.* **477**:47 (1997), arXiv:astro-ph/9602033.
3. M.-N. Celerier, *Astron. Astrophys.* **353**:63-71 (2000), arXiv:astro-ph/9907206.
4. H. Alnes, M. Amarzguioui and O. Gron *Phys. Rev. D* **73**:083519 (2006), arXiv:astro-ph/0512006.
5. J. Garcia-Bellido and T. Haugboelle, *JCAP* **0804**:003 (2008), arXiv:0802.1523.
6. E. Bunn, P. Ferreira and J. Silk, *Phys. Rev. Lett.* **77**, 2883 (1996), arXiv:astro-ph/9605123v1.
7. T. Koivisto, D. Mota, M. Quartin and T. Zlosnik, arXiv:1006.3321 (2010).
8. M. H. Partovi and B. Mashhoon, *Astrophys. J.* **276**, 4 (1984).
9. A. Sandage, *Astrophysical Journal* **136**, p.319 (1962).
10. A. Loeb, *Astrophysical Journal* **499**:L111-L114 (1998), arXiv:astro-ph/9802122.
11. J.-P. Uzan, C. Clarkson and G. F. R. Ellis, *Physical Review Letters* **100**, 191303 (2008), arXiv:0801.0068.
12. M. Quartin and L. Amendola, *Phys. Rev. D* **81**, 043522 (2010), arXiv:0909.4954
13. C. Quercellini, M. Quartin and L. Amendola, *Phys. Rev. Lett.* **102**, 151302 (2009), arXiv:0809.3675.
14. F. Ding & R. A. C. Croft, *MNRAS* **397** 1739 (2009), arXiv:0903.3402v2.
15. M. Fontanini, M. Trodden and E. J. West, arXiv:0905.3727v1.
16. C. Quercellini, P. Cabella, L. Amendola, M. Quartin and A. Balbi, *Phys. Rev. D* **80**, 063527 (2009), arXiv:0905.4853.
17. L. Pasquini, S. Cristiani, H. Dekker *et al.*, *The Messenger* **122**, 10 (2005).
18. M. A. C. Perryman *et al.*, *Astron. Astrophys.* **369**:339-363, (2001).
19. C. A. L. Bailer-Jones, edited by D. W. Kurtz, in *IAU Colloq.* **196**, pp. 429-443 (2005).
20. H. Alnes and M. Amarzguioui, *Phys. Rev. D* **74**, 103520 (2006), arXiv:astro-ph/0607334.
21. H. Alnes and M. Amarzguioui, *Phys. Rev. D* **75**, 023506 (2007), arXiv:astro-ph/0610331.

22. M. Blomqvist and E. Mortsell, arXiv:0909.4723v1 [astro-ph.CO].
23. P.-S. Corasaniti, D. Huterer and A. Melchiorri, Phys. Rev. D **75** 062001 (2007).
24. A. Balbi and C. Quercellini, MNRAS **382**:1623-1629 (2007), arXiv:0704.2350v3.
25. J. Liske, A. Grazian, E. Vanzella *et al.*, MNRAS **386**:1192-1218 (2008), arXiv:0802.1532.
26. C. Quercellini, L. Amendola, A. Balbi, P. Cabella and M. Quartin, *in preparation*.

5. **Theory**

MODELS OF DARK ENERGY

EDMUND J. COPELAND

*School of Physics and Astronomy, University of Nottingham, University Park,
Nottingham, NG7 2RD, England*

A number of models of dark energy are reviewed. These include a cosmological constant, dynamical models where a scalar field may be responsible for the observed late time acceleration through to the possibility that we are not fully in control of the gravity sector and the acceleration may be some manifestation of modified gravity.

1 Introduction

Through the 1980's and early 1990's a number of observations of the large scale structure in the universe began to question the accepted paradigm of a cold dark matter (CDM) dominated $\Omega_{\text{matter}} = 1$ universe. For example in a study of the large scale clustering of IRAS galaxies performed in¹ it was realised that it was difficult to reconcile the observed clustering of these galaxies with that predicted in the standard paradigm at the time. In fact it led a number of authors to begin questioning the paradigm and in 1990 Efstathiou et al,³ actually proposed that a better fit to the data available at that time would be a scenario with a "spatially flat cosmology in which as much as 80 percent of the critical density is provided by a positive cosmological constant." This remarkable conclusion was reached well before the observations of distant Type Ia supernova hit the headlines in 1998. Their reasoning was reinforced in the analysis of the APM Galaxy Survey data in which there was strong evidence for more large-scale structure in the survey than predicted by the standard scale-invariant CDM model². Perhaps we should not be too surprised that there were people back in the 80's and 90's who were turning their attention to the prospect of a cosmological constant. After all, there were many groups of astronomers trying to reconcile the fact that the large scale structure data was looking so inconsistent with a standard CDM scenario. However, I think it is fair to say that not too many people (especially from the particle physics camp) were prepared to face the prospect that we had to have a Λ present today if our cosmology was to make sense. Two exceptions to this were Weinberg⁴ and Linde⁵, as they argued for a Λ but from an anthropic standpoint. However, as will shortly see the real catalyst which sparked theorists into action was the reported observations by the Supernova groups in 1998^{6,7} of deviations in the Hubble diagram at large redshifts providing evidence of an accelerating Universe. It seemed to galvanise people into action and has led to an unprecedented amount of attention being lavished on the question of the origin of the dark energy as the source of the accelerating universe. In this brief review I will try and give a flavour of the many attempts that have been made to access the nature of dark energy. Given that there have been over 2000 papers written on the subject since 1998, I apologise from the outset. I can not cover the field properly, nor give proper references. There are a number of reviews on the subject and I urge the interested reader to look there for details. Here are just a few of

them^{8,9,10,11,12,13,14,15,16}. Neither will I go into great details over any particular approach, this is going to be a schematic review, aimed at giving the reader a flavour of the attempts that have been made to understand the nature of the dark energy.

In what follows I will describe attempts to model the dark energy as a pure cosmological constant Λ . This remains the best fit to the data, although from a particle physics perspective it is fraught with problems. I will then discuss a range of dynamical dark energy models in which we assume there is some as yet unknown mechanism which has forced the real cosmological constant to vanish to day, and the dark energy is associated with say the potential energy of some slowly rolling scalar field. This too has problems, not least being the fact such a field generally has to have a very small mass, which means that it is subject to the severe constraints that exist in the form of fifth force experiments. Finally, we will look at attempts to modify the left hand side of Einstein's equations, the geometry part. Perhaps it is not the matter that needs looking at, it is the spacetime to which the matter is coupled. However, we will see that even in this case, it is pretty hard to modify Einstein's theory too much to accommodate the late time accelerating universe. All in all, the dark energy issue remains one of the most interesting and perplexing problems in physics and astrophysics.

2 The basic equations

We have principally the Friedmann and fluid equations describing the evolution of the scale factor $a(t)$ in an isotropic and homogeneous universe of spatial curvature K containing matter of density ρ and pressure p , related by an equation of state $p = w\rho$.

$$H^2 \equiv \left(\frac{\dot{a}}{a}\right)^2 = \frac{8\pi G\rho}{3} - \frac{K}{a^2}, \quad (1)$$

$$\dot{H} = -4\pi G(p + \rho) + \frac{K}{a^2}, \quad (2)$$

$$\dot{\rho} + 3H(\rho + p) = 0. \quad (3)$$

where H is the Hubble parameter.

Equation (3) can be derived from Eqs. (1) and (2), which means that two of Eqs. (1), (2) and (3) are independent. Eliminating the K/a^2 term from Eqs. (1) and (2), we obtain

$$\frac{\ddot{a}}{a} = -\frac{4\pi G}{3}(\rho + 3p). \quad (4)$$

Hence the accelerated expansion occurs for $\rho + 3p < 0$.

Let us consider the evolution of the universe filled with a barotropic perfect fluid with an equation of state

$$w = p/\rho, \quad (5)$$

where w is assumed to be constant. Then by solving the Einstein equations given in Eqs. (1) and (2) with $K = 0$, we obtain

$$H = \frac{2}{3(1+w)(t - t_0)}, \quad (6)$$

$$a(t) \propto (t - t_0)^{\frac{2}{3(1+w)}}, \quad (7)$$

$$\rho \propto a^{-3(1+w)}, \quad (8)$$

where t_0 is constant. We note that the above solution is valid for $w \neq -1$. The radiation dominated universe corresponds to $w = 1/3$, whereas the dust dominated universe to $w = 0$. In

these cases we have

$$\text{Radiation : } a(t) \propto (t - t_0)^{1/2}, \quad \rho \propto a^{-4}, \quad (9)$$

$$\text{Dust : } a(t) \propto (t - t_0)^{2/3}, \quad \rho \propto a^{-3}. \quad (10)$$

Both cases correspond to a decelerated expansion of the universe.

From Eq. (4) an accelerated expansion ($\ddot{a}(t) > 0$) occurs for the equation of state given by

$$w < -1/3. \quad (11)$$

In order to explain the current acceleration of the universe, we require an exotic energy dubbed “dark energy” with equation of state satisfying Eq. (11). From Eq. (3) the energy density ρ is constant for $w = -1$. This is the famous cosmological constant case and it follows that the Hubble rate is also constant from Eq. (1), giving the evolution of the scale factor:

$$a \propto e^{Ht}, \quad (12)$$

which is the de-Sitter universe.

Now introducing the dimensionless density parameter $\Omega(t) = \rho(t)/\rho_c(t)$ where $\rho_c(t) = 3H^2(t)/8\pi G$ is the critical density (gives a spatially flat universe), we can rewrite the Friedmann equation as an elegant algebraic expression $\Omega_m + \Omega_\Lambda + \Omega_k = 1$ where I have divided the density up into three contributions arising from matter (including baryons, cold dark matter and massive neutrinos), a cosmological constant type term and spatial curvature. Turning briefly to the observational constraints on these three quantities. First Ω_m the contribution from matter. Well a number of surveys of large scale structure, measurements of the Baryon Acoustic Oscillation (BAO) scale, weak lensing tests, cluster baryon abundance measurements using X-ray measurements of intracluster gas, or SZ measurements and numerical simulations of structure growth all appear to indicate that $\Omega_m \sim 0.25$. For example the most recent work measuring the BAO scale by combining 2dFGRS and SDSS data suggests the best fit cosmological parameters are $\Omega_m = 0.25$, $\Omega_b h^2 = 0.0223$ and $h = 0.72$ ¹⁷. The bottom line is that $\Omega_m \ll 1$. Analysing the peak structure of the CMB anisotropies provides evidence for the contribution of Ω_k . In fact to a good approximation, the position of the first peak in ℓ space is given by $\ell_{\text{peak}} \sim \frac{220}{\sqrt{\Omega_m + \Omega_\Lambda}}$.

The most recent beautiful WMAP5 data when combined with the distance measurements from the Type Ia supernovae and the BAO in the distribution of galaxies probably provides the most powerful constraints to date on the cosmological parameters¹⁸. For instance assuming the standard Λ CDM paradigm the following values are obtained (including 68% uncertainties): $\Omega_b h^2 = 0.02265 \pm 0.00059$, $\Omega_{\text{cdm}} h^2 = 0.1143 \pm 0.0034$, $\Omega_\Lambda = 0.721 \pm 0.015$, which allows for the following to be derived: $H_0 = 70.1 \pm 1.3 \text{ km s}^{-1} \text{ Mpc}^{-1}$, $\Omega_b = 0.0462 \pm 0.0015$, $\Omega_{\text{cdm}} = 0.233 \pm 0.013$ and $\Omega_m h^2 = 0.1369 \pm 0.0037$. Tight constraints (95% CL) follow on the (constant) equation of state for dark energy, $-0.11 < 1 + w < 0.14$ and on the spatial curvature of the universe $-0.0175 < \Omega_k < 0.0085$ implying that the universe is perfectly consistent with being spatially flat $\Omega_k \simeq 0$ and dominated by a true cosmological constant $w = -1$ ¹⁸. However a slight word of caution, always be aware that these numbers come with certain prior assumptions made about some of the other parameters. There could well be some residual dependence on these parameters that has not been properly taken into account. For example when the constraint of a constant dark energy equation of state is relaxed to allow for dynamical dark energy, we find for the present value w_0 , $-0.38 < 1 + w_0 < 0.14$ ¹⁸, not as tight a bound as before.

Finally, the observations of the Type Ia supernova indicates that the Hubble diagram is no longer well fitted by a CDM dominated universe, and prefers a universe that is dominated with a cosmological constant today – well not actually today. We don’t know what the universe is doing right now, we can only know what it was doing around a redshift of $z \sim 0.2 - 1$ as far as the supernova are concerned. For all we know it has actually stopped accelerating today and we just haven’t received the information yet!

3 Models of Λ

Why is the observed value of the cosmological constant a problem? For many it isn't, it is just another parameter that makes up the cosmological parameter set, and its observed contribution should just be taken as an empirical fact. However, for those who believe it has something to do with the world of particle physics then it is a real problem because its energy scale is so small compared to the value we would naively expect it to have. This cosmological constant problem has been with us for a long time. It was assumed the cosmological constant (or Λ) was zero today, but we did not have any real reason to set it to that value, rather we relied on some as yet unknown symmetry to protect it and maintain it at zero. To be a bit more precise, as we have seen today it is of order the critical density inferring an energy density scale of $10^{-47}(GeV)^4$. Now in the world of quantum field theory we expect that the zero point fluctuations of any scalar fields (for example) present will contribute towards an effective cosmological constant. Moreover the scale of that constant will be governed by the cut-off scale associated with the theory. So if I associated that with the Planck scale, I would expect a contribution of vacuum fluctuations to be at a scale of $10^{71}(GeV)^4$ a mere 10^{118} orders of magnitude larger than is observed. If you didn't trust Planck scale physics (and who could blame you!) then how about the electroweak scale at around a TeV. Then we would expect a contribution of around $1(TeV)^4$ which is a mismatch of 10^{61} or so. Thus even invoking supersymmetry (which brings us down to a TeV scale) we still have an incredible mismatch of scales. This is the cosmological constant problem, why has the universe not been completely dominated by these energy sources before now? Why are they effectively decoupling from the cosmological dynamics? Needless to say there has been a great deal of interest in the possibility that a cosmological constant may pop out of string theory and in the braneworld. This has met with mixed success but has opened up an area of research which has led people into the myriad of possibilities known as the String Landscape. It was known for some time that in conventional supergravity models there were 'No go' theorems which forbid cosmic acceleration in cosmological solutions arising from compactification of pure supergravity models where the internal space is a time-independent, non-singular compact manifold without boundary^{19,20}. Now one way of avoiding the theorem is to relax the conditions under which it applies such as allowing the internal space to be time-dependent, the analogue of a time-dependent scalar fields (radion). However, doing this, whilst leading to some solutions which have an accelerating late time evolution, they generally had mixed fortune in that they were preceded by a kinetic energy dominated evolution rather than a more useful matter dominated era. An alternative approach was developed by a number of authors who were interested in the pressing issue of stabilising the extra dimensions (moduli fields) in string theory^{21,22}. They realised that by using antisymmetric tensor fields to stabilise the extra dimensions (basically by wrapping them in fluxes), the net effect was that the resulting effective cosmological constant was described as a combination of the bare cosmological constant and the energy density of the fluxes (see also earlier work by Linde⁵). Given suitably quantised fluxes they argued that it was possible to have the required precision to account for the observed cosmological constant with of order 100 fluxes. This was easy to formulate in string theory. In fact given that there are believed to be of order 10^{500} possible vacua in string theory, it opened up the possibility that this new Landscape would inevitably have regions (possibly many of them) where the vacuum energy matched our observed one²³. This Landscape is good and bad. The good aspect of it, is that should it exist, it seems quite plausible that we can expect there to be many many Λ 's and a large number of these will be in the range of values we require. Indeed in a pioneering paper back in the late 1980's Weinberg effectively predicted we would have to find a Λ term today with the kind of scale it appears to have⁴. Anything larger would have meant the universe would expand too rapidly for structures to collapse to form galaxies. The downside is that it is proving almost impossible to calculate anything properly in this framework. We don't yet have exact

solutions we can use and so tend to end up adopting Anthropic arguments to justify our claims. The Landscape is clearly an interesting feature of string theory, and the hope for many of us is that one day we will be able to really test the notion that this is the origin of our observed universe. Other string related approaches to Λ include: using the extra dimensions to remove the gravitational effect of the vacuum energy, leaving us with an effectively flat four dimensional theory²⁴; of using a mechanism whereby Λ relaxes through the nucleation of branes coupled to a gauge potential²⁵ and by using the Cyclic universe as a means to give the cosmological constant plenty of time to relax to its present day value²⁶.

4 Rolling scalar fields – Quintessence and K-essence

An alternative approach to explain the nature of the dark energy is to say that we don't know why Λ is zero, but accept it is and try to find an alternative explanation for the dark energy in the form of an evolving scalar field – a late time inflaton field if you like. Many of us have had a go at this, far too many to mention, but I will briefly describe some of the neat features associated with it. Many Quintessence scenarios have the attractive feature that there are attractor solutions where the system evolves so as to not dominate the dynamics at early times but come to dominate at late times. This means that the system can evolve from a wide range of initial conditions in the safe knowledge that it will inevitably dominate the evolution at late times. The idea first developed by Ratra and Peebles²⁷ as well as Wetterich²⁸ in the mid 1980's was later used for this purpose in^{29,30}. I am not going to go into the details of any of the scalar field models – there are so many of them, but I feel it should be made clear that they all have the same basic fine tuning issues. First of all the parameters in the potential need to be generally adjusted so that today the scalar field potential matches that required for it to be dark energy. The potentials have to be flat enough to have slow roll inflation and this needs to be protected against supergravity corrections. Secondly, it has to come to dominate at the correct time, namely in the recent past. In almost all cases of Quintessence the net effect is that the mass of the Quintessence field has to be very small, $m_Q \simeq 10^{-33} \text{eV}$, with an associated energy density of the field being $V_0 \simeq (10^{-3} \text{eV})^4$. Such small mass scale should cause a few alarm bells to go off. A light field implies long range interactions, hence fifth force tests. There are strong limits on the allowed couplings of such fields to matter, and basically any such field needs to be protected from having too strong a coupling to matter otherwise we would have seen it as a fifth force. One possible route therefore is to consider models that have protected masses such as through using Nambu-Goto Goldstone bosons^{31,32,33}. Following the equation of state for the scalar field during its evolution we see how it tracks that of the background radiation, then matter before coming to dominate like a cosmological constant today. However, it is not a constant, it is evolving. One of the biggest questions we face is how can we test whether dark energy is evolving and moreover can we see that it might be different from a true cosmological constant?

An alternative approach to having a suitably flat potential, is to consider the case of a non-canonical kinetic sector to the theory driving the late time acceleration^{34,35}. Such an approach is called K-essence and has generated a lot of interest because of the fact that non-canonical terms appear often in string models. One of the nice features of the approach is that a long period of perfect tracking is followed by domination of dark energy triggered by the transition to matter domination – an epoch during which structures can form. This solution of the ‘why now’ problem is therefore addressed because rather than being put in as an arbitrary time scale, the transition occurs around the epoch of radiation-matter equality an epoch we know happened. However, a word of warning. It is not clear that K-essence solves the coincidence problem. The basin of attraction into the regime of tracker solutions is small compared to those where it immediately goes into K-essence domination, and so there may well be a degree of fine tuning

required in the scenario that is not obvious at first sight³⁶.

Before leaving the idea of scalar fields let me just mention that there have been a number of dark energy papers written making use of tachyon fields, phantom fields, chameleon fields, acceleron fields (scalar fields coupled to massive neutrinos) and chaplygin gases amongst others. The idea of the chameleon field is worth describing in a bit more detail³⁷. The key idea is that in order to avoid fifth force type constraints on Quintessence models, why not have a situation where the mass of the field depends on the local matter density? It can then be massive in high density regions (i.e. solar system) and light ($m \sim H$) in low density regions (i.e. cosmological scales). In that way it can explain dark energy without violating solar system bounds. There is plenty of work currently going on to investigate the nature and consistency of chameleon fields.

5 Modifying gravity

Up to now we have worked on the assumption that the dark energy is to be explained as a new form of matter, such as the cosmological constant. However, it could well be that it has nothing to do with the matter, but rather the gravity of the universe that we have got wrong. In other words perhaps we need to modify Einstein's gravity. Two recent reviews on the subject are^{12,16}. It is worth mentioning one approach in a bit more detail, but it gives a flavour of the many attempts that have been made over the past few years. In the same spirit of the pioneering work of Starobinsky³⁸, Carroll et al looked at a modification of the usual Einstein action³⁹ in which late time acceleration can be realized by terms containing inverse powers of the Ricci scalar added to the Einstein Hilbert action. Unfortunately the original model ($\mathcal{L} \propto R + 1/R$) is not compatible with solar system experiments and this remains the real test of modified gravity models today. A large number of people have generalised the model of Carroll et al to more general $R + f(R)$ type models. However usually $f(R)$ struggles to satisfy both solar system bounds on deviations from General Relativity and late time acceleration. It brings in an extra light degree of freedom which once again implies fifth force constraints come into play. A possible get out clause that has been investigated is to make the scalar degree of freedom massive in the high density solar vicinity and therefore hidden from solar system tests by a chameleon type mechanism. In general it appears to require a form for $f(R)$ where the mass squared of the scalar is large and positive at high curvature. In fact very recently Amendola and Tsujikawa have analysed these models and concluded that the $f(R)$ models satisfying cosmological and local gravity constraints are practically indistinguishable from the Lambda CDM model, at least at the background level⁴⁰. Other modified gravity models include ideas based on Braneworlds, where the extra dimensions can lead to modifications of the four dimensional gravity we are used to. Of particular popularity has been the model of Dvali-Gabadadze-Porrati (DGP)⁴¹ in which the brane is embedded in a *Minkowski* bulk. In a DGP braneworld, gravity remains four dimensional at short distances but can leak into the bulk at large distances leading to infrared modifications to Einstein gravity. There is a cross-over scale around which gravity manifests these higher-dimensional properties. This scenario is a simple one parameter model which can account for the current acceleration of the universe provided the cross-over scale is fine tuned to match observations. However there are problems with the model, perhaps the most significant and potentially lethal one being the fact that in the Self accelerating branch there are ghosts in the spectrum for any value of the brane tension. Such an instability is serious and suggests that all is not well with the model⁴².

I will finish on an area which is proving very difficult to rule out – perhaps there is no such thing as dark energy, we don't need to modify General Relativity, rather we just have to abandon the aspect of the cosmological principle that assumes large scale homogeneity. Although this is not the view of the majority of cosmologists who are happy with the Λ CDM paradigm, it has been suggested by a small but increasing number of authors that the apparent acceleration

is due to the fact we are in an inhomogeneous universe containing appreciable sized voids. In other words all we need to do is solve for General Relativity in an inhomogeneous background – easy to write, difficult to do of course. As an example Hunt and Sarkar ⁴³ have recently suggested that we can do away with the need for dark energy if we allow for the possibility that we live in an inhomogeneous universe, where inflation proceeded leading to features (bumps) in the primordial spectrum so that it is not scale free. We could be living in a local void where the Hubble flow is 30% faster than the global rate. They acknowledge a possible problem making their data consistent with the observed baryon oscillations in the large scale structure power spectra but otherwise they fit the data very well. Another inhomogeneous model has also been proposed recently by Wiltshire ⁴⁴, and alternatives to Dark Matter and Dark Energy have been proposed by Mannheim ⁴⁵. Kolb, Matarrese and collaborators ⁴⁶ have demonstrated the possibility of explaining away dark energy by solving the Einstein equations in a particular class of inhomogeneous Swiss Cheese universes and demonstrating the role averaging and backreaction can play in interpreting the dynamical evolution of these models. I think it is fair to say that we should always be prepared for the unexpected in this field.

6 Conclusions

Dear energy is a subject in which observations are driving us forward, transforming the field, especially through the CMBR and LSS. The data suggests that the universe is accelerating and its evolution is consistent with the driving force being due to a pure cosmological constant. However we don't really know why it is accelerating and what if anything has generated the constant to be the value it is. Moreover we don't even know if it is a cosmological constant and determining that must be one of the most important questions we would like to know the answer to. In particular, is $w = -1$, the cosmological constant and if not, then what value has it? On the other hand is $w(z)$ dynamical? Perhaps we are actually seeing some new Gravitational Physics. There are lots of models of dark energy but it may yet prove too difficult to separate one from another such as cosmological constant. However we need to try though! Rather frustratingly for some of us, perhaps we will only be able to determine Λ from anthropic arguments and not from fundamental theory. And finally, perhaps we are wrong and we do not need a lambda term at all. The next decade is certainly going to be exciting in this field !

Acknowledgments

I am very grateful to the organisers of the 45th Rencontres de Moriond for the invitation to participate in this fun meeting in such wonderful surroundings and with such nice people. I am also grateful to the Royal Society for financial support through the Wolfson Merit Award.

References

1. G. Efstathiou *et al*, *Mon. Not. Roy. Astron. Soc.* **247**, 10 (1990).
2. S. J. Maddox *et al*, *Mon. Not. Roy. Astron. Soc.* **283**, 1227 (1996).
3. G. Efstathiou *et al*, *Nature* **348**, 705 (1990).
4. S. Weinberg, *Rev. Mod. Phys.* **61**, 1 (1989).
5. A. D. Linde, *Rept. Prog. Phys.* **47**, 925 (1984).
6. S. Perlmutter *et al.*, *Astrophys. J.* **517**, 565 (1999).
7. A. G. Riess *et al.*, *Astron. J.* **116**, 1009 (1998); *Astron. J.* **117**, 707 (1999).
8. V. Sahni and A. A. Starobinsky, *Int. J. Mod. Phys. D* **9**, 373 (2000); V. Sahni, *Lect. Notes Phys.* **653**, 141 (2004).
9. S. M. Carroll, *Living Rev. Rel.* **4**, 1 (2001).

10. T. Padmanabhan, *Phys. Rept.* **380**, 235 (2003); *Current Science* **88**, 1057 (2005).
11. P. J. E. Peebles and B. Ratra, *Rev. Mod. Phys.* **75**, 559 (2003).
12. S. Nojiri and S. D. Odintsov, *eConf* **C0602061**, 06 (2006); *Int. J. Geom. Meth. Mod. Phys.* **4**, 115 (2007)
13. E. J. Copeland *et al.*, *Int. J. Mod. Phys. D* **15**, 1753 (2006).
14. E. V. Linder, *Rept. Prog. Phys.* **71**, 056901 (2008)
15. J. Frieman *et al.*, *Ann. Rev. Astron. Astrophys.* **46**, 385 (2008)
16. T. P. Sotiriou and V. Faraoni, arXiv:0805.1726 [gr-qc].
17. W.J. Percival *et al.*, *Mon. Not. Roy. Astron. Soc.* **381**, 1053 (2007)
18. E. Komatsu *et al.* [WMAP Collaboration], *Astrophys. J. Suppl.* **180**, 330 (2009)
19. G.W. Gibbons, *Aspects of Supergravity Theories*, in *Supersymmetry, Supergravity, and Related Topics*, eds. F. del Aguila, J.A. de Azcárraga and L.E. Ibañez (World Scientific 1985) pp. 346-351.
20. D.H. Wesley, *JCAP* **0901**, 041 (2009)
21. R. Bousso and J. Polchinski, *JHEP* **0006**, 006 (2000)
22. S. Giddings, S. Kachru and J. Polchinski, *Phys. Rev. D* **66**, 106006 (2002).
23. L. Susskind, arXiv:hep-th/0302219.
24. S. Kachru *et al.*, *Phys. Rev. D* **62**, 045021 (2000); N. Arkani-Hamed *et al.*, *Phys. Lett. B* **480**, 193 (2000)
25. J. L. Feng *et al.*, *Nucl. Phys. B* **602**, 307 (2001)
26. P. J. Steinhardt and N. Turok, *Science* **312**, 1180 (2006) [arXiv:astro-ph/0605173].
27. B. Ratra and J. Peebles, *Phys. Rev. D* **37**, 321 (1988).
28. C. Wetterich, *Nucl. Phys. B* **302**, 668 (1988).
29. R. R. Caldwell *et al.*, *Phys. Rev. Lett.* **80**, 1582 (1998).
30. I. Zlatev *et al.*, *Phys. Rev. Lett.* **82**, 896 (1999); P. J. Steinhardt *et al.*, *Phys. Rev. D* **59**, 123504 (1999).
31. J. A. Frieman *et al.*, *Phys. Rev. Lett.* **75**, 2077 (1995).
32. K. Choi, *Phys. Rev. D* **62**, 043509 (2000).
33. J. E. Kim and H. P. Nilles, *Phys. Lett. B* **553**, 1 (2003).
34. C. Armendáriz-Picón *et al.*, *Phys. Rev. Lett.* **85**, 4438 (2000).
35. C. Armendáriz-Picón *et al.*, *Phys. Rev. D* **63**, 103510 (2001).
36. M. Malquarti *et al.*, *Phys. Rev. D* **67**, 123503 (2003); M. Malquarti *et al.*, *Phys. Rev. D* **68**, 023512 (2003).
37. J. Khoury and A. Weltman, *Phys. Rev. Lett.* **93**, 171104 (2004).
38. A. A. Starobinsky, *Phys. Lett. B* **91**, 99 (1980).
39. S. M. Carroll *et al.*, *Phys. Rev. D* **70**, 043528 (2004).
40. L. Amendola and S. Tsujikawa, *Phys. Lett. B* **660**, 125 (2008)
41. G. R. Dvali *et al.*, *Phys. Lett. B* **485**, 208 (2000).
42. C. Charmousis *et al.*, *JHEP* **0610**, 066 (2006)
43. P. Hunt and S. Sarkar, *Phys. Rev. D* **76**, 123504 (2007); arXiv:0807.4508 [astro-ph]
44. D. L. Wiltshire, *New J. Phys.* **9**, 377 (2007); *Phys. Rev. Lett.* **99**, 251101 (2007); arXiv:0909.0749 [astro-ph.CO]
45. P. D. Mannheim, *Prog. Part. Nucl. Phys.* **56**, 340 (2006)
46. E. W. Kolb *et al.*, *New J. Phys.* **8**, 322 (2006); *Phys. Rev. D* **78**, 103002 (2008); arXiv:0901.4566 [astro-ph.CO]; V. Marra *et al.*, *Phys. Rev. D* **76**, 123004 (2007)

PRIMORDIAL GRAVITATIONAL WAVES AND THE LOCAL B-POLARIZATION OF THE CMB

JUAN GARCIA-BELLIDO

*Instituto de Física Teórica CSIC-UAM and Departamento de Física Teórica,
Universidad Autónoma de Madrid, Cantoblanco 28049 Madrid, Spain*

*Département de Physique Théorique, Université de Genève,
24 quai Ernest Ansermet, CH-1211 Genève 4, Switzerland*

A stochastic background of primordial gravitational waves could be detected soon in the polarization of the CMB and/or with laser interferometers. There are at least three GWB coming from inflation: those produced during inflation and associated with the stretching of space-time modes; those produced at the violent stage of preheating after inflation; and those associated with the self-ordering of Goldstone modes if inflation ends via a global symmetry breaking scenario, like in hybrid inflation. Each GW background has its own characteristic spectrum with specific features. We discuss the prospects for detecting each GWB and distinguishing between them with a very sensitive probe, the local B-mode of CMB polarization.

Cosmological Inflation^{1,2} naturally generates a spectrum of density fluctuations responsible for large scale structure formation which is consistent with the observed CMB anisotropies.³ It also generates a spectrum of gravitational waves, whose amplitude is directly related to the energy scale during inflation and which induces a distinct B-mode polarization pattern in the CMB.⁴ Moreover, Inflation typically ends in a violent process at preheating,⁵ where large density waves collide at relativistic speeds generating a stochastic background of GW⁶ with a non-thermal spectrum characterized by a prominent peak at GHz frequencies for GUT-scale models of inflation (or at mHz-kHz for low scale models of inflation), and an amplitude proportional to the square of the mass scale driving/ending inflation. Such a background could be detected with future GW observatories like Adv-LIGO⁷, LISA⁸, BBO⁹, etc. Furthermore, if inflation ended with a global phase transition, like in certain scenarios of hybrid inflation, then there is also a GWB due to the continuous self-ordering of the Goldstone modes at the scale of the horizon,¹⁰ which is also scale-invariant on subhorizon scales,¹¹ with an amplitude proportional to the quartic power of the symmetry breaking scale, that could be detectable with laser interferometers as well as indirectly with the B-mode polarization of the CMB.¹²

Gravitational waves produced during inflation arise exclusively due to the quasi-exponential expansion of the Universe², and are not sourced by the inflaton fluctuations, to first order in perturbation theory. They have an approximately scale invariant and Gaussian spectrum whose amplitude is proportional to the energy density during inflation. GUT scale inflation has good chances to be discovered (or ruled out) by the next generation of CMB anisotropies probes, Planck¹³ and CMBpol¹⁴, see Fig. 1 for present bounds. At the end of inflation, reheating typically takes place in several stages. There is first a rapid (explosive) conversion of energy from the inflaton condensate to the fields that couple to it. This epoch is known as preheating⁵

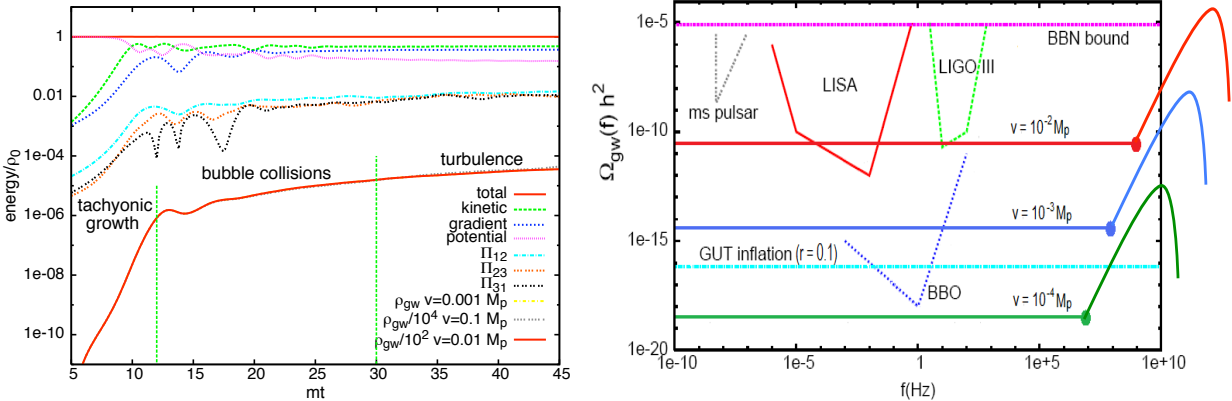


Figure 1: LEFT: The time evolution of the GW energy density during the initial stages of preheating after hybrid inflation, from Ref.[6]. Note the three stages of tachyonic growth, bubble collisions and turbulence. RIGHT: The observational bounds on GW. Flat spectra correspond to GUT Inflation (dashed line) and global phase transitions (continuous lines), while the peaks at the end of the latter spectra correspond to preheating at high scales.

and occurs in most models of inflation. It can be particularly violent in the context of hybrid inflation, where the end of inflation is associated with a symmetry breaking scenario, with a huge range of possibilities, from GUT scale physics down to the Electroweak scale. Gravitational waves are copiously produced at preheating from the violent collisions of high density waves moving and colliding at relativistic speeds⁶, see Fig. 1. The GW spectrum is highly peaked at the mass scale corresponding to the symmetry breaking field, which could be very different from the Hubble scale.

In low-scale models of hybrid inflation it is possible to attain a significant GWB at the range of frequencies and sensitivities of LIGO or BBO. The origin of these GW is very different from that of inflation. Here the space-time is essentially static, but there are very large inhomogeneities in the symmetry breaking (Higgs) field due to the random spinodal growth during preheating. Although the transition is not first order, “bubbles” form due to the oscillations of the Higgs field around its minimum. The subsequent collisions of the quasi-bubble walls produce a rapid growth of the GW amplitude due to large field gradients, which source the anisotropic stress-tensor⁶. The relevant degrees of freedom are those of the Higgs field, for which there are exact analytical solutions in the spinodal growth stage, which later can be input into lattice numerical simulations in order to follow the highly non-linear and out-of-equilibrium stage of bubble collisions and turbulence. However, the process of GW production at preheating lasts only a short period of time around symmetry breaking. Soon the amplitude of GW saturates during the turbulent stage and then can be directly extrapolated to the present with the usual cosmic redshift scaling. Such a GWB spectrum from preheating would have a characteristic bump, worth searching for with GW observatories based on laser interferometry, although the scales would be too small for leaving any indirect signature in the CMB polarization anisotropies. Moreover, the mechanism generating GW at preheating is also active in models where the SB scenario is a local one, with gauge fields present in the plasma, and possibly related to the production of magnetic field flux tubes¹⁵. In such a case, one could try to correlate the GWB amplitude and the magnitude and correlation length of the primordial magnetic field seed.

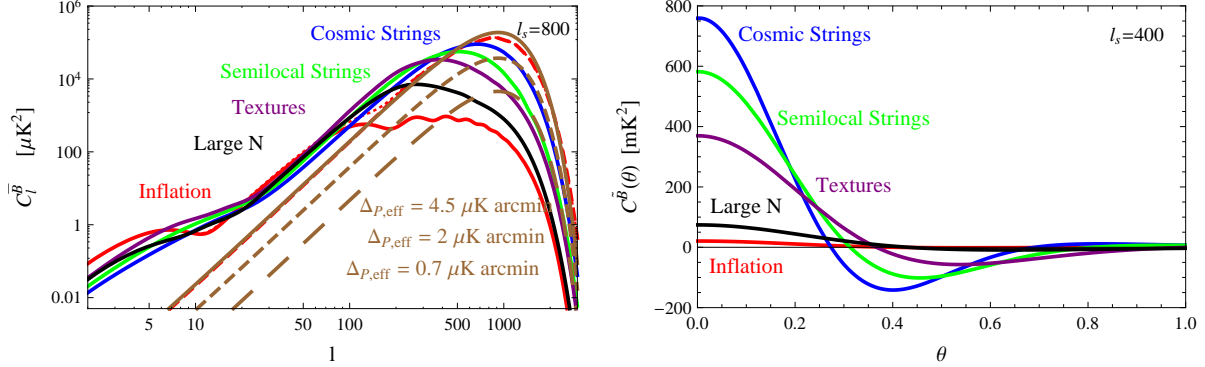


Figure 2: LEFT: The local \tilde{B} -polarization power spectra for tensor perturbations from inflation, cosmic strings, textures and the large- N limit of the non-linear sigma-model. All spectra are normalized such that they make up 10% of the observed temperature anisotropy at $\ell = 10$. Note that the lensed EE modes (red dashed line) contribute as colored noise to the local-BB angular power spectrum. RIGHT: The local \tilde{B} -polarization angular correlation functions for $\theta < 1^\circ$ for inflation, cosmic strings, textures and the large- N limit of NL sigma model.

In the case that inflation ends with a global or local symmetry breaking mechanism, then there generically appear cosmic defects associated with the topology of the vacuum manifold. For instance, global cosmic strings are copiously produced during preheating if the Higgs field is a complex scalar with a U(1) global symmetry⁵. In principle, all kinds of topological and non-topological defects could form at the end of inflation and during preheating. Such defects will have contributions to all three different metric perturbations: scalar, vector and tensor, with similar amplitudes¹⁶. In a recent work¹¹, we analyzed the production of GW at preheating for a model with O(N) symmetry. The dynamics at subhorizon scales was identical to that of the usual tachyonic preheating. However, in this model even though the Higgs potential fixed the radial component to its vev, there remained the free (massless) Goldstone modes to orient themselves in an uncorrelated way on scales larger than the causal horizon. In the subsequent evolution of the Universe, as the horizon grows, spatial gradients at the horizon will tend to reorder these Goldstone modes in the field direction of the subhorizon domain. This self-ordering of the fields induces an anisotropic stress-tensor which sources GW production. In the limit of large N components, it is possible to compute exactly the scaling solutions, and thus the amplitude and shape of the GWB spectrum. It turns out that the GWB has a scale-invariant spectrum on subhorizon scales¹⁰ and a k^3 infrared tail on large scales¹¹, which can be used to distinguish between inflation and these non-topological defects.

Apart from the IR tail, the main difference between inflationary and global defect contributions to the CMB anisotropies arises from the fact that defects generically contribute with all modes: scalar, vector and tensor modes, with similar amplitudes, while inflationary tensor modes could be negligible if the scale of inflation is well below the GUT scale. Since (curl) B-modes of the polarization anisotropies only get contributions from the vector and tensor modes, the detection of the B-mode from inflation may be challenging, and dedicated experiments like Planck and CMBpol have been designed to look for them. On the other hand, defects' contribution to the temperature anisotropies have a characteristic smooth hump in the angular power spectrum, which allows one to bound their amplitude (and thus the scale of symmetry breaking) below 10^{16} GeV.¹⁷ However, the contribution to the B-mode coming from defects have both tensor and vector components, and the latter can be up to ten times larger than the former, and actually peaks at a scale somewhat below the horizon at last scattering (in harmonic space the corresponding multipole is $\ell \sim 1000$).

In a recent paper¹² we analyzed the possibility of disentangling the different contributions

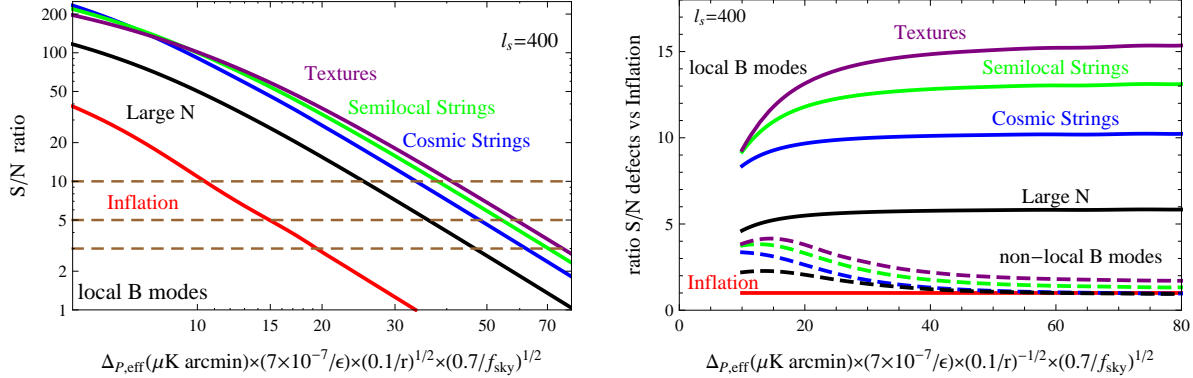


Figure 3: LEFT: The signal-to-noise ratio as a function of the normalized polarization sensitivity, for inflation, cosmic strings, textures and the large- N limit of the non-linear sigma-model. RIGHT: The relative signal-to-noise ratio for defect models versus inflation for local (continuous lines) and non-local (dashed lines) B-modes.

to the B-mode polarization coming from defects versus that from inflation. The main difficulty, for both defects and tensor modes from inflation, is that the B-mode power spectrum is “contaminated” by the effect of lensing from the intervening matter distribution on the dominant E-mode contribution on similar angular scales. Using the temperature power spectrum to determine the underlying matter perturbation from evolved large scale structures responsible for CMB lensing, it is possible to engineer an iterative scheme to clean the primordial B-modes from lensed E-modes¹⁸. This procedure leaves a significantly smaller polarization noise background $\Delta_{P,\text{eff}}$ which allows one to detect the GW background at high confidence level (3σ) if the scale of inflation or that of symmetry breaking is high enough. What we realized is that the usual E- and B-modes used for computing the angular power spectra are complicated non-local functions of the Stokes parameters, involving both partial differentiation and inverse laplacian integration. Such a non-local function requires knowledge of the global polarization on scales as large as the horizon, where the B-mode angular correlation function is negligible and thus prone to large systematic errors. In contrast, the so-called “local” \tilde{E} - and \tilde{B} -modes^{4,19} can be constructed directly from the Stokes parameters and do not involve any non-local inversion. A direct consequence in this change of variables is that the angular power spectrum of local \tilde{B} -modes has a extra factor $n_\ell = (\ell + 2)!/(\ell - 1)! \sim \ell^4$, which boosts the high- ℓ peak in the defects’ power spectra. When compared with the angular correlation function of inflation, it gives a significant advantage to the defects’ prospects for detection in future CMB experiments, see Fig. 3 and Table 1.

Table 1: The limiting amplitude for inflation ($r=T/S$) and various defects ($\epsilon = Gv^2$), at 3σ in the range $\theta \in [0, 1^\circ]$, for Planck ($\Delta_{P,\text{eff}} = 11.2 \mu\text{K}\cdot\text{arcmin}$), CMBpol-like exp. ($\Delta_{P,\text{eff}} = 0.7 \mu\text{K}\cdot\text{arcmin}$) and a dedicated CMB experiment with $\Delta_{P,\text{eff}} = 0.01 \mu\text{K}\cdot\text{arcmin}$. We have assumed $f_{\text{sky}} = 0.7$ for all CMB experiments.

$S/N = 3$	Inflation	Strings	Semilocal	Textures	Large-N
Planck	0.03	$1.2 \cdot 10^{-7}$	$1.1 \cdot 10^{-7}$	$1.0 \cdot 10^{-7}$	$1.6 \cdot 10^{-7}$
CMBpol	10^{-4}	$7.7 \cdot 10^{-9}$	$6.9 \cdot 10^{-9}$	$6.3 \cdot 10^{-9}$	$1.0 \cdot 10^{-8}$
\tilde{B} exp	10^{-7}	$1.1 \cdot 10^{-10}$	$1.0 \cdot 10^{-10}$	$0.9 \cdot 10^{-10}$	$1.4 \cdot 10^{-10}$

Acknowledgments

I thank Ruth Durrer, Martin Kunz, Elisa Fenu and Daniel Figueroa for a very enjoyable collaboration. This work is supported by the Spanish MICINN under project AYA2009-13936-C06-06.

References

1. A. D. Linde, “Particle Physics and Inflationary Cosmology,” *Harwood* (1990)
2. V. Mukhanov, “Physical foundations of cosmology,” *Cambridge Univ. Press* (2005).
3. E. Komatsu *et al.*, “Seven-Year WMAP Observations: Cosmological Interpretation,” [arXiv:1001.4538 \[astro-ph.CO\]](https://arxiv.org/abs/1001.4538).
4. R. Durrer, “The Cosmic Microwave Background”, *Cambridge Univ. Press* (2008).
5. L. Kofman, A. D. Linde and A. A. Starobinsky, Phys. Rev. Lett. **73**, 3195 (1994); Phys. Rev. D **56**, 3258 (1997). Y. Shtanov, J. H. Traschen and R. H. Brandenberger, Phys. Rev. D **51**, 5438 (1995); S. Y. Khlebnikov and I. I. Tkachev, Phys. Rev. Lett. **77**, 219 (1996); Phys. Rev. Lett. **79**, 1607 (1997); S. Khlebnikov, L. Kofman, A. D. Linde and I. Tkachev, Phys. Rev. Lett. **81**, 2012 (1998); J. García-Bellido and A. D. Linde, Phys. Rev. D **57**, 6075 (1998); G. N. Felder, J. García-Bellido, P. B. Greene, L. Kofman, A. D. Linde and I. Tkachev, Phys. Rev. Lett. **87**, 011601 (2001); G. N. Felder, L. Kofman and A. D. Linde, Phys. Rev. D **64**, 123517 (2001); J. García-Bellido, M. García Perez and A. González-Arroyo, Phys. Rev. D **67**, 103501 (2003).
6. S. Y. Khlebnikov and I. I. Tkachev, Phys. Rev. D **56**, 653 (1997); J. García-Bellido, “Preheating the universe in hybrid inflation,” [arXiv:hep-ph/9804205](https://arxiv.org/abs/hep-ph/9804205); R. Easther and E. A. Lim, JCAP **0604**, 010 (2006); J. García-Bellido and D. G. Figueroa, Phys. Rev. Lett. **98**, 061302 (2007); R. Easther, J. T. Giblin and E. A. Lim, Phys. Rev. Lett. **99**, 221301 (2007); J. García-Bellido, D. G. Figueroa and A. Sastre, Phys. Rev. D **77**, 043517 (2008); J. F. Dufaux, A. Bergman, G. N. Felder, L. Kofman and J. P. Uzan, Phys. Rev. D **76**, 123517 (2007); J. F. Dufaux, G. N. Felder, L. Kofman and O. Navros, JCAP **0903**, 001 (2009); A. Kusenko and A. Mazumdar, Phys. Rev. Lett. **101**, 211301 (2008); J. F. Dufaux, Phys. Rev. Lett. **103**, 041301 (2009).
7. B. Abbott *et al.* [LIGO Scientific Collaboration], Nature **460**, 990 (2009); LIGO URL: <http://www.ligo.caltech.edu/>
8. LISA URL’s: <http://lisa.esa.int> or <http://lisa.jpl.nasa.gov/>
9. G. M. Harry, P. Fritschel, D. A. Shaddock, W. Folkner and E. S. Phinney, Class. Quant. Grav. **23**, 4887 (2006); BBO URL: <http://universe.nasa.gov/new/program/bbo.html>
10. L. M. Krauss, Phys. Lett. B **284**, 229 (1992); K. Jones-Smith, L. M. Krauss and H. Mathur, Phys. Rev. Lett. **100** (2008) 131302; L. M. Krauss, K. Jones-Smith, H. Mathur and J. Dent, [arXiv:1003.1735 \[astro-ph.CO\]](https://arxiv.org/abs/1003.1735).
11. E. Fenu, D. G. Figueroa, R. Durrer and J. García-Bellido, JCAP **0910**, 005 (2009).
12. J. García-Bellido, R. Durrer, E. Fenu, D. G. Figueroa and M. Kunz, “The local B-polarization of the CMB: a very sensitive probe of cosmic defects,” [arXiv:1003.0299 \[astro-ph.CO\]](https://arxiv.org/abs/1003.0299).
13. The ESA satellite Planck, URL: <http://www.esa.int/planck>
14. CMB polarization satellite project, <http://cmbpol.uchicago.edu/>
15. A. Diaz-Gil, J. Garcia-Bellido, M. Garcia Perez and A. Gonzalez-Arroyo, Phys. Rev. Lett. **100**, 241301 (2008); JHEP **0807**, 043 (2008).
16. R. Durrer, M. Kunz, A. Melchiorri, Phys. Rept. **364**, 1 (2002).
17. U. Seljak and A. Slosar, Phys. Rev. D **74**, 063523 (2006); N. Bevis, M. Hindmarsh, M. Kunz and J. Urrestilla, Phys. Rev. Lett. **100**, 021301 (2008); Phys. Rev. D **76**, 043005 (2007); L. Pogosian and M. Wyman, Phys. Rev. D **77**, 083509 (2008); N. Bevis, M. Hindmarsh, M. Kunz and J. Urrestilla, Phys. Rev. D **75**, 065015 (2007); J. Urrestilla, P. Mukherjee, A. R. Liddle, N. Bevis, M. Hindmarsh and M. Kunz, Phys. Rev. D **77**, 123005 (2008).
18. U. Seljak and C. M. Hirata, Phys. Rev. D **69**, 043005 (2004).
19. D. Baumann and M. Zaldarriaga, JCAP **0906**, 013 (2009).

Charge, domain walls and dark energy

JONATHAN A PEARSON

*Jodrell Bank Centre for Astrophysics, The University of Manchester,
Manchester M13 9PL, U.K*

One idea to explain the mysterious dark energy which appears to pervade the Universe is that it is due to a network of domain walls which has frozen into some kind of static configuration, akin to a soap film. Such models predict an equation of state with $w = P/\rho = -2/3$ and can be represented in cosmological perturbation theory by an elastic medium with rigidity and a relativistic sound speed. An important question is whether such a network can be created from random initial conditions. We consider various models which allow the formation of domain walls, and present results from an extensive set of numerical investigations. The idea is to give a mechanism which prevents the natural propensity of domain walls to collapse and lose energy, almost to the point where a domain wall network freezes in. We show that when domain walls couple to a field with a conserved charge, there is a parameter range for which charge condenses onto the domain walls, providing a resistive force to the otherwise natural collapse of the walls.

1 Introduction and motivation

Modern cosmology has found itself a problem. If observational data are understood within the framework of the FRW model in General Relativity, one must invent a “dark energy” component within the content of the universe, to explain acceleration (in the absence of a cosmological constant). The alternative is to move away from the FRW model, or to modify the gravitational theory.

In this paper we provide fresh theoretical evidence for the viability of the elastic dark energy model – a model which uses frozen domain wall networks to accelerate the universe¹. The equation of state for a gas of domain walls moving at velocity v is $w_{\text{dw}} = v^2 - 2/3$, hence our requirement for a frustrated “frozen” network, for which $w_{\text{dw}} = -2/3$. We present a mechanism which freezes domain wall networks. If symmetry currents interact with domain walls, a pseudo-stable glass-like network forms.

We will begin by giving a quick review of features and results of the proto-typical domain wall forming model. We will then discuss two models, which have the feature that a field with discrete minima interacts with a second field with continuous $U(1)$ symmetry.

2 \mathbb{Z}_2 domain walls

If a field theory has a potential, and if the potential has multiple disconnected vacua, domain walls form. Domain walls are the interpolations between spatially adjacent vacuum states². The simplest example of such a field theory is described by the Lagrangian

$$\mathcal{L} = \frac{1}{2} \partial_\mu \phi \partial^\mu \phi - \frac{\lambda}{4} (\phi^2 - \eta^2)^2. \quad (1)$$

The vacuum in this theory – the configurations of the scalar field $\phi(x^\mu) \in \mathbb{R}$ that minimise the potential – is just the set $\mathcal{V} = \{+\eta, -\eta\}$. If we imagine two chunks of space, one with $\phi = +\eta$ and another with $\phi = -\eta$, then the field must continuously interpolate at the boundary between the “domains”. There is a static solution to the equations of motion which captures such an interpolation, $\phi(x) = \eta_\phi \tanh(x/\Delta)$, where $\Delta := \sqrt{2/\lambda\eta^2}$, the so-called kink solution. The symmetry properties of this model are rather interesting. Consider the full model (1), and transforming $\phi \rightarrow -\phi$: the model is totally invariant under this transformation. However, if one expands about each of the minima, the symmetry is lost. This is a simple example of spontaneous symmetry breaking.

By a rather simple dimensional argument, as well as substantial numerical investigations^{3 4}, the number of domain walls formed by the standard Kibble scenario drops, $n \propto t^{-1}$. This result is also observed in many other models (so long as discrete vacua are present) – even with 3 or more vacua (with junctions). The standard result, therefore, is that domain walls collapse under their own tension.

Numerical simulation Throughout the rest of the paper we will refer to simulations that we have performed. We evolve the equations of motion in $(2+1)$ -dimensions, using a leapfrog evolver, imposing periodic boundary conditions. We use random initial conditions: each grid-point is randomly assigned to be in one of the vacuum states of the theory. We also apply damping for a small amount of the total simulation time, to ease condensation into domains: results are only meaningful once this damped period has elapsed.

3 Kinky vortons

The kinky vorton model allows a charged condensate to live on a domain wall kink solution. The model has Lagrangian

$$\mathcal{L} = \partial_\mu \phi \partial^\mu \phi + \partial_\mu \sigma \partial^\mu \bar{\sigma} - \frac{\lambda_\phi}{4} (\phi^2 - \eta_\phi^2)^2 - \frac{\lambda_\sigma}{4} (|\sigma|^2 - \eta_\sigma^2)^2 - \beta \phi^2 |\sigma|^2. \quad (2)$$

The first two terms are the kinetic terms of the real and complex scalar fields, ϕ, σ , respectively. Third is the symmetry breaking term of the real scalar – this allows domain walls to form. Next is a term which has a $U(1)$ symmetry, where the complex scalar takes on a non-zero value in the vacuum. Finally, a quartic interaction term between the fields. This theory has a global $\mathbb{Z}_2 \times U(1)$ symmetry. The model parameters are chosen such that the \mathbb{Z}_2 symmetry is broken in the vacuum, and the $U(1)$ symmetry retained. A consequence of the $U(1)$ symmetry is that there exists a conserved symmetry current and charge (Noether’s theorem):

$$J_\mu := \bar{\sigma} \partial_\mu \sigma - \sigma \partial_\mu \bar{\sigma}, \quad \partial_\mu J^\mu = 0, \quad \frac{d}{dt} \int d^3x J_0 = 0.$$

One will immediately notice that there are a large number of model parameters, whose values must be chosen. A range of different choices have been discussed in ref.⁵, but in the present paper will only consider a single parameter set: $\lambda_\phi = \lambda_\sigma = 2, \beta = \eta_\phi = 1, \eta_\sigma = \sqrt{3}/2$.

A kinky vorton is a stable solution to the Euler-Lagrange equations of motion, which corresponds to a circular kink solution with a current-carrying charged condensate living on the domain wall⁶. The radius of the loop is entirely determined by the charge and current that reside on the loop: one can imagine the loop being stabilized by the existence of the conserved charge/current (without the condensate, the loop collapses).

3.1 Formation from random initial conditions

The loops just described are entirely idealized: single loops, carefully setup in numerical simulations. So, we ask the question: can these charged loops form from random initial conditions, and can they aid network stabilization?

We initially setup a homogeneous charged background, and random vacuum occupation. We specify an initial charge density $\rho_Q(0)$, and let the equations of motion evolve. Figure 1 has images of the ϕ -field, over time, for various initial charge densities $\rho_Q(0)$. It is clear from inspecting these images that as the initial charge is increased, the rate at which the network “dilutes” slows down. This is quantified by inspecting a plot of the evolution of the total number of domain walls, for various initial charge densities (not included in the present paper, but can be found another publication⁷). We have also isolated some of the loops, and analyzed their properties (winding number, charge and radius). We have shown that they have properties very close to kinky vortons.

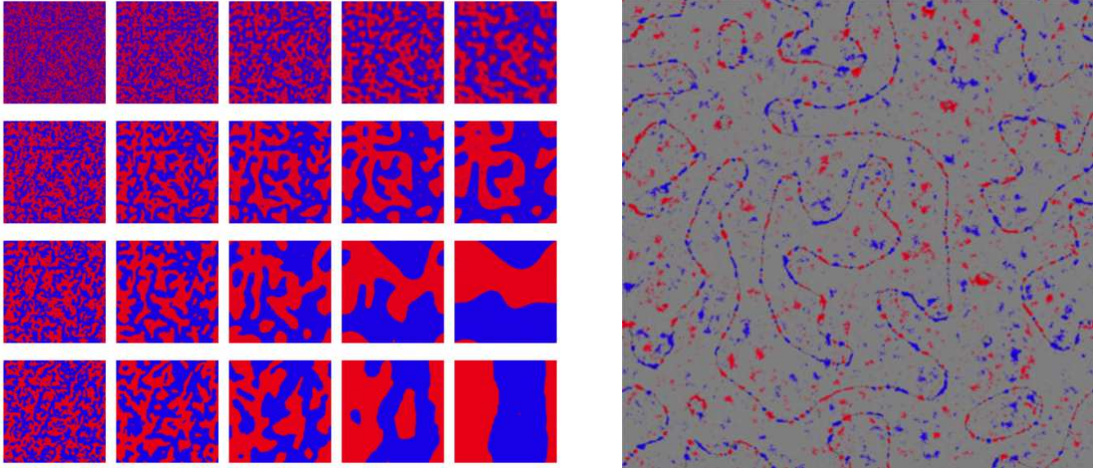


Figure 1: *Left* Images of the evolution of the ϕ -field at $t = 80, 160, 320, 640, 1280$ (left to right) for initial charge densities $\rho_Q(0) = 0, 0.01, 0.09, 0.25$ (bottom to top). *Right* Image of $\Re(\sigma)$, of the $\rho_Q(0) = 0.09$ simulation at $t = 640$. In both sets of images, red/blue denotes positive/negative values (i.e. the two vacua, and a winding, respectively).

4 Charge-coupled cubic anisotropy model

The charged-coupled cubic anisotropy model is constructed by interacting a real vector field $\phi(x^\mu) \in \mathbb{R}^N$ with a complex scalar field σ , so that the model has a broken $O(N) \times U(1)$ global symmetry. It is only the $O(N)$ symmetry that is broken in the vacuum – so that domain walls form, and there exists a conserved charge. The potential is

$$V = \frac{\lambda_\phi}{4} (|\phi|^2 - \eta_\phi^2)^2 + \epsilon \sum_{i=1}^N \phi_i^4 + \frac{\lambda_\sigma}{4} (|\sigma|^2 - \eta_\sigma^2)^2 + \beta |\phi|^2 |\sigma|^2. \quad (3)$$

The first two terms create discrete vacua in the vector field, then the introduction of the condensate field, and finally the term which interacts the condensate and vector fields. As there are more than 2 vacua, junctions and multiple tensions of domain walls can form (a junction is where more than two vacua cycle around a point in space: if four vacua cycle, an X -type junction is formed, and if there are three then a Y -type junction). A known result is that the number of domain walls in the cubic anisotropy model drops $n \propto t^{-1}$: junctions do nothing to prevent the collapse of a network³.

We have performed a set of simulations with this model, taking $\phi(x^\mu) \in \mathbb{R}^2$. As in the kinky vorton model, we start off with homogeneous initial charge and random initial domain occupation (this time there are 4 vacua/colours to choose from). The parameter choice in this model becomes less trivial, but an interesting parameter worthy of note is the interaction constant β , where we take $4\beta^2 = \lambda_\phi \lambda_\sigma + 4\epsilon \lambda_\sigma$, chosen to avoid the phase-separation phenomenon⁵.

In Figure 2 we display images of the ϕ -field, all of which are at the same time-step, but with different initial charge densities. Again, the implication is clear: more charge freezes the pattern in more. Plots of $\Re(\sigma)$, charge and current densities look qualitatively identical to their kinky vortons counterparts, having become associated exclusively with domain walls.

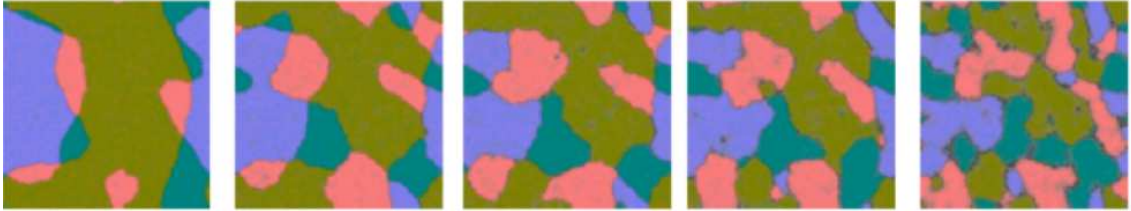


Figure 2: Images of the ϕ -field at $t = 320$, for $\rho_Q(0) = 0.09, 0.16, 0.2, 0.25, 0.36$.

5 Conclusions and summary

Our first result is that networks with higher initial charge density freezes wall networks in “more”. Secondly, charge and current condense on domain walls, and almost exclusively live on them. Finally, some of the loops that form have the specific properties of kinky vortons.

The elastic dark energy model was proposed to use domain walls as a model, requiring the wall network to freeze in. The conserved charge of the condensate field discussed here provides a resisting force against the tension of a domain wall, enabling a network to become pseudo-stable.

Acknowledgements

The work presented here was carried out in collaboration with R. Battye, P. Sutcliffe and S. Pike; our image creation software was largely developed by C. Welshman.

References

1. M. Bucher and D.N. Spergel, *Phys. Rev. D* **60**, 043505 (1999); R.A. Battye, M. Bucher and D. Spergel, *astro-ph/9908047* (1999)
2. A. Vilenkin and E.P.S. Shellard, *Cosmic strings and other topological defects*, Cambridge University Press, Cambridge, UK (1994)
3. R.A. Battye and A. Moss, *Phys. Rev. D* **74**, 023528 (2006)
4. P.P. Avelino et al, *Phys. Lett. B* **647**, 63 (2007), *Phys. Rev. D* **73**, 123520 (2006), *Phys. Rev. D* **78**, 103508 (2008)
5. R.A. Battye and J.A. Pearson, *in prep* (2010)
6. R.A. Battye and P.M. Sutcliffe, *NPB* **805**, 287 (2008)
7. R.A. Battye, J.A. Pearson, P.M. Sutcliffe and S. Pike, *JCAP* **09**, 039 (2009)

TESTING GENERIC PREDICTIONS OF DARK ENERGY

M.J. MORTONSON

*Center for Cosmology and AstroParticle Physics,
The Ohio State University, Columbus, OH 43210*

Constraints on the expansion history of the universe from measurements of cosmological distances make predictions for large-scale structure growth. Since these predictions depend on assumptions about dark energy evolution and spatial curvature, they can be used to test general classes of dark energy models by comparing predictions for those models with direct measurements of the growth history. I present predictions from current distance measurements for the growth history of dark energy models including a cosmological constant and quintessence. Although a time-dependent dark energy equation of state significantly weakens predictions for growth from measured distances, for quintessence there is a generic limit on the growth evolution that could be used to falsify the whole class of quintessence models. Understanding the allowed range of growth for dark energy models in the context of general relativity is a crucial step for efforts to distinguish dark energy from modified gravity.

1 Introduction

Although several ideas have been proposed to explain the observed acceleration of the cosmic expansion rate, none has yet emerged as a clear favorite from a theoretical viewpoint. Even if we restrict the possibilities to models where general relativity (GR) is valid even on the largest scales and dark energy drives the accelerated expansion, there are still numerous models of dark energy that can fit existing cosmological data. One method for distinguishing among these possibilities is to compare constraints from probes of geometry (distances and the expansion rate) with those from probes of the growth of large-scale structure. Here I present predictions for the growth history from existing measurements of distances and show that while these predictions can vary significantly depending on the specific model of dark energy, there are some generic aspects of the growth predictions that offer the possibility of simultaneously testing large classes of dark energy models.

To maximize the potential for cutting down the allowed space of dark energy models, the goal here is to identify *general features* of broad classes of dark energy models rather than to place constraints on specific models of dark energy individually. The example of a model class that I will use here is the set of all scalar field quintessence models. A second important point is that for the purposes of this study, the constraints on dark energy parameters themselves are unimportant; instead, the main output of the analysis consists of *observable predictions* that provide tests of each class of dark energy models. In particular, I will focus on predictions for the growth of large-scale structure.

The growth function describes how initial density fluctuations in the universe grow under the influence of gravity. On large scales, where the density fluctuations δ are small enough that the equations for the evolution of perturbations can be linearized, the growth function is

independent of scale and can be expressed relative to its value at some redshift z_{MD} during matter domination as $G(z) = [(1+z)\delta(z)]/[(1+z_{\text{MD}})\delta(z_{\text{MD}})]$. During matter domination, $\delta(z) \propto (1+z)^{-1}$ so $G(z) = 1$, but at late times cosmic acceleration typically causes $G(z)$ to fall below unity. The linear evolution of the growth is related to the Hubble expansion rate $H(z)$ by

$$G'' + \left(4 + \frac{H'}{H}\right)G' + \left[3 + \frac{H'}{H} - \frac{3}{2}\Omega_{\text{m}}(z)\right]G = 0, \quad (1)$$

where $\Omega_{\text{m}}(z) = \Omega_{\text{m}}(1+z)^3[H_0/H(z)]^2$ is the fraction of density in matter with present value Ω_{m} , and primes denote derivatives with respect to $\ln a = -\ln(1+z)$. The Hubble constant, $H_0 = H(z=0)$, can also be expressed in the dimensionless form $h = H_0/(100 \text{ km s}^{-1} \text{ Mpc}^{-1})$.

The expansion rate is constrained observationally through measurements of cosmological distances as a function of redshift,

$$D(z) = \frac{1}{\sqrt{\Omega_{\text{K}}}H_0} \sinh \left[\sqrt{\Omega_{\text{K}}}H_0 \int_0^z \frac{dz'}{H(z')} \right], \quad (2)$$

where Ω_{K} parametrizes spatial curvature. Observations of Type Ia supernovae (SNe), the Hubble constant, baryon acoustic oscillations (BAO), and the cosmic microwave background (CMB) all provide constraints on the distance-redshift relation at various redshifts. The inferred evolution of $H(z)$ can be used to predict the linear growth history $G(z)$ using Eq. (1).

2 Methods

By varying the parameters of some model for dark energy and comparing $D(z)$ from Eq. (2) for each set of parameters with measurements of $D(z)$, Markov Chain Monte Carlo (MCMC) analysis provides an estimate of the joint probability distribution for the model parameters. Uncertainties on the model parameters can then be propagated to redshift-dependent observables like $H(z)$ and $G(z)$. The strength of these predictions depends on many factors, particularly the precision of the available data and the choice of dark energy parameters and priors.

The range allowed for many observable quantities can be predicted from data using these methods; for example, predictions for several different functions describing large-scale structure growth as well as for $H(z)$ and $D(z)$ (at redshifts where it is not directly constrained by data) are presented by Mortonson, Hu, and Huterer^{1,2} for both current data sets and forecasts. Here I will focus on the predictions for $G(z)$ from current data.

The data sets I use to constrain the distance-redshift relation and make predictions for the growth history include the following: (1) A recent compilation of SN data, called the Union compilation,³ including 307 Type Ia supernovae mostly at $0.1 < z < 1$. (2) CMB observations from the 5-year data release of the WMAP satellite.⁴ For the purposes of constraining dark energy evolution, the main quantities measured by the CMB are the distance to recombination at $z \approx 1100$ and the matter density $\Omega_{\text{m}}h^2$. [Note that $\Omega_{\text{m}}(z)$ in Eq. (1) depends only on $H(z)$ and $\Omega_{\text{m}}h^2$.] (3) A 4% constraint on the volume-averaged distance $D_V(z=0.35) = (zD^2/H)^{1/3}|_{z=0.35}$ from the correlation of SDSS luminous red galaxies.⁵ (4) A 5% constraint on H_0 from the analysis of the SHOES team⁶ which anchors the distance-redshift relation at low z .

The parametrizations of dark energy that I will consider here include (1) a cosmological constant model (Λ CDM), characterized by a constant equation of state $w = -1$, and (2) scalar field quintessence models with a time-dependent equation of state that satisfies $-1 \leq w(z) \leq 1$. To provide a complete description of the effects of dark energy at low redshifts ($z < 1.7$), $w(z)$ for quintessence models is expressed as a linear combination of basis functions $e_i(z)$ which are the principal components (PCs) of the Fisher matrix forecast for future space-based SN data and Planck CMB data,¹

$$w(z) = -1 + \sum_i \alpha_i e_i(z), \quad (3)$$

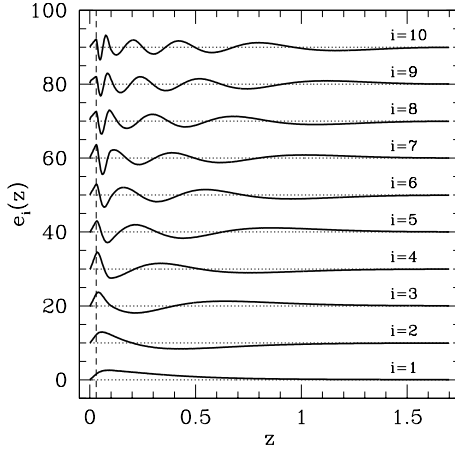


Figure 1: The 10 lowest-variance principal components (increasing variance from bottom to top) of $w(z)$ at $z < 1.7$ for SN and CMB forecasts. Different components are offset vertically for clarity, with zero points indicated by dotted lines. The vertical dashed line shows the assumed minimum SN redshift, $z = 0.03$.

where α_i are the PC amplitudes. The PCs are constructed to be orthogonal for the forecasts and remain nearly uncorrelated for current data,⁷ and they are ordered by the accuracy with which they can be measured. The latter property allows the set of PCs to be truncated, keeping only the modes of $w(z)$ that produce measurable changes in the cosmological observables. For current data, the first 10 PCs are sufficient for completeness (see Fig. 1).

Variations in the dark energy equation of state at high redshifts are poorly constrained by current data and are expected to be less important than low-redshift evolution since dark energy makes up a much smaller fraction of the total density at early times. Nevertheless, we can allow for the possibility of early dark energy in the quintessence model class by including a constant equation of state parameter at $z > 1.7$, w_∞ . Additionally, it is important to consider the possibility of nonzero spatial curvature (for both Λ CDM and quintessence) due to degeneracies between curvature and dark energy evolution.

3 Growth predictions

Figure 2 shows examples of the predicted ranges of the growth function $G(z)$ allowed by current data for a few representative classes of dark energy models: Λ CDM assuming a flat universe ($\Omega_K = 0$), quintessence models without early dark energy ($w_\infty = -1$) in a flat universe, and quintessence models with both early dark energy and nonzero curvature.

For Λ CDM where the dark energy equation of state is fixed to $w = -1$, the evolution of the growth function is very well predicted by current data with a precision better than 2% at all redshifts. These predictions only weaken slightly if spatial curvature is allowed to vary. Generalizing dark energy evolution to include all quintessence models (without early dark energy or curvature) weakens the growth predictions significantly, and including uncertainty in early dark energy and curvature has an even more dramatic effect.

Nevertheless, for each of these model classes the *upper limit* on $G(z)$ is robust; even in the most general class of quintessence models, growth cannot be larger than in the best-fit Λ CDM model by more than $\sim 2\%$. This one-sided expansion of the predictions is due to the quintessence bounds on $w(z)$. Relative to Λ CDM with $w = -1$, $w(z)$ for any quintessence model must be equal or larger, resulting in dark energy density that can only increase with redshift (or remain constant). This asymmetry in quintessence dark energy evolution relative to the cosmological constant leads to asymmetric predictions for $G(z)$ and other observables.^{1,2}

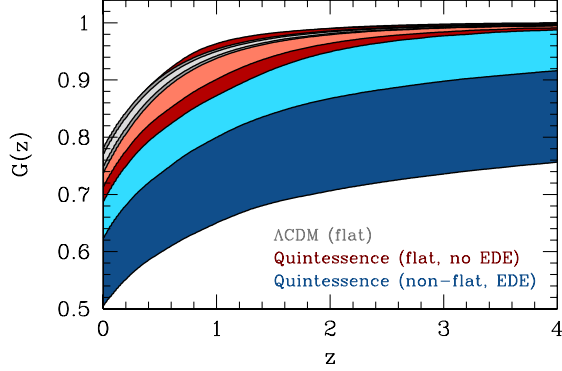


Figure 2: Growth function predictions for three classes of dark energy models: flat Λ CDM (gray, top), flat quintessence without early dark energy (red, middle), and non-flat quintessence with early dark energy (blue, bottom), showing 68% CL (light shading) and 95% CL (dark shading) regions.

Predictions like these provide a way to test general classes of dark energy models by comparing growth predictions from distance measurements to independent measurements of the growth history, e.g. from weak lensing or galaxy cluster surveys. As Fig. 2 shows, measured growth that is far below the Λ CDM prediction could falsify the cosmological constant model and indicate the need for a more complicated dark energy model like quintessence. Measured growth that is much greater than the Λ CDM prediction would rule out not only a cosmological constant but also all quintessence models.

Although strong predictions are best for the purpose of falsifying models, weak predictions that allow a broad range of observables can be useful for constraining model parameters. For example, the ratio $G(z)/G(z=0)$ is strongly correlated with Ω_K in growth predictions from distance measurements for quintessence and even more general models of dark energy, so measurement of this growth ratio is one way to obtain precise constraints on curvature that are independent of dark energy modeling.⁸

Finally, understanding the range of growth histories allowed by distance constraints in the context of GR is important for distinguishing dark energy from modified gravity. Many tests of modified gravity rely on comparing the expected growth for a Λ CDM model to direct growth measurements; however, since dark energy evolution and spatial curvature can also significantly change the growth evolution predicted by precise distance and expansion rate measurements, studying these predictions is a necessary step in obtaining robust tests of GR from combined distance and growth probes.

Acknowledgments

MJM is supported by CCAPP at Ohio State.

References

1. M.J. Mortonson, W. Hu, and D. Huterer, *Phys. Rev. D* **79**, 023004 (2009).
2. M.J. Mortonson, W. Hu, and D. Huterer, *Phys. Rev. D* **81**, 063007 (2010).
3. M. Kowalski, *et al.*, *Astrophys. J.* **686**, 749 (2008).
4. J. Dunkley, *et al.*, *Astrophys. J. Suppl.* **180**, 306 (2009).
5. D.J. Eisenstein, *et al.*, *Astrophys. J.* **633**, 560 (2005).
6. A.G. Riess, *et al.*, *Astrophys. J.* **699**, 539 (2009).
7. M.J. Mortonson, D. Huterer, and W. Hu (2010), arXiv:1004.0236.
8. M.J. Mortonson, *Phys. Rev. D* **80**, 123504 (2009).

THE STRING REVOLVER: HOW ROTATION OF BACKGROUND GALAXIES COULD BE A SMOKING GUN FOR THE EXISTENCE OF COSMIC STRINGS

D.B.THOMAS

Theoretical Physics, Blackett Laboratory, Imperial College, London, England SW7 2AZ

Vector perturbations sourced by topological defects can generate rotations in the lensing of background galaxies. This is a potential smoking gun for the existence of defects since rotation generates a curl-like component in the weak lensing signal that is not generated by standard density perturbations at linear order. Future large scale weak lensing surveys should be able to detect this signal even for string tensions an order of magnitude lower than current constraints. See Phys. Rev. Lett. 103, 181301 (2009) for more detail.

1 Introduction

Weak lensing of background galaxies has earned a place in the growing observational toolkit of the era of precision cosmology. The conventional picture first proposed in ¹ is one where correlations in the weak lensing of photon bundles can be related statistically to the power spectrum of the evolving density field along the line of sight. The correlations can be observed by measuring the shearing of background objects such as galaxies or higher redshift objects such as Ly- α emitters or CMB anisotropies. The statistical effect of the weak lensing is well understood. Scalar perturbations such as density fluctuations generate three independent components of the matrix relating the original source to the distorted image. The first is a trace κ which gives the amplification, or convergence of the image and the second are two shear components, γ_1 and γ_2 , which describe a symmetric, traceless, and divergenceless contribution to the distortion matrix. A fourth independent component ρ , describing rotations, can be added as an anti-symmetric contribution. However, ρ cannot be generated by linear perturbations transforming as scalars under 3d rotations. In fact any rotational, or curl-like, component in the surveys has been used as measure of systematic contamination of the data².

We suggest a source of curl-like distortions at first order in the perturbation amplitude. The source of the signal are vector metric perturbations induced by cosmic strings along the line of sight. The signal induced in cosmic shear surveys by the scalar source of a network of strings is smaller than that due to dark matter density perturbations along the line of sight given current constraints on string tensions $G\mu < 0.7 \times 10^{-6}$ (for the Abelian model³). In contrast, the signal due to vector and tensor perturbations sourced by strings generates rotations which have no counterpart, at the same order of magnitude, from density perturbations. Thus any observations of curl-like lensing signal would provide a candidate detection of cosmic strings.

Here, we focus on the vector mode induced signal which is expected to be an order of magnitude greater than the tensor induced one⁴. We calculate the lensing distortion generated by a generic vector source and then specialise to cosmic strings and calculate the statistical signal due to a network of strings. This is compared with the expected variance of future weak

lensing surveys.

Generalised, vector-type perturbations to the flat Friedmann-Robertson-Walker metric are given by the contributions $g_{0i} = -a^2 V_i$ and $g_{ij} = a^2 (F_{i,j} + F_{j,i})$, with both F_i and V_i are divergenceless vectors and $a(\eta)$ is the scale factor. Two of the four independent modes specified by the two vectors can be fixed by a choice of gauge and $F_i = 0$ is adopted for this calculation. The geodesic equation can then be used to derive the effect of the perturbed metric on the trajectory of photons⁵. The coordinates can be aligned such that $x^i = (x, y, \chi) \equiv \chi(\theta_1, \theta_2, 1)$ where χ is the comoving radial distance with $d\chi/d\eta = 1$ and $\vec{\theta}$ is the vector spanning the plane orthogonal to the line of sight. Using the relation $d\eta/d\lambda = p/a$, where p is the modulus of the photon 3-momentum, a second order differential equation for the transverse projection of the trajectory is obtained

$$\frac{\partial^2(\chi\theta_i)}{\partial\chi^2} = \frac{\dot{V}_i}{a^2} + \frac{V_{\chi,i}}{a^2} - \frac{V_{i,\chi}}{a^2} \quad (1)$$

where $i = 1$ and 2 only. In the small angle approximation the transverse deflection can be derived as a 2×2 jacobian matrix relating the observed source position θ_i to its true position on the transverse source plane θ'_j as $\partial\theta'_i/\partial\theta_j = \delta_{ij} + \psi_{ij}$ such that

$$\psi_{ij} = \int_0^{\chi_\infty} d\chi g(\chi) \left(\frac{\dot{V}_{i,j} + V_{\chi,ij} - V_{i,\chi j}}{a^2} \right) \quad (2)$$

with $g(\chi) \equiv \chi \int_\chi^{\chi_\infty} d\tilde{\chi} (1 - \chi/\tilde{\chi}) W(\tilde{\chi})$ a weighted integral of the normalised source distribution function $W(\chi)$ along the line of sight.

In the case examined here, the metric perturbations V_i are sourced by vector perturbations in the cosmic string stress-energy tensor. These are described in terms of a divergenceless vector contribution to the string momentum ω_i and a divergenceless and traceless contribution to the anisotropic stress Π_i . The sources are coupled to the metric perturbation via the Einstein equations

$$\begin{aligned} V_i &= \frac{16\pi G a^2}{k^2} \omega_i \\ \dot{V}_i &= -\frac{8\pi G a^2 \Pi_i}{k} - \frac{2\dot{a}}{a} \left(\frac{16\pi G a^2}{k^2} \right) \omega_i \end{aligned} \quad (3)$$

where the perturbations have been implicitly expanded in 3d plane waves $\exp(-i\vec{k} \cdot \vec{x})$. V_i and \dot{V}_i can then be eliminated to obtain the distortion tensor ψ_{ij} in terms of the vector sources ω_i and Π_i

$$\psi_{ij} = \frac{2G}{\pi^2} \int_0^{\chi_\infty} d\chi g(\chi) \int_{-\infty}^{\infty} d^3 k e^{i\vec{k} \cdot \vec{x}} \times \hat{k}_j \left(\hat{k}_\chi \omega_i - \hat{k}_i \omega_\chi - 2i \frac{\dot{a}}{a} \frac{\omega_i}{k} - \frac{i}{2} \Pi_i \right) \quad (4)$$

where $\hat{k}_i \equiv k_i/|\vec{k}|$. The convergence, shear, and rotation modes can then be inferred from the distortion tensor using

$$-\psi_{ij} \equiv \begin{pmatrix} \kappa + \gamma_1 & \gamma_2 + \rho \\ \gamma_2 - \rho & \kappa - \gamma_1 \end{pmatrix} \quad (5)$$

2 Vector power spectrum

In the presence of a network of strings the signal must be calculated in terms of power spectra averaged over the sky. In this case the signal is assumed to be generated by a scaling network of cosmic strings with tension μ with the limit $G\mu < 10^{-6}$ set by the allowed contribution to the scalar angular power spectrum of the Cosmic Microwave Background³. In the small angle limit the quantity of interest is the 2d power spectrum of ψ_{ij} , $\langle \psi_{ij}(\vec{l}) \psi_{lm}^*(\vec{l}') \rangle = (2\pi)^2 \delta^2(\vec{l} - \vec{l}') P_{ijlm}^\psi(l)$,

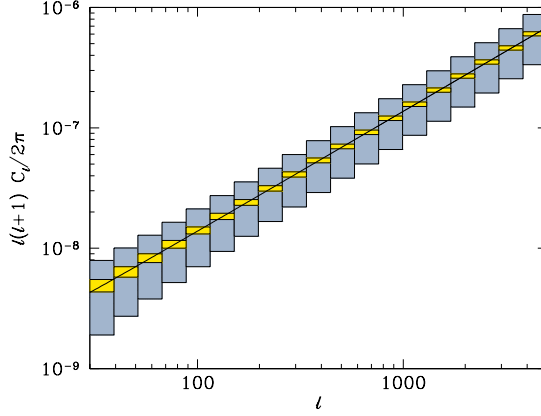


Figure 1: The angular power spectrum of rotation for a network of strings with $G\mu = 1 \times 10^{-7}$. The blue and yellow boxes show the forecasted error for two surveys with $f_{\text{sky}} = 0.1$ and $f_{\text{sky}} = 0.5$ respectively. The errors include both sample and intrinsic ellipticity noise contributions.

where \vec{l} is the 2d fourier transform reciprocal of $\vec{\theta}$. The 2d power spectrum for the rotation is then

$$P_\rho(l) = \int_0^{\chi_\infty} d\chi \frac{g^2(\chi)}{\chi^3} 64\pi^2 G^2 \times \left(\frac{4\dot{a}^2 \chi^2}{a^2 l^2} P_\omega(l) + \frac{P_{\Pi}(l)}{4} + \frac{2\dot{a}\chi}{al} P_{\Pi\omega}(l) \right), \quad (6)$$

where the power spectra for the source terms $P_\omega(l)$, $P_{\Pi}(l)$, and their cross-correlation $P_{\Pi\omega}(l)$ in the small angle limit ($k_\chi \ll l/\chi$) have been introduced.

The source spectra for scaling networks of cosmic strings can be written in terms of structure functions $P_X(k\chi, k\chi')$ which have been measured from numerical simulations^{6,4,7} and computed from semi-analytical models^{8,9}. The unequal time correlators for the source terms are related to the structure functions through scaling laws

$$\langle \omega_i(\vec{k}, \eta) \omega_j^*(\vec{k}', \eta') \rangle = (2\pi)^3 \delta^3(\vec{k} - \vec{k}') P_{ij} \frac{P_\omega(k\chi, k\chi')}{\sqrt{\chi\chi'}}, \quad (7)$$

with projector $P_{ij} = \delta_{ij} - \hat{k}_i \hat{k}_j$ and similar relations for $\langle \Pi\Pi^* \rangle$ and $\langle \Pi\omega^* \rangle$ correlations. For this case, in the small angle limit, only the diagonal of the structure functions is relevant with $P_\omega(k\chi, k\chi') \rightarrow P_\omega(l)$ where $l \approx k\chi$. To determine whether a cosmic string network could potentially be detected, (6) can be computed numerically. For the structure functions, an inverse scaling with l is assumed such that $P_\omega(l) = (G\mu)^2 l^{-1}$ with relative normalisations $\omega : \Pi : \Pi\omega = 1 : 0.25 : 0.1$, from the numerical results of^{10,11,7}. An overall amplitude $(G\mu)^2 = 10^{-14}$ is used throughout.

Fig. 1 shows the power spectrum of the rotation C_ℓ^ρ where in the small angle limit $\ell \approx l$ and $C_\ell^\rho \sim (2\pi)^2 P_\rho(l)$. The integral in (6) is computed assuming a background galaxy distribution as a function of redshift z as $w(z) \sim z^2 \exp(-z/z_0)$ with $z_0 = 0.4$ and taking the maximum redshift to be $z = 6$. Cosmological parameters $\Omega_m = 0.3$, $\Omega_\Lambda = 0.7$ and $h = 0.72$ are used. Expected errors for two surveys covering 10% and 50% of the sky are also shown. The errors include contributions from both sample and intrinsic ellipticity noise variance although the latter dominates the errors at these scales. For both surveys a background galaxy density of 100 galaxies per square arcminute and an average intrinsic ellipticity of 0.3 was assumed.

As shown a distinct weak lensing signal generated by cosmic strings is predicted: rotation with a specific power spectrum. Its intensity is below current sensitivity but provides an ideal target for projected observations. If cosmic string networks exist with $G\mu \sim 10^{-7}$ then the effect should be detectable with the next generation of surveys^{12,13}. Should it not be observed then

the constraints on a string network will become considerably tighter. The only caveat is that at this level we can no longer assume that no curl-like modes are generated by lensing. Separating the corresponding systematics out in these surveys will therefore be more challenging. Yet, the distinct spectral signature of the string signal is likely to provide a simple solution to this problem.

References

1. N. Kaiser. Weak gravitational lensing of distant galaxies. *Astrophys. J.*, 388:272–286, April 1992.
2. H. Hoekstra, Y. Mellier, L. van Waerbeke, E. Semboloni, L. Fu, M. J. Hudson, L. C. Parker, I. Tereno, and K. Benabed. First Cosmic Shear Results from the Canada-France-Hawaii Telescope Wide Synoptic Legacy Survey. *Astrophys. J.*, 647:116–127, August 2006.
3. N. Bevis, M. Hindmarsh, M. Kunz, and J. Urrestilla. Fitting Cosmic Microwave Background Data with Cosmic Strings and Inflation. *Physical Review Letters*, 100(2):021301–+, January 2008.
4. C. Contaldi, M. Hindmarsh, and J. Magueijo. Power Spectra of the Cosmic Microwave Background and Density Fluctuations Seeded by Local Cosmic Strings. *Physical Review Letters*, 82:679–682, January 1999.
5. S. Dodelson. *Modern cosmology*. 2003.
6. B. Allen, R. R. Caldwell, S. Dodelson, L. Knox, E. P. S. Shellard, and A. Stebbins. Cosmic Microwave Background Anisotropy Induced by Cosmic Strings on Angular Scales $>\sim 15'$. *Physical Review Letters*, 79:2624–2627, October 1997.
7. N. Bevis, M. Hindmarsh, M. Kunz, and J. Urrestilla. CMB power spectrum contribution from cosmic strings using field-evolution simulations of the Abelian Higgs model. *Phys. Rev. D*, 75(6):065015–+, March 2007.
8. A. Albrecht, R. A. Battye, and J. Robinson. Detailed study of defect models for cosmic structure formation. *Phys. Rev. D*, 59(2):023508–+, January 1999.
9. L. Pogosian and T. Vachaspati. Cosmic microwave background anisotropy from wiggly strings. *Phys. Rev. D*, 60(8):083504–+, October 1999.
10. C. Contaldi. Theories of Structure Formation in the Early Universe. *PhD Thesis, University of London*, 2000.
11. J. Magueijo and R. Brandenberger. Cosmic defects and cosmology. *Large Scale Structure Formation' (Kluwer, Dordrecht)*., 2000.
12. J. A. Tyson. Large Synoptic Survey Telescope: Overview. In J. A. Tyson and S. Wolff, editors, *Society of Photo-Optical Instrumentation Engineers (SPIE) Conference Series*, volume 4836 of *Society of Photo-Optical Instrumentation Engineers (SPIE) Conference Series*, pages 10–20, December 2002.
13. N. Kaiser. Pan-STARRS: a wide-field optical survey telescope array. In J. M. Oschmann, Jr., editor, *Society of Photo-Optical Instrumentation Engineers (SPIE) Conference Series*, volume 5489 of *Society of Photo-Optical Instrumentation Engineers (SPIE) Conference Series*, pages 11–22, October 2004.

GRAVITATIONAL WAVES FROM COSMOLOGICAL PHASE TRANSITIONS

C. CAPRINI

CEA, IPhT & CNRS, URA 2306, F-91191 Gif-sur-Yvette, France

First order phase transitions in the early universe can give rise to a stochastic background of gravitational waves. A hypothetical first order electroweak phase transition is particularly interesting in this respect, since the signal is in the good frequency range to be detectable by the space interferometer LISA. Three main processes lead to the production of the gravitational wave signal: the collision of the broken phase bubbles, the magnetohydrodynamical turbulence in the plasma stirred by the bubble collisions, and the magnetic fields amplified by the magnetohydrodynamical turbulence. The main features of the gravitational wave spectrum, such as the peak frequency, the amplitude, and the slopes both at low and high wave-number can be predicted by general arguments based on the characteristics of the source: in particular, the structure of its space and time correlation. We find that the gravitational wave signal from a first order phase transition occurring at electroweak symmetry breaking falls into the LISA sensitivity range if the phase transition lasts for about one hundredth of the Hubble time and the energy density of the turbulent motions is about twenty percent of the total energy density in the universe at the phase transition time.

1 Introduction

It is likely that in the years to come the interferometers LIGO ¹ and VIRGO ² will provide the first direct detection of gravitational waves (GWs). Terrestrial interferometers operate in the frequency range 10-1000 Hz, while the space-based interferometer LISA ³ will have its best sensitivity around the milliHertz frequency. A possible target of these experiments is a stochastic background of GWs of cosmological origin. The detection of such a background, relic of the early universe, would have a profound impact both on cosmology and on high energy physics. Once GWs have been emitted, in fact, they propagate freely through the universe, carrying direct information on the physical process that generated them: their detection would therefore provide a new way of probing the primordial universe, and correspondingly physics at very high energies, which would not be accessible otherwise.

One of the processes that can generate such a stochastic background of GWs is a relativistic first order phase transition ⁴. In the course of its adiabatic expansion, the universe might have undergone several phase transitions driven by the temperature decrease. The nature of the phase transitions depends on the particle theory model, but if they are first order they proceed through the nucleation of broken phase bubbles, which is a very violent and inhomogeneous process capable of sourcing GWs. In the following we review the different mechanisms of generation of GWs by a first order phase transition, and show that the characteristic frequency and amplitude of the GW signal are related respectively to the temperature at which the phase transition occurs and to its strength. We also review the analytical method developed in Refs. ^{5,6,7}, which predicts the main features of the GW spectrum starting from a description of the source which we tried to make as simple and as model independent as possible. The GW signal depends explicitly on a

few free parameters: under specific choices for these parameters, it can be potentially interesting for observation with LISA or, more speculatively, advanced LIGO.

2 Gravitational wave background of cosmological origin

In the cosmological context GWs are small perturbations of the FRW metric represented by the transverse-traceless tensor h_{ij} which is first order in cosmological perturbation theory:

$$ds^2 = a^2(t)(dt^2 - (\delta_{ij} + 2h_{ij})dx^i dx^j), \quad h_i^i = h_i^j|_j = 0, \quad (1)$$

where we assume flat spatial sections and t denotes conformal time. Inserting the perturbed metric into Einstein's equations $G_{\mu\nu} = 8\pi G T_{\mu\nu}$ one obtains the evolution equation for the tensor perturbation, which in a radiation dominated universe takes the form

$$\ddot{h}_{ij}(\mathbf{k}, t) + \frac{2}{t}\dot{h}_{ij}(\mathbf{k}, t) + k^2 h_{ij}(\mathbf{k}, t) = 8\pi G a^2 T_{ij}^{(TT)}(\mathbf{k}, t), \quad (2)$$

where $T_{ij}^{(TT)}(\mathbf{k}, t)$ is the transverse-traceless part of the energy momentum tensor sourcing the GWs, *i.e.* the tensor anisotropic stress. A source of GWs operating in the primordial universe is described as a stochastic process, and generates a stochastic background of GWs statistically homogeneous, isotropic, unpolarised and assumed to be gaussian. The energy density of the GWs, normalised by the critical energy density of the universe today ρ_c , is given by the integral over wave-number of the power spectrum

$$\Omega_{\text{GW}} = \frac{\langle \dot{h}_{ij} \dot{h}^{ij} \rangle}{8\pi G \rho_c a^2} = \int \frac{dk}{k} \frac{d\Omega_{\text{GW}}}{d \log k}, \quad \text{where} \quad \frac{d\Omega_{\text{GW}}}{d \log k} = \frac{k^3 |\dot{h}|^2}{2(2\pi)^3 G \rho_c a^2}, \quad (3)$$

$$\text{and} \quad \langle \dot{h}_{ij}(\mathbf{k}, t) \dot{h}_{ij}^*(\mathbf{q}, t) \rangle = (2\pi)^3 \delta(\mathbf{k} - \mathbf{q}) |\dot{h}(k, t)|^2. \quad (4)$$

If we consider a source of GWs operating at a given time t_* while the universe is in a phase of standard FRW expansion (*i.e.* anytime besides inflation), then causality constrains the characteristic frequency of the emitted GWs to be larger than the causal horizon of the universe at the time of generation: $k_* \geq \mathcal{H}_*$, where \mathcal{H}_* denotes the conformal Hubble parameter and k_* is the comoving wave-number. For example, GWs generated at the electroweak phase transition (EWPT) at $T_* \simeq 100$ GeV must have a characteristic frequency $k_* \geq 10^{-5}$ Hz, while the characteristic frequency of GWs generated at the QCD phase transition at $T_* \simeq 100$ MeV can be much lower, $k_* \geq 10^{-8}$ Hz. This estimation, based on the causality argument, shows that GWs generated during the EWPT are potentially interesting for detection with the space interferometer LISA, which operates in the frequency window from 10^{-4} to 1 Hz. On the other hand, GW production at the QCDPT can fall into the frequency range of detection with pulsar timing array⁸. We now proceed to analyse which kind of processes can act as sources of GWs during a relativistic phase transition occurring in the early universe.

3 Gravitational waves from phase transitions

There are a variety of processes related to primordial phase transitions that can lead to the production of GWs, as for example cosmic strings⁹ or scalar field relaxation¹⁰. Here we concentrate specifically on the processes driven by bubble nucleation during a first order phase transition⁴. The EWPT in the standard model is a crossover, and it is not expected to lead to any appreciable cosmological signal; however, deviations from the standard model in the Higgs sector or introducing supersymmetry can lead to a first order EWPT¹¹. Similarly, the QCDPT which is also predicted to be a crossover by lattice simulations¹², can become first order if the neutrino

chemical potential is sufficiently large¹³. GWs detection would help to probe the nature of these phase transitions, and provide interesting information on the underlying particle theory.

A first order phase transition proceeds through the nucleation of true-vacuum bubbles, which in the end of the transition collide and convert the entire universe to the broken phase. The collisions break the spherical symmetry of the bubble walls, generating a non-zero anisotropic stress which acts as a source of GWs. Moreover, bubble collision causes an injection of energy in the primordial plasma, which has a very high Reynolds number (of the order of 10^{13} at 100 GeV and at the typical scale of the bubbles⁷): the energy injection leads to the formation of magnetohydrodynamic (MHD) turbulence in the fluid, which also sources GWs through the anisotropic stresses of the chaotic fluid motions. MHD turbulence also leads to the amplification of small magnetic fields generated by charge separation at the bubble wall, which have non-zero anisotropic stress and act as an independent source of GWs.

There are in summary three processes which can lead to the production of GWs towards the end of a first order phase transition. They are all related to the collision of bubbles, which involves two quantities: the duration of the phase transition, commonly denoted by the parameter β^{-1} , and the typical size of the bubbles at the moment of collision, $R_* \simeq v_b \beta^{-1}$, where v_b is the bubble wall velocity. The characteristic frequency of the GWs generated by the three processes can correspond either to the duration of the phase transition or to the bubble size: $k_* \simeq \beta$, R_*^{-1} , depending on the details of the time evolution of the source (*cf.* section 4). Assuming for the moment $k_* \simeq \beta$, one obtains the following order of magnitude estimate of the characteristic frequency in Hz:

$$k_* \simeq 10^{-2} \frac{\beta}{\mathcal{H}_*} \frac{T_*}{100 \text{ GeV}} \text{ mHz}. \quad (5)$$

The parameter β/\mathcal{H}_* represents the ratio of the duration of the phase transition with respect to the Hubble time. Since the entire universe must be converted to the broken phase, the phase transition must complete faster than Hubble time: a typical value for the EWPT is $\beta/\mathcal{H}_* \simeq 100$ ¹⁴. From Eq. (5) one gets that the characteristic frequency of GWs emitted at the EWPT is of the order of the milliHertz, and falls in the frequency range of the space interferometer LISA, which covers the frequency region $10^{-4} \text{ Hz} \leq k \leq 1 \text{ Hz}$. LISA reaches its best sensitivity precisely around a milliHertz, where it can detect GWs with amplitude corresponding to $\Omega_{\text{GW}} \simeq 10^{-12}$.

Starting from the perturbed Einstein equations $\delta G_{\mu\nu} = 8\pi G \delta T_{\mu\nu}$, one can give a simple order of magnitude estimate of the GW amplitude, which shows how the result depends on the duration and the energy density of the GW source. Since we are merely interested in determining the scaling of the GW amplitude, we rewrite Einstein equations simply as $\beta^2 h \sim 8\pi G T$, where h denotes the amplitude of the tensor perturbation, T the energy momentum tensor, and we inserted $1/\beta$ as the characteristic time on which the perturbation is evolving (we have dropped indices for simplicity). This suggests that $\dot{h} \sim 8\pi G T/\beta$, and the GW energy density becomes then $\rho_{\text{GW}} \sim \dot{h}^2/(8\pi G) \sim 8\pi G T^2/\beta^2$. For the three processes under analysis here, the energy momentum tensor of the GW source can be rewritten in all generality as $T/\rho_* \sim \Omega_s^*$, where ρ_* denotes the energy density in the universe at the GW generation time, and the parameter Ω_s^* denotes the relative energy density available in the source for the GW generation. We can now rearrange the equation for ρ_{GW} accounting for the fact that the phase transition takes place in the radiation-dominated universe, that the GW energy density also evolves like radiation, and inserting Friedmann equation $3\mathcal{H}_* = 8\pi G \rho_*$. It becomes then

$$\Omega_{\text{GW}} \sim \Omega_{\text{rad}} \left(\frac{\mathcal{H}_*}{\beta} \right)^2 (\Omega_s^*)^2, \quad (6)$$

where Ω_{rad} denotes the radiation energy density parameter today. The above equation shows that the GW energy density scales like the square of the ratio of the GW source duration and the Hubble time, and the square of the energy density in the source. Using $h^2 \Omega_{\text{rad}} = 4.2 \cdot 10^{-5}$

and $\mathcal{H}_*/\beta \simeq 0.01$, it turns out that a GW source with relative energy density of the order of $\Omega_s^* \sim 0.1$ could generate a GW signal above the lowest sensitivity of the space interferometer LISA. A detectable signal can therefore arise only from very energetic processes, which must involve at least 10% of the total energy density in the universe: namely, the phase transition must be strongly first order.

4 The gravitational wave power spectrum

Having demonstrated that GWs generated by a first order phase transition have a characteristic frequency and amplitude which can be interesting for detection, we now proceed to evaluate the main features of the GW power spectrum. The aim of this section is to show how the form of the power spectrum depends on the characteristics of the stochastic source, in particular the structure of its spatial and temporal correlation. It is based on the work done in Refs.^{5,6,7}.

As derived in⁷, Eq. (2) can be solved in the radiation era (neglecting changes in the number of effective relativistic degrees of freedom), and once combined with definitions (3) and (4) it leads to the following formula for the GW power spectrum today :

$$\frac{d\Omega_{\text{GW}}}{d \log k} = \frac{4\Omega_{\text{rad}}}{3\pi^2} k^3 \int_{t_{\text{in}}}^{t_{\text{fin}}} \frac{dt_1}{t_1} \int_{t_{\text{in}}}^{t_{\text{fin}}} \frac{dt_2}{t_2} \cos[k(t_2 - t_1)] \Pi(k, t_1, t_2), \quad (7)$$

where $\Pi(k, t_1, t_2)$ is the unequal time power spectrum of the source anisotropic stress,

$$\langle \Pi_{ij}(\mathbf{k}, t_1) \Pi_{ij}^*(\mathbf{q}, t_2) \rangle = (2\pi)^3 \delta(\mathbf{k} - \mathbf{q}) \Pi(k, t_1, t_2), \quad (8)$$

and we denote Π_{ij} the dimensionless anisotropic stress: $T_{ij}^{(TT)} = (\rho + p) \Pi_{ij}$ (ρ and p are the energy density and pressure of the primordial relativistic fluid, *cf.* Eq. (2) and Ref.⁷). The part of the energy momentum tensor which contributes to the tensor anisotropic stress is the spatial and off-diagonal one. In the bubble collisions case it is given by $T_{ij} = (\rho + p) v_i v_j / (1 - v^2)$, where v_i is the velocity of the relativistic fluid at the bubble wall position⁵. In the case of MHD turbulence, the energy momentum tensor can be decomposed into a part representing the turbulent velocity field and a part representing the magnetic field (for details, see⁷). The turbulent velocity field part takes the form $T_{ij} = (\rho + p) v_i v_j$ (where we omit the gamma factor since we assume non-relativistic velocities), and the magnetic field one takes the form $T_{ij} = B_i B_j / (4\pi)$. We see that for all the three GW generation processes the tensor anisotropic stress is radiation-like, since the phase transition takes place in the radiation dominated universe. The parameter Ω_s^* introduced in section 3 is therefore given simply by $\Omega_s^* \sim \langle v^2 \rangle$ in the case of the turbulence and $\Omega_s^* \sim \langle b^2 \rangle$ in the case of the MHD processed magnetic field, where $b_i = B_i / \sqrt{\rho_{\text{rad}}}$ is the dimensionless magnetic field parameter⁷. In the bubble case, the definition of Ω_s^* is a bit more involved, depending on whether the phase transition happens in a thermal bath or in vacuum: it is anyway related to the ratio of the kinetic energy density due to the bubble wall motions and the total energy density in the universe⁶.

Eq. (7) shows that the GW power spectrum is given by the double integral of the Green function of Eq. (2) multiplied by the unequal time anisotropic stress power spectrum, and its general shape as a function of wave-number k depends on the interplay among these two quantities. In particular, the spatial and temporal correlation of the source, together with its overall time evolution, determine the k and time dependence of the anisotropic stress power spectrum both at equal and unequal time, and in turns the GW spectrum. Much of the analytical work of Refs.^{5,6,7} has dealt with the problem of modeling the statistical source for bubble collisions and MHD turbulence, and here we summarise the results obtained there.

First of all, the k -dependence of the equal time power spectrum $\Pi(k, t_1, t_1)$ is relatively easy to determine, following mainly from a causality argument. The bubble collisions and subsequent

MHD turbulence are causal processes, characterised by a typical length-scale: the size of the bubbles at the moment of collision R_* , which also corresponds to the scale of energy injection in the primordial fluid generating the MHD turbulence. On scales larger than R_* , the anisotropic stresses are not correlated and we expect the power spectrum to be flat, up to the wave-number corresponding to the inverse characteristic scale R_*^{-1} . Beyond $k \simeq R_*^{-1}$, the power spectrum decays with a slope that depends on the details of the source, and turns out to be k^{-4} for bubble collisions⁵, and $k^{-11/3}$ for MHD turbulence⁷. The spatial correlation structure of the source completely determines the k -dependence of $\Pi(k, t_1, t_1)$, shown in Fig. 1 for the MHD turbulence case.

Concerning the time dependence of $\Pi(k, t_1, t_1)$, it is due to the overall evolution of the GW source in time. In the case of bubble collisions, the source turns off right at the end of the phase transition, and lasts therefore for much less than one Hubble time. The overall time dependence of the source in this case comes mainly from the bubble expansion⁶. In the case of MHD turbulence on the other hand, the dissipation of the turbulent motions in the primordial fluid is not very efficient due to the extremely low viscosity of the fluid itself⁷. MHD turbulence is therefore maintained in the primordial fluid for several Hubble times, and the overall time dependence of the source depends both on the slow decay of the turbulent motions and on the growth of the turbulence characteristic scale associated with the decay. The influence of the total duration of the source on the shape of the GW spectrum shows up mainly at very large scales: if the source lasts several Hubble times, the GW signal is amplified on scales larger than the Hubble scale at the phase transition time $k < \mathcal{H}_*$ ⁷.

Moreover, in order to find the GW spectrum one needs to know the unequal time power spectrum of the anisotropic stress, as given in Eq. (7). This is much less obvious to determine, but one can identify a few simple models which are easy to deal with analytically and represent the main properties of the source. These have been discussed in^{5,6,7}, and in what follows we present the main results. In the bubble collision case, the source can be modeled as *completely coherent*, meaning that its time dependence is deterministic. In this case, the unequal time anisotropic stress power spectrum can be decomposed in terms of the equal time one as

$$\Pi(k, t_1, t_2) = \sqrt{\Pi(k, t_1, t_1)} \sqrt{\Pi(k, t_2, t_2)}. \quad (9)$$

This is a consequence of two main facts: first of all, the signal comes from the individual collision events, and each collision event can be assumed to be uncorrelated in time with the others; second, each collision event can also be assumed to be coherent, since the time evolution of the anisotropic stress related to the collisions is deterministic (it is basically only due to the growth in time of the bubbles⁶). In the case of MHD turbulence, the situation is different. The turbulence can be viewed as a superposition of eddies of different size, each with its proper turnover time related to the eddy size. In the Kraichnan model¹⁵, the eddy turnover time is the typical decorrelation time of turbulent motions. Therefore, the source has a finite decorrelation time which depends on the eddy size: this can be modeled with a *top-hat decorrelation*:

$$\Pi(k, t_1, t_2) = \{ \Pi(k, t_1, t_1) \Theta[t_2 - t_1] \Theta[1 - k(t_2 - t_1)] + t_1 \leftrightarrow t_2 \}, \quad (10)$$

meaning that the source is correlated for time differences larger than about one wavelength $|t_1 - t_2| < k^{-1}$ ⁷.

The behaviour of the anisotropic stress unequal time power spectrum strongly influences the GW spectrum, and in particular the position of the peak. For a coherent source, the GW spectrum becomes the square of the temporal Fourier transform of the source, as can be seen by inserting Eq. (9) into (7)⁶. The source is characterised by the spatial correlation scale R_* and the temporal correlation scale β^{-1} , related by $R_* = v_b \beta^{-1}$. Since $v_b \leq 1$, one has $R_* < \beta^{-1}$. On scales larger than both the characteristic spatial correlation scale R_* and temporal correlation

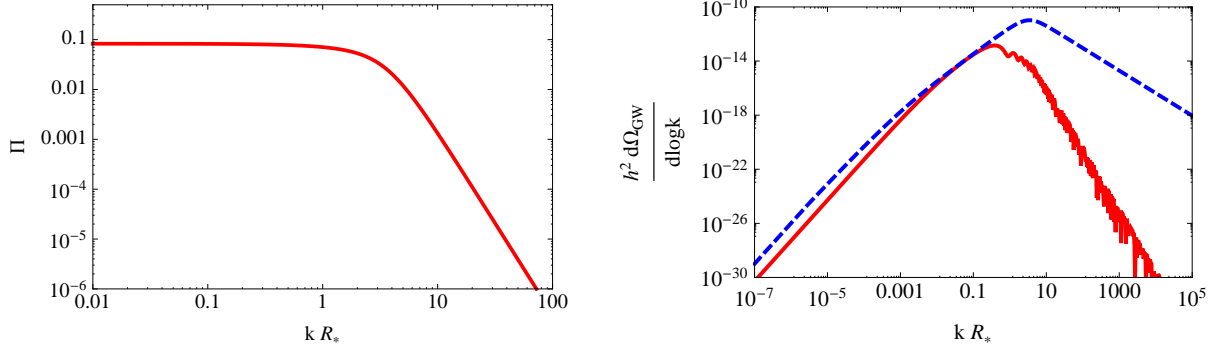


Figure 1: Left panel: the anisotropic stress power spectrum at equal time as a function of the dimensionless variable $k R_*$ for the MHD turbulence. On scales larger than the characteristic scale R_* the spectrum is flat since the source is uncorrelated, while on scales smaller than R_* the spectrum decays as $k^{-11/3}$ (we assumed Kolmogorov turbulence). Right panel: the qualitative behaviour of the GW spectrum from the MHD turbulent source modeled as completely coherent (red, solid line) and as top-hat decorrelation (blue, dashed line). The peak position corresponds to the characteristic time-scale of the source $k_* \simeq \beta$ for the coherent case, and to the characteristic length-scale $k_* \simeq 1/R_*$ for the top-hat decorrelation case. The low frequency increase is k^3 by causality, and the high frequency slope depends both on the time decorrelation assumption and on the k -dependence of the source power spectrum (left panel).

scale β^{-1} , the space and time Fourier transforms of the source are constant because the source is not correlated (white noise). Therefore, for wave-numbers $k < \beta < 1/R_*$, the GW spectrum simply increases as k^3 (cf. Eq. (7)). However, for $k > \beta$ the time Fourier transform is no longer constant and starts to decay as a power law, the exponent depending on the time differentiability properties of the source⁶. In the bubble collision case, it turns out that this implies a k^{-1} decay for the GW spectrum at intermediate scales $\beta < k < 1/R_*$: the peak of the GW spectrum corresponds therefore to the characteristic time of the source, $k_* \simeq \beta^6$. For a source with finite decorrelation time as in Eq. (10), on the other hand, the GW spectrum is no longer related to the temporal Fourier transform of the source, and the situation changes. The spectrum still increases as k^3 on large scales, but the characteristic time of the source β^{-1} does not lead to any feature in the spectrum, which peaks instead at the inverse characteristic scale of the source $k_* \simeq R_*^{-1}$. The qualitative shape of the GW spectra coming from a coherent source and a top-hat decorrelating one is shown in Fig. 1.

5 Results

Fig. 2 shows the GW spectra generated by bubble collisions and MHD turbulence, as derived in Refs.^{5,6,7}. The parameter representing the duration of the phase transition is set to $\mathcal{H}_*/\beta = 0.01$, and the parameter representing the relative energy density available in the source for the GW generation is set to $\Omega_s^* = 0.2$ in both cases (cf. Eq. 6). This high value of Ω_s^* implies a strongly first order phase transition, for which the vacuum energy density is about one third of the radiation one $\alpha = 1/3$, and the bubble wall speed is close to the speed of light, $v_b = 0.87$. Correspondingly, the mean velocity of the turbulent motions must be of the order of the speed of sound, $\langle v^2 \rangle = 1/3$, and equipartition is assumed among the kinetic and the magnetic energies in the turbulence such that $\langle b^2 \rangle \simeq \langle v^2 \rangle$.

In the two GW spectra of Fig. 2 we can distinguish the features presented in the previous sections. Both spectra rise as k^3 for small wave-numbers: this is simply the phase space volume (cf. Eq. (7)) combined with the k -dependence of the anisotropic stress power spectrum, which is flat at small wave-numbers because of causality. In the GW spectrum generated by bubble collisions the k^3 slope is maintained up to the peak, while in the one generated by MHD tur-

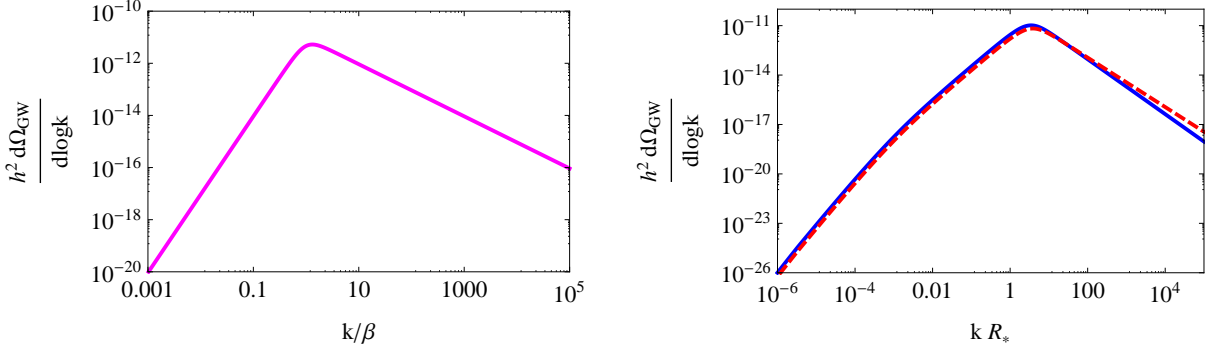


Figure 2: Left panel: the GW power spectrum generated by bubble collisions as a function of the dimensionless variable k/β . The spectrum increases as k^3 at low frequency, peaks at $k_* \simeq \beta$ since the source is coherent, and decreases at high frequency as k^{-1} , due both to the fact that the source is coherent and to the thin wall approximation. Right panel: the GW power spectrum generated by MHD turbulence as a function of kR_* : blue, solid by the turbulent velocity field and red, dashed by the magnetic field. The spectra increase as k^3 at low frequency, turn to a k^2 increase at subhorizon scales $k > \mathcal{H}_*$ because the source lasts for several Hubble times, and peak at a frequency corresponding to the characteristic scale of the source $k_* \simeq 2\pi/R_*$ due to the top-hat decorrelation holding in the case of MHD turbulence. At high frequency, the spectra decay as $k^{-5/3}$ for the kinetic turbulence (Kolmogorov spectrum for the source) and as $k^{-3/2}$ for the magnetic field (Iroshnikov-Kraichnan spectrum for the source). The duration of the phase transition and the energy density of the sources are given the values $\mathcal{H}_*/\beta = 0.01$ and $\Omega_s^* = 0.2$.

bulence the slope changes to k^2 at sub-horizon scales $k > \mathcal{H}_*$: this difference is due to the fact that bubble collisions are a short lasting source, while MHD turbulence acts a source of GWs for several Hubble times⁷. The GW spectrum due to bubble collisions peaks at a wave-number corresponding to the duration of the source $k_* \simeq \beta$, since the source is modeled as completely coherent in its time decorrelation; while the GW spectrum due to MHD turbulence peaks at a wave-number corresponding to the characteristic length-scale of the source, given by the bubble size at the end of the phase transition: $k_* \simeq 2\pi/R_*$, since the source is modeled following the top-hat Ansatz and has a finite decorrelation time corresponding to the eddy turnover time⁷. At frequencies smaller than the peak, the GW spectrum from bubble collisions decays as k^{-1} : this decay is related both to the fact that the source is coherent and to the thin wall approximation, which has been inserted in the analytical analysis to recover the result of numerical simulations^{16,6}. The GW spectrum from MHD turbulence decays at high frequencies with slopes that also depend both on the top-hat decorrelation structure and on the source power spectrum: they turn out to be $k^{-5/3}$ for the kinetic turbulence (coming directly from the assumption of a Kolmogorov spectrum) and $k^{-3/2}$ for the magnetic field (due to the assumption of an Iroshnikov-Kraichnan spectrum)⁷.

Fig. 3 shows the final GW power spectrum given by the sum of the bubble collisions signal and the MHD turbulence signal for the EWPT at $T_* \simeq 100$ GeV. The parameters are again $\mathcal{H}_*/\beta = 0.01$ and $\Omega_s^* = 0.2$, so that the phase transition is assumed to be strongly first order. The signal is compared with the sensitivity curves of LISA and BBO: for a strongly first order EWPT the signal falls into the sensitivity range of LISA. Clearly this can only be achieved in the context of theories that go beyond the standard model of particle physics. Fig. 3 also shows an even more speculative case of a phase transition occurring at temperature $T_* = 5 \cdot 10^6$ GeV, with $\mathcal{H}_*/\beta = 0.02$ and $\Omega_s^* = 0.2$: in this case, the signal could be interesting for advanced LIGO.

References

1. URL <http://www.ligo.caltech.edu/>
2. URL <http://www.virgo.infn.it/>

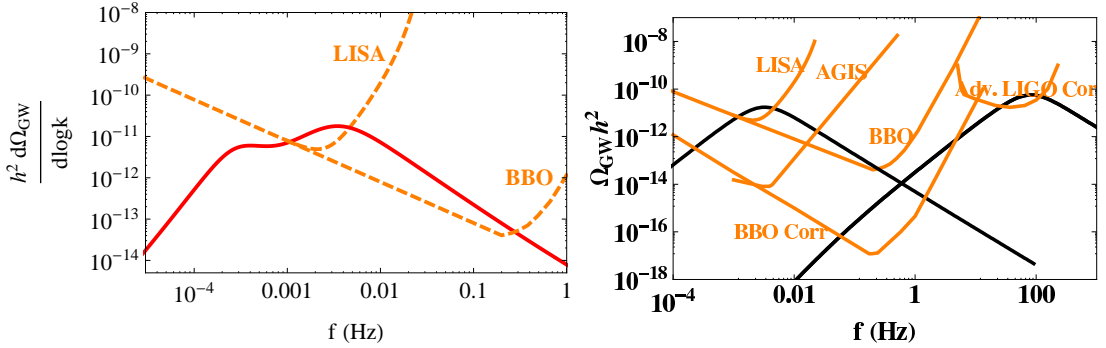


Figure 3: Left panel: the total GW spectrum for bubble collisions and MHD turbulence generated at a strongly first order EWPT as a function of frequency in Hz. The duration of the phase transition and the energy density of the sources are given the values $\mathcal{H}_*/\beta = 0.01$ and $\Omega_s^* = 0.2$, and the signal falls into the sensitivity range of the space interferometer LISA. Right panel: the total GW spectrum from MHD turbulence only, generated at a strongly first order EWPT (left black curve) and at a hypothetical first order phase transition at temperature $T_* = 5 \cdot 10^6$ GeV. The parameters are $\mathcal{H}_*/\beta = 0.01$ and $\Omega_s^* = 0.2$ for the EWPT and $\mathcal{H}_*/\beta = 0.02$ and $\Omega_s^* = 0.2$ for the PT at $T_* = 5 \cdot 10^6$ GeV. Figure from⁷.

3. URL <http://lisa.jpl.nasa.gov/>
4. For a review, see M. Maggiore, *Phys. Rept.* **331**, 283 (2000) and references therein.
5. C. Caprini *et al*, *Phys. Rev. D* **77**, 124015 (2008).
6. C. Caprini *et al*, *Phys. Rev. D* **79**, 083519 (2009).
7. C. Caprini *et al*, *JCAP* **0912** 024 (2009)
8. G. Hobbs *et al*, *Class. Quantum Grav.* **27**, 084013 (2010)
9. See LIGO Scientific Collaboration: B. Abbott *et al*, *Phys. Rev. D* **80**, 062002 (2009) and references therein
10. L.M. Krauss, *Phys. Lett. B* **284**, 229 (1992); E. Fenu *et al*, *JCAP* **10**, 005 (2009)
11. See for example C. Grojean *et al*, *Phys. Rev. D* **71**, 036001 (2005); S. J. Huber and T. Konstandin, *JCAP* **0805**, 017 (2008)
12. See for example Y. Aoki *et al*, *JHEP* **0906** 088 (2009)
13. D. J. Schwarz and M. Stuke, *JCAP* **11**, 025 (2009)
14. M. S. Turner *et al*, *Phys. Rev. D* **46**, 2384 (1992); A. Kosowsky and M. S. Turner, *Phys. Rev. D* **47**, 4372 (1993)
15. R.H. Kraichnan, *Phys. Fluid* **7**, 1163 (1964)
16. S. J. Huber and T. Konstandin, *JCAP* **0809**, 022 (2008)

F-TERM UPLIFTED RACETRACK INFLATION

MARCIN BADZIAK

*Institute of Theoretical Physics, University of Warsaw
ul. Hoża 69, PL-00-681 Warsaw, Poland*

It is shown that two classes of racetrack inflation models, saddle point and inflection point ones, can be constructed in a fully supersymmetric framework with the matter field F -term as a source of supersymmetry (SUSY) breaking and uplifting. Two models of F -term SUSY breaking are considered: the Polonyi model and the quantum corrected O’Raifeartaigh model. In the former case, both classes of racetrack inflation models differ significantly from the corresponding models with non-SUSY uplifting. The main difference is a quite strong dominance of the inflaton by the matter field. In addition, fine-tuning of the parameters is relaxed as compared to the original racetrack models. In the case of the racetrack inflation models coupled to the O’Raifeartaigh model, the matter field is approximately decoupled from the inflationary dynamics.

1 Introduction

Recent progress in moduli stabilization, due to the proposal of the KKLT mechanism¹, allowed for constructing viable inflationary models within the string theory. Particularly interesting are those in which the volume modulus drives inflation. In this kind of models, called racetrack inflation, superpotential consists of two non-perturbative terms (originating e.g. from the gaugino condensation in the hidden sector) and a constant contribution from fluxes:

$$W = W_0 + Ce^{-cT} + De^{-dT}, \quad (1)$$

With the use of the above superpotential and the tree-level Kähler potential,

$$K = -3 \ln(T + \bar{T}), \quad (2)$$

two different inflationary scenarios have been realized. In the first of them, inflation takes place in the vicinity of a saddle point of the potential with the axion τ , associated with the volume modulus, being the inflaton². In the second scenario, the real part of the volume modulus t is the inflaton and inflation takes place in the vicinity of an inflection point of the potential³. The crucial element of both scenarios is the uplifting term $\Delta V = \frac{E}{t^2}$, originating from the $\overline{D3}$ -branes, which is added to the potential in order to break SUSY and cancel cosmological constant in the post-inflationary vacuum. However, in the effective field theoretical description the $\overline{D3}$ -branes break SUSY explicitly. This is the main drawback of the KKLT stabilization on which racetrack inflation models are based. In these proceedings we show that both racetrack inflation models can be constructed in a fully supersymmetric framework with the matter field F -term as a source of uplifting and SUSY breaking.

It is known that the moduli stabilization at a Minkowski (or dS) minimum can be achieved using F -term uplifting⁴. Nevertheless, successful F -term uplifting of inflationary models does

not have to be straightforward. The moduli stabilization is a local problem in a sense that the only issue which matters is the stability of the potential at a Minkowski (or dS) stationary point. On the other hand, the problem of constructing an inflationary model involves also the global structure of the potential. The reason is that the Minkowski vacuum and the inflationary region are in separate domains of the field space. A priori one cannot be sure that there always exists a trajectory connecting these two regions. It is especially not obvious that such a trajectory exists when one increases the dimensionality of the field space by introducing a matter field. Therefore, it is encouraging that racetrack inflation models can be successfully realized with uplifting from the matter field F -term.

2 Conditions for Kähler potential

It was pointed out in⁵ that the role of uplifting in racetrack inflation models is two-fold. Besides the cancelation of the cosmological constant, uplifting is also crucial for the stability of the vacuum and for fulfilling slow-roll conditions. We explain this point below. The necessary condition for the stable dS vacuum and/or slow-roll inflation depends on the Kähler potential in the following way^{5,6}:

$$R(f^i) < \frac{2}{\hat{G}^2}, \quad (3)$$

where $R(f^i) \equiv R_{i\bar{j}p\bar{q}} f^i f^{\bar{j}} f^p f^{\bar{q}}$ is the sectional curvature of the Kähler manifold (defined by the metric given by the second derivative of the Kähler potential $K_{i\bar{j}}$) along the direction of SUSY breaking and $f_i \equiv G_i/\hat{G}$ is the unit vector defining that direction. We also introduced the quantity $\hat{G} \equiv \sqrt{G^i G_i}$ related in a simple way to the value of the potential: $\hat{G}^2 = 3 + e^{-G} V$. For the tree-level Kähler potential (2) the scalar curvature $R_T \equiv R_{T\bar{T}T\bar{T}} f^T f^{\bar{T}} f^T f^{\bar{T}} = 2/3$ and the necessary condition (3) is violated for non-negative values of the potential. Nevertheless, racetrack inflation models can be realized because the uplifting term is non-supersymmetric so after adding it to the potential the necessary condition (3) is no longer valid.

However, our goal is to construct racetrack inflation models in which SUSY is broken spontaneously by the matter field F -term and without invoking explicitly SUSY breaking terms. This cannot be achieved if the no-scale Kähler potential $K = -3 \ln(T + \bar{T} - |\Phi|^2)$ is used because in such a case $R(f^i) = 2/3$ ⁷ and the necessary condition (3) is violated. This fact motivates us to study Kähler potentials of the form: $K = K^{(T)}(T, \bar{T}) + K^{(\Phi)}(\Phi, \bar{\Phi})$. In such a case the necessary condition (3) reduces to:

$$R_T \Theta_T^4 + R_\Phi \Theta_\Phi^4 < \frac{2}{\hat{G}^2}, \quad (4)$$

where R_i are the scalar curvatures of the one dimensional submanifolds associated with each of the fields and $\Theta_i^2 \equiv G_{i\bar{i}} f^i f^{\bar{i}}$ (no summation over i or \bar{i}) are the spherical coordinates parameterizing SUSY breaking. They satisfy the condition $\Theta_T^2 + \Theta_\Phi^2 = 1$. For the canonically normalized matter field (i.e. with $K^{(\Phi)} = \Phi \bar{\Phi}$), the scalar curvature R_Φ vanishes. Therefore, if the canonically normalized matter field dominates SUSY breaking during inflation (i.e. $\Theta_T^2 \ll 1$) then the condition (4) is satisfied and slow-roll inflation is possible.

3 Racetrack inflation with Polonyi uplifting

Consider a racetrack model coupled to the canonically normalized matter field as follows:

$$W = W_0 + C e^{-cT} + D e^{-dT} - \mu^2 \Phi, \quad K = -3 \ln(T + \bar{T}) + \Phi \bar{\Phi}. \quad (5)$$

The matter field part of the above model corresponds to the well-known Polonyi model of SUSY breaking. The cancelation of the cosmological constant is due to the fine-tuning of the

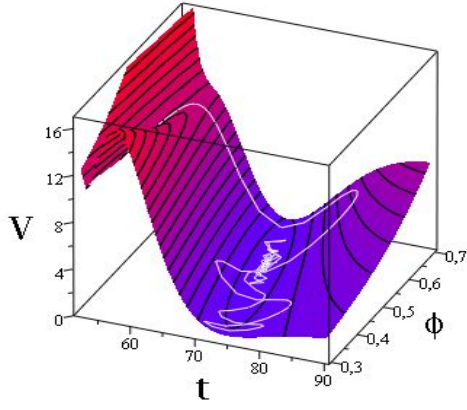


Figure 1: The potential for the inflection point model coupled to the Polonyi sector for $\tau = \theta = 0$. The white curve represents the field trajectory.

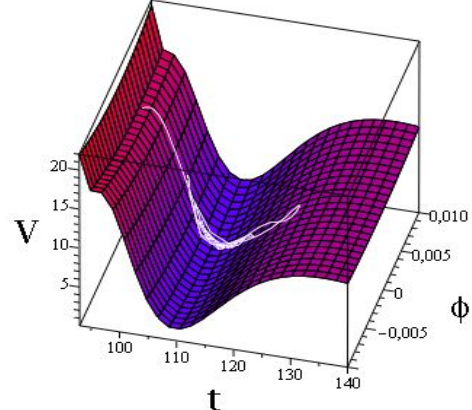


Figure 2: The potential for the inflection point model coupled to an effective O'Raifeartaigh model for $\tau = \theta = 0$. The white curve represents the field trajectory.

parameter μ . We found that in the above simple setup both racetrack inflation models can be successfully realized. However, racetrack inflation with Polonyi uplifting is significantly different from original racetrack models^{2,3} with non-SUSY uplifting.

Let us focus first on the inflection point model. Potential and the trajectory of the inflaton for this model is shown in figure 1. It can be seen that the real part of the matter field ϕ dominates inflation so the volume modulus is no longer the inflaton. SUSY breaking during inflation is strongly dominated by the matter field F -term. In consequence, $R(f^i) \approx 0$ and the necessary condition for slow-roll inflation (3) is easily satisfied.

In the original racetrack inflection point inflation³ fine-tuning of parameters, required for obtaining more than 60 e-folds of inflation, is related to the height of the barrier which prevents the inflaton t from running away to infinity after inflation⁸. Avoiding the overshooting problem requires fine-tuning of one parameter (e.g. W_0) at the level of 10^{-8} . In the inflection point model with Polonyi uplifting this problem is less severe and the fine-tuning of W_0 at the level of 10^{-3} is enough to obtain 60 e-folds of inflation ending in the Minkowski minimum.

Saddle point racetrack inflation with Polonyi uplifting also significantly differs from the original model² with non-SUSY uplifting. In the present case the imaginary part of the matter field θ is the main component of the inflaton. Fine-tuning of parameters is of order 10^{-3} so it is slightly weaker than in the original model² in which fine-tuning is at the level of 10^{-4} .

4 Racetrack inflation with O'uplifting

Let us now consider the following generalization of the previous model:

$$W = W_0 + Ce^{-cT} + De^{-dT} - \mu^2\Phi, \quad K = -3\ln(T + \bar{T}) + \Phi\bar{\Phi} - \frac{(\Phi\bar{\Phi})^2}{\Lambda^2}. \quad (6)$$

The model with Polonyi uplifting is recovered in the limit $\Lambda \rightarrow \infty$. The matter field sector of the above model can be treated as an effective quantum corrected O'Raifeartaigh model with the superpotential $W^{(O')} = mXY + \lambda\Phi X^2 - \mu^2\Phi$ in which the heavy fields X and Y have been integrated out⁹. The parameter Λ corresponds to the mass scale of the fields that have been integrated out so a natural value of Λ is much smaller than one (in Planck units). The parameter μ is, again, adjusted in such a way that the cosmological constant at the post-inflationary vacuum (almost) vanishes. The value of the real part of the matter field during inflation, as well as at

the Minkowski minimum, is $\phi \sim \mathcal{O}(\Lambda^2)$. So, in the region important for inflation the following hierarchy is present: $\phi \ll \Lambda \ll 1$. One can show that in the limit $\phi \ll \Lambda \ll 1$ the mass matrix is nearly diagonal and the matter field is heavier than the volume modulus. In consequence, the matter field is approximately decoupled from the inflationary dynamics.

Both racetrack inflation models resemble original ones^{2,3} with non-SUSY uplifting. As an example illustrating this fact we present the plot for the inflection point model in figure 2. It can be seen that the volume modulus t plays the role of the inflaton (as in the original model³) while the matter field is almost frozen during inflation. Another similarity to the original model is that the fine-tuning of parameters is related to the height of the barrier which separates the Minkowski vacuum from the runaway region. It is worth to note that in the inflection point model with O'uplifting (or with uplifting from $\overline{D3}$ -brane) it is possible to arrange inflation with arbitrary low scale. However, this would require extremely large values of parameters C and D . The saddle point model with O'uplifting is also similar to the corresponding one with non-SUSY uplifting. In particular, axion τ dominates inflation and fine-tuning of W_0 is of order 10^{-4} .

5 Conclusions

In these proceedings we have shown that both racetrack inflation models^{2,3} can be constructed in a fully supersymmetric framework with the matter field F -term being a source of uplifting and SUSY breaking. The details of inflationary scenarios depend on the choice of the matter field sector. If the Polonyi model is chosen for the uplifting sector, the real (imaginary) part of the matter field dominates the inflection (saddle) point racetrack inflation. With this kind of uplifting the fine-tuning of parameters is significantly weaker than in models with non-SUSY uplifting (especially in the inflection point model). On the other hand, if the O'Raifeartaigh model is responsible for uplifting, the matter field is decoupled from the inflationary dynamics and racetrack inflation models are similar to the original ones but with one important difference: SUSY is now broken spontaneously. In these models, the volume modulus is the inflaton even though SUSY breaking is dominated by the matter field F -term. More detailed analysis of models presented here can be found in¹⁰.

Acknowledgments

M.B. would like to thank M. Olechowski for many fruitful discussions and collaboration. M.B. was partially supported by the EC 6th Framework Project MRTN-CT-2006-035863 “The Origin of Our Universe: Seeking Links between Fundamental Physics and Cosmology” and by Polish MNiSzW scientific research grants N N202 103838 and N N202 285038.

References

1. S. Kachru *et al.*, Phys. Rev. D **68** (2003) 046005 [arXiv:hep-th/0301240].
2. J. J. Blanco-Pillado *et al.*, JHEP **0411** (2004) 063 [arXiv:hep-th/0406230].
3. A. Linde and A. Westphal, JCAP **0803** (2008) 005 [arXiv:0712.1610 [hep-th]].
4. O. Lebedev *et al.*, Phys. Lett. B **636** (2006) 126 [arXiv:hep-th/0603047].
5. M. Badziak and M. Olechowski, JCAP **0807** (2008) 021 [arXiv:0802.1014 [hep-th]].
6. L. Covi *et al.*, JHEP **0806** (2008) 057 [arXiv:0804.1073 [hep-th]]; JHEP **0808** (2008) 055 [arXiv:0805.3290 [hep-th]].
7. M. Gomez-Reino and C. A. Scrucca, JHEP **0609** (2006) 008 [arXiv:hep-th/0606273].
8. M. Badziak and M. Olechowski, JCAP **0902** (2009) 010 [arXiv:0810.4251 [hep-th]].
9. R. Kallosh and A. Linde, JHEP **0702** (2007) 002 [arXiv:hep-th/0611183].
10. M. Badziak and M. Olechowski, JCAP **1002**, 026 (2010) [arXiv:0911.1213 [hep-th]].

INITIAL CONDITIONS IN HYBRID INFLATION: EXPLORATION BY MCMC TECHNIQUE

SEBASTIEN CLESSE

Service de Physique Théorique, Université Libre de Bruxelles, CP225, Boulevard du Triomphe, 1050 Brussels, Belgium

Center for Particle Physics and Phenomenology, Louvain University, 2 chemin du cyclotron, 1348 Louvain-la-Neuve, Belgium

In hybrid inflation, initial field values leading to sufficiently long inflation were thought to be fine-tuned in a narrow band along the inflationary valley. A re-analysis of this problem has shown that there exist a non negligible proportion of successful initial conditions exterior to the valley, organised in a complex structure with fractal boundaries, and whose origin has been explained. Their existence in a large part of the parameter space has been demonstrated using a bayesian Monte-Carlo-Markov-Chain (MCMC) method, and natural bounds on potential parameters have been established. Moreover, these results are shown to be valid not only for the original hybrid model, but also for other hybrid realizations in various frameworks.

1 Introduction and original hybrid model

Recent observations of the Cosmic Microwave Background (CMB) and its anisotropies have provided strong arguments in favour of a phase of accelerated expansion in the early universe. If the simpler way to realize this inflation era is to assume the universe initially filled with a unique homogeneous scalar field slowly rolling along its potential, many other realizations have been proposed ^a. In hybrid models, an inflaton field is coupled to an auxiliary field, and accelerated expansion usually occurs when inflaton slow-rolls along a nearly flat valley of the potential and ends abruptly due to a tachyonic instability. The advantages of hybrid models are that the energy scale of inflation can be low and initial field values do not need to be larger than the Planck mass. Moreover, the model can be embedded in some high energy frameworks like supersymmetry, supergravity and grand unified theories. A generic prediction of the original hybrid model ^{2,3} is a blue spectrum of scalar perturbations, and thus it is strongly disfavoured by WMAP constraints on the scalar spectral index ⁴. It remains nevertheless a good toy model for other hybrid realizations in various frameworks, whose dynamics is similar.

The potential for the original hybrid model reads ^{2,3}

$$V(\phi, \psi) = \Lambda^4 \left[\left(1 - \frac{\psi^2}{M^2} \right)^2 + \frac{\phi^2}{\mu^2} + 2 \frac{\phi^2 \psi^2}{\phi_c^2 M^2} \right] \quad (1)$$

in which ϕ is the inflaton, ψ is the auxiliary Higgs-type field, and M, μ, ϕ_c are three mass parameters. Inflation occurs in the false-vacuum along the nearly flat valley $\psi = 0$. A tachyonic instability appears when inflaton reaches $\phi = \phi_c$. From this point, the trajectory falls through one of the global minima of the potential $\phi = 0, \psi = \pm M$ whereas tachyonic preheating occurs ⁵.

It is a natural question to ask how the fields have to be tuned initially along the inflationary valley in order to generate more than around 60 e-folds of inflation inside the valley. If trajectories are initially displaced slightly in the transverse direction, they perform damped oscillations along the valley before the slow-roll regime engages the realisation of a large number of e-folds. On the contrary, if the initial value of the auxiliary field ψ_i is too large, the damping can not proceed sufficiently quickly and slow-roll regime do not begin before the critical point of instability is reached. Tetradis ⁶ and afterward Mendes and Liddle ⁷ determined that the successful region

^asee e.g.¹ for a recent review.

in the initial field space was a very narrow band along the valley such that the initial value of the auxiliary field had to be fine-tuned compared to initial inflaton values. However, some inconsistencies can be pointed out and have lead to the reanalysis of the problem in ^{8,9,10}. Both ⁶ and ⁷ observed some unexplained successful initial conditions outside the valley, who seem organised in some structures in ⁶, but apparently isolated and very subdominant in the higher-resolution analysis of ⁷. These previous studies were also restricted to some similar sets of potential parameters. A full quantitative study of the problem of initial field values in the whole parameter space was still lacking.

By integrating numerically the classical 2-field dynamics, the behaviour of such successful trajectories starting outside the valley can be understood. The relative area that these points can occupy can be evaluated for some sets of parameters, and their dominance in the whole space of potential parameters, initial field-values and initial velocities can be probed using a statistical Monte-Carlo-Markov-Chain method. Our results indicate that the model do not suffer of fine-tuning any more because successful trajectories start more probably outside the valley. It is also shown that initial velocities do not affect the probability to generate sufficient inflation. Finally, some bounds on potential parameters can be established with the only requirement of sufficiently long period of inflation and the absence of some fine-tuning of initial conditions. The important questions of the robustness of these observations for other hybrid realisations, as well as the effects of quantum fluctuations on such trajectories can be pointed out and will be addressed briefly in the conclusion.

2 Space of initial conditions

2.1 Grids of initial field values for fixed parameters

High-resolution grids of initial field values have been plotted by integrating numerically the classical 2-field dynamics. In a flat FLRW universe, dynamics is governed by Friedmann-Lemaître equations

$$H^2 = \frac{8\pi}{3m_{\text{pl}}^2} \left[\frac{1}{2} (\dot{\phi}^2 + \dot{\psi}^2) + V(\phi, \psi) \right], \quad \frac{\ddot{a}}{a} = \frac{8\pi}{3m_{\text{pl}}^2} \left[-\dot{\phi}^2 - \dot{\psi}^2 + V(\phi, \psi) \right], \quad (2)$$

as well as Klein-Gordon equations in an expanding universe

$$\ddot{\phi} + 3H\dot{\phi} + \frac{\partial V(\phi, \psi)}{\partial \phi} = 0, \quad \ddot{\psi} + 3H\dot{\psi} + \frac{\partial V(\phi, \psi)}{\partial \psi} = 0, \quad (3)$$

where a dot denotes derivative with respect to cosmic time, m_{pl} is the Planck mass ^b $H \equiv \dot{a}/a$ and a is the scale factor. In a first step, initial velocities are assumed to be vanishing. White regions in the grid represented in figure 1 correspond to initial conditions leading to more than 60 e-folds of inflation. As expected, a band of fine-tuned initial field values is found along the valley, as well as successful points outside the valley. But instead of being isolated, as it was suggested in ⁷, they form a complex structure of thin lines and crescents, and with successive zooming it is observed that the structure form a connected set. Moreover, the fractal properties of these successful initial conditions have been studied ⁸. The box-counting dimension of the boundaries has been determined numerically and found to be non-integer. Nevertheless, the structure itself exhibits a non-fractal finite area. These properties are similar to the well known Mandelbrot set whose area is finite with infinite fractal boundaries.

Finally, the relative area covered by successful points have been quantified. These points are found to cover up to 20% of the space of initial field values, depending on potential parameter sets ⁹. Therefore, the amount of fine-tuning necessary to have successful inflation is strongly reduced for these particular sets of parameters.

^b M_{pl} is used for the reduced Planck mass $m_{\text{pl}}/\sqrt{8\pi}$

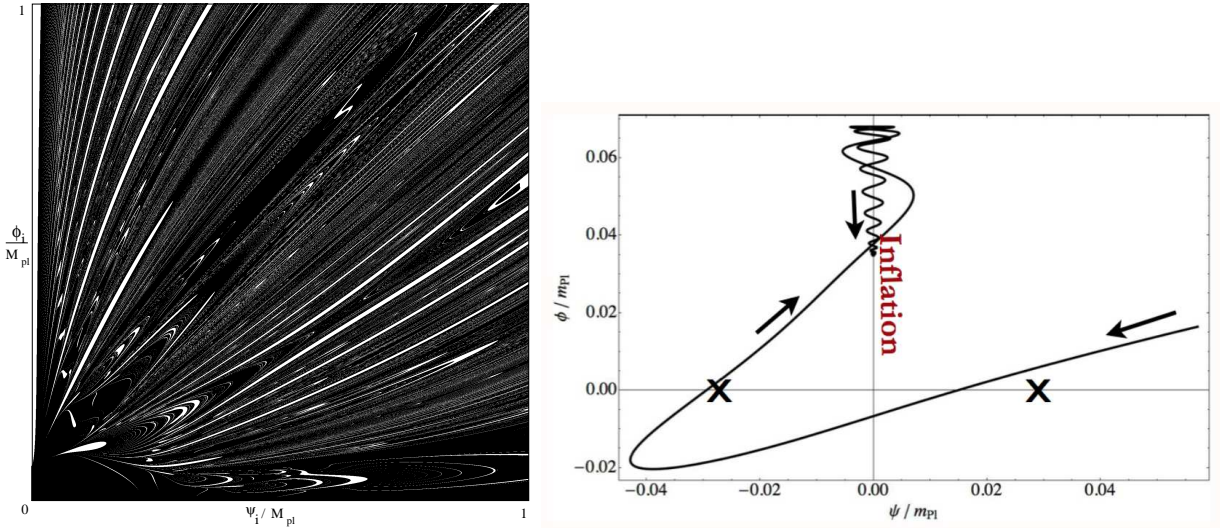


Figure 1: Left: grid (2040x2040 points) of initial field values producing more/less than 60 e-folds of inflation (white/black regions). The potential parameters are set to $M = 0.03 m_{\text{pl}}$, $\mu = 636 m_{\text{pl}}$, $\phi_c = \sqrt{2} \times 10^{-2} m_{\text{pl}}$. Right: typical behaviour of successful trajectory starting outside the inflationary valley, falling towards the bottom of the potential, then climbing the inflationary valley ($\psi = 0$ direction) instead of being trapped by one of the global minima of the potential (represented by crosses). Inflation occurs when it slow-rolls back.

2.2 Successful trajectories initially outside the valley

The typical behaviour of successful trajectories starting outside the inflationary valley (see fig.1, right) has been studied more precisely. Three successive phases have been identified. First, a fast-rolling phase pushing the trajectories through the bottom of the potential, without generating a significant number of e-folds. Then, after some rebonds on the sides of the potential, these trajectories become oriented along the valley, and climb it. Arriving at an extremum point with a quasi-vanishing velocity^c, they start to slow roll back along the valley while producing a large number of e-folds.

2.3 Statistical MCMC analysis

Grids of initial conditions demonstrates that a severe fine-tuning of initial field values is not required in hybrid inflation for particular sets of potential parameters. However, the full initial fields and potential parameter space including initial velocities is 7-th dimensional^d and thus is hardly explored with such grids. For this reason, a statistical bayesian MCMC analysis of this space has been performed. Priors are chosen to be flat for initial field values, initial velocities, and for the logarithm of the potential parameters, in order to avoid fine-tuning of the initial fields and to not favour any precise scale for the potential parameters. Only the sub-planckian regime has been considered, but it was shown in⁹ that for super-Planckian trajectories, the realisation of at least 60 e-folds of inflation becomes generic. More details about the MCMC method can be found in⁸. Only the main results will be discussed below.

The first result concerns the posterior probability density distribution of ψ_i marginalised over the rest of the space (see figure 2). It exhibits a maximum at $\psi_i = 0$ corresponding to

^cThis extremum point is located inside the fine-tuned successful band, thus there exists a correspondence between each initial value inside and exterior to the valley.

^dLet notice that Λ has not been considered since it only normalises the potential without influencing the dynamics.

successful trajectories starting inside the valley. However, it is important to remark that the probability distribution is widely spread over large values of ψ_i , so that the probability to have a successful trajectory starting exterior to the valley is dominant over the probability to start along it. It can therefore be concluded that in the original hybrid model, there is no need of fine-tuned initial conditions along the valley to generate sufficient inflation. Concerning initial velocities, posterior probability distributions are flat, and they do not play a role in the game of finding trajectories leading to many e-folds of inflation. Finally, from the only requirement of having more than 60 e-folds of inflation, natural bounds on the potential parameters ϕ_c and μ can be established,

$$\phi_c < 0.004 m_{\text{pl}} \text{ 95\%C.L.}, \quad \mu > 1.7 m_{\text{pl}} \text{ 95\%C.L..} \quad (4)$$

From the first bound, inflaton value at instability point is shown to be smaller than the reduced planck mass, and the last 60 e-folds are sure to be generated in the sub-planckian regime inside the valley. The second bound is linked to the non-existence of a small field phase of inflation along the valley for small values of μ . This regime was put in evidence in⁹.

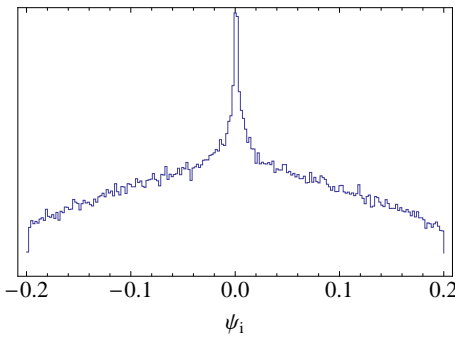


Figure 2: Posterior probability density distribution for ψ_i (in m_{pl} units) with the requirement of at least 60 e-folds generated, marginalised over initial values of ϕ , potential parameters and initial field velocities.

3 Conclusion and discussion

By integrating the classical 2-field dynamics, it has been shown that the original hybrid model does not require fine-tuned initial field values in order to generate a sufficient number of e-folds to solve the standard cosmological problems. Actually, trajectories do not need to be initially tuned inside a narrow band along the inflationary valley. They can start exterior to the valley, and after a fast-roll phase and some rebonds on the sides of the potential, they join it and enter in the slow-roll regime. A bayesian MCMC method has been used to show that this observation is valid, not only for some specific potential parameter sets, but in a large part of the 7-D space of initial field values, initial velocities and potential parameters. Initial velocities do not influence the probability to generate sufficient inflation, and bounds on potential parameters have been deduced from the only requirement of a sufficiently long period of inflation.

If the analysis of the successful initial conditions has been conducted essentially for original hybrid model, the results remain generic for other hybrid realisations in various framework^{9,8}. A large part of the space of initial field values (up to 80%) has been found to be successful for supersymmetric smooth¹¹ and shifted^{13,14} inflation, both in their SUSY and SUGRA versions, as well as for radion assisted gauge inflation¹⁵. The MCMC analysis have been conducted for F-term hybrid inflation¹⁶ in supergravity, with similar results. In particular, a bound on the only parameter M of the model has been established,

$$\log(M/M_{\text{pl}}) < -1.33 \text{ 95\% C.L.}, \quad (5)$$

comparable to the upper bound obtained from cosmic strings formation in¹⁸.

One could argue that there is a remaining problem in the sense that successful initial conditions are subdominant (they do not exceed 25% of the space of initial field values for original hybrid model) compared to unsuccessful trajectories. However, it is without noticing that successful points outside the valley form a complex fractal structure covering roughly all parts of the space of initial conditions. Due to quantum fluctuations along trajectories, we can imagine that each initial patch of the universe will contain at least one region for which inflation will undergo while in other regions inflation will not occur. At the end, the volume occupied by the regions in which inflation occurred is largely dominant, similarly to what happens in a self-reproducing universe. If the following reasoning is correct, all initial conditions would become successful. This effect should be studied more in details in a future work.

Acknowledgments

This work has been done in collaboration with J. Rocher and C. Ringeval. It is a pleasure to thank T. Carletti, A. Fuzfa, A. Lemaitre and M. Tytgat for fruitful discussions and comments. S.C. is supported by the Belgian Fund for research F.R.I.A.

1. Anupam Mazumdar and Jonathan Rocher. Particle physics models of inflation and curvaton scenarios. 2010.
2. Andrei D. Linde. Hybrid inflation. *Phys. Rev.*, D49:748–754, 1994.
3. Edmund J. Copeland, Andrew R. Liddle, David H. Lyth, Ewan D. Stewart, and David Wands. False vacuum inflation with Einstein gravity. *Phys. Rev.*, D49:6410–6433, 1994.
4. Jerome Martin and Christophe Ringeval. Inflation after WMAP3: Confronting the slow-roll and exact power spectra to CMB data. *JCAP*, 0608:009, 2006.
5. Gary N. Felder et al. Dynamics of symmetry breaking and tachyonic preheating. *Phys. Rev. Lett.*, 87:011601, 2001.
6. N. Tetradis. Fine tuning of the initial conditions for hybrid inflation. *Phys. Rev.*, D57:5997–6002, 1998.
7. Luis E. Mendes and Andrew R. Liddle. Initial conditions for hybrid inflation. *Phys. Rev.*, D62:103511, 2000.
8. Sebastien Clesse, Christophe Ringeval, and Jonathan Rocher. Fractal initial conditions and natural parameter values in hybrid inflation. *Phys. Rev.*, D80:123534, 2009.
9. Sebastien Clesse and Jonathan Rocher. Avoiding the blue spectrum and the fine-tuning of initial conditions in hybrid inflation. *Phys. Rev.*, D79:103507, 2009.
10. Sebastien Clesse. Anamorphosis in hybrid inflation: How to avoid fine-tuning of initial conditions? 2009.
11. George Lazarides and C. Panagiotakopoulos. Smooth hybrid inflation. *Phys. Rev.*, D52:559–563, 1995.
12. George Lazarides and Achilleas Vamvasakis. New smooth hybrid inflation. *Phys. Rev.*, D76:083507, 2007.
13. R. Jeannerot, S. Khalil, George Lazarides, and Q. Shafi. Inflation and monopoles in supersymmetric $SU(4)_c \times SU(2)_L \times SU(2)_R$. *JHEP*, 10:012, 2000.
14. R. Jeannerot, S. Khalil, and George Lazarides. New shifted hybrid inflation. *JHEP*, 07:069, 2002.
15. M. Fairbairn, Laura Lopez Honorez, and M. H. G. Tytgat. Radion assisted gauge inflation. *Phys. Rev.*, D67:101302, 2003.
16. G. R. Dvali, Q. Shafi, and Robert K. Schaefer. Large scale structure and supersymmetric inflation without fine tuning. *Phys. Rev. Lett.*, 73:1886–1889, 1994.
17. Rachel Jeannerot and Marieke Postma. Confronting hybrid inflation in supergravity with CMB data. *JHEP*, 05:071, 2005.

Conformal Invariance, Dynamical Dark Energy and the CMB

Emil Mottola

Theoretical Div., Los Alamos National Laboratory, Los Alamos, NM 87545 USA

E-mail: emil@lanl.gov

and

Theoretical Physics Group, PH-TH, CERN CH-1211, Geneva 23, Switzerland

E-mail: emil.mottola@cern.ch

General Relativity receives quantum corrections relevant at cosmological distance scales from conformal scalar degrees of freedom required by the trace anomaly of the quantum stress tensor in curved space. In the theory including the trace anomaly terms, the cosmological “constant” becomes dynamical and hence potentially dependent upon both space and time. The fluctuations of these anomaly scalars may also influence the spectrum and statistics of the Cosmic Microwave Background. Under the hypothesis that scale invariance should be promoted to full conformal invariance, an hypothesis supported by the exact equivalence of the conformal group of three dimensions with the de Sitter group $O(4, 1)$, the form of the CMB bi-spectrum can be fixed, and the tri-spectrum constrained. The non-Gaussianities predicted by conformal invariance differ from those suggested by simple models of inflation.

1 Cosmological Dark Energy and the Effective Field Theory of Gravity

Observations of type Ia supernovae at moderately large redshifts ($z \sim 0.5$ to 1) have led to the conclusion that the Hubble expansion of the universe is *accelerating*.¹ According to Einstein’s equations this acceleration is possible if and only if the energy density ρ and pressure p of the dominant component of the universe satisfies the inequality,

$$\rho + 3p \equiv \rho (1 + 3w) < 0. \quad (1)$$

A vacuum energy with $\rho_v > 0$ and $w \equiv p_v/\rho_v = -1$ leads to an accelerated expansion, a kind of “repulsive” gravity in which the relativistic effects of a negative pressure can overcome a positive energy density in (1). Taken at face value, the observations imply that some 74% of the energy in the universe is of this hitherto undetected $w = -1$ dark variety. This leads to a non-zero inferred cosmological term in Einstein’s equations of

$$\Lambda_{\text{meas}} \simeq (0.74) \frac{3H_0^2}{c^2} \simeq 1.4 \times 10^{-56} \text{ cm}^{-2} \simeq 3.6 \times 10^{-122} \frac{c^3}{\hbar G}. \quad (2)$$

Here H_0 is the present value of the Hubble parameter, approximately 73 km/sec/Mpc $\simeq 2.4 \times 10^{-18} \text{ sec}^{-1}$. The last number in (2) expresses the value of the cosmological term inferred from the SN Ia data in terms of Planck units, $L_{\text{pl}}^{-2} = \frac{c^3}{\hbar G}$. Explaining the value of this smallest number in all of physics is the basic form of the *cosmological constant problem*.

If the universe were purely classical, L_{pl} would vanish and Λ , like the overall size or total age of the universe, could take on any value whatsoever without any technical problem of naturalness. On the other hand, if $G = 0$ and there are also no boundary effects to be concerned with, then the cutoff dependent zero point energy of flat space could simply be subtracted, with no observable consequences. A naturalness problem arises only when the effects of quantum zero point energy on the large scale curvature of spacetime are considered. Thus this is a problem of the gravitational energy of the quantum vacuum or ground state of the system at *macroscopic* distance scales, very much greater than L_{pl} , when both $\hbar \neq 0$ and $G \neq 0$.

The treatment of quantum effects at distances much larger than any ultraviolet cutoff is precisely the context in which effective field theory (EFT) techniques should be applicable. This means that we assume that we do not need to know every detail of physics at extremely short

distance scales of 10^{-33} cm or even 10^{-13} cm in order to discuss cosmology at 10^{28} cm scales. In extending Einstein's classical theory to take account of the quantum properties of matter, the classical stress-energy tensor of matter T_b^a becomes a quantum operator, with an expectation value $\langle T_b^a \rangle$. In this *semi-classical* theory with both \hbar and G different from zero, quantum zero-point and vacuum energy effects first appear, while the spacetime geometry can still be treated classically. Since the expectation value $\langle T_b^a \rangle$ suffers from the quartic divergence, a regularization and renormalization procedure is necessary in order to define the semi-classical EFT. The result of the renormalization program for quantum fields and their vacuum energy in curved space is that General Relativity can be viewed as a low energy quantum EFT of gravity, provided that the classical Einstein-Hilbert classical action is augmented by the additional terms required by the *trace anomaly* when $\hbar \neq 0$.

Massless quantum matter or radiation fields have stress-energy tensors which are traceless classically. However it is impossible to maintain both conservation and tracelessness of the quantum expectation value $\langle T_b^a \rangle$. Instead a well-defined conformal or trace anomaly for this expectation value in curved spacetime is obtained,² *i.e.*

$$\langle T_a^a \rangle = bF + b' \left(E - \frac{2}{3} \square R \right) + b'' \square R, \quad (3)$$

where

$$E \equiv {}^*R_{abcd} {}^*R^{abcd} = R_{abcd}R^{abcd} - 4R_{ab}R^{ab} + R^2, \quad (4a)$$

$$F \equiv C_{abcd}C^{abcd} = R_{abcd}R^{abcd} - 2R_{ab}R^{ab} + \frac{R^2}{3}. \quad (4b)$$

in terms of the Riemann curvature tensor R_{abcd} . The coefficients b and b' in (3) do not depend on any ultraviolet short distance cutoff, but instead are determined only by the number and spin of massless fields via

$$b = \frac{\hbar}{120(4\pi)^2} (N_S + 6N_F + 12N_V), \quad (5a)$$

$$b' = -\frac{\hbar}{360(4\pi)^2} (N_S + \frac{11}{2}N_F + 62N_V), \quad (5b)$$

with (N_S, N_F, N_V) the number of massless fields of spin $(0, \frac{1}{2}, 1)$ respectively. The number of massless fields of each spin is a property of the low energy effective description of matter, having no direct connection with physics at the ultrashort Planck scale. Indeed massless fields fluctuate at all distance scales and do not decouple in the far infrared, relevant for cosmology.

One can find a covariant action functional whose variation gives the trace anomaly (3). This functional is *non-local* in terms of just the curvature, and hence describes long distance infrared physics. The non-local anomaly action may be put into a local form, but only by the introduction of two new scalar fields φ and ψ . Then the local effective action of the anomaly in a general curved space may be expressed in the form^{3,4}

$$S_{\text{anom}} = b'S_{\text{anom}}^{(E)} + bS_{\text{anom}}^{(F)}, \quad (6)$$

where

$$\begin{aligned} S_{\text{anom}}^{(E)} &\equiv \frac{1}{2} \int d^4x \sqrt{-g} \left\{ -(\square\varphi)^2 + 2 \left(R^{ab} - \frac{R}{3}g^{ab} \right) (\nabla_a\varphi)(\nabla_b\varphi) + \left(E - \frac{2}{3}\square R \right) \varphi \right\}; \\ S_{\text{anom}}^{(F)} &\equiv \int d^4x \sqrt{-g} \left\{ -(\square\varphi)(\square\psi) + 2 \left(R^{ab} - \frac{R}{3}g^{ab} \right) (\nabla_\mu\varphi)(\nabla_\nu\psi) \right. \\ &\quad \left. + \frac{1}{2}C_{abcd}C^{abcd}\varphi + \frac{1}{2} \left(E - \frac{2}{3}\square R \right) \psi \right\}. \end{aligned} \quad (7)$$

The free variation of the local action (6)-(7) with respect to ψ and φ yields their eqs. of motion. Each of these terms when varied with respect to the background metric gives a stress-energy tensor in terms of these anomaly scalar fields φ and ψ . The scalar fields of the local form (7) of the anomaly effective action describe massless scalar degrees of freedom of low energy gravity, not contained in classical General Relativity. The effective action of low energy gravity is thus

$$S_{eff}[g] = S_{EH}[g] + S_{anom}[g; \varphi, \psi] \quad (8)$$

with S_{EH} the Einstein-Hilbert action of classical General Relativity and S_{anom} the anomaly action given by (6)-(7).

2 Dynamical Dark Energy

In order to understand the *dynamical* effects of the kinetic terms in the anomaly effective action (7), one can consider simplest case of the quantization of the conformal factor in the case that the fiducial metric is flat, *i.e.* $g_{ab} = e^{2\sigma} \eta_{ab}$. In this case the Wess-Zumino form of the effective anomaly action (6) simplifies to^{4,5}

$$S_{anom}[\sigma] = -\frac{Q^2}{16\pi^2} \int d^4x (\square\sigma)^2, \quad (9)$$

where

$$Q^2 \equiv -32\pi^2 b'. \quad (10)$$

This action quadratic in $\sigma = \varphi/2$ is the action of a free scalar field in flat space, with a kinetic term that is fourth order in derivatives.

The classical Einstein-Hilbert action for a conformally flat metric $g_{ab} = e^{2\sigma} \eta_{ab}$ is

$$S_{EH}[g = e^{2\sigma} \eta] = \frac{1}{8\pi G} \int d^4x [3e^{2\sigma} (\partial_a \sigma)^2 - \Lambda e^{4\sigma}], \quad (11)$$

which has derivative and exponential self-interactions in σ . It is remarkable that these complicated interactions can be treated systematically using the the fourth order kinetic term of (9). These interaction terms are renormalizable and their anomalous scaling dimensions due to the fluctuations of σ can be computed in closed form^{4,5}. Direct calculation of the conformal weight of the Einstein curvature term shows that it acquires an anomalous dimension β_2 given by the quadratic relation,

$$\beta_2 = 2 + \frac{\beta_2^2}{2Q^2}. \quad (12)$$

In the limit $Q^2 \rightarrow \infty$ the fluctuations of σ are suppressed and we recover the classical scale dimension of the coupling G^{-1} with mass dimension 2. Likewise the cosmological term in (11) corresponding to the four-volume acquires an anomalous dimension given by

$$\beta_0 = 4 + \frac{\beta_0^2}{2Q^2}. \quad (13)$$

Again as $Q^2 \rightarrow \infty$ the effect of the fluctuations of the conformal factor are suppressed and we recover the classical scale dimension of Λ/G , namely 4. The solution of the quadratic relations (12) and (13) determine the scaling dimensions of these couplings at the conformal fixed point at other values of Q^2 .

The positive corrections of order $1/Q^2$ (for $Q^2 > 0$) in (12) and (13) show that both G^{-1} and Λ/G *flow to zero* at very large distances. Because both of these couplings are separately dimensionful, at a conformal fixed point one should properly speak only of the dimensionless

combination $\hbar G \Lambda / c^3 = \lambda$. By normalizing to a fixed four volume $V = \int d^4x$ one can show that the finite volume renormalization of λ is controlled by the anomalous dimension,

$$2\delta - 1 \equiv 2 \frac{\beta_2}{\beta_0} - 1 = \frac{\sqrt{1 - \frac{8}{Q^2}} - \sqrt{1 - \frac{4}{Q^2}}}{1 + \sqrt{1 - \frac{4}{Q^2}}} \leq 0. \quad (14)$$

This is the anomalous dimension that enters the infrared renormalization group volume scaling relation,⁴

$$V \frac{d}{dV} \lambda = 4(2\delta - 1) \lambda. \quad (15)$$

The anomalous scaling dimension (14) is negative for all $Q^2 \geq 8$. This implies that the dimensionless cosmological term λ has an infrared fixed point at zero as $V \rightarrow \infty$. Thus the cosmological term is *dynamically driven to zero* as $V \rightarrow \infty$ by infrared fluctuations of the conformal part of the metric described by (9).

No fine tuning is involved here and no free parameters enter except Q^2 , which is determined by the trace anomaly coefficient b' by (10). Once Q^2 is assumed to be positive, then $2\delta - 1$ is negative, and λ is driven to zero at large distances by the conformal fluctuations of the metric, with no additional assumptions. Thus the fluctuations of the conformal scalar degrees of freedom of the anomaly generated effective action S_{anom} may be responsible for the observed small value of the cosmological dark energy density (2) inferred from the supernova data. Note also that the fields φ and ψ are scalar degrees of freedom in cosmology which arise naturally from the effective action of the trace anomaly in the Standard Model, without the *ad hoc* introduction of an inflaton field. Recent progress in evaluating their effects of these anomaly scalars in de Sitter space indicate that they have potentially large effects at the cosmological horizon.⁶ Even in the absence of a complete theory of dynamical cosmological vacuum energy, it is reasonable to assume that the conformal fluctuations of S_{anom} could be observable in the signatures of conformal invariance should be imprinted on the spectrum and statistics of the CMB.

3 Conformal Invariance and the CMB

Our earlier studies of fluctuations in de Sitter space suggest that the fluctuations responsible for the screening of λ take place at the horizon scale.⁴ In that case then the microwave photons in the CMB reaching us from their surface of last scattering should retain some imprint of the effects of these fluctuations. It then becomes natural to extend the classical notion of scale invariant cosmological perturbations to full conformal invariance. In that case the classical spectral index of the perturbations should receive corrections due to the anomalous scaling dimensions at the conformal phase.⁷ In addition to the spectrum, the statistics of the CMB should reflect the non-Gaussian correlations characteristic of conformal invariance.

Consider first the two-point function of any observable \mathcal{O}_Δ with dimension Δ . Conformal invariance requires

$$\langle \mathcal{O}_\Delta(x_1) \mathcal{O}_\Delta(x_2) \rangle \sim |x_1 - x_2|^{-2\Delta} \quad (16)$$

at equal times in three dimensional flat spatial coordinates. In Fourier space this gives

$$G_2(k) \equiv \langle \tilde{\mathcal{O}}_\Delta(k) \tilde{\mathcal{O}}_\Delta(-k) \rangle \sim |k|^{2\Delta-3}. \quad (17)$$

Thus, we define the spectral index of this observable by

$$n \equiv 2\Delta - 3. \quad (18)$$

In the case that the observable is the primordial density fluctuation $\delta\rho$, and in the classical limit where its anomalous dimension vanishes, $\Delta \rightarrow p = 2$, we recover the Harrison-Zel'dovich spectral index of $n = 1$.

In order to convert the power spectrum of primordial density fluctuations to the spectrum of fluctuations in the CMB at large angular separations we follow the standard treatment relating the temperature deviation to the Newtonian gravitational potential φ at the last scattering surface, $\frac{\delta T}{T} \sim \delta\varphi$, which is related to the density perturbation in turn by

$$\nabla^2\delta\varphi = 4\pi G \delta\rho . \quad (19)$$

Hence, in Fourier space,

$$\frac{\delta T}{T} \sim \delta\varphi \sim \frac{1}{k^2} \frac{\delta\rho}{\rho} , \quad (20)$$

and the two-point function of CMB temperature fluctuations is determined by the conformal dimension Δ to be

$$C_2(\theta) \equiv \left\langle \frac{\delta T}{T}(\hat{r}_1) \frac{\delta T}{T}(\hat{r}_2) \right\rangle \sim \int d^3k \left(\frac{1}{k^2} \right)^2 G_2(k) e^{ik \cdot r_{12}} \sim \Gamma(2 - \Delta) (r_{12}^2)^{2-\Delta} , \quad (21)$$

where $r_{12} \equiv (\hat{r}_1 - \hat{r}_2)r$ is the vector difference between the two positions from which the CMB photons originate. They are at equal distance r from the observer by the assumption that the photons were emitted at the last scattering surface at equal cosmic time. Since $r_{12}^2 = 2(1 - \cos\theta)r^2$, we find then

$$C_2(\theta) \sim \Gamma(2 - \Delta)(1 - \cos\theta)^{2-\Delta} \quad (22)$$

for arbitrary scaling dimension Δ .

Expanding the function $C_2(\theta)$ in multipole moments,

$$C_2(\theta) = \frac{1}{4\pi} \sum_{\ell} (2\ell + 1) c_{\ell}^{(2)}(\Delta) P_{\ell}(\cos\theta) , \quad (23)$$

$$c_{\ell}^{(2)}(\Delta) \sim \Gamma(2 - \Delta) \sin[\pi(2 - \Delta)] \frac{\Gamma(\ell - 2 + \Delta)}{\Gamma(\ell + 4 - \Delta)} , \quad (24)$$

shows that the pole singularity at $\Delta = 2$ appears only in the $\ell = 0$ monopole moment. This singularity is just the reflection of the fact that the Laplacian in (19) cannot be inverted on constant functions, which should be excluded. Since the CMB anisotropy is defined by removing the isotropic monopole moment (as well as the dipole moment), the $\ell = 0$ term does not appear in the sum, and the higher moments of the anisotropic two-point correlation function are well-defined for Δ near 2. Normalizing to the quadrupole moment $c_2^{(2)}(\Delta)$, we find

$$c_{\ell}^{(2)}(\Delta) = c_2^{(2)}(\Delta) \frac{\Gamma(6 - \Delta)}{\Gamma(\Delta)} \frac{\Gamma(\ell - 2 + \Delta)}{\Gamma(\ell + 4 - \Delta)} , \quad (25)$$

which is a standard result. Indeed, if Δ is replaced by $p = 2$ we obtain $\ell(\ell + 1)c_{\ell}^{(2)}(p) = 6c_2^{(2)}(p)$, which is the well-known predicted behavior of the lower moments ($\ell \leq 30$) of the CMB anisotropy where the Sachs-Wolfe effect should dominate.

Turning now from the two-point function of CMB fluctuations to higher point correlators, we find a second characteristic prediction of conformal invariance, namely non-Gaussian statistics

for the CMB. The first correlator sensitive to this departure from gaussian statistics is the three-point function of the observable \mathcal{O}_Δ , which takes the form⁷

$$\langle \mathcal{O}_\Delta(x_1) \mathcal{O}_\Delta(x_2) \mathcal{O}_\Delta(x_3) \rangle \sim |x_1 - x_2|^{-\Delta} |x_2 - x_3|^{-\Delta} |x_3 - x_1|^{-\Delta} , \quad (26)$$

or in Fourier space,^a

$$G_3(k_1, k_2) \sim \int d^3p |p|^{\Delta-3} |p + k_1|^{\Delta-3} |p - k_2|^{\Delta-3} \sim \frac{\Gamma(3 - \frac{3\Delta}{2})}{[\Gamma(\frac{3-\Delta}{2})]^3} \times \int_0^1 du \int_0^1 dv \frac{[u(1-u)v]^{\frac{1-\Delta}{2}} (1-v)^{-1+\frac{\Delta}{2}}}{[u(1-u)(1-v)k_1^2 + v(1-u)k_2^2 + uv(k_1 + k_2)^2]^{3-\frac{3\Delta}{2}}} . \quad (27)$$

This three-point function of primordial density fluctuations gives rise to three-point correlations in the CMB by reasoning precisely analogous as that leading from Eqns. (17) to (21). That is,

$$C_3(\theta_{12}, \theta_{23}, \theta_{31}) \equiv \left\langle \frac{\delta T}{T}(\hat{r}_1) \frac{\delta T}{T}(\hat{r}_2) \frac{\delta T}{T}(\hat{r}_3) \right\rangle \sim \int \frac{d^3k_1 d^3k_2}{k_1^2 k_2^2 (k_1 + k_2)^2} G_3(k_1, k_2) e^{ik_1 \cdot r_{13}} e^{ik_2 \cdot r_{23}} \quad (28)$$

where $r_{ij} \equiv (\hat{r}_i - \hat{r}_j)r$ and $r_{ij}^2 = 2(1 - \cos \theta_{ij})r^2$.

In the general case of three different angles, this expression for the non-Gaussian three-point correlation function (28) is quite complicated, although it can be rewritten in parametric form analogous to (27) to facilitate numerical evaluation. In the special case of equal angles, it follows from its global scaling properties that the three-point correlator is

$$C_3(\theta) \sim (1 - \cos \theta)^{\frac{3}{2}(2-\Delta)} . \quad (29)$$

Expanding the function $C_3(\theta)$ in multiple moments as in (23) with coefficients $c_\ell^{(3)}$, and normalizing to the quadrupole moment, we find

$$c_\ell^{(3)}(\Delta) = c_2^{(3)}(\Delta) \frac{\Gamma(4 + \frac{3}{2}(2 - \Delta))}{\Gamma(2 - \frac{3}{2}(2 - \Delta))} \frac{\Gamma(\ell - \frac{3}{2}(2 - \Delta))}{\Gamma(\ell + 2 + \frac{3}{2}(2 - \Delta))} . \quad (30)$$

In the limit $\Delta \rightarrow 2$, we obtain $\ell(\ell + 1)c_\ell^{(3)} = 6c_2^{(3)}$, which is the same result as for the moments $c_\ell^{(2)}$ of the two-point correlator but with a different quadrupole amplitude. The value of this quadrupole normalization $c_2^{(3)}(\Delta)$ cannot be determined by conformal symmetry considerations alone, and requires more detailed dynamical information about the origin of conformal invariance in the spectrum.

For higher point correlations, conformal invariance does not determine the total angular dependence. Already the four-point function takes the form,

$$\langle \mathcal{O}_\Delta(x_1) \mathcal{O}_\Delta(x_2) \mathcal{O}_\Delta(x_3) \mathcal{O}_\Delta(x_4) \rangle \sim \frac{A_4}{\prod_{i < j} r_{ij}^{2\Delta/3}} , \quad (31)$$

where the amplitude A_4 is an arbitrary function of the two cross-ratios, $r_{13}^2 r_{24}^2 / r_{12}^2 r_{34}^2$ and $r_{14}^2 r_{23}^2 / r_{12}^2 r_{34}^2$. Analogous expressions hold for higher p -point functions.

An important point to emphasize is that all of these results depend upon the hypothesis of conformal invariance on the spatially homogeneous and isotropic flat spatial sections of geometries. This is only one way in which conformal invariance may be realized, for example, if the universe went through a de Sitter like inflationary expansion. That this is actually related to the geometric symmetries of de Sitter space is shown next.

^aNote that (27) corrects two minor typographical errors in eq. (16) of Ref. ⁷

4 Conformal Invariance as a Consequence of de Sitter Invariance

In cosmology the line element of de Sitter space is usually expressed in the form

$$ds^2 = -d\tau^2 + a^2(\tau) d\vec{x} \cdot d\vec{x} = -d\tau^2 + e^{2H\tau} (dx^2 + dy^2 + dz^2) \quad (32)$$

with flat spatial sections, and the Hubble parameter $H = \sqrt{\Lambda/3}$. This de Sitter geometry has an $O(4, 1)$ symmetry group with 10 Killing generators satisfying

$$\nabla_a \xi_b^{(\alpha)} + \nabla_b \xi_a^{(\alpha)} = 0, \quad \alpha = 1, \dots, 10, \quad (33)$$

which leave the de Sitter metric invariant. In coordinates (32), (33) becomes

$$\partial_\tau \xi_\tau^{(\alpha)} = 0, \quad (34a)$$

$$\partial_\tau \xi_i^{(\alpha)} + \partial_i \xi_\tau^{(\alpha)} - 2H \xi_i^{(\alpha)} = 0, \quad (34b)$$

$$\partial_i \xi_j^{(\alpha)} + \partial_j \xi_i^{(\alpha)} - 2H a^2 \delta_{ij} \xi_\tau^{(\alpha)} = 0. \quad (34c)$$

For $\xi_\tau = 0$ we have the three translations, $\alpha = T_j$,

$$\xi_\tau^{(T_j)} = 0, \quad \xi_i^{(T_j)} = a^2 \delta_i^j, \quad j = 1, 2, 3, \quad (35)$$

and the three rotations, $\alpha = R_\ell$,

$$\xi_\tau^{(R_\ell)} = 0, \quad \xi_i^{(R_\ell)} = a^2 \epsilon_{i\ell m} x^m, \quad \ell = 1, 2, 3. \quad (36)$$

This accounts for 6 of the 10 de Sitter isometries which are self-evident in the spatially flat homogeneous and isotropic Robertson-Walker coordinates (32) with $\xi_\tau = 0$. The 4 additional solutions of (34) have $\xi_\tau \neq 0$. They are the three special conformal transformations of \mathbb{R}^3 , $\alpha = C_n$,

$$\xi_\tau^{(C_n)} = -2Hx^n, \quad \xi_i^{(C_n)} = H^2 a^2 (\delta_i^n \delta_{jk} x^j x^k - 2\delta_{ij} x^j x^n) - \delta_i^n, \quad n = 1, 2, 3, \quad (37)$$

and the dilation, $\alpha = D$,

$$\xi_\tau^{(D)} = 1, \quad \xi_i^{(D)} = H a^2 \delta_{ij} x^j. \quad (38)$$

This last dilational Killing vector is the infinitesimal form of the finite dilational symmetry,

$$\vec{x} \rightarrow \lambda \vec{x}, \quad (39a)$$

$$a(\tau) \rightarrow \lambda^{-1} a(\tau) \quad (39b)$$

of de Sitter space. The existence of this symmetry explains why Fourier modes of different $|\vec{k}|$ leave the de Sitter horizon at a shifted RW time τ , so in an eternal de Sitter space, in which there is no preferred τ , one expects a scale invariant spectrum.

The existence of the three conformal modes of \mathbb{R}^3 (37) implies in addition that any $O(4, 1)$ de Sitter invariant correlation function must decompose into representations of the conformal group of three dimensional flat space. Fundamentally this is because the de Sitter group $O(4, 1)$ is the conformal group of flat Euclidean \mathbb{R}^3 , as eqs. (33)-(38) shows explicitly. Moreover, because of the exponential expansion in de Sitter space, the decomposition into representations of the conformal group become simple at distances large compared to the horizon scale $1/H^8$. Thus if the universe went through an exponentially expanding de Sitter phase for many e-foldings when the fluctuations responsible for the CMB were generated, then the CMB should exhibit full conformal invariance in addition to simple scale invariance. Neither the form nor magnitude

of the CMB power or bi-spectrum depend upon an inflaton or “slow-roll” parameters as in conventional scalar models of inflation.

Another quite distinct possibility for realizing conformal invariance from de Sitter space is if the fluctuations due to the anomaly scalars are generated in the vicinity of the cosmological horizon at $r = 1/H$ in the *static* coordinates of de Sitter space, *i.e.*..

$$ds^2 = -(1 - H^2 r^2) dt^2 + \frac{dr^2}{(1 - H^2 r^2)} + r^2 d\Omega^2. \quad (40)$$

Conformal invariance on the sphere $r = 1/H$ leads to a different characteristic form of the non-Gaussian bi-spectrum and higher angular correlations. This form will be presented in a forthcoming article.

References

1. A. G. Riess *et. al.*, *Astron. J.* **116**, 1009 (1998); *Astron. J.* **607** 665 (2004);
S. Perlmutter *et. al.*, *Astrophys. J.* **517** 565 (1999);
J. L. Tonry *et. al.*, *Astrophys. J.* **594**, 1 (2003).
2. N. D. Birrell and P. C. W. Davies, *Quantum Fields in Curved Space* (Cambridge University Press, Cambridge, 1982), and references therein.
3. E. Mottola and R. Vaulin, *Phys. Rev. D* **74**, 064004 (2006).
4. I. Antoniadis, P. O. Mazur and E. Mottola, *New J. Phys.* **9**, 11 (2007).
5. I. Antoniadis and E. Mottola, *Phys. Rev. D* **45**, 2013 (1992).
6. P. R. Anderson, C. Molina-Páris, and E. Mottola, *Phys. Rev. D* **80**, 084005 (2009).
7. I. Antoniadis, P. O. Mazur and E. Mottola, *Phys. Rev. Lett.* **79**, 14 (1997).
8. I. Antoniadis, P. O. Mazur and E. Mottola, e-print arxiv: astro-ph/9705200.

6. Herschel

MODELLING GALAXIES CLUSTERING IN THE COSMIC INFRARED BACKGROUND

A. PÉNIN, O. DORÉ, G. LAGACHE, M. BÉTHERMIN

Institut d'Astrophysique Spatiale, bâtiment 121, Université Paris-XI, 91405 Orsay, France

Abstract

The Cosmic Infrared Background (CIB) is the contribution of starburst galaxies (SB) integrated over the whole history of the Universe. Its energy is of the order of that emitted in the optical whereas in the local Universe the energy emitted in the infrared (IR) is around one third of that emitted in the optical. It implies that the Universe went through an IR era billions of years ago. Indeed, the star formation rate was dominated by SB galaxies at $0.5 < z < 3$.

In the far-IR data are limited by confusion which makes impossible the study of the clustering of IR galaxies using the correlation function. At small spatial scales the clustering constrains the physics inside one halo of dark matter and at large scales it probes the linear bias of IR galaxies and thus the underlying dark matter distribution. A way of circumventing confusion is the study of the anisotropies of the CIB as they contain the clustering.

We present a clustering model of IR galaxies based on a dark matter distribution model linked to a model of the evolution of IR galaxies and show how we can constrain cosmological parameters and starburst galaxies luminosity function by applying the former to available data at several wavelength and later to Planck and Herschel.

1 Introduction

The Cosmic Infrared Background (CIB) is the contribution of all starburst galaxies (SB) integrated on the whole history of the Universe (Puget et al. (1996), Fixsen et al. (1998)), it peaks around 150 μm . These SB galaxies are mainly characterized by a high star formation rate, ten or even a hundred times higher than that of the Milky Way, therefore they host many young stars that heat surrounding dust which reprocesses UV light and reemits it in the infrared (IR). At these wavelengths (far IR and sub-millimeter), observations are limited by confusion, small spatial scales are lost because of the poor angular resolution of the instruments. In the near and mid IR a large fraction of the CIB is resolved whereas in the far IR only a few percents is, unless statistical methods are used. Indeed, Papovich et al. (2004) resolve 70 % of the 24 μm and Dole et al. (2004) resolve 23% and 7% of the CIB at 70 and 160 μm respectively. However, Dole et al. (2006) resolve more than 70 % of the CIB at 70 and 160 μm stacking 24 μm sources. As a result, sources detected at 24 μm are the main sources of the CIB around its peak. The CIB is dominated by objects that get more and more massive as the redshift increases from luminous IR galaxies (LIRGs) with $10^{11}L_\odot < L_{IR} < 10^{12}L_\odot$ at $0.8 < z < 1.2$ with intermediate mass to extremely LIRGs with $10^{12}L_\odot < L_{IR} < 10^{14}L_\odot$ that dominate at $z > 2$ and with masses $> 10^{11}M_\odot$ (Caputi et al. (2006)).

Using 24 μm detected sources Magliocchetti et al. (2007) was able to derive the two-point-correlation of Ultra LIRGs at $z \simeq 1.6 - 2.7$ and found that these SB galaxies are strongly clustered and that they are embedded in dark matter halos more massive than $\simeq 10^{13.4}M_\odot$. The two-point correlation function cannot be computed in the far-IR because of confusion, but the clustering of SB galaxies can be measured in the anisotropies of the CIB. Indeed, it has been recently detected at several wavelengths: at 160 μm by Lagache et al. (2007) and by Grossan & Smoot (2007) in the Spitzer

Multiband Imaging Photometer (MIPS) data and from 250 to 500 μm by Viero et al. (2009) in the Balloon-borne Large Aperture Submillimeter Telescope (BLAST) data. The three of them detected an excess of signal at intermediate scales due to the clustering of starburst galaxies which enabled them to derive the bias parameter b that links the fluctuations of the density field of galaxies to that of dark matter. The former found $b = 2.4 \pm 0.2$ and the latter $b = 3 \pm 0.3$. The difference is due to a selection effect: at longer wavelength, higher redshift SB galaxies are probed (Lagache et al. (2005), Fernandez-Conde et al. (2008)) and thus are found to be more biased. Indeed, SB galaxies are a highly biased tracer of the underlying dark matter density field as they formed in very massive DM halos in the early times of the Universe. These measurements have been followed by those of Hall et al. (2009) at 1.3 and 2 mm with the South Pole Telescope and by Fowler & Atacama Cosmology Telescope Team (2010) at 2mm with the Atacama Cosmology Telescope. They either derive or set an upper limit to the clustered power spectra and to the Poisson noise at these longer wavelengths. The clustering has been thus measured over a large range of wavelength, and potentially a large range of redshift has been probed.

The analysis of these measurements require a model including a description of the evolution of SB galaxies and of the underlying dark matter distribution. Previous measurements have either neglected the dark matter distribution assuming a linear power spectrum (Lagache et al. (2007), Hall et al. (2009)) or used a pre-Herschel model of evolution of SB galaxies (Viero et al. (2009) used Lagache et al. (2003)). However future measurements analysis such as that of Planck and Herschel need a model including both description and in agreement with already existing data. Moreover we use a trustworthy halo occupation distribution. We present a new model of the clustering of galaxies in the CIB that contains the evolution of SB galaxies fitted on number counts at several wavelengths (Béthermin et al. in prep) linked to the formalism of the halo model (Cooray & Sheth (2002)) that describes the DM density field.

2 The model

2.1 The parametrised galaxies evolution

In order to reproduce measured number counts we use two galaxy populations, starburst and spirals galaxies. The former emit most of their energy in the infrared because of their high star formation rate and the latter are nearby 'normal' galaxies similar to the Milky Way that emit half or less of their energy in the infrared. At low z the emission is dominated by spiral galaxies and at higher z starbursts dominate. We compute number counts for each population.

Differential counts at a wavelength λ and at flux S are given by

$$\frac{dN}{dS} = \int_z \int_L \frac{dN}{d \log_{10} L dz} \frac{d \log_{10} L}{dS} dz \quad (1)$$

The second part of the integral is computed with spectral energy density templates from Lagache et al. (2003) and the first part is derived with the following luminosity function (Le Floc'h et al. (2005)):

$$\phi(L) = \frac{dN(L)}{dV d \log_{10}(L)} \quad (2)$$

$$= \phi^*(z) \left(\frac{L}{L^*(z)} \right)^{1-\alpha} \exp \left[-\frac{1}{2\sigma^2} \log_{10}^2 \left(1 + \left(\frac{L}{L^*(z)} \right) \right) \right] \quad (3)$$

Where $\phi(L^*) = \phi^*$ and dV the comoving volume. The luminosity function is fully described by four parameters: α , σ which do not depend on z and L^* , ϕ^* which are redshift dependent:

$$L^*(z) = L^*(z=0)(1+z)^{r_L} \quad (4)$$

$$\phi^*(z) = \phi^*(z=0)(1+z)^{r_\phi} \quad (5)$$

r_L and r_ϕ take different values for low and high z , the limit between high and low z is defined by another parameter z_{break} . The last parameters are the luminosity transition at which starburst galaxies start to dominate the IR emission and its width.

Best parameters are computed using a χ^2 minimisation with measured differential number counts

with Spitzer MIPS at 24, 70, 160 μm (Dole et al. (2006), Béthermin et al. (2010)), BLAST at 250, 350, 500 μm (Patanchon et al. (2009)) and SCUBA at 850 μm . They are very well fitted as shows Fig. 2.1. This model will be presented in Béthermin et al. in prep.

Using best fits we compute emissivities which are an input for the CIB angular power spectrum.

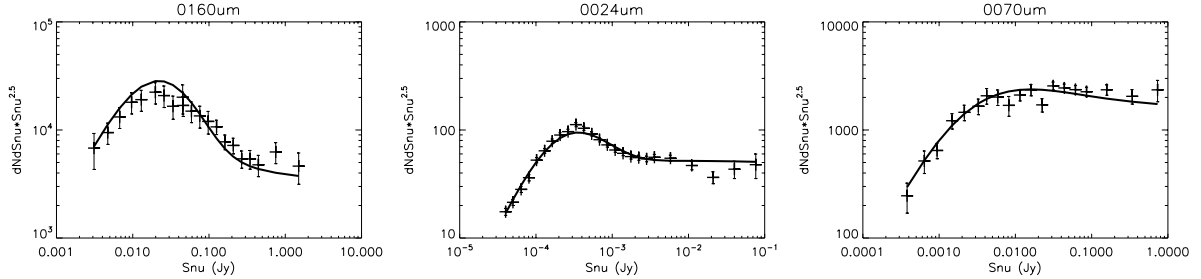


Figure 1: Fits of differential number counts at 160, 24 and 70 μm .

2.2 The angular power spectrum

The CIB fluctuations angular power spectrum can be written (Knox et al. (2001)), using the Limber assumption:

$$C_{\ell}^{\lambda\lambda'} = \int dz \frac{dr}{dz} \frac{a^2(z)}{d_A^2} \bar{i}_{\lambda}(z) \bar{i}_{\lambda'}(z) P_{ss}(k = \frac{l}{d_A}, z) \quad (6)$$

where r is the conformal distance from the observer, d_A the comoving angular diameter distance, $\bar{i}_{\lambda}(z)$ is the mean emissivity per comoving unit volume at wavelength λ as a function of z . $P_{ss}(k)$ is the galaxy power spectrum computed in the formalism of the halo model (Cooray & Sheth (2002)) which describes the dark matter distribution. $P_{ss}(k)$ is written as the sum of the clustering in one single halo (1h) and in two different halos (2h):

$$P_{ss}(k) = P_{1h}(k) + P_{2h}(k) \quad (7)$$

Where

$$P_{2h}(k) = P_{lin}(k) \left[\int dM \frac{dN}{dM} b(M) \frac{\langle N_{gal}|M \rangle}{\bar{n}_{gal}^2} U(k, M) \right]^2 \quad (8)$$

$$P_{1h}(k) = \int dM \frac{dN}{dM} \frac{\langle N_{gal}(N_{gal}-1)|M \rangle}{\bar{n}_{gal}^2} U(k, M)^2 \quad (9)$$

(10)

Where M is the halo mass, $P_{lin}(k)$ is the dark matter linear power spectrum, $U(k, M)$ is the Fourier transform of the halo density profile (Navarro Frenk White), $b(M)$ the galaxy bias and \bar{n}_{gal} the mean number density of galaxies. $\langle N_{gal}|M \rangle$ is the probability of having N galaxies in a halo of mass M . Moreover the distribution of galaxies in one halo is also needed. These two descriptions are also called the halo occupation distribution. Following the halo model, galaxies are separated between central and satellite ones and we use the distribution of galaxies used by Tinker et al. (2009). For clarity we now write $\langle N_{gal}|M \rangle$ as $\langle N_{gal} \rangle$

$$\langle N_{gal} \rangle = \langle N_c \rangle + \langle N_s \rangle \quad (11)$$

$$\langle N_s \rangle = \left(\frac{M}{M_1} \right)^{\alpha_{sat}} \exp \left(-\frac{M_{cut}}{M} \right) \quad (12)$$

$$\langle N_c \rangle = \text{erf} \left[5 \left(1 - \frac{M}{M_{min}} \right) \right] \quad (13)$$

(14)

Where $\langle N_c \rangle$ and $\langle N_s \rangle$ are respectively the probability of having N_c central galaxies and N_s satellite galaxies in a halo of mass M . They consider $\alpha_{sat} = 1$, $M_1/M_{min}=15.7$ and $M_{cut}/M_{min}=1.14$ with $M_{min} = 9 \times 10^{11} h^{-1} M_\odot$. M_{min} and α_{sat} are some of the parameters that we constrain. The others are cosmological ones : w_0 , Ω_0 , w_A and σ_8 .

Emissivities are computed using the previous parametrised luminosity function following :

$$j_\nu = a \frac{d\chi}{dz} \int_L S \frac{dN}{dz d(\ln L)} d(\ln L) \quad (15)$$

where

$$\frac{d\chi}{dz} = \frac{c}{H_0 \sqrt{\Omega_\Lambda + \Omega_m(1+z)^3}} \quad (16)$$

Best parameters are derived using a χ^2 minimisation on measured power spectra at $160 \mu\text{m}$ (Lagache et al. (2007), Pénin et al. in prep.), and $250, 350, 500 \mu\text{m}$ (Viero et al. (2009)).

3 A work in progress

Using the best fit parameters obtained using source counts data, we compute the associated Fisher matrices coming from differential number counts and angular power spectra on. Fig. 3 shows likelihood contours computed with number counts data around selected parameters (see Sect. 2.1) of the galaxy evolution model. Clear degeneracies are visible. In the next step of our work, we will show how the use of angular power spectra allow to break some of these degeneracies. In principle, this approach will allow us to constrain simultaneously and in a statistically sound manner the DM distribution, SB galaxies luminosity functions, the clustering of starburst galaxies, their luminosity function and its evolution. We plan to apply this model to forthcoming data in order to constrain the 1-halo term with Herschel, the 2-halo term with Planck, as well as measurements of the luminosity functions that should alleviate further some degeneracies.

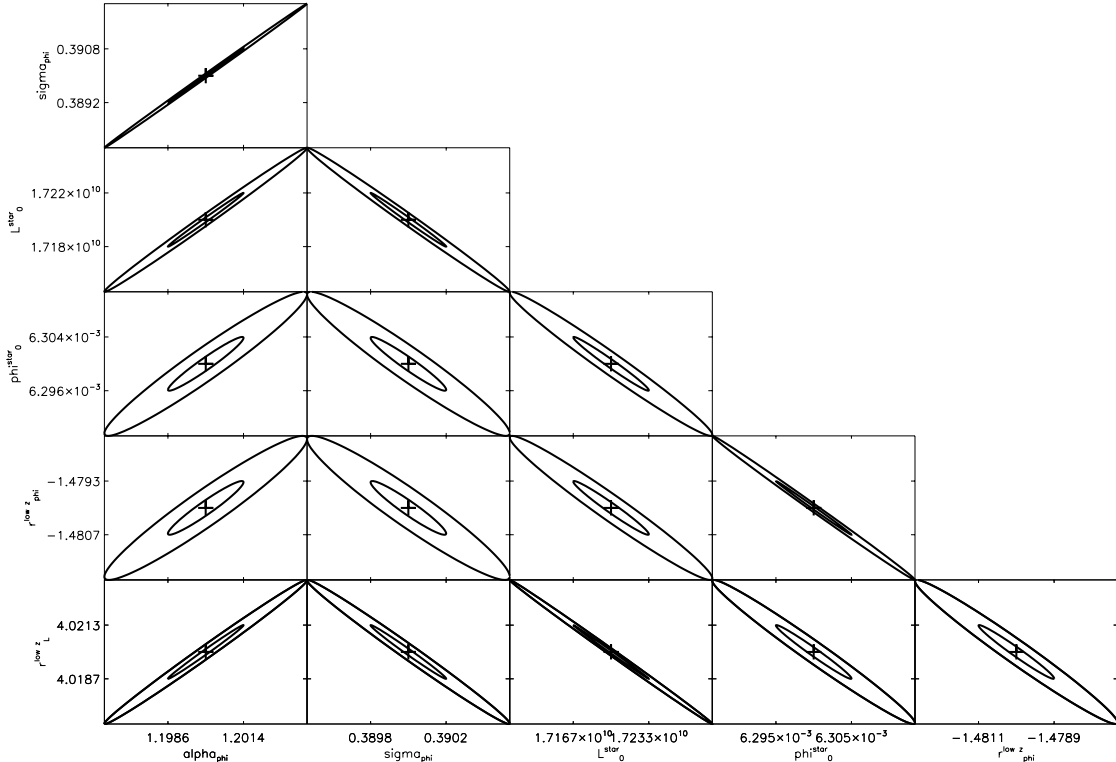


Figure 2: Likelihood ellipses (1 and 2σ) for several parameters of the model of galaxy evolution computed with number counts data.

References

- Béthermin, M., Dole, H., Beelen, A., & Aussel, H. 2010, A&A, 512, A78+
- Caputi, K. I., Dole, H., Lagache, G., & Puget, J. 2006, ArXiv Astrophysics e-prints
- Cooray, A. & Sheth, R. 2002, PhysRev, 372, 1
- Dole, H., Lagache, G., Puget, J.-L., et al. 2006, A&A, 451, 417
- Dole, H., Le Floc'h, E., Pérez-González, P. G., et al. 2004, Astrophysical Journal Supplement Series, 154, 87
- Fernandez-Conde, N., Lagache, G., Puget, J.-L., & Dole, H. 2008, A&A, 481, 885
- Fixsen, D. J., Dwek, E., Mather, J. C., Bennett, C. L., & Shafer, R. A. 1998, ApJ, 508, 123
- Fowler, J. W. & Atacama Cosmology Telescope Team. 2010, in Bulletin of the American Astronomical Society, Vol. 41, Bulletin of the American Astronomical Society, 599–+
- Grossan, B. & Smoot, G. F. 2007, A&A, 474, 731
- Hall, N. R., Knox, L., Reichardt, C. L., et al. 2009, ArXiv e-prints
- Knox, L., Cooray, A., Eisenstein, D., & Haiman, Z. 2001, ApJ, 550, 7
- Lagache, G., Bavouzet, N., Fernandez-Conde, N., et al. 2007, ApJ, 665, L89
- Lagache, G., Dole, H., & Puget, J.-L. 2003, MNRAS, 338, 555
- Lagache, G., Puget, J., & Dole, H. 2005, ARA&A, 43, 727
- Le Floc'h, E., Papovich, C., Dole, H., et al. 2005, ApJ, 632, 169
- Magliocchetti, M., Silva, L., Lapi, A., et al. 2007, MNRAS, 375, 1121
- Papovich, C., Dole, H., Egami, E., et al. 2004, Astrophysical Journal Supplement Series, 154, 70
- Patanchon, G., Ade, P. A. R., Bock, J. J., et al. 2009, ApJ, 707, 1750
- Puget, J., Abergel, A., Bernard, J., et al. 1996, A&A, 308, L5+
- Tinker, J. L., Wechsler, R. H., & Zheng, Z. 2009, ArXiv e-prints
- Viero, M. P., Ade, P. A. R., Bock, J. J., et al. 2009, ArXiv e-prints

7.

Testing the Cosmological Model

No Evidence for Dark Energy Dynamics from a Global Analysis of Cosmological Data

P. SERRA

*Center for Cosmology, Department of Physics and Astronomy,
University of California, Irvine, CA 92697*

We use a variant of principal component analysis to investigate the possible temporal evolution of the dark energy equation of state, $w(z)$. We constrain $w(z)$ in multiple redshift bins, utilizing the most recent data from Type Ia supernovae, the cosmic microwave background, baryon acoustic oscillations, the integrated Sachs-Wolfe effect, galaxy clustering, and weak lensing data. Unlike other recent analyses, we find no significant evidence for evolving dark energy; the data remains completely consistent with a cosmological constant. We also study the extent to which the time-evolution of the equation of state would be constrained by a combination of current and future-generation surveys, such as Planck and the Joint Dark Energy Mission.

1 Introduction

One of the defining challenges for modern cosmology is understanding the physical mechanism responsible for the accelerating expansion of the Universe^{1,2}. The origin of the cosmic acceleration can be due to a new source of stress-energy, called “dark energy”, a modified theory of gravity, or some mixture of both³.

In the absence of a well-defined and theoretically motivated model for dark energy, it is generally assumed that the dark energy equation of state (the ratio of pressure to energy density) evolves with redshift with an arbitrary functional form. Common parameterizations include a linear variation, $w(z) = w_0 + w_z z$ ⁴, or an evolution that asymptotes to a constant w at high redshift, $w(z) = w_0 + w_a z/(1+z)$ ^{5,6}. However, given our complete ignorance of the underlying physical processes, it is advisable to approach our analysis of dark energy with a minimum of assumptions. Fixing an ad hoc two parameter form could lead to bias in our inference of the dark energy properties.

In this paper we measure the evolution history of the dark energy using a flexible and almost completely model independent approach, based on a variant of the principal component analysis (PCA) introduced in Huterer (2003)⁷; in order to be conservative, we begin by using data we determine the equation only from geometric probes of dark energy, namely the cosmic microwave background radiation (CMB), Type Ia supernovae (SNe) and baryon acoustic oscillation data (BAO). We perform a full likelihood analysis using the Markov Chain Monte Carlo approach⁸. We then consider constraints on $w(z)$ from a larger combination of datasets, including probes of the growth of cosmological perturbations, such as large scale structure (LSS) data. An important consideration for such an analysis is to properly take into account dark energy perturbations, and we make use of the prescription introduced in⁹. This method implements a Parameterized Post-Friedmann (PPF) prescription for the dark energy perturbations following¹⁰.

2 Analysis and results

The method we use to constrain the dark energy evolution is based on a modified version of the publicly available Markov Chain Monte Carlo package CosmoMC⁸, with a convergence diagnostics based on the Gelman-Rubin criterion¹². We consider a flat cosmological model described by the following set of parameters:

$$\{w_i, \omega_b, \omega_c, \Theta_s, \tau, n_s, \log[10^{10} A_s]\} , \quad (1)$$

where ω_b ($\equiv \Omega_b h^2$) and ω_c ($\equiv \Omega_c h^2$) are the physical baryon and cold dark matter densities relative to the critical density, Θ_s is the ratio of the sound horizon to the angular diameter distance at decoupling, τ is the optical depth to re-ionization, and A_s and n_s are the amplitude of the primordial spectrum and the spectral index, respectively. We bin the dark energy equation of state in five redshift bins, $w_i(z)$ ($i = 1, 2, \dots, 5$), representing the value at five redshifts, $z_i \in [0.0, 0.25, 0.50, 0.75, 1.0]$ and, for $z > 1$, we fix the equation of state parameter at its $z = 1$ value, since we find that current data place only weak constraints on $w(z)$ for $z > 1$. To summarize, our parameterization is given by:

$$w(z) = \begin{cases} w(z=1), & z > 1; \\ w_i, & z \leq z_{max}, z \in \{z_i\}; \\ \text{spline}, & z \leq z_{max}, z \notin \{z_i\}. \end{cases} \quad (2)$$

Finally, we follow¹¹ to determine uncorrelated estimates of the dark energy parameters. For the CMB, we use data and likelihood code from the WMAP team's 5-year release¹³ (both temperature TT and polarization TE; we will refer to this analysis as WMAP5). We also checked that results don't change if we use the latest data release from WMAP¹⁴. Supernova data come from the Union data set (UNION) produced by the Supernova Cosmology Project¹⁵; however, to check the consistency of our results, we also used the recently released Constitution dataset (Constitution)¹⁸ which, with 397 Type Ia supernovae, is the largest sample to date. We also used the latest SDSS release (DR7) BAO distance scale^{16,17}. Weak lensing (WL) data are taken from CFHTLS²² and we use the weak lensing module provided in^{19,20}, with some modifications to assess the likelihood in terms of the variance of the aperture mass (Eq. 5 of²²) with the full covariance matrix²¹. The cross-correlation between CMB and galaxy survey data is employed using the public code at²³. We modify it to take into account the temporal evolution of the dark energy equation of state, since the code only considers w CDM cosmologies. We refer to^{24,25} for a description of both the methodology and the datasets used. Finally, we use the recent value of the Hubble constant from the SHOES (Supernovae and H_0 for the Equation of State) program, $H_0 = 74.2 \pm 3.6 \text{ km s}^{-1} \text{ Mpc}^{-1}$ (1σ)²⁶. We also incorporate baryon density information from Big Bang Nucleosynthesis $\Omega_b h^2 = 0.022 \pm 0.002$ (1σ)²⁷, as well as a top-hat prior on the age of the Universe, $10 \text{ Gyr} < t_0 < 20 \text{ Gyr}$.

As we can see from Fig. 1, all values are compatible with a cosmological constant ($w = -1$) at the 2σ level; in particular, there is no discrepancy between the Union and Constitution datasets. Moreover, as we can see from Fig. 2, the addition of cosmological probes of cosmic clustering noticeably reduces the uncertainty in the determination of the dark energy parameters, especially at high redshifts.

To reinforce our conclusions, we also created several mock datasets for upcoming and future SN, BAO, and CMB experiments. The quality of future datasets allows us to constrain the dark energy evolution beyond redshift $z = 1$. We thus consider an additional bin at $z = 1.7$, with a similar constraint: $w(z > 1.7) = w(z = 1.7)$. We consider a mock catalog of 2,298 SNe, with 300 SNe uniformly distributed out to $z = 0.1$, as expected from ground-based low redshift samples, and an additional 1998 SNe binned in 32 redshift bins in the range $0.1 < z < 1.7$, as

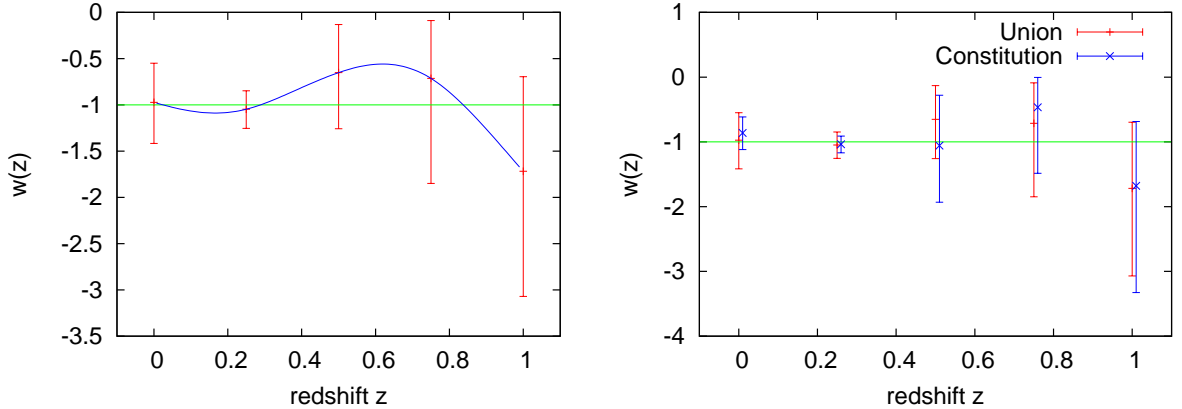


Figure 1: Left: uncorrelated constraints on the dark equation of state parameters using WMAP+UNION+BAO. Right: comparison between WMAP+UNION+BAO and WMAP+Constitution+BAO; the points for the Constitution dataset have been slightly shifted to facilitate comparison between the two cases: we find no significant difference between UNION and Constitution.

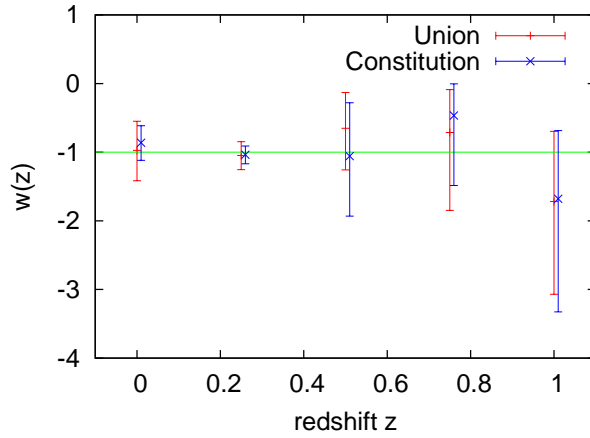


Figure 2: Results using data from a “global” dataset which includes WMAP+UNION+BAO+WL+ISW+LSS; error bars are at 2σ .

expected from JDEM or similar future surveys²⁸. The error in the distance modulus for each SN is given by the intrinsic error, $\sigma_{\text{int}} = 0.1$ mag. In addition, we use a mock catalog of 13 BAO estimates, including 2 BAO estimates at $z = 0.2$ and $z = 0.35$, with 6% and 4.7% uncertainties (in D_V), respectively, 4 BAO constraints at $z = [0.6, 0.8, 1.0, 1.2]$ with corresponding fiducial survey precisions (in D_V) of [1.9, 1.5, 1.0, 0.9]% (V5N5 from²⁹), and 7 BAO estimates with precision [0.36, 0.33, 0.34, 0.33, 0.31, 0.33, 0.32]% from $z = 1.05$ to $z = 1.65$ in steps of 0.1³⁰.

We simulate Planck data using a fiducial Λ CDM model, with the best fit parameters from WMAP5, and noise properties consistent with a combination of the Planck 100–143–217 GHz channels of the HFI³¹, and fitting for temperature and polarization using the full-sky likelihood function given in³². In addition, we use the same priors on the Hubble parameter and on the baryon density as considered above. As can be seen from Table 1 and Figure 3, future data will reduce the uncertainties in w_i by a factor of at least 2, with the relative uncertainty below 10% in all but the last bin (at $z = 1.7$).

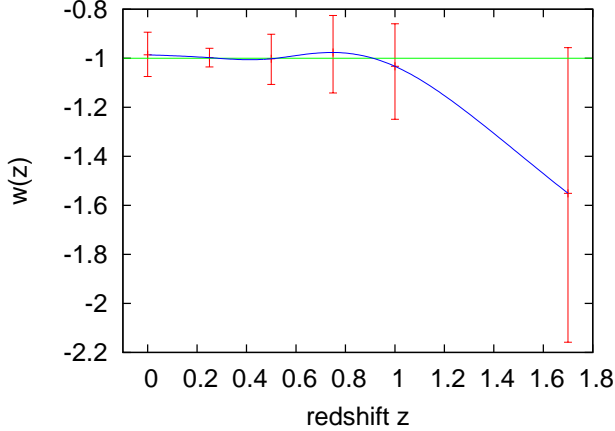


Figure 3: Uncorrelated constraints on the dark energy equation of state parameters, for mock datasets from Planck and JDEM; error bars are at 2σ .

3 Conclusions

One of the main tasks for present and future dark energy surveys is to determine whether or not the dark energy density is evolving with time.

We have performed a global analysis of the latest cosmological datasets and have constrained the dark energy equation of state using a very flexible and almost model independent parameterization. We determine the equation of state $w(z)$ in five independent redshift bins, incorporating the effects of dark energy perturbations. We find no evidence for a temporal evolution of dark energy—*the data is completely consistent with a cosmological constant*. This agrees with most previous results, but significantly improves the overall constraints. We show that future experiments, such as Planck or JDEM, will be able to reduce the uncertainty on $w(z)$ to less than 10% in multiple redshift bins, thereby mapping any temporal evolution of dark energy with high precision. With this data it will be possible to measure the temporal derivative of the equation of state parameters, dw/dz , useful in discriminating between two broad classes of “thawing” and “freezing” models³³.

References

1. A. G. Riess *et al.* [Supernova Search Team Collaboration], Astron. J. **116**, 1009 (1998).
2. S. Perlmutter *et al.* [Supernova Cosmology Project Collaboration], Astrophys. J. **517**, 565 (1999).
3. J. P. Uzan, Gen. Rel. Grav. **39**, 307 (2007).
4. A. .R. Cooray and D. Huterer, Astrophys. J. **513**, L95 (1999).
5. M. Chevallier and D. Polarski, Int. J. Mod. Phys. D, **10**, 213 (2001).
6. E. V. Linder, Phys. Rev. Lett. **90**, 091301 (2003).
7. D. Huterer and G. Starkman, Phys. Rev. Lett. **90**, 031301 (2003).
8. A. Lewis and S. Bridle, Phys. Rev. D **66**, 103511 (2002), Available at cosmologist.info.
9. W. Fang, W. Hu and A. Lewis, Phys. Rev. D **78**: 087303 (2008).
10. W. Hu and I. Sawicki, Phys. Rev. D **76**:104043,2007.
11. D. Huterer and A. .R. Cooray, Phys. Rev. D **71**:023506, (2005).
12. A. Gelman and D. B. Rubin, Statistical Science, 7, 457-472 (1992).
13. J. Dunkley *et al.* [WMAP collaboration], Astrophys.J. 701:1804-1813, 2009.
14. E. Komatsu *et al.* [WMAP collaboration], [[arXiv:astro-ph/1001.4538](https://arxiv.org/abs/1001.4538)], submitted to Astrophysical Journal Supplement Series.

15. M. Kowalski *et al.*, *Astrophys. J.* **686**:749-778,2008.
16. B. A. Reid *et al.*,[SDSS collaboration], *MNRAS*, Vol. **404** Issue 1, Pages 60-85.
17. W. J. Percival *et al.* [SDSS collaboration], *MNRAS*, Vol **401**, Issue 4, pp. 2148-2168.
18. M. Hicken *et al.*, *Astrophys. J.* **700**: 331-357,2009.
19. R. Massey *et al.*, *Astrophys. J. Suppl.* **172**:239-253,2007.
20. J. Lesgourgues *et al.*, *JCAP* **0711**, 008 (2007).
21. M. Kilbinger, private communication (2008).
22. L. Fu *et al.*, *Astron. Astrophys.* **479**:9-25,2008.
23. see <http://www.astro.princeton.edu/~shirley/ISWWL.html>.
24. S. Ho *et al.*, *Phys. Rev. D* **78**:043519, (2008).
25. C. Hirata *et al.*, *Phys. Rev. D* **78**:043520, (2008).
26. A. G. Riess *et al.*, *Astrophys. J.*, **699**, 539 (2009).
27. S. Burles, K. M. Nollett and M. S. Turner, *Astrophys. J.* **552**: L1, 2001.
28. A. G. Kim *et al.* 2004, *MNRAS*, 347, 909.
29. H-J. Seo and D. J. Eisenstein, *Astrophys. J.* **598**, 720 (2003).
30. A. Riess (private communication).
31. Planck collaboration, [[arXiv:astro-ph/0604069](https://arxiv.org/abs/astro-ph/0604069)].
32. A. Lewis, *Phys. Rev. D* **71**: 083008, (2005).
33. R. R. Caldwell and M. Kamionkowski, *Ann. Rev. Nucl. Part. Sci.* **59**:397-429,2009.

THE GAMMA-RAY VIEW OF THE EXTRAGALACTIC BACKGROUND LIGHT

J. D. Finke^{1,2} for the *Fermi*-LAT Collaboration

¹ *U.S. Naval Research Laboratory, Space Science Division, Code 7653, 4555 Overlook Ave. SW, Washington, DC, 20375 USA*

² *NRL/NRC Research Associate*

The Extragalactic Background Light (EBL) from the infrared (IR) through the ultraviolet (UV) is dominated by emission from stars, either directly or through absorption and reradiation by dust. It can thus give information on the star formation history of the universe. However, it is difficult to measure directly due to foreground radiation fields from the Galaxy and solar system. Gamma-rays from extragalactic sources at cosmological distances (blazars and gamma-ray bursts) interact with EBL photons creating electron-positron pairs, absorbing the gamma-rays. Given the intrinsic gamma-ray spectrum of a source and its redshift, the EBL can in principle be measured. However, the intrinsic gamma-ray spectra of blazars and GRBs can vary considerably from source to source and the from the same source over short timescales. A maximum intrinsic spectrum can be assumed from theoretical grounds, to give upper limits on the EBL absorption from blazars at low redshift with very high energy (VHE) gamma-ray observations with ground-based Atmospheric Cherenkov telescopes. The *Fermi*-LAT observations of blazars and GRBs can probe EBL absorption at higher redshifts. The lower energy portion of the LAT spectrum of these sources is unattenuated by the EBL, so that extrapolating this to higher energies can give the maximum intrinsic spectrum for a source. Comparing this to the observed higher energy LAT spectrum will then give upper limits on the EBL absorption. For blazars which have been detected by both the *Fermi*-LAT and at higher energies by Cherenkov telescopes, combined LAT-VHE observations can put more stringent constraints on the low redshift EBL. These procedures above can also be reversed: for sources with an unknown redshift, a given EBL model and gamma-ray spectrum can lead to an upper limit on the source's redshift.

1 Introduction

The night sky appears dark to the naked eye, but in fact glows faintly in the IR through the optical and UV. At these wavelengths, the background light is dominated by emission from the atmosphere, solar system, and Milky Way. There is also a much smaller extragalactic component from all of the stars which have ever existed, through direct emission (in the UV-optical) and through absorption and reradiation by dust (in the IR). Due to the weakness of this extragalactic background light (EBL) to other components, direct measurement of the EBL is extremely difficult ^{1,2,3}. The other background components can be avoided to some extent by using instruments on spacecraft which have left the atmosphere ^{1,4} or the solar system ^{5,6}. However, it is unlikely that spacecraft will leave our Galaxy in the near future, so uncertainties in direct measurements will remain. Number counts in the IR and optical can be used to find EBL lower limits ^{7,8}, as discussed by Beelen and Penin in these proceedings. Modeling ^{9,10,11,12,13} has been an important tool for constraining the EBL intensity and tying it to basic astrophysics

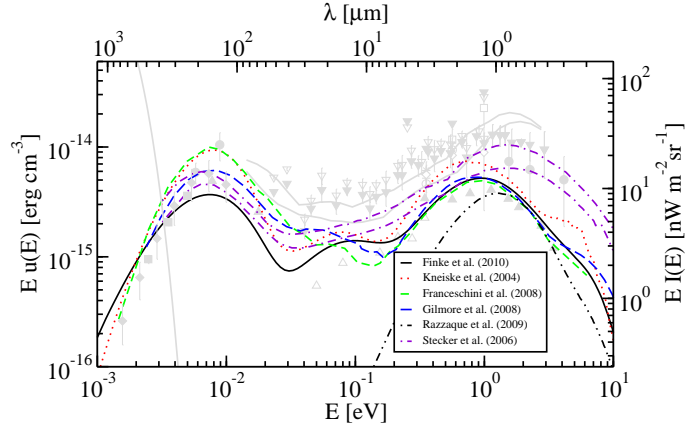


Figure 1: EBL models, measurements, and constraints. See Finke *et al.* for details and references.

such as the star formation rate density, dust absorption, initial mass function, cosmological expansion rate, and others. Fig. 1 shows many EBL measurements, constraints and models, and Hauser & Dwek¹⁴ present a thorough review.

The EBL photons interact with γ -rays from cosmological sources to produce e^+e^- pairs, absorbing the γ -rays so that the observed flux $F_{obs}(E) = F_{int}(E) \exp[-\tau_{\gamma\gamma}(E)]$ where $F_{int}(E)$ is the unabsorbed source flux as a function of observed energy E , and $\tau_{\gamma\gamma}(E)$ is the EBL absorption optical depth. If $F_{int}(E)$ is known, a measurement of the observed γ -ray spectrum from these sources can be used to probe the EBL. The intrinsic spectrum is not generally known, however it is possible to determine an upper limit either from theory or from extrapolating a lower energy, unattenuated spectrum to higher energies. This is discussed further in the next sections. From the upper limit on $F_{int}(E)$ and the measurement of $F_{obs}(E)$ with a γ -ray telescope, an upper limit on $\tau_{\gamma\gamma}(E)$ can be calculated and compared to theoretical predictions.

2 Constraints with Atmospheric Cherenkov Telescopes

Nearby blazars—active galactic nuclei with relativistic jets pointed along our line of sight—are γ -ray-emitting sources up to VHE energies and are located at cosmological distances. They are thus a good candidate for constraining the EBL by measuring their γ -ray attenuation. Atmospheric Cherenkov telescopes (ACTs) such as HESS, MAGIC, and VERITAS detect γ -rays through the Cherenkov radiation from particle cascades produced by γ -rays interacting with the Earth’s atmosphere. TeV blazars are located nearby and VHE γ -rays are generally attenuated by the mid-IR EBL. Although they seem to be persistent sources, they are highly variable and the intrinsic spectrum cannot be determined. However, theory allows the determination of a maximum possible intrinsic spectrum. Assuming the γ -rays are produced by Compton scattering off of electrons accelerated by naïve test particle acceleration theory, the hardest possible photon index will be $\Gamma_{int,max} = 1.5$ where the photon flux is $dN/dE \propto E^{-\Gamma}$. Using this, results from several blazars (e.g. 1ES 1011-232¹⁵, 1ES 0229+200¹⁶, 3C 279¹⁷) have ruled out high levels of the IR EBL. However, physical mechanisms have been suggested to produce intrinsic VHE γ -ray spectra harder than $\Gamma = 1.5$ ^{18,19,20}. Without a strong constraint on $F_{int}(E)$, the constraining upper limits on the EBL intensity are not well-accepted by some in the community.

3 Constraints with the *Fermi*-LAT

Higher z sources can be probed in the GeV range using the *Fermi* telescope. The *Fermi* Gamma-Ray Space Telescope’s primary instrument, the Large Area Telescope (LAT) is a pair conversion

detector which surveys the entire sky every three hours in the 20 MeV to 300 GeV range²¹. Sources located at higher z will have their VHE γ -ray spectrum completely absorbed; however, in the range accessible by the LAT, these sources will have their spectra attenuated by optical-UV EBL photons, yet not so attenuated that they cannot be observed. Approximately 600 blazars are listed in the first year LAT AGN catalog²². Unfortunately, many of these exhibit intrinsic spectral breaks and do not have many photons ≥ 10 GeV needed to probe the EBL²³. Using statistics of the LAT blazars, as suggested by Chen *et al.*²⁴ is thus not possible²⁵. However, a smaller sample of blazars do not exhibit spectral breaks and do have high energy photons, and these can be used to probe the EBL on a case-by-case basis. Additionally, 6 Gamma-Ray Bursts (GRBs)^a with measured redshifts have been detected by the LAT as of this writing (2010 May 13). Together, these blazars and GRBs can be used to constrain EBL models.

Abdo *et al.*²⁵ use two methods to do this: the highest energy photon (HEP) method and the Likelihood Ratio Test (LRT) method. Both of these techniques make use of the fact that below 10 GeV, all EBL models predict essentially no attenuation. This lower energy spectrum can be extrapolated to higher energies to give the maximum possible intrinsic spectrum, which can then be compared to the observed LAT spectrum at > 10 GeV. The HEP method uses a Monte Carlo simulation to randomly draw the highest energy photon from a distribution created with the extrapolated 0.1–10 GeV spectrum and a particular EBL model. Repeating this many times builds up a distribution of HEPs which can be compared to the actual HEP observed from a source to give the probability of rejecting the particular EBL model used. The LRT technique assumes as a null-hypothesis the extrapolated 0.1–10 GeV spectrum and a certain EBL model. A fit is then performed with the normalization of this EBL model’s opacity as a free parameter. From the likelihood ratio of these two fits, Wilks’ theorem can be used to determine the probability of rejecting the null hypothesis, which is essentially the probability of rejecting the EBL model being tested.

Combining the results from several sources, the Stecker *et al.*¹⁰ baseline model is rejected with a high significance. It should be noted however that this rejection is only applicable to the UV; at the mid-IR and longer wavelengths, the model predictions are still viable. The Stecker *et al.* fast evolution model predicts a greater opacity than their baseline model, and is rejected at an even greater significance. All other EBL models tested by Abdo *et al.*²⁵ are allowed.

An additional way of using the LAT to constrain the EBL has been suggested: using the Compton-scattering of the EBL in the lobes of radio galaxies²⁷. The recent detection of the giant lobes of the nearby radio galaxy Cen A by the LAT²⁶ demonstrates the feasibility of this method, since Compton-scattering of the cosmic microwave background alone cannot explain this emission. Georganopoulos *et al.*²⁷ suggest the well-constrained lobes of Fornax A would be an ideal candidate for this technique.

4 Constraints Combining ACTs and the LAT

The problems with theoretical uncertainties in the intrinsic VHE γ -ray spectra of blazars (§ 2) can be sidestepped by using the *Fermi*-LAT. The LAT spectrum can be extrapolated into the TeV range, giving the maximum possible TeV spectrum, assuming that the γ -ray spectrum of a blazar would be concave upwards. This technique has been used by Georganopoulos *et al.*²⁸ with the blazar 1ES 1218+304 to reject the Stecker *et al.*¹⁰ baseline and fast evolution models with 2.6σ and 4.7σ significance, respectively, and the “best fit” models of Kneiske *et al.*⁹ with a 2.9σ significance. Future applications of this technique to combined LAT-ACT observations could give even stronger constraints.

The opposite of this technique can also be used to constrain the redshift of a blazar for which it is unknown. Assuming a certain model for the EBL, the VHE spectrum of a source can be

^aBrief, beamed γ -ray emission from exploding stars.

deabsorbed until it is at a higher level than the extrapolated LAT spectrum. This technique has been used to constrain $z < 0.75$ for PG 1553+113²⁹ and $z < 0.66$ for PKS 1424+240³⁰.

Acknowledgments

The *Fermi* LAT Collaboration acknowledges generous ongoing support from a number of agencies and institutes that have supported both the development and the operation of the LAT as well as scientific data analysis. These include the National Aeronautics and Space Administration and the Department of Energy in the United States, the Commissariat à l'Energie Atomique and the Centre National de la Recherche Scientifique / Institut National de Physique Nucléaire et de Physique des Particules in France, the Agenzia Spaziale Italiana and the Istituto Nazionale di Fisica Nucleare in Italy, the Ministry of Education, Culture, Sports, Science and Technology (MEXT), High Energy Accelerator Research Organization (KEK) and Japan Aerospace Exploration Agency (JAXA) in Japan, and the K.A. Wallenberg Foundation, the Swedish Research Council and the Swedish National Space Board in Sweden.

References

1. R.A. Bernstein, W.L. Freedman, & B.F. Madore, *Astrophys. J.* **571**, 107 (2002)
2. K. Mattila, *Astrophys. J.* **591**, 119 (2003)
3. R.A. Bernstein, *Astrophys. J.* **666**, 663 (2007)
4. M.G. Hauser *et al.*, *Astrophys. J.* **508**, 25 (1998)
5. G.N. Toller, *Astrophys. J. Lett.* **266**, L79 (1983)
6. J. Edelstein, S. Bowyer, & M. Lampton, *Astrophys. J.* **539**, 187 (2000)
7. P. Madau & L. Pozzetti, *MNRAS* **312**, L9 (2000)
8. G. Marsden *et al.*, *Astrophys. J.* **707**, 1729 (2009)
9. T.M. Kneiske *et al.*, *Astro. & Astrophys.* **413**, 807 (2004)
10. F.W. Stecker, M.A. Malkan, & S.T. Scully, *Astrophys. J.* **648**, 774 (2006)
11. A. Franceschini, G. Rodighiero, & M. Vaccari, *Astro. & Astrophys.* **487**, 837 (2008)
12. R.C. Gilmore *et al.*, *MNRAS* **399**, 1694 (2009)
13. J.D. Finke, S. Razzaque, & C.D. Dermer, *Astrophys. J.* **712**, 238 (2010)
14. M.G. Hauser & E. Dwek, *An. Rev. Astro. & Astrophys.* **39**, 249 (2001)
15. F. Aharonian *et al.*, *Nature* **440**, 1018 (2006)
16. F. Aharonian *et al.*, *Astro. & Astrophys.* **475**, L9 (2007)
17. J. Albert *et al.*, *Science* **320**, 1752 (2008)
18. F.W. Stecker, M.G. Baring, & E.J. Summerlin, *Astrophys. J. Lett.* **667**, L29 (2007)
19. M. Böttcher, C.D. Dermer, & J.D. Finke, *Astrophys. J. Lett.* **679**, L9 (2008)
20. F.A. Aharonian, D. Khangulyan, & L. Costamante, *MNRAS* **387**, 1206 (2008)
21. W.B. Atwood *et al.*, *Astrophys. J.* **697**, 1071 (2009)
22. A. Abdo *et al.*, *Astrophys. J.* **715**, 429 (2010)
23. A.A. Abdo *et al.*, *Astrophys. J.* **710**, 1271 (2010)
24. A. Chen, L.C. Reyes, & S. Ritz, *Astrophys. J.* **608**, 686 (2004)
25. A. Abdo *et al.*, *Astrophys. J.*, submitted, arXiv:1005.1003, (2010)
26. A. Abdo *et al.*, *Science* **328**, 725 (2010)
27. M. Georganopoulos *et al.*, *Astrophys. J. Lett.* **686**, L5 (2008)
28. M. Georganopoulos, J.D. Finke, & L.C. Reyes, *Astrophys. J. Lett.* **714**, L157 (2010)
29. A.A. Abdo, *et al.*, *Astrophys. J.* **708**, 1310 (2010)
30. V.A. Acciari *et al.*, *Astrophys. J. Lett.* **708**, L100 (2010)

Constraints on the linear fluctuation growth rate from future surveys

Cinzia Di Porto

Università degli Studi “Roma Tre”, Dip. di Fisica, via della Vasca Navale 84, 00146, Roma, Italy

Luca Amendola

Inst. Theor. Phys., U. Heidelberg, Philosophenweg 16, 69120 Heidelberg, Germany and INAF/Roma

Many experiments in the near future will test dark energy through its effects on the linear growth of matter perturbations. In this paper we discuss the constraints that future large-scale redshift survey experiments can put on three different parametrizations of the linear growth factor and how these constraints will help ruling out dark energy models.

Many years since its first discovery^{1,2} the evidence for dark energy (DE) still rests primarily on background quantities like the luminosity distance and the angular diameter distance^{3,4,5}. The cross-correlation of the integrated Sachs-Wolfe effect with the large scale structure yielded an independent proof of the existence of dark energy that relies on the linear growth of the gravitational potential⁶. In the future, galaxy and Lyman- α power spectra at high redshift and weak lensing surveys from ground and from space will offer the opportunity to test competing dark energy models to a very high precision using a mix of background, linear and non-linear indicators. We aim to find the constraints that future surveys can put on cosmological parameters through the information contained in the power spectrum.

In order to constrain the parameters, we use the Fisher matrix method, an approximation to the likelihood function that provides under some conditions the minimal errors that a given experiment may attain.

Following Eisenstein *et al.*⁷ we estimate the observed power spectrum at redshift z in any cosmology which will depend on a number of parameters such as the matter and baryon fraction, Ω_m and Ω_b , the spectral tilt n_s , the growth index γ , the dark energy equation of state w , etc. In addition we adopt redshift dependent parameters such as the growth factor $G(z)$, the angular diameter distance $D(z)$, a scale-independent offset due to incomplete removal of shot-noise $P_s(z)$, the redshift distortion parameter $\beta(z)$ and the bias $b(z)$, assumed to be independent in each redshift bin. Then we calculate, numerically or analitically, the derivatives of the spectrum respect to the parameters, evaluated at a fiducial model that we assume to be the standard Λ CDM. Finally we obtain the Fisher matrix⁸ which depends on $n(z)$, the number density of galaxies expected to be observed in every redshift bin.

For what concerns the bias, we assumed a fiducial constant bias, $b(z) = 1$ in each redshift bin but we also tested that a different choice, $b(z) = \sqrt{1+z}$, does not seriously affect our results.

The future surveys we consider in this work represent realistic large-scale surveys of the next decade, as for instance Euclid⁹. In particular we adopt for $n(z)$ the values in Tab. 1 where the n_1, n_2, n_3 are the expected observable galaxy number densities for three different flux limits ($5,4$ and $3 \cdot 10^{-16}$ erg m $^{-2}$ s $^{-1}$) and a conservative choice for the luminosity function at $z < 2$. The survey area is 20000 deg 2 and we assume two different values for the efficiency (the spectroscopic redshift success rate): $\varepsilon_{1,2} = 0.3, 0.5$. So we defined and analyzed three different cases: a “reference case” with $n(z) = \varepsilon_2 \cdot n_2(z)$, an “optimistic case” $n(z) = \varepsilon_2 \cdot n_1(z)$ and a “pessimistic case” $n(z) = \varepsilon_1 \cdot n_3(z)$.

We also analyzed three different parametrizations. First, we estimated the errors on the growth rate s , defined as $s = d \ln \delta_m / d \ln a$, where a is the scale factor, related to the redshift by the equation $a = 1/(1+z)$. Since $s(z)$ is degenerate with $b(z)$, in this case we were forced to assume an external arbitrary constraint on $b(z)$. We call this the s -parametrization.

Then we assumed

Table 1: Expected galaxy number densities for Euclid survey.

z	0.5-0.7	0.7-0.9	0.9-1.1	1.1-1.3	1.3-1.5	1.5-1.7	1.7-1.9	1.9-2.1
$10^3 \cdot n_1(z)$	4.69	3.33	2.57	2.1	1.52	0.92	0.54	0.31
$10^3 \cdot n_2(z)$	3.56	2.42	1.81	1.44	0.99	0.55	0.29	0.15
$10^3 \cdot n_3(z)$	2.8	1.84	1.33	1.03	0.68	0.35	0.17	0.08

$$s \equiv \Omega_m(z)^\gamma , \quad (1)$$

where the the matter density parameter follows the standard Λ CDM evolution. However, this usual parametrization of the growth factor can describe only a set of dark energy models so we decided to use a more general γ index, with an explicit dependence on the redshift, which can be parameterized as

$$\gamma(z) = \gamma_0 + \gamma_1 \frac{z}{1+z} ; \quad (2)$$

we denote this as the γ parametrization. As pointed out by Wu *et al.*¹⁰, this parametrization is more accurate than that of eq. (1) for both Λ CDM and DGP models. Furthermore, γ_1 is negative for dark energy models with a constant equation of state, lying in the range $-0.021 < \gamma_1 < -0.015$ (for $0.2 < \Omega_m < 0.35$ and $-1.2 < w < 0.8$) and positive for the DGP model ($0.042 > \gamma_1 > 0.035$ for $0.2 < \Omega_m < 0.35$), thus providing another signature to discriminate them. Moreover, even if the constant growth index parametrization is very simple and useful for several models, γ evolves with time in modified gravity theories in general¹¹.

Finally, we explored a parametrization more suitable to models where perturbations grow faster than they do in Λ CDM, as for instance in models where there is a coupling between dark energy and dark matter. For those models we found that a better parametrization is given by

$$s \equiv \Omega_m(z)^\gamma (1 - \eta) . \quad (3)$$

We denote this as the η -parametrization. As shown by Di Porto and Amendola¹², in the coupled quintessence model the numerical solution for the growth rate can be fitted by the formula (3), with $\eta = c\beta_c$, where β_c is the dark energy-dark matter coupling constant. The best fit values are $\gamma = 0.56$ and $c = 2.1$, thus constraints for η can be transformed into constraints over β_c .

For the equation of state of the dark energy we used the Chevallier-Polarski-Linder (CPL) parametrization

$$w(z) = w_0 + w_1 \frac{z}{1+z} . \quad (4)$$

As a further case we also considered constant γ and w .

For the case of the s -parametrization, after we have calculated the Fisher matrix, we marginalize over all parameters but the 8 $\beta(z)$'s, thus obtaining their marginalized errors. Note that the fiducial $\beta(z)$'s values are computed through $\beta(z) = \Omega_m(z)^\gamma / b(z)$. Now we can transform to the growth rates parameters $s(z) = \beta(z) \cdot b(z)$ and assuming for the $b(z)$'s arbitrary errors of 1% and 10% we can compute, through standard error propagation, the errors over $s(z)$. Results are shown in Fig. 1.

Now we explicit the dependence of the growth factor and the distortion parameter on the growth index γ , through the relations (1) and $\beta(z) = s(z)/b(z)$, while $\Omega_m(z)$ and $D(z)$ depend on w . As a first case we consider constant γ and w and we draw their marginalized probability regions at 1 and 2σ levels (left panel of Fig. 2). If we use instead of constant γ and w their z -dependent parametrizations (2), (4) and marginalize over the parameters γ_1 and w_1 , the ellipses will obviously expand. This is shown in Fig. 3. Using the γ parametrizations (2) we can also

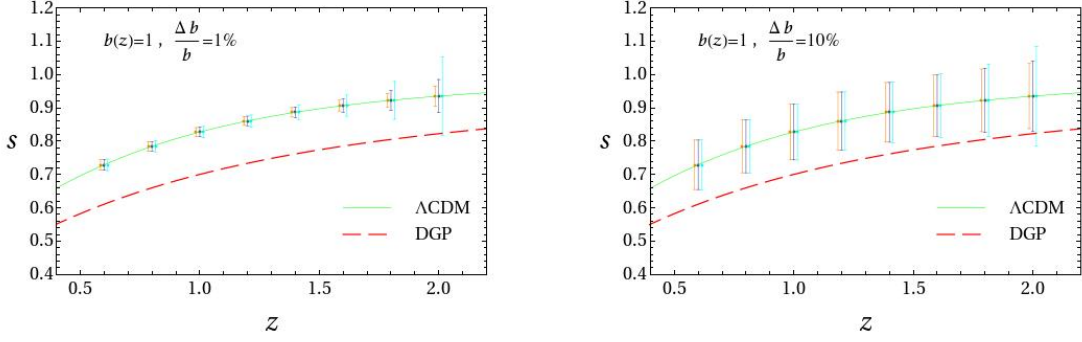


Figure 1: Expected constraints on the growth rates in each redshift bin, assuming for the bias a relative error of 1% (left panel) and 10% (right panel). For each z the central error bars refer to the reference case while those referring to the optimistic and pessimistic case have been shifted by -0.015 and +0.015 respectively. The growth rates for two different models such as the fiducial Λ CDM (green solid curve) and the DGP (red dashed curve) are also plotted. The errors bars are obviously centered on the fiducial model, but one can see that, even in the case of large errors (10%) for the bias values, it will be possible to distinguish these models with next generation data.

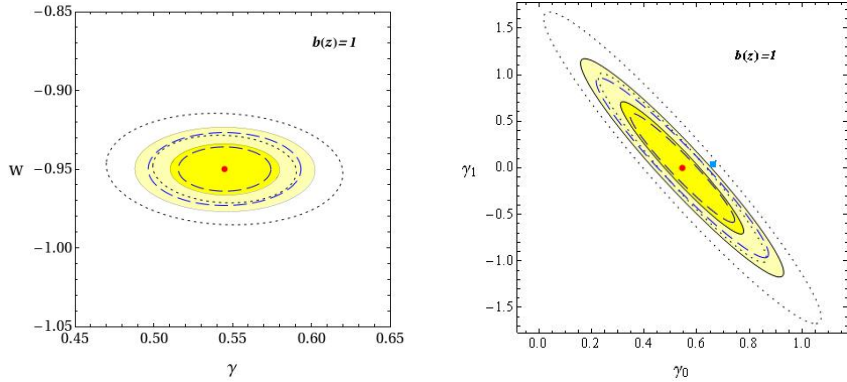


Figure 2: 1 and 2σ marginalized probability regions for constant γ and w (left panel) and for the parameters γ_0 and γ_1 (right panel) in the γ -parametrization, relative to the reference case (shaded yellow regions), to the optimistic case (blue long-dashed ellipses), and to the pessimistic case (black dotted ellipses). Red dots represent the fiducial model; the flat DGP model is not marked in the left panel being far outside the ellipses ($\gamma = 0.68$, $w=-0.8$) while is represented by the blue square in the right panel. Then, in the case of γ -parametrization, one could distinguish these two models only in the reference and in the optimistic case.

project the probability regions for the parameters γ_0 and γ_1 (right panel of Fig. 2) and calculate their marginalized errors (Tab. 2) and obviously we can do the same for the η parametrizations (3), drawing the marginalized probability ellipses for the parameters γ and η (left panel of Fig. 4); comparing their marginalized errors to those obtained using present data (right panel of Fig. 4), we found that the constraints will improve at least by a factor 10 for γ and 2 for η (further details in Amendola and Di Porto, in preparation).

In this work we showed how future deep and wide surveys will be able to put tight constraints on the cosmological parameters, in particular on the quantities related to the growth of matter perturbations, and how they will help to distinguish dark energy models with very different physical origins such as the Λ CDM and the DGP, now degenerate respect to present data.

CDP wishes to thank the organizers of the 45th Rencontres de Moriond for partial support.

References

1. A. G. Riess *et al.*, Astron. J. **116** 1009 (1998), astro-ph/9805201

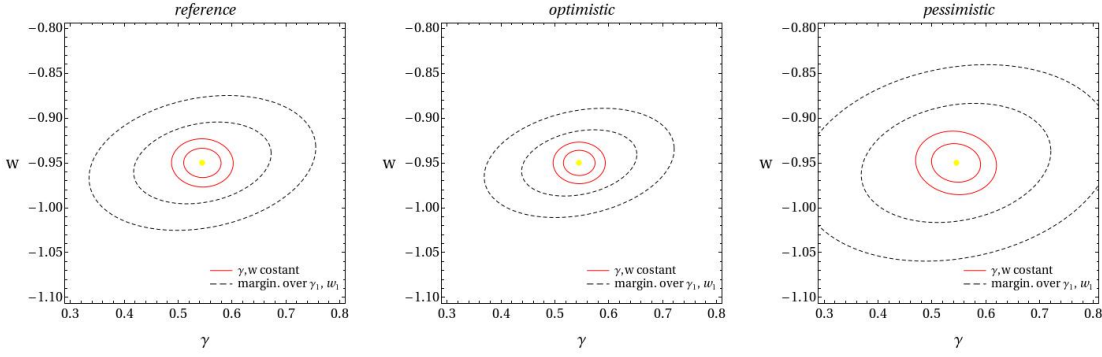


Figure 3: 1 and 2σ marginalized probability regions obtained assuming constant γ and w (red solid curves) or assuming the parametrizations (2),(4) and marginalizing over γ_1 and w_1 (black dashed curves); marginalized error values are in columns σ_{γ_m} , σ_{w_m} of Tab. 2. Yellow dots represent the fiducial model.

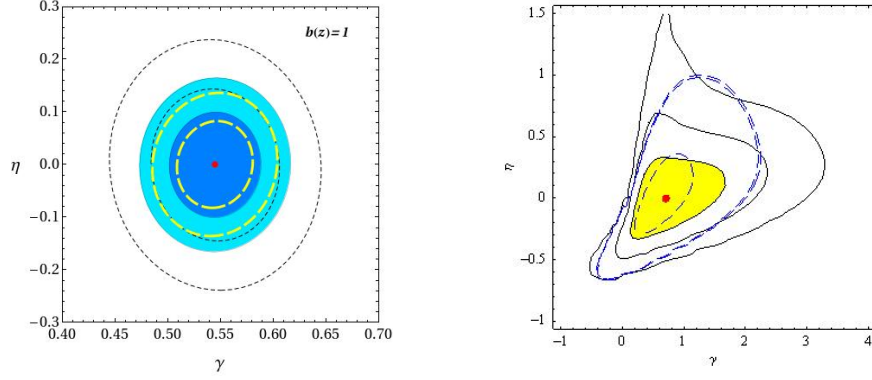


Figure 4: left panel: 1 and 2σ marginalized probability regions for the parameters γ and η in eq.3 relative to the reference case (shaded blue regions), to the optimistic case (yellow long-dashed ellipses) and to the pessimistic case (black short-dashed ellipses); the red dot is the fiducial model. Right panel: present constraints on γ and η computed through a full likelihood method (here the red dot marks the likelihood peak)¹²; long-dashed contours are obtained assuming a prior for $\Omega_{m,0}$.

2. S. Perlmutter *et al.*, *Astrophys. J.* **517** 565 (1999), astro-ph/9812133
3. P. Astier *et al.*, *Astron. Astrophys.* **447** 31 (2006)
4. D. N. Spergel *et al.* [WMAP collaboration] *ApJS* **170** 377, (2007), astro-ph/0603449
5. D. Eisenstein *et al.* [SDSS collaboration] *Astrophys. J.* **633**, 560 (2005) astro-ph/0501171
6. S. Boughn and R. Crittenden, *Nature*, 427, 45 (2004)
7. D. Eisenstein *et al.*, *The Astrophysical Journal*, 664:660Y674, 2007
8. M. Tegmark, *Phys. Rev. Lett.* 79, 3806–3809 (1997)
9. Euclid yellow book, <http://sci.esa.int/science-e/www/object/index.cfm?fobjectid=46176>
10. P. Wu *et al.* *JCAP06*(2009)019
11. R. Gannouji *et al.* *JCAP02*(2009)034
12. C. Di Porto & L. Amendola, *Phys. Rev. D* 77, 083508 (2008)

Table 2: Numerical values for 1σ constraints on parameters in Fig. 2, Fig. 3 and left panel of Fig. 4 respectively.

bias	case	σ_γ	σ_w	σ_{γ_0}	σ_{γ_1}	σ_{γ_m}	σ_{w_m}	σ_γ	σ_η
$b = 1$	reference	0.02	0.01	0.15	0.47	0.08	0.03	0.02	0.07
	optimistic	0.02	0.01	0.13	0.39	0.07	0.02	0.02	0.05
	pessimistic	0.03	0.01	0.21	0.67	0.12	0.04	0.04	0.09

8.
Reionization / Radio

Efficiently Simulating the High-Redshift 21-cm Signal with 21cmFAST

A. Mesinger

*Department of Astrophysical Sciences, Princeton University,
Princeton, NJ 08544, USA*

We introduce a powerful semi-numeric modeling tool, 21cmFAST, designed to efficiently simulate the cosmological 21-cm signal. Our code generates 3D realizations of evolved density, ionization, peculiar velocity, and spin temperature fields, which it then combines to compute the 21-cm brightness temperature. Although the physical processes are treated with approximate methods, we compare our results to a state-of-the-art large-scale hydrodynamic simulation, and find good agreement on scales pertinent to the upcoming observations ($\gtrsim 1$ Mpc). The power spectra from 21cmFAST agree with those generated from the numerical simulation to within 10s of percent, down to the Nyquist frequency. We show results from a 1 Gpc simulation which tracks the cosmic 21-cm signal down from $z = 250$, highlighting the various interesting epochs. Depending on the desired resolution, 21cmFAST can compute a redshift realization on a single processor in just a few minutes. Our code is fast, efficient, customizable and publicly available, making it a useful tool for 21-cm parameter studies.

1 Introduction

The dawn of the first astrophysical objects and their subsequent evolution, remains one of the most compelling frontiers of modern cosmology. This epoch culminated in the epoch of reionization (EoR), when light from these early generations of stars (and black holes) began flowing through and eventually permeating the Universe. Unfortunately, precious little is known about this fundamental epoch, as well as the dark ages which preceded it.

Some of the most important and timely information on the EoR and the dark ages should come in the form of the redshifted 21-cm line of neutral hydrogen. Several interferometers will attempt to observe the cosmological 21-cm signal, including the Mileura Wide Field Array (MWA;¹^a, the Low Frequency Array (LOFAR)^b, the Giant Metrewave Radio Telescope (GMRT;²), the Precision Array to Probe the Epoch of Reionization (PAPER;³), and eventually the Square Kilometer Array (SKA)^c.

However, interpreting this data will be quite challenging and no-doubt controversial, as foreshadowed by the confusion surrounding the scant, currently-available observations. There are two main challenges to overcome: (1) an extremely large parameter space, due to our poor understanding of the high-redshift Universe; (2) an enormous dynamic range (i.e. range of relevant scales).

Theoretically, the dawn of the first astrophysical objects and reionization could be modeled from first principles using numerical simulations, which include the complex interplay of many

^a<http://web.haystack.mit.edu/arrays/MWA/>

^b<http://www.lofar.org>

^c<http://www.skatelescope.org/>

physical processes. In practice however, simulating these epochs requires enormous (gigaparsec) simulation boxes and at the same time very high resolution to resolve the underlying sources and sinks of ionizing photons and the complex small-scale feedback mechanisms which regulate them. Furthermore, large-scale simulations are computationally costly and thus are inefficient in large parameter studies. On the other hand, analytic models, while more approximate, are fast and can provide physical insight into the import of various processes. However, analytical models are hard-pressed to go beyond the linear regime, and beyond making fairly simple predictions.

Here, we follow a path of compromise, attempting to preserve the most useful elements of both analytic and numeric approaches. We introduce a self-consistent, semi-numerical^d simulation, specifically optimized to predict the high-redshift 21-cm signal. Through a combination of the excursion-set formalism and perturbation theory, our code can generate full 3D realizations of the density, ionization, velocity, spin temperature, and ultimately 21-cm brightness temperature fields. Although the physical processes are treated with approximate methods, our results agree well with a state-of-the-art hydrodynamic simulation of reionization. However, unlike numerical simulations, realizations are computationally cheap and can be generated in a matter of minutes on a single processor, with modest memory requirements. Most importantly, our code is publicly available at <http://www.astro.princeton.edu/~mesinger/Sim.html>. We name our simulation *21cmFAST*. More details can be found in⁴.

2 Comparing 21cmFAST to State-of-the-Art Simulations

The offset of the 21-cm brightness temperature from the CMB temperature, T_γ , along a line of sight (LOS) at observed frequency ν , can be written as (c.f. ⁵):

$$\delta T_b(\nu) = 27x_{\text{HI}}(1 + \delta_{\text{nl}}) \left(\frac{H}{dv_r/dr + H} \right) \left(1 - \frac{T_\gamma}{T_S} \right) \left(\frac{1+z}{10} \frac{0.15}{\Omega_M h^2} \right)^{1/2} \left(\frac{\Omega_b h^2}{0.023} \right) \text{mK}, \quad (1)$$

where x_{HI} is the hydrogen neutral fraction, T_S is the gas spin temperature, τ_{ν_0} is the optical depth at the 21-cm frequency ν_0 , $\delta_{\text{nl}}(\mathbf{x}, z) \equiv \rho/\bar{\rho} - 1$ is the evolved (Eulerian) density contrast, $H(z)$ is the Hubble parameter, dv_r/dr is the comoving gradient of the line of sight component of the comoving velocity, and all quantities are evaluated at redshift $z = \nu_0/\nu - 1$. The above equation also assumes that $dv_r/dr \ll H$, which is generally true for the pertinent redshifts and scales.

The components of eq. 1 are the density, δ_{nl} , the ionization, x_{HI} , the velocity gradient, dv_r/dr , and the spin temperature, T_S , fields. We compare the first three fields generated by 21cmFAST to those generated by the hydrodynamic cosmological simulation of⁶, *using the same initial conditions (ICs)*^f. Unfortunately, there is currently no numerical simulation which includes the computationally expensive radiative transfer of both X-rays and Ly α photons from atomically or molecularly cooled sources required to compute T_S numerically (though see the recent work of⁷, who perform RT simulations on a small subset of sources, with $M \gtrsim 10^{10} M_\odot$). Therefore we cannot directly compare our the spin temperature fields to numerical simulations.

We perform “by-eye” comparisons at various redshifts/stages of reionization, as well as one and two-point statistics: the PDFs (smoothed on several scales), and the power spectra. Since our code is designed to simulate the cosmological 21-cm signal from neutral hydrogen, we study

^dBy “semi-numerical” we mean using more approximate physics than numerical simulations, but capable of independently generating 3D realizations.

^eThe simulations of⁶ are the current “state-of-the-art” reionization simulations. They include simultaneous treatment of dark matter (DM) and gas, five-frequency radiative transfer (RT) on a 512^3 grid, and they resolve $M_{\text{halo}} \gtrsim 10^8 M_\odot$ ionizing sources with $\gtrsim 40$ DM particles in a 143 cMpc box.

the regime before the likely completion of reionization, $z \gtrsim 7$ (though present data is even consistent with reionization completing at $z \lesssim 6$; ⁸).

We find good agreement with the numerical simulation on scales pertinent to the upcoming observations ($\gtrsim 1$ cMpc). The power spectra from 21cmFAST agree with those generated from the numerical simulation to within 10s of percent down to the Nyquist frequency.

Most importantly, the model uncertainties of the semi-numerical schemes are smaller than the evolution due to reionization over a range $\Delta \bar{x}_{\text{HI}} \sim 0.2$. Naively therefore, one can predict that the semi-numerical schemes are accurate enough to estimate \bar{x}_{HI} from the power spectra to $\pm \lesssim 0.1$, or even better if the behavior of the models are understood. However, there are many astrophysical uncertainties associated with prescriptions for sources and sinks of ionizing photons during the epoch of reionization, and it will likely be these which regulate the achievable constraints on \bar{x}_{HI} . *Therefore it is imperative for models to be fast and be able to span large regions of parameter space.* A single 21cmFAST realization of the δT_b fields shown in this section (generated from 1536^3 ICs) takes ~ 30 minutes to compute on a single-processor computer.

3 Results: complete δT_b evolution

Our code also derives the full 21-cm brightness temperature offset from eq. (1), *including the spin temperature field*. Our derivations are similar to other semi-analytic models (e.g. ⁹). However, unlike ¹⁰ and ¹¹, we do not explicitly resolve the halo field as an intermediary step. Instead we operate directly on the evolved density fields, using excursion set formalism to estimate the mean number of sources inside spherical shells corresponding to some higher redshift. Bypassing the halo field allows the code to be faster, with modest memory requirements. Our detailed formalism for computing the spin temperature can be found in ⁴.

In Fig. 1, we show slices through our fiducial δT_b box (*left*), and the corresponding 3D power spectra (*right*). The slices were chosen to highlight various epochs in cosmic 21-cm signal discussed above: the onset of Ly α pumping, the onset of X-ray heating, the completion of X-ray heating, and the mid-point of reionization are shown from top to bottom. We encourage the interested reader to see more evolutionary stages through the movie at <http://www.astro.princeton.edu/~mesinger/Movies/delT.mov>. When normalized to the same epoch, our power-spectrum evolution agrees fairly well with the analytical model of ¹², as well as its application to a numerical ¹⁰ and a semi-numerical (¹³) simulation (¹¹; c.f. see their Fig. 11).

Acknowledgments

Support for this work was provided in part by NASA through Hubble Fellowship grant HST-HF-51245.01-A to AM, awarded by the Space Telescope Science Institute, which is operated by the Association of Universities for Research in Astronomy, Inc., for NASA, under contract NAS 5-26555.

References

1. J. D. Bowman, M. F. Morales, and J. N. Hewitt. Probing the Epoch of Reionization with Power Spectrum Measurements by the First Generation of Low Frequency Radio Arrays. In *Bulletin of the American Astronomical Society*, volume 37 of *Bulletin of the American Astronomical Society*, pages 1217–+, December 2005.
2. Ue-Li Pen et al. The GMRT EoR Experiment: Limits on Polarized Sky Brightness at 150 MHz. 2008.

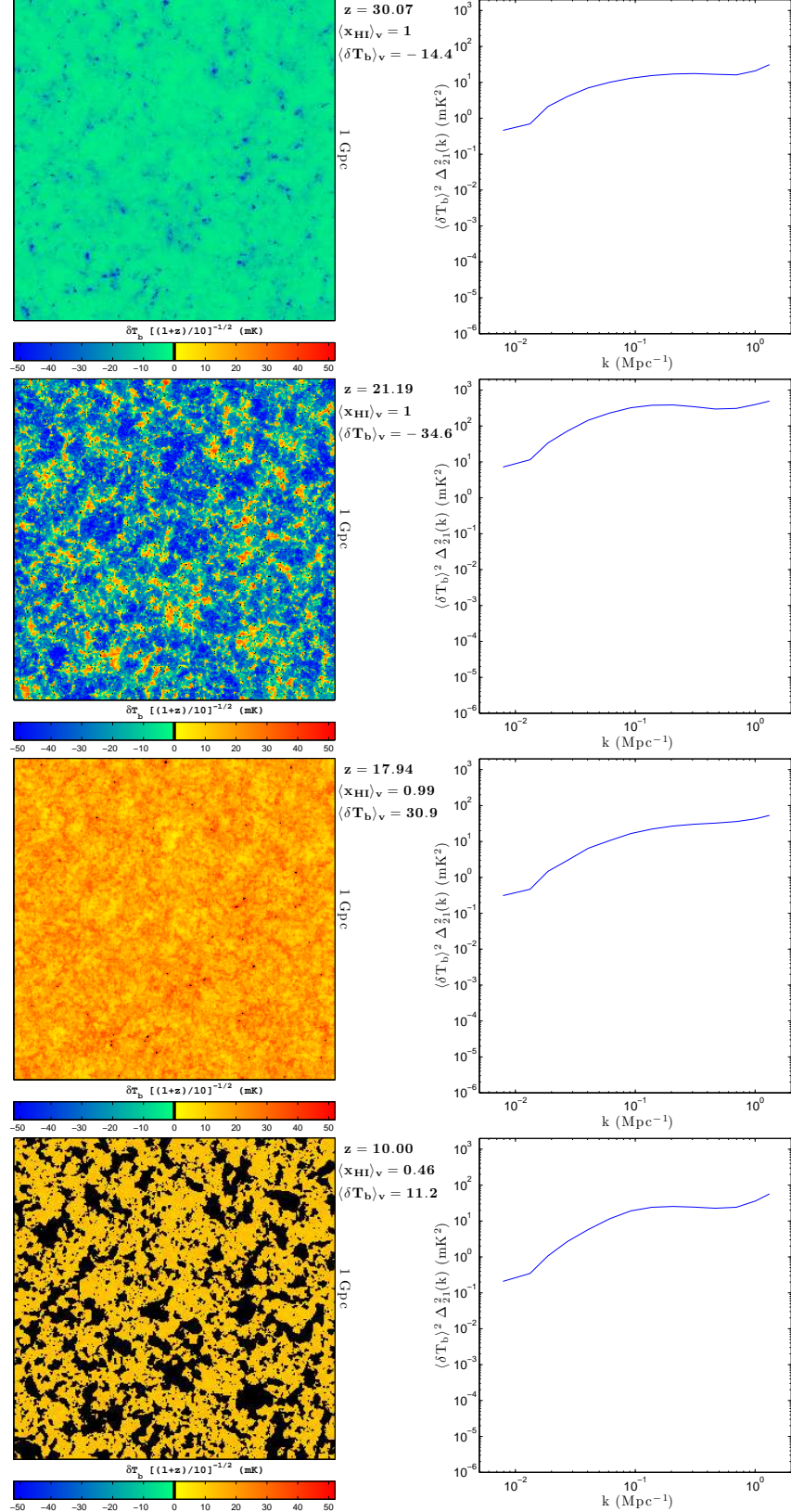


Figure 1: Slices through our δT_b simulation box (*left*), and the corresponding 3D power spectra (*right*), for our fiducial model at $z = 30.1, 21.2, 17.9, 10.0$ (*top to bottom*). The slices were chosen to highlight various epochs in the cosmic 21-cm signal: the onset of Ly α pumping, the onset of X-ray heating, the completion of X-ray heating, and the mid-point of reionization are shown from top to bottom. All slices are 1 cGpc on a side and 3.3 cMpc deep. For a movie of this simulation, see <http://www.astro.princeton.edu/~mesinger/Movies/delT.mov>.

3. Aaron R. Parsons et al. The Precision Array for Probing the Epoch of Reionization: 8 Station Results. 2009.
4. A. Mesinger, S. Furlanetto, and R. Cen. 21cmFAST: A Fast, Semi-Numerical Simulation of the High-Redshift 21-cm Signal. *ArXiv e-prints:1003.3878*, March 2010.
5. S. R. Furlanetto, S. P. Oh, and F. H. Briggs. Cosmology at low frequencies: The 21 cm transition and the high-redshift Universe. *Physics Reports*, 433:181–301, October 2006.
6. H. Trac, R. Cen, and A. Loeb. Imprint of Inhomogeneous Hydrogen Reionization on the Temperature Distribution of the Intergalactic Medium. *ApJ*, 689:L81–L84, December 2008.
7. S. Baek, B. Semelin, P. Di Matteo, Y. Revaz, and F. Combes. Reionization by UV or X-ray sources. *ArXiv e-prints*, March 2010.
8. A. Mesinger. Was reionization complete by $z \sim 5-6$? *ArXiv e-prints:0910.4161*, October 2009.
9. S. R. Furlanetto. The global 21-centimeter background from high redshifts. *MNRAS*, 371:867–878, September 2006.
10. M. G. Santos, A. Amblard, J. Pritchard, H. Trac, R. Cen, and A. Cooray. Cosmic Reionization and the 21 cm Signal: Comparison between an Analytical Model and a Simulation. *ApJ*, 689:1–16, December 2008.
11. M. G. Santos, L. Ferramacho, M. B. Silva, A. Amblard, and A. Cooray. Fast and Large Volume Simulations of the 21 cm Signal from the Reionization and pre-Reionization Epochs. *ArXiv e-prints*, November 2009.
12. J. R. Pritchard and S. R. Furlanetto. 21-cm fluctuations from inhomogeneous X-ray heating before reionization. *MNRAS*, 376:1680–1694, April 2007.
13. A. Mesinger and S. Furlanetto. Efficient Simulations of Early Structure Formation and Reionization. *ApJ*, 669:663–675, November 2007.

FAST LARGE VOLUME SIMULATIONS OF THE 21 CM SIGNAL FROM THE REIONIZATION AND PRE-REIONIZATION EPOCHS

M. G. SANTOS¹

L. FERRAMACHO¹, M. B. SILVA¹, A. AMBLARD², A. COORAY²

¹*CENTRA, Departamento de Física, Instituto Superior Técnico,
1049-001 Lisboa, Portugal*

²*Center for Cosmology, Department of Physics and Astronomy,
University of California, Irvine, CA 92697*

We present a new type of simulation of the 21cm signal from the Reionization and pre-Reionization epoch capable of quickly generating the signal up to very high redshifts with the large field of view of the next generation of radio telescopes. This simulation uses a semi-numerical prescription based on 3-d Monte-Carlo realizations of the dark matter density field, achieving a much higher dynamical range than previous time-consuming N-body codes with radiative transfer algorithms. The simulation extends to high redshifts ($z \sim 25$) thus including the effect of the Lyman alpha and collisional coupling as well as X-ray heating and corrections due to the gas bulk velocities. With the new algorithm we were able to achieve very large volumes (1000 Mpc)³, thus fully probing the large scale structure of the 21cm signal. This fast simulation also allows to quickly test the effect of different astrophysical parameters on the 21cm signal.

1 Introduction

Observations of the 21 cm line of neutral hydrogen are currently considered to be one of the most promising probes of the epoch of reionization (EoR) and possibly even the preceding period, during the so called dark ages. Motivated by the observational possibilities offered by the current and upcoming low frequency radio interferometers^{abc} a great deal of effort has been underway in order to fully understand and generate the expected 21 cm signal that will be seen by these experiments (see Furlanetto et al.⁴ for a review). Numerical simulations can potentially provide an improved description of the 21 cm brightness temperature signal but are slow to run, being constrained in dynamical range to sizes typically smaller than 100 Mpc/h. We propose a semi-numerical technique, capable of quickly generating an end-to-end simulation of the 21 cm signal even at high redshifts when the spin temperature is non-negligible. Moreover, this method can be used to simulate very large volumes (e.g. 1000 Mpc), crucial to simulate the field-of-view of next generation of radio telescopes, without sacrificing the speed or requiring unpractical amounts of computer memory. The code to generate this type of simulation is now provided publicly online^d and it will be subject to continuous improvement through calibration against full radiative transfer/hydrodynamic simulations. The large volume simulations created with

^aLOFAR: <http://lofar.org>

^bMWA: <http://web.haystack.mit.edu/arrays/MWA>

^cSKA: <http://www.skatelescope.org>

^d<http://www.simfast21.org>

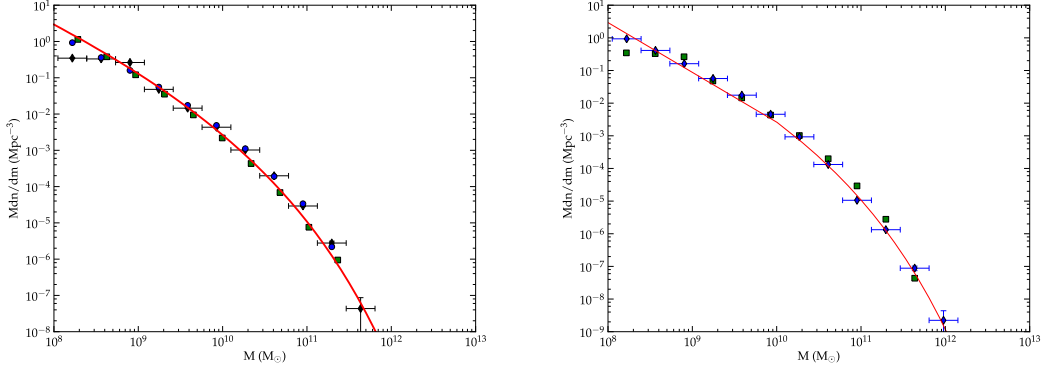


Figure 1: Left: Mass functions at $z=10$ taken from our halo filtering prescription with $L=142$ Mpc and $N=1536^3$ (blue circles) and $L=300$ Mpc and $N=1800^3$ (black diamonds). The results for the N-body simulation of Trac et al.¹³ with $L=142$ Mpc are also shown as green squares. The red line shows the theoretical mass function. Right: mass function for our simulation with $L=300$ Mpc and $N=1800^3$ (green squares) compared with the large volume simulation with $L=1000$ Mpc and $N=1800^3$ (blue diamonds).

this method are part of the SKA Design Studies Simulated Skies initiative and we hope this approach can prove useful to generate sky models for the future 21 cm experiments, which is crucial to test for calibration issues and foreground removal methods.

2 From linear density fluctuations to the ionization field

The underlying basis for our simulation is the Monte-Carlo generation of the dark matter linear density field assuming a Gaussian probability distribution function for the linear overdensity as the initial state, which is then later evolved and used to find the collapsed structures and the corresponding ionized bubbles. This implementation partially follows the algorithm prescribed in Mesinger & Furlanetto⁷, which is based on the “peak-patch” approach introduced by Bond & Myers¹. Figure 1 shows the obtained halo mass function. In the left panel, we can see that our simulations agree quite well with the theoretical curve and N-body simulation, although the number of low mass halos in the simulation with the lower resolution ($L=300$ Mpc) is slightly underestimated. However, we have checked that this effect has a minor impact on the ionized hydrogen distribution and can be seen as a good compromise in order to cover the largest possible volume with this algorithm.

The positions of both the halos and the dark matter were then corrected to include non-linear dynamics using the Zel'dovich approximation¹⁶ and with the corrected halo and density fields, the ionization regions can be determined using a similar excursion-set algorithm. The principle behind this procedure is that the galaxies formed inside dark matter halos will produce a given amount of photons (dependent of the halo mass) that will ionize the surrounding hydrogen generating ionized bubbles. The efficiency of this process can be quantified by one parameter ζ . Figure 2 shows two slices of our ionization field at the beginning and ending of reionization. These figures exhibit the characteristic bubble structure of ionized hydrogen increasing in size at lower redshifts until converging into a completely ionized IGM. In order to characterize the statistical distribution of the ionization field we computed its power spectrum, $P_{x_i x_i}$ (figure 3). We see that the excursion-set formalism allows to obtain a bubble power spectrum that matches the one from a full N-body radiative transfer simulation when the volume size and cell resolution are the same. However, at large scales we find an increase in power with larger boxes, which we believe is due to the fact that we are finding larger bubbles in the 300 Mpc box, while smaller bubbles are absorbed in larger ones.

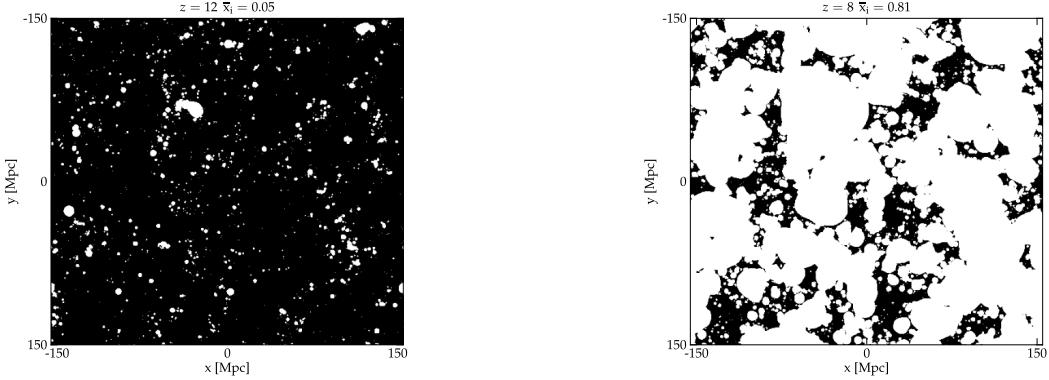


Figure 2: Slices of the ionization field at the beginning and ending of reionization (left: $z = 12$, $\bar{x}_i = 0.05$; right: $z = 8$, $\bar{x}_i = 0.81$)

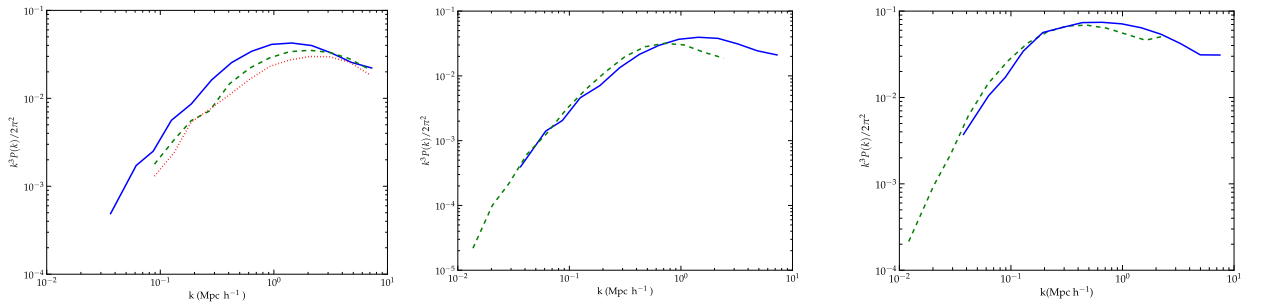


Figure 3: First panel: power spectrum of the ionization field for our simulation with $L=143$ Mpc, $N=768^3$ (red dotted curves), $L=300$ Mpc, $N=600^3$ (solid blue curves) and the simulation of Trac et al.¹³ with $L=143$ Mpc, $N=768^3$ (dashed green curves), for $z = 9$ and $\bar{x}_i = 0.15$. The boxes were smoothed to a common resolution. Two right panels: power spectrum of the ionization field for the very large volume simulation (green dashed curves), compared to the same result for the $L=300$ Mpc simulation. Both plots are for $z=9$ but using different efficiency parameters ($\zeta=5.0$ and $\zeta=14.0$) so that $\bar{x}_i = 0.1$ (left) and $\bar{x}_i = 0.55$ (right).

3 Extending the simulation to very large volumes

Although quite fast, the semi-numerical simulation presented so far still imposes some limitations regarding the volume it can cover since it requires a very large number of cells in order to achieve sufficient resolution to filter scales corresponding to $10^8 M_\odot$ halos and cover large volumes at the same time. However, we can use a low resolution box and use the expected halo mass function to place the smaller halos in our large volume simulation cells by following the prescription of Wilman et al.¹⁴. By the definition of the mass function, the quantity $n = dn/dM\Delta M\Delta V$ corresponds to the mean number of halos that can be found in a given cell with comoving volume ΔV . If one would simply perform a Poisson sampling for each cell with a mean n , the distribution of obtained halos would yield a correct mass function but their positions would be completely random. In order to correlate the halo positions with the underlying density field, a normalized bias term can be added,

$$n_{cell} = K e^{b(z, M)\delta(z)} \frac{dn}{dM} \Delta M \delta V , \quad (1)$$

where $b(z, M)$ is the bias model for halos at a given redshift and $\delta(z, M)$ the density field at the same redshift. The factor K is a normalization constant that ensures the consistency of the above expression with the mass function $\frac{dn}{dM}$ when averaging over the large volume box. The above equation introduces a dependence of the halo locations on the density field, by amplifying

the overdense regions with respect to underdense ones. As for the bias term, it describes the difference in clustering between dark matter halos and the mass density field.

We have then used this prescription in complement with the excursion-set formalism to perform a dark matter simulation with $L=1000$ Mpc. In figure 1 right panel, we plot (blue diamonds) the obtained mass function for this run and compare it to the higher resolution, $L=300$ Mpc simulation obtained using only the excursion set formalism. We also checked that this formalism can reproduce the spatial distribution of halos with its correlation with the underlying matter density field. We then proceed to derive the ionization bubbles using the same method as in Section 2. The results for the power spectrum of the ionization field are shown in figure 3 (two right panels) compared to those obtained with the full excursion-set method with $L=300$ Mpc and for two different efficiency parameters at $z=9$. The curves seem to agree reasonable well showing convergence with the 300 Mpc box, although if we go to even larger ionization fractions we still find slightly larger bubbles in the 1Gpc box (the largest bubble for the 1Gpc box with $x_i = 0.55$ has a size of 20 Mpc).

4 The 21 cm signal up to $z=25$

With ionization maps at different redshifts we can focus on the predicted 21 cm signal from neutral hydrogen during the pre-EOR and the EOR. At high redshifts ($z > 10$) the spin temperature (T_S) is no longer high enough to saturate the effect in the brightness temperature and we need to take into account the contribution of fluctuations from the spin temperature to the 21 cm signal. These originate from fluctuations in the coupling between the spin temperature and the gas temperature and the perturbations in the gas temperature itself (T_K) and we can write:

$$1 - \frac{T_\gamma}{T_S} = \frac{x_{tot}}{1 + x_{tot}} \left(1 - \frac{T_\gamma}{T_K} \right), \quad (2)$$

where $x_{tot} = x_\alpha + x_c$ is the sum of the radiative and collisional coupling parameters. Collisions can be important for decoupling the HI 21 cm spin temperature from the CMB, especially at very high redshifts ($z > 30$)⁸ and are straightforward to apply to the simulation⁶. The radiative coupling due to the absorption of Ly_α photons (the Wouthuysen-Field effect^{15,3}), on the other hand, should be dominant for $z < 25$ and we shall concentrate on calculating this effect here. The radiative coupling is given by

$$x_\alpha = \frac{S_\alpha J_\alpha}{J_c}, \quad (3)$$

with $J_c \approx 5.552 \times 10^{-8}(1+z) \text{ m}^{-2}\text{s}^{-1}\text{Hz}^{-1}\text{sr}^{-1}$ and S_α is a correction factor of order unity^{5,2,4}. We follow the prescription in Santos et al.⁹ to calculate J_α . For this, we need the comoving star formation rate, $\psi(\mathbf{x}, z)$ and $\epsilon_\alpha(\nu)$, the spectral distribution function of the sources (defined as the number of Ly_n photons per unit frequency emitted at ν per baryon in stars). We can easily assume any model for $\epsilon_\alpha(\nu)$ in our code to test for different sources of radiation. For this simulation we used: $A\nu^{-\alpha}$, with $\alpha = 0.9$ and A set such that we get a total of 20000 $Ly\alpha$ photons per baryon. We used the halo catalogue to obtain the star formation rate density which was then normalized to the one in Shin et al.¹². The gas in the IGM is also heated as the reionization progresses. In our simulation, we assume that this heating is done by x-rays with an emission connected to the star formation rate (see Santos et al.⁹). This X-ray emissivity is again assumed to be a power law, with a spectral index and amplitude compatible with what is observed for starburst galaxies. Figure 4 left panel, shows the evolution of the gas temperature with redshift, where we can see that most of the IGM is heated above 100K for $z < 11$. The spin temperature starts very close to the CMB one (no signal) and approaches the gas temperature as x_α increases, following it for $z < 17$.

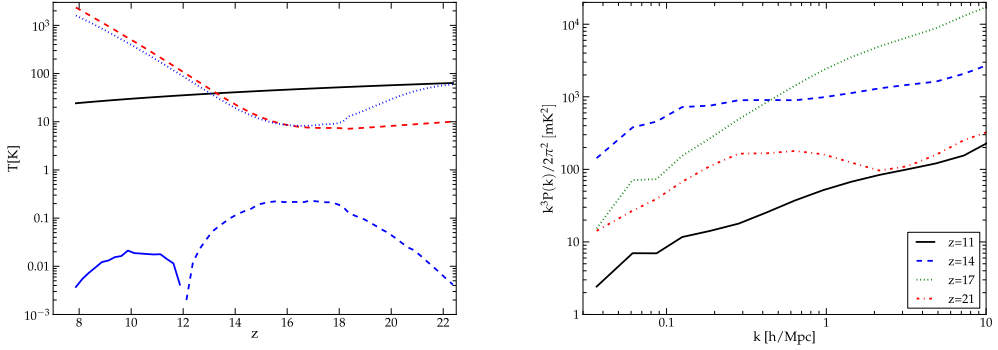


Figure 4: Left: the evolution of the gas temperature, spin temperature and brightness temperature with redshift. Solid black line - CMB; Red dashed - gas temperature; Blue dotted - spin temperature; Dark blue solid/dashed (below) - brightness temperature. Right: The power spectrum of the 21-cm signal at high redshifts including all fluctuations in the spin temperature.

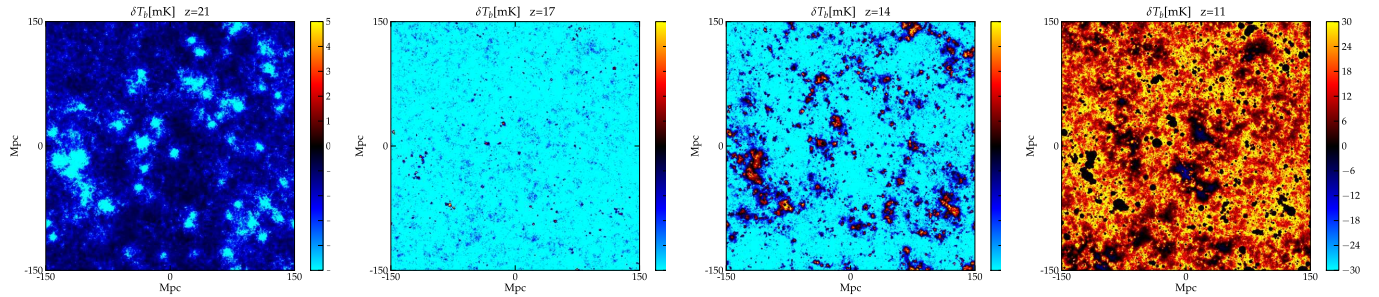


Figure 5: Maps of the 21 cm signal at very high redshifts from the simulation, including all sources responsible for the fluctuations.

Putting it all together we can calculate the 21 cm signal. Calculation of x_α and the gas temperature takes around 5 minutes for each redshift in our machine using 20 CPUs. In figure 4 left panel, we can also see the evolution of the average brightness temperature with redshift, which is observed in absorption down to $z = 12$ where it becomes approximately zero when $T_K \approx T_{CMB}$. In figure 5 we show maps of the 21 cm signal for a few very high redshifts taking into account all the effects while figure 4 right panel, shows the corresponding power spectrum. At high redshifts ($z = 21$) most of the temperature is zero ($T_s \sim T_{CMB}$) but we already start to see some cold spots where the Ly α sources couple the spin temperature to the cold gas temperature and the fluctuations in x_α dominate. At $z = 17$ the spin temperature is basically following the gas one everywhere and we can see fluctuations in the 21 cm signal due essentially to the gas temperature (although most of the Universe is still cold at this epoch). At $z = 14$ we can already see the higher temperature regions surrounding the light sources located in the halos. Finally at $z = 11$ basically all the IGM is heated above the CMB and we start seeing the ionization bubbles ($\bar{x}_i \approx 0.1$, but note that some of the dark regions here are not due to the ionized bubbles but because $T_S = T_K \sim T_{CMB}$).

5 Summary

We presented a semi-numerical method capable of quickly generating end-to-end simulations of the 21 cm signal even at the high redshifts where the spin temperature is non-negligible (see Santos et al.¹⁰ for further details). The algorithm allows to generate brightness temperature boxes with very large volumes, e.g. $(1000 \text{ Mpc})^3$, crucial to properly simulate the field of view

of the next generation of radio-telescopes. The corresponding code (SimFast21) takes about 1 hour to run for each redshift, which can be considered remarkably fast. We are expecting that further optimization of the code can still reduce this time. This is on going research that will be implemented as we update the numerical code. Although much faster than hydrodynamical numerical simulations, our analysis shows that relevant quantities such as the halo mass function, the halo mass power spectrum or the ionization fraction power spectrum are all consistent with the numerical simulations with which we compared our results to. The dependence on the astrophysical parameters of the simulation was encoded in three functions: the ionization efficiency, ζ , the Ly α spectral distribution function of the sources, ϵ_α and the X-ray spectral distribution function, ϵ_X . These functions can be easily changed for a model of our choice and the code can then quickly generate new simulations of the signal (even faster if we keep the same cosmology). By combining all the unknowns into a physically meaningful small set of parameters we can easily probe the huge intrinsic parameter space available to 21 cm observations. The code is now publicly available and we welcome the community participation in its updating and upgrading as well as development of additional applications on observational probes of reionization beyond the 21 cm observations.

Acknowledgements

This work was partially supported by FCT-Portugal under grant PTDC/FIS/66825/2006. This work was supported by the European Commission Framework Program 6, Project SKADS, Square Kilometre Array Design Studies (SKADS), contract no 011938.

References

1. Bond, J. R. & Myers, S. T. 1996, ApJS, 103, 1
2. Chuzhoy, L. & Shapiro, P. R. 2007, ApJ, 655, 843
3. Field, G. B. 1959, ApJ, 129, 536
4. Furlanetto, S. R., Oh, S. P., & Briggs, F. H. 2006, Phys. Rep., 433, 181
5. Hirata, C. M. 2006, MNRAS, 367, 259
6. Kuhlen, M., Madau, P., & Montgomery, R. 2006, ApJ, 637, L1
7. Mesinger, A. & Furlanetto, S. 2007, ApJ, 669, 663
8. Nusser, A. 2005, MNRAS, 359, 183
9. Santos, M. G., Amblard, A., Pritchard, J., et al. 2008, ApJ, 689, 1
10. Santos, M. G., Ferramacho, L., Silva, M. B., Amblard, A., & Cooray, A. 2009, ArXiv e-prints, MNRAS2010
11. Sheth, R. K. & Tormen, G. 1999, MNRAS, 308, 119
12. Shin, M.-S., Trac, H., & Cen, R. 2007, ArXiv e-prints, 708
13. Trac, H., Cen, R., & Loeb, A. 2008, ApJ, 689, L81
14. Wilman, R. J., Miller, L., Jarvis, M. J., et al. 2008, MNRAS, 388, 1335
15. Wouthuysen, S. A. 1952, AJ, 57, 31
16. Zel'Dovich, Y. B. 1970, A&A, 5, 84

COSMOLOGICAL OBSERVATIONS IN THE RADIO DOMAIN: THE CONTRIBUTION OF EXTRAGALACTIC SOURCES

A.TARTARI, M.ZANNONI, M.GERVASI, G.SIRONI & S.SPINELLI

*Dip. di Fisica "G.Occhialini" - Università degli Studi di Milano-Bicocca
Piazza della Scienza, 3 - 20126 Milano, Italy*

The low frequency tail of the CMB spectrum, down along the radio range (~ 1 GHz), may carry weak spectral distortions which are fingerprints of processes occurred during different epochs of the thermal history of the Universe, from $z \sim 3 \times 10^6$ to reionization. TRIS and ARCADE2 are the most recent experiments dedicated to the exploration of this chapter of CMB cosmology. The level of instrumental accuracy they reached in the determination of the absolute sky temperature is such that the removal of galactic and extra-galactic contamination is the true bottleneck towards the recovery of the cosmological signal. This will be certainly the case also for future experiments in the radio domain. Here we present an update of a study originally done to recognize the contribution of unresolved extra-galactic radio sources to the sky brightness measured by TRIS. Despite the specific context which originated our analysis, this is a study of general interest, improved by the inclusion of all the source counts available up-to-date from 150 MHz to 8.4 GHz.

1 Scientific case

The frequency spectrum of the Cosmic Microwave Background (CMB) recovered by the FIRAS instrument¹ on board the COBE satellite is an almost perfect planckian spectrum at the thermodynamic temperature of 2.728 ± 0.004 K, even if a more recent analysis and an update of this result can be found in a recent work by Fixsen². No signatures of spectral distortions have been found on the monopole scale. Nevertheless, there are important arguments³ suggesting that deviations from a blackbody curve originated in the pre-recombination Universe, may be present in the CMB spectrum. In particular, we know that if an energy injection in the photon-baryon fluid occurred in the redshift range $\sim 10^5 < z < \sim 3 \times 10^6$, corresponding to a temperature of the photon-baryon fluid $\sim 0.1\text{keV} < T < \sim 1\text{keV}$, than the system relaxes towards a kinetic equilibrium, the photons having Bose-Einstein spectrum with a chemical potential $\mu \neq 0$. Several mechanisms have been proposed as possible sources of perturbation, among them decay of relic massive particles⁴, dissipation of primordial magnetic fields⁶, annihilation of relic particles⁵ and dissipation of acoustic oscillations in the fluid⁷. Was the spectrum a Bose-Einstein one, we would observe a dip in the plot Temperature *vs* Frequency of the CMB at frequencies ~ 1 GHz, given the present estimate of H_0 (Hubble parameter) and Ω_b (baryon density). The amplitude of this distortion, $\Delta T/T \simeq \mu(\Omega_b h^2)^{-2/3}$ (h being H_0 in units of 100 (km/s)/Mpc), is strongly model dependent. Extrapolating to lower frequencies the FIRAS upper limit on μ , we expect a temperature dip smaller than few tens of mK.

Another effect able to produce a monopole scale spectral distortion is free-free emission during reionization. This effect produces a signal $\Delta T/T \propto Y_{ff} \lambda^2$, which is essentially the

optical depth to bremsstrahlung, λ being the wavelength and Y_{ff} a distortion parameter as defined by Bartlett and Stebbins⁸. Despite new tighter limits on Y_{ff} obtained by Gervasi et al.⁹, we are still far from the possibility of testing reionization scenarios like those investigated by Weller et al.¹⁰.

Both effects are more relevant at decimetric wavelengths, where (1) calibrations are more difficult due to the size of antennas, (2) the brightness of the Galaxy overcomes the CMB and (3) the signal of Unresolved Extragalactic Radio Sources (UERS), the subject of this study, may introduce a temperature offset if not properly evaluated and subtracted.

Two recent experiments searched for low frequency CMB spectral distortions: TRIS¹¹ and ARCADE2¹². In the framework of TRIS, a new estimate of the brightness temperature of UERS has been proposed by Gervasi et al.¹³. Here we present an update of those results, exploiting all the most recent radio source counts from 150 MHz to 8.4 GHz and adding a new frequency to those used in the previous study.

2 Unresolved Extragalactic Radio Sources contamination

2.1 Aims and Methods of this study

As stated in the previous section, the purpose of this work is to develop the earlier work by Gervasi et al.¹³ enlarging the data-set described in table 1 of this reference. Here we included all the deepest radio source counts done in the last few years, especially those obtained at VLA and GMRT. In particular, we enriched our analysis taking into account new results at 150 MHz¹⁴, 610 MHz¹⁵ and 1400 MHz¹⁶. We completed the 8400 MHz counts by adding the results by Henkel and Partridge¹⁷.

We added also a new frequency in our analysis, namely the 325 MHz channel (Oort et al.¹⁸, Owen et al.¹⁹).

Typical experiments looking for spectral distortions in the CMB spectrum have beams $> 7^\circ$ (e.g. FIRAS), so that, on average, pointing in different directions, the radiometer will detect the same blend of AGNs, quasars and normal galaxies, with only a poissonian fluctuation in their number. Therefore, UERS are seen as an isotropic diffuse radiation. We calculate its temperature in two steps. First, we fit the differential source counts normalized to the euclidean counts, that is $Q(S) = S^{2.5}dN/dS$, S being the flux. Then we use the definition of brightness temperature,

$$T_{b,UERS} = \frac{\lambda^2}{2k_B} \int_{S_{min}}^{S_{max}} Q(S) S^{-3/2} dS \quad (1)$$

(k_B Boltzmann constant), to calculate the integrated contribution of sources between two limiting values of flux. Here a problem is evident: given the fact that a survey will be complete at a flux limit S_{min} , how can we take into account the contribution of sources fainter than that? If we stop our integration within the data range, we get a lower limit of the temperature of UERS, introducing a bias in our analysis. A solution is to extrapolate our integral at fainter fluxes. In absence of a physical cut-off, to circumvent this problem we simply look for a functional form of $Q(S)$ such that $T_{b,UERS}$ remains finite when $S_{min} \rightarrow 0$, avoiding a kind of Olbers'paradox.

2.2 Radio Source counts

As originally proposed by Gervasi et al.¹³ we assume

$$Q(S) = Q_1(S) + Q_2(S) = \frac{1}{A_1 S^{\varepsilon_1} + B_1 S^{\beta_1}} + \frac{1}{A_2 S^{\varepsilon_2} + B_2 S^{\beta_2}} \quad (2)$$

where A_i, B_i, ε_i and β_i ($i = 1, 2$) are parameters to be fitted. This analytical description, inspired by source evolutionary models proposed by Danese, Franceschini and collaborators (see Danese et al.²⁰ and Franceschini et al.²¹), has the property of being integrable at faint fluxes, even if it is not good as $\log(S)$ polynomials to describe features within the experimental range. One of the basic assumptions underlying our approach is that the four parameters of $Q(S)$ giving the slopes (ε_i and β_i) are frequency independent. Moreover, following again a suggestion of the model by Franceschini et al., and analyzing the data at 600, 1400 and 5000 MHz (frequencies where both faint and strong fluxes are well sampled), we fix $\varepsilon_1 = \varepsilon_2$, simplifying further the description of source counts. Now, the Q_1 and Q_2 terms, following the notation of Gervasi et al.¹³, are dominant respectively in the strong and faint flux regimes, so that two ratios can be calculated at the three frequencies with the widest flux coverage: $r_A = A_2/A_1$ and $r_B = B_2/B_1$, at 600, 1400 and 5000 MHz. These ratios, r_A in particular, can be used to reconstruct the faint flux tails of counts at those frequencies where data are not deep enough. Since they show a weak frequency dependence (see tab. 1 for A_2/A_1), our choice has been to use the r_A and r_B calculated at the frequency closest to the one we want to reconstruct.

Table 1: The measured A_2/A_1 ratios.

	600 MHz	1400 MHz	5000 MHz
A_2/A_1	0.17 ± 0.02	0.23 ± 0.01	0.31 ± 0.03

3 Results

The main result we have obtained is a new estimate of the brightness temperature of the blend of UERS in the range 150 MHz - 8400 MHz. The calculated temperature values are well described by a single power law (eq. 3) with spectral index -2.75 (see fig.1). Our estimates are well in agreement with those found by other authors²², and the main result is

$$T_{b,UERS}(\nu) = (0.91 \pm 0.02) \left(\frac{\nu}{610 \text{ MHz}} \right)^{-(2.75 \pm 0.02)} K \quad (3)$$

for the contribution of unresolved sources to the overall temperature of the radio sky.

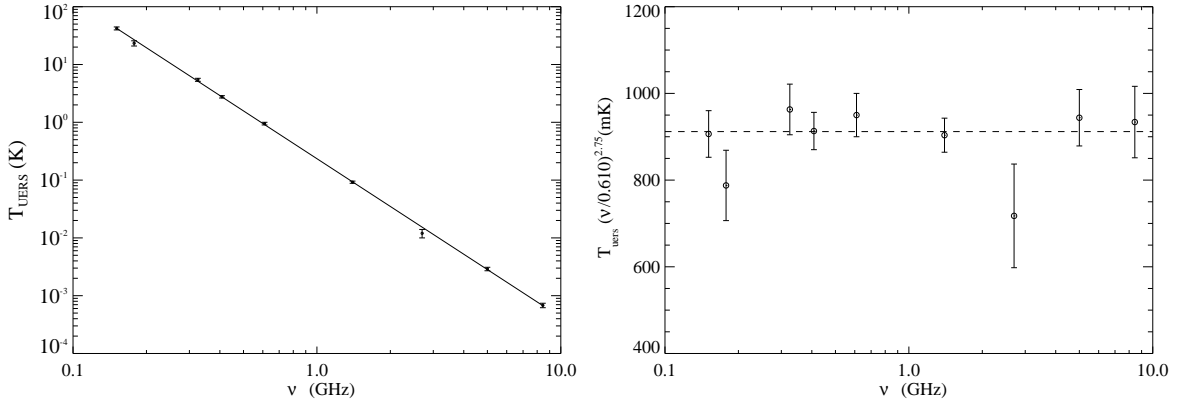


Figure 1: Left panel: Temperature vs Frequency plot; calculated temperatures and power law fit (solid line); 1σ error bars. Right panel: the same as in left panel, but with temperature rescaled by a factor $\propto \nu^{2.75}$ to appreciate the scatter of points around the single power law fit.

This formula allows us to calculate the UERS temperature in correspondence of TRIS frequency channels, namely 600, 820 and 2500 MHz: we find, respectively, 950 ± 20 mK, 408 ± 9 mK and 20.6 ± 0.7 mK.

4 Conclusions

This update of our previous work allowed us a better reconstruction of differential source counts, especially at faint fluxes. In fact, unlike the first study, we could determine the ratio A_2/A_1 finding a hint for weak frequency dependence. Improved source count fits lead directly to a more accurate estimate of the brightness temperature: this is very well described by a single power-law frequency spectrum. Then, using eq. 3, we could evaluate the UERS contribution at TRIS frequencies with uncertainties almost a factor 10 smaller than those commonly assumed before new estimates by Gervasi et al.¹³. By virtue of that, the subtraction of this foreground is no longer a limiting factor in low frequency CMB experiments, the overall error budget being now dominated by the reconstruction of the absolute temperature scale and by the disentangling of galactic and cosmological signals. Finally, we conclude that the estimate given by eq.3, exclusively based on source counts, doesn't agree with the extragalactic radio excess detected as a diffuse signal by the ARCADE2 collaboration²³. The discrepancy is around a factor 5 at 600 MHz, and still the origin of the radio excess remains mysterious. If its origin is truly extragalactic, there must be a number of sources able to produce an intense integrated signal, but individually so weak to escape from detection with radio interferometers. The case is intriguing and again tells us how non trivial is searching for CMB spectral distortions, and how unpredictable are the outcomes.

References

1. D.J.Fixsen, et al., ApJ **473**, 576 (1996)
2. D.J.Fixsen, ApJ **707**, 916 (2009)
3. R.A.Sunyaev & Ya.B. Zeldovich, Ap&SS **7**, 20 (1970)
4. W.Hu & J.Silk, PRL **70**, 2661 (1993)
5. P.McDonald, R.J.Scherrer & T.P. Walker, PRD **63**, 023001 (2000)
6. K.Jedamzik, V.Katalinić & A.V.Olinto, PRL **85**, 700 (2000)
7. J.D.Barrow & P.Coles, MNRAS **248**, 52 (1991)
8. J.G.Bartlett & A.Stebbins, ApJ **371**, 8 (1991)
9. M.Gervasi, et al., ApJ **688**, 24 (2008)
10. J.Weller, R.A.Battye & A.Albrecht, PRD **60**, 103520 (1999)
11. M.Zannoni, et al., ApJ **688**, 12 (2008)
12. J.Singal, et al., ApJ *accepted*, arXiv:0901.0546
13. M.Gervasi, et al., ApJ **682**, 223 (2008)
14. C.H.Ishwara-Chandra, et al., MNRAS *accepted*, arXiv:1002.0691
15. T.Garn, et al., MNRAS **387**, 1037 (2008)
16. E. Ibar, et al., MNRAS **397**, 281 (2009)
17. B.Henkel & R.B. Partridge, ApJ **635**, 950 (2005)
18. M.J.A., Oort , W.J.G. Steemers & R.A Windhorst, A&A **73**(Suppl), 103 (1988)
19. F.N. Owen, et al., Astron.J. **137**, 4846 (2009)
20. L.Danese, G. De Zotti, A.Franceschini, & L. Toffolatti, ApJ **318**, L15 (1987)
21. A.Franceschini, L. Toffolatti, L. Danese & G. De Zotti, ApJ **344**, 35 (1989)
22. G. De Zotti et al, A& A Rev. **18**, 1 (2010)
23. D.J.Fixsen, et al., arXiv:0901.0555

COSMIC STRUCTURE FORMATION AT HIGH REDSHIFT

ILIAN T. ILIEV

Astronomy Centre, Department of Physics & Astronomy, Pevensey II Building, University of Sussex, Falmer, Brighton BN1 9QH, United Kingdom

KYUNGJIN AHN

Department of Earth Science Education, Chosun University, Gwangju 501-759, Korea

JUN KODA, PAUL R. SHAPIRO

Department of Astronomy, University of Texas, Austin, TX 78712-1083, U.S.A.

UE-LI PEN

Canadian Institute for Theoretical Astrophysics, University of Toronto, 60 St. George Street, Toronto, ON M5S 3H8, Canada

We present some preliminary results from a series of extremely large, high-resolution N-body simulations of the formation of early nonlinear structures. We find that the high- z halo mass function is inconsistent with the Sheth-Tormen mass function, which tends to over-estimate the abundance of rare halos. This discrepancy is in rough agreement with previous results based on smaller simulations. We also show that the number density of minihaloes is correlated with local matter density, albeit with a significant scatter that increases with redshift, as minihaloes become increasingly rare. The average correlation is in rough agreement with a simple analytical extended Press-Schechter model, but can differ by up to factor of 2 in some regimes.

1 Introduction

The properties of the first luminous objects in the universe remain a big enigma at present due to the scarcity of observational data. These objects, the first stars and galaxies, started forming very early, only about 100-200 million years after the Big Bang, and their ionizing radiation eventually completely reionized the intergalactic medium¹. This complex process can be studied through numerical simulations and semi-analytical models. The former have the advantage of being able to describe complex situations and, in particular, the non-linearities of the cosmic structures, but are expensive to run and have limited dynamic range. The latter are much cheaper to run and thus allow studies of the full parameter space, but inevitably involve many approximations and simplifications. The distribution and properties of the low-mass halos which host the first stars is an important ingredient in any semi-analytical model of reionization. Such small-scale structure potentially has very different properties from larger structures we see at later times, as they probe a very different part of the initial power spectrum of density fluctuations. Therefore, it is important to check the validity of any models and fits to the halo mass function and bias in this new regime.

2 Simulations

The results we present in this work are based on series of very large N-body simulations, as summarized in Table 1. They follow between 1728^3 (5.2 billion) and 5488^3 (165 billion) particles (the latter at present is the largest cosmic structure formation simulation ever performed) in a wide range of box sizes from $2/h$ Mpc up to $3.2/h$ Gpc. Spatial resolution ranges from 50 pc/h to 40 kpc/h, while the particle masses range from $100 M_\odot$ up to $\sim 6 \times 10^{10}$, which yields minimum resolved halo masses (with 20 particles) between $2 \times 10^3 M_\odot$ and $10^{12} M_\odot$. The simulations were performed with the code CubeP³M^a².

Table 1: N-body simulation parameters. Background cosmology is based on the WMAP 5-year results.

boxsize	N_{part}	mesh	spatial resolution	$m_{particle}$	$M_{halo,min}$
$2 h^{-1} \text{Mpc}$	2048^3	4096^3	$48.8 h^{-1} \text{pc}$	$99.8 M_\odot$	$1996 M_\odot$
$6.3 h^{-1} \text{Mpc}$	1728^3	3456^3	$182 h^{-1} \text{pc}$	$5.19 \times 10^3 M_\odot$	$1.04 \times 10^5 M_\odot$
$11.4 h^{-1} \text{Mpc}$	3072^3	6114^3	$186 h^{-1} \text{pc}$	$5.47 \times 10^3 M_\odot$	$1.10 \times 10^5 M_\odot$
$20 h^{-1} \text{Mpc}$	5488^3	10976^3	$182 h^{-1} \text{pc}$	$5.19 \times 10^3 M_\odot$	$1.04 \times 10^5 M_\odot$
$114 h^{-1} \text{Mpc}$	3072^3	6144^3	$1.86 h^{-1} \text{kpc}$	$5.47 \times 10^6 M_\odot$	$1.09 \times 10^8 M_\odot$
$1 h^{-1} \text{Gpc}$	3072^3	6144^3	$16.3 h^{-1} \text{kpc}$	$3.62 \times 10^9 M_\odot$	$7.24 \times 10^{10} M_\odot$
$3.2 h^{-1} \text{Gpc}$	4000^3	8000^3	$40.0 h^{-1} \text{kpc}$	$5.67 \times 10^{10} M_\odot$	$1.14 \times 10^{12} M_\odot$

3 Cosmological structure formation

In Figure 1 we show the matter (green) and halo (orange) distributions in a thin slice at redshift $z = 8$ from our largest, 20 Mpc/h box simulation with 5488^3 particles. The cosmic web is already well-developed and highly nonlinear at these small scales even at such an early time. At this point there are over 110 million resolved dark matter halos in the box. The larger, rare halos are strongly clustered, with a spatial distribution which is highly biased with respect to the underlying density field, and largely follows the high-density filaments and knots. However, there are a fair number of smaller halos (minihaloes) which are found in mean and low-density (void) regions. The reason for this is that at this time the smallest minihaloes become very common haloes, with $\nu = \delta_c/\sigma(M) < 1$, where $\delta_c \sim 1.69$ is the linear overdensity at collapse time predicted by the top-hat model and $\sigma(M)$ is the density field variance at the appropriate mass scale M . A number of large-scale voids, from a few to ~ 10 Mpc in size, are found in our computational volume, as well as a large number of high density peaks. The density therefore varies very significantly between sub-volumes. For example, at ~ 0.5 Mpc scale the density variation is 1 order of magnitude even at $z = 28$ and reaches ~ 2 orders of magnitude at $z = 8$.

3.1 Halo mass function

We locate the collapsed halos on-the-fly, as the code is running, using a spherical overdensity halo finder with overdensity of 178. This is done by first interpolating the particles onto a gridded density field (at resolution twice the number of particles per dimension, as listed in Table 1). Local density peaks (with density at least 100 times the average) are located and spherical shells are expanded around each peak until the threshold overdensity is reached. The resulting object is then marked as a halo (objects with less than 20 particles are discarded as they cannot be reliably identified). The halo centre position is calculated more precisely by quadratic interpolation within the cell and the particles within the halo virial radius are identified and

^a<http://www.cita.utoronto.ca/mediawiki/index.php/CubePM>

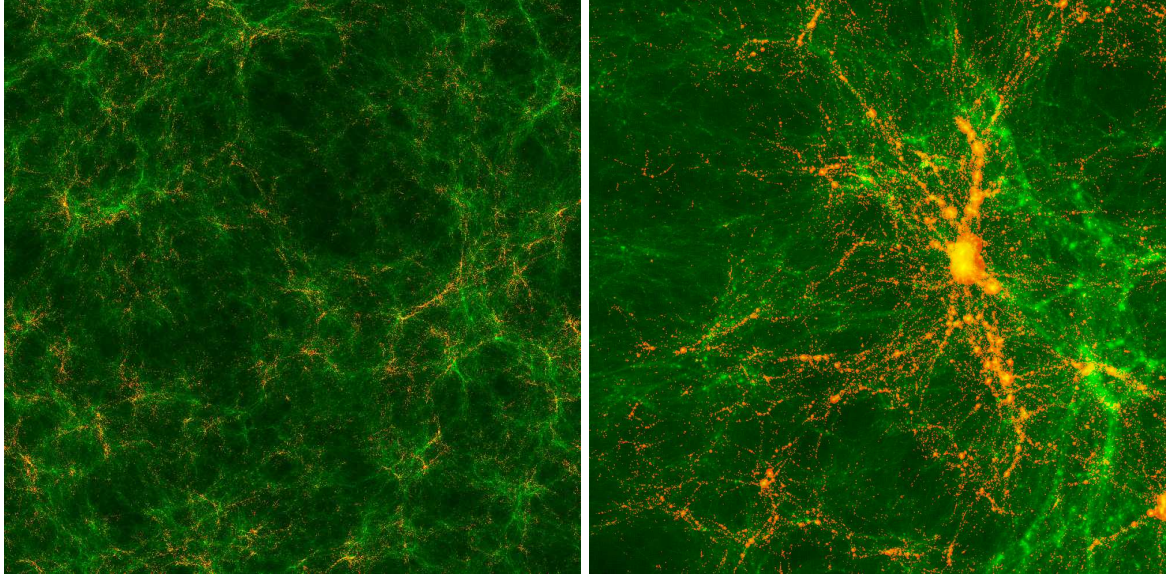


Figure 1: Cosmic Web at redshift $z = 8$ from simulation with boxsize $20 h^{-1}$ Mpc and $5488^3 = 165$ billion particles resolving halos with minimum masses of $10^5 M_\odot$. Shown are projections of the total density (green) and halos (actual size; orange). Slice is $444 h^{-1}$ kpc thick, images are of the full box (left) and of a zoomed sub-region $1.8 \times 1.8 h^{-1}$ Mpc in size (right).

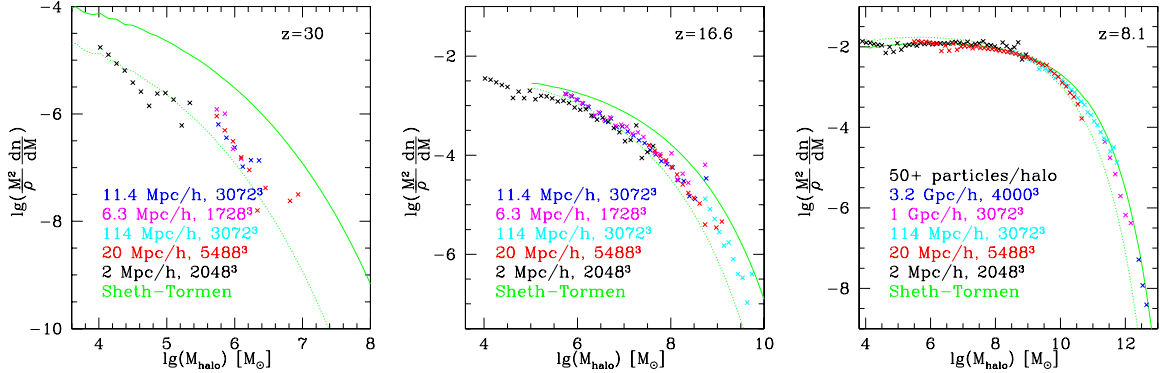


Figure 2: Halo multiplicity functions at redshifts $z = 30$ (left), $z = 16.6$ (middle) and $z = 8.1$ (right).

then the halo properties, e.g. mass, velocity dispersion, center-of-mass, angular momentum, radius, etc. are calculated and saved in the halo catalogue.

The resulting halo multiplicity functions, $(M^2/\rho)(dn/dM)$, at $z = 30$, 16.6 and 8.1 are shown in Figure 2. Here we conservatively only include well-resolved halos, with at least 50 (100) particles at $z = 8$ (higher redshifts). The halo mass functions show significant differences from the widely-used Sheth-Tormen (ST) approximation³ (solid green line), particularly for rare halos. At $z = 8.1$, ST is a reasonably good fit for halos with $M_{halo} < 10^9 M_\odot$ (corresponding roughly to ν up to a few), but over-predicts the abundances of more massive halos by a significant factor of up to a few. This is consistent with previous results on the halo mass function at high- z ^{4,5,6}. At higher redshifts the numerical mass functions do not agree with ST by ever larger factors, over-predicting the halo abundances by up to an order of magnitude at $z = 30$. In fact, at highest redshift, the classic Press-Schechter mass function (green dotted line) is a better fit, although it somewhat underestimates the halo abundances.

3.2 Halo bias

The halo mass function is a strongly nonlinear function of the local density. Overdense regions behave locally as universe with higher mean density producing exponentially more halos. This is directly related to the bias of the halo distribution with respect to the underlying density

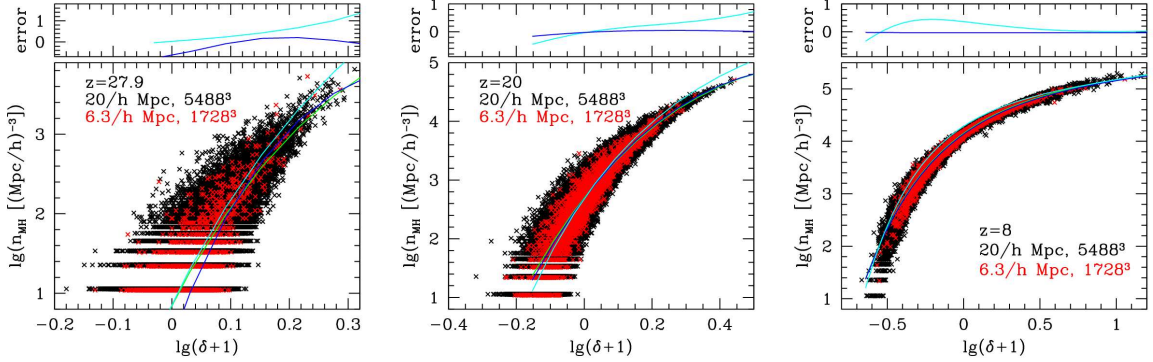


Figure 3: Number of minihaloes per unit volume vs. local overdensity, $1 + \delta$, for sub-volumes of size $440 h^{-1}\text{kpc}$ at $z = 28$ (left), $z = 20$ (middle) and $z = 8$ (right). Shown are the results based on 2 simulations with same resolution, with boxesizes $6.3 h^{-1}\text{Mpc}$ (red points) and $20 h^{-1}\text{Mpc}$ (black points). Also shown are the best mean fits for $6.3 h^{-1}\text{Mpc}$ (dark blue line) and $20 h^{-1}\text{Mpc}$ (green line) and the extended Press-Schechter (extPS) model predictions (light blue line). Top panel shows the extPS (light blue) and $6.3 h^{-1}\text{Mpc}$ mean (dark blue) in units of the respective $20 h^{-1}\text{Mpc}$ box results.

field and is an important ingredient in many semi-analytical models of structure formation and reionization. Such models are also used as sub-grid physics in simulations when they do not have sufficient resolution to resolve all halos relevant to the questions being asked. It is therefore very important to have a handle on the correlation of mass function with local density. To this end, we use data from two of our simulations, with box sizes $20 \text{ Mpc}/h$, $6.3 \text{ Mpc}/h$. Scatter plots of the number of minihalos ($M_{\text{halo}} < 10^8 M_{\odot}$) vs. local density in units of the mean are shown in Figure 3. The best-fit mean relations are plotted as well. For comparison we also show an analytical bias prescription based on extended Press-Schechter theory⁷. The first observation is that results are fairly consistent between the $6.3 \text{ Mpc}/h$ and the $20 \text{ Mpc}/h$ runs, which have the same spatial and mass resolution, but very different volume. Both extremes, high overdensity and underdensity, are less well sampled by the smaller box, which is especially evident at high redshift, $z = 28$, but the best mean fits for each box agree with each other reasonably well. At later times, $z < 20$, they become virtually indistinguishable. The analytical model gives a relatively good prediction for the correlation at mean density and high redshift, and at high density and lower redshift, but can be off by up to a factor of 2 at other regimes. Finally, we note that there is a significant scatter in the halo number - local density relation, particularly at higher redshifts. At later times the correlation tightens, although mostly in relative terms, because the density variation range increases significantly, while the absolute value of the scatter remains roughly constant. The origins of this scatter and its effects on semi-analytical and sub-grid numerical models are currently under investigation.

Acknowledgements

We thank the Texas Advanced Computing Center for providing HPC resources and excellent support (special thanks to Bill Barth), and grants NSF AST 0708176, NASA NNX 07AH09G and NNG04G177G, and Chandra SAO TM8-9009X.

References

1. S. R. Furlanetto, S. P. Oh, and F. H. Briggs. *Physics Reports*, 433:181, 2006.
2. I. T. Iliev, P. R. Shapiro, G. Mellema, H. Merz, and U.-L. Pen. *in proceedings of Tera-Grid08, ArXiv e-prints (0806.2887)*, 2008.
3. R. K. Sheth and G. Tormen. *MNRAS*, 329:61–75, 2002.
4. I. T. Iliev, G. Mellema, U.-L. Pen, H. Merz, P. R. Shapiro, and M. A. Alvarez. *MNRAS*, 369:1625–1638, 2006.
5. D. S. Reed, R. Bower, C. S. Frenk, A. Jenkins, and T. Theuns. *MNRAS*, 374:2, 2007.
6. Z. Lukić, K. Heitmann, S. Habib, S. Bashinsky, and P. M. Ricker. *ApJ*, 671:1160, 2007.
7. R. Barkana and A. Loeb. *ApJ*, 609:474, 2004.

DISTRIBUTION OF MAXIMAL LUMINOSITY OF GALAXIES IN THE SLOAN DIGITAL SKY SURVEY

E. REGŐS, A. SZALAY, Z. RÁCZ, M. TAGHIZADEH, K. OZOGANY

CERN (Geneva), Johns Hopkins U. (Baltimore), ELTE (Budapest)

Extreme value statistics (EVS) is applied to the pixelized distribution of galaxy luminosities in the Sloan Digital Sky Survey (SDSS). We analyze the DR6 Main Galaxy Sample (MGS), divided into red and blue subsamples, as well as the Luminous Red Galaxy Sample (LRGS). A non-parametric comparison of the EVS of the luminosities with the Fisher-Tippett-Gumbel distribution (limit distribution for independent variables distributed by the Press-Schechter law) indicates a good agreement provided uncertainties arising both from the finite size of the samples and from the sample size distribution are accounted for.

1 Introduction

Extreme value statistics analyzes the behavior of the tails of distributions. The distribution of extreme values for i.i.d. (independent, identically distributed) variables converge to a few limiting distributions depending on the tail behavior of the parent population (Fisher-Tippett-Gumbel, Weibull, Fisher-Tippet-Frechet). The onset of the scaling behavior is quite slow, therefore requires very large samples. This is the reason why astronomy has seen very few applications of EVS to date. The galaxy samples in the SDSS redshift survey may be just large enough to attempt such an analysis, and we present here a study of the distribution of maximal luminosities (selected from the luminosities in a given direction and solid angle).

Since EVS is well known only for i.i.d. variables, we try to minimize the correlations between luminosities and positions by selecting the maximal luminosities from the batches of galaxies in elongated conical regions (defined by the footprints of HEALPix cells on the sky).

The shape of the galaxy luminosity function is important for the EVS. This function is well described by the Schechter function, functionally similar (and motivated by) the theoretically derived Press-Schechter formula, with a power law distribution and an exponentially falling tail. Such a tail would imply a Fisher-Tippett-Gumbel (FTG) EVS distribution, with corrections for the finite sample sizes depending on the power law at low luminosities. In this analysis we will show that there is an excellent agreement with these expectations, implying that the Schechter function extends to very high luminosities, i.e. there is no indication for a sharp cutoff at a high but finite luminosity.

In order to arrive at the above results, it was important to notice that the galaxies can be divided into three types with significantly distinct luminosities and spatial distributions. It turned out that an EVS analysis of the luminosities for the joint populations of these three types is practically impossible. This is due to the large differences in the luminosity scales of the three

types which results from the morphology–density relation combined with the presence of voids and clusters in the galaxy distribution.

Even though the SDSS sample is large, the residual from the FTG distribution can be explained only when we consider the corrections due to both the finite size of the samples and the distribution present in the sample sizes (the number of galaxies in a cone is finite and varies from cone to cone).

In Section 2, we describe our galaxy sample, the data acquisition methods, the details of the separation of the sample according to cuts in a color-magnitude diagram. The distributions of the galaxy luminosities and the galaxy counts in pencil beams are also constructed here. Section 3 discusses extreme value statistics with deviations from the expected limit distributions due to finite number of the galaxies in the pencil beams and the pencil-to-pencil fluctuations in the galaxy counts. Section 4 are the results about the distribution of maximal luminosities with the conclusion that within the uncertainties the Fisher–Tippett–Gumbel distribution is a good fit.

2 Sample Creation

We use data from SDSS-DR6, available in a MS-SQL Server database that can be queried online via CasJobs (<http://casjobs.sdss.org>). The spectroscopic survey renders a complicated geometry defined by **sectors**, whose aggregated area covers 6807.94 deg² in the sky.

We explore 4 different galaxy samples: the Luminous Red Galaxies (LRGs) (Eisenstein 2001) and the Main Galaxy Sample (MGS, hereafter MGSall) (Strauss 2002), which is segregated into a blue (MGSblue) and red populations (MGSred). The LRGs are slowly evolving and intrinsically luminous red galaxies composed of old stellar populations, selected for tracing the structure at a higher redshift than MGSs. For selecting the latter we impose a redshift interval of [0.02, 0.18]. A total of $N_T = 383791$ MGSall and $N_T = 66960$ LRG galaxies is obtained in a survey’s comoving volume of $V_S = 2.75 \times 10^8$ Mpc³ and $V_S = 4.31 \times 10^9$ Mpc³ respectively, where we used the parameters $(\Omega_L, \Omega_M, \Omega_r, h_0, w_0) = (0.726, 0.274, 0.0, 0.705, -1)$.

2.1 Color and Magnitude Cuts

In order to segregate the MGSall sample into MGSblue and MGSred, we construct a color-magnitude diagram (CMD) of MGSall and follow the work done in Baldry (2004). The color $C_{ur} \equiv u - r$ is calculated using model magnitudes, whereas the absolute magnitude M_r is derived from the petrosian magnitudes. All magnitudes are galactic extinction and k-corrected. The k-corrections are calculated by using a non-negative least squares fitting method against 30 templates drawn from the Bruzual & Charlot catalogue. Fig.1 shows a smooth separation between MGSblue and MGSred, resembling a bimodal gaussian in color space.

We use the naive Bayes classifier under the classes *Red* and *Blue* in order to construct a color-separating curve $C_S(M_r)$, on top of which the galaxies have the same probability of belonging to either populations. The separator leads to $N_T = 188354$ and $N_T = 195437$ galaxies in the MGSblue and MGSred samples respectively, whose luminosity functions are in Fig.1.

We use 13 JackKnife regions defined as HEALPix cells in the sky, which are part of a $N_{side} = 4$ low resolution HEALPix map of the SDSS-DR6 footprint. Each region has at least 90% of its area inside the footprint.

2.2 Footprint and HEALPix based pencil beams, Distributions of galaxy counts in a HEALPix cell

In order to have close-to-i.i.d realizations (batches) from which to draw the maximal luminosities, we tessellate the sphere into regions defined by individual HEALPix cells (Gorski 2005), all of

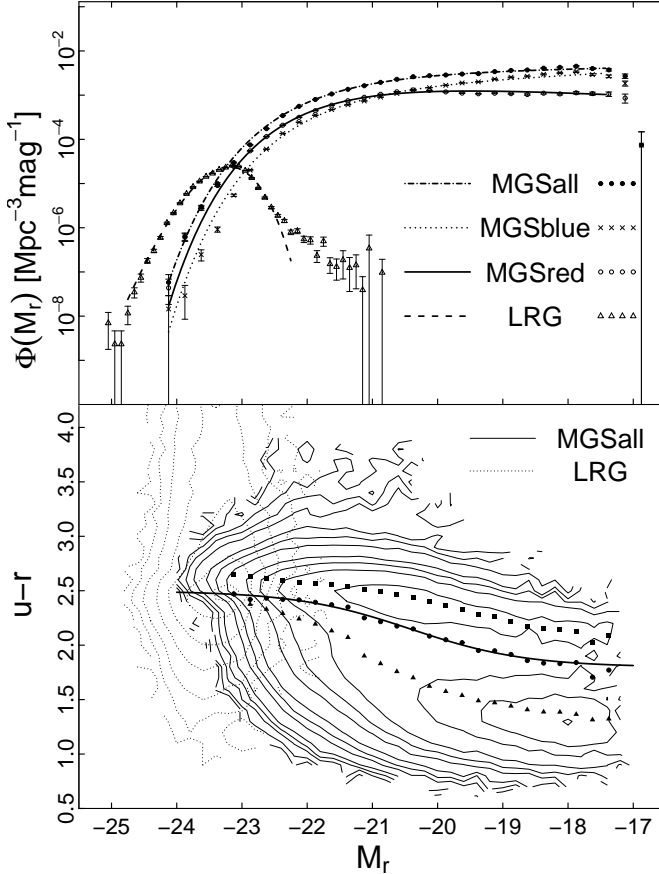


Figure 1: Top: Luminosity functions of the different galaxy samples, together with the best Schechter and generalized gamma fits. The fits are shown only in the range of M_r inside which they were calculated. The magnitude bin widths are $\Delta M_r = 0.25$ and 0.1 for the MGS and LRG samples respectively. Bottom: Color magnitude diagrams of the MGSall and LRG samples. The contour level curves are in \log_{10} scale, set for MGSall at $\{1, 1.8, 3.5\} \times 10^n$ ($n = 0, \dots, 4$); and at $\{1, 3\} \times 10^n$ ($n = 0, 1, 3$) for the LRG sample. The triangles and squares indicate the fitted values of μ for the blue and red populations respectively, whereas the solid thick line is the population separator fitted to the filled circles.

which have the same area. This creates 3-dimensional pencil-like beams that sample the galaxy populations across different redshifts.

We create the entire SDSS-DR6 spectroscopic footprint with resolution $N_{side} = 512$ ($\sqrt{\Omega_{pix}} \simeq 6.87'$). The total area of the HEALPix footprint is 6806.61 deg^2 , close to the joint area of all sectors (6807.94 deg^2).

We degrade the footprint to 3 lower resolution maps defined by $N_{side} = 16, 32$ and 64 , creating thus the cells that define the pencil beams. We use only the group of cells which satisfy that their fractional area occupancy inside the footprint $f \geq 0.98$. HEALPix maximal luminosity maps are shown for MGSall in Fig. 2.

3 Theory of Extreme Value Statistics

Extreme value statistics (EVS) is concerned with the probability of the largest value in a batch of N measurements. For us, they are galaxy luminosities in a given solid angle of the sky and N is the number of galaxies in the given angle.

The results of the EVS are simple for i.i.d. variables. The limit distribution belongs to one of three types and the determining factor is the large-argument tail of the parent distribution. Frechet type distribution emerges if the parent distribution f decays as a power law, Fisher-

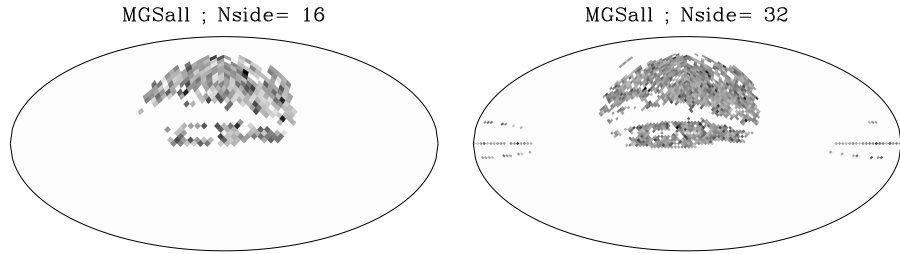


Figure 2: HEALPix Maps of maximal luminosities (in linear scale) for the MGSSall galaxy sample at different values of N_{side} . Darker color means higher luminosity. The SDSS-DR6 footprint becomes easily recognizable at resolution $N_{side} = 64$.

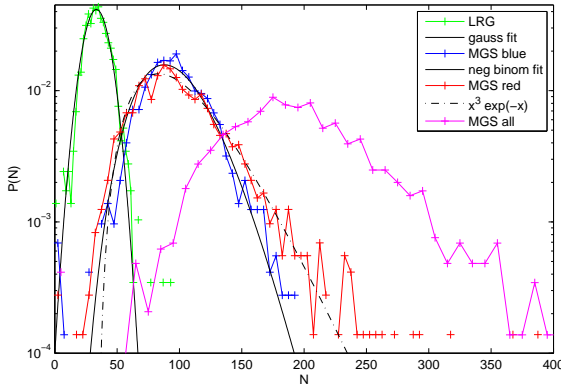


Figure 3: Distribution $P(N)$ of the number of galaxies N in the pencil beams for the case of $N_{side} = 32$. The results are for the MGS-red, MGS-blue, and the LRG samples (red, blue, and green lines, respectively) and for the sample containing all the galaxies (magenta) are plotted on the top panel. Fits to the empirical data on MGS-red, MGS-blue and LRG data are also shown.

Tippett-Gumbel (FTG) distribution is generated by fs which decays faster than any power law and parent distributions with finite cutoff and power law behavior around the cutoff yield the Weibull distribution. All the above cases can be unified as a generalized EVS whose integrated distribution $F_N(v)$ is given in the $N \rightarrow \infty$ limit by $F(v) = \exp [-(1 + \xi v)^{-1/\xi}]$ where $\xi > 0, = 0, < 0$ correspond to the Frechet, FTG, Weibull classes, respectively, with the parameter ξ being the exponent of the power law behavior.

The parent distribution for galaxy luminosities is known, it is the Gamma-Schechter distribution. For this the limit distribution of extremal luminosities belongs to the FTG class ($\xi \rightarrow 0$)

$$P(v) = \frac{dF(v)}{dv} = \frac{1}{b} \exp \left[-\frac{v-a}{b} - \exp \left(-\frac{v-a}{b} \right) \right]. \quad (1)$$

where the parameters can be fixed by setting $\langle v \rangle = 0$ and $\sigma = \sqrt{\langle v^2 \rangle - \langle v \rangle^2} = 1$. This choice ($a = \pi/\sqrt{6}$ and $b = \gamma_E \approx 0.577$) leads to a parameter-free comparison with the experiments provided the histogram of the maximal luminosities $P(v)$ is plotted in terms of the variable $x = (v - \langle v \rangle_N)/\sigma_N$ where $\langle v \rangle_N$ is the average the maximal luminosity while $\sigma_N = \sqrt{\langle v^2 \rangle_N - \langle v \rangle_N^2}$ is its standard deviation. The resulting scaling function is the universal function (1) in the limit $L \rightarrow \infty$: $\Phi_N(x) = \sigma_N P_N(\sigma_N x + \langle v \rangle_N) \rightarrow \Phi(x)$.

3.1 Deviations from the ideal case

In addition to the assumption of i.i.d. variables, there are two additional problems with comparing data with theory. A notorious aspect of EVS is the slow the convergence to the limit distribution. Second, the batch size N (the number of galaxies in a given solid angle) varies with the direction of the angle. Thus the histogram of the maximal luminosities $P_N(v)$ is built from a distribution of N s. Both effects introduce corrections to the limit distribution.

3.2 Finite size corrections

Finite size corrections in EVS have been studied with the conclusion that to first order the scaling function can be written as $\Phi_N(x) \approx \Phi(x) + q(N)\Phi_1(x)$, where $q(N \rightarrow \infty) \rightarrow 0$ and the shape correction $\Phi_1(x)$ is universal function. Both the amplitude q and the shape correction Φ_1 are known for Press-Schechter type parent distributions. The convergence to the limit distribution is slow since $q(N) = -\theta/\ln^2 N$. The value of θ is roughly 1 thus for characteristic range of $N \approx 10 - 200$, the amplitude is of the order of 0.2-0.04. Thus one can expect a 20-4% deviations coming from finite-size effects.

The finite-size shape correction is $\Phi_1(x) = [M_1(x)]'$ where

$$M_1(x) = \Phi(x) \left[\frac{ax^2}{2} - \frac{\zeta(3)x}{a^2} - \frac{a}{2} \right]. \quad (2)$$

3.3 Variable batch size

Variable sample size raises basic questions about EVS.

We use various approximations for the $F(N)$, including using the experimentally observed one. We carried out simulations for the following $N_{side} = 32$ cases: (a) $F(N)$ is approximated as a Gaussian for the LRG sample, (b) $F(N)$ of the MGS red sample is fitted to $(aN+b)^3 \exp(-(aN+b))$, (c) $F(N)$ of MGS blue sample is described by a binomial distribution whose parameters were determined from the empirical values of the average and mean-square fluctuations of N and (d) $F(N)$ is just the exact empirical distribution for the MGS red sample.

Combining the finite-size effects with the effects coming from the variable batch-size can produce the features observed in the deviations from the FTG limit.

4 Distribution of Maximal Luminosities, Discussion

When considering only cells with $N > 10$, leads to a good agreement for the MGSall sample.

If the distributions obtained are FTG distributions then we can claim that at large distances, r , the luminosity-luminosity correlations should decay with an exponent $C(r) \sim r^{-\sigma}$ with $\sigma > 2$.

The FTG-s found suggest weak correlations, and the noise, or more precisely, the correlated features of the noise are, in principle, explainable by the combination of finite-size and variable batch-size effects.

References

- [Bruzual & Charlot (2003)] Bruzual A.,G. & Charlot S. 2003, MNRAS 344, 1000
- [Baldry et al. (2004)] Baldry, I. K. et al. 2004, ApJ, 600:681-694
- [Fisher Tippet (1928)] Fisher, R.A and Tippet, L.H.C. 1928. Proc. Camb. Phil. Soc. 24,180-190
- [Gnedenko (1943)] Gnedenko, B.V 1943. Ann. Math. 44, 423-453
- [Górski et al. (2005)] Górska, K. M. et al. 2005, ApJ, 622:759 , 109, 301

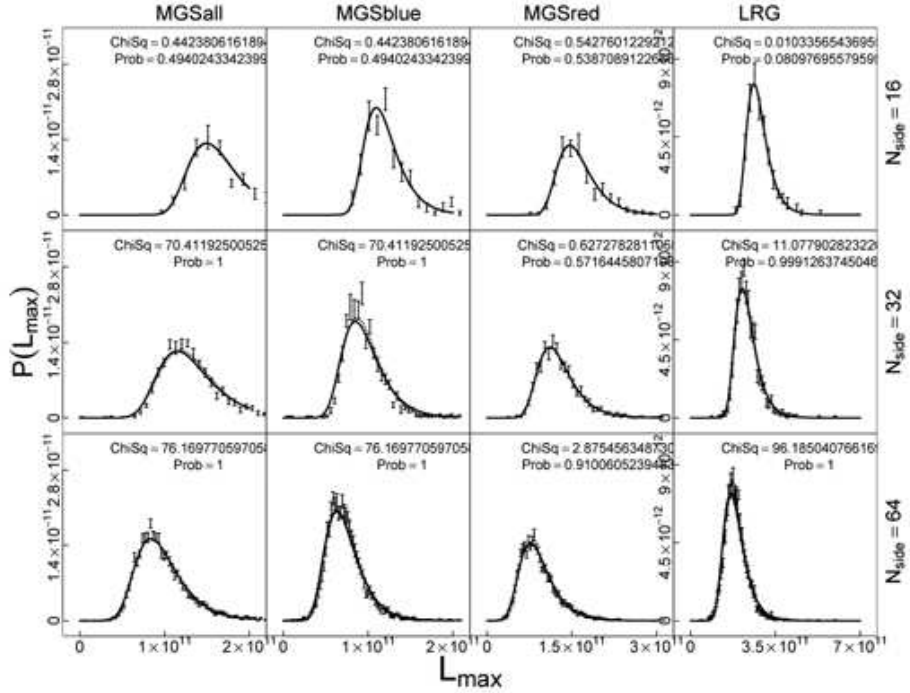


Figure 4: Histogram of the maximal luminosities L_{max} . The continuous line corresponds to the GEV fit, whereas the dotted shows the Gumbel model. The χ^2 values are for the Likelihood ratios between the 2 models, with the corresponding probability of accepting the Gumbel model.

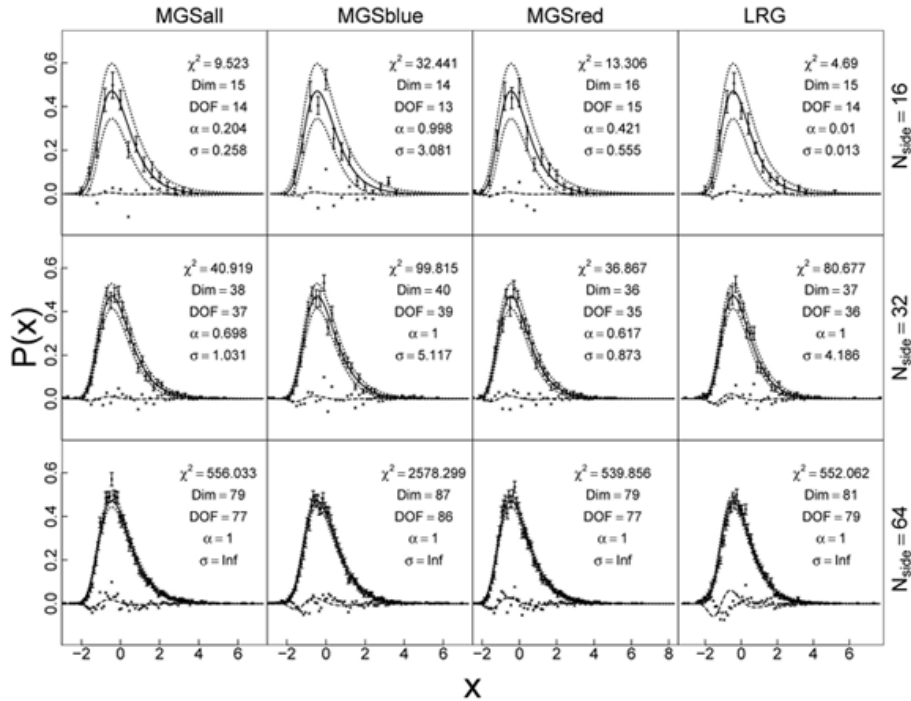


Figure 5: The filled dots represent the normalized maximum luminosity histograms for $N_{side} = 16, 32, 64$ and for the 4 galaxy samples. The continuous line is the theoretical FTG universal curve with $\sigma = 1$ and the dotted curve is its first order correction. The crosses are the residuals.

9. Posters

A MULTIFREQUENCY METHOD BASED ON THE MATCHED MULTIFILTER FOR THE DETECTION OF POINT SOURCES IN CMB MAPS

L.F. LANZ, D. HERRANZ, J.L. SANZ, M. LÓPEZ-CANIEGO

*Instituto de Física de Cantabria (CSIC-UC),
Av. de Los Castros s/n, Santander, 39005, Spain*

J. GONZÁLEZ-NUEVO

SISSA,

via Beirut 4, Trieste, I-34014, Italy

In this work we deal with the problem of simultaneous multifrequency detection of extragalactic point sources in maps of the Cosmic Microwave Background. We developed a linear filtering technique that takes into account the spatial and the cross-power spectrum information at the same time.

1 Introduction

A big effort has been devoted to the problem of detecting point sources in Cosmic Microwave Background (CMB) experiments. The main reasons are that the point sources contaminate the CMB radiation. It is therefore necessary to detect the maximum possible number of extragalactic point sources (EPS) and to estimate their flux with the lowest possible error. However, EPS are not just a contaminant that should be eliminated. They are a very important source of knowledge from the point of view of extragalactic astronomy.

For this reason, in order to reduce the threshold detection level of point sources, we use multi-wavelength information: statistical information of the background and the spatial profile of the sources for both channels at the same time. We also take into account the spectral behaviour of the sources without making any a priori assumption (for a more detailed description of the method and the obtained results, see⁵).

2 Method and simulations

Once we filter the maps with the multifrequency method, the total filtered field w is *optimal* for the detection of sources if $\langle w(\mathbf{0}) \rangle = A$ (source position) and the variance of $w(\mathbf{b})$ is minimum.

If the spatial profiles of the sources τ_ν and the frequency dependence f_ν are known and if the crosspower spectrum is known or can be estimated from the data, the solution to the problem is already known: the *matched multifilter*⁴(MMF):

$$\Psi(q) = \alpha \mathbf{P}^{-1} \mathbf{F}, \quad \alpha^{-1} = \int d\mathbf{q} \mathbf{F}^t \mathbf{P}^{-1} \mathbf{F}, \quad (1)$$

where $\Psi(q)$ is the column vector of filters $\Psi(q) = [\psi_\nu(q)]$, \mathbf{F} is the column vector $\mathbf{F} = [f_\nu \tau_\nu]$, \mathbf{P}^{-1} is the inverse matrix of the cross-power spectrum \mathbf{P} and α is a factor of normalisation.

The frequency dependence f_ν is modelled in the following way:

$$I(\nu) = I_0 \left(\frac{\nu}{\nu_0} \right)^{-\gamma}, \quad (2)$$

where $I(\nu)$ is the flux at frequency ν , ν_0 is a frequency of reference, I_0 is the flux at that frequency of reference and γ is the *spectral index*. This equation is widely used in the literature.

When we have the different simulated maps with the point sources (see next paragraph), these images are iteratively filtered with different MMFs (in fact, we modify γ , but MMF depends

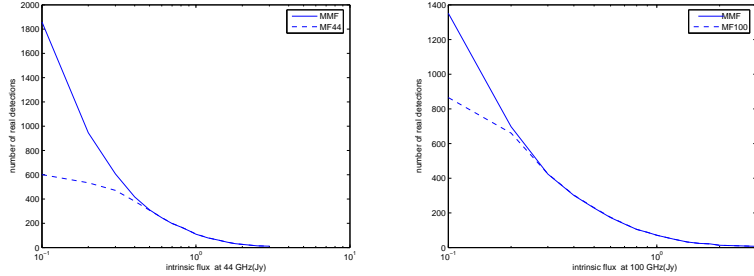


Figure 1: Number of real sources recovered by the MMF (solid line) and the MF (dashed line) at 44 GHz (left panel) and 100 GHz (right panel) whose intrinsic fluxes are higher than the corresponding value in the x axis.

on γ). The value of γ that maximises the SNR for a given source is an unbiased estimator of the real value of the spectral index of that source. After that, results are compared with the *matched filter* (MF).

The simulations that we use to check the power of the multifrequency method are a set of realistic patches simulated from the Planck Sky Model, with the instrumental characteristics of the channels of the *Planck* mission at 44 and 100 GHz, and lied far away from the Galactic plane. Then, point sources are added in such a way that in the same image we have sources with the same flux and spectral index. The threshold detection level is established at 5σ .

3 Results

We compare the performance of the MMF with the MF in terms of source detection, flux and spectral estimation, reliability and spurious detections.

It is very important to give a good estimation of the spectral index and the flux at the reference frequency. In both cases, we can see that the MMF improves the results obtained with the MF: the values are closer to the input values with smaller error bars.

Additionally, in order to study and compare both filters in terms of the spurious detections, we have made a set of more realistic simulations (see ^{1, 2} and ³ for more details). We have also changed the threshold detection level from 5σ to 3σ to find more spurious sources and make a more complete statistical analysis. First of all, we compare the number of real detections that we obtain with both techniques at 44 and 100 GHz. At fluxes below ~ 0.3 Jy, we detect more real sources with the MMF than with the MF (see Figure 1).

Moreover, the reliability of the MMF is much higher than the reliability of the MF for low fluxes. This difference is particularly important at 44 GHz, where the MF obtains similar values to the reliability of the MMF only for fluxes close to 1 Jy. At 100 GHz, the MF has the same reliability of the MMF only for fluxes greater than ~ 0.3 Jy.

Finally, we look at the number of real sources that we have for a fixed number of spurious detections. The most efficient method is the one that has higher number of real detections for a given value of spurious detections. According to this analysis, we observe that the MMF recovers a larger number of real objects if the number of spurious detections is fixed.

References

1. G. De Zotti *et al*, A&A **431**, 893 (2005).
2. J. González-Nuevo *et al*, ApJ **621**, 1 (2005).
3. J. González-Nuevo *et al*, MNRAS **384**, 711 (2008).
4. D. Herranz *et al*, MNRAS **336**, 1057 (2002).
5. L.F. Lanz *et al*, MNRAS **403**, 2120 (2010).

PLANCK-HFI TIME ORDERED DATA ANALYSIS

D. Girard

Laboratoire de Physique Subatomique et de Cosmologie, Grenoble, France

The main missions of the Planck satellite are the ultimate measurements of the CMB temperature anisotropies (which is not limited by instrumental errors but only by the cosmic variance and by the component separation capacities) and an important improvement of the measurements of its polarisation. I shortly present the Planck satellite and the HFI instrument. To reach the ambitious scientific objectives of the project, it is necessary to have extremely sensitive detectors but also an optimised data analysis chain which allows to get rid of instrumental systematic effects up to a very high level. In this document I take as an example some simulations of the interaction between cosmic rays and detectors and I show how it is detected, evaluated and suppressed in the time ordered data analysis.

1 The Planck mission - The HFI instrument and its bolometers

The satellite has been launched on May the 14th, 2009. It has been cooled down to its nominal temperature during the flight to the L2 Lagrange point of the Earth-Sun system. Detectors cooling is made in 4 steps. A passive cooling brings down to 40 K. Then 3 cryogenic machines are used to reach 0.1 K. Its nominal mission should last 15 month at least, which corresponds to two full sky surveys. The 52 detectors of the High Frequency Instrument (HFI) are grid bolometers (spider web shaped grid for temperature, grid of parallel wires for polarisation). They measure the CMB temperature at 100, 143, 217, 353, 545, 857 GHz and its polarisation at 100, 143, 217, 353 GHz. For a better description of the Planck mission, satellite, instruments and scientific objectives, please refer to the Planck Bluebook^a.

2 Data analysis

The first step is the time ordered data analysis. It is followed by the projection of data on sky maps after calibration and focal plane reconstruction. The frequency maps then go through a component separation step to obtain astrophysical components maps. From the CMB map we calculate the angular power spectrum and finally the cosmological parameters. The main goal of time ordered data analysis is to clean or correct some time domain systematic effects. The main steps are: time response deconvolution and electronic effect filtering, thermal effect decorrelation, 4K cooler parasitic lines removal, detection and flagging of data affected by cosmic rays. It is a very interesting topic as it is one of the main systematic effects. Its detection, evaluation, and correction are therefore very important for the whole Planck results. When a particle interacts with one of the detectors, energy is deposited and a parasitic signal appears. If not treated, this

^aThe Planck Bluebook; ESA; 2005; [http://www.rssd.esa.int/SA/PLANCK/docs/Bluebook-ESA-SCI\(2005\)1_V2.pdf](http://www.rssd.esa.int/SA/PLANCK/docs/Bluebook-ESA-SCI(2005)1_V2.pdf)

effect dominates the signal in the resulting maps. Figure 1 shows the projected sky maps from two simulations, one with and one without cosmic rays.

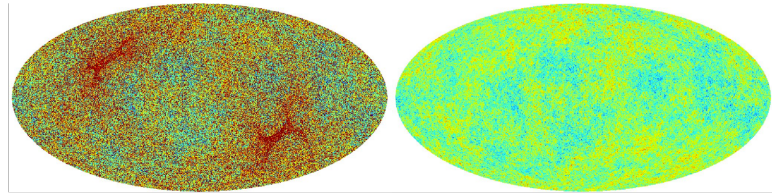


Figure 1: Projected sky maps from two simulations, left with and right without cosmic rays

Data affected by cosmic rays are not valid and should not be projected on the maps. It is necessary to flag them. For this purpose our team has developed data analysis tools designed to recognise the signature of cosmic rays in time ordered data and flag them as invalid. Figure 2 shows the principle of invalid data flagging when a cosmic ray is identified. Data flagged as invalid will not be projected on the maps. The pointing strategy followed by the satellite makes 40 measurements (on average) of each point of the sky, therefore there is no hole in the projected maps when invalid data are flagged.

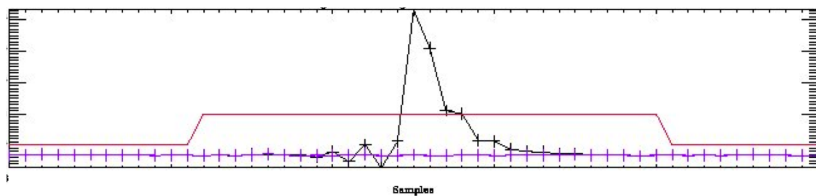


Figure 2: Simulated time ordered data for a HFI detector. The reference simulation without cosmic ray is in purple, the simulation with cosmic rays is in black, the red curve shows invalid data flagging. Some data are flagged before the impact to get rid of the oscillation effect from data filtering.

3 Conclusion

The HFI instrument of the Planck satellite has been built for the ultimate measurements of the CMB temperature anisotropies and an important improvement of its polarisation measurements. To reach these ambitious scientific objectives it is necessary to optimise the data analysis and particularly the systematic effects processing. As an example the processing applied on cosmic ray systematic effect already allows us to reach a sensitivity very close to the one expected without this effect. Figure 3 shows the first published data from Planck: the *First Light Survey* in which we already see very clearly the temperature anisotropies of the CMB. It is a first confirmation of the performance of both the instruments and the data processing chains.

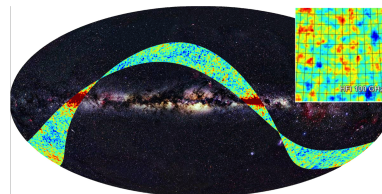


Figure 3: Planck's first light. Up left square is a zoom of $10^{\circ} \times 10^{\circ}$ degrees where CMB is clearly visible. (Credit: ESA / LFI-HFI consortia / background image : Alex Mellinger)

CLUSTERING OF RADIO GALAXIES

W.Godłowski

*Institut of Physics, Opole University
Oleska 48 45-052 Opole Poland*

We discuss the clustering of the radio-identified galaxies. We analyzed the autocorrelation function $\xi(r)$ for the sample of 1157 radio-identified galaxies. For separation $2 - 15h^{-1}$ Mpc autocorrelation function $\xi(s)$ can be approximated by the power law with correlation length $3.75h^{-1}$ and slope $-\gamma = -1.8$. We do not find any clearly evidence for differences of the correlation length between AGN and SB galaxies while slope value for both sub samples are different: $\gamma = 2.4$ for AGN and $\gamma = 1.7$ for SB. We found that correlation length for radiogalaxies is significantly smaller than found for whole sample of galaxies and also that radiogalaxies clusters more strongly than normal galaxies. The discovery of clustering in our sample means, that clustering of radiogalaxies is presented at least till $z = 0.26$.

1 Introduction

Clustering of the radio galaxies was detected for the first time by Peacock and Nicholson¹ in 3D analysis redshift survey of 329 galaxies with $z < 0.1$ and $S(1.4\text{GHz}) > 500\text{mJy}$ (PN91). The obtained result was that the correlation function measured in the redshift space has the form $\zeta = [s/11h^{-1}\text{Mpc}]^{-1.8}$ In the 1999 Peacock² analyzed a sample of 451 radio identified galaxies selected of the base LCRS (Las Campanas Redshift Survey³ and NVSS survey⁴ (P99). Based on the projected correlation function $\Xi(r) = \int \xi[(r^2 + x^2)^{0.5}]dx$ he found the for optical galaxies correlation length are $5h^{-1}\text{Mpc}$ while correlation length for radio-loud subsample is approximately $6.5h^{-1}\text{Mpc}$. Peacock² suggested that these differences are probably because his sample is dominated by SB galaxies while PN91 sample are mostly luminous AGN. The aim of our investigation was to analyse possible clustering of the radio galaxies on the base of a sample of 1157 galaxies selected on the base of LCRS and NVSS by Machalski and Condon⁵.

2 Results.

At first we decided to test our procedure, computing angular correlation function for the sample of the optical galaxies taking from LCRS the slice -12 . We can observe that the power law exponent $-\epsilon = -0.67$. If we assume that correlation function $\xi(r) = r^{-\gamma}$ is a pure power law on all scales, the $-\epsilon$ value is equal $-\gamma + 1$. In such a case $-\gamma + 1 = -0.67$ what means that the our value $\gamma = 1.67$ is not far from value $\gamma = 1.52$ found by Tucker et al. for LCRS optical galaxies from 3D analysis⁶. We also found that angular correlation function $w(\theta)$ breaks from power law on a distance 0.0095rad . It gives the scale of the correlation length $w(\theta D)7.4h^{-1}\text{Mpc}$ again close to value found by Tucker et al.⁶ $6.28h^{-1}\text{Mpc}$. It shows that even from 2D correlation function we could obtain correct and important information. It is very important because when

we analyzed radiogalaxies, the sample, comparing with the number of optical galaxies, is small and comparing results of 2D and 3D analysis is crucial.

Result of the analysis for sample of the 1157 radio-identified galaxies shows $-\epsilon = -\gamma + 1 = -0.97$ for all radio galaxies, -1.13 for AGN and -0.86 for SB. The function $w(\theta)$ breaks from the power law on a distance 0.0065rad that is significantly less than value obtained for "all" LCRS galaxies. Our sample is three times larger than sample P99. However number of our radiogalaxies is still small with that, require for precious measurements of the autocorrelation function. So, in my opinion it is not possible check the Peacock suggestion that clustering of radiogalaxies is changing with redshift.

In the case of 3D analysis of autocorrelation function $\xi(r)$ for optical galaxies we again found good agreement between our result and that obtained by Tucker et al. Now we can start 3D analysis of the radiogalaxies. The main result is that for radio galaxies the function can be also approximated as a power law and the correlation lengths are $3.75h^{-1}\text{Mpc}$ in all cases (all radio-identified galaxies, AGN and SB). However, slopes are different in all cases and we obtain the value $-\gamma = -1.76$ for all galaxies, -2.39 for AGN and -1.66 for SB. It means that analysis spatial correlation function confirm result obtained from analysis of angular correlation function $w(\theta)$ that power law exponent are significantly different for AGN and SB radiogalaxies. Moreover comparing the amplitude of clustering of optical galaxies and radiogalaxies shows, that effect of clustering is stronger for radiogalaxies. This result is going both, from analysis of angular correlation function and spatial correlation function

3 Conclusions

We have presented a detailed study of radiogalaxies clustering on the base of the Machalski and Condon sample of 1157 radio-identified galaxies⁵. Our main result is that for separation $2 - 15h^{-1}\text{Mpc}$ autocorrelation function $\xi(s)$ can be approximated by the power law with slope $-\gamma = -1.8$ and correlation length $3.75h^{-1}\text{Mpc}$. This result means that correlation length for radiogalaxies is significantly smaller than found for whole sample of galaxies. Moreover radiogalaxies clusters more strongly than normal galaxies. The discovery of redshift clustering in our sample means that clustering of radiogalaxies is presented at least till $z = 0.26$ (deep of the LCRS). We found significant difference for slope coefficients for AGN and SB radiogalaxies. I interpreted it as following: AGN are the radiosources type FRI and FRII. We have no information if particular AGN is belong to the type FRI or FRII. However it is clear, that significant number of the radio sources classified as AGN is connected with elliptical galaxies laying in the centre of galaxies. Instead, SB are mostly spiral galaxies. Their galaxies are rather distributed on the outer part of cluster or even on the border of filaments where processes of the galaxies formation connected with the starburst process are strong.

Acknowledgments: Author thanks prof J.Machalski for the permission of using his radio-galaxies data and the helpful discussion.

References

1. Peacock J.A., Nicholson D. 1991, MNRAS, 253, 307
2. Peacock J. A. The Most Distant Radio Galaxies, Proceedings of the colloquium, Amsterdam, 15-17 October 1997, Royal Netherlands Academy of Arts and Sciences. Edited by H. J. A. Rttgering, P. N. Best, and M. D. Lehnert. 1999, p. 377.
3. Shectman S.A, et al. 1996 ApJ, 470, 172
4. Condon J.J., et.al. 1998, AJ, 115, 1693
5. Machalski J., Condon J.J. 1999 ApJS, 123, 21
6. Tucker D. L., et al. 1997, MNRAS, 285, L5

VOID MERGING TREE IN HIERARCHICAL CLUSTERING

Esra Tigrak, Johan Hidding, Rien van de Weygaert

Kapteyn Astronomical Institute, Landleven 12, 9747 AD, Groningen, The Netherlands

In this study, we formulate an analytical model to construct a merger tree of large and small void populations in terms of the two-barrier EPS formalism suggested by Sheth and van de Weygaert. To do this, we apply Lacey and Cole's tree algorithm based on the extended Press Schechter formalism for the merging history of dark halos to void structures. We extend their formalism into an analytical framework to describe complex void merging history which is strongly correlated with the environment in terms of large and small void populations.

1 Introduction

Observational studies show that a large fraction of Universe is dominated by empty regions called voids which evolve from under-densities in the primordial Universe. N-body simulations and theoretical models propose that complex hierarchical evolution of voids can be modeled by the extended Press Schechter¹ (EPS) formalism³ and the evolution of voids is highly dependent on their internal substructure. In the hierarchical evolution procedure, voids exhibit two different behaviors related with their surroundings and environments, they can merge (void in void problem in the EPS formalism) or collapse (void in cloud problem in the EPS formalism). To construct the void merging tree formalism, we modify Lacey and Cole²'s tree algorithm for haloes and apply it to a two-barrier EPS formalism for spherical voids in the Einstein de Sitter (EdS) Universe ($\Omega = 1$).

2 Void Merging Tree

Sheth and van de Weygaert suggested that the collapse and merging of voids can be described by a two-barrier EPS formalism³. In our study, we use two barriers represented by the merging threshold of spherical voids with a fixed threshold value $\delta_v = -2.81$ and the void collapse of an under-density embedded within a contracting over-density with a fixed threshold value for the collapse barrier $\delta_c = 1.686$ in the EdS Universe. The analytical evaluation of the two-barrier random walk problem takes into account a prediction of the distribution function $f_v(M)$ for voids on a mass scale M corresponding to a fractional under density function given as

$$f_v(M)dM = \frac{1}{\sqrt{2\pi}} \frac{v(M)}{\sigma^2} \exp\left[-\frac{v^2(M)}{2}\right] \exp\left[-\frac{|\delta_v|}{\delta_c} \frac{D^2}{4v^2(M)} - \frac{2D^4}{v^4(M)}\right] dM \quad (1)$$

where $v(M) = |\delta_v|/\sigma(M)$ is the scaled mass function, $\sigma(M)$ is the mass variance function, δ_v is the spherical density function and D is the void and cloud parameter $D \equiv 1 - \delta_c/(\delta_c + |\delta_v|)$ which parameterizes the impact of the halo evolution on the evolving population of voids including two barriers for over-dense δ_c and under-dense δ_v regions³. Mass fraction function in Eq. 1 represents

the four dynamical stages of the EPS formalism with respect to the two barriers called "cloud in cloud", "cloud in void", "void in cloud" and "void in void".

2.1 Merging Tree of Large Voids

The model of the merging tree of isolated spherical large voids not embedded in over-dense regions is directly obtained by the "void in void" process. This means that we can assume the density function of the over dense regions as zero $\delta_c \rightarrow \infty$ which causes the void in cloud parameter D to tend to unity ($D \rightarrow 1$) then mass fraction function in Eq. 1 is reduced to the following form including one barrier δ_v for large voids

$$f_v(S, \delta_v) dS = \frac{1}{\sqrt{2\pi}} \frac{|\delta_v|}{S^{3/2}} \exp \left[-\frac{|\delta_v|^2}{2S} \right] dS \quad (2)$$

where S is the mass scale function which is defined in terms of the mass variance function $\sigma(M)$ as $S(M) = \sigma^2(M)$. Hence the merging rate of the large voids is interpreted as the probability of a void with mass M_1 which will merge with another void with mass $\Delta M = M_1 - M_2$ at the corresponding time interval $d|\delta_v|$ is calculated as

$$\frac{d^2 p}{d \ln \Delta M d \ln t} = \sqrt{\frac{2}{\pi}} \frac{\Delta M}{M_2} \frac{|\delta_v(t)|}{\sigma_2} \left| \frac{d \ln \sigma_2}{d \ln M_2} \right| \left| \frac{d \ln |\delta_v(t)|}{d \ln t} \right| \frac{1}{(1 - \sigma_2^2/\sigma_1^2)^{3/2}} \exp \left[-\frac{|\delta_v(t)|^2}{2} \left(\frac{1}{\sigma_2^2} - \frac{1}{\sigma_1^2} \right) \right] \quad (3)$$

where $\sigma_1 = \sigma(M_1)$ and $\sigma_2 = \sigma(M_2)$ are mass variance functions and $\delta_v(t)$ is linear density function of the under-dense regions in the EdS Universe. We find that the merger rate of the large voids in Eq. 3 has the same appearance as the merger rates of the dark matter halos and the merger rates of the large voids are independent from the redshift value.

2.2 Merging Tree of Small Voids

The model of the merging tree of small voids embedded into over dense regions includes four barriers which are reduced to the two barriers in the EdS Universe while the model of large voids includes one barrier. The merging tree model of small voids is constructed by using mass fraction function Eq. 1 but unlike the model of large voids, the model of small voids takes into account the void in cloud parameter D . Hence the merging rate of small voids is given as

$$\begin{aligned} \frac{d^2 p}{d \ln \Delta M d \ln t} &= \sqrt{\frac{2}{\pi}} \frac{\Delta M}{M_2} \frac{|\delta_v(t)|}{\sigma_2} \left| \frac{d \ln \sigma_2}{d \ln M_2} \right| \left| \frac{d \ln |\delta_v(t)|}{d \ln t} \right| \frac{1}{(1 - \sigma_2^2/\sigma_1^2)^{3/2}} \exp \left[-\frac{|\delta_v(t)|^2}{2} \left(\frac{1}{\sigma_2^2} - \frac{1}{\sigma_1^2} \right) \right] \\ &\quad \exp \left[-\frac{1}{(\delta_c + |\delta_v|)} \left(\frac{1}{4} \frac{|\delta_v|}{\delta_c} (\sigma_2^2 - \sigma_1^2) + \frac{2}{(\delta_c + |\delta_v|)} (\sigma_2^4 - \sigma_1^4) \right) \right] \end{aligned} \quad (4)$$

where $\delta_c(t)$ linear density function of spherical over-dense regions in the EdS Universe. We conclude that merger rate of small void populations is strongly dependent on the redshift value unlike the merger rate of large voids.

References

1. W. H. Press, P. Schechter, *Astrophysical Journal* **187**, 425 (1974).
2. C. Lacey and S. Cole, *Monthly Notices of Royal Astronomical Society* **262**, 627 (1993).
3. R. K. Sheth and R. van de Weygaert, *Monthly Notices of Royal Astronomical Society* **350**, 517 (2004).
4. E. Tigrak *et al*, *In preparation* (2010).

SuperNova Legacy Survey 5-years sample analysis : a new differential photometry method

N. Fourmanoit

Laboratoire de Physique Nucléaire et des Hautes Énergies (UPMC Paris 6)

Determining accurate flux measurements of Type Ia supernovae with well understood uncertainty budget is a crucial point for 2nd generation Type Ia supernovae search projects like the SuperNova Legacy Survey. The differential photometry consists in fitting simultaneously a large set of images of the supernova with a model of the supernova flux and position plus a galaxy background and a sky level (see SNLS 1st year paper¹, hereafter A06). We present here an improvement of that technique that intends to offer better constraints of fluxes uncertainties. Geometrical transformations and kernel convolution that match the image position and PSF are applied to the model rather to the pixels, as previously done in A06. Without any resampling nor convolution of the image pixel grid, the pixels entering the fit remain uncorrelated and then prevent the fit uncertainties to be underestimated. This on-going analysis is applied on the SNLS survey 5-years data set, with a large statistics of 419 supernovae Ia with redshifts from 0.01 to 1.1

Data sample This study takes advantages of the large sample supplied by the 5 years SNLS survey carried out from summer 2003 to summer 2008. It consists in more than 400 000 science images (2048×4612 CCDs from MegaCam/CFHT) dispatched among 4 fields (D1:25%, D2:22%, D3:29%, D4:24%) and 4 filters (g':18%, r':24%, i':35%, z':23%). 419 Type Ia SNe have been spectroscopically identified and photometrically monitored within this sample.

A06 photometry The differential photometry presented in A06 (hereafter A06 photometry) and still used for SNLS 3rd year analysis² consisted in simultaneously fitting all images in a given filter with a model that includes (1) a spatially variable galaxy (constant with time), and (2) a time variable point source (the supernova). Previously to the fit, all images are resampled to the pixel grid defined by the image of best quality (IQ) chosen as a reference. The intensity $D_{i,p}$ in a pixel p of image i is modeled as :

$$D_{i,p} = \left[\left(\textcolor{red}{flux}_i \times PSF_{ref}(x - \textcolor{red}{x}_{sn}, y - \textcolor{red}{y}_{sn}) + \textcolor{red}{gal}_{ref}(x, y) \right) \otimes Kern_{ref \rightarrow i} \right]_p + \textcolor{red}{sky}_i \quad (1)$$

where the fit parameters are : $flux_i$ is the supernova flux in image i , gal_{ref} the non parametric galaxy model made of independent pixels which represents the galaxy in the reference image. PSF_{ref} is the normalized Point Spread Function of the reference image centered on the supernova position, $Kern_{ref \rightarrow i}$ the convolution kernel that matches the PSF of the reference image to the PSF of image i and sky_i the local background level. In A06, the kernel is a semi analytical model fit based on several hundred objects selected for their high, but unsaturated, peak flux (see Alard, 2000³). These convolution kernels not only match the PSFs, but also contain the photometric ratios of each image to the reference through their integral values. Eventually a least squares minimization is done including all images that contains the supernova position, and all pixels in the fitted stamp of this image. We typically fit 50×50 galaxy pixels and several hundred images, thus each supernova fit as several thousands parameters.

Flux uncertainties in A06 photometry However a current problem is the minimization does not take into account the correlations between neighboring pixels introduced by image resampling. In order to derive accurate uncertainties, we used the fact that for each epoch, several images in the same night are available which measure the same object flux. We fit a common flux per night to the fluxes measured on each individual image by minimizing a χ^2_{night} . The covariance of the per-night fluxes is then extracted, and normalized so that the minimum χ^2_{night}/ndf is 1.

New differential photometry Keeping the previous point in mind, we developed a new differential photometry we actually called WNR photometry for “Without aNy Resampling” since the images are not resampled anymore. The intensity $D_{i,p}$ in a pixel p of coordinates (x, y) of image i is now modeled as :

$$D_{i,p} = \text{flux}_i \times \text{PSF}_i \left[\text{TF}x(x - x_{sn}, y - y_{sn}), \text{TF}y(x - x_{sn}, y - y_{sn}) \right] + \text{gal}_{ref} \left[\text{TF}x(x - x_{sn}, y - y_{sn}), \text{TF}y(x - x_{sn}, y - y_{sn}) \right] \otimes \text{Kern}_{ref \rightarrow i} + \text{sky}_i , \quad (2)$$

where the model is resampled using the pixel coordinates transformations $\text{TF}_x(x, y)$ and $\text{TF}_y(x, y)$. PSF_i is the PSF of the image i centered on the supernova position. Note that PSFs are not normalized here. $\text{Kern}_{ref \rightarrow i}$ is now computed using the PSF_{ref} and the PSF_i . The photometric ratio, applied on image i , is now computed using the stars PSF flux measured on the image i and the reference image. We mention that SDSS-II SNe Survey uses a similar technique, based on the same principle that A06 photometry, with non-resampled images but with a different implementations of the PSFs, the geometrical transformations and the galaxy model (see Holtzman, 2008⁴).

Flux uncertainties in WNR photometry The pixels entering the least-squares photometric fit minimizing (2) are now uncorrelated. As a consequence, uncertainties on fluxes estimations are up to 20% larger, which is what we expected for more realistic uncertainties.

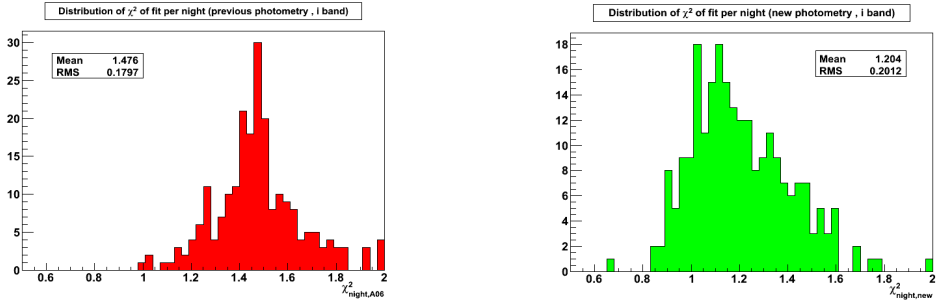


Figure 1: A shown by the distribution of χ^2_{night} with A06 (left) and WNR photometry (right), the correction obtained by measuring the additional scatter between measurements on a same night is reduced by 20-25% depending on filter.

Conclusion and acknowledgments

The differential photometry without any resampling nor convolution we presently exposed is a part of a more global effort for a better control of systematics budget in the the SuperNova Legacy Survey. It shows very promising features and has been check extensively with field star photometry. A posteriori scatter correction is minimised with the same photometric precision guaranteed. Next step of the analysis will be to undertake an investigation for an impact on cosmological results.

I would like to express my gratitude to D. Hardin, P. Astier and J. Guy, and all other members of the SNLS team without whom this work would not have been brought to a successful conclusion.

References

1. P. Astier, J. Guy, N. Regnault, et al. (2006). *The Supernova Legacy Survey: measurement of Ω_M , Ω and w from the first year data set*. *Astronomy & Astrophysics*, 447:31–48.
2. J. Guy, A. Conley, M. Sullivan, N. Regnault (2010) *The Supernova Legacy Survey 3-year sample: Type Ia Supernovae photometric distances and cosmological constraints*. (in prep)
3. C. Alard (2000). *Image subtraction using a space-varying kernel*. *Astronomy & Astrophysics Supplement*, 144:363–370.
4. J. A. Holtzman, J. Marriner, R. Kessler, et al. (2008). *The Sloan Digital Sky Survey-II: Photometry and Supernova IA Light Curves from the 2005 Data*. *Astronomical Journal*, 136:2306–2320.

DARK ENERGY ACCRETION ONTO BLACK HOLES

E. O. BABICHEV^{1,2}, V. I. DOKUCHAEV¹ AND Yu. N. EROSHENKO¹

¹*Institute for Nuclear Research of the Russian Academy of Sciences,
60th October Anniversary Prospect 7a, 117312 Moscow, Russia*

²*APC, UMR 7164 (CNRS-Université Paris 7),
10 rue Alice Domon et Léonie Duquet, 75205 Paris Cedex 13, France*

We study the spherically symmetric stationary accretion of a perfect fluid with an arbitrary equation of state in the Reissner-Nordström metric. In the case of the Reissner-Nordström naked singularity we show that stationary accretion is not a solution of equations of motion. Instead of, a static atmosphere of fluid is formed around singularity. We show that the third law of black hole thermodynamics is violated in a test fluid approximation in the process of phantom energy accretion onto rotating or electrically charged black hole.

We describe the spherically symmetric steady-state accretion of a test perfect fluid with an arbitrary equation of state $p = p(\rho)$, where ρ and p are a fluid energy density and pressure correspondingly, onto a black hole with mass m and electric charge q . For fluid with a linear equation of state $p = \alpha(\rho - \rho_0)$ and for the Chaplygin gas we find analytical solutions for stationary accretion onto the Reissner-Nordström black hole. See in Fig. 1 (left panel) an example for the distribution of thermal photon gas ($\alpha = 1/3$) around the charged black hole. In the case of eternal charged black hole, the accreting fluid does not reach the central singularity. Instead of, after reaching the minimal radius r_{\min} inside the event horizon, the inflowing fluid moves out to the other asymptotically flat internal spacetime (wormhole). In the case of “astrophysical” black holes, formed by the gravitational collapse, the are no of internal spacetimes and inflowing fluid will be accumulated near r_{\min} . This accumulated fluid will transform the internal part of the electro-vacuum Reissner-Nordström metric to the some self-consistent one, providing the stationarity for accretion.

The accreting fluid reaches sound velocity at the critical point

$$r_* = \frac{1 + 3c_*^2}{4c_*^2} \left\{ 1 + \left[1 - \frac{8c_*^2(1 + c_*^2)}{(1 + 3c_*^2)^2} e^2 \right]^{1/2} \right\} m, \quad (1)$$

where $c_* = c_s(x_*) = (\partial p / \partial \rho)^{1/2}$ is the sound speed at critical radius and $e = q/m$. The black hole mass changes at the rate

$$\dot{m} = 4\pi A m^2 [\rho_\infty + p(\rho_\infty)], \quad (2)$$

where ρ_∞ — is an energy density far from the black hole and numerical constant A depends on the equation of state . For the linear equation of state¹

$$A = \alpha^{1/2} x_*^2 \left(\frac{2\alpha x_*^2}{x_* - e^2} \right)^{\frac{1-\alpha}{2\alpha}}. \quad (3)$$

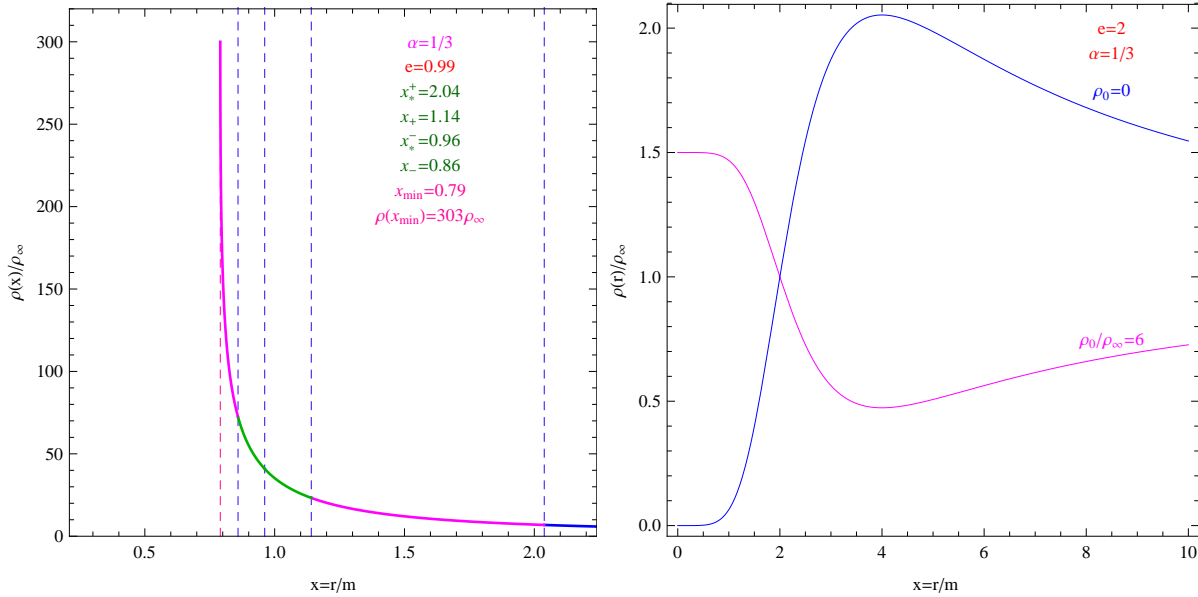


Figure 1: *Left panel:* Radial distribution of the energy density $\rho(r)$ of the thermal photon gas ($\alpha = 1/3$) around the charged black hole with electric charge $e = 0.99$. After the reaching the minimal radius r_{\min} , the fluid is expands into the internal asymptotically flat space. *Right panel:* An example of energy density distribution for the thermal radiation ($\alpha = 1/3$, $\rho_0 = 0$) and the phantom energy ($\alpha = 1/3$, $\rho_0 = 6\rho_\infty$) in a static atmosphere around the Reissner-Nordström naked singularity with electric charge $e = 2$. The inverse energy density profile of thermal radiation near the singularity is a manifestation of the repulsive character of naked singularity.

It is clear from equation (2) that accretion of a phantom energy, defined by the condition $\rho_\infty + p(\rho_\infty) < 0$, is always accompanied with a diminishing of the black hole mass. This is in accordance with previous finding for the Schwarzschild black hole². The result is valid for any equation of state $p = p(\rho)$ with $p + p(\rho) < 0$.

When the Reissner-Nordström metric is a naked singularity, i. e. when $m^2 < q^2$, a perfect fluid does not accrete onto a naked singularity, instead, a static atmosphere around a singularity is formed. See in Fig. 1 (right panel) the energy density distribution for the thermal radiation and phantom energy in a static atmosphere around the Reissner-Nordström naked singularity.

In the case of phantom energy accretion a charged black hole loses its mass and the extreme state with $m = q$ is reached in a finite time with a threat of violation of the the third law of black hole thermodynamics³. We argue, however, that the test fluid approximation is inevitably violated when the Reissner-Nordström black hole or a naked singularity is nearly extremal. This would mean that back reaction of the accreting fluid on the background geometry may prevent black hole transformation into the naked singularity in accordance with the Penrose cosmic censorship conjecture⁴.

References

1. E. Babichev, S. Chernov, V. Dokuchaev and Yu. Eroshenko; arXiv:0806.0916 [gr-qc].
2. E. Babichev, V. Dokuchaev and Yu. Eroshenko, *Phys. Rev. Lett.* **93**, 021102 (2004); [arXiv:gr-qc/0402089].
3. J. M. Bardeen, B. Carter and S. W. Hawking, *Commun. Math. Phys.* **31**, 161 (1973).
4. R. Penrose, *Riv. Nuovo Cim.* **1**, 252 (1969).

Measuring unified DM and DE properties with 3D cosmic shear

S. Camera¹, T.D. Kitching², A.F. Heavens², D. Bertacca^{3,4} & A. Diaferio¹

¹*Dip.to di Fisica Generale, Università degli Studi di Torino, and INFN, Sez. di Torino, Torino, Italy*

²*SUPA, Institute for Astronomy, University of Edinburgh, Royal Observatory, Edinburgh, UK*

³*Dip.to di Fisica, Università di Padova, and INFN, Sez. di Padova, Padova, Italy*

⁴*Institute of Cosmology and Gravitation, University of Portsmouth, Portsmouth, UK*

We investigate how 3D cosmic shear can constrain a class of cosmological models in which both the matter-dominated epoch of the evolution of the Universe and its current, accelerated expansion can be driven by a single, exotic scalar field with a non-canonical kinetic term in its Lagrangian, which behaves both as Dark Matter (DM) and Dark Energy (DE).

1 Unified Dark Matter and Dark Energy models

Rather than considering DM and DE as two distinct components, the alternative hypothesis that DM and DE are two states of the same fluid has recently been suggested. Compared with the standard DM plus DE models (e.g. Λ CDM), these models have the advantage that we can describe the dynamics of the Universe with a single scalar field which triggers both the accelerated expansion at late times and the Large-Scale Structures (LSS) formation at earlier times. Specifically, for these models, we can use Lagrangians with a non-canonical kinetic term, namely a term which is an arbitrary function of the square of the time derivative of the scalar field, in the homogeneous and isotropic background.

We investigate a class of these models^{6,1} which can reproduce the same expansion history of the concordance Λ CDM model, as well as the LSS we see today and the power spectrum of the temperature anisotropies of the Cosmic Microwave Background (CMB). The scalar field energy density has two terms, one behaving like DM and another which is constant, and thus plays the role of a cosmological constant Λ .

However, the DM-like component of the scalar field presents a non-negligible speed of sound, which is parameterized by its late-time value c_∞ . This corresponds to the appearance an effective Jeans length $\lambda_J(a)$ for the gravitational potential, below which the dark fluid does not cluster. Thus, the viability of this UDM model strictly depends on the value of this effective sound speed.

2 The 3D cosmic shear signal

In Fig. 1a we present the 3D shear matrix $C^{\gamma\gamma}(k_1, k_2; \ell)$. The oscillatory features of the UDM gravitational potential, due to the sound speed⁴, can be clearly seen in the shear signal of the UDM model with $c_\infty = 4 \cdot 10^{-3}$ (in units of the speed of light $c = 1$). Instead, when the sound speed is small enough, the matter power spectrum of UDM models is in agrees well with Λ CDM, and we do not see any oscillations, even at non-linear scales $k \gtrsim 0.2 h \text{ Mpc}^{-1}$.

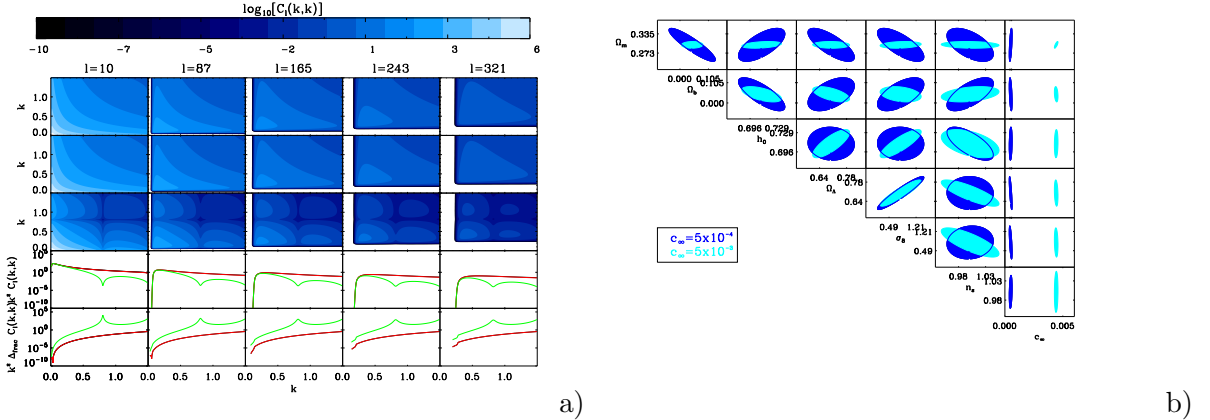


Figure 1: (a) The 3D shear matrix $\log_{10} C^{\gamma\gamma}(k_1, k_2; \ell)$ for ℓ values of ℓ in (blue)grey-scale. In the first row we show the CDM signal, while in the second and third rows we present the UDM signal for $c_\infty = 5 \cdot 10^{-4}$ and $c_\infty = 4 \cdot 10^{-3}$, respectively. The fourth row shows the diagonal elements $k^2 C^{\gamma\gamma}(k, k; \ell)$, and each curve, from top to bottom, refers to the corresponding matrix above. The CDM curve is virtually on top of the small- c_∞ UDM curve. The fifth row shows the fractional error. (b) Expected marginal errors on UDM model cosmological parameters from a 20,000 deg² Euclid-like survey with a median redshift $z_m = 0.8$. Ellipses show the 1σ errors for two parameters (68% confidence regions), marginalized over all the other parameters. Dark (light) ellipses refer to a UDM model with $c_\infty = 5 \cdot 10^{-4}$ ($c_\infty = 4 \cdot 10^{-3}$).

Beyond the oscillations, these signals, expected for two different values of c_∞ , show us the effect of the effective Jeans length of the gravitational potential. In fact, the Newtonian potential in UDM models behaves like Λ CDM at scales much larger than $\lambda_J(a)$, while at smaller scales it starts to decay and oscillate. Hence, at high values of ℓ and k , which correspond to small angular and physical scales, respectively, the signal of weak lensing observables, like cosmic shear, shows the decay of the gravitational potential.

3 Parameter forecasts

Fig. 1b shows the Fisher matrix elements marginalized over different parameters. It is well known that weak lensing can tightly constrain the (Ω_m, σ_8) -plane, using standard cosmic shear techniques, and 3D weak lensing constrains σ_8 in the same way by measuring the overall normalization of the matter power spectrum. The expected marginal errors on Ω_m and σ_8 are in fact very promising, particularly in the perspective of combining the cosmic shear data with other datasets, i.e. CMB or SNeIa. In UDM models, there is another aspect which is particularly interesting to notice: we are able to lift the degeneracy between Ω_m and Ω_b without using early-Universe data. That is because Ω_{DM} and Ω_b enter in the growth of structures in two different ways. The expansion history of the Universe takes into account only their joint effect, through Ω_m , whereas the speed of sound is determined by Ω_{DM} alone. In fact we have to keep in mind that in UDM models there is a scalar field which mimics both DM and Λ , but it still has a proper dynamics different from that of its respectives in the Λ CDM model.

References

1. D. Bertacca *et al.*, *JCAP* **0810**, 023 (2008).
2. P.G. Castro *et al.*, *Phys. Rev. D* **72**, 023516 (2005).
3. A. Refregier *et al.*, *preprint* arXiv:1001.0061 (2010).
4. S. Camera *et al.*, *Mon. Not. R. Astron. Soc.* **399**, 1995 (2009).
5. S. Camera *et al.*, *preprint* arXiv:1002.4740 (2010).
6. D. Bertacca *et al.*, *JCAP* **0711**, 026 (2007).

Multi-scalar field cosmology from SFT: Exactly solvable approximation

F. Galli^a and A. S. Koshelev^b

*Theoretische Natuurkunde, Vrije Universiteit Brussel and
The International Solvay Institutes, Pleinlaan 2, B-1050 Brussels, Belgium*

The main result of this note is the introduction of an exactly solvable model which obeys an exact solution in the cosmological context for the Friedmann equations and restores the asymptotic behavior expected from SFT.

1 Introduction and the Model

In this note we briefly review a new class of cosmological models based on the string field theory (SFT) (for details see reviews¹) and the p -adic string theory². We introduce an exactly solvable model incorporating the most of the behavior of the asymptotic regime. The reader is referred to^{3,4,5,6} and refs. therein for a more detailed analysis on the subject. It is known that the SFT and the p -adic string theory are UV-complete ones. Thus one can expect that resulting (effective) models should be free of pathologies. Furthermore, models originating from the SFT exhibit one general non-standard property, namely, they have terms with infinitely many derivatives, i.e. non-local terms. Higher derivative terms usually produce the well known Ostrogradski instability⁷. However the Ostrogradski result is related to higher than two but finite number of derivatives. In the case of infinitely many derivatives it is possible that instabilities do not appear.

Contemporary cosmological observational data^{8,9} strongly support that the present Universe exhibits an accelerated expansion providing thereby an evidence for a dominating DE component¹⁰. Recent results of WMAP⁹ together with the data on Ia supernovae give the following bounds for the DE state parameter $w_{\text{DE}} = -1.02^{+0.14}_{-0.16}$. Note that the present cosmological observations do not exclude an evolving DE state parameter w . Non-local models of the type obtained from SFT may have effective phantom behavior and are of interest for the present cosmology. To construct a stable model with $w < -1$ one should construct from the fundamental theory, which is stable and admits quantization, an effective theory with the Null Energy Condition (NEC) violation. This is a hint towards SFT inspired cosmological models.

We stress here that appearance of non-localities is a general feature of SFT based models and exactly the one we are going to explore. The starting point is the Lagrangian

$$S = \int d^4x \sqrt{-g} \left(\frac{R}{16\pi G_N} + \frac{1}{2g_o^2} \tau \mathcal{F}(\square) \tau - \Lambda \right), \quad (1)$$

where we manifestly indicate four dimensions. The function $\mathcal{F}(\square)$ may be not a polynomial producing thereby manifest non-locality. The cornerstone of the succeeding analysis is the fact

^aAspirant FWO-Vlaanderen, e-mail: fgalli@vuba.ac.be

^bPostdoctoral researcher of FWO-Vlaanderen, e-mail: alexey.koshelev@vuba.ac.be

that action (1) is fully equivalent to the following action with many free local scalar fields

$$S_{local} = \int d^4x \sqrt{-g} \left(\frac{R}{16\pi G_N} - \frac{1}{g_o^2} \sum_i \frac{\mathcal{F}'(J_i)}{2} (g^{\mu\nu} \partial_\mu \tau_i \partial_\nu \tau_i + J_i \tau_i^2) - \Lambda \right). \quad (2)$$

Here J_i are roots of the characteristic equation $\mathcal{F}(J) = 0$ and there are as many scalar fields as many roots of the characteristic equation. The details of the equivalence statement can be found in^{4,6}. The crucial point is that the roots J_i can be complex. It is much more convenient to continue with local action (2). We specialize to the spatially flat Friedmann–Robertson–Walker (FRW) Universe characterized by the scale factor $a(t)$ with t being the cosmic time. The Hubble parameter is as usual $H = \dot{a}/a$ and the dot denotes a derivative with respect to the cosmic time t . Background solutions for τ_i are considered to be space-homogeneous as well. In⁶ it was proven that cosmological perturbations in the free theory with one non-local scalar field (1) and in the corresponding local theory (2) with many scalar field are equivalent as well.

2 Exactly solvable generalized model

An exact analytic solution for equations of motion following from the action (2) (and furthermore (1)) is not known. However, it is much more transparent working with exact solutions rather than with asymptotics when one wants to study cosmological perturbations. There is a chance to modify the potential such that: first, the model becomes exactly solvable and, second, in the regime of interest all the new terms vanish rapidly so that the previous picture is restored. Furthermore an exactly solvable model in cosmology has its own value just because not so many exactly solvable models are known. In our particular case we deal with many scalar fields and this complicates the problem. Moreover we have complex coefficients in the Lagrangian and this is an unexplored problem.

By adding a potential $-\frac{3\pi G}{2g_o^2} (\sum_i \mathcal{F}'(J_i) \alpha_i \tau_i^2)^2$ where $J_i = -\alpha_i(\alpha_i + 3H_0)$, $H_0 = \sqrt{\frac{8\pi G_N \Lambda}{3}}$ and $G = G_N/g_o^2$ in action (2) one yields exactly solvable equations of motion with a solution

$$\tau_i = \tau_{i0} e^{\alpha_i t}, \quad H = H_0 - 2\pi G \sum_i \mathcal{F}'(J_i) \alpha_i \tau_{i0}^2 e^{2\alpha_i t}. \quad (3)$$

This solution is valid for any number of fields (including single field model) and for any values of parameters α_i (i.e. real, complex, etc.). Moreover, we see that if $\text{Re}(\alpha_i) < 0$ for all i then the quartic term in the scalar fields potential vanishes and we are left with free fields. Thus for large times the model (2) is restored and we can speak about SFT based models.

Eliminate $\mathcal{F}'(J_i)$ by the fields rescaling, one has the following perturbation equations:

$$\ddot{\zeta}_{ij} + \dot{\zeta}_{ij} (3H + \alpha_i + \alpha_j) + \zeta_{ij} \frac{k^2}{a^2} = \frac{1}{H} (\alpha_i - \alpha_j) \left(4\pi G \sum_k \tau_{0k}^2 \alpha_k^2 e^{2\alpha_k t} (\dot{\zeta}_{ik} + \dot{\zeta}_{jk}) + 3H^2 \varepsilon \right), \quad (4)$$

$$\begin{aligned} \ddot{\varepsilon} + \dot{\varepsilon} \left(5H + 4\frac{\dot{H}}{H} - \frac{\ddot{H}}{H} \right) + \varepsilon \left(6H^2 + 14\dot{H} + 2\frac{\dot{H}^2}{H^2} - 3H \frac{\ddot{H}}{H} + \frac{k^2}{a^2} \right) = \\ \frac{k^2}{a^2} \frac{4(4\pi G)^2}{3\dot{H}H^2} \sum_{k,l} \alpha_k^3 \alpha_l^2 \tau_{0k}^2 \tau_{0l}^2 e^{2(\alpha_k + \alpha_l)t} \zeta_{kl}. \end{aligned} \quad (5)$$

These equations form the main result of the present note. Analysis of these equations is a very important problem and is the ongoing project.

The example of perturbations with complex roots in the original linearized action (2) was carried out in¹⁴. Linear perturbations in such a configurations can be confined thus not destroying the system. This result is not evident from the very beginning and it supports the claim that the SFT based models are stable. The case of complex J_i has never been studied in general and deserves deeper investigation. Analysis of perturbations with complex roots in the exactly solvable model will be addressed in forthcoming publications.

Acknowledgments

A.K. thanks the organizers of “Rencontre de Moriond” meeting for the possibility to present this work. Authors are grateful to I.Ya. Aref’eva, F. Bezrukov, B. Craps, B. Dragovich, G. Dvali, V. Mukhanov, and S.Yu. Vernov for useful comments and stimulating discussions. This work is supported in part by the Belgian Federal Science Policy Office through the Interuniversity Attraction Poles IAP VI/11, the European Commission FP6 RTN programme MRTN-CT-2004-005104 and by FWO-Vlaanderen through the project G.0428.06. A.K. is supported in part by RFBR grant 08-01-00798 and state contract of Russian Federal Agency for Science and Innovations 02.740.11.5057.

References

1. K. Ohmori, [hep-th/0102085]; I.Ya. Aref’eva, D.M. Belov, A.A. Giryavets, A.S. Koshelev and P.B. Medvedev, [hep-th/0111208]; W. Taylor, [hep-th/0301094].
2. L. Brekke, P.G.O. Freund, M. Olson, E. Witten, Nucl. Phys. **B302** (1988) 365; P.H. Frampton, Ya. Okada, Phys. Rev. **D37** (1988) 3077; V.S. Vladimirov, I.V. Volovich, E.I. Zelenov, “*p-adic Analysis and Mathematical Physics*”, WSP, Singapore, 1994; B. Dragovich, A. Yu. Khrennikov, S. V. Kozyrev, I. V. Volovich, Anal. Appl. **1** (2009) 1, [arXiv:0904.4205].
3. I.Ya. Aref’eva, AIP Conf. Proc. **826** (2006) 301, [astro-ph/0410443]; I.Ya. Aref’eva, AIP Conf. Proc. **957** (2007) 297, [arXiv:0710.3017].
4. A.S. Koshelev, JHEP **0704** (2007) 029, [hep-th/0701103].
5. I.Ya. Aref’eva and A.S. Koshelev, JHEP **0809** (2008) 068, [arXiv:0804.3570].
6. A.S. Koshelev and S.Yu. Vernov, [arXiv:0903.5176].
7. M. Ostrogradski, Mem. Ac. St. Petersburg, VI **4** (1850) 385.
8. S.J. Perlmutter et al., Astrophys. J. **517** (1999) 565, [astro-ph/9812133]; A. Riess et al., Astron. J. **116** (1998) 1009, [astro-ph/9805201]; A. Riess et al., Astrophys. J. **607** (2004) 665, [astro-ph/0402512]; R.A. Knop et al., Astrophys. J. **598** (2003) 102, [astro-ph/0309368]; M. Tegmark et al., Astrophys. J. **606** (2004) 702, [astro-ph/0310723]; D.N. Spergel et al., Astrophys. J. Suppl. **148** (2003) 175, [astro-ph/0302209]; P. Astier et al., Astron. Astrophys. **447** (2006) 31, [astro-ph/0510447]; W.M. Wood-Vasey et al., Astrophys. J. **666** (2007) 694, [astro-ph/0701041].
9. E. Komatsu, Astrophys. J. Suppl. **180** (2009) 330, [arXiv:0803.0547]; M. Kilbinger et al., [arXiv:0810.5129].
10. T. Padmanabhan, Phys. Rep. **380** (2003) 235, [hep-th/0212290]; P. Frampton, [astro-ph/0409166]; E. J. Copeland, M. Sami, Sh. Tsujikawa, [hep-th/0603057]; A. Albrecht, et al., [astro-ph/0609591].
11. J.M. Bardeen, Phys. Rev. **D22** (1980) 1882.
12. V.F. Mukhanov, H.A. Feldman, and R.H. Brandenberger, Phys. Rep. **215** (1992) 203; V.F. Mukhanov, “*Physical Foundations of Cosmology*”, Cambridge University Press, 2005.
13. J. Hwang and H. Noh, Class. Quant. Grav. **19** (2002) 527, [astro-ph/0103244].
14. A.S. Koshelev, [arXiv:0912.5457].

ON LEPTOGENESIS AND LEPTON ASYMMETRY EFFECTS IN THE EARLY UNIVERSE

D. P. KIRILOVA

Institute of Astronomy, Bulgarian Academy of Sciences, Sofia, Bulgaria

Lepton asymmetry generation in MSW resonant neutrino oscillations in the early Universe is discussed. The evolution of dynamically generated lepton asymmetry and its effect on Big Bang Nucleosynthesis are numerically studied. The case of initially present lepton asymmetry is also analyzed. BBN and lepton asymmetry constraints on oscillation parameters are obtained.

1 Introduction

Although generally assumed that lepton asymmetry (LA) $L = (n_l - n_{\bar{l}})/n_\gamma$ is of the order of the baryon one $\beta \sim 10^{-10}$, this may not be the case. Big LA may hide in the neutrino sector. At present BBN provides the strongest constraint on its value $L < 0.07$ ¹, CMB and LSS provide much looser bounds. Considerable LA generation in MSW active sterile resonant neutrino oscillations in the early Universe was found for mass differences $\delta m^2 > 10^{-5}$ eV² and very small mixings in collisions dominated oscillations² and for small mass differences $\delta m^2 \sin^4 2\theta < 10^{-7}$ eV² and relatively large θ in the collisionless case³. Here we discuss the interplay between LA, either initially present or generated by oscillations, and neutrino oscillations in the early Universe and LA effect on BBN. LA effects oscillations by: changing neutrino number densities; neutrino distribution and neutrino oscillations pattern (depending on its value it can suppress them or lead to their resonant enhancement). On the other hand, oscillations also may suppress or amplify LA.

We studied numerically the evolution of the oscillating neutrinos, accounting simultaneously for Universe expansion, neutrino oscillations and neutrino forward scattering, in case of oscillations effective after neutrino decoupling, $\delta m^2 \sin^4 2\theta < 10^{-7}$ eV². The evolution of LA, and the evolution of nucleons and LA role during pre-BBN epoch were calculated simultaneously with that of neutrino ensembles. Since these type of oscillations may strongly distort neutrino energy spectrum^{3,4} precise description of the neutrino momenta distribution plays extremely important role for the correct determination of LA evolution and of its effect. In this analysis 1000 bins were used to describe it in the non-resonant case, and up to 5000 in the resonant case.

2 Oscillations Generated Lepton Asymmetry and BBN

In the analyzed oscillations case the evolution of LA is dominated by oscillations and typically LA has rapid oscillatory behavior: it oscillates and changes sign. We have determined the region of parameter space for which large generation (by 4-5 orders of magnitude) of LA is possible:

$$|\delta m^2| \sin^4 2\theta \leq 10^{-9.5} \text{ eV}^2. \quad ^a$$

Oscillations generated LA changes energy spectrum distribution and the number densities of neutrinos from standard BBN case. This influences the kinetics of nucleons during BBN and changes the produced light element abundances⁶. Evolution of nucleons in the presence of oscillations was numerically analyzed. Production of primordial ${}^4\text{He}$ Y_p was calculated. Over-production of Y_p decreases at small mixings due to asymmetry growth for these parameters (see figure), therefore, the BBN constraints, obtained on the basis of observational data of Y_p , are less stringent at small mixing angles than the ones obtained without asymmetry growth account⁷. See also.

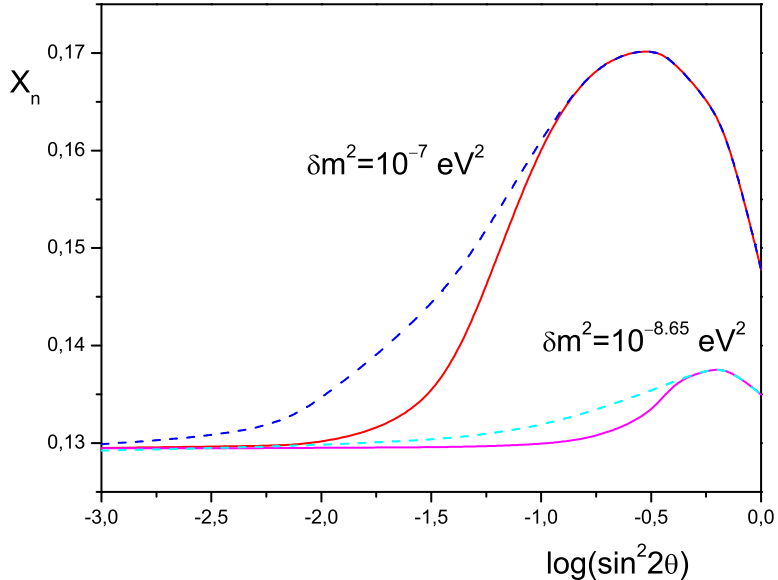


Figure 1: Neutron-to-nucleons freezing ratio dependence on the mixing for two mass differences in case of the account of asymmetry growth and without asymmetry growth account (dashed curves).

3 Initial lepton asymmetry, oscillations and BBN

The numerical analysis^{5,9} has proved that for oscillations with small mass differences discussed $L < 10^{-7}$ does not effect oscillations, $L \sim 10^{-7}$ enhances oscillations, while $L > 0.1(\delta m^2)^{2/3}$ suppress oscillations, and asymmetries as big as $L > (\delta m^2)^{2/3}$ inhibit oscillations. Numerical analysis of $Y_p(\delta m^2, \theta, L)$ dependence has been provided for the entire range of mixing parameters of the model and L . Small L , $10^{-7} < L << 0.01$, that do not effect directly BBN kinetics, influence indirectly BBN via oscillations. Hence, in case of neutrino oscillations: BBN can feel extremely small L . LA enhancing oscillations leads to a higher production of Y_p . Large enough L , suppressing oscillations, decreases Y_p overproduction by oscillations.

Therefore, initially present LA may change BBN bounds: The analysis showed that it relaxes them at large mixings and strengthens them at small mixings. LA bigger than 10^{-5} leads to

^aIn some cases increasing the resolution of momentum space leads to changes of the oscillatory character and diminishes the LA amplitude. This observation is in accordance with the studies of other authors in other parameter regions⁸. Further analysis is required to decide if the oscillatory behavior and LA strong growth is induced by numerical error in these cases.

a total suppression of oscillations effect on BBN and hence, eliminates the BBN bounds on oscillation parameters. Instead the following approximate bound holds: $\delta m^2(eV^2) < L^{3/2}$.

4 CONCLUSIONS

The lepton asymmetry of the Universe may be non-negligible, i.e. much bigger than the baryon asymmetry, and hidden in the neutrino sector. It may be measured by its influence on Universe expansion, Big Bang Nucleosynthesis, Cosmic Microwave Background and Cosmic Neutrino Background. Active-sterile Mikheyev-Smirnov-Wolfenstein oscillations propose an example for effective neutrino-antineutrino asymmetry generation mechanism. We performed a detail numerical analysis of the interplay between small lepton asymmetry $<< 0.01$, either relic (initially present) or dynamical (generated by MSW active-sterile neutrino oscillations) and neutrino oscillations for the case of active-sterile oscillations occurring after electron neutrino decoupling. Higher resolution for the description of the neutrino momenta distribution was provided for the investigation of the asymmetry behavior in this oscillation parameter region.

The parameter range for which relic lepton asymmetry is able to enhance, suppress or inhibit oscillations was determined. Asymmetry growth in case of small mass differences and relatively big mixing angles by 5 orders of magnitude was found possible.

Cosmological influence of such small lepton asymmetries, which do not have direct effect on nucleons kinetics during BBN, was shown not to be negligible. Such small asymmetries are invisible by CMB, but may be felt by BBN: lepton asymmetries as small as 10^{-7} may be felt by BBN in case of neutrino oscillations. Depending on its value, relic lepton asymmetry can strengthen, relax or wave out BBN constraints on oscillations. In the latter case LA constraint on oscillation parameters is determined. Dynamically generated asymmetry relaxes BBN constraints at small mixing angles.

Acknowledgments

The author thanks the organizers for the partial financial support for her participation in the conference and acknowledges the perfect organization and the pleasant and stimulating atmosphere of the meeting.

References

1. A. Dolgov *et al*, *Nucl. Phys. B* **632**, 363 (2002).
2. R. Foot, M. Thomson, R. Volkas, *Phys. Rev. D* **53**, R5349 (1996).
3. D. Kirilova, M. Chizhov, *Neutrino96*, 478 (1996); D. Kirilova, M. Chizhov, *Phys. Lett. B* **393**, 375 (1997).
4. D. Kirilova, *Int. J. Mod. Phys. D* **13**, 831 (2004).
5. D. Kirilova, 2010 (in preparation).
6. D. Kirilova, M. Chizhov, *Nucl. Phys. B* **591**, 457 (2000); D. Kirilova, M. Chizhov, *in Verbier 2000, Cosmology and particle physics*, 433 (2001), astro-ph/0101083
7. D. Kirilova, M. Panayotova, *JCAP* **12**, 014 (2006); D. Kirilova, *Int. J. Mod. Phys. D* **16**, 1197 (2007).
8. P. Di Bari, R. Foot, *Phys. Rev. D* **61**, 105012 (2000).
9. D. Kirilova, M. Chizhov, *Nucl. Phys. B* **534**, 447 (1998).

**Liste
of
Participants**

XLVth Rencontres de Moriond

Cosmology

List of Participants

Family name	First name	Home institution address	Country	Email address
Abate	Alexandra	LAL	France	abate@lal.in2p3.fr
Albert	Joshua	Duke University	USA	jba10@phy.duke.edu
Amblard	Alexandre	University of California	USA	amblard@uci.edu
Andersen	Jeppe	CERN	Switzerland	jeppe.andersen@cern.ch
Badziak	Marcin	University of Warsaw	Poland	mbadziak@fuw.edu.pl
Baracchini	Elisabetta	University of California	USA	ebaracch@uci.edu
Battye	Richard	Jodrell Bank Centre for Astrophysics	UK	Richard.Battye@manchester.ac.uk
Bazin	Gurvan	Ludwig Maximilians University	Germany	gbazin@usm.uni-muenchen.de
Begel	Michael	BNL	USA	begel@bnl.gov
Bernal	Nicolás	IST - CPTP	Portugal	nicolas.bernal@cftp.ist.utl.pt
Besançon	Marc	CEA Saclay - SPP	France	marc.besancon@cea.fr
Bird	Simeon	Institute of Astronomy	UK	spb41@cam.ac.uk
Borgani	Stefano	University of Trieste	Italy	borgani@oats.inaf.it
Braidot	Ermes	University Utrecht	The Netherlands	braidot@rcf.rhic.bnl.gov
Brentjens	Michiel	ASTRON	The Netherlands	brentjens@astron.nl
Camera	Stefano	Univ. degli Studi di Torino	Italy	stefano.camera@ph.unito.it
Chang	Ming-Chuan	Fu Jen Catholic University	Taiwan	068190@mail.fju.edu.tw
Chareyre	Eve	LPNHE	France	eve.chareyre@lpnhe.in2p3.fr
de Rújula	Alvaro	Autonoma University of Madrid	Spain	alvaro.derujula@cern.ch
Debove	Johnathan	LPSC	France	debove@lpsc.in2p3.fr
Demina	Regina	University of Rochester	USA	demina@fnal.gov
Dickinson	Clive	Jodrell Bank Centre for Astrophysics	UK	Clive.Dickinson@manchester.ac.uk
Djouadi	Abdelhak	LPTO / CERN	France	djouadi@th.u-psud.fr
Dokuchaev	Viacheslav	Institute for Nuclear Research - RAS	Russia	dokuchaev@lngs.infn.it
Dokuchaev	Viacheslav	Institute for Nuclear Research - RAS	Russia	dokuchaev@lngs.infn.it
Dorigo	Mirco	INFN	Italy	mirco.dorigo@ts.infn.it
Dudziak	Fany	LAL	France	dudziak@lal.in2p3.fr
Ellwanger	Ulrich	LPTTh	France	ellwanger@th.u-psud.fr
Errard	Josquin	APC	France	josquin@apc.univ-paris7.fr
Fauvet	Lauranne	LPSC	France	fauvet@lpsc.in2p3.fr
Ferrari	Chiara	Observatoire de la Côte d'Azur	France	chiara.ferrari@oca.eu
Ferrera	Giancarlo	University of Florence	Italy	ferrera@fi.infn.it
Finoguenov	Alexis	MPE/UMBC	Germany	alexis@mpe.mpg.de
Foëx	Gaël	LATT	France	gfoex@ast.obs-mip.fr
Fourmanoit	Nicolas	LPNHE	France	fourmanoit@lpnhe.in2p3.fr
Garcia-Bellido	Juan	University of Geneva	Switzerland	juan.garcia-bellido@unige.ch
Garcia-Bellido	Aran	University of Rochester	USA	aran@pas.rochester.edu
Garra	Ticó Jordi	University of Barcelona	Spain	jordix@slac.stanford.edu
Girard	Damien	LPSC	France	damien.girard@lpsc.in2p3.fr
Gonzalez-Alonso	Martin	Instituto de Fisica Corpuscular	Spain	Martin.Gonzalez@ific.uv.es
Gottloeber	Stefan	Astrophysical Institute Potsdam	Germany	sgottloeber@aip.de
Goudzovski	Evgueni	University of Birmingham	UK	eg@hep.ph.bham.ac.uk
Grinstein	Sebastian	IAFE	Spain	sgrinstein@ifae.es
Gripaios	Ben	CERN	Switzerland	ben.gripaios@cern.ch
Grosse-Oetringhaus	Jan Fiete	CERN	Switzerland	Jan.Fiete.Grosse-Oetringhaus@cern.ch
Gubitosi	Giulia	University of Rome "La Sapienza"	Italy	giulia.gubitosi@roma1.infn.it
Han	Liang	University of Science & Technology	China	hanl@ustc.edu.cn
Hays	Jonathan	Imperial College	UK	jonathan.hays@imperial.ac.uk
Hektor	Andi	NICPB	Estonia	andi.hektor@cern.ch
Houdeau	Nicolas	LPTHE	France	secretariat@lpthe.jussieu.fr
Iliev	Ilian	University of Sussex	UK	I.T.Iliev@sussex.ac.uk
Ishimori	Hajime	Niigata University	Japan	ishimori@muse.sc.niigata-u.ac.jp
Kadastik	Mario	KBFI	Estonia	mario.kadastik@cern.ch
Kannike	Kristjan	NICPB	Estonia	kannike@cern.ch
Kayser	Boris	Fermilab	USA	boris@fnal.gov
Khoze	Valeri	IPPP	UK	v.a.khoze@Durham.ac.uk
Koshelev	Alexey	VUB - ULB	Belgium	alexey.koshelev@vub.ac.be
Kovner	Alex	University of Connecticut	USA	kovner@phys.uconn.edu
Kraml	Sabine	LPSC	France	sabine.kraml@lpsc.in2p3.fr
Lansberg	Jean-Philippe	Ecole Polytechnique - CPHT	France	Jean-Philippe.Lansberg@cpht.polytechnique.fr
Lanz	Luis Fernando	Instituto de Física de Cantabria (CSIC-UC)	Spain	lanz@ifca.unican.es
Leahy	Paddy	Jodrell Bank Centre for Astrophysics	UK	j.p.leahy@manchester.ac.uk
Lee	Kang Young	Konkuk University	Korea	kylee@muon.kaist.ac.kr

Lee Hyun Su	University of Chicago	USA	hslee@fnal.gov
Lefevre Gwenaelle	University of Sussex	UK	g.lefeuvre@sussex.ac.uk
Lewis Antony	University of Sussex	UK	antony@cosmologist.info
Li Shi-Yuan	Shandong University	China	lisy@sdu.edu.cn
Long Owen	University of California	USA	owen.long@ucr.edu
Lu Cai-Dian	Institute of High Energy Physics	China	lucd@ihep.ac.cn
Markovic Katarina	Excellence Cluster Universe	Germany	markovic@usm.lmu.de
Marra Valerio	University of Jyväskylä	Finland	valerio.marra@jyu.fi
Marshall Glen	Triumf	Canada	glen_marshall@triumf.ca
Martin Christopher	California Institute of Technology	USA	cmartin@srl.caltech.edu
Mazzotta Pasquale	University of Rome "Tor Vergata"	Italy	mazzotta@roma2.infn.it
Mesinger Andrei	Princeton University	USA	mesinger@astro.princeton.edu
Meyer Jean-Pierre	CEA Saclay - SPP	France	jpmeyer@cea.fr
Mocioiu Irina	Pennsylvania State University	USA	irina@phys.psu.edu
Nemevšek Miha	University of Hamburg	Germany	miha.nemevsek@desy.de
Nerling Frank	University of Freiburg	Germany	nerling@cern.ch
Oakes Louise	Oxford University	UK	l.oakes1@physics.ox.ac.uk
Oki Haruna	Tokyo Metropolitan University	Japan	haruna@phys.metro-u.ac.jp
Osmanov Bari	University of Florida	USA	osmanov@fnal.gov
Parke Stephen	Fermilab	USA	parke@fnal.gov
Peters Yvonne	University of Manchester	UK	peters@fnal.gov
Pierog Tanguy	Institut für Kernphysik - KIT	Germany	tanguy.pierog@kit.edu
Pointecouteau Etienne	CESR	France	pointeco@cesr.fr
Porteboeuf Sarah	LLR	France	sarah.porteboeuf@llr.in2p3.fr
Price Darren	Indiana University	USA	dprice@fnal.gov
Qiao Congfeng	Chinese Academy of Sciences	China	qiaocf@gucas.ac.cn
Quartin Miguel	ITP	Germany	m.quartin@thphys.uni-heidelberg.de
Raidal Martti	NICPB	Estonia	martti.raidal@cern.ch
Rangel Murilo	LAL	France	rangel@fnal.gov
Rauch Michael	ITP	Germany	rauch@particle.uni-karlsruhe.de
Riva Francesco	Istituto Galileo Galilei	Italy	riva@pd.infn.it
Robertson Steven	McGill University	Canada	steven@physics.mcgill.ca
Sapeta Sebastian	LPTHE	France	sapeta@lpthe.jussieu.fr
Schaeffer Arthur	LAL	France	R.D.Schaffer@cern.ch
Schmid Christoph	ETH	Switzerland	chschmid@itp.phys.ethz.ch
Schoeffel Laurent	CEA Saclay - SPP	France	laurent.schoeffel@cea.fr
Serra Paolo	University of California	USA	pserra@uci.edu
Servant Géraldine	CERN	Switzerland	geraldine.servant@cern.ch
Shaw John	Kavli Institute for Cosmology	UK	jrs65@cam.ac.uk
Shitov Yuri	Imperial College	UK	y.shitov@imperial.ac.uk
Smith Christopher	ITP	Germany	chsmith@particle.uni-karlsruhe.de
Sorin Veronica	IFAE	Spain	vsorin@ifae.es
StDenis Richard	University of Glasgow	UK	r.stdenis@physics.gla.ac.uk
Stevens Justin	Indiana University	USA	stevens4@indiana.edu
Studenikin Alexander	Moscow State University	Russia	studenik@srn.sinp.msu.ru
Tang Jiayu	IPMU, University of Tokyo	Japan	jiayu.tang@ipmu.jp
Thomas Daniel	Imperial College	UK	dbt08@ic.ac.uk
Tristram Matthieu	LAL	France	tristram@lal.in2p3.fr
Ubiali Maria	University of Edinburgh	UK	M.Ubiali@sms.ed.ac.uk
Urquijo Philip	Syracuse University	USA	Phillip.Urquijo@cern.ch
Uwer Peter	Humboldt University	Germany	Peter.Uwer@physik.hu-berlin.de
Valencia German	Iowa State University	USA	valencia@iastate.edu
Viel Matteo	INAF - OATS	Italy	viel@oats.inaf.it
Vieregg Abigail	University of California	USA	agoodhue@physics.ucla.edu
Villadoro Giovanni	CERN	Switzerland	giovanni.villadoro@cern.ch
Wang Jianxiong	Institute of High Energy Physics	China	jxwang@ihep.ac.cn
Weller Jochen	Ludwig Maximilians Universiity	Germany	jochen.weller@usm.lmu.de
Wenniger Jorg	CERN	Switzerland	Jorg.Wenninger@cern.ch
Williams Ciaran	IPPP	UK	ciaran.williams@durham.ac.uk
Winter Jan-Christophe	Fermilab	USA	jwinter@fnal.gov
Wozniak Krzysztof	Institute of Nuclear Physics - PAN	Poland	krzysztof.wozniak@ifj.edu.pl
Yacoob Sahal	Northwestern University	USA	sahal@northwestern.edu
Yao Weiming	LBNL	USA	wmyao@lbl.gov
Ylinen Tomi	Royal Institute of Technology - KTH	Sweden	tomi@particle.kth.se
Yokoyama Masashi	University of Tokyo	Japan	masashi@phys.s.u-tokyo.ac.jp
Zakharov Alexander	Inst. Theoretical and Experimental Physics	Russia	zakharov@itep.ru, alex.fed.zakharov@gmail.com